Transactions of the ASME®

FLUIDS ENGINEERING DIVISION
Technical Editor
DEMETRI P. TELIONIS (1999)
Assistant to the Editor
J. E. POWELL
Executive Secretary
PAT WHITE (1999)
Calendar Editor
M. F. ACKERSON

Associate Technical Editors
R. E. A. ARNDT (1995)
P. R. BANDYOPADHYAY (1997)
M. GHARIB (1995)
A. F. GHONIEM (1995)
F. GIRALT (1997)
H. HASHIMOTO (1996)
J. A. C. HUMPHREY (1997)
F. HUSSAIN (1998)
O. C. JONES (1995)
G. E. KARNIADAKIS (1995)
J. KATZ (1998)
J. H. KIM (1996)
R. W. METCALFE (1995)
L. NELIK (1995)
W.-F. NG (1995)
M. W. REEKS (1996)
W. S. SARIC (1995)
M. M. SINDIR (1997)
D. E. STOCK (1996)
S. P. VANKA (1996)

BOARD ON COMMUNICATIONS
Chairman and Vice-President
R. MATES
Members-at-Large
T. BARLOW, N. H. CHAO, A. ERDMAN, G. JOHNSON, L. KEER, E. M. PATTON, S. PATULSKI, S. ROHDE, R. SHAH, F. WHITE, J. WHITEHEAD, K. T. YANG

OFFICERS OF THE ASME
President, **D. T. KOENIG**
Exec. Director
D. L. BELDEN
Treasurer
R. A. BENNETT

PUBLISHING STAFF
Managing Director, Engineering
CHARLES W. BEARDSLEY
Director, Technical Publishing
JANET M. WEINRIB
Managing Editor, Technical Publishing
CYNTHIA B. CLARK
Managing Editor, Transactions
CORNELIA MONAHAN
Production Assistant
MARISOL ANDINO

Transactions of the ASME, Journal of Fluids Engineering (ISSN 0098-2202) is published quarterly (Mar., June, Sept., Dec.) for $175.00 per year by The American Society of Mechanical Engineers, 345 East 47th Street, New York, NY 10017. Second class postage paid at New York, NY and additional mailing offices. POSTMASTER: Send address changes to Transactions of the ASME, Journal of Fluids Engineering, c/o THE AMERICAN SOCIETY OF MECHANICAL ENGINEERS, 22 Law Drive, Box 2300, Fairfield, NJ 07007-2300.
CHANGES OF ADDRESS must be received at Society headquarters seven weeks before they are to be effective. Please send old label and new address.
PRICES: To members, $40.00, annually: to nonmembers, $175.00. Add $30.00 for postage to countries outside the United States and Canada.
STATEMENT from By-Laws. The Society shall not be responsible for statements or opinions advanced in papers or . . . printed in its publications (B7.1, Par. 3).

INDEXED by Applied Mechanics Reviews and Engineering Information, Inc. Canadian Goods & Services Tax Registration #126148048.

Journal of Fluids Engineering

Published Quarterly by The American Society of Mechanical Engineers

VOLUME 117 • NUMBER 4 • DECEMBER 1995

(Contents continued on page 563)

(Contents continued)

Technical Briefs

Announcements and Special Notices

Dr. Owen M. Griffin

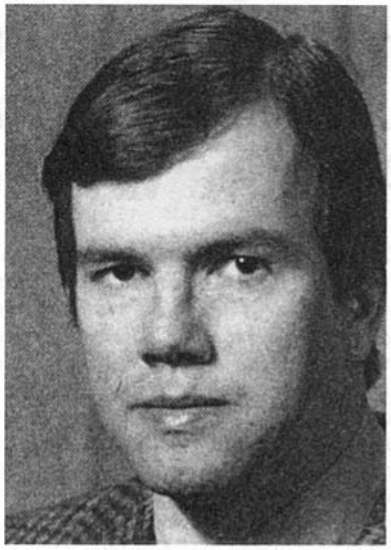

Dr. Owen M. Griffin

Dr. Owen M. Griffin died on 29 September, 1995, at the age of 54, at his home in Fort Washington, Maryland. He was one of the outstanding men of our subject and of our times. As a likable, happy man with an uncomplicated character and a sharp scientific mind, he made numerous contributions to the understanding of vortex shedding, flow-induced oscillations, and remote sensing. His deep physical insight, computational, conceptual, and experimental ability of high order in the design and execution of many experiments resulted in seminal contributions and inspired researchers around the world. His work is his legacy to us and will be a source of inspiration to the disciples of fluid/structure interactions for generations to come. His untimely death impoverishes us all. His innumerable friends and colleagues, the Fluids Engineering community, and the American Society of Mechanical Engineers mourn his loss and extend their deepest sympathies to Mrs. Sherry Griffin and their children Dan and Jennifer.

Testing Three-Dimensional Bluff-Body Models in a Low-Speed Two-Dimensional Adaptive Wall Test Section

D. Sumner

E. Brundrett

Department of Mechanical Engineering,
University of Waterloo,
Waterloo, Ontario,
Canada, N2L 3G1

Thin, sharp-edged disk models were evaluated in a low-speed two-dimensional adaptive flexible wall test section to determine the optimum adaptive wall testing environment for three-dimensional bluff-body models, by providing model testing recommendations for nominal solid blockage ratio and model span ratio. Drag coefficient measurements obtained under straight wall and adapted wall conditions showed that for a two-dimensional adaptive wall test section, the model span ratio imposes a more severe restriction upon model size than does the nominal solid blockage ratio. Minimum wall interference conditions were achieved with adapted walls for nominal solid blockage ratios less than 3 percent and model span ratios less than 21 percent, independent of the nominal test section aspect ratio, based on favorable comparison with previously-published experimental data. Data obtained under straight wall conditions confirmed that wall interference effects can only be neglected in conventional, straight-walled test sections for solid blockage ratios less than 0.5 percent and model span ratios less than 10 percent. The post-test boundary correction method of Maskell was successfully used to adjust the straight wall test section drag coefficient measurements of the larger models for wall interference effects, but no direct measurements of wall interference are used with this method. The results support the careful use of a two-dimensional wall adjustment strategy for three-dimensional nonlifting flows.

Introduction

Wind tunnel experiments have always been complicated by the presence of the test section boundaries and their undesirable influence on the flowfield surrounding a model. The problem is often further complicated by the difficulty of determining, quantitatively, the degree of wall interference present during an experiment, and to what extent it affects the results. Solutions to the problem of wall interference have included the use of semi-empirical procedures to apply corrections to the experimental data, testing small models in proportionally-large test sections to the degree that wall effects are reduced to a minimum, use of ventilated walls (slotted or perforated), and simply avoiding its mention entirely. Often, however, these traditional solutions are impractical, and may not satisfy demands for high-quality wind tunnel data. At a minimum, high-quality wind tunnel data must be accompanied by a quantified assessment of wall interference and its effect on any measured quantities. With or without such an assessment, selection of an applicable means of correcting data is still a difficult task. Ideally, a test environment should be selected with the lowest possible levels of interference and effect a minimum amount of post-test correction to the data.

A unique solution to the problem of obtaining high-quality wind tunnel data free from wall interference effects has been the development and use of the adaptive flexible wall test section (AWTS), wherein the shape of the test section boundaries can be freely controlled. By adapting the test section walls to approximate streamline shapes, the flow about a model is permitted to closely approximate that of an infinite flowfield, and the net result is a flowfield environment with minimum wall interference. The use of rigid, flexible (nonporous) walls permits accurate measurement of flow conditions along the test section boundaries, for a more confident assessment of wall interference. The AWTS has been shown to demonstrate greater tolerance to high blockage models, consequently permitting reliable experimental data to be obtained at higher Reynolds numbers in proportionally-smaller test sections (Kankainen and Brundrett, 1991; Wolf, 1991, and others).

Adaptive wall wind tunnel technology originated with transonic airfoil testing at NPL in 1938 (Wolf, 1991, and others), and gained renewed interest in the early 1970s (Hornung, 1990). Goodyer (1975) and others at the University of Southampton in particular have demonstrated interference-free two-dimensional model testing up to and through the speed of sound (Lewis et al., 1992). Wall adaptation in a two-dimensional AWTS, in which only the solid but flexible test section roof and floor are freely adjustable in single curvature, has been shown to effectively eliminate wall interference for two-dimensional models, such as a cylinder or airfoil. For low-speed flows, solid blockage ratios greater than 30 percent have been tolerated (Kankainen and Brundrett, 1991).

Recently, two-dimensional wall adaptation has been successfully applied to three-dimensional bodies, including those of lifting configuration at high subsonic speeds (Lewis et al., 1992), demonstrating that the more difficult problem of wall-induced upwash can also be accommodated in addition to blockage. Equally significant, by being able to achieve low levels of residual interference in a decidedly three-dimensional flow with only two-dimensional wall adaptation, the mechanical and computational complexities of a full three-dimensional flexible wall AWTS are then avoided (Wolf, 1991).

Objectives of the Study

Research on three-dimensional models in two-dimensional AWTS's has been confined to slender bodies and aerodynamic

Contributed by the Fluids Engineering Division for publication in the JOURNAL OF FLUIDS ENGINEERING. Manuscript received by the Fluids Engineering Division August 11, 1994; revised manuscript received April 14, 1995. Associate Technical Editor: M. Gharib.

shapes of relatively small size. For semi-aerodynamic bodies of revolution, solid blockage ratios less than 3 percent and model span ratios less than 20 percent have been accommodated (Hornung, 1990). For reliable and more versatile application of the AWTS, such as a research tool in more fundamental fluid mechanics studies, a better understanding is needed of the operational constraints and optimum test section configuration for testing larger, less aerodynamic, three-dimensional models (such as bluff-bodies).

The first objective of this study was to provide a contribution towards testing three-dimensional, axisymmetric bluff-body models in a minimum wall interference environment in a low-speed two-dimensional AWTS, and to identify some restrictions and recommendations on the model size and test section configuration. For a two-dimensional AWTS of width, b, nominal height, h, and an axisymmetric bluff-body model of diameter, d, the parameters of interest were the permissible nominal solid blockage ratio, A_{model}/A_{ts}; the model span in the cross-stream direction and its proximity to the fixed test section side walls, defined as the model span ratio, d/b; and the nominal test section dimensions, specifically the nominal test section aspect ratio, b/h.

As a second objective, the study would identify operational constraints for wind tunnel experiments conducted in conventional, straight-wall test sections, and demonstrate where straight-wall test sections fail for testing bluff-body models and under what conditions of solid blockage ratio and model span they may be used successfully (for the effects of wall interference to be negligible).

The disk was selected as the bluff-body model for the study, a model that to the authors' knowledge had never been tested in an adaptive wall wind tunnel. The disk generates sufficient solid and wake blockage for examining the limits of wall adaptation's effectiveness. Since the disk flowfield is essentially Reynolds number independent, drag coefficient measurements can be obtained under straight wall and adapted wall conditions with the confidence that Reynolds number effects are negligible.

Conventional Wind Tunnel Testing

The simplest rules for testing models in conventional wind tunnels have been to keep the model small, and to apply post-test corrections to the wind tunnel data to account for blockage and other boundary effects. For example, it has been recommended to keep the solid blockage ratio as low as 0.5 percent (Saltzman and Ayers, 1982) in order for the effects of wall interference to be negligible. The influence of the boundary layer growth on the fixed test section walls must also be accounted for, since it induces an undesirable longitudinal static pressure gradient.

Maskell's method (1963) is a well-known semi-empirical post-test boundary correction procedure for bluff-body flows, used to determine a representative induced dynamic pressure, q_{ind}, caused by wake blockage. The correction is based on A_{model}/A_{ts}, the measured drag coefficient, C_{Du} (corrected only for induced longitudinal static pressure gradient effects), and an empirically-determined blockage factor, ϵ.

Adaptive Wall Wind Tunnel Technology

Wall adaptation uses a wall adjustment strategy (WAS) and a method of wall interference assessment (WIA) to establish a minimum wall interference flowfield for a given model at a given set of test conditions. Typically, a wall adjustment strategy for a two-dimensional AWTS will use measurements of static pressure distribution along the centerlines of the two flexible test section boundaries, along with the test section wall geometry or shape, to predict streamlined wall contours for minimum wall interference. The process of predicting wall shapes is generally iterative and is independent of the model being tested.

The Predictive Wall Adjustment Strategy of Wolf and Goodyer (1988) is one of the most commonly-used and one of the few adequately-described wall adjustment strategies. It is applicable to (but not limited to) low-speed, incompressible flows of a two-dimensional nature, in a two-dimensional AWTS with rigid but flexible test section roof and floor.

For minimum wall interference, the adapted walls must be contoured in such a way that they establish effective streamlines in an infinite flowfield about the model (in the cases where such a flowfield is desired). Without going into extensive detail, the Predictive Strategy divides the flowfield into a region of real flow within the test section boundaries, and regions of imaginary flow extending to infinity outside the test section boundaries, with the flexible walls as the interfaces between the two regions (Wolf and Goodyer, 1988). The real flowfield along the inside of the flexible test section walls is determined from the measured static pressure distributions, and the imaginary flowfield is computed by the WAS. Velocity or pressure imbalances across the wall interfaces arising from the presence of the model in a straight-walled test section, between the real and imaginary flow regions, are minimized through successive iterations of the WAS and successive wall adjustments. When there are no remaining velocity or pressure imbalances across the flexible wall interfaces, the walls are considered streamlined.

Since zero imbalance cannot practically be achieved, any velocity or pressure imbalance remaining once the iterative adaptation process is ended can be considered a measure of the effectiveness of the wall adaptation. With the Predictive Strategy, wall streamlining quality is evaluated using the average absolute difference between the real and imaginary flowfield static pressure distributions along the interfaces, known as the wall setting error, E_{avg}. Satisfactory results for two-dimensional flow are typically obtained for $E_{\text{avg}} < 0.01$ (Lewis, 1988).

Wall interference assessment (WIA) provides a measure of the distribution of wall-induced velocity perturbations. For a non-lifting flow such as that of the bluff-body, the interference component distribution of interest is the streamwise (or blockage) component, often expressed as the ratio u_{ind}/U_∞. In the present study, wall interference effects were considered neg-

Nomenclature

A_{disk} = frontal area of disk model [m^2]
A_{model}/A_{ts} = nominal solid blockage ratio
A_{ts} = nominal cross-sectional area of the wind tunnel test section [m^2]
b = width of wind tunnel test section [m]
b/h = nominal test section aspect ratio
C_D = drag coefficient
C_{Du} = uncorrected drag coefficient
d = diameter [m]
d/b = model span ratio (for an axisymmetric model of diameter d)
E_{avg} = average wall setting error for Predictive Strategy
h = nominal height of wind tunnel test section [m]
L_{ts} = effective length of wind tunnel test section [m]
q_{ind} = induced dynamic pressure [Pa]
Re_d = Reynolds number based on disk diameter
U_∞ = freestream velocity [m/s]
u_{ind} = streamwise (blockage) component of induced velocity [m/s]
x = streamwise (axial) coordinate [m]
ϵ = blockage factor for Maskell's method ($\epsilon = 2.75$ for bluff-bodies)

ligible when the residual blockage (i.e. after wall adaptation) was everywhere less than 0.25 percent (based partly on some past two-dimensional model experiments), even though tolerable levels of residual interference are difficult to determine precisely. This limiting boundary is consistent with Lewis et al. (1992), while noting that their work was undertaken at high subsonic speeds as opposed to the low-speed experiments conducted as part of this study.

For three-dimensional model testing in a two-dimensional AWTS, more sophisticated wall adjustment strategies and methods of wall interference assessment have been developed. Though the three-dimensional WAS code of Lamarche and Wedemeyer (1984) relies solely on information along the test section centerline for wall adaptation, other three-dimensional WAS codes such as the University of Southampton procedure (Lewis and Goodyer, 1991; Lewis et al., 1992) generally require more extensive test section boundary measurements than those needed for two-dimensional testing (such as at off-centerline and side wall locations).

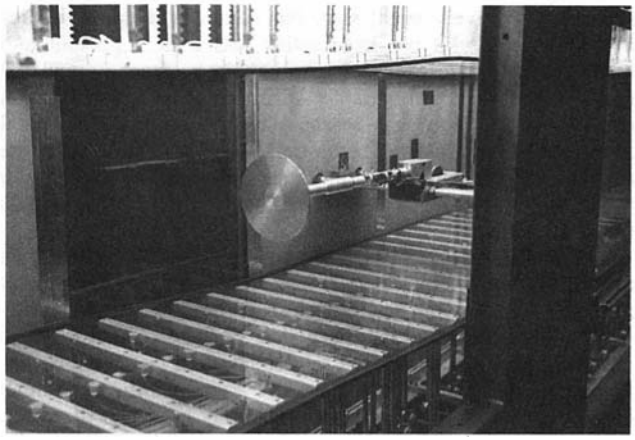

Fig. 2 Disk model (d/b = 0.29, A_{disk}/A_{ts} = 0.089) mounted in AWTS (b/h = 1.35), with adapted wall contours

Experiment Apparatus and Instrumentation

The experiments for the study were undertaken in the University of Waterloo Flexible Wall Wind Tunnel (UWFWWT), a low-speed wind tunnel of open return design incorporating a two-dimensional AWTS with a flexible roof and floor (Brundrett and Kankainen, 1991; Kankainen et al., 1994). The test section has a width of b = 0.615 m, a nominal height of h = 0.890 m, and an overall length of L_{ts} = 6.63 m (of which 5.99 m contains the flexible roof and floor). In its standard form, freestream velocities of up to U_∞ = 50 m/s (freestream Mach number of M ≈ 0.14) can be attained, though with a reduced test section area, speeds of $U_\infty > 80$ m/s (M ≈ 0.23) have been reached.

The flexible roof and floor run the full length of the test section, and are constructed of Lexan polycarbonate sheets. Each is positioned manually with 48 pairs of rack and pinion jacks. Static pressure measurements along the flexible roof and floor of the test section are obtained from 70 static pressure taps along the centerlines of each surface.

By adapting the inlet and exit portions of the test sections into two-dimensional contraction and diffuser sections respectively, straight-wall test sections of different nominal aspect ratio, b/h (and cross-sectional area, A_{ts}), can be established (at constant width b = 0.615 m). By being able to freely set test sections of any desired b/h, test section dimensions can be tailored to meet the specific needs of a particular model or application (Fig. 1).

The disk models were manufactured as thin, circular plates with sharp leading edges and chamfered trailing edges (with an average thickness-to-diameter ratio of 1:20). Each disk was oriented normal to the mean flow direction on the test section centerline (at x/L_{ts} = 0.46), and was supported by a sting at the rear (Fig. 2). The sting was mounted from an airfoil-shaped section spanning the width of the test section and supported by the fixed side walls (leading edge at x/L_{ts} = 0.54).

A computer-controlled data acquisition and control system was used, including three pressure transducers and a system of four Scanivalve® switching units. Drag force measurements were acquired with a six-component straingauge balance in a sting configuration. A comprehensive uncertainty analysis yielded a total combined uncertainty for the drag coefficient of $C_D \pm 0.02$, for all experiment configurations (Sumner, 1994).

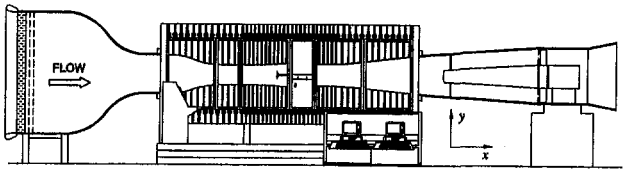

Fig. 1 The University of Waterloo flexible wall wind tunnel, with disk model (b/h = 1.35, d/b = 0.29, A_{disk}/A_{ts} = 0.089, adapted wall contours)

Wall Adjustment Strategy and Method of Wall Interference Assessment

Wall adaptation was undertaken with the two-dimensional Predictive Wall Adjustment Strategy of Wolf and Goodyer (1988), in conjunction with a two-dimensional wall interference assessment (WIA) code (Sumner, 1994). The WIA code computed streamwise two-dimensional induced velocities along the test section centerline from the same real and imaginary flowfield computations used by the Predictive Strategy. Three to four iterations were typically required for convergence to the final adapted wall contours. Wall interference assessment data, the average wall setting error (E_{avg}), and the amount of wall movement (i.e., if the predicted movement was less than the wall setting resolution) were used as roof and floor streamlining criteria. Model-induced changes in the test section wall boundary layer displacement thicknesses (Lewis, 1988) were accounted for in the application of the Predictive Strategy and in the WIA computations (Sumner, 1994).

At the outset, the use of two-dimensional WAS and WIA methods appears to be a poor approximation for a three-dimensional flow. But since considerable experience had already been gained with the Predictive Strategy for two-dimensional model testing (Kankainen and Brundrett, 1991; Kankainen et al., 1994), it was of interest to explore its potential application for three-dimensional model testing. If reasonable minimum wall interference results could be achieved for non-lifting three-dimensional flows with careful use of the two-dimensional Predictive Strategy, then there would be less reason to justify going to a full three-dimensional wall adjustment strategy, such as that of Lamarche and Wedemeyer (1984) for example, for which first-hand experience had yet to be obtained.

The instrumentation capabilities of the UWFWWT were also considered in the choice of the two-dimensional Predictive Strategy, since this method needs roof and floor centerline static pressure measurements only (like that of Lamarche and Wedemeyer, 1984). Initial measurements with laterally-positioned roof and floor static pressure taps suggested that they were of insufficient number and density for use with three-dimensional WIA codes and more sophisticated three-dimensional WAS codes (though ideal numbers and densities of these taps and their effect on WIA accuracy are generally unknown).

Description of Experiments

Each of the seven disk models was tested at $Re_d = 2.95 \times 10^5$. Twenty experiment combinations were chosen from the seven different model span ratios from $0.15 \leq d/b \leq 0.29$ and nominal test section aspect ratios of $b/h = 0.69$, 1.06, and 1.35. Fourteen different nominal solid blockage ratios were obtained in the range of $0.015 \leq A_{disk}/A_{ts} \leq 0.089$. It is noted that the nominal test section aspect ratio, model span ratio, and nominal solid blockage ratio were not fully independent variables for the disks, since a change in nominal solid blockage ratio was coincident with either a change in span ratio or a change in nominal test section aspect ratio. Using the adaptive wall terminology of AGARD, it should be noted that the experiments fall into the Group 1 flow category (Hornung, 1990).

For each of the twenty experiment configurations, drag coefficient measurements were acquired under the influence of geometrically-straight walls (GSW), aerodynamically-straight walls (ASW) in which the longitudinal static pressure gradient was removed (for an empty test section), and adapted walls computed using the Predictive Strategy. Data were compared to the disk drag coefficient result of Fail et al. (1957), at $C_D = 1.12$ for $Re_d > 10^4$. The experiments of Fail et al. (1957) were judged to be of high enough quality to be considered "interference-free," since particular attention was given to the model support system, the solid blockage was kept to less than $A_{disk}/A_{ts} = 0.0145$, and the results were corrected by Maskell's method (1963).

Effects of Longitudinal Static Pressure Gradient

The effects of the longitudinal static pressure gradient were removed experimentally by setting aerodynamically-straight walls (ASW), which was a necessary step in determining the final adapted wall solution with the Predictive Strategy (see also Kankainen and Brundrett, 1991; Kankainen et al., 1994). The longitudinal static pressure gradient effects on the disk drag coefficient were found to be independent of b/h and A_{disk}/A_{ts}. Results (Table 1) showed typically a 3 to 4 percent decrease in the disk drag coefficient under ASW conditions, when these data were compared to those acquired under straight-wall conditions (GSW). The noted differences in the disk drag coefficient results between GSW and ASW test section boundaries contradict the claims of Awbi and Tan (1981), that longitudinal static pressure gradient correction for high-drag bluff bodies is insignificant.

Blockage Effects

When the disk C_D measurements acquired under straight wall (GSW) and adapted wall conditions are plotted against the nominal solid blockage ratio (Fig. 3), with comparison to the accepted disk drag coefficient of $C_D = 1.12$, the adapted

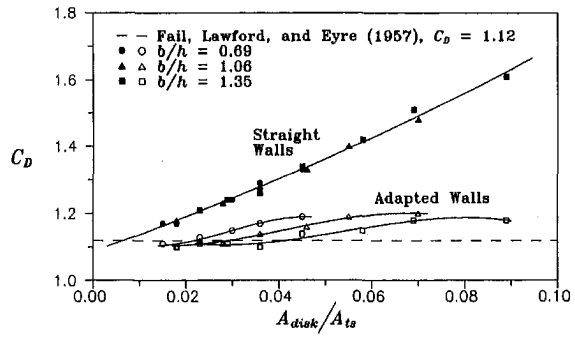

Fig. 3 Disk drag coefficient data plotted against nominal solid blockage ratio, for straight walls (GSW) and adapted walls ($C_D \pm 0.02$ total combined uncertainty)

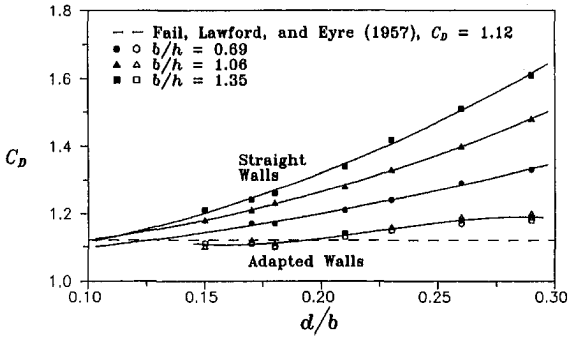

Fig. 4 Disk drag coefficient data plotted against the model span ratio, for straight walls (GSW) and adapted walls ($C_D \pm 0.02$ total combined uncertainty)

wall results suggest that two-dimensional wall adaptation can achieve near-interference-free conditions for bluff-bodies of $A_{disk}/A_{ts} < 0.03$. This ratio falls within the range of three-imensional aerodynamic model sizes previously tested in a two-dimensional AWTS (Hornung, 1990).

Though the straight wall drag coefficient data (Fig. 3) are independent of b/h, the adapted wall drag coefficient data seem to indicate that the smaller-height test section configuration ($b/h = 1.35$) is the most blockage-tolerant, and could permit minimum wall interference testing up to $A_{disk}/A_{ts} = 0.06$ with adapted walls. However, given that (circular) disks were tested, the same nominal solid blockage ratio in a different test section also represents a different model span ratio (because A_{ts} cannot be kept constant when varying b/h). The test section configuration with $b/h > 1$ is apparently more blockage-tolerant simply because the disk models being tested actually have a proportionally-smaller span ratio; i.e., the aspect ratio effect (or blockage ratio effect) is coupled with a span ratio effect.

Model Span Ratio Effects

When the disk C_D data for straight walls (GSW) and adapted walls are plotted against the model span ratio, d/b, the adapted wall C_D data now fall on a single curve, indicating that the model span ratio defines the adaptive wall testing limitations for this type of bluff-body flow (Fig. 4). The experimental data suggest that provided $d/b < 0.21$, a two-dimensional AWTS can be used to create a minimum-interference flow environment (based on comparison to the previously-published data of Fail et al., 1957), and that the model span ratio recommendations are generally independent of b/h. This model span ratio recommendation for bluff-body flows agrees with model span ratio values used in previous experiments in a two-dimensional AWTS, for axisymmetric, slender bodies (Hornung, 1990).

The results indicate that the primary constraint in tests of this nature is the model proximity to the fixed test section side walls. The model span ratio imposes a more severe restriction on model size than does the nominal solid blockage ratio, with the $d/b < 0.21$ recommendation defining the upper limit on permissible model size.

It was observed that the straight wall C_D data of Fig. 4 (for all three b/h conditions) could be collapsed onto a single curve by plotting C_D versus $d/(bh)^{1/2}$, rather than as C_D versus d/b. However, because the h-dependency in adaptive wall testing is effectively eliminated through roof and floor adaptation, the C_D versus d/b correlation (i.e., for adapted wall C_D data) was considered to be more relevant.

Post-Test Boundary Correction Methods

Data obtained under ASW conditions were corrected with Maskell's method (1963), and showed excellent agreement with the published results of Fail et al. (1957), even up to $A_{disk}/$

$A_{ts} = 0.089$ and $d/b = 0.29$ (Table 1), since the scope of the investigation was within the capabilities of the method. The corrected straight wall C_D results were blockage-independent and model-span-ratio-independent, and were in good agreement with the adapted wall data for $d/b \leq 0.21$.

Though Maskell's method was effective over a greater range of blockage and model span ratios than two-dimensional wall adaptation with a two-dimensional WAS, the method is likely to fail under conditions of significant wall interference, under which the basic nature of a flowfield might be altered, and generally provides only an estimate of C_D.

Implications for Conventional, Straight-Wall Test Sections

The disk C_D measurements acquired under GSW conditions have important consequences for testing bluff-body models in conventional wind tunnels with fixed, straight-wall test sections. Extension of a best-fit line through the straight-wall C_D data (Fig. 3) shows that the accepted, interference-free value for the disk drag coefficient can only be achieved for $A_{disk}/A_{ts} \leq 0.005$ (0.5 percent), a result consistent with the recommendation quoted by Saltzman and Ayers (1982). Extrapolation of the straight wall C_D data plotted against span ratio (Fig. 4) shows that negligible wall interference conditions would be obtained for $d/b \leq 0.10$.

Average Wall Setting Errors

The investigation demonstrated that the two-dimensional Predictive Strategy could be successfully used to establish minimum wall interference flowfields for three-dimensional bluff-body models at low speeds, even when using only centerline static pressure measurements along the flexible test section boundaries. However, the $E_{avg} < 0.01$ criterion (Lewis, 1988) was not a good indicator of a minimum-interference flow environment. The results showed that tolerable levels of residual wall interference in three-dimensional flows were found for $E_{avg} < 0.007$.

Wall Interference Assessment

Using the two-dimensional WIA method for $d/b < 0.21$, test section centerline distributions of $u_{ind}/U_\infty < 0.0025$ were established with adapted walls over the entire length of test section (Fig. 5). This level of residual blockage, with the disk model installed, was on the order of the test section induced wall interference tolerated in wind tunnels of high aerodynamic quality, but without a model present.

It should be noted, however, that though the results of the two-dimensional WIA suggest that a minimum wall interference environment has been approximated, a full three-dimensional WIA method would be needed to verify off-centerline residual interference levels, and to properly account for side-wall-induced interference.

Table 1 Disk drag coefficient data for $b/h = 1.06$ ($C_D \pm 0.02$ total combined uncertainty)

d/b	A_{disk}/A_{ts}	C_D GSW	C_D ASW	C_D Adapted walls	C_D Maskell's method
0.15	0.018	1.18	1.15	1.10	1.09
0.17	0.023	1.21	1.18	1.12	1.10
0.18	0.028	1.23	1.18	1.11	1.08
0.21	0.036	1.28	1.24	1.14	1.10
0.23	0.046	1.33	1.29	1.16	1.11
0.26	0.055	1.40	1.35	1.19	1.12
0.29	0.070	1.48	1.43	1.20	1.12

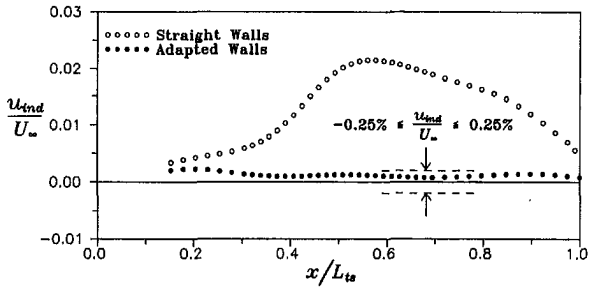

Fig. 5 Two-dimensional streamwise wall interference assessment ($\mu_{ind}/U_\infty \pm 0.0010$ total combined uncertainty) for disk model ($b/h = 0.69$, $d/b = 0.18$, $A_{disk}/A_{ts} = 0.018$) before wall adaptation ($C_D = 1.13$) and after ($C_D = 1.10$). The disk model is located at $\chi/L_{ts} = 0.46$.

Conclusions

Two-Dimensional Adaptive Wall Test Sections The model span ratio was found to be the limiting parameter for successfully testing three-dimensional bluff-body models in a two-dimensional AWTS with a two-dimensional WAS, for minimum wall interference (confirming the influence of the fixed test section side walls on the natural flow about the model). Though adapted walls were shown to minimize wall interference effects for $A_{model}/A_{ts} < 0.03$ (preferably with $b/h > 1$), a model testing criterion of $d/b < 0.21$ (which was generally independent of b/h) was found to be the more significant restriction on model size.

While experiments with three-dimensional wall adjustment strategies (and three-dimensional wall interference assessment methods) might demonstrate that these blockage and model span limits can be extended, the present results suggest that careful use of a two-dimensional wall adjustment strategy precludes the need to employ a full three-dimensional wall adjustment strategy for such low-speed flows, provided the currently-identified span and blockage restrictions are met (for bluff-bodies).

When using the Predictive Strategy (Wolf and Goodyer, 1988) in particular, for testing three-dimensional models, the wall streamlining convergence criterion should be $E_{avg} = 0.007$, rather than $E_{avg} = 0.01$ recommended for two-dimensional transonic model tests (Lewis, 1988). Computation of two-dimensional residual induced velocity distributions on the order of $u_{ind}/U_\infty \approx 0.0025$ demonstrated that the two-dimensional WAS was performing effectively.

Lastly, disk models represent one of the worst cases for bluff-body flows, given the prominent separation point and significant wake size and blockage. Preliminary investigations with an instrumented sphere model have suggested that semi-aerodynamic shapes are more tolerant of model span and blockage (Sumner, 1994), and that the adaptive wall model testing limitations which have been identified for bluff-bodies could be relaxed for these flows.

Conventional, Straight-Walled Test Sections The investigation confirmed that wall interference should be a major concern when designing an experiment for a conventional, straight-walled wind tunnel test section, and when assessing the quality of experimental data obtained in such wind tunnels. Specifically, significant wall interference effects were found to be negligible for $A_{model}/A_{ts} < 0.005$ (0.5 percent), a recommendation quoted by Saltzman and Ayers (1982). For axisymmetric bluff-body flows in particular, the model span ratio should be kept to $d/b < 0.10$. The correction for longitudinal static pressure gradient should be applied to straight-wall test section data, and may, for example, result in a 3 to 4 percent difference in C_D.

Maskell's method (1963) was shown to be satisfactory in correcting drag coefficient measurements obtained under straight-wall test section conditions up to $A_{disk}/A_{ts} = 0.089$ and

$d/b = 0.29$, provided the induced pressure gradient effects were removed before the method was applied. However, post-test boundary correction methods of this nature use no quantitative assessment of wall interference, and are often restricted to adjusting a single mean flow property. Since significant wall interference can distort streamlines to the point where the entire fundamental nature of the flow is changed, generalized post-test boundary correction methods must fail under such conditions. Certainly, no reliable correction method exists apart from wall adaptation to remove the effects of wall interference on more sophisticated aspects of fluid mechanics, such as separation and transition points, turbulence structure, and convection-dominated heat transfer.

Acknowledgments

The first author acknowledges the financial support of a postgraduate scholarship from the Natural Sciences and Engineering Research Council of Canada (NSERC). The second author acknowledges the partial support of NSERC for the UWFWWT, in the form of an operating grant.

References

Awbi, H. B., and Tan, S. H., 1981, Effect of Wind-Tunnel Walls on the Drag of a Sphere," ASME JOURNAL OF FLUIDS ENGINEERING, Vol. 103, Sept., pp. 461–465.

Brundrett, E., and Kankainen, P., 1991, "The Construction and Commissioning of a Flexible Walled Wind Tunnel," *CASI Journal,* Vol. 27, No. 3, Sept.

Fail, R., Lawford, J. A., and Eyre, R. C. W., 1957, "Low-Speed Experiments on the Wake Characteristics of Flat Plates Normal to an Air Stream," Aeronautical Research Council Reports and Memoranda No. 3120.

Goodyer, M. J., 1975, "A Low Speed Self-Streamlining Wind Tunnel," *Wind Tunnel Design and Testing Techniques,* AGARD Conference Proceedings No. 174, Fluid Dynamics Panel Symposium, London, Oct.

Hornung, H. G., ed., 1990, *Adaptive Wind Tunnel Walls: Technology & Applications,* AGARD Advisory Report No. 269, Fluid Dynamics Panel Working Group 12.

Kankainen, P., and Brundrett, E., 1991, "Two-Dimensional Airfoil Testing in a Flexible Walled Wind Tunnel Facility," *Proceedings of the 3rd Canadian Symposium on Aerodynamics,* Canadian Aeronautics and Space Institute, Toronto, Canada, Nov.

Kankainen, P., Brundrett, E., and Kaiser, J. A., 1994, "A Small Wind Tunnel Significantly Improved by a Multi-Purpose Two Flexible Wall Test Section," ASME JOURNAL OF FLUIDS ENGINEERING, Vol. 116, Sept., pp. 419–423.

Lamarche, L., and Wedemeyer, E., 1984, "Minimization of Wall Interference for Three-Dimensional Models with Two-Dimensional Wall Adaptation," VKI TN 149.

Lewis, M. C., 1988, "Aerofoil Testing in a Self-Streamlining Flexible Walled Wind Tunnel," NASA CR 4128, 1988.

Lewis, M. C., and Goodyer, M. J., 1991, "Two-Dimensional Wall Adaptation for Three-Dimensional Flows," ICAW 1991, International Conference on Adaptive Wall Wind Tunnel Research and Wall Interference Correction, Xian, China, Proceedings, pp. A2-1-24.

Lewis, M. C., Taylor, N. J., and Goodyer, M. J., 1992, "Adaptive Wall Technology for Three-Dimensional Models at High Subsonic Speeds and Aerofoil Testing Through the Speed of Sound," *Wind Tunnels and Wind Tunnel Test Techniques,* European Forum on Wind Tunnels and Wind Tunnel Test Techniques, University of Southampton, U.K., September 1992, Royal Aeronautical Society, pp. 42.1–42.12.

Maskell, E. C., 1963, "A Theory of the Blockage Effects on Bluff Bodies and Stalled Wings in a Closed Wind Tunnel," Aeronautical Research Council Reports and Memoranda No. 3400.

Saltzman, E. J., and Ayers, T. G., 1982, "Review of Flight-to-Wind-Tunnel Drag Correlation," *Journal of Aircraft,* Vol. 19, No. 10, pp. 801–811.

Sumner, D., 1994, "An Experimental Investigation of Three-Dimensional Models in a Two-Dimensional Adaptive Wall Test Section," M.A.Sc. thesis, Department of Mechanical Engineering, University of Waterloo, Waterloo, Ontario, Canada.

Wolf, S. W. D., 1991, "Adaptive Wall Technology for Minimization of Wind Tunnel Boundary Interferences—A Review," ICAW, International Conference on Adaptive Wall Wind Tunnel Research and Wall Interference Correction, Xian, China, Proceedings, pp. A1-1-15.

Wolf, S. W. D., and Goodyer, M. J., 1988, "Predictive Wall Adjustment Strategy for Two-Dimensional Flexible Walled Adaptive Wind Tunnel—A Detailed Description of the First One-Step Method," NASA CR 181635.

Hugh W. Coleman
Eminent Scholar in Propulsion and Professor,
Propulsion Research Center,
Department of Mechanical and Aerospace Engineering,
University of Alabama in Huntsville,
Huntsville, AL 35899

W. Glenn Steele
Professor and Head.

Robert P. Taylor
Professor.

Thermal & Fluid Dynamics Laboratory,
Department of Mechanical Engineering,
Mississippi State University,
Mississippi State, MS 39762

Implications of Correlated Bias Uncertainties in Single and Comparative Tests

The effects of correlated bias uncertainties are considered for both single and comparative tests, and the implications of these effects on experimental results and their uncertainties are investigated. In single tests, correlated bias uncertainties can cause a significant increase or a significant decrease in uncertainty in the result as compared to the uncertainty when there are no correlation effects. In comparative tests, the experimental result is the difference of two test results or the ratio of two test results. If the same test apparatus and instrumentation are used to obtain the two test results, the systematic uncertainty in the difference or the ratio can be significantly less than the systematic uncertainty in the individual test results. However, the effects of systematic uncertainties do not cancel out in comparative tests in which the result is the difference in the results of two tests, contrary to assertions made in some engineering standards.

1 Introduction

The authors' objectives in this article are to examine the implications of correlated bias uncertainties (Coleman and Steele, 1989; Brown et al., 1994) in both single and comparative (back-to-back) tests, to draw some general conclusions that can be useful in designing such experiments and in analyzing their results, and to correct some erroneous ideas about uncertainties in comparative tests that have appeared in some engineering standards (ANSI/ASME, 1984; ANSI/ASME, 1986). In this section, we will review some basic uncertainty analysis concepts. In Section 2, correlated bias effects on single tests are considered, and in Section 3 the effects of correlated bias uncertainties in comparative tests (both difference and ratio) are discussed. The general conclusions of the study are summarized in Section 4.

A general representation of a data reduction equation (DRE) is

$$r = r(X_1, X_2, \ldots, X_J) \tag{1}$$

where r is the experimental result determined from J measured variables, X_i. Each of the measurements of the variables contains bias (systematic) errors and precision errors. These errors in the measured values then propagate through the data reduction equation, thereby generating the bias and precision errors in the experimental result, r. Only in rare instances is the true value of a quantity known, thus, it is necessary to make an estimate of an error, and that estimate is called an uncertainty, U. Uncertainty estimates are made at some confidence level—a 95 percent confidence estimate, for example, means that the true value of the quantity is expected to be within the $\pm U$ interval about the experimentally-determined value 95 times out of 100.

As an estimator of the true but known bias error, a bias limit B is often defined. A 95 percent confidence estimate of B is interpreted as the experimenter being 95 percent confident that the true value of the bias error, if known, would fall within $\pm B$. (It is assumed that corrections have been made for all bias errors whose values are known—the remaining bias errors are thus equally as likely to be positive as negative.) A useful approach to estimating a bias limit is to assume that the bias error for a given case is a single realization drawn from some statistical parent distribution of possible bias errors. For example, one might assume that a bias error belongs to a Gaussian parent distribution with a zero mean and a standard deviation b so that the interval defined by $\pm B = \pm 2b$ would include about 95 percent of the possible bias errors that could be realized from the parent distribution. (The bias limit is sometimes referred to as the "systematic uncertainty".)

As an estimator of the magnitude of the precision errors, a precision limit P is often defined. A 95 percent confidence estimate of P is interpreted to mean that the $\pm P$ interval about a single reading of X_i (or about a single result r) should cover the appropriate parent population mean 95 times out of 100. (The precision limit is sometimes referred to as the "precision uncertainty".)

As developed in the recently issued AGARD report (AGARD, 1994), the 95 percent confidence "large sample" uncertainty analysis equations recommended for use in the vast majority of engineering tests are

$$U_r^2 = B_r^2 + P_r^2 \tag{2}$$

where

$$B_r^2 = \sum_{i=1}^{J} \theta_i^2 B_i^2 + 2 \sum_{i=1}^{J-1} \sum_{k=i+1}^{J} \theta_i \theta_k B_{ik} \tag{3}$$

and

$$P_r^2 = \sum_{i=1}^{J} \theta_i^2 P_i^2 \tag{4}$$

assuming no correlated precision uncertainties. In Eqs. (2)–(4), U_r, B_r, and P_r are the uncertainty, bias limit, and precision limit, respectively, of the result given by Eq. (1); the B_i and P_i are the bias limits and precision limits, respectively, of the variables X_i in Eq. (1); B_{ik} is the covariance estimator for the bias errors in X_i and X_k; and

$$\theta_i = \frac{\partial r}{\partial X_i} \tag{5}$$

These equations incorporate the assumptions and approximations discussed in detail in AGARD (1994) and are consistent

Contributed by the Fluids Engineering Division for publication in the JOURNAL OF FLUIDS ENGINEERING. Manuscript received by the Fluids Engineering Division September 29, 1994; revised manuscript received March 29, 1995. Associate Technical Editor: D. P. Telionis.

with the methodology of ISO (1993). The necessity of estimating the P_i's and P_r over an appropriate time interval is discussed in detail in Coleman and Steele (1989) and AGARD (1994).

When estimating the bias limits B_i of the individual variables in Eq. (3), it is often useful to consider the elemental sources of bias that arise from such categories as calibration errors, data acquisition errors, data reduction errors, test technique errors, etc. For instance, if for the Jth variable, X_J, there are M elemental bias errors identified as significant and whose bias limits are estimated as $(B_J)_1$, $(B_J)_2$, . . . , $(B_J)_M$, then the bias limit for the measurement of X_J is calculated as the root-sum-square (RSS) combination of the elemental limits

$$B_J = [\sum_{k=1}^{M} (B_J)_k^2]^{1/2} \tag{6}$$

As discussed in Brown et al. (1994), the approximation that is recommended for the covariance estimator B_{ik} in Eq. (3) is

$$B_{ik} = \sum_{\alpha=1}^{L} (B_i)_\alpha (B_k)_\alpha \tag{7}$$

where the summation is over the L elemental systematic error sources that are common for measurements of variables X_i and X_k. In the authors' experience, the only way to identify correlated bias uncertainties is to recognize elemental sources that are common for more than one measured variable and that therefore cause the measurements in the different variables to be either consistently high or consistently low. In such cases, the covariance estimator (as given by Eq. (7)) is always positive. In principle, it is possible for the true covariance of the systematic errors in different measured variables to be negative, but the authors have never encountered such a case (that they recognized).

It is not unusual for the uncertainties in the results of engineering experiments to be influenced by the effects of correlated bias uncertainties in the measurements of several of the variables. A typical example occurs when different variables are measured using the same transducer, such as multiple pressures sequentially ported to and measured with the same transducer or temperatures at different positions in a flow measured with a single probe that is traversed across the flow field. Obviously, the bias errors in the variables measured with the same transducer are not independent of one another. Another common example occurs when different variables are measured using different transducers all of which have been calibrated against the same standard, a situation typical of the electronically scanned pressure (ESP) measurement systems in wide use in aerospace test facilities. In such a case, at least a part of the bias error arising from the calibration procedure will be the same for each transducer, and thus some of the elemental bias error contributions in the measurements of the variables will be correlated.

2 Correlated Bias Effects in Single Tests

Consider a case for which the data reduction equation is

$$r = r(x, y) \tag{8}$$

Then the bias limit for r is (applying Eq. (3))

$$B_r^2 = \theta_x^2 B_x^2 + \theta_y^2 B_y^2 + 2\theta_x\theta_y B_{xy} \tag{9}$$

Depending on the particular experimental approach, the effect of correlated bias errors in the measurements of different variables can lead either to increased or to decreased systematic uncertainty in the final experimental result as compared to the same approach with no correlated bias errors. Consider the final term in Eq. (9)—if some bias errors are correlated ($B_{xy} > 0$) and the partial derivatives (θ_x and θ_y) are of the same sign, the term is positive and B_r is increased. On the other hand, if some bias errors are correlated and the partial derivatives are of opposite signs, the term is negative and B_r is decreased. This observation suggests that the effect of correlated bias errors can sometimes be used to advantage if the proper strategies are applied in planning and designing the experiment—sometimes one would want to force correlation of bias errors using appropriate calibration approaches, sometimes not.

This point was evident in previously reported work (Brown et al., 1994) in which four experiments were investigated using a Monte Carlo simulation technique. In temperature difference, pressure coefficient, and compressor efficiency experiments, the presence of correlated bias effects decreased B_r, and it was shown that if the correlated effects were ignored, the resulting B_r estimate could be too large by several orders of magnitude. In the experiment in which the result was the average of three temperatures, the presence of correlated bias effects increased B_r, and it was shown that if the correlated effects were ignored, the resulting B_r estimate could be much too small.

Consider, as a specific example for this article, the situation in which an average velocity of air flow at a duct cross-section is needed so that a volumetric or mass flow rate can be determined. This occurs in a variety of heating, ventilating, and air conditioning (HVAC) applications, in heat exchanger heat rate determinations, and in turbine efficiency tests (Hudson, 1994). In the determination of this average velocity of air flow in a duct, measurements are made at various positions in the duct cross-section (either by traversing a probe or using a rake) and an area weighted average velocity is determined as

$$V_{\text{avg}} = \frac{1}{A_{\text{tot}}} \sum_{i=1}^{N} A_i V_i \tag{10}$$

where each V_i is measured at the midpoint of the area A_i and A_{tot} is the duct cross-sectional area. If all of the A_i's are equal, then the average velocity becomes

$$V_{\text{avg}} = \frac{1}{N} \sum_{i=1}^{N} V_i \tag{11}$$

Applying Eq. (3) to Eq. (11), the bias limit for the average velocity due to the systematic uncertainties in the measurements of the velocities V_i is

$$B_{V_{\text{avg}}}^2 = \sum_{i=1}^{N} \left(\frac{1}{N}\right)^2 (B_{V_i})^2 + 2 \sum_{i=1}^{N-1} \sum_{k=i+1}^{N} \left(\frac{1}{N}\right)\left(\frac{1}{N}\right) B_{V_i V_k} \tag{12}$$

The B_{V_i}'s are all equal (to B_V, say) for cases where (a) a single probe is traversed (or a rake of probes is used with all transducers having been identically calibrated against the same standard), (b) the installation error is the same at each measurement position, and (c) the B_{V_i}'s are a fixed value (''% of full scale'' rather than ''% of reading''). For such cases Eq. (7) gives

$$B_{V_i V_k} = (B_{V_i})(B_{V_k}) = B_V^2 \tag{13}$$

and Eq. (12) reduces to

$$B_{V_{\text{avg}}} = B_V \tag{14}$$

For this set of circumstances, then, the bias limit for the average velocity is equal to the bias limit for a single measurement of velocity. Note, however, that this would not be the case if the B_{V_i}'s were specified as ''% of reading'' or some other function of the measured value, since Eq. (7) would not yield the relationship shown by Eq. (13).

On the other hand, if all of the B_{V_i}'s are of the same magnitude (B_V) but are totally uncorrelated (perhaps when a rake of probes is used but none of the transducers have been calibrated against the same standard), then the bias limit for the average velocity is, from Eq. (12),

$$B_{V_{avg}} = \frac{1}{\sqrt{N}} B_V \tag{15}$$

There are several important points to be made from this example. First, the bias limits for V_{avg} for the two situations differ by a factor of $1/\sqrt{N}$, with the bias limit being smaller when there are no correlated biases. It cannot be said, therefore, that it is always "conservative" to ignore the correlated bias contributions. Second, in HVAC applications minimum values of $N = 20$ for round ducts and $N = 16$ for rectangular ducts are recommended (ASHRAE, 1989), meaning that ignoring the correlated bias effects would lead to estimates of $B_{V_{avg}}$ that were about $\frac{1}{5}$ to $\frac{1}{4}$ of the value estimated by proper consideration of the correlated bias effects. This effect, then, can be quite considerable.

3 Correlated Bias Effects in Comparative Tests

Many misconceptions have appeared in the engineering literature regarding the effects of bias uncertainties in comparative tests. Even in some engineering standards, statements about the uncertainties associated with comparative (back-to-back) experiments are made such as

> "uncertainty in the difference measurement will be composed only of precision errors" (ANSI/ASME, 1986)

and

> ". . . all the fixed, constant bias errors will cancel out. The measurement uncertainty is composed of precision errors only" (ANSI/ASME, 1984)

The authors of such statements try to account for the correlated error effects without using the mathematics as derived in Eq. (3), and the statements are incorrect in general.

In this section, we will examine the effects of correlated bias uncertainties in two cases: (1) where the experimental result of interest is the difference of the results from two tests, and (2) where the experimental result of interest is the ratio of the results from two tests. The effects can be most easily seen for the simple test in which the result is a function of two measured variables, so that the data reduction equation for a single test is given by Eq. (8)

$$r = r(x, y) \tag{8}$$

Difference of Results of Two Tests. Consider the case in which the experimental result of interest is the difference in the results of two tests. An example would be a wind tunnel test program to determine the drag increment due to a configuration change on a model for a given freestream condition. Labeling the tests as a and b, the data reduction equation is

$$\delta = r(x_a, y_a) - r(x_b, y_b) \tag{16}$$

Application of Eq. (3) gives the expression for the bias limit for δ

$$\begin{aligned} B_\delta^2 = &\left(\frac{\partial \delta}{\partial x_a}\right)^2 B_{x_a}^2 + \left(\frac{\partial \delta}{\partial x_b}\right)^2 B_{x_b}^2 + 2\left(\frac{\partial \delta}{\partial x_a}\right)\left(\frac{\partial \delta}{\partial x_b}\right) B_{x_a x_b} \\ &+ \left(\frac{\partial \delta}{\partial y_a}\right)^2 B_{y_a}^2 + \left(\frac{\partial \delta}{\partial y_b}\right)^2 B_{y_b}^2 + 2\left(\frac{\partial \delta}{\partial y_a}\right)\left(\frac{\partial \delta}{\partial y_b}\right) B_{y_a y_b} \\ &+ 2\left(\frac{\partial \delta}{\partial x_a}\right)\left(\frac{\partial \delta}{\partial y_a}\right) B_{x_a y_a} + 2\left(\frac{\partial \delta}{\partial x_b}\right)\left(\frac{\partial \delta}{\partial y_b}\right) B_{x_b y_b} \\ &+ 2\left(\frac{\partial \delta}{\partial x_b}\right)\left(\frac{\partial \delta}{\partial y_a}\right) B_{x_b y_a} + 2\left(\frac{\partial \delta}{\partial x_a}\right)\left(\frac{\partial \delta}{\partial y_b}\right) B_{x_a y_b} \end{aligned} \tag{17}$$

Derivatives with respect to a variable with an a subscript are evaluated at the conditions of test a, while derivatives with respect to a variable with a b subscript are evaluated at the conditions of test b. Noting that

$$\frac{\partial \delta}{\partial x_a} = \frac{\partial r}{\partial x_a}; \quad \frac{\partial \delta}{\partial y_a} = \frac{\partial r}{\partial y_a}$$
$$\frac{\partial \delta}{\partial x_b} = -\frac{\partial r}{\partial x_b}; \quad \frac{\partial \delta}{\partial y_b} = -\frac{\partial r}{\partial y_b} \tag{18}$$

and substituting into Eq. (17) gives

$$\begin{aligned} B_\delta^2 = &\left(\frac{\partial r}{\partial x_a}\right)^2 B_{x_a}^2 + \left(\frac{\partial r}{\partial x_b}\right)^2 B_{x_b}^2 + 2\left(\frac{\partial r}{\partial x_a}\right)\left(-\frac{\partial r}{\partial x_b}\right) B_{x_a x_b} \\ &+ \left(\frac{\partial r}{\partial y_a}\right)^2 B_{y_a}^2 + \left(\frac{\partial r}{\partial y_b}\right)^2 B_{y_b}^2 + 2\left(\frac{\partial r}{\partial y_a}\right)\left(-\frac{\partial r}{\partial y_b}\right) B_{y_a y_b} \\ &+ 2\left(\frac{\partial r}{\partial x_a}\right)\left(\frac{\partial r}{\partial y_a}\right) B_{x_a y_a} + 2\left(-\frac{\partial r}{\partial x_b}\right)\left(-\frac{\partial r}{\partial y_b}\right) B_{x_b y_b} \\ &+ 2\left(-\frac{\partial r}{\partial x_b}\right)\left(\frac{\partial r}{\partial y_a}\right) B_{x_b y_a} + 2\left(\frac{\partial r}{\partial x_a}\right)\left(-\frac{\partial r}{\partial y_b}\right) B_{x_a y_b} \end{aligned} \tag{19}$$

The third term on the right-hand-side (RHS) accounts for the correlated bias uncertainties in the measurement of x in test a and the measurement of x in test b, and the sixth term does the same for the y measurements. Since in most comparative tests a variable will be measured by the same system in test a and in test b, most (if not all) of the elemental error sources will be identical in the measurements of a variable in the two tests and the covariance estimator will be nonzero and positive.

The final four terms on the RHS account for the possibility that the x measurements and the y measurements might share some elemental error sources. This usually occurs when x and y are both pressures, or both temperatures, etc., and are either measured with the same instrument or with different instruments that have been calibrated against the same standard.

For this discussion, assume measurements of x and measurements of y share no elemental error sources so that the final four RHS terms are zero. Equation (19) then becomes

$$\begin{aligned} B_\delta^2 = &\left(\frac{\partial r}{\partial x_a}\right)^2 B_{x_a}^2 + \left(\frac{\partial r}{\partial x_b}\right)^2 B_{x_b}^2 - 2\left(\frac{\partial r}{\partial x_a}\right)\left(\frac{\partial r}{\partial x_b}\right) B_{x_a x_b} \\ &+ \left(\frac{\partial r}{\partial y_a}\right)^2 B_{y_a}^2 + \left(\frac{\partial r}{\partial y_b}\right)^2 B_{y_b}^2 - 2\left(\frac{\partial r}{\partial y_a}\right)\left(\frac{\partial r}{\partial y_b}\right) B_{y_a y_b} \end{aligned} \tag{20}$$

As stated at the beginning of this section, two Standards documents indicate that B_δ is always zero. What are the conditions necessary for B_δ to be zero? First, all of the elemental bias error sources for x measurements must be the same in test a and in test b, and the bias limits for all of the elemental sources must be constants (% of full scale type) rather than a function of the measured value (% of reading type, for instance). The same must be true for the systematic errors in the y measurements. Then

$$B_{x_a} = B_{x_b} = B_x; \quad B_{x_a x_b} = B_x^2$$
$$B_{y_a} = B_{y_b} = B_y; \quad B_{y_a y_b} = B_y^2 \tag{21}$$

Second, the derivatives evaluated at test a conditions must equal the corresponding derivatives evaluated at test b conditions, i.e.,

$$\frac{\partial r}{\partial x_a} = \frac{\partial r}{\partial x_b}; \quad \frac{\partial r}{\partial y_a} = \frac{\partial r}{\partial y_b} \tag{22}$$

For the conditions represented by Eqs. (21) and (22), the first, second and third terms on the RHS of Eq. (20) add to give zero, as do the fourth, fifth and sixth terms. Equation (20) then yields $B_\delta = 0$.

Now consider the experiment mentioned previously investigating the drag increment due to a model configuration change. The data reduction equation is

$$\delta = \frac{F_a}{\frac{1}{2}\rho_a V_a^2 A_a} - \frac{F_b}{\frac{1}{2}\rho_b V_b^2 A_b} \tag{23}$$

The derivatives with respect to V, for example, are

$$\frac{\partial \delta}{\partial V_a} = \frac{-2F_a}{\frac{1}{2}\rho_a V_a^3 A_a}; \quad \frac{\partial \delta}{\partial V_b} = \frac{2F_b}{\frac{1}{2}\rho_b V_b^3 A_b} \tag{24}$$

Even if the denominators of the two derivatives are equal (test a and test b freestream conditions exactly the same), the numerators will not be the same except for the very special instance of the dependent test variable (drag force in this case) having the same value in the two tests. This is a highly unlikely occurrence—even if a test is replicated with everything the same, including configuration, the measured values of the variables will be slightly different in tests a and b. In the more likely case of interest in this section, the drag forces F_a and F_b will be different, so $\delta \neq 0$ and the conditions of Eqs. (21) and (22) are not fulfilled.

Based on the discussion above, it must be concluded that the effects of systematic uncertainties *do not* cancel out in comparative experiments in which the result is the difference in the results of two tests. When the same test apparatus and instrumentation are used in the two tests, however, the systematic uncertainty in δ (from Eq. (19) or (20)) can be significantly less than the systematic uncertainty in either the result of test a or of test b.

When considering the question "How small an increment can be distinguished in a comparative test?" the *overall uncertainty* associated with δ must be considered, since it can be argued that the minimum distinguishable increment must certainly be larger than its uncertainty. The uncertainty in δ is given by

$$U_\delta^2 = B_\delta^2 + P_\delta^2 \tag{25}$$

where B_δ is given by Eq. (19) or (20). The determination of the appropriate estimate for P_δ warrants further discussion.

The estimate of P_δ must include the influence of *all* of the significant factors that cause variation in δ, considering the process by which δ is determined. Consider a case similar to the drag increment experiment, for instance, in which the wind tunnel was shut down after test a; the model was removed, altered, and reinstalled; the tunnel was re-started and reset to the freestream conditions of test a; and then the test b data were taken. For a DRE given by Eq. (16), using Eq. (4) to determine P_δ by propagation gives

$$P_\delta^2 = \left(\frac{\partial r}{\partial x_a}\right)^2 P_{x_a}^2 + \left(\frac{\partial r}{\partial x_b}\right)^2 P_{x_b}^2 + \left(\frac{\partial r}{\partial y_a}\right)^2 P_{y_a}^2 + \left(\frac{\partial r}{\partial y_b}\right)^2 P_{y_b}^2 \tag{26}$$

This will not, in general, give an appropriate estimate of P_δ if the P_x's and P_y's are estimated based on data taken within a test without tunnel conditions reset and model re-installation effects included. A more appropriate estimate would be given by substituting

$$r_a = r(x_a, y_a); \quad r_b = r(x_b, y_b) \tag{27}$$

into Eq. (16) and applying Eq. (4) to yield

$$P_\delta^2 = (1)^2 P_{r_a}^2 + (-1)^2 P_{r_b}^2 \tag{28}$$

where the P_r's are determined directly from a sample of multiple results (Coleman and Steele, 1989; AGARD, 1994) that includes all of the effects discussed above.

In many practical engineering tests (such as the drag increment experiment example), one might determine an estimate of P_r directly from a sample of previous results (for a similar model if possible) that includes the effects of resetting tunnel conditions and model re-installation, and assume that

$$P_{r_a} = P_{r_b} = P_r \tag{29}$$

so that Eq. (27) gives

$$P_\delta = \sqrt{2} P_r \tag{30}$$

It should be noted that depending on how the comparative experiments are performed, some factors listed above that can affect δ may not occur during the testing period. For instance, if the model angle is the only parameter changed between tests a and b with the wind tunnel continually operating at the same nominal conditions during both tests, then the precision limit associated with the comparison would not contain the effects of shutting the tunnel down and restarting it or of model removal and reinstallation. The P_r values in Eq. (29) should represent only those precision factors that exhibit variations in the comparison of results from tests a and b.

Ratio of Results of Two Tests. Consider the case in which the experimental result of interest is the ratio of the results of two tests. Such cases occur, for example, in heat transfer testing when data are presented as ratios of heat transfer coefficients for different wall boundary conditions on a given test article. A recent example, including discussion of the uncertainty aspects, was published by Chakroun et al. (1993). Labeling the tests as a and b, the data reduction equation is

$$\eta = \frac{r(x_a, y_a)}{r(x_b, y_b)} \tag{31}$$

Application of Eq. (3) gives the expression for the bias limit for η

$$\begin{aligned} B_\eta^2 = {} & \left(\frac{\partial \eta}{\partial x_a}\right)^2 B_{x_a}^2 + \left(\frac{\partial \eta}{\partial x_b}\right)^2 B_{x_b}^2 \\ & + 2\left(\frac{\partial \eta}{\partial x_a}\right)\left(\frac{\partial \eta}{\partial x_b}\right) B_{x_a x_b} \left(\frac{\partial \eta}{\partial y_a}\right)^2 B_{y_a}^2 + \left(\frac{\partial \eta}{\partial y_b}\right)^2 B_{y_b}^2 \\ & + 2\left(\frac{\partial \eta}{\partial y_a}\right)\left(\frac{\partial \eta}{\partial y_b}\right) B_{y_a y_b} + 2\left(\frac{\partial \eta}{\partial x_a}\right)\left(\frac{\partial \eta}{\partial y_a}\right) B_{x_a y_a} \\ & + 2\left(\frac{\partial \eta}{\partial x_b}\right)\left(\frac{\partial \eta}{\partial y_b}\right) B_{x_b y_b} + 2\left(\frac{\partial \eta}{\partial x_b}\right)\left(\frac{\partial \eta}{\partial y_a}\right) B_{x_b y_a} \\ & + 2\left(\frac{\partial \eta}{\partial x_a}\right)\left(\frac{\partial \eta}{\partial y_b}\right) B_{x_a y_b} \end{aligned} \tag{32}$$

Noting that

$$\begin{aligned} \frac{\partial \eta}{\partial x_a} &= \frac{1}{r_b}\frac{\partial r}{\partial x_a}; \quad \frac{\partial \eta}{\partial y_a} = \frac{1}{r_b}\frac{\partial r}{\partial y_a} \\ \frac{\partial \eta}{\partial x_b} &= \frac{-r_a}{r_b^2}\frac{\partial r}{\partial x_b}; \quad \frac{\partial \eta}{\partial y_b} = \frac{-r_a}{r_b^2}\frac{\partial r}{\partial y_b} \end{aligned} \tag{33}$$

and substituting into Eq. (32) gives

$$\begin{aligned} B_\eta^2 = {} & \frac{1}{r_b^2}\left(\frac{\partial r}{\partial x_a}\right)^2 B_{x_a}^2 + \frac{r_a^2}{r_b^4}\left(\frac{\partial r}{\partial x_b}\right)^2 B_{x_b}^2 \\ & - 2\frac{r_a}{r_b^3}\left(\frac{\partial r}{\partial x_a}\right)\left(\frac{\partial r}{\partial x_b}\right) B_{x_a x_b} + \frac{1}{r_b^2}\left(\frac{\partial r}{\partial y_a}\right)^2 B_{y_a}^2 \\ & + \frac{r_a^2}{r_b^4}\left(\frac{\partial r}{\partial y_b}\right)^2 B_{y_b}^2 - 2\frac{r_a}{r_b^3}\left(\frac{\partial r}{\partial y_a}\right)\left(\frac{\partial r}{\partial y_b}\right) B_{y_a y_b} \end{aligned}$$

$$+ 2\,\frac{1}{r_b^2}\left(\frac{\partial r}{\partial x_a}\right)\left(\frac{\partial r}{\partial y_a}\right)B_{x_a y_a} + 2\,\frac{r_a^2}{r_b^4}\left(\frac{\partial r}{\partial x_b}\right)\left(\frac{\partial r}{\partial y_b}\right)B_{x_b y_b}$$
$$- 2\,\frac{r_a}{r_b^3}\left(\frac{\partial r}{\partial x_b}\right)\left(\frac{\partial r}{\partial y_a}\right)B_{x_b y_a} - 2\,\frac{r_a}{r_b^3}\left(\frac{\partial r}{\partial x_a}\right)\left(\frac{\partial r}{\partial y_b}\right)B_{x_a y_b} \quad (34)$$

This expression is identically zero only for the relatively uninteresting case in which tests a and b are exactly the same. In that case, $\eta = 1$ and the first, second and third terms on the RHS of Eq. (34) add to zero, as do the fourth, fifth, and sixth terms and the seventh, eighth, ninth, and tenth terms. For a more practical situation, the study by Chakroun et al. (1993) showed that when heat transfer test results were presented as a ratio to results from a baseline test, the bias uncertainty of the ratio was less than the bias uncertainty associated with the results from either test. The study included the complexity of the measurements of x and y variables sharing an identical source of bias error, so that all six covariance terms in Eq. (34) were non-zero.

As in the case in which the experimental result was the difference in two results, when the same test apparatus and instrumentation are used in two tests the ratio of the two test results can have a lower systematic uncertainty than the systematic uncertainty in either of the individual test results (as shown by Chakroun, et al. (1993)). The same precision uncertainty considerations discussed for the difference tests apply in the case of ratio tests.

4 Conclusions

In single tests, correlated bias uncertainties can cause a significant increase or a significant decrease in uncertainty in the result as compared to the uncertainty when there are no correlation effects. It cannot be said, therefore, that it is always "conservative" to ignore correlated bias contributions.

In comparative tests, the experimental result is the difference of two test results or the ratio of two test results. If the same test apparatus and instrumentation are used to obtain the two test results, the systematic uncertainty in the difference or the ratio can be significantly less than the systematic uncertainty in the individual test results. However, the effects of systematic uncertainties do not cancel out in comparative tests in which the result is the difference in the results of two tests, contrary to assertions made in some engineering standards (ANSI/ASME, 1984: ANSI/ASME, 1986).

References

AGARD, 1994, *Quality Assessment for Wind Tunnel Testing,* AGARD-AR-304. (This document, with minor editorial revisions, has also been issued as AIAA Standard S-071-1995, *Assessment of Wind Tunnel Data Uncertainty,* 1995.)

ANSI/ASME, 1986, *Measurement Uncertainty,* ANSI/ASME PTC 19.1–1985.

ANSI/ASME, 1984, *Measurement Uncertainty for Fluid Flow in Closed Conduits,* ANSI/ASME MFC-2M-1983.

ASHRAE, 1989, *Fundamentals,* American Society of Heating, Refrigerating and Air Conditioning Engineers, Inc.

ISO, 1993, *Guide to the Expression of Uncertainty in Measurement,* International Organization for Standardization.

Brown, K. K., Coleman, H. W., Steele, W. G., and Taylor, R. P., 1994, "Evaluation of Correlated Bias Approximations in Experimental Uncertainty Analysis," AIAA Paper 94–0772 presented at the 32nd AIAA Aerospace Sciences Meeting.

Chakroun, W., Taylor, R. P., Steele, W. G., and Coleman, H. W., 1993, "Bias Error Reduction in Experimental Results by Presentation as a Ratio to a Baseline Experiment—A Heat Transfer Case Study," *J. Thermophysics and Heat Transfer,* Vol. 7, No. 4.

Coleman, H. W., and Steele, W. G., 1989, *Experimentation and Uncertainty Analysis for Engineers,* Wiley, New York, NY.

Hudson, S. T., 1994, personal communication, NASA Marshall Space Flight Center.

Assessment of a Reynolds Stress Closure Model for Appendage-Hull Junction Flows

Hamn-Ching Chen
Ocean Engineering Program,
Department of Civil Engineering,
Texas A & M University,
College Station, TX 77843

A multiblock numerical method, for the solution of the Reynolds-Averaged Navier-Stokes equations, has been used in conjunction with a near-wall Reynolds stress closure and a two-layer isotropic eddy viscosity model for the study of turbulent flow around a simple appendage-hull junction. Comparisons of calculations with experimental data clearly demonstrate the superior performance of the present second-order Reynolds stress (second-moment) closure over simpler isotropic eddy viscosity models. The second-moment solutions are shown to capture the most important features of appendage-hull juncture flows, including the formation and evolution of the primary and secondary horseshoe vortices, the complex three-dimensional separations, and interaction among the hull boundary layer, the appendage wake and the root vortex system.

Introduction

The vorticities shed from the hull, appendages, and intersections of a submarine are a major cause of the spatial nonuniformity in propeller inflow. These flows are typically characterized by thick boundary layers in the stern region, counterrotating longitudinal vortices generated by appendage-hull junctures, and appendage turbulent wakes. The spatial nonuniformity of axial velocities and redistribution of turbulent Reynolds stresses significantly affect the propulsor noise and powering performance. In order to address the propulsor/hull/appendage interactions and the associated acoustics, it is necessary to develop accurate and robust hydrodynamic assessment capabilities for detailed resolution of the appendage-hull juncture vortices and nonuniform inflow to submarine propulsors.

Recently, Chen and Korpus (1993) and Chen et al. (1994) developed a multiblock Reynolds-Averaged Navier-Stokes (RANS) method in conjunction with the two-layer $k-\epsilon$ model of Chen and Patel (1988) for calculations of viscous incompressible flow around practical submarine and ship configurations. The method successfully captured many important features of ship and submarine flows including the thick boundary layers, viscous wakes, and nonlinear free surface waves. However, these studies also revealed several critical deficiencies of isotropic eddy viscosity models for the tracking of longitudinal vortices behind submarine appendages and ship sterns. In particular, the isotropic eddy viscosity models were found to produce excessive eddy viscosity in regions of strong surface curvatures or significant vortical motions. The extra diffusion caused by excessive eddy viscosity is responsible for the overprediction of mean velocities in the inner part of the stern boundary layer, and the rather poor resolution of longitudinal vortices behind the submarine appendages.

In order to improve the predictions of the inflow to submarine propulsors, it is necessary to employ advanced turbulence closures which can more accurately resolve the Reynolds stress anisotropy for complex three-dimensional flows involving large surface curvatures and strong vortical motions. In the past several years, there has been significant progress in the second-moment closure models for engineering flow calculations involving significant curvatures, swirling motions, buoyancy, or density stratifications. The review of many comparative calculations by Launder (1989) and So et al. (1991) clearly demonstrated the superior predictive capability of second-order Reynolds stress closures in comparison with simpler eddy viscosity models. In a recent study, Chen (1992, 1993) examined several high-Reynolds-number and near-wall second-order Reynolds stress models with the specific objectives of evaluating their performance for submarine flow simulations. Very encouraging results have been obtained using the second-moment closure model of Speziale, Sarkar, and Gatski (SSG, 1991) and Shima (SH, 1988) for applications involving simple submarine configurations.

In the present study, a practical near-wall Reynolds stress closure model has been devised by extending the SSG second-moment closure all the way to the solid surface to enable direct resolution of the laminar sublayer and buffer layer in the near-wall region. Calculations have been performed using the generalized SSG second-moment closure for viscous incompressible flows around an appendage/flat-plate junction and several practical submarine configurations. The present paper is concerned specifically with a detailed validation and critical assessment of the proposed near-wall second-moment closure model for the appendage/flat-plate junction flow of Dickinson (1986). Applications of the present second-moment RANS method for the simulation of turbulent incompressible flow around practical submarine and ship configurations are reported in Chen (1994, 1995).

Governing Equations

Consider the nondimensional Reynolds-Averaged Navier-Stokes equations in general curvilinear coordinates (ξ^i, t), $i = 1, 2, 3$, for unsteady incompressible flow:

$$U^i_{,i} = 0 \tag{1}$$

$$\frac{\partial U^i}{\partial t} + U^m U^i_{,m} = -g^{im} p_{,m} + \frac{1}{\mathrm{Re}} g^{mn} U^i_{,mn} - R^{im}_{,m} + F^i \tag{2}$$

where $R^{ij} = \overline{u^i u^j}$ is the Reynolds stress tensor. Overbars imply the ensemble Reynolds averaging and the summation convention is used for repeated indices. The subscripts $,m$ and $,mn$ represent the first and second covariant derivatives with respect to ξ^m. g^{mn} is the conjugate metric tensor in general curvilinear coordinates. U^i and u^i are contravariant components of the mean and fluctuating velocities, F^i are contravariant components of

Contributed by the Fluids Engineering Division for publication in the JOURNAL OF FLUIDS ENGINEERING. Manuscript received by the Fluids Engineering Division February 21, 1994; revised manuscript received February 7, 1995. Associate Technical Editor: O. Baysal.

the body force field, t is time, p is pressure, and $\mathrm{Re} = U_o L/\nu$ is the Reynolds number, based on a reference velocity U_o, a reference length L, and the kinematic viscosity ν. All quantities are made dimensionless using U_o, L and density ρ.

The Reynolds stress tensor R^{ij} is a solution of the transport equations

$$\frac{\partial R^{ij}}{\partial t} + U^m R^{ij}_{,m} = P^{ij} + D_u^{ij} + D_p^{ij} + D_v^{ij} + \Phi^{ij} - \epsilon^{ij} \quad (3)$$

with

$$P^{ij} = -(R^{im}U^j_{,m} + R^{jm}U^i_{,m}); \quad D_u^{ij} = -(\overline{u^i u^j u^m})_{,m} \quad (4)$$

$$D_p^{ij} = -g^{jm}(\overline{u^i p'})_{,m} - g^{im}(\overline{u^j p'})_{,m}$$

$$D_v^{ij} = (1/\mathrm{Re})g^{mn}R^{ij}_{,mn} \quad (5)$$

$$\Phi^{ij} = \overline{p'(g^{im}u^j_{,m} + g^{jm}u^i_{,m})}; \quad \epsilon^{ij} = (2/\mathrm{Re})g^{mn}\overline{u^i_{,m}u^j_{,n}} \quad (6)$$

where P^{ij}, D_u^{ij}, D_p^{ij}, D_v^{ij}, Φ^{ij}, and ϵ^{ij} represent the production, diffusion by velocity fluctuation, diffusion by pressure fluctuation, viscous diffusion, pressure-strain, and viscous dissipation, respectively. To solve these equations, appropriate closure models must be provided for the diffusion, pressure-strain and dissipation terms. A comprehensive review of various second-moment closure models can be found in, among others, Launder (1989), Speziale (1991), and So et al. (1991). Chen (1992, 1993) has recently examined several of these advanced Reynolds stress closure models in order to ascertain their general performance for submarine flow simulations. Very encouraging results have been obtained using a second-moment closure model which combines the pressure-strain correlations of Speziale, Sarkar, and Gatski (SSG, 1991) with the near-wall Reynolds stress closure of Shima (SH, 1988). In the present study, the high-Re SSG closure has been extended directly to the solid surface with a consistent near-wall closure model to further improve the prediction of near-wall turbulent flows involving strong pressure gradients and three-dimensional separations.

High-Re Second-Moment Closure. It is well known that the pressure-strain correlation Φ^{ij} plays a pivotal role in determining a wide variety of the turbulence structures for complex three-dimensional flows. There are two distinct kinds of interactions giving rise to the pressure-strain correlations; one involving just fluctuating quantities (Φ_1^{ij}) and the other arising from the presence of the mean rate of strain (Φ_2^{ij}). In addition, wall-reflection terms Φ_{1w}^{ij} and Φ_{2w}^{ij} are often added to account for the wall proximity effects due to the presence of solid boundaries. In the present study, the high-Re SSG pressure-strain correlations of Speziale, Sarkar, and Gatski (1991) have been generalized to arbitrary curvilinear coordinates system as follows:

$$\Phi^{ij} = \Phi_1^{ij} + \Phi_2^{ij} \quad (7)$$

where

$$\Phi_1^{ij} = -(C_1\epsilon + C_1^* P)b^{ij} + C_2\epsilon(g_{mn}b^{im}b^{jn} - \tfrac{1}{3}g^{ij}II) \quad (8)$$

$$\Phi_2^{ij} = (C_3 - C_3^* II^{1/2})kS^{ij} + C_4 k(g_{mn}b^{im}S^{jn} + g_{mn}b^{jm}S^{in} - \tfrac{2}{3}g^{ij}g_{mr}g_{ns}b^{mn}S^{rs}) + C_5 k(g_{mn}b^{im}W^{jn} + g_{mn}b^{jm}W^{in}) \quad (9)$$

and

$$b^{ij} = \frac{R^{ij}}{2k} - \frac{1}{3}g^{ij}; \quad II = g_{mr}g_{ns}b^{mn}b^{rs}$$

$$S^{ij} = \tfrac{1}{2}(g^{jm}U^i_{,m} + g^{im}U^j_{,m}); \quad W^{ij} = \tfrac{1}{2}(g^{jm}U^i_{,m} - g^{im}U^j_{,m})$$

where the model constants (C_1, C_1^*, C_2, C_3, C_3^*, C_4, C_5) are equal to (3.4, 1.80, 4.2, 0.8, 1.30, 1.25, 0.40). In addition to the pressure-strain terms, appropriate closure models are also needed for the diffusion and dissipation terms. In the present study, the gradient-diffusion model of Daly and Harlow (1970) was generalized to curvilinear coordinates to provide necessary closures for the combined turbulent diffusions $D^{ij} = D_u^{ij} + D_p^{ij}$ as:

$$D^{ij} = C_s'\left(\frac{k}{\epsilon}R^{mn}R^{ij}_{,n}\right)_{,m}; \quad C_s' = 0.22 \quad (10)$$

For fully turbulent flow away from the solid walls, the dissipation terms are assumed to be isotropic with $\epsilon^{ij} = (2/3)g^{ij}\epsilon$.

Near-Wall Reynolds Stress Closure. It is well known that a solid boundary exerts many important effects on the characteristics of the near-wall turbulence. A rigid wall enforces no-slip conditions, thus ensuing that the turbulence stresses are negligible within a laminar sublayer where the viscous effects become of vital importance. Furthermore, it raises the dissipation rates in the wall region by reducing the length scales of the fluctuation. The solid wall also reflects pressure fluctuations and inhibits turbulence energy transfer into fluctuations normal to the wall. Most of the wall-reflection terms introduced in high-Re closure models do not explicitly account for the viscous damping effects, they actually reflected pressure fluctuations and provided a desirable "echo" effect in the proximity of a wall. In addition to these wall-reflection effects, several near-wall models have been proposed to explicitly account for the viscous damping effects in the dissipation and pressure-strain processes. A comprehensive review of these models was given in So et al. (1991). The majority of these near-wall closure models introduced viscous damping functions in the dissipation and pressure-strain terms, while retaining the high-Re closure for diffusion terms.

Most of the existing near-wall models were formulated in Cartesian tensors with explicit reference to surface normal directions n_i. It is noted, however, that the contravariant Reynolds stress component $\overline{u^i u^i}$ does not strictly represent the normal stress perpendicular to the solid surface n_i unless a triply-orthogonal coordinate system is employed. Moreover, the surface normal n_i may not be uniquely defined for concave surfaces with strong curvatures such as the corner region of the appendage-hull junction considered here. In order to avoid possible ambiguity in the determination of n_i for complex geometries, it is desirable to employ a near-wall closure which does not depend explicitly on the surface normal n_i. In the present study, the high-Re second-moment closure described above has been extended all the way to solid walls using a practical near-wall closure which depends only upon the near-wall distance y, but not the surface normal directions n_i. In particular, we have modified one of the more successfully near-wall closures, namely that of Shima (1988), to facilitate a direct resolution of the laminar sublayer and buffer layer in the near-wall region.

Instead of modeling the near-wall Φ^{ij} and ϵ_{ij} separately, we shall rearrange these two terms following the arguments of Lumley (1980) as

$$\Phi^{ij} - \epsilon^{ij} = \bar{\Phi}_1^{ij} + \Phi_2^{ij} + \Phi_w^{ij} - \tfrac{2}{3}g^{ij}\epsilon \quad (11)$$

where $\bar{\Phi}_1^{ij} = \Phi_1^{ij} - \epsilon^{ij} + (2/3)g^{ij}\epsilon$ includes only the turbulence (fluctuation) part of the pressure-strain and dissipation terms, while Φ_2^{ij} represents the mean-strain part of pressure-strain correlation given in Eq. (6). In the present study, both $\bar{\Phi}_1^{ij}$ and Φ_w^{ij} are modeled using near-wall damping functions similar to those proposed by Shima (1988):

$$\bar{\Phi}_1^{ij} = -\bar{C}_1\{1 - (1 - 1/\bar{C}_1)f_w\}\epsilon b^{ij} + C_2(1 - f_w)\epsilon(g_{mn}b^{im}b^{jn} - \tfrac{1}{3}g^{ij}II) \quad (12)$$

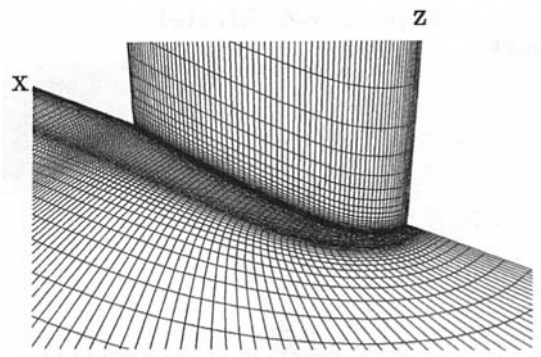

Fig. 1 Partial view of the numerical grid

$$\Phi_w^{ij} = f_w\{0.45(P^{ij} - \tfrac{2}{3}g^{ij}P) - 0.03(Q^{ij} - \tfrac{2}{3}g^{ij}P) + 0.08k(2S^{ij})\} \quad (13)$$

$$\bar{C}_1 = C_1 + C_1^* \frac{P}{\epsilon}; \quad f_w = \exp[-(0.015\sqrt{k}y/\nu)^4] \quad (14)$$

$$P = \tfrac{1}{2}g_{mn}P^{mn}; \quad Q^{ij} = -g_{lm}(g^{in}R^{jl} + g^{jn}R^{il})U^m_{,n} \quad (15)$$

where y is the normal distance from the nearest solid surface. Away from solid walls, the effects of damping functions diminish exponentially to zero with $\bar{\Phi}^{ij} = \Phi^{ij}$ and $\Phi_w^{ij} = 0$ in the fully turbulent regions. Unlike the earlier SSG/SH closure of Chen (1992, 1993) which combines the high-Re SSG and near-wall SH models in a two-layer approach, the present near-wall closure is completely consistent with the high-Re SSG model and can be used in both the near-wall and fully turbulent flow regions. Consequently, the needs for consistent matching of the Reynolds stresses described in the hybrid SSG/SH closure model is completely alleviated.

Results and Discussion

Calculations have been performed for viscous flow around an appendage-hull junction to provide a thorough assessment of the present near-wall second-moment closure model. In particular, we consider the flow past a symmetric appendage mounted on a flat plate at zero incidence to a uniform stream. This simple model problem has been used in several previous experimental (e.g., Dickinson, 1986; Pierce and Harsh, 1988; Devenport and Simpson, 1990) and numerical (among others, Sung and Yang, 1988; Chen and Patel, 1989) investigations to study flow phenomena associated with junctions in practical configurations, such as those in appendage-hull junctions in hydrodynamics, wing-fuselage intersections in aerodynamics, and blade-hub junctions in propellers and turbomachinery. In the present study, the appendage/flat-plate experiment of Dickinson (1986), which is representative of many previous experimental studies, has been selected for the validation and assessment of the new near-wall Reynolds stress closure. In this experiment, a 25.9 cm (10.2 in) chord appendage, consisting of a 3:2 semielliptic nose and a NACA 0020 aft section, was mounted in a 0.61 m wide, 1.22 m high (2 ft × 4 ft) wind tunnel. The maximum thickness of the appendage was 6.1 cm (2.4 in), which gives a nominal area blockage of 10 percent. Pressure, velocity and Reynolds stress data were taken at seven axial stations $X/C = -0.75$, 0.18, 0.64, 0.75, 0.93, 1.05 and 1.50, under different inflow conditions.

Calculations were performed at the experimental Reynolds number of 5×10^5 using an $101 \times 81 \times 41$ numerical grid shown in Fig. 1. The grid was constructed with adaptive refinement of grid density along the trajectory of the primary horseshoe vortex to improve the resolution around the vortex core region. This fine adaptive grid has been demonstrated to yield grid-independent solutions in a systematic grid refinement study performed by Chen (1994). Therefore, any discrepancies between the measurements and present numerical results must be attributed primarily to the difference in test conditions or turbulence modeling.

Several experimental investigations of steady and unsteady horseshoe vortices in the plane of symmetry have been made by Baker (1979, 1980), Kawahashi and Hosei (1989), Devenport and Simpson (1990), and other researchers. Detailed numerical studies of the horseshoe vortex systems have also been performed recently by Visbal (1991), Hung et al. (1992) and Chen and Hung (1992) for both laminar and turbulent flows at various Reynolds and Mach numbers. For laminar flows, detailed particle traces in the plane of symmetry reveals an evolution of the vortex system from a saddle point of attachment with no spiral horseshoe vortex, to a single spiral vortex, and finally to a complex flow structure with multiple spiral horseshoe vortices. On the other hand, the turbulent flow calculations indicated a quite different flow topology with the outermost singular point changes from a saddle point of attachment to a saddle point of separation.

To understand the detailed vortex system produced by the two-layer and second-moment simulations, plots of particle traces which originated from an upstream station in the plane of symmetry are shown in Fig. 2. In addition, the computed surface streamlines on the bottom plate are also plotted to provide a complete description of the three-dimensional vortical flow patterns. It is seen that the two-layer solutions incorrectly predicted a saddle point of attachment without any spiral vortex. As noted in Hung et al. (1992), this flow topology is a fundamental pattern associated with low-Re laminar, but not high-Re turbulent, horseshoe vortex systems. On the contrary, the second-moment solutions clearly displayed a spiral primary horseshoe vortex which wraps around the root of the appendage-hull junction. The helical motion of the primary horseshoe vortex creates a three-dimensional separation surface ahead and alongside the appendage. The primary separation line formed at the intersection of the three-dimensional separation surface and the bottom flat plate can be clearly seen in Fig. 2. Furthermore, the second-moment solutions also indicated the presence of a distinct shear-stress gradient line between the separation line and the leading edge. As noted in Dickinson (1986), this line delineates a region of high shear stress near the appendage from an area of lower shear outside. The shear stress gradient line wraps around the leading edge and merges with the primary separation line alongside the appendage. Both the location and shape of the calculated shear stress gradient line are in close agreement with the oil-film flow visualization reported in Dickinson (1986).

Figure 3 shows a comparison of the calculated and measured pressure distributions on the flat plate. The calculated pressures were interpolated along constant-Y lines to facilitate direct comparisons with the measurements. It is seen that the second-moment and two-layer solutions are nearly identical in the middle section of the appendage. Significant differences, however, were observed around the leading and trailing edges of the appendage. In particular, it is noted that the isotropic two-layer model considerably underpredicted the pressure peak near the trailing edge while the second-moment solutions accurately captured the pressure recovery in the tail region. A close examination of the flat-plate pressure contours shown in Fig. 4 further revealed major differences in the second-moment and two-layer pressure distributions around the leading edge of the appendage. More specifically, the second-moment solutions exhibited a distinct line of pressure bulge along the trajectory of the primary horseshoe vortices. The observed pressure bulge is obviously caused by the strong helical motion in the core region of the primary horseshoe vortex. The two-layer solution, on the other

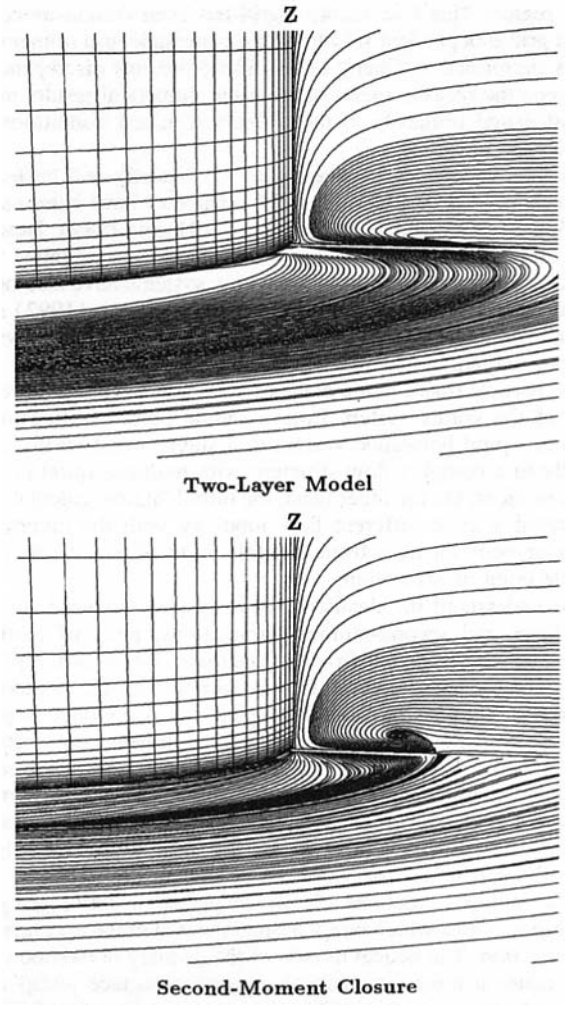

Fig. 2 Particle traces in the symmetry plane and on flat plate: (top) two-layer model, (bottom) second-moment closure

hand, predicted only a weak pressure bulge in conjunction with the secondary horseshoe vortex.

In addition to the pressure distributions and particle traces shown earlier, it is desirable to examine also the turbulent kinetic energy distributions in order to provide a more critical assessment of the isotropic eddy viscosity and second-order Reynolds stress closure models. Figure 5 shows a detailed comparison of the calculated and measured turbulent kinetic energy contours in two transverse sections, $X/C = 0.64$ and 1.50 where detailed

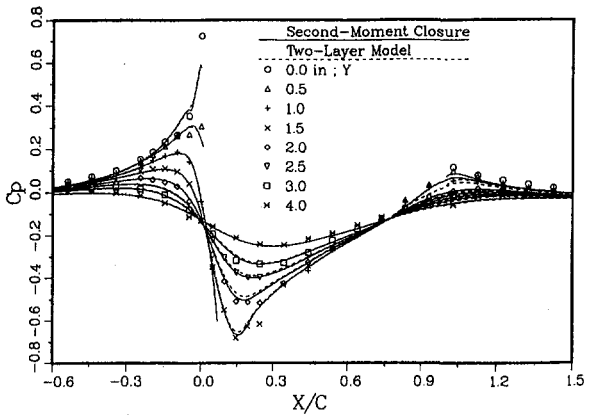

Fig. 3 Comparison of pressure distributions on flat plate

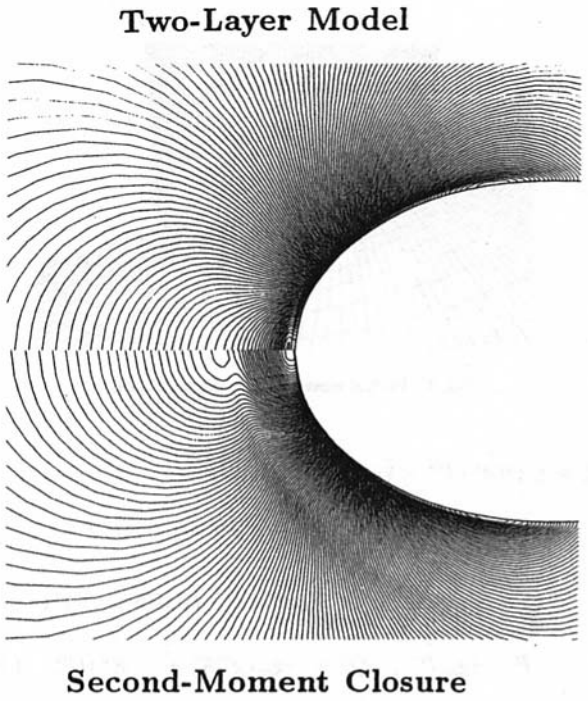

Fig. 4 Comparison of two-layer (top) and second-moment (bottom) pressure contours around the leading edge of appendage

measurements were made. This provides by far the most convincing evidence regarding the deficiencies of the $k - \epsilon$ type isotropic eddy-viscosity models. Under the isotropic eddy viscosity assumption, the generation of turbulent kinetic energy is linearly proportional to the mean flow gradient without any directional preference. While this seems appropriate for two-dimensional boundary layer flows with only one predominant flow gradient, serious problems arose when the flow is subjected to more than one predominant gradients in different directions. For the appendage/flat-plate junction considered here, the turbulent kinetic energy distributions in the flat plate boundary layer ahead of the appendage were quite well resolved by both the two-layer $k - \epsilon$ and second-moment closure models. Outside the flat plate boundary layer, $Z \geq 3.0$ in (7.6 cm), the development of appendage boundary layer flow was also well predicted by both turbulence models. Around the appendage-hull junction, however, the flow is subjected to a complex three-dimensional velocity gradient due to two distinct strain rates generated independently by two different walls. The first one being the flat plate boundary layer flow originating from far upstream, and the second is the appendage boundary layer developed from the leading edge of the appendage. Since the isotropic eddy-viscosity models cannot distinguish these two different rates of strain, an enormous amount of turbulent kinetic energy was generated along the corner of appendage and flat plate. This is particularly evident at $X/C = 0.64$ where the excessive eddy viscosity completely overpowered the primary and secondary horseshoe vortices. Because the horseshoe vortices are buried in an oncoming stream with very high turbulence intensity and low effective Reynolds number, it is not surprising that the two-layer solutions produced a laminar flow topology as shown earlier in Fig. 2.

The experiments of Dickinson (1986) indicated that the primary horseshoe vortex lies completely outside the appendage boundary layer. Two distinct regions of high turbulence level developed almost independently, one along the appendage surface, and the other following the core of the primary vortex. In addition, a third high turbulence core associated with the secondary horseshoe vortex is also clearly visible in the corner of appendage/flat-plate junction. In the two-layer solutions,

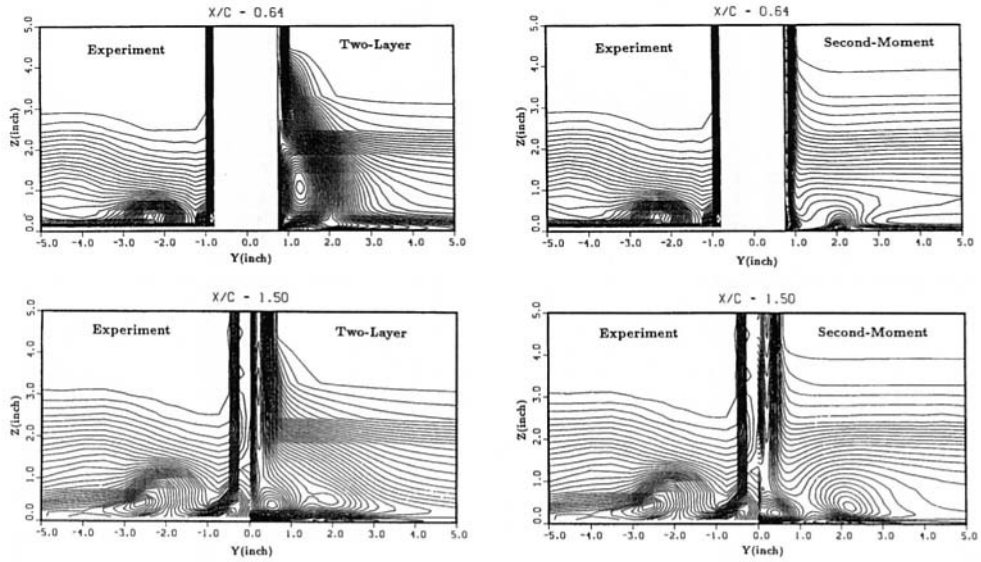

Fig. 5 Comparison of calculated and measured turbulent kinetic energy: (left) two-layer model, (right) second-moment closure

however, these three distinct regions of high turbulence intensity were merged into one high turbulence region as seen at station $X/C = 0.64$. The remnants of the primary and secondary root vortices are visible only at the last station $X/C = 1.50$. It is quite obvious that the excessive eddy viscosities produced by improper turbulence modeling assumptions are responsible for the quick dissipation of root horseshoe vortices in the two-layer solutions.

Unlike the isotropy two-layer models which failed completely to resolve anisotropic turbulence due to different rates of strain, the present Reynolds stress closure model successfully captured the separate developments of the flat-plate boundary layer, appendage boundary layer and wake, and the appendage root vortices. Furthermore, the second-moment solutions also closely predicted the size and shape of both the primary and secondary horseshoe vortices even though the strength of the primary vortex was somewhat underpredicted. In spite of some minor discrepancies between the second-moment results and the experimental data, the numerical solutions obtained here clearly demonstrated the superior performance of the Reynolds stress closure models over simpler isotropic eddy viscosity models.

In addition to the detailed mean flow and turbulent kinetic energy measurements, the experimental data also contain five of the six Reynolds stress components at all measurement stations. Comparisons have been made in Fig. 6 for all five available Reynolds stresses at $X/C = 0.93$ and 1.50 to enable a detailed examination of the effects of Reynolds stress anisotropy in the development and evolution of the appendage-hull juncture flows. It should be remarked here that the turbulence intensities $\sqrt{\overline{uu}}$ and $\sqrt{\overline{vv}}$ are Cartesian components which, in general, do not align with the tangents of the appendage surface. Consequently, the effects of Reynolds stress anisotropy may be skewed for the station $X/C = 0.93$ ahead of the appendage trailing edge. Nevertheless, both the measured and calculated turbulence intensities clearly exhibit a significant level of anisotropy with $\sqrt{\overline{uu}} > \sqrt{\overline{vv}} > \sqrt{\overline{ww}}$. It is quite obvious that the flat plate has significantly inhibited the turbulence level $\sqrt{\overline{ww}}$ in the z-direction. Similarly, the presence of the appendage has led to a reduction of $\sqrt{\overline{vv}}$ which is approximately normal to the appendage wall in the tail region. The predicted shear stresses $\overline{uv}$ and $\overline{uw}$ are also in very good agreement with the corresponding measurements. The slight underprediction of the turbulence intensities and shear stresses are most likely due to the wind-tunnel blockage effects which were not modeled in the present study.

Conclusions

The multiblock RANS method of Chen and Korpus (1993) has been generalized to incorporate a practical near-wall second-order Reynolds stress closure models for the calculation of turbulent, incompressible flows. The numerical results obtained for appendage-hull juncture flows clearly demonstrated the superiority of the present second-order Reynolds stress closure models over simpler isotropic eddy viscosity models. In general, the second-moment solutions exhibit a significant level of anisotropy in the normal components of Reynolds stress tensor. Near a solid boundary, the Reynolds stress component perpendicular to the wall is significantly reduced below the averaged isotropic level as the solid surface inhibits the turbulence energy transfer into fluctuations normal to the wall. The anisotropic response of Reynolds stresses in the streamwise and normal directions has led to the attenuation of turbulence intensity on convex curvatures, and the amplification of turbulence level along concave walls. The same Reynolds stress anisotropy is also responsible for the augmentation of shear stresses and turbulence intensity in the core region of the horseshoe vortices generated by appendage-hull junctions.

Although the isotropic eddy viscosity models appeared to be quite useful for boundary layer flows with only one predominant flow gradient, the applications of these models for complex three-dimensional vortical flows involving several predominant flow gradients must be carefully scrutinized. For appendage/flat-plate junction flows considered here, the two-layer eddy viscosity model failed completely to distinguish the two distinct strain rates generated independently by the upstream flat plate boundary layer and by the newly developed appendage boundary layer. On the contrary, the second-moment calculations successfully resolved the detailed turbulence structures associated with the developments of the appendage boundary layer, the formation of the spiral primary horseshoe vortex and the corner secondary horseshoe vortex, and the evolution of both vortices around the appendage/flat-plate junction. With some further improvements in the Reynolds stress closures, the method can be readily generalized to study the complex interaction between the boundary layers, wakes and vortex systems around complex three-dimensional geometries.

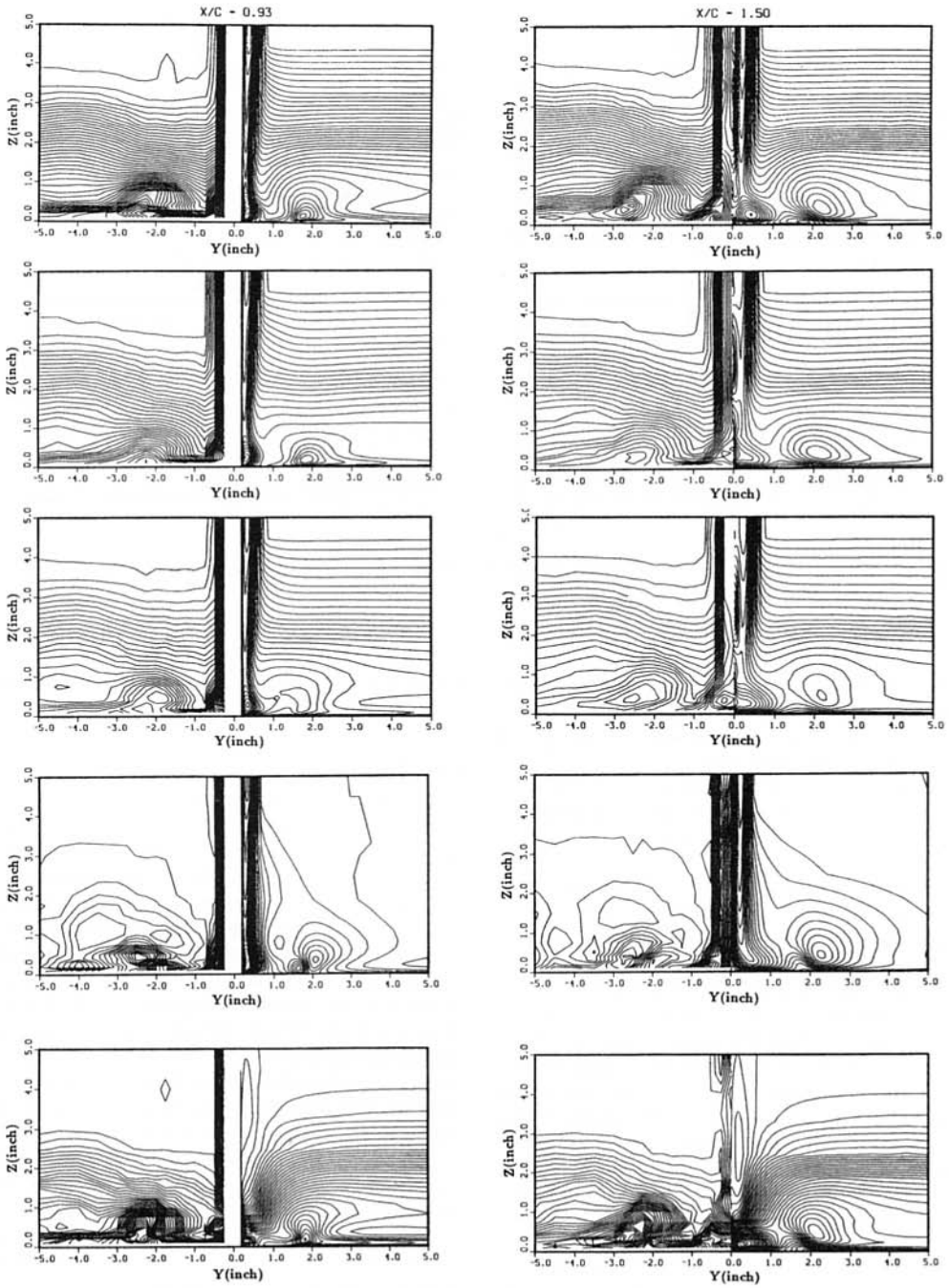

Fig. 6 Calculated and measured turbulence intensities and shear stresses: (left) $X/C = 0.93$, (right) $X/C = 1.50$

Acknowledgments

This research was sponsored by the Office of Naval Research (ONR) and the Submarine Technology Program, Underwater Warfare Program Office of Advanced Research Project Agency (ARPA), under Contract N00014-91-J-4048. The author appreciated the support of ONR Program Manager, Mr. James A. Fein, and ARPA Program Manager, Mr. Gary Jones, during the course of this research. All the computations were performed on the CRAY C90 and YMP of Cray Research Inc. at Eagen, Minnesota. The author is grateful to Cray Research Inc. and Mr. Chris Hempel for the use of these computing resources.

References

Baker, C. J., 1979, "The Laminar Horseshoe Vortex," *Journal of Fluid Mechanics,* Vol. 95, Part 2, pp. 347–367.

Baker, C. J., 1980, "The Turbulent Horseshoe Vortex," *Journal of Wind Engineering and Industrial Aerodynamics,* Vol. 6, No. 11-12, pp. 9–23.

Chen, C. L., and Hung, C. M., 1992, "Numerical Study of Juncture Flows," *AIAA Journal,* Vol. 30, No. 7, pp. 1800–1807.

Chen, H. C., 1992, "Calculations of Submarine Flows by a Second-Moment RANS Method," COE Report No. 325, Texas A & M University Research Foundation, College Station, TX.

Chen, H. C., 1993, "Calculations of Submarine Flows by a Multiblock Reynolds-Averaged Navier-Stokes Method," *Engineering Turbulence Modeling and Experiments 2,* W. Rodi and F. Martelli, eds., Elsevier Science Publishers B.V., pp. 711–720.

Chen, H. C., 1994, "Assessment of Reynolds Stress Closure Models for Submarine and Ship Flows," COE Report No. 333, Texas A & M University Research Foundation, College Station, TX.

Chen, H. C., 1995, "Studies of Submarine Flows By a Second-Moment Closure," *Journal of Engineering Mechanics,* to appear.

Chen, H. C., and Korpus, R., 1993, "A Multi-block Finite-Analytic Reynolds Averaged Navier-Stokes Method for 3D Incompressible Flows," ASME FED-Vol. 150, *Individual Papers in Fluid Engineering,* pp. 113–121.

Chen, H. C., Lin, W. M., and Weems, K. M., 1994, "Interactive Zonal Approach for Ship Flows Including Viscous and Nonlinear Wave Effects," *Proceedings of the 6th International Conference on Numerical Ship Hydrodynamics,* V. C. Patel and F. Stern, eds., National Academy Press, Washington, D.C., pp. 341–363.

Chen, H. C., and Patel, V. C., 1988, "Near-Wall Turbulence Models for Complex Flows Including Separation," *AIAA Journal,* Vol. 26, pp. 641–648.

Chen, H. C., and Patel, V. C., 1989, "The Flow Around Wing-Body Junctions," *Proceedings of the 4th Symposium on Numerical and Physical Aspects of Aerodynamic Flows,* Jan., Long Beach, CA, pp. 16–19.

Daly, B. J., and Harlow, F. H., 1970, "Transport Equations in Turbulence," *The Physics of Fluids,* Vol. 13, pp. 2634–2649.

Devenport, W. J., and Simpson, R. L., 1990, "Time-Dependent and Time-Averaged Turbulence Structure Near the Nose of a Wing-Body Junctions," *Journal of Fluid Mechanics,* Vol. 210, pp. 23–55.

Dickinson, S. C., 1986, "An Experimental Investigation of Appendage-Flat Plate Junction Flow, Volume I: Description, Volume II: Elliptical Nose Appendage Data Base," DTNSRDC-86/052, David Taylor Research Center, MD.

Hung, C. M., Sung, C. H., and Chen, C. L., 1992, "Computation of Saddle Point of Attachment," *AIAA Journal,* Vol. 30, No. 6, pp. 1561–1569.

Kawahashi, M., and Hosai, K., 1989, "Beam-Sweep Laser Speckle Velocimetry," *Experiments in Fluids,* Vol. 8, No. 1/2, pp. 109–111.

Launder, B. E., 1989, "Second-Moment Closure: Present . . . and Future?" *International Journal of Heat and Fluid Flow,* Vol. 10, No. 4, pp. 282–300.

Lumley, J. L., 1980, "Second-Order Modeling of Turbulent Flows," *Prediction Methods for Turbulent Flows,* W. Kollmann, ed., Hemisphere, NY, pp. 1–31.

Pierce, F. J., and Harsh, M. D., 1988, "The Mean Flow Structure Around and Within a Turbulent Junction or Horseshoe Vortex-Part II. The Separated and Junction Vortex Flow," ASME JOURNAL OF FLUIDS ENGINEERING, Vol. 110, pp. 415–423.

Shima, N., 1988, "A Reynolds-Stress Model for Near-Wall and Low-Reynolds-Number Regions," ASME JOURNAL OF FLUIDS ENGINEERING, Vol. 110, pp. 38–44.

So, R. M. C., Lai, Y. G., Zhang, H. S., and Hwang, B. C., 1991, "Second-Order Near-Wall Turbulence Closures: A Review," *AIAA Journal,* Vol. 29, No. 11, pp. 1819–1835.

Speziale, C. G., 1991, "Analytical Methods for the Development of Reynolds-stress Closure in Turbulence," *Annual Review of Fluid Mechanics,* Vol. 23, pp. 107–157.

Speziale, C. G., Sarkar, S., and Gatski, T. B., 1991, "Modelling the Pressure-Strain Correlation of Turbulence: An Invariant Dynamical Systems Approach," *Journal of Fluid Mechanics,* Vol. 227, pp. 245–272.

Sung, C. H., and Yang, C. I., 1988, "Validation of Turbulent Horseshoe Vortex Flows," *Proceedings of the 17th ONR Symposium on Naval Hydrodynamics,* The Hague, The Netherlands, pp. 241–255.

Visbal, M. R., 1991, "Structure of Laminar Juncture Flows," *AIAA Journal,* Vol. 29, No. 8, pp. 1273–1282.

M. J. Donnelly

O. K. Rediniotis

S. A. Ragab

D. P. Telionis

Department of Engineering Science and Mechanics, Virginia Polytechnic Institute and State University, Blacksburg, VA 24061-0219

The Interaction of Rolling Vortices With a Turbulent Boundary Layer

(Data Bank Contribution)*

Laser-Doppler velocimetry is employed to measure the periodic field created by releasing spanwise vortices in a turbulent boundary layer. Phase-averaged vorticity and turbulence level contours are estimated and presented. It is found that vortices with diameter of the order of the boundary layer quickly diffuse and disappear while their turbulent kinetic energy spreads uniformly across the entire boundary layer. Larger vortices have a considerably longer life span and in turn feed more vorticity into the boundary layer.

1 Introduction

In a variety of engineering applications, one encounters the interaction of coherent vortical structures with a turbulent boundary layer. Vortical structures comparable in size or larger than the thickness of the boundary layer could be generated downstream of obstructions which induce separation. Dynamic motions of solid surfaces with sharp edges like propeller blades or impeller fins generate free shear layers which roll up and form vortical structures. Such structures again may interact with a turbulent boundary layer.

Researchers are interested in the effects of vortical structures on the wall shear stress, the heat transfer, the turbulent characteristics of the boundary layer, or the interaction of the external structures with the natural organization of the boundary layer. In this paper we will refer to such initially coherent vortical structures as "vortices." These vortices are far from ideal and soon lose their coherence but one can easily trace their location. Ideal vortices are the vortices with a circumferential velocity component varying inversely with distance from their center, in a frame of reference attached to the center. There is no rigorous definition for the "coherence" of a vortex but many authors imply by this term a well-ordered distribution of vorticity, continuously decreasing from the center of the vortex.

Broadly speaking, studies of the interaction of vortices with a turbulent boundary layer can be grouped into two categories: (i) those which focus on the effect of the externally imposed vortical structure on the turbulent boundary layer and (ii) those which explore the effect of the turbulent boundary layer on the organization of the vortex. This distinction is usually dictated by the interest in a specific engineering application. The problem of course is highly nonlinear and the two effects are strongly coupled. In the present paper we present information on the temporal development of both the turbulence characteristics and the organized character of the disturbing vortex.

The effects of a variety of disturbances imposed on a turbulent boundary layer have been investigated in the past. A long line of investigators introduced axial vortices ("streamers") in turbulent boundary layers. One of the initial contributions is due to Shabaka et al. (1985). A more recent example is the work of Littell and Eaton (1991) who generated a disturbance by rapidly pitching a half delta wing. Three-dimensional disturbances can also be introduced locally. Makita et al. (1989) create artificial horse-shoe vortices in their turbulent boundary layers. Disturbances can be introduced in a uniform spanwise direction to create structures with spanwise vorticity. Such vortical structures are commonly known as "rollers." Rollers can be generated by pitching airfoils in a free stream or by periodically lifting spanwise fences on a wall. A number of investigators have employed pitching fences to study the structure of unsteady separation (Francis et al., 1979; Reisenthel et al., 1985; Consigny et al., 1984; Nagib et al., 1985). In another line of work, disturbances were created in a free stream in order to study their interaction with blades further downstream (Poling and Telionis, 1986; Poling et al., 1988; Booth and Yu, 1986; Wilder et al., 1990). More recently, careful investigations of the interaction of rollers with turbulent boundary layers were carried out (Nelson et al., 1990; Kothmann and Pauley, 1992; Macrorie and Pauley, 1992). The present contribution belongs to this category.

Nelson et al. (1990) lift a fence from the floor of a flat plate on which a turbulent boundary layer has developed. They then measure periodic velocity fields by ensemble averaging LDV data. Pauley and his co-workers (Kothmann and Pauley, 1992; Macrorie and Pauley, 1992) instead pitch a small airfoil upstream of the leading edge of a flat plate and allow the disturbances to enter the boundary layer which grows downstream. In the work reported here we create a disturbance in a manner very similar to the one employed by Nelson et al. (1990).

Nelson et al. (1990) employ a fence with a chordlength approximately half of the boundary layer thickness. As a result their vortices are embedded in their boundary layers. A very interesting result for this choice of parameters is that the vortex disintegrates very quickly and completely disappears only a few chordlengths downstream of the fence. In this paper, we report on experiments conducted with fence chordlengths comparable with the boundary layer thickness and we confirm the fact that disturbances created in this way have a very short life span. We also report on vortices that are about twice and three times as large as the thickness of the boundary layer and provide evidence that such vortices can be sustained for longer distances downstream of the disturbing blade.

Shear flows developing away from solid surfaces have a nearly two-dimensional structure. On the other hand, turbulence in a boundary layer developing over a solid wall is dominated by three-dimensional structures. The problem of interaction between an artificially created two-dimensional disturbance and a boundary layer is therefore a complex problem. In a future publication we will report on the three-dimensional character of such flows.

* Data have been deposited in the JFE Data Bank. To access the file for this paper, see instructions on p. 740 of this issue.

Contributed by the Fluids Engineering Division for publication in the JOURNAL OF FLUIDS ENGINEERING. Manuscript received by the Fluids Engineering Division June 27, 1994; revised manuscript received September 1, 1995. Associate Technical Editor: F. M. White.

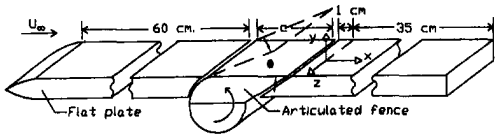

Fig. 1 Schematic of the flat plate including the embedded articulated fence

2 The Experimental Rig

A turbulent boundary layer was allowed to develop on a flat plate inserted in the test section of the Engineering Science and Mechanics (ESM) water tunnel. This facility has a test section of 25.4 cm × 30.5 cm and can provide flow speeds of up to 3 m/sec. at turbulence levels ranging from 0.6 to 1.5 percent. A detailed description of this facility and its calibration is included in Koromilas and Telionis (1980) and Mathioulakis and Telionis (1987). An articulated fence can be lifted 60 cm downstream of the leading edge of the plate to generate a local disturbance (Fig. 1). The origin of the coordinate system, $x = 0$, was positioned on the plate, 10 mm downstream of the trailing edge of the fence.

Measurements were carried out with laser-Doppler velocimetry (LDV). A TSI, three-beam, two-component LDV system was employed. Two of the beams were shifted at 60 MHz and 40 MHz, respectively. It was thus possible to separate the two components by electronic filters and therefore employ only one photomultiplier. The original system described in Mathioulakis and Telionis (1987) was capable of obtaining two velocity components in planes parallel to the side walls of the tunnel. A system of coordinates was defined with its x-direction aligned with the freestream and the y direction normal to the plate, as shown in Fig. 1. The design of the traversing system allowed traversing in the directions of x and y. This design was dictated by the need to study nominally two-dimensional flows. In the present effort we employ a modified system which allows traversing in the spanwise direction as well.

A large optical bench and a more powerful laser (35 mW, Helium-Neon) are now employed. The TSI design was modified to mount the laser next to the train of optics instead of underneath it. The long side of the optical bench and therefore the direction of the optical beam was positioned normal to the axis of the test section. A mirror tower was again employed for traversing. The tower is now mounted on a precision sliding table to allow traversing in the spanwise direction. The position of the upper mirror of the tower is controlled by a lead screw, thus facilitating traversing in the y direction. A second set of mirrors was also mounted on traversing brackets and the system allows the beams to be directed either from the side wall of the tunnel or from the ceiling of the tunnel. In this way, all three components of the velocity can be obtained, although not all simultaneously.

Traversing is achieved by two stepping motors and monitored by two linear variable differential transducers (LVDT). The latter provide an independent analog feedback to confirm the accurate positioning of the measuring volume. In this way, two-dimensional grids along planes xy or yz can be traversed. The accuracy in positioning the measuring volume is 0.05 mm. Phase referencing and instantaneous fence inclination information is obtained through optical methods. The optical encoder used has an accuracy of 0.1 deg.

The entire operation is controlled by two serially communicating laboratory computers which are programmed to operate the pitching mechanism and the stepping motors, collect the information on the instantaneous angle of the fence inclination, perform the LDV data acquisition, reduce the data and transfer them to a mainframe IBM 3090 for calculations and plotting. The entire data acquisition process is fully automated.

In our initial design, lifting of the fence generated a slot which prevented the formation of a wake downstream of the fence by supplying fluid from the other side of the plate. The flow thus entering our field contained vorticity generated on the other side of the plate which has the opposite sign. It was decided that the real-life situation of large separated bubbles which are convected with the flow can be better simulated if the fence lifts out of a cavity. This design is not without a disadvantage, because when the fence returns to its initial position it ejects the fluid in the cavity and thus imparts some momentum to the vortex generated by the fence. To minimize this effect, the cavity was filled with rubber foam.

Three fences were employed with chordlengths c equal to 12.7, 25.4, and 38.1 mm. The fences were pitched through a four-bar linkage by a motor which in turn was controlled by one of the laboratory computers. The schedule of their motion is shown in Fig. 2. The fences were lifted sharply to an angle of 28 deg and then returned to their initial position, flush with the plate, and remained there for a short period, in order to allow the flow to settle again to steady-state, turbulent boundary-layer flow. The period of the fence's motion was $\tau = 3.33$ s which is equivalent to a dimensionless time of 925 if the momentum thickness, θ, and the freestream velocity are used for nondimensionalization. Dimensionless times $T/\Delta T$, where $\Delta T = \tau/100$, were defined and all the results are presented here in terms of this time parameter. In other words, the period is divided into one hundred time units. As shown in Fig. 2, the fences are lifted within 10 or 20 time units, returned to their initial position after at most 50 time units and remain flush with the plate for the duration of the period.

An LED (light-emitting diode) sensor was employed to provide a trigger. This allowed us to conditionally average the data. The average and RMS of the fluctuation of a quantity g was thus calculated according to

$$\bar{g}(t) = \frac{1}{N}\sum_{i=1}^{N} g_i(t) \tag{1}$$

$$g_{\text{rms}}(t) = \left[\frac{1}{N}\sum_{i=1}^{N}[g_i(t) - \bar{g}(t)]^2\right]^{1/2} \tag{2}$$

where $g_i(t)$ is the ith realization. Note that the quantity $g_{\text{rms}}(t)$ is a statistical measure of the deviation of the quantity $g(t)$ from its average at a time t. We also obtained the ensemble average of the sum of the velocity component fluctuations. We were thus able to obtain the phase-averaged value of the turbulent kinetic energy

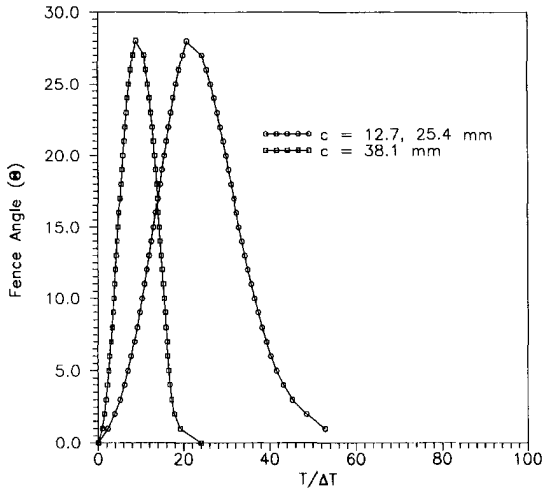

Fig. 2 Schedule of the fence motion (Uncertainty in $\theta = \pm 0.5$ deg)

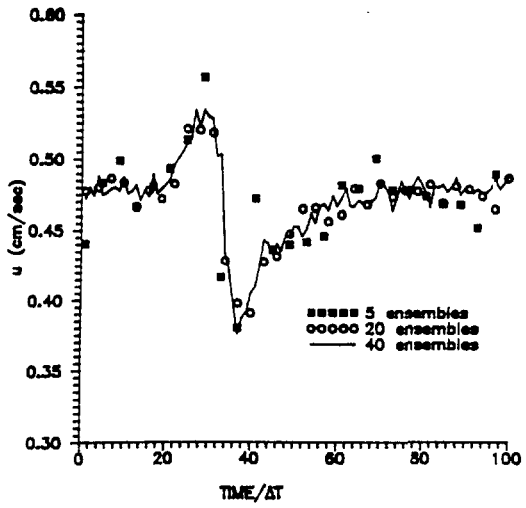

Fig. 3 Effect of the number of ensembles per cycle on the waveform

$$q(t) = \frac{1}{N}\sum_{i=1}^{N}[u_i'^2(t) + v_i'^2(t)] \tag{3}$$

where $u_i'(t)$ and $v_i'(t)$ are the fluctuations of the two components of the velocity. An example of waveforms obtained within a period by employing 5, 20, or 40 ensembles is shown in Fig. 3. These data were obtained at $x/c = 1.0$ and $y/\delta = 0.5$ behind the smallest fence. They indicate the scatter of the data and the character of the waveform produced by a pitching fence.

Results and Discussion

Experiments were conducted at a free-stream velocity of 51 cm/s. The boundary layer was allowed to freely transition to a fully turbulent state. Data were obtained in the center plane of the tunnel and along normals to the plate. The boundary-layer thickness based on 99 percent recovery of the free-stream velocity and the momentum thickness were measured at $\delta = 14.0$ mm and $\theta = 1.837$ mm. The latter value corresponds to a Reynolds number of 913, while the Reynolds number based on the distance from the leading edge was $\mathrm{Re}_L = U_\infty L/\nu = 2.98 \times 10^5$. In order to confirm the canonical nature of the turbulent boundary layer, the boundary layer thickness was calculated according to the empirical formula (White, 1974)

$$\frac{\delta}{\bar{x}} = \frac{0.16}{\mathrm{Re}_x^{1/7}} \tag{4}$$

where $\bar{x}$ is the distance from the leading edge of the plate. At the origin of measurements, this yields a boundary layer thickness of 14.6 mm, which is very near the measured value of 14.0 mm. The quantities $\bar{u}$, u_{rms}, and v_{rms} were obtained for steady flow and compared to earlier measurements to confirm the reliability of the method (not displayed here due to lack of space). The same quantities averaged over cycles of the disturbance imposed display similar trends with those of undisturbed flow, except that now the fluctuating components are approximately equal in magnitude, and the scatter is somewhat enhanced, requiring larger number of ensembles to arrive at converged profiles.

Data were obtained on 50 points along normals to the plate, along 10 stations for the 25.4 mm fence and 11 stations for the 12.7 mm and the 38.1 mm fences. The size of the fence and the approximate size of the vortical disturbance are of the same order. All distances were normalized with the chordlength of the fence. These data correspond to the same oncoming turbulent boundary layer. The thickness of the boundary layer is therefore different if expressed in terms of the chord lengths of the plates.

Vorticity was calculated in terms of the measured velocity components. For an undisturbed boundary layer, the term $\partial u/\partial y$ is much larger than the term $\partial v/\partial x$. However, in the present case, this assumption is no longer valid in the presence of a large vortical disturbance. Our spacing is very fine in the y direction, so the term $\partial u/\partial y$ can be accurately calculated, but the estimation of the term $\partial v/\partial x$ may involve considerable error. We estimated that the error in the calculation of vorticity may be as high as 30 percent of its corresponding maximum value. Nevertheless, we believe that vorticity thus calculated offers insight into the physics of the problem and for this reason, in the following figures we superimposed vorticity contours on the velocity vector fields.

Some understanding of the phenomena under consideration was gained by flow visualization. This was accomplished simply by releasing dye a little upstream of the plate. For very low speeds, the boundary layer was laminar and the dye streak was well defined. The motion of the dye was captured in a video tape. In Fig. 4 we display a few instantaneous frames of visualization which indicate that a strong and tightly coiled vortex develops behind the fence. The vortex is then released but the dye quickly loses its coherence a few chordlengths downstream of the plate. It is not clear from the visualization if this is due to turbulence or to the fact that the vortex itself disintegrates.

In Fig. 5 we present ensemble-averaged velocity vectors downstream of the 12.7 mm fence, corresponding to six phase

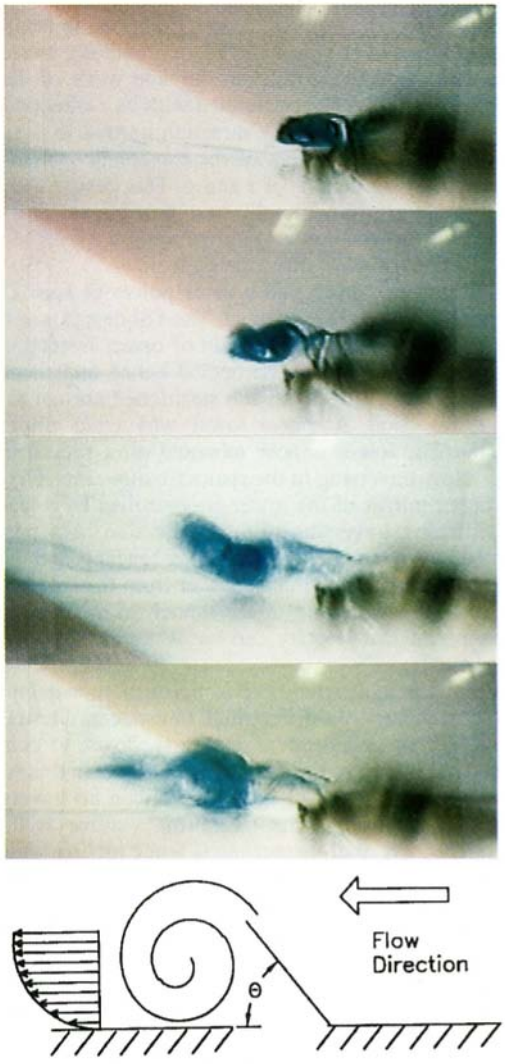

Fig. 4 Flow visualization of vortex interaction

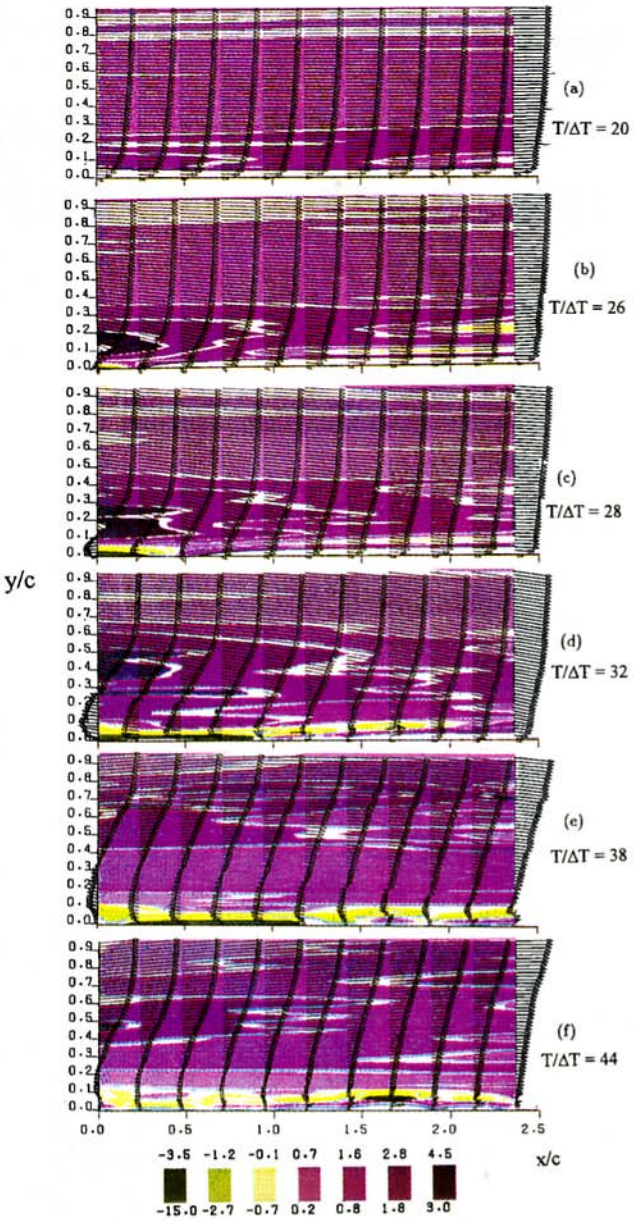

Fig. 5 Velocity vectors and velocity contours for chordlength c = 12.7 mm

angles, or equivalently six instants within the period of the motion. Superposed on these fields are vorticity contours. The boundary layer thickness in terms of dimensionless units based on the chord of the fence is approximately equal to 1.1. The height of the frame of data therefore is a little less than the thickness of the boundary layer. In the first frame, the disturbance has not yet entered the domain of observation. The field corresponds to the undisturbed turbulent boundary layer. In Fig. 5(b) the presence of the vortex is evident from the larger magnitude of vorticity as well as the appearance of reversed flow. Note that vorticity of the opposite sense is present right next to the wall. In Fig. 5(c) we observe that the vortex is moving more clearly into the domain of observation and the opposite-sign vorticity is more evident. Figure 5(d) corresponds to a dimensionless time of 32 for which the projected height of the fence is about 20 percent of its maximum. At this time, the disturbance on the velocity field has propagated over the entire domain of observation. However, the region with elevated vorticity does not propagate any further. On the other hand, vorticity of the opposite sign is creeping downstream at the bottom of the boundary layer. In the frame 5e, which corresponds to time 38, we observe that the vorticity disturbance has practically disappeared but the reverse flow region is well-defined and extends beyond the domain of observation.

A good indication of the location of the center of the disturbance is the slope of the velocity vectors on the upper region of the domain of measurement. In the undisturbed flow, the directions of the velocity vectors are very nearly parallel to the wall. As the vortex enters this domain, the velocity vectors above its center slope upward and downward, upstream and downstream of its center, respectively. Figure 5 thus indicates that the vortex practically disintegrates by the time its center propagates to a dimensionless distance of about 1.0. The peak vorticity value is drastically reduced, the contours of vorticity are disconnected, disorganized and spread to an area much larger than originally occupied by the vortex. Moreover, flow reversal spreads to a considerable distance downstream and although the influence is weak, it covers the entire domain at $T/\Delta T = 44$.

At $T/\Delta T = 38$, the disturbance takes on the appearance of recirculating flow behind a backward facing step, because all velocity vectors are nearly parallel to the wall and the magnitude of the backward flow velocities is rather small. This is only reminiscent of the flow over an obstacle, because the projection of the fence normal to the wall by this time does not extend more than 0.05 units above the wall. Finally, in Fig. 5(f) we observe that the velocity is further reduced along the entire field of measurement. This disturbance appears more like a dead-fluid region. And yet, the secondary vorticity survives intact and continues propagating downstream. Apparently, the vortex disintegrates before it propagates more than one chordlength downstream of the fence. This is in qualitative agreement with the results of Nelson et al. (1990) who also examined the case of a vortex comparable in size with the thickness of the boundary layer.

Next we considered the case of a vortex approximately twice as large as the thickness of the boundary layer, generated by a fence with a chordlength equal to 25.4 mm. These results are not displayed here due to lack of space. A sequence of frames similar to Fig. 5 indicates that the events are quite similar to the events with the small vortex. Vorticity is considerably dispersed and by the time $T/\Delta T = 38$, vorticity contours do not indicate any coherence of a vortex. However, vorticity levels are considerably larger than the vorticity normally contained in a turbulent boundary layer.

Finally, we consider a fence with a chordlength of c = 38.1 mm. In the results presented in Fig. 6, the boundary layer thickness corresponds to about 0.3 length units. The vortex now penetrates much further downstream into the domain of measurement. The net amount of vorticity decreases with time. The velocity vectors in Fig. 6(d) indicate that while on the left the flow is moving to the right all along the width of the domain, further downstream, there exists a recirculating region. The vortex therefore retains its character while convecting downstream. Notice also by comparison with Fig. 5(e) that for the same time, the large vortex drifts much faster downstream than the small vortex, but its extent is constrained because the relative duration of the fence deployment is much shorter.

Only two components of the velocity were obtained here. Moreover, the data were conditionally averaged. It is therefore not possible to track the development of this three-dimensional vortical field in space and time. We offer here a physical picture of the phenomena observed based only on the limited data and the analytical formulations that govern vorticity transport.

The vorticity disturbance is created in our experiments in the form of straight vortex lines that are normal to the oncoming stream. The turbulent boundary layer though is dominated by random disturbances with a strong three-dimensional character which includes axial vorticity and locally swirling motions. As

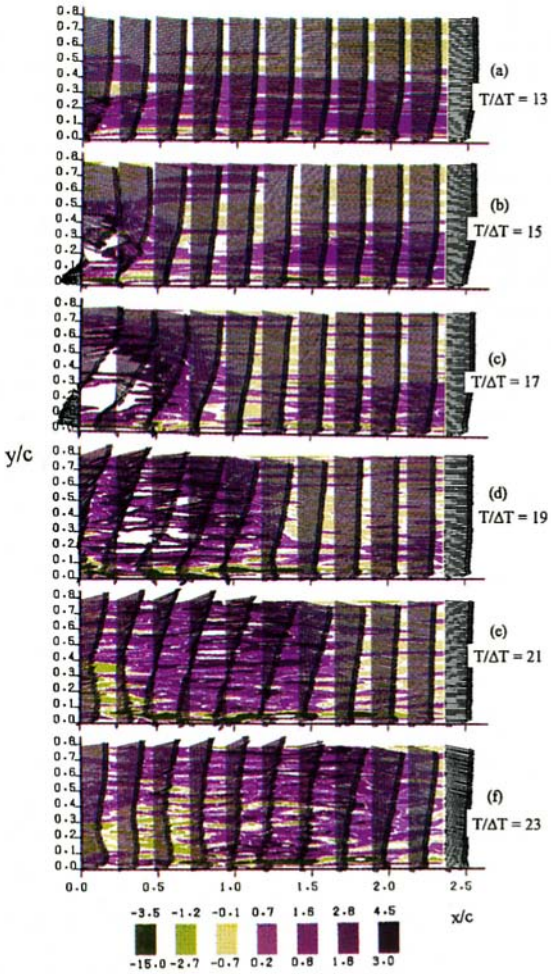

Fig. 6 Velocity vectors and vorticity contours for chordlength c = 38.1 mm

a result, the disturbance vortex lines which are convected with the flow stretch locally in the downstream direction. This effect alone reduces the component of the vorticity which we measure. It is also possible that with great distortions of the vortex lines, vorticity disconnects and reconnects to form vortex rings (Kida and Takaoka, 1994) of which only cross-sections we capture by our measurement technique. These three-dimensional structures will bring vortex filaments of opposite sense in close proximity and therefore will contribute to vorticity annihilation due to cross-diffusion by the mechanism described by Morton (1984) and later calculated by Kida et al. (1991). Turbulent diffusion is probably also responsible for the overall reduction of the measured levels of vorticity, because it transports vorticity outside the measuring domain, and also cascades it to smaller scales which are lost during our ensemble averaging procedure.

To examine more carefully the character of the disturbance, we plotted in Fig. 7 the temporal variation of the u-component of the velocity at different elevations and x-stations. If an ideal vortex is approaching a certain station, one would expect the velocity to increase above the center of the vortex and decrease below it. For an ideal vortex, the deviation from the undisturbed value should be the largest nearest the center. But if the vortex has a core with uniform vorticity, then within the core, the disturbance should be increasing with distance from the center. It appears from Fig. 7(a) that the 12.7 mm fence creates a disturbance of the latter case, therefore a vortical core exists. In fact, we notice that the increase of the velocity at higher elevations is much smaller than the decrease of the velocity below it. Further downstream, at $x/c = 1.417$ the flow appears much more like a wake rather than a vortical disturbance. That is, there is no acceleration above the disturbance but considerable deceleration below it, in agreement with our earlier observation.

A larger vortex displays a more pronounced increase of the velocity above its center as shown in Fig. 8(a), but the general trend is quite similar in character. Of interest here is also the appearance of a secondary structure which trails the primary vortex. This is evident by the following behavior. At low eleva-

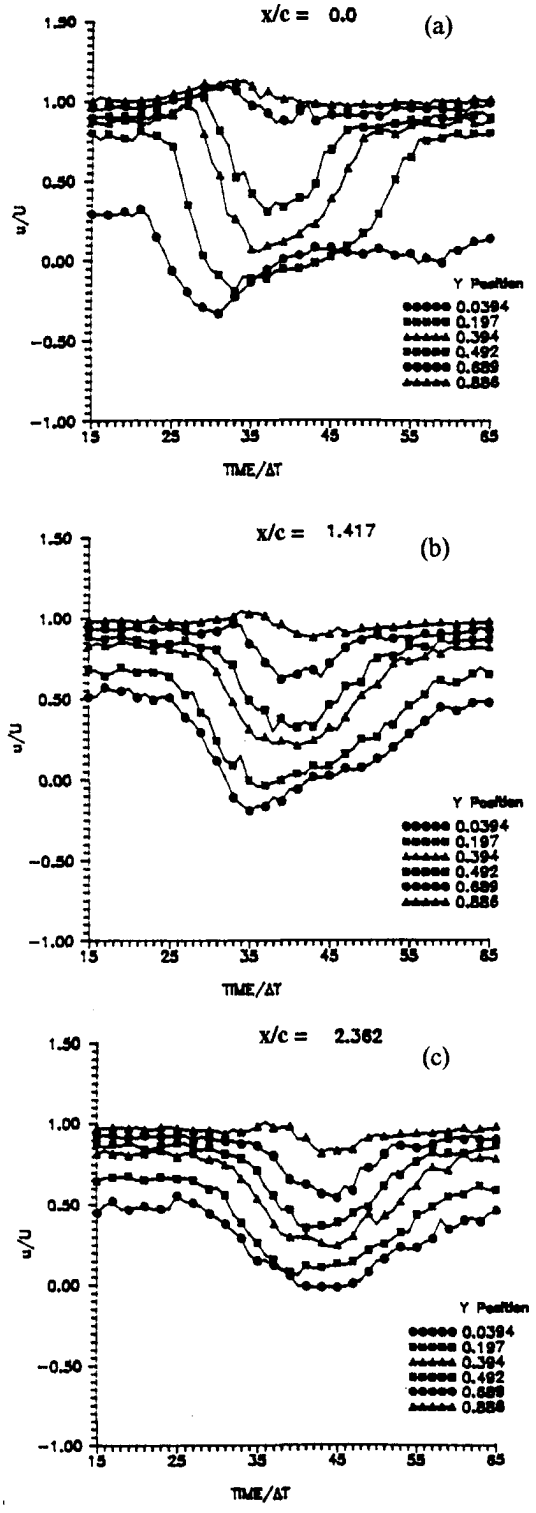

Fig. 7 Temporal variation of the u-component of velocity for chordlength c = 12.7 mm (Uncertainty in u/U = ±0.27)

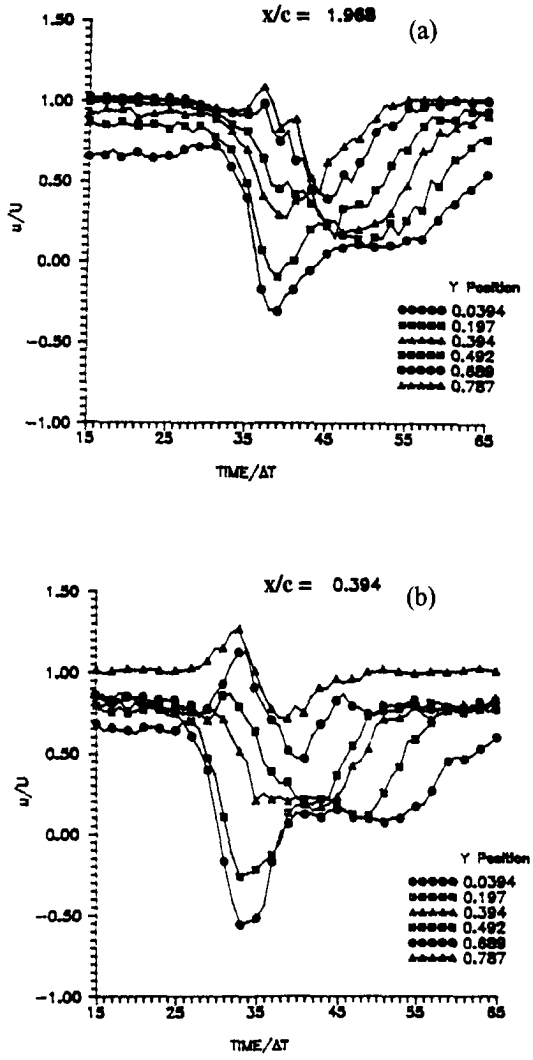

Fig. 8 Temporal variation of the u-component of velocity for chordlength c = 25.4 mm (Uncertainty in u/U = ±.027)

tions, one would expect a decrease followed by an increase to the undisturbed value. Instead we observe in Fig. 8(a) that the velocity at y = 0.0394 decreases first, regains some magnitude, but then decreases again for a time as long as 55 units. In Fig. 8(b) we observe that the behavior is again reminiscent of a wake rather than a disturbing vortex. However, it is significant to note that now the velocity near the wall reverses its direction at distances much further downstream than in the case of the small fence.

Useful information is also contained in the temporal variation of turbulent kinetic energy. Turbulent kinetic energy contours were constructed and a few representative frames are presented in Fig. 9. In the first frame we observe the levels of turbulent kinetic energy normally distributed in a steady turbulent boundary layer. This quantity decreases monotonically with distance from the wall and is independent of the axial distance. As the vortex enters the domain of measurement (Figs. 9(b) and (c)) a region of increased turbulent kinetic energy appears which coincides approximately with the region of high vorticity (see Fig. 7). By the time $T/\Delta T$ = 32, the high intensity turbulence level has spread across the entire field. Even though the coherence of the vorticity is by now virtually eliminated, the turbulent kinetic energy remains elevated and the distribution almost uniform across the entire boundary layer.

Turbulent kinetic energy for the largest fence, c = 38.1 cm is displayed in Fig. 10. The bulk of the turbulent energy which enters the domain and drifts downstream seems to be trailing the center of the disturbance. For example, at the time $T/\Delta T$ the center of gravity of the turbulent kinetic energy appears to be a little upstream of x/c = 0.5 but in the corresponding frame of Fig. 9, the center of the vortex is approximately at x/c = 0.7. It therefore appears that the vortex is lifting turbulence from the boundary layer. And yet, this mechanism could not account for the total amount of turbulence contained in the vortical structure. It therefore seems that vorticity in this vortical structure loses its organization and breaks down into turbulence. Eventually, the turbulent energy diffuses and passes out of the domain of measurement.

Conclusions

This experimental study indicates that a coherent spanwise vortex suddenly planted in the middle of a fully-developed turbulent boundary layer quickly loses its coherence if its size is comparable to the thickness of the boundary layer. At the beginning, up to two chordlengths downstream of its creation, it retains the character of a vortex with a viscous core. By the time the vortex drifts to three chordlengths downstream, its behavior is reminiscent of a wake behind a backward facing

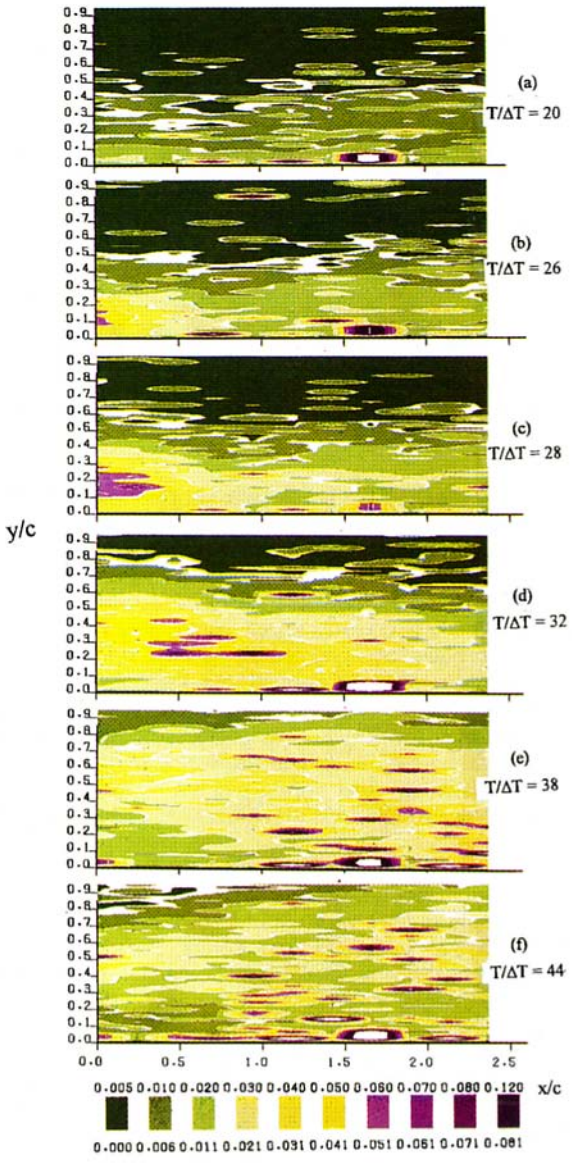

Fig. 9 Turbulent kinetic energy contours for chordlength c = 12.7 mm

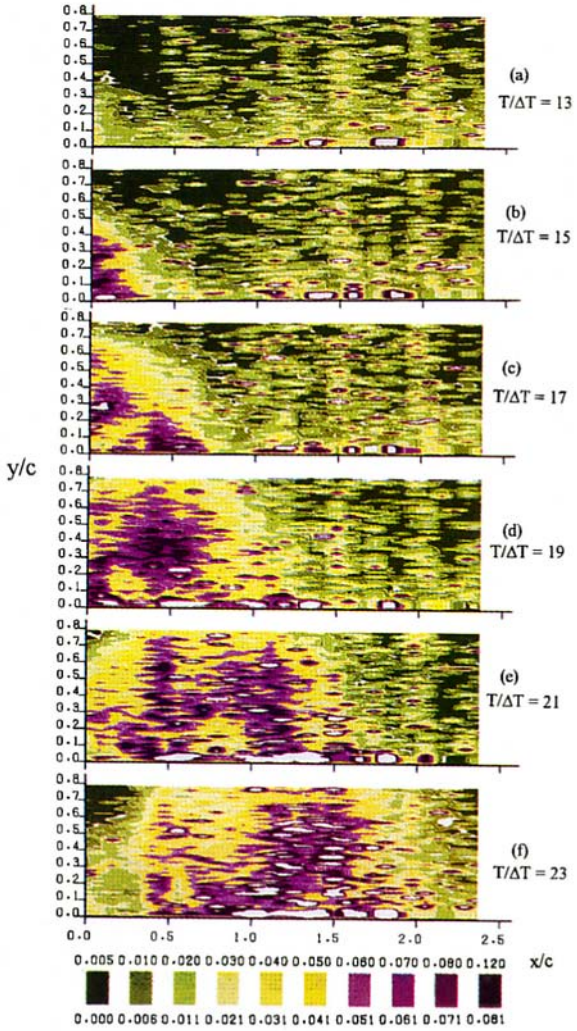

Fig. 10 Turbulent kinetic energy contours for chordlength c = 38.1 mm

step and by four to five chordlengths downstream, the effect of the disturbance has been practically eliminated.

For a disturbance about twice as large as the thickness of the boundary layer, the behavior is qualitatively similar. However, in this case, the identity of the vortex is preserved to a longer distance. The largest vortex tested, about three times the thickness of the boundary layer retains its character for the entire length of the measuring domain, but loses the coherence of its vorticity. On the other hand, the turbulence kinetic energy associated with the vortex experiences some diffusion, but its overall level appears to remain unaffected by the downstream drift. This indicates that vorticity in the vortex breaks down into turbulence which drifts downstream and leaves the domain of integration.

In all cases, the disturbing vortices appear to carry a higher level of turbulence than contained in the turbulent boundary layer. For the smaller vortex, turbulent kinetic energy quickly falls but in the case of the large vortex, the turbulence levels reach values as high as 25 percent. These high levels of turbulence are convected downstream with rather little diffusion and energize the mixing in the turbulent boundary layer for many chordlengths downstream.

Data Bank Contribution

The raw digital data obtained on this project are deposited to the JFE Data Bank. For the plates 12.7 mm and 26.5 mm, the data are presented for each integral value of $T/\Delta T$ in the range $0 < T/\Delta T < 40$ (see Fig. 2). For each value of $T/\Delta T$, data are provided in columns corresponding to the four quantities x, y, u, and v. For the 38.1 mm plate, time records are provided for $20 < T/\Delta T < 40$. The files are organized in the same way. Enlarged and individual color figures are also deposited in the Data Bank.

Acknowledgments

The support of the Office of Naval Research under grant no. N00014-93-1-0264, Edwin Rood, monitor, is gratefully acknowledged.

References

Booth, E. R., Jr., and Yu, Y. C., 1986, "Two-Dimensional Blade-Vortex Visualization Investigation," *AIAA Journal,* Vol. 24, pp. 1468–1473.

Booth, E. R., 1986, "Surface Pressure Measurement During Low Speed Two-Dimensional Blade-Vortex Interaction," AIAA Paper No. 86-1856.

Consigny, H., Gravelle, A., and Molinaro, R., 1984, "Aerodynamic Characteristics of a Two-Dimensional Moving Spoiler in Subsonic and Transonic Flow," *Journal of Aircraft,* Vol. 21, pp. 687–693.

Francis, M. S., Keesee, J. E., Lang, J. D., Sparks, G. W., and Sisson, G. E., 1979, "Aerodynamic Characteristics of an Unsteady Separated Flow," *AIAA Journal,* Vol. 17, pp. 1332–1339.

Kida, S., Takaoka, M., and Hussain, F., 1991, "Collision of Two Vortex Rings," *Journal of Fluid Mechanics,* Vol. 230, pp. 583–646.

Kida, S., and Takaoka, M., 1994, "Vortex Reconnection," *Annual Reviews of Fluid Mechanics,* Vol. 25, pp. 169–189.

Kothmann, B. C., and Pauley, W. P., 1992, "Interaction of Unsteady Turbulent, Vortical Structures with a Turbulent Boundary Layer," AIAA Paper No. 92-0060.

Koromilas, C., and Telionis, D. P., 1980, "Unsteady Laminar Separation—An Experimental Study," *Journal of Fluid Mechanics,* Vol. 97, pp. 347–384.

Littell, H. S., and J. K. Eaton, 1991, "Unsteady Flowfield Behind a Vortex Generator Rapidly Pitched to Angle of Attack," *AIAA Journal,* Vol. 29, pp. 577–584.

Macrorie, M., and Pauley, W. R., 1992, "Experimental Development of Spanwise Vortex Models with Streamwise Decay Due to Wall Interaction," AIAA Paper 92-2688.

Makita, H., K. Sassa, M., and Itabashi, A., 1989, "Decay Processor of a Manipulated Large-Scale Horseshoe Vortex in a Turbulent Boundary Layer," *AIAA Journal,* Vol. 27, pp. 155–160.

Mathioulakis, D. S., and Telionis, D. P., 1987, "Velocity and Vorticity Distribution in Periodic Separating Flow," *Journal of Fluid Mechanics,* Vol. 184, pp. 303–333.

Morton, B. R., 1984, "The Generation and Decay of Vorticity," *GeophysicoAstrophysics Fluid Dynamics,* Vol. 28, pp. 277–308.

Nagib, H. M., Reisenthel, P. H., and Koga, D. J., 1985, "On the Dynamical Scaling of Forced Unsteady Flows," AIAA Paper No. 85-0553.

Nelson, C. F., Koga, D. J., and Eaton, J. K., 1990, "Unsteady, Separated Flow Behind an Oscillating, Two-Dimensional Spoiler," *AIAA Journal,* Vol. 28, pp. 845–852.

Poling, D. R., and Telionis, D. P., 1986, "The Response of Airfoils to Periodic Disturbances—The Unsteady Kutta Condition," *AIAA Journal,* Vol. 24, pp. 193–199.

Poling, D. R., Wilder, M. C., and Telionis, D. P., 1988, "Two-Dimensional Interaction of Vortices with a Blade," AIAA Paper No. 88-0044.

Reisenthel, P. H., Nagib, H. M., and Koga, D. J., 1985, "Control of Separated Flows Using Forced Unsteadiness," AIAA Paper No. 85-0556.

Shabaka, I. M. M. A., Mehta, R. D., and Bradshaw, P., 1985, "Longitudinal Vortices Imbedded in Turbulent Boundary Layers, Part 1, Single Vortex," *Journal of Fluid Mechanics,* Vol. 155, pp. 37–57.

Wilder, M. C., Pesce, M. M., Telionis, D. P., Poling, D. R., and Dadone, L., 1990, "Blade-Vortex Interaction Experiments—Velocity and Vorticity Fields," AIAA Paper No. 90-0030.

White, F. M., 1974, *Viscous Fluid Flow,* McGraw-Hill, 2nd Edition, New York.

The Effect of Constriction Size on the Pulsatile Flow in a Channel

Moshe Rosenfeld
Lecturer.

Shmuel Einav
Associate Professor.

Department of Fluid Mechanics
and Heat Transfer and
Department of Biomedical Engineering,
Faculty of Engineering,
Tel Aviv University, Tel Aviv 69978, Israel

The effect of the constriction size on the pulsatile flow in a channel is studied by solving the time-dependent incompressible Navier-Stokes equations. A pulsating incoming flow is specified at the upstream boundary and the flow is investigated for several constriction sizes. Large flow structures are developed downstream of the constriction even for very small constriction size. The flow structures consist of several vortices that are created in each cycle and propagate downstream until they are washed away with the acceleration of the incoming flow. Additional vortices are created by a vortex multiplication process. The strength and total number of vortices generated in each cycle increase with the severity of the constriction. The maximal size of the vortices as well as their propagation speed are independent of the constriction size. These findings may be used for devising noninvasive methods for detecting the severity of stenoses in blood vessels and the potential damage to blood elements and thrombus formation caused by vortices.

1 Introduction

The study of internal pulsating flows received increased attention in the past few years both in engineering and biofluid applications, e.g., Sobey (1985), Armaly et al. (1983), Pedley and Stephanoff (1985), Ralph and Pedley (1988), Park (1989), Tutty (1992), and Tutty and Pedley (1993). Unsteady flows in general and pulsating flows in particular exhibit an exceptionally large variety of flow structures that depend on the incoming flow properties and on the geometry of the problem. Of special interest are the vortical structures that develop in nonuniform channels even for low Reynolds (Re) numbers. The swirling motion of the vortices alters significantly the characteristics of the flow field and derived quantities, such as the heat transfer and mixing rates. Desired flow properties can be obtained by changing the governing parameters, allowing direct control on the flow properties behind constrictions. Thus, the identification of possible flow structures in pulsating flows and their dependence on the governing parameters are of importance to both fundamental and applied fluid mechanics.

In the present study, we focus on incompressible viscous flows in two-dimensional constricted channels. Even cases with steady entrance flow exhibit complex flow patterns, Armaly et al. (1983). Several separation eddies are generated behind the constriction, and at $\mathrm{Re} = O(10^3)$ the flow becomes unsteady. A multiple vortex system is found at substantially lower $\mathrm{Re}(O(10^2))$, if a periodic flow is imposed by a moving portion of the wall (Pedley and Stephanoff 1985), by oscillating (Sobey, 1985; Tutty and Pedley, 1993) or pulsating (Park, 1989; Tutty, 1992) incoming flow. The pulsatile flow characteristics were found to be significantly different from their steady flow counterparts.

These and other works reveal that the pulsating flow field in non-uniform channels depends on a large number of factors, such as the Strouhal and Reynolds numbers and the constriction size. Most existing works studied the dependence of the flow on the Reynolds and Strouhal numbers, but the effects of the shape and size of the constriction were less well studied. The shape was found to have a minor effect on the global features of the flow, Sobey (1985), so that the constriction size remains the most significant geometric factor. Tutty and Pedley (1993) studied the effect of the step-size, along with other factors, for the case of an oscillating incoming flow in a stepped channel. They found that the increase of the step size increased the size of the vortices and the wavelength of the core flow, but still the vortices remained stationary. Park (1989) found for significantly larger St and lower Re that increasing the severity of the constriction increases the amplitude of the core flow, the vortices survive for a longer time and their shape becomes more circular. In contrary to most other works, the vortices propagated downstream because the flow was driven by a pulsating flow with a non-zero mean.

A systematic parametric study that includes all the governing parameters is far beyond the extent of a single investigation and therefore in the present work we concentrate on the least studied parameter—the effect of the constriction size. The effect of the Strouhal and Reynolds numbers were studied in several previous works, Tutty (1992), Tutty and Pedley (1993) and Rosenfeld (1995).

2 Methodology

2.1 Formulation. The geometry of the problem is shown in figure 1; it is similar to that used in the experiments of Park (1989). The channel is composed of two straight parallel plates at a distance of h from each other (all length units are scaled by h). On the upper wall, a circular-arc constriction with a size of a/h is added. Four different sizes are considered in the present study: $a/h = 0.07$, 0.14, 0.28 and 0.56.

The equations governing the flow of a constant density isothermal incompressible fluid in a fixed control volume with face S and volume V are the conservation of mass

$$\oint_S d\mathbf{S}\cdot\mathbf{u} = 0 \tag{1}$$

and the Navier-Stokes equations

$$\frac{d}{dt}\int_V \mathbf{u}\,dV = \oint_S d\mathbf{S}\cdot\mathbf{T}, \tag{2a}$$

where $\mathbf{u}$ is the velocity vector, t is the time, dV is a volume element and $d\mathbf{S}$ is the area element vector. For Newtonian fluids, the tensor $\mathbf{T}$ is given by

Contributed by the Fluids Engineering Division for publication in the JOURNAL OF FLUIDS ENGINEERING. Manuscript received by the Fluids Engineering Division April 26, 1994; revised manuscript received January 9, 1995. Associate Technical Editor: S. P. Vanka.

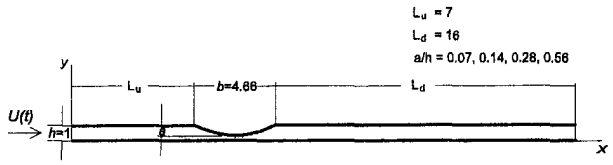

Fig. 1 The geometry of the problem (not to scale)

$$\mathbf{T} = -\mathbf{uu} - P\mathbf{I} + \nu(\nabla\mathbf{u} + (\nabla\mathbf{u})^T), \qquad (2b)$$

where $\mathbf{I}$ is the identity tensor, $\nabla\mathbf{u}$ is the gradient of $\mathbf{u}$ and $(\nabla\mathbf{u})^T$ is its transpose. The pressure is P and ν is the kinematic viscosity.

The waveform of the average incoming axial velocity $U(t)$ is defined for each cycle as in the experiments of Park (1989):

$$U(t) = U_s \qquad 0 < \frac{t}{T} \leq \frac{1}{2}$$

$$U(t) = U_s - U_p \sin\left(2\pi \frac{t}{T}\right) \qquad \frac{1}{2} < \frac{t}{T} \leq 1\,, \qquad (3)$$

where T is the period, and U_s, U_p are the steady and oscillating components of the spatially averaged inflow velocity, respectively. In the present study different values of U_s, U_p are used, $U_s = 0.1$ and $U_p = 4$, yielding a peak velocity of $U_M = U_s + U_p = 4.1$. The starting of each cycle corresponds to $t/T = 0$, i.e., t/T is the phase of the cycle (not the absolute time). We shall also refer to a phase inside a cycle according to the variation of the incoming flow. Thus, the steady incoming flow phase refers to the first half of the cycle, $\frac{1}{2} \geq t/T \geq 0$, while the acceleration and deceleration phases refer to $\frac{3}{4} \geq t/T > \frac{1}{2}$ and $1 > t/T > \frac{3}{4}$, respectively.

At the upstream boundary, a fully developed flow between two straight plates is specified for the waveform (3). At the downstream boundary, that is assumed to be far away from the region of interest, Neumann type boundary conditions are given for the velocity components: $\partial\mathbf{u}/\partial x = 0$, where x is the streamwise Cartesian coordinate. On the upper and lower solid walls, the no-slip and the no-injection conditions are specified, $\mathbf{u} = 0$.

To make the problem tractable, the Reynolds and Strouhal numbers are kept constant at $\mathrm{Re} = U_M h/\nu = 2100$ and $\mathrm{St} = h/U_M T = 0.016$. These values are similar to that found in the aorta, although the present study does not concentrate on biofluid applications. The Strouhal number is in the regime studied in several previous studies (for other geometries and incoming waveforms, e.g., Tutty 1992). The Reynolds number is higher than in previous studies. Tutty (1993) and Rosenfeld (1995) found that Re affects the strength of the vortices, but has no effect on the global properties of the flow (such as the wavelength).

2.2 Numerical Method. The laminar unsteady incompressible Navier-Stokes equations with primitive variables are solved with a solution procedure developed by Rosenfeld et al. (1991) and Rosenfeld and Kwak (1991, 1993). The formulation of the governing equations, the discretization procedure and the numerical solution stages are combined to yield an accurate and efficient solution method of complex time-dependent flows in generalized coordinate systems. The governing equations, written in the integral form (1) and (2), are discretized by finite volumes using a staggered arrangement of the variables. The Cartesian velocity components are replaced by the volume fluxes across the faces of the computational cells. The discretization is equivalent to second-order-accurate central differences. Possible numerical oscillations are smoothed out by adding a small amount of fourth-order numerical diffusion. The discrete equations are solved by a fractional step method with an approximate factorization of the momentum equations. A three-level temporal discretization is employed to yield an implicit second-order-accurate scheme in time as well. The implicit terms include contributions from both the advection and diffusion terms. The terms that do not fit into the tri- or penta-diagonal structure of each stage of the approximate factorization method are treated explicitly (without destroying the temporal accuracy). The convergence rate of the Poisson equation is accelerated by a multigrid procedure. The interested reader may find the details of the method in the references cited above.

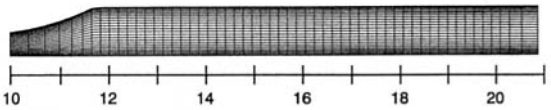

Fig. 2 The mesh in the region downstream of the constriction for the case of $a/h = 0.56$ (only every fourth mesh point is shown)

2.3 Mesh and Numerical Details. A transfinite algebraic mesh generator was employed with 289×97 points in the axial and transverse directions, respectively. The finest resolution in the axial direction is specified downstream of the constriction, where the flow field is the most complex. A blow-up of the mesh in this region is shown in Fig. 2; for clarity, only every *fourth* point is shown in each direction.

The solution was started from a fully developed parabolic velocity profile and was marched in time until a (graphically accurate) time periodic flow was attained in the whole region of interest (it requires three full cycles). All the results to be presented refer to the fully periodic solution. The numerical method itself was validated for a series of internal and external flow problems, e.g., Rosenfeld et al. (1991) and Rosenfeld and Kwak (1991). Detailed comparisons with the experimental results of Park (1989) were made by Rosenfeld (1993) (for $a/h = 0.56$ and a different regime of St, Re, U_s, and U_p). The vortical flow field was accurately captured by the numerical

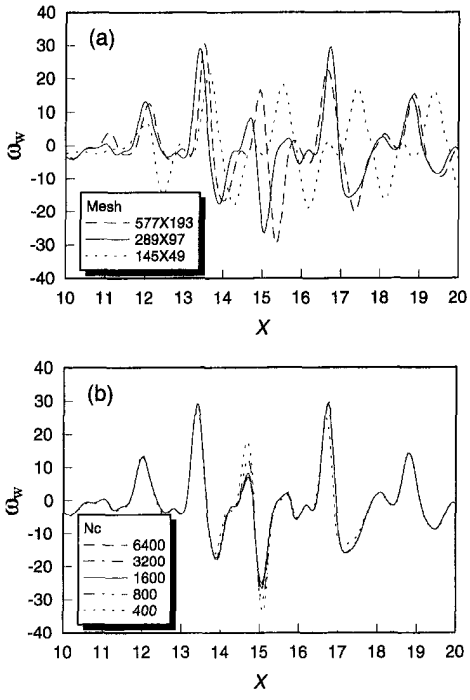

Fig. 3 (*a*) Mesh- and (*b*) time-step refinement studies of the lower wall vorticity ($a/h = 0.28$)

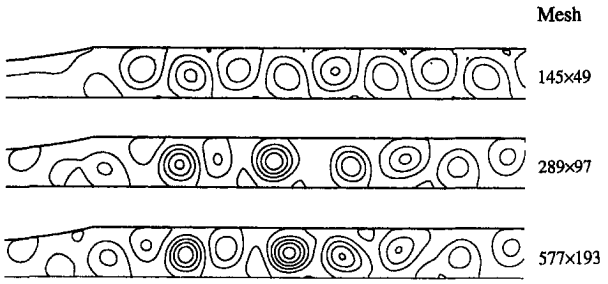

Fig. 4 The dependence of the instantaneous streamlines on the mesh ($t/T = 0.4$)

simulations and very good agreement was obtained in the propagation speed of the vortices for a wide range of parameters. In the present study, we rely on these favorable results to extend the study to regimes not studied previously.

Nevertheless, additional mesh and time step refinement studies were carried out mainly because of the larger Re of the present case. The wall-vorticity was found to be the most sensitive quantity for performing the tests. Figure 3(a) summarizes a mesh refinement study on the lower wall vorticity for $a/h = 0.28$ at $t/T = 0.4$. Three meshes with 145×49, 289×97 and 577×193 points were employed; 3 cycles with 1600 time steps per cycle were simulated in all the cases. The solution shows sensitivity to the mesh size, but the grid of 289×97 points seems to result in a reasonable compromise between accuracy and efficiency in most of the region (except for $15.5 > x > 14$).

Other flow variables are less mesh dependent and show good accuracy even for the mesh of 289×97 points, as can be seen in Fig. 4, that plots the instantaneous streamlines for $t/T = 0.4$ in the region downstream of the constriction. The coarsest mesh gives unacceptable prediction, but the next two meshes result in reasonable agreement. The main interest of the present paper is the study of the structure of the flow field (e.g., the number and size of the vortices). Figure 4 shows that these properties are predicted accurately even for the intermediate mesh. Therefore, we conclude that the mesh of 289×97 points is adequate.

A time step refinement study for the mesh of 289×97 points is given in Fig. 3(b) for $t/T = 0.4$. The solution is time step independent for $N_c > 800$, where N_c is the number of time steps per cycle. Therefore, in all the calculations at least 800 time steps per cycle were used.

In addition, the location of the upstream and downstream boundaries, as well as the type of the upstream boundary conditions were tested. The conditions given in Section 2.1 reflect the values that were found not to affect the solution in the region of interest (about 10 channel width units downstream of the constriction).

3 Results

3.1 Description of the Flow Field. The periodic flow field is depicted in Fig. 5 by the instantaneous streamlines and vorticity contours for the cases of $a/h = 0.07$, 0.14, 0.28 and 0.56 (it should be noted that the increments between the contour lines are not identical in all the plots). The solution of each case is shown for ten equally spaced instances along the *third*

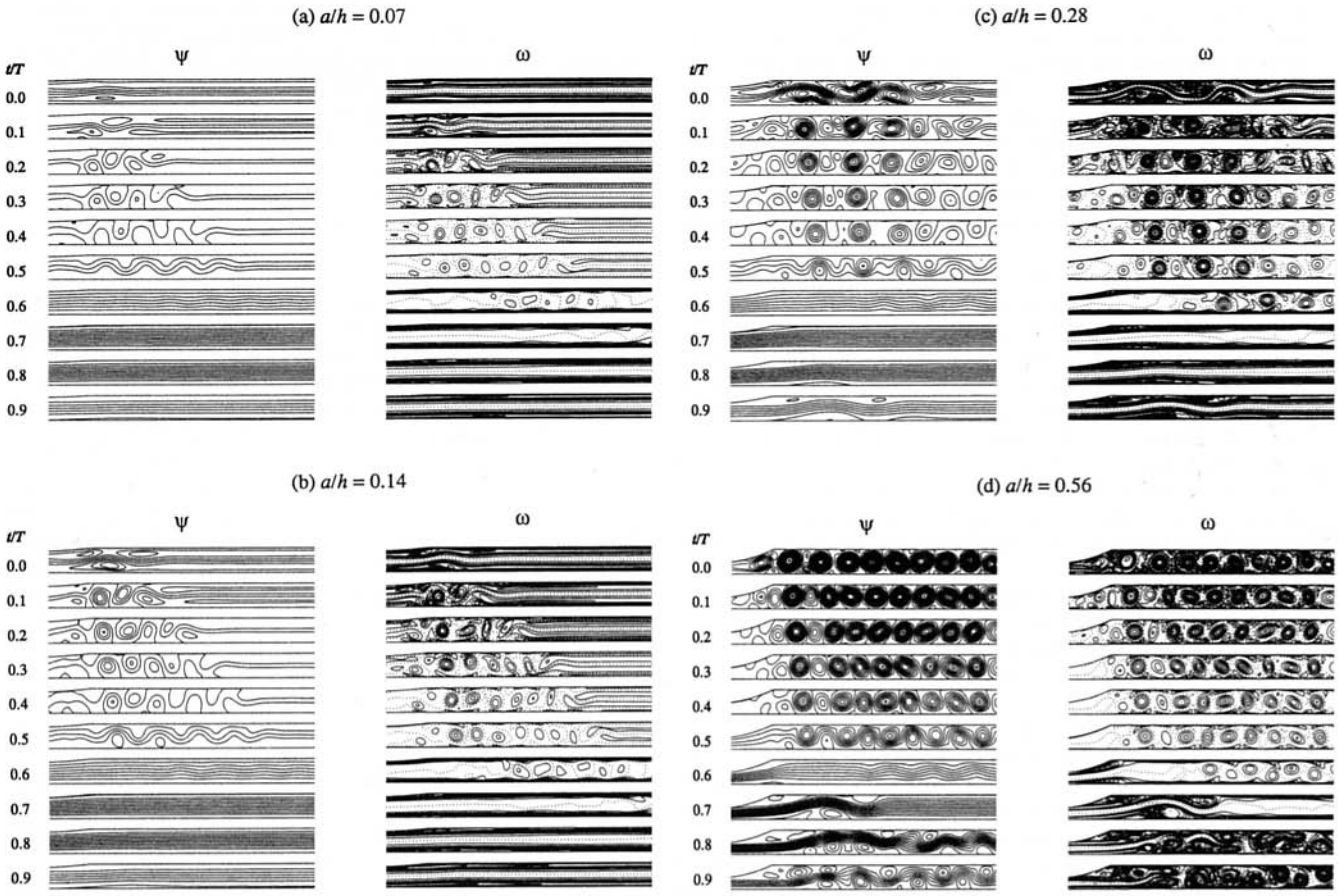

Fig. 5 The instantaneous streamlines (ψ) and vorticity (ω) contours. The increment between the streamlines is 0.1 and 0.4 in the first- and second-half cycles, respectively. The vorticity contour lines are given for $-100 < \omega < 100$ with an increment of 2.5 for (*a*) (*b*) (*c*), and 10 for (*d*). Zero vorticity is shown by dotted lines.

cycle of the simulation (when a periodic flow was already established).

The flow downstream of the smallest constriction, $a/h = 0.07$, is nonparallel with transverse variations considerably larger than the size of the constriction, Fig. 5(a). Closed streamlines and closed vorticity contour lines are found in the first half of the cycle. These closed lines indicate the presence of vortices in the flow field. At the beginning of the cycle ($t/T = 0$), two very small vortices are found and by $t/T = 0.1$, three larger vortices form. In the rest of the steady incoming flow phase ($0.5 > t/T$), the vortices expand in size and additional vortices are formed downstream. In the second half of the cycle ($1 > t/T > 0.5$), the incoming flow velocity increases by more than one order of magnitude (3), leading to streamlines parallel to the walls. However, the vorticity contour lines exhibit significant transverse variations even in the acceleration phase of the cycle ($0.75 > t/T > 0.5$). For the case of a more severe constriction, $a/h = 0.14$ (Fig. 5(b)), larger vortices are developed during the steady phase of the incoming flow. The vortices start to develop as early as $t/T = 0.9$ and by $t/T = 1$ (or $t/T = 0$), three large vortical regions are formed.

For the case of $a/h = 0.28$ (Fig. 5(c)), additional and stronger vortices form and they fill the whole domain shown. To aid in the description of the flow details, the streaklines of this case are also presented in figure 6 for the same ten instances. The sequence that leads to the formation of the vortices starts at the deceleration phase of the cycle. Two small eddies are formed by $t/T = 0.8$, one near the constriction and the other on the opposite wall, downstream of the first separation (see also Fig. 5(c)). The flow separated regions expand during the rest of the deceleration phase. By $t/T = 0.9$, the separated regions roll up into two vortices and a third vortex is observed to be forming near the upper wall farther downstream. In the beginning of the steady incoming flow phase, when the net mass flow rate is small ($U = U_s = 0.1$), the strength of the vortices increases and additional vortical structures are formed downstream. The large vortical structures transform into a number of smaller vortices by the vortex multiplication phenomenon, as described in Section 3.3. The vortices decay slowly in the rest of the cycle up to $t/T = 0.5$. In the acceleration phase ($0.75 > t/T > 0.5$) the vortices are not destroyed, but are washed rapidly downstream with the increase in the incoming velocity.

In the most severe constriction considered, $a/h = 0.56$ (Fig. 5(d)), the similar flow processes are considerably augmented. Large vortices are formed as early as $t/T = 0.7$, when the bulk-flow still accelerates. The first two vortical structures apparently split into several vortices ($t/T = 0.8$), along with the creation of additional vortices farther downstream. In the second half of the cycle, the size of the vortices is limited by the presence of a fast core flow (where most of the flow rate is conveyed). In the steady incoming flow phase of the cycle, the mass flow rate almost vanishes, allowing the expansion of the vortical regions up to the full height of the channel.

3.2 Generation of Vortices. The flow processes leading to the vortical flow field are first discussed for the case of $a/h = 0.14$, (Fig. 5(b)). In the deceleration phase of the cycle ($1 > t/T > 0.75$), the flow is displaced from the lee of the constriction because of the diverging cross-section of the channel. This causes the displacement of the flow from the opposite (lower) wall farther downstream. Large vorticity is convected away from both walls into the core flow, where it rolls up and forms two well-defined vortices even before $t/T = 0$. The displacement of the streamlines downstream of the lower vortex enhances the convection of vorticity from the upper wall into the core region, forming a third eddy ($t/T = 0$). This process of vortex generation, that was also described by Tutty and Pedley (1993), repeats itself along with a secondary process of vortex multiplication (see Section 3.3), forming nine vortices by $t/T = 0.5$. In the second half of the cycle, with the increase in the mass flow rate, the vortices are washed downstream.

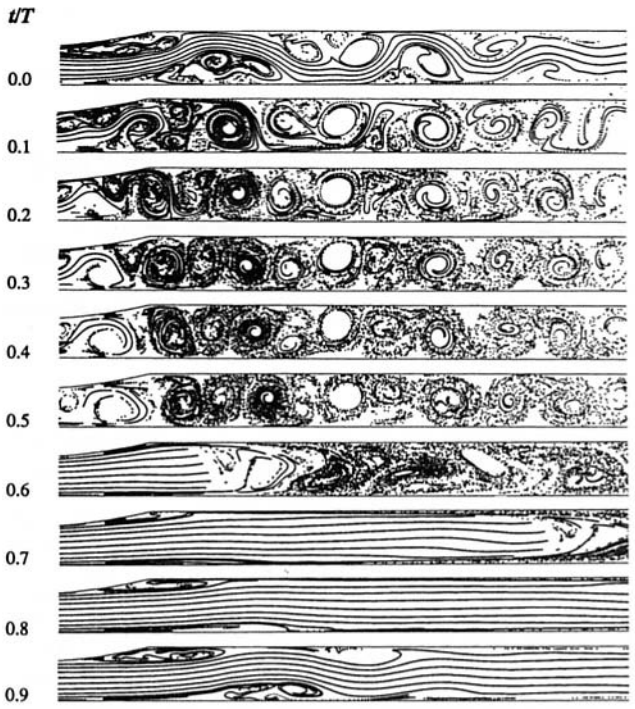

Fig. 6 The streaklines for the case of $a/h = 0.28$

Figure 5 reveals that the flow field is dominated by a propagating wave in the core flow and by the vortices upstream of the wave front. This wave is referred to in many works as *vorticity wave* (Pedley and Stephanoff, 1985; Sobey, 1985; Tutty and Pedley, 1993). The front of the propagating wave has a group velocity equal to the velocity of the core flow, see also Tutty and Pedley (1993). The group velocity of the propagating core flow wave is an order of magnitude larger than the incoming velocity during the first half of the cycle. The propagation (phase) velocity of the vortices, on the other hand, is proportional to the incoming velocity, see below.

The formation mechanism of the vortices is similar for all the constriction sizes considered. The vortices start to develop in the second half of the cycle. Additional vortices form during the first half of the cycle until they are washed away in the acceleration phase. The roll up time of the first vortex, however, does depend on the constriction size. Figure 5 reveals that as the size of the constriction increases, the vortices form sooner. The formation time of the first vortex is estimated from the figure to be $t/T = 0.15$, 0, 0.95, 0.65 for the constriction sizes of $a/h = 0.07$, 0.14, 0.28 and 0.56, respectively (i.e., in the most severe constriction the vortex forms in the acceleration phase). The total number of vortices generated in each cycle decreases with the reduction in the constriction size, because they are washed away closer to their time of formation. This finding may be utilized for detecting the severity of constrictions by using non-invasive methods, such as acoustic devises.

It should be noted that the generation and propagation of the vortices is a stable process, in contrary to the vortex shedding that results from the instability of shear layers. Similar propagating vortices form even for $\mathrm{Re} = O(10^2)$ (Park, 1989; Rosenfeld, 1995). Shedding of vortices was found for steady incoming flows in the same geometry only for Re (based on the mean velocity) more than twice as large as in the present case.

The streamwise location x_v of the most upstream lower wall vortex is plotted in Fig. 7 as a function of time. The strong dependence of x_v on the constriction size (at a given time) is attributed to the different formation time of the vortices. Yet,

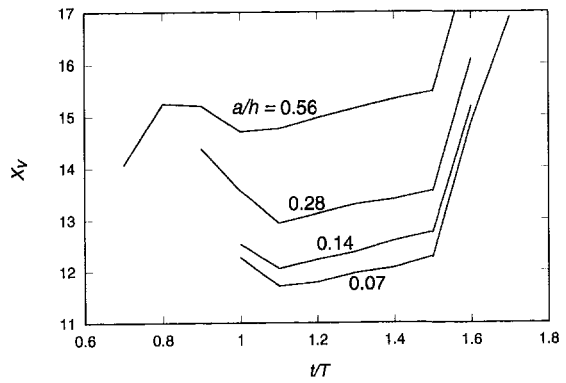

Fig. 7 The motion of the upstream lower-wall vortex

the propagation speed (given by the slope of x_v) is essentially independent of the constriction size. In most parts of the cycle, the phase velocity is proportional to the incoming velocity, proving that convection dominates the propagation of the vortices. Moreover, in a series of (unreported) simulations, the problem was solved for other Re, but the propagation speed was not found to be affected, indicating that the motion of the vortices is essentially inviscid.

3.3 Vortex Multiplication. In the present regime of parameters, the number of vortices generated in each cycle is determined by two related mechanisms: (i) the generation of the primary vortical structures and (ii) a secondary effect of vortex multiplication that further increases the number of vortices. The first mechanism was elaborated in the previous section. The vortex multiplication mechanism is described in this section for the typical case of $a/h = 0.28$, using the instantaneous streamlines and vorticity field shown in Fig. 8. This figure is a blow up of the region next to the constriction.

Three primary vortical structures (A, B_1, and D_1) are formed by $t/T = 0.9$. On the lower wall, a single eddy B_1 is found and a very small eddy C_1 is observed beneath B_1. The convection of counter-vorticity away from the lower wall is augmented by the swirling motion of B_1, causing the expansion of C_1 ($t/T = 0.94$). At the same time, the vorticity contour lines upstream of B_1 reveal a small downstream extension due to the non-uniform velocity field. This extension develops in time and generates a well-defined shear layer that rolls up by $t/T = 0.98$ to form yet another corotating vortex (B_2) upstream of B_1. The roll up process is accompanied by the migration of B_2 into the center of the channel. During the roll up of B_2 ($1.02 > t/T > 0.98$), the strengths and especially the sizes of B_1 and C_1 do not change. At the beginning of the steady incoming flow phase ($t/T = 1.02$), B_2 is larger than B_1 (see also figure 6) and a second contra-rotating vortex (C_2) is induced by B_2 upstream of C_1. Both B_1 and C_1 start to increase in size and strength, while B_2 decays and moves upstream. By $t/T = 1.10$, B_1 occupies a major portion of the height of the channel and C_1 has its maximal size. At the last instance shown in Fig. 8 ($t/T = 1.14$), B_1 remains almost unchanged, while B_2 is significantly weaker.

At the end of the process, three vortices (B_1, C_1, and B_2) are formed instead of the single vortex B_1 and therefore this process is referred to as *vortex multiplication.* The corotating vortex B_2 develops independently of B_1, while the contrarotating vortex C_1 is created by B_1. A similar sequence is noticed for the other primary structures, such as the development of the E and D vortices near the upper wall, downstream of the B-C vortices. Yet, there is a time lag of about 0.04 non-dimensional time units between them (the pattern of the vortices D_1-E_1-D_2 at $t/T = 1.10$ is similar to the pattern of B_1-C_1-B_2 at $t/T = 1.06$). The delay in the development is caused by the later formation of the downstream vortical structures.

3.4 Other Properties. The strength of the vortices increases with the size of the constriction. Larger constriction sizes generate stronger vortices lee of the constriction. This leads to a larger displacement of the flow from the lower wall, enforcing the rapid convection of vorticity into the core region. The process repeats itself, resulting in stronger vortices in the whole flow field. In the initial stages of their development, the

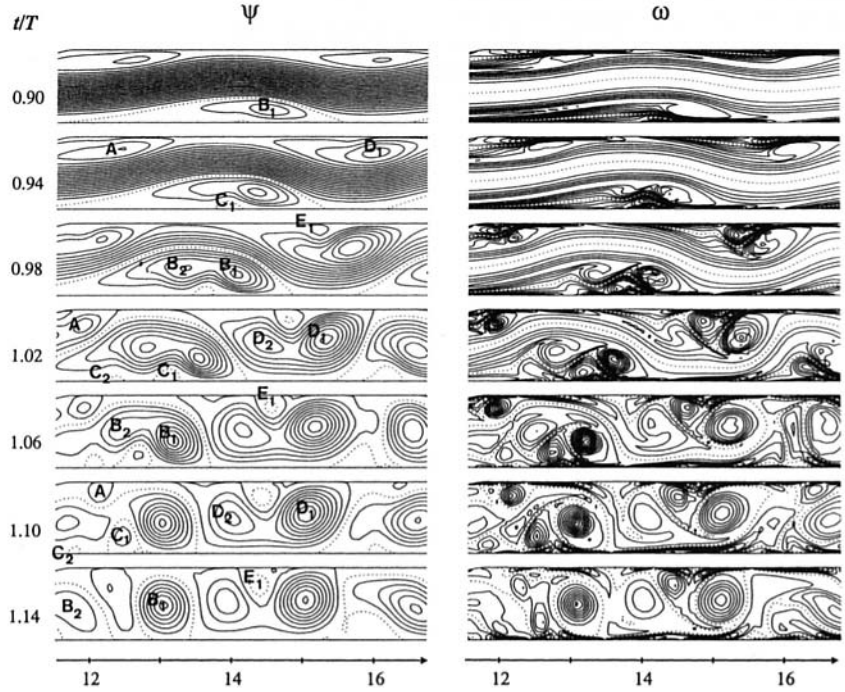

Fig. 8 The development of the multiple-vortex structure ($a/h = 0.28$). The increments between the streamlines (ψ) and the vorticity (ω) contours are 0.1 and 5, respectively. The vorticity contour lines are given for $-60 < \omega < 60$. Zero values are shown by the dotted lines.

size of the vortices increases with the constriction size. However, the vortex multiplication phenomenon leads to a flow field where the maximal size of the vortices is almost independent of the constriction size for a large portion of the steady incoming flow phase (Fig. 5). The maximal size is determined by the height of the channel. It should be recalled, however, that the number of vortices does depend on the size of the constriction.

Development of large vortical structures during the deceleration phase was observed in other works as well, see for example Tutty (1992) and Tutty and Pedley (1993). The latter study observed phenomena similar to that described in the present work. Although similarities may be found in several other global features (e.g., propagating wave front, multiple vortices), the details differ because in the present study the incoming waveform includes a relatively large mean flow and a long steady incoming flow phase. Moreover, in the present case the downstream propagating vortices do not decay in place, as was found by Tutty and Pedley (1993), but are washed out of the region. Tutty and Pedley (1993) found that the increase in the step size strengthen the vortices, as in the present case. However, they found that the sizes of the vortices depend on the step-size, while our simulations of smooth constrictions did not reveal such a dependence. Moreover, they found for constriction sizes smaller than 0.2 (in our notation) that the flow is quasi-steady downstream of the step. In the present pulsatile flow, significant time variations occur even for very small obstructions.

If only the instantaneous streamlines are considered (Fig. 8), the vortex multiplication phenomenon looks very similar to the *eddy-doubling* described by Pedley and Stephanoff (1985) and Ralph and Pedley (1988). They found for the case of an oscillating indentation that a single eddy splits into two co-rotating vortices. Yet, the vorticity field reveals that this term is inappropriate for the present case. The vortex B_1 does not split to form B_2; rather, the second corotating vortex B_2 is generated independently by vorticity originating from the same origin as that of B_1.

4 Concluding Remarks

The effect of the constriction size on the flow field was studied for a pulsating incoming flow with Re = 2100 and St = 0.016. It was found that the strength and number of vortices increase with the constriction size, indicating that these parameters might be used for detecting the severity of stenosis of blood vessels using non-invasive methods. The number and strength of vortices can serve as a basis for evaluating the potential damage and thrombus formation to blood flowing in stenosed vessels. Also, the vortices form sooner as the constriction size increases. However, the constriction size does not affect the maximal size of the vortices or their propagation speed.

Changing the Re and St numbers or the incoming waveform may affect the details of the flow field. However, based on our experience and numerous previous simulations, we believe that the global effects of the constriction size should be similar for a wide range of St and Re. Also, the results should not be affected significantly for incoming flows with waveforms that do not deviate significantly.

Acknowledgment

This work was supported in part by BSF Grant 91-00-217 and a grant from Drown Foundations.

References

Armaly, B. F., Durst, F. J., Pereira, C. F., and Schonung, B., 1983, "Experimental and Theoretical Investigation of Backward-Facing Step Flow," *Journal of Fluid Mechanics,* Vol. 127, pp. 473–496.

Park, D. K., 1989, "A Biofluid Mechanics Study of Arterial Stenoses," M.Sc. thesis, Lehigh University, Bethlehem, PA.

Pedley, T. J., and Stephanoff, K. D., 1985, "Flow Along a Channel with a Time-Dependent Indentation in One Wall: The Generation of Vorticity Waves," *Journal of Fluid Mechanics,* Vol. 160, pp. 337–367.

Ralph, M. E., and Pedley, T. J., 1988, "Flow in a channel with a moving indentation," *Journal of Fluid Mechanics,* Vol. 190, pp. 87–112.

Rosenfeld, M., 1993, "Validation of numerical simulation of incompressible pulsatile flow in a constricted channel," *Computers & Fluids,* Vol. 22, pp. 139–156.

Rosenfeld, M., 1995, "A Numerical Study of Incompressible Laminar Pulsating Flow Behind a Constriction," *Journal of Fluid Mechanics,* in press.

Rosenfeld, M., and Kwak, D., 1991, "Time-dependent solutions of viscous incompressible flows in moving coordinates," *International Journal for Numerical Methods in Fluids,* Vol. 13, pp. 1311–1328.

Rosenfeld, M., and Kwak, D., 1993, "Multi-Grid Acceleration of Fractional Step Solvers of Incompressible Navier-Stokes Equations in Generalized Curvilinear Coordinate Systems," *AIAA Journal,* Vol. 31, pp. 1792–1800.

Rosenfeld, M., Kwak, D., and Vinokur, M., 1991, "A Fractional-Step Solution Method for the Unsteady Incompressible Navier-Stokes Equations in Generalized Coordinate Systems," *Journal of Computational Physics,* Vol. 94, pp. 102–137.

Sobey, I. J., 1985, "Observation of Waves during Oscillatory Channel Flow," *Journal of Fluid Mechanics,* Vol. 151, pp. 395–426.

Tutty, O. R., 1992, "Pulsatile Flow in a Constricted Channel," ASME *Journal of Biomechanical Engineering,* Vol. 114, pp. 50–54.

Tutty, O. R., and Pedley, 1993, "Pulsatile Flow in a Constricted Channel," *Journal of Fluid Mechanics,* Vol. 247, pp. 179–204.

An Experimental Study of Pulsatile Flow in Canine Larynges

F. Alipour
Department of Speech Pathology and Audiology,
The University of Iowa,
334 WJSHC,
Iowa City, Iowa 52242-1012

R. C. Scherer
Wilbur James Gould Voice Research Center,
The Denver Center for the Performing Arts,
Denver, CO 80204

V. C. Patel
Department of Mechanical Engineering & Iowa Institute of Hydraulic Research,
The University of Iowa
Iowa City, Iowa

Pulsatile flow in an excised canine larynx was investigated with simultaneous recordings of air velocity, subglottal pressure, volume flow rate, and the signal from an electro-glottograph (EGG) for various conditions of phonation. Canine larynges were mounted on a pseudotrachea and sustained oscillations were established and maintained with sutures attached to cartilages to mimic the function of laryngeal muscles. The pitch and amplitude of the oscillations were controlled by varying the airflow, and by adjusting glottal adduction and vocal-fold elongation. Measurements with hot-wire probes suggest that subglottal inlet flow to the larynx is pulsatile but mostly laminar, while the exiting jet is non-uniform and turbulent. In the typical ranges of flow rate, subglottal pressure, and oscillation frequencies, the Reynolds number based on the mean glottal velocity and glottal hydraulic diameter varied between 1600 to 7000, the Strouhal number based on the same parameters varied between 0.002 and 0.032, and the Womersley number ranged from 2.6 to 15.9. These results help define the conditions required for computational models of laryngeal flow.

Introduction

Human speech sounds are created as a result of the conversion of aerodynamic power to acoustic power through oscillatory tissue dynamics. The mechanism of this conversion process to air flow through the glottis is poorly understood. The glottis is a three dimensional space between the vocal folds that changes dynamically during phonation. As a dynamic valve, it creates pulsatile flow which becomes the source of sound in phonation. In addition, from a biomechanical point of view, the calculation of the driving forces on the vocal folds requires the knowledge of both the pressure distribution and the velocity pattern within the glottis (Alipour and Titze, 1988).

The pulsatile flow within the glottis has not been studied in detail except with simple one-dimensional, experimental and computational models such as collapsible-tube model of vocal folds (Conrad, 1980), which was based on the theory developed by Shapiro (1977). However, unsteady flows in constricted channels are studied in other applications. For example, Thornburg et al. (1992) studied steady and unsteady laminar flows through an axisymmetric rigid cosine-shaped constriction. They found that the flow became unsteady at a Reynolds number of 2000 and a constriction area ratio of 0.75. Rosenfeld (1993) simulated pulsatile laminar flow in a two-dimensional constricted channel and validated his model with the flow-visualization results of Park (1989). The constriction ratio in Rosenfeld's simulation was no more than 0.75 and the Reynolds number was less than 140. In contrast, laryngeal flow, for which the constriction ratios exceed 0.9 and the Reynolds numbers frequently exceed 1500, is both unsteady and turbulent. Einav and Sokolov (1993) discuss pulsatile pipe flow with ranges of transitional Reynolds number and Stokes parameter similar to those of the present study (also see Nakamura, Sugiyama and Haruna, 1993; Ahmed and Giddens, 1984), although their application is more appropriate to stenoses rather than flow-induced dynamic valving as in the larynx.

There has been much experimental work on laryngeal fluid mechanics, but few studies have measured air velocities. The first attempt to quantify the glottal velocity profile appears to have been made by Berke et al. (1989). Using constant-temperature hot-wire anemometry, they measured the velocity waveform in an in-vivo canine larynx at five locations along the midline of the glottis. Although the data were limited in scope, they demonstrated that the canine larynx is a feasible model for the study of pulsatile flow during phonation. The results can be reasonably extrapolated to human phonation due to the close similarity between the canine and human glottographic waveforms (Slavit et al., 1990).

Experimental and computational techniques for diagnostics of pulsatile flow in the larynx complement each other. Experimental investigations with excised larynx models provide realistic laryngeal flow information that is useful for validation of computational models. In particular, experiments guide establishment of the inlet and outlet flow conditions, and the range of Reynolds and Strouhal numbers that occur in typical operating conditions. The present study was undertaken to quantify the laryngeal flow below and above the vocal folds, to establish the procedures for making measurements in such a pulsatile flow, and to obtain the range of Womersley number, and the Reynolds and Strouhal numbers under typical oscillation conditions. The results provide an understanding of the flow in the glottis, and could be used to define the conditions required in computational models of laryngeal flow.

Experimental Arrangement

Fresh excised canine larynges were acquired from other laboratories at the University of Iowa Hospitals and Clinics. The larynges were kept in saline solution prior to their use in the experiments. Figure 1 shows the overall experimental arrangement. After establishing an air supply with 100 percent relative humidity and a temperature of about 37°C using a Conchatherm heater unit (RCI Laboratories), the larynx was mounted on the rigid vertical tube of a pseudo-lung mechanism. The glottis was easily viewed by a camera and was accessible to other equipment. Adduction (the mechanism of bringing the vocal folds together) and tension controls were established by connecting the cartilages to micrometers with sutures (see Fig. 2). Vocal

Contributed by the Fluids Engineering Division for publication in the JOURNAL OF FLUIDS ENGINEERING. Manuscript received by the Fluids Engineering Division September 22, 1994; revised manuscript received April 26, 1995. Associate Technical Editor: F. Giralt.

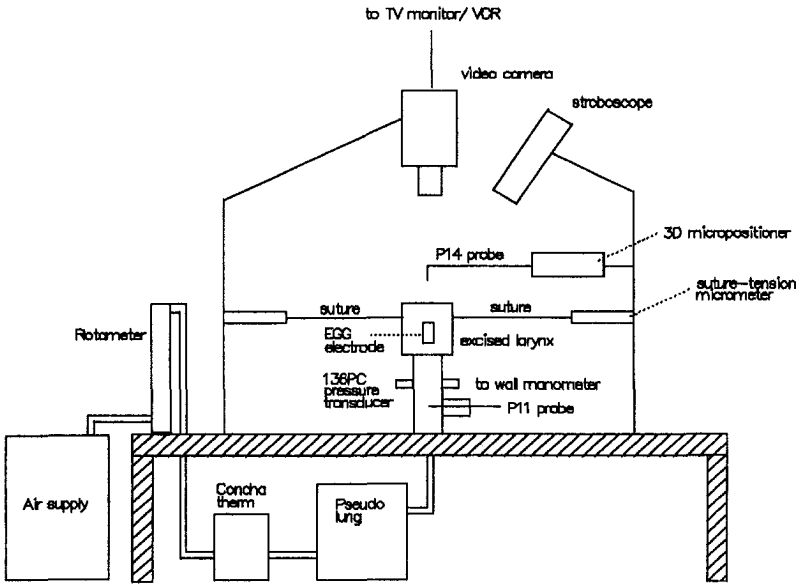

Fig. 1 Experimental arrangement (not to scale)

fold length was controlled by sutures attached to the thyroid cartilage anteriorly and the cricoid cartilages posteriorly (the latter are not shown in Fig. 2). A suture was sewn to each arytenoid cartilage and passed laterally through the other to control adduction.

Electrodes from an electroglottograph (EGG) made by Synchrovoice Inc. were attached to the laminae of the thyroid cartilage with push pins to pick up the EGG signal during oscillations. The EGG signal represents the change in impedance through the neck via a 5 MHz electric field, and has been related to vocal fold contact area (Childers, 1985; Scherer et al., 1988). It can be used to identify the approximate opening and closing phases of the glottis (exemplified below). The EGG signal was also used in the data analysis as a trigger signal to process the phase-averaged waveform from the instantaneous air velocity signal.

The mean pressure in the subglottal region (measured about 10 cm below the vocal folds) was monitored with a wall mounted well-type water manometer with an accuracy of ±10 Pa (Dwyer No. 1230-8). The mean flow rate was monitored with an in-line flowmeter (Gilmont rotameter model J197; accuracy: ±3 percent) as shown in Fig. 1. The time varying subglottal pressure was measured with a piezoresistive pressure sensor (Microswitch 136PC01G1). This pressure (accuracy: ±2.3 percent) was measured at the same location as the manometer tap (Fig. 1) for ease of calibration.

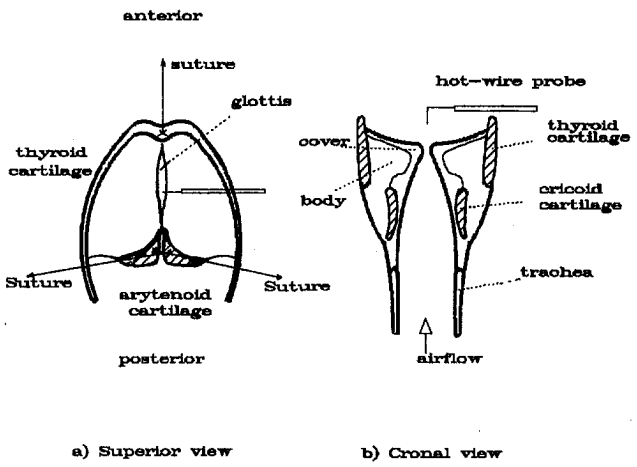

Fig. 2 Schematic of the superior (top) view and coronal (vertical sectional) cut of the excised larynx. The top view shows the glottal slit frozen at maximum excursion.

The velocity was measured with a constant-temperature hot-wire anemometer system (Dantec 56C01). A straight miniature probe (Dantec 55P11) was positioned in the subglottal tube about 12 cm below the vocal folds (Fig. 1) to measure velocity upstream of the glottis. The velocity in the jet above the glottis was measured at various locations with a miniature probe (with right-angled prongs, Dantec P14) with the sensor's direction perpendicular to the flow axis. The probe was mounted on a three-dimensional micropositioner (Deadal model 393M) access any location in the glottal jet (Fig. 2). Experiments were conducted with several frequencies and mean subglottal pressures.

The subglottal pressure signal was amplified with a bridge amplifier (Bioamp model 205) and calibrated against the manometer at regular intervals. The hot-wire signal was calibrated against a pitot tube placed over the center of an air jet exiting a 0.6 cm diameter uniform tube. Humidified air at 35–37°C was used during both the hot-wire calibration and the larynx experiments. A best fit to the calibration was obtained with a least-square polynomial and used in subsequent data reduction. The velocity measurement accuracy was estimated to be no worse than ±4 percent in the experimental range.

During the experiment, analog data from the hot-wire probes, EGG, and pressure transducer were monitored on a digital oscilloscope (Data 6000 Universal Waveform Analyzer, Data Precision) and simultaneously recorded on a Sony model PC-108M Digital Audio Tape (DAT) recorder. Portions of these recordings were digitized later with a 16-bit analog/digital convertor and analyzed on VAX-station computers. The multiple channels of signals were DC-coupled and digitized at the rate of 20 kHz (to ensure full waveform specification) for at least one second per channel (between 1.1 to 1.5 seconds). During the experiment, the top view of the larynx and vocal folds was recorded onto video tape for later analysis of the glottal images during oscillations.

To separate the turbulence from the periodic component of the velocity signal, the technique of phase shift averaging was employed. In this method, the EGG signal was used as the trigger signal to obtain cycle information. Every instantaneous velocity measurement on consecutive cycles corresponding to

a phase point on the EGG trigger cycle was averaged over 100 to 300 cycles for the range of frequencies encountered in the experiments. This averaging process provided the so-called deterministic component of the oscillatory flow (the ensemble average). This average was then cross correlated to a shifted raw cycle to obtain the maximum correlation coefficient (see Kitney and Giddens, 1984, for details). This process was iterated until a reasonable convergence was achieved. This phase-averaged velocity shows the deterministic or pulsatile nature of the flow. When this signal is subtracted from the instantaneous velocity, the turbulent component is obtained. However, as noted by Walburn et al. (1983), when there is a cycle-to-cycle variation of oscillation period, using the phase averaged velocity will over predict the turbulent component. Thus, a nonrecursive digital low-pass filter (Hamming, 1973) was first used to smooth the velocity, so that the turbulent velocity fluctuations could be obtained independently of the phase shift averaged velocity. The turbulence intensity was calculated by taking the root mean square of the turbulent velocity fluctuation signal.

The recorded stroboscopic superior view of the larynx showed an essentially elliptical glottal opening that changed from a minimum to a maximum during each cycle. To obtain estimates of the oscillation amplitude, the strobe light was externally triggered with the EGG signal to freeze the image. By controlling the delay between the EGG and the trigger signal, the glottal view was set to its maximum area. The selected frame of glottal area was captured by a frame grabber and saved for digital image analysis. This image (Fig. 3) was analyzed by the WinTrace software (developed at the Image Analysis Facilities of the University of Iowa). The calibration procedure for length and area was performed using a known distance on the image (a digitized millimeter grid) within the software itself. The maximum glottal area value (A_g) and glottal perimeter were measured by tracing the glottis contour with accuracy of ± 2 percent for area and ± 5 percent for perimeter. The mean glottal velocity (U_m; accuracy: ± 5 percent) was calculated by dividing the mean volume flow rate obtained from the rotameter by this maximum glottal area. The maximum glottal area, together with the corresponding measured glottal perimeter (G_p; accuracy: ± 5 percent), was used to obtain the hydraulic diameter ($D_h = 4A_g/G_p$; accuracy: ± 7 percent) of the glottis during oscillations. The mean Reynolds number was calculated based on this length scale and mean glottal velocity ($\mathrm{Re} = U_m D_h/\nu$; accuracy: ± 12 percent). The Strouhal number was also calculated based on these parameters and the frequency of oscillation ($\mathrm{St} = fD_h/U_m$; accuracy: ± 8 percent). The Womersley number, defined on the basis of hydraulic diameter, frequency and viscosity ($\alpha = 0.5D_h(2\pi f/\nu)^{0.5}$; accuracy: ± 8 percent), was also calculated.

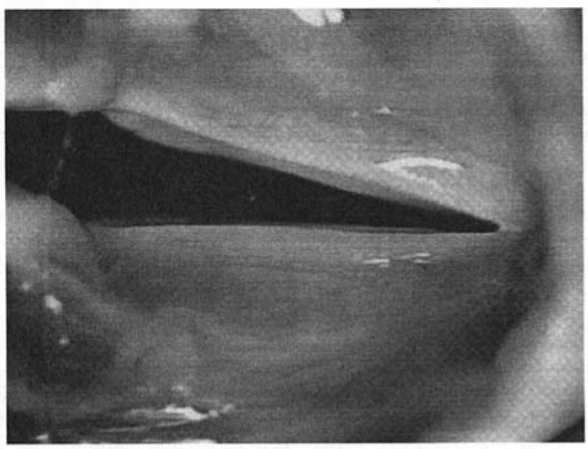

Fig. 3 A digitized image of the glottis

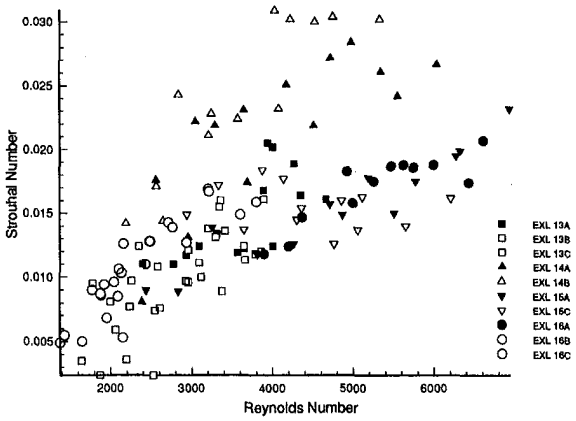

Fig. 4 Strouhal and Reynolds numbers in tests with four excised larynges. Each larynx represented by different symbol. For these cases, the mean subglottal pressure ranged between 0.7 and 3.0 kPa, and mean flowrate ranged between 92 and 970 ml/s. (Experimental uncertainty in Reynolds number = ±12 percent and in Strouhal number = ±8 percent).

Results and Discussion

The experiments performed with four excised larynges: (1) male, weight of 22 kg, in situ vocal fold length of 14.0 mm; (2) male, 27 kg, 18.0 mm; (3) male, 25 kg, 17.5 mm; (4) female, 27 kg, 18.4 mm. For each larynx there was a range of pressure and flow rate for which the oscillation was audibly stable. For each larynx, one to three cases of oscillation with different adductory configurations were considered. The pressure and flow rate were varied within the stable range for each larynx and signals were recorded while the phonation was stable. Figure 4 shows the operation of the four larynges with ten cases of pressure and flow variations. Every point on the figure represents a stable working condition of a larynx, and each symbol corresponds to one particular larynx. The overall data indicate that flow at the exit was mostly turbulent with a Reynolds number ranging between 1600 to 7000. The Strouhal number ranged between 0.002 and 0.03 with an average of 0.016. The corresponding range of the unsteadiness parameter was 2.6 to 15.9 with an average of 9.1. The data of Fig. 4, obtained for realistic ranges of glottal pressure and flow, give values of Re and St which may be used in numerical simulations of pulsatile flow in the larynx.

Figure 5 shows a sample of the data from one particular larynx indicating, from the bottom, the EGG signal, the subglottal pressure (Ps), the subglottal velocity measured in the trachea (Vs), the supraglottal jet velocity (V_j), the phase-averaged jet velocity ($\langle V \rangle$), and the turbulent component of the jet velocity (V'), respectively. There are four points indicated on the EGG waveform. Points 1 and 4 correspond to the approximate start of the glottal opening (Anastaplo and Karnell, 1988), point 2 is the approximate location of the beginning of glottal closing, and point 3 is where glottal closing is completed. In this example, the glottis was open longer than it was closed. This finding can be seen also from the velocity signals.

The subglottal pressure increased during the glottal closing portion of the cycle (interpreted from the EGG signal), continued to build up until the vocal folds began to open, and then decreased to a minimum. At lower frequencies, resonance in the subglottal system causes the subglottal pressure to contain more than one spectral component.

The subglottal velocity was pulsatile and appeared to be laminar (that is, had no apparent turbulence component). The pulsatile flow fell to a non-negligible minimum, indicating that the vocal folds did not close completely, or there was subglottal tracheal expansion near the time of glottal closure and maximum subglottal pressure. The peak of this signal fell in the region of the fully-open glottis (between points 1 and 2). This velocity

may also have been affected by the resonance in the subglottal system.

In Fig. 5, the hot-wire probe (P14) was positioned over the midline of the glottis and 10 mm above the vocal folds. At the instants of glottal opening and closing, the instantaneous velocity signal, as well as the phase-averaged velocity signal, show very large gradients, and these large gradients appear to be responsible for the spikes in the turbulent velocity fluctuations.

Figure 6 shows six velocity profiles in the subglottal section of the larynx. The probe was traversed in a direction parallel to the glottal edge (anterior-posterior). The profiles are foreshortened on the right of the figure because the hot-wire probe was kept away from the wall on that side to protect it from damage. These velocity profiles were selected at different phase positions of the oscillation cycle as indicated by the numbers on the single cycle of the subglottal velocity (insert). The same larynx was used for all 6 profiles. Ten cycles of each subglottal velocity waveform were averaged at 18 transverse locations and at 6 phases of the cycles. The resulting instantaneous velocity profiles are plotted in Fig. 6. The first marker was selected at the peak of the EGG signal which, from Fig. 5, is seen to be near maximum glottal closure. These subglottal velocity profiles changed in shape with time and were nearly parabolic in shape. The overall averaged subglottal velocity waveform (Figure 6 insert) was skewed to the right (asymmetric).

To quantify the shape of the jet exiting the glottis at various phases of the oscillation cycle, the following experiment was conducted. First a stable phonation was obtained. Then, by locking the strobe light with the EGG signal and adjusting the delay, the maximum opening was observed on the video in a stationary

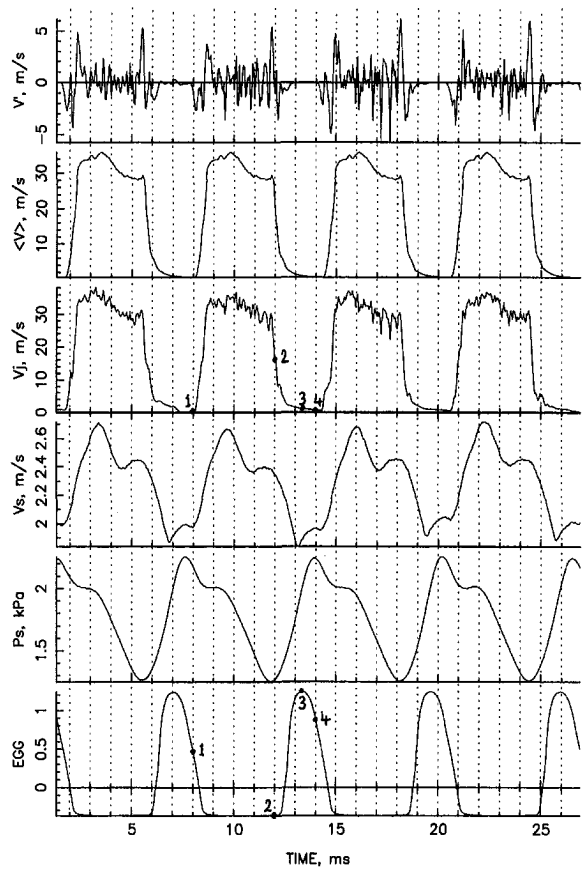

Fig. 5 Waveforms of flow in typical larynx. The signals are, from the bottom, electroglottograph (EGG), subglottal pressure (Ps), subglottal velocity (Vs), jet velocity 10 mm above the vocal folds (Vj), phase-averaged velocity ($\langle V \rangle$), and the turbulent velocity fluctuation (V'). (Experimental uncertainty in pressure = ±2 percent and in velocity = ±4 percent)

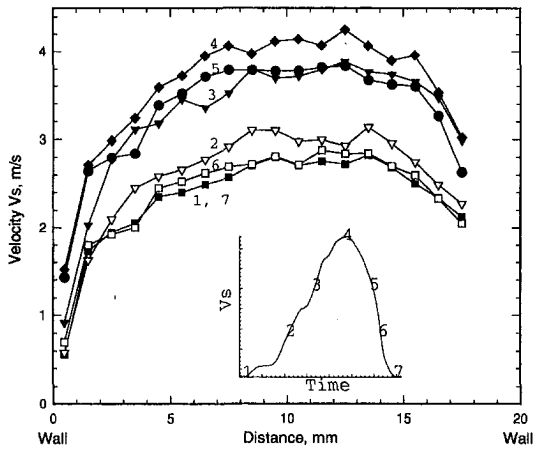

Fig. 6 Velocity profiles upstream of the glottis (in the subglottal section). Profiles are selected at different phase positions in the oscillation cycle. (Experimental uncertainty in distance = ±0.1 percent and in velocity = ±4 percent).

(freeze) mode. The area of the opening was divided into a 9 × 13 point grid with 0.25 mm spacing laterally (in the X direction, across the glottis) and 1 mm spacing longitudinally (in the Y direction, parallel to the glottis). The hot-wire probe (P14) was located at every grid point for about 5 seconds and moved to the next position using the X-Y micropositioner. The data were digitized later and processed on a VAX-station computer.

Figure 7 shows a velocity surface in the cross section of the glottal jet time-averaged over a duration of one second. For this case, the mean flow rate was approximately 230 ml/s and the subglottal pressure was approximately 1.4 kPa. The maximum glottal opening was about 1.25 mm. The measurement grid included a 0.25 mm extension on each side. Figure 7 clearly shows a highly nonuniform average velocity distribution in the glottal jet. There are large variations in velocity especially in the Y direction. The maximum velocity of approximately 25 m/s occurred at a location of about 3 mm from the anterior glottal commissure, whereas maximum glottal opening (as measured from the video tape recording) was approximately 5 mm from the anterior commissure. The location of the point of maximum velocity in the anterior glottis, anterior to the maximum vocal fold displacement, is similar to that reported by Berke et al. (1989) who measured a mean velocity as large as 40 m/s. The dynamic glottal configuration and flow impedance need further study to explain these data.

Conclusions

This study was concerned with the pulsatile flow from the glottis during phonation. Air velocities in excised canine larynges were measured using hot-wire anemometry, and were accompanied by simultaneous measurement of subglottal pressure, subglottal air velocity, and the electroglottographic signal. Phase-averaging of the velocity signals was performed to obtain the deterministic velocity. Subtracting the digital low-pass filtered velocity from the instantaneous velocity gave the turbulent velocity fluctuations. Recordings of velocity were made over the glottal midline as well as over a measurement grid above the glottis to map the velocity field in the three-dimensional jet exiting the vocal folds.

Results of this study suggest the following:

1. The flow regime above the glottis in the excised canine larynx is turbulent over most of the open glottis portion of the vibratory cycle. The subglottal velocity did not show turbulence.

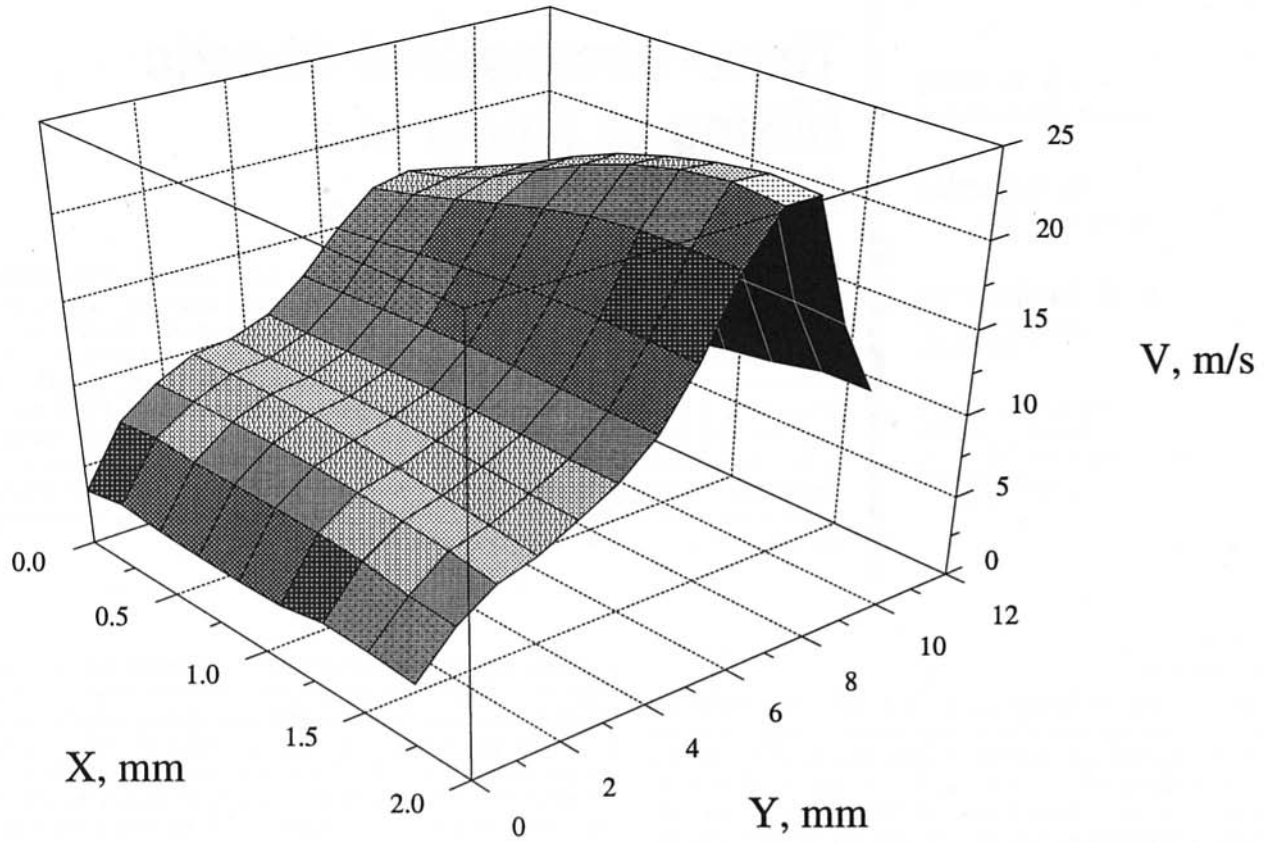

Fig. 7 Time-averaged (mean) velocity 10 mm above the glottal cross-section

2. The Reynolds number ranged from 1600 to 7000; the corresponding Strouhal number range was 0.002 to 0.03, the Womersley number range was 2.6 to 15.9. The turbulence intensity ranged between 1.1 to 5.7 m/s.
3. The largest velocity values occurred through the anterior glottal region, anterior to the location of the cyclic maximum glottal excursion, in the example given.

These results together provide guidance to development of a theory or model of phonatory aeroacoustics.

Acknowledgments

The authors would like to thank Jim Knowles, Daryl Lorel, and Katie Sacket for their assistance in larynx preparation and data collection. This work was supported by National Institute on Deafness and other Communication Disorders, Grant No. DC00831-03.

References

Ahmed, S. A., and Giddens, D. P., 1984, "Pulsatile Poststenotic Flow Studies with Laser Doppler Anemometry," *Journal of Biomechanics,* Vol. 17, pp. 695–705.

Alipour, F., and Titze, I. R., 1988, "A Finite-Element Simulation of Vocal Fold Vibration," *Proceedings of the Fourteenth Annual Northeast Bioengineering Conference,* Durham, N.H., IEEE publication #88-CH2666-6, pp. 186–189.

Anastaplo, S., and Karnell, M. P., 1988, "Synchronized Videostroboscopic and Electroglottographic Examination of Glottal Opening," *Journal of the Acoustical Society of America,* Vol. 83, pp. 1883–98.

Berke, G. S., Moore, D. M., Monkewitz, P. A., Hanson, D. G., and Gerratt, B. R., 1989, "A Preliminary Study of Particle Velocity During Phonation in an In-Vivo Canine Model," *Journal of Voice,* Vol. 3, No. 4, pp. 306–313.

Childers, D. G., 1985, "A Critical Review of Electroglottography," *CRC Critical Reviews in Biomedical Engineering,* Vol. 12, Issue 2, pp. 131–161.

Conrad, W. A., 1980, "A New Model of the Vocal Cords Based on a Collapsible Tube Analogy," *Medical Research Engineering,* Vol. 13, pp. 7–10.

Einav, S., and Sokolov, M., 1993, "An Experimental Study of Pulsatile Pipe Flow in the Transition Range," ASME JOURNAL OF BIOMECHANICAL ENGINEERING, Vol. 115, pp. 404–411.

Hamming, R. W., 1973, *Numerical Methods for Scientists and Engineers,* Second Edition, McGraw-Hill, New York.

Kitney, R. I., and Giddens, D. P., 1983, "Analysis of Blood Velocity Waveforms by Phase Shift Averaging and Autoregressive Spectral Estimation," ASME JOURNAL OF BIOMECHANICAL ENGINEERING, Vol. 106, pp. 398–401.

Nakamura, M., Sugiyama, W. and Haruna, M., 1993, "An Experiment on the Pulsatile Flow at Transitional Reynolds Numbers—The Fluid Dynamical Meaning of the Blood Flow Parameters in the Aorta," ASME JOURNAL OF BIOMECHANICAL ENGINEERING, Vol. 115, pp. 412–417.

Park, D. K., 1989, "A Biofluid Mechanics Study of Arterial Stenoses," M.Sc. thesis, Lehigh University, Bethlehem, PA.

Rosenfeld, M., 1993, "Validation of Numerical Simulation of Incompressible Pulsatile Flow in a Constricted Channel," *Computers and Fluids,* Vol. 22, No. 2/3, pp. 139–156.

Scherer, R. C., Druker, D. G., and Titze, I. R., 1988, "Electroglottography and Direct Measurement of Vocal Fold Contact Area," O Fujimura ed., *Vocal Physiology: Voice Production, Mechanisms, and Functions,* Raven Press, Ltd., New York, pp. 279–291.

Shapiro, A. H., 1977, "Steady Flow in Collapsible Tubes," ASME JOURNAL OF BIOMECHANICAL ENGINEERING, Aug., pp. 126–147.

Slavit, D. H., Lipton, R. J., and McCaffrey, T. V., 1990, "Glottographic Analysis of Phonation in the Excised Canine Larynx," *Annals of Otology, Rhinology & Laryngology,* Vol. 99, No. 5, pp. 396–402.

Thornburg, H. J., Ghia, U., Osswald, G. A., and Ghia, K. N., 1992, "Efficient Computation of Unsteady Vortical Flow Using Flow-Adaptive Time-Dependent Grids," *Fluid Dynamics Research,* Vol. 10, pp. 371–397.

Tu, C., Deville, M., Dheur, L., and Vanderschuren, L., 1992, "Finite Element Simulation of Pulsatile Flow Through Arterial Stenosis," *Journal of Biomechanics,* Vol. 25, No. 10, pp. 1141–1152.

Tutty, O. R., 1992, "Pulsatile Flow in a Constricted Channel," ASME JOURNAL OF BIOMECHANICAL ENGINEERING, Vol. 114, pp. 50–54.

Walburn, F. J., Sabbah, H. N., and Stein, P. D., 1983, "An Experimental Evaluation of the Use of an Ensemble Average for the Calculation of Turbulence in Pulsatile Flow," *Annals of Biomedical Engineering,* Vol. 11, pp. 385–399.

K. C. Miles
Graduate Research Assistant.

B. Nagarajan
Graduate Research Assistant.

D. A. Zumbrunnen
Associate Professor.
Mem ASME.

Thermal and Fluid Sciences
Research Laboratory,
Department of Mechanical Engineering,
Clemson University,
Clemson, SC 29634-0921

Three-Dimensional Chaotic Mixing of Fluids in a Cylindrical Cavity

Three-dimensional chaotic mixing of Newtonian fluids in a previously uninvestigated cylindrical cavity was studied both experimentally and numerically for creeping flow conditions. Such mixing processes have practical application to the blending of viscous fluids, biological suspensions, or can be used as test beds to study waterborne pollutant formation. A mixing chamber was fabricated which consisted of a cylindrical glass cavity with independently rotating upper and lower circular disks. Fluid motion was revealed by digitizing successive video images of a small neutrally buoyant sphere placed into the mixing cavity and also by photographing dyed blobs. Experimental particle tracking studies were supplemented by numerical simulations. Phase-space trajectories, return maps, and Lyapunov exponents were used to characterize the mixing process and to confirm chaotic behavior.

Introduction

The transport of thermal energy or a molecular species in a fluid is greatly enhanced by mixing. Often, mixing occurs due to turbulence that arises above some critical Reynolds number owing to inertial effects. However, in very viscous fluids or in situations where inertial forces can have adverse effects on components conveyed by a fluid, the flow may be laminar either as a consequence of very low Reynolds numbers or by design. For example, desirable properties in plastics are sometimes obtained by blending molten polymers. Due to very high viscosities, the mixing process is performed at low velocities in order to suppress viscous dissipation and the resulting degeneration of long-chain polymer molecules. Individual components comprising synthesized or purified blood or other biological suspensions must be combined gently such that cellular components are not damaged. Particles are sometimes formed in industrial processes through the agglomeration of separate components suspended in a fluid. In such cases, inertial forces can limit particle sizes or preclude agglomeration. The creation of waterborne pollutants in the environment from precursors can occur in complex time-varying flows prevailing in large quiescent lakes or ponds. Mixing in the laminar flow regime can provide a good laboratory model to study pollutant formation.

Although the foregoing examples illustrate a broad rationale for investigating three-dimensional chaotic mixing, this study was primarily motivated by the realization that chaotic behavior in multiphase molten polymeric systems can be utilized to create in situ very fine-scale structures which may be captured by solidification. This technique has been employed to synthesize simple polymeric composites with very fine lamellae or fibers from single and multiple minor phase clusters in a mixing cavity closely related to the one considered in the present paper (Zumbrunnen et al., 1995). It should be noted that interesting fine-scale interfacial structures of solidified specimens can also be inspected by microscopy and photography, so the technique also has direct application to studies of multiphase flows.

Chaotic mixing has been investigated recently in two-dimensional flows within cavities. Much of this work has been done to elucidate fundamental mixing processes and has been summarized by Chien et al. (1986) and Ottino (1989). Aref (1984) and Aref and Balachandar (1986) demonstrated that the equations governing the mixing process in two-dimensional incompressible flows constitute a Hamiltonian system and are characterized by phase spaces in which the sizes of enclosed areas are preserved upon deformation. By contrast, when fluids are compressible or the flow field is three-dimensional, the governing equations constitute dissipative systems which have contracting areas in phase spaces leading to fractal structures in Poincaré sections.

Three-dimensional chaotic mixing was achieved in this study under creeping flow conditions within a previously uninvestigated cylindrical cavity formed between rotatable upper and lower circular disks and a stationary lateral surface. Chaotic mixing involves the chaotic motion of individual fluid particles and not necessarily chaotic fluctuations in the velocity field, which may be regular. Chaos therefore occurs in a Lagrangian sense; and it is instructive to first consider pathlines associated with the steady flow field. In Fig. 1, the pathlines in the mixing cavity are shown for the steady rotation of an upper concentric disk and the simultaneous rotation of an offset lower disk. Simultaneous and steady rotation of both disks establishes a locus of hyperbolic points within the flow field and associated homoclinic orbits. For creeping flows, the momentum equations for fluid motion are linear so that the steady pathlines of Fig. 1 are evident in return maps prior to the onset of chaos in the mixing cavity.

The cavity flow of Fig. 1 is related to the blinking vortex first studied by Aref (1984) and later also investigated by Khakhar et al. (1986), which was shown to be a two-dimensional Hamiltonian flow. Although the mixing process in the cavity was three-dimensional, the kinematical description for two-dimensional flows can be applied in a qualitative sense to better convey underlying events leading to chaos in fluid particle motions. Chaotic mixing was instilled by rotating separately the upper and lower disks to the cylindrical mixing cavity of Fig. 1. In the blinking vortex, a two-dimensional flow is established by the action of identical vortices separated by a small distance. When both vortices act steadily, a single hyperbolic point is formed at the midpoint between them. The rotational motion of the vortices and the hyperbolic point in the pathlines for the steady flow field resemble the rotational motions of the disks and the locus of hyperbolic points in Fig. 1. As with the disks of the mixing cavity, when the vortices acted alternately, chaotic motion in fluid particles was induced. The extent of chaotic regions in the vicinities of the vortices was determined by a

Contributed by the Fluids Engineering Division for publication in the JOURNAL OF FLUIDS ENGINEERING. Manuscript received by the Fluids Engineering Division June 9, 1994; revised manuscript received February 7, 1995. Associate Technical Editor: M. Gharib.

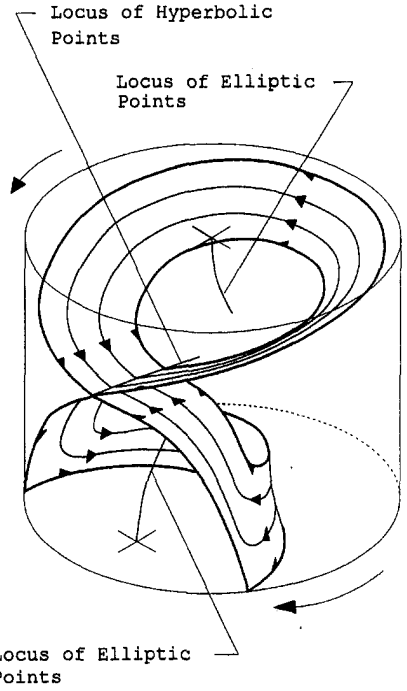

Fig. 1 Illustration of loci of elliptic and hyperbolic points. (Note: The orientation of the cavity in subsequent figures is identical to the one shown.)

perturbation strength that was proportional to the overall time, or period, for the separate and equal flow of each vortex. At small perturbation strengths, particle motion was regular. However, at higher perturbation strengths, chaotic motion was first evident in Poincaré sections in the vicinity of each vortex. At still higher perturbation strengths, chaotic motion evolved also from the vicinity of the location of the central hyperbolic point. Separate regions of chaotic behavior formed heteroclinic intersections at higher perturbation strengths until chaotic mixing occurred throughout a large domain between the vortices. A similar encroachment on nonchaotic regions was disclosed for the cylindrical mixing cavity of this study when the rotational displacements of the disks were increased.

Three-dimensional chaotic mixing in a previously uninvestigated cylindrical cavity is demonstrated experimentally and numerically in light of the aforementioned applications. The mixing cavity has many attributes. It can be easily constructed and driven. Liquids can be readily contained. Heat can also be removed effectively through the large, accessible disk surfaces in order to capture by solidification interesting emergent features of interfaces between phases.

Experimental Apparatus and Methods

The apparatus is shown schematically in Fig. 2. A cylindrical mixing cavity of 7.87 cm diameter was contained within a cylin-

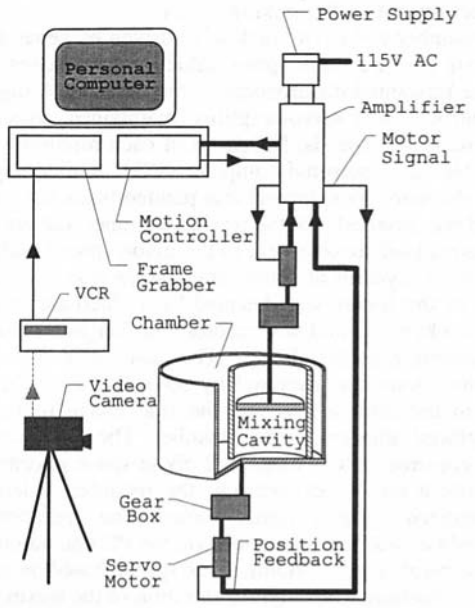

Fig. 2 Schematic representation of the apparatus

Nomenclature

A = aspect ratio of the mixing cavity = H/D
D = inner diameter of mixing cavity = 7.87 cm
e = eccentricity between the axes of rotation of the upper and lower disks = E/R
E = radial distance between centers of upper and lower disks (m)
H = height of mixing cavity
N = number of periods, where one period comprises the separate rotation of both disks
N_R = total angular displacement of both disks in terms of number of rotations = $2\,N\mu$
P = dimensionless pressure = P_*/P_0
P_* = pressure (N/m^2)
P_0 = scale factor for pressure = $\mu V_\theta/H$
r = dimensionless radial coordinate (Fig. 4) = r_*/R
r_0 = initial radial location of center of tracked sphere or dyed minor phase cluster
r_* = radial coordinate (m)
R = inner radius of mixing cavity
Re = Reynolds number = $\omega R^2(1 + e)/\nu$
t = dimensionless time = t_*/T
t_* = time
T = time interval equivalent to one-half period, where one period comprises the separate rotation of each disk
u_r = radial velocity component (m/s)
u_z = vertical velocity component (m/s)
u_θ = angular velocity component (m/s)
v_r = dimensionless radial velocity component = u_r/V_r
v_z = dimensionless vertical velocity component = u_z/V_z
v_θ = dimensionless angular velocity component = u_θ/V_θ
V_r = radial velocity scale factor = $e\omega R$
V_z = vertical velocity scale factor = $e\omega R$
V_θ = angular velocity scale factor = $\omega R(1 + e)$
z = dimensionless vertical coordinate (Fig. 4) = z/z_*
z_0 = initial vertical position of center of tracked sphere or dyed discrete phase cluster (m)
z_* = vertical coordinate (m)
θ = dimensionless angular coordinate = θ_*/Φ
θ_0 = initial angular location of center of tracked sphere or dyed minor phase (radians)
θ_* = angular coordinate (radians)
μ = perturbation strength in terms of the fraction of a complete rotation in each period for the upper and lower disks
ν = kinematic viscosity (m^2/sec)
ρ = mass density of fluid (kg/m^3)
Φ = angular displacement per disk per period (radians) = ωT
ω = rotational velocity of disks (radians/s)

drical chamber of 15.24 cm diameter. Both the cavity and chamber were filled with glycerin and were constructed of transparent glass. A small vertical distance of less than about 250 μm was maintained between the lower side walls of the mixing cavity and the lower surface of the chamber to separate the liquid within the mixing cavity from the liquid within the chamber. The floor of the chamber and a disk suspended into the mixing cavity of 7.62 cm diameter were rotated separately in order to induce mixing. Thus, the chamber floor was effectively a lower disk with respect to the mixing cavity. The axes of the mixing cavity and the chamber were offset in order to establish a three-dimensional flow field and pathlines of the type depicted in Fig. 1. The offset distance between the rotational axes was fixed at 2.76 cm. This axis offset placed the chamber axis at a position located 70 percent (i.e., $e = 0.70$) of the distance from the mixing cavity axis to the mixing cavity wall. The height of the suspended disk above the chamber floor was adjustable to vary the aspect ratio A of the mixing cavity.

The chamber and cavity disk were driven by separate servomotors via zero-backlash speed reduction gear boxes so as to minimize unwanted disturbances during mixing. A digital motion controller and servo-amplifier maintained constant prescribed rotational speeds. Durations of each rotation were programmable via a personal computer (PC). A nylon sphere of 2.4 mm diameter (not shown) was painted black for good contrast and was inserted into the mixing chamber. Layers of black paint were added successively to the nylon sphere until neutral buoyancy in glycerin at room temperature was obtained. The position of the sphere was detected by a video camera against a white background and was recorded on magnetic tape with a video cassette recorder (VCR). The position of the sphere in three-dimensions was captured by recording both the images normal to the camera lens and the side image reflected in a mirror placed adjacent to the chamber. These positions were used to construct return maps and phase space portraits. After completing a mixing experiment, the recorded video images were digitized using a frame grabber. The operation of the frame grabber was programmable via the PC and automatically identified pixels corresponding to the sphere based on a contrast threshold criterion. Although the duration of the mixing experiments was as long as 4 hours, this feature provided for the automatic detection and recording of the sphere positions in three-dimensional space. The uncertainty in position stemmed principally from the accuracy of the digitization process and slight mismatches in the densities of the glycerin and painted nylon sphere. This uncertainty was estimated by constructing a time series of the difference in the sphere positions at the completion of successive mixing periods when the particle motion was nonchaotic. An uncertainty of 0.004 D was determined for a 95 percent confidence interval. This distance, 0.38 mm, was small in comparison to the 2.4 mm sphere.

In all experiments, the top and bottom disks of the mixing cavity were rotated alternately with the rotation of one disk comprising one-half period. The total rotational displacement of each disk within each period was held constant in each experiment and was identical for both disks. The rotational displacement was expressed in terms of a perturbation strength μ defined as the fraction of a complete rotation for one disk. This definition is analogous to the one given for the blinking vortex, which was discussed previously. Identical rotational speeds of 0.69 revolutions per minute for each disk were employed that corresponded to the creeping flow regime as verified by the numerical model. Refraction due to the curved lateral surface of the glass mixing chamber introduced error in the detected position of the suspended sphere. However, this position error was deemed acceptable since a critical comparison between experimental and numerical results with regard to regular or chaotic behavior could still be made.

A 1.5 cm–2.0 cm diameter spherical minor phase cluster of a dyed glycerin-water mixture was injected into the mixing cavity in order to visualize the effect of stretching and folding processes for differing perturbation strengths with $A = 0.4$. The densities of the dyed minor phase and the transparent major phase in the mixing cavity were matched by diluting glycerin with a concentration of water similar to the dyed phase. Striations in the minor phase were recorded on photographic film and video tape. Interfacial morphologies have also been inspected by optical microscopy by solidifying low density polyethylene in a related mixing cavity. Full descriptions and micrographs of thin sections have been presented separately (Zumbrunnen et al., 1995; Liu and Zumbrunnen, 1995).

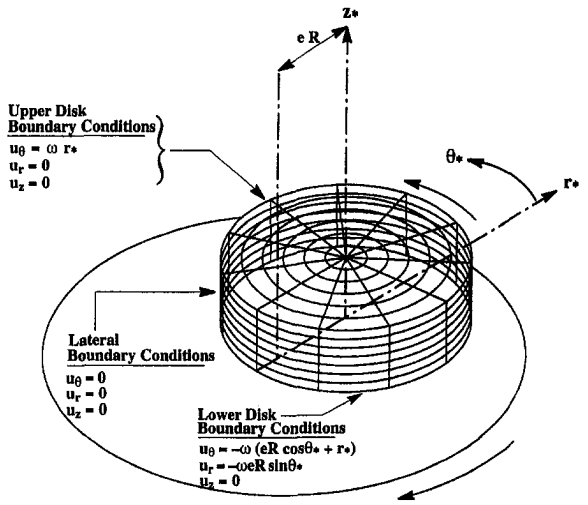

Fig. 3 Computational domain and boundary conditions employed in the numerical modeling of the mixing process

Governing Equations and Numerical Modeling

Numerical modeling was performed under conditions pertaining to the following assumptions: (i) steady, isothermal laminar flow, (ii) constant thermophysical properties, (iii) negligible body forces in comparison to viscous forces, (iv) inertial forces negligible in comparison to viscous forces. The computational domain and applicable velocity boundary conditions for the numerical model are shown in Fig. 3. The computational domain was a cylindrical region resembling the mixing cavity of Fig. 2 and was of identical dimensions. The radial and angular velocity components for both disks were expressed with respect to the reference frame aligned with the cavity axis by employing trigonometric relationships between the respective velocity components of the offset and aligned reference frames. Expressions are given in Fig. 3. The Navier-Stokes equations were scaled with suitable dimensionless parameters and variables defined in the Nomenclature. For example, since flow was deflected upward by the cavity wall (Fig. 1), the velocity scale V_z for u_z was taken to be the maximum rotational velocity of the offset lower disk. Other velocity scales followed directly from the expressions in Fig. 3. The velocity scale for pressure, P_0, was related to maximal viscous shear stresses since mixing was performed under creeping flow conditions. The corresponding scaled Navier-Stokes equations in cylindrical coordinates are given by Eqs. (1)–(3).

r momentum:

$$\mathrm{Re}\left[\frac{e}{\Phi}\frac{\partial v_r}{\partial t} + e^2 v_r \frac{\partial v_r}{\partial r} + \frac{e(1+e)}{\Phi}\frac{v_\theta}{r}\frac{\partial v_r}{\partial \theta} - (1+e)^2\frac{v_\theta^2}{r}\right.$$

$$\left. + \frac{e^2}{2A} v_z \frac{\partial v_r}{\partial z}\right] = -\frac{1}{2A}(1+e)^2\frac{\partial p}{\partial r} + e(1+e)\frac{\partial}{\partial r}$$

$$\times \left(\frac{1}{r}\frac{\partial}{\partial r}(rv_r)\right) + \frac{e(1+e)}{\Phi^2}\frac{1}{r^2}\frac{\partial^2 v_r}{\partial\theta^2} + \frac{e(1+e)}{4A^2}\frac{\partial^2 v_r}{\partial z^2} - \frac{(1+e)^2}{\Phi}\frac{2}{r^2}\frac{\partial v_\theta}{\partial\theta} \quad (1)$$

θ momentum:

$$\mathrm{Re}\left(\frac{1}{\Phi}\frac{\partial v_\theta}{\partial t} + ev_r\frac{\partial v_\theta}{\partial r} + \frac{1+e}{\Phi}\frac{v_\theta}{r}\frac{\partial v_\theta}{\partial\theta} + e\frac{v_r v_\theta}{r} + \frac{e}{2A}v_z\frac{\partial v_\theta}{\partial z}\right)$$
$$= (1+e)\left[-\frac{1}{2Ar}\frac{\partial p}{\partial\theta} + \frac{\partial}{\partial r}\left(\frac{1}{r}\frac{\partial}{\partial r}(rv_\theta)\right) + \frac{1}{\Phi^2 r^2}\frac{\partial^2 v_\theta}{\partial\theta^2} + \frac{1}{4A^2}\frac{\partial^2 v_\theta}{\partial z^2} + \frac{e}{\Phi(1+e)}\frac{2}{r^2}\frac{\partial v_r}{\partial\theta}\right] \quad (2)$$

z momentum:

$$\mathrm{Re}\left(\frac{1}{\Phi}\frac{1}{1+e}\frac{\partial v_z}{\partial t} + \frac{e}{1+e}v_r\frac{\partial v_z}{\partial r} + \frac{1}{\Phi}v_\theta\frac{\partial v_z}{\partial\theta} + \frac{e}{1+e}\frac{1}{2A}v_z\frac{\partial v_z}{\partial z}\right) = \frac{1}{r}\frac{\partial}{\partial r}\left(r\frac{\partial v_z}{\partial r}\right)$$
$$+ \frac{1}{r^2\Phi^2}\frac{\partial^2 v_z}{\partial\theta^2} + \frac{1}{4A^2}\frac{\partial^2 v_z}{\partial z^2} - \frac{1+e}{e}\frac{1}{4A^2}\frac{\partial p}{\partial z} + \frac{1}{e}\frac{gR}{\omega\nu} \quad (3)$$

The selection of the appropriate Reynolds number Re for the experiments was based on reducing inertial forces while also minimizing the time for molecular diffusion of the dyed minor phase clusters (Leong and Ottino, 1989). As in the experiments, most numerical results pertained to $e = 0.7$ and $A = 0.3$. However, aspect ratio was varied within the range $0.3 < A < 0.5$ to assess the influence on the chaotic mixing process. For these parametric conditions, Eqs. (1)–(3) indicate that inertial forces are not large away from the cavity axis ($r = 0$) in comparison to viscous forces with $\mathrm{Re} \ll 1$. Due to singularities at $r = 0$ in some inertial terms in Eqs. (1)–(3), terms with singularities were retained in numerical calculations. With the stated values of A, e, and with $\mathrm{Re} = 0.5$, creeping flow was closely attained as confirmed by agreement to within 0.82 percent between numerically generated steady velocity components determined with and without the neglected inertial terms present in Eqs. (1)–(3). This Reynolds number was therefore adopted in the calculations and experiments. Experimental confirmation of creeping flow conditions was also obtained by reversing the rotation of the disks and ensuring that the tracked sphere returned to its initial location for various rotational velocities. Such *kinematic reversibility* is characteristic of steady creeping flows and is consistent with steady solutions to Eqs. (1)–(3) for $\mathrm{Re} \to 0$. It is important to note that, as a result of kinematic reversibility, the pathlines for creeping flows are independent of the magnitude of the fluid velocity. Since chaotic behavior is evident when a Lagrangian perspective is adopted, results are presented in terms of fluid particle positions within the mixing cavity in lieu of detailed velocity fields. Inspection of Eqs. (1)–(3) indicates that results under creeping flow conditions (Re 0) are independent of the fluid viscosity. Results are therefore generally applicable to all Newtonian fluids when mixing is performed in accordance with the assumptions given earlier. The aspect ratio A, the eccentricity e between the disk shafts, and the dimensionless angular displacement Φ of the disks are the relevant parameters according to the scaling analysis.

With the inertial and transient terms removed excepting terms with singularities at $r = 0$, Eqs. (1)–(3) were solved numerically for the cases where each disk moved separately and steadily. Neglecting some terms in accordance with the scaling analysis yielded faster computations and results applicable to creeping flows which were of interest. The momentum equations were discretized using the finite-volume approach and were solved according to the SIMPLER method (Patankar, 1980). A uniform mesh was used in the radial, angular, and axial directions. Insensitivity to mesh size was assessed by determining differences upon mesh refinement in calculated velocities at twelve unique reference points within the computational domain. The selected mesh included 51 nodes in the angular direction and 31 nodes in both the radial and axial directions. (The mesh in Fig. 3 is coarser for clarity.) Convergence in a line-by-line tridiagonal matrix algorithm was assessed by monitoring the change in calculated velocities at all offset grid locations where velocities were greater than five percent of the maximum velocity specified at one of the disk surfaces. Iterations were continued until successive values at all monitored locations differed by less than 0.004 percent and the total residual for all velocity components was less than 10^{-6}. Typically, 800 iterations were required. The accuracy of the numerical solutions was estimated by comparison to an available exact analytical solution for creeping flow in a related cylindrical cavity with a rotating concentric bottom disk, stationary lateral surface, and stationary upper confining disk (Pao, 1972). Numerical solutions were determined to be within 1.34 percent at all offset grid locations. In addition, experimental and numerical pathlines and return maps were found to be in excellent agreement.

The velocity protocol for the rotations of the disks was identical to the one described earlier for the experiments. Velocity fields from the numerical model were used to track a particle placed at an initial location within the computational domain. In this manner, numerical and experimental results could be directly compared. Velocities within the mesh were estimated by linear interpolation in the three orthogonal directions based on proximity with neighboring finite volume faces where velocities were determined numerically. The change $\Delta\mathbf{r}$ in the particle position was then calculated from the velocity v according to $v\Delta t$, where the time step $\Delta t = 0.001/\omega$. This time step was selected by successively reducing its value until periodic particle trajectories produced closed curves for long integration times as required for periodic behavior.

Lyapunov exponents for the mixing process were calculated with the numerically generated velocity fields by determining the distance of six tracked particles from a fiduciary particle after the completion of successive mixing periods. With the six particles initially placed symmetrically a small distance $d_0 = 0.0001\ D$ from the fiduciary, the subsequent positions of all particles, including the fiduciary, were determined. The positions of the tracked particles were returned to their initial orientation about the subsequent positions of the fiduciary in the event that the distance of any tracked particle from the fiduciary exceeded $0.1\ D$. Tracking six particles in lieu of one particle about a fiduciary provided more rapid convergence in the calculated Lyapunov exponents and thereby reduced the computational effort. The algorithm is summarized by Eq. (4), where $d_{n,i}$ was the distance between the i^{th} particle and the fiduciary particle at the completion of N periods.

$$\lambda = \lim_{N\to\infty}\frac{1}{N}\sum_{n=0}^{N}\frac{1}{6}\sum_{i=1}^{6}\log_2\frac{d_{n+1,i}}{d_{n,i}} \quad (4)$$

This algorithm for Lyapunov exponent is related directly to those used for the evaluation of dynamical responses for iterated mappings (Moon, 1992). Positive Lyapunov exponents indicate sensitivity to initial conditions and thereby chaotic behavior. Regular behavior is indicated by this algorithm when Lyapunov exponents approach zero or a negative value. Calculated Lyapunov exponents were found to differ by about 12 percent when particle pathlines were calculated with time increments Δt of $0.001/\omega$, $0.0005/\omega$, and $0.0001/\omega$. Uniform convergence with decreasing Δt could not be obtained due to accumulated round-off errors and small inaccuracies in the numerically determined velocity field. Calculated Lyapunov exponents were therefore

useful in distinguishing between regular and chaotic behavior except when calculated values were near zero and a mild chaotic condition may have prevailed.

Results and Discussion

Experiments were performed for ranges in the mixing cavity aspect ratio A, the perturbation strength μ, and for various initial positions (r_0, θ_0, z_0) of the suspended sphere. The perturbation strength is a measure of the angular displacement of each disk during each period, where one period is comprised of identical time intervals for each disk to rotate separately. Since the experiments and numerical studies pertained to creeping flow conditions, inertial effects were negligible and the position of the tracked sphere with either disk rotating steadily thereby depended only on elapsed time for any specific rotational speed. For example, doubling the rotational speed caused the sphere to move twice the distance along the *same* path in a given time interval. Thus, rotational speed was not varied as a parameter.

Representative phase space portraits of the tracked sphere located within the experimental mixing cavity are shown in Fig. 4 for two different perturbation strengths. (The orientation of the mixing cavity in this and subsequent figures is identical to the one specified for Fig. 1.) Results for only the first 5 to 10 periods are shown in order to avoid filling the phase space and thereby obscuring individual trajectories, where each period corresponded to the successive rotation of both disks by an identical amount. With the perturbation strength $\mu < 0.4$, trajectories formed closed loops in regions of the cavity corresponding to the elliptic points in Fig. 1 and the pathlines of Fig. 1 were reconstructed owing to the linearity of the momentum equations under creeping flow conditions. For $\mu = 0.4$, differences in the locations of the tracked sphere along the left-upper portions of the trajectories in Fig. 4 exceeded the experimental uncertainty in the position of the tracked sphere. The sphere motion was therefore not periodic. Numerical simulations indicated that adjacent chaotic regions that evolved from the vicinity of the hyperbolic points of the steady flow field in Fig. 1 encroached upon the loops and degraded them. This degradation in the elliptic flow structures will be further examined in experimental and numerical return maps. With $\mu = 0.8$, the tracked sphere was transported to a markedly larger region within the mixing cavity and trajectories clearly did not repeat. Continued plotting of the trajectories would yield a darkened region as the trajectories increasingly occupied a greater portion of the phase space.

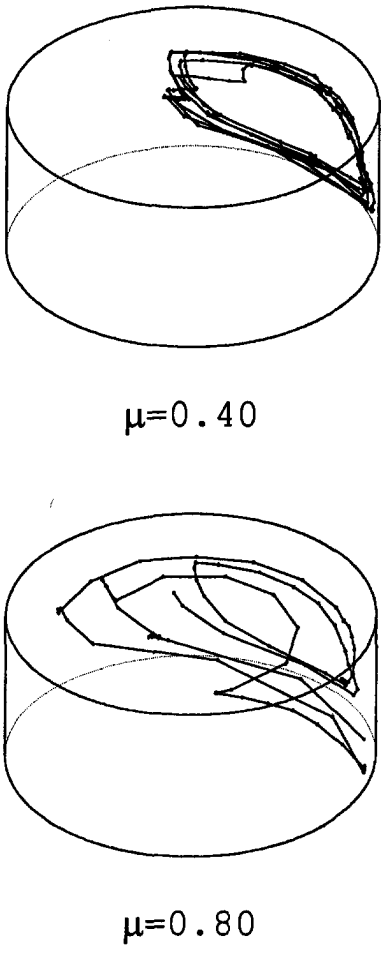

Fig. 4 Experimental phase space portraits indicating a degradation of the periodic trajectories of the tracked sphere within the mixing cavity due to an increase in the perturbation strength μ with $A = 0.3$, $r_0 = 0.45\ D$, $\theta_0 = \pi/4$ and $z_0 = 0.5\ H$

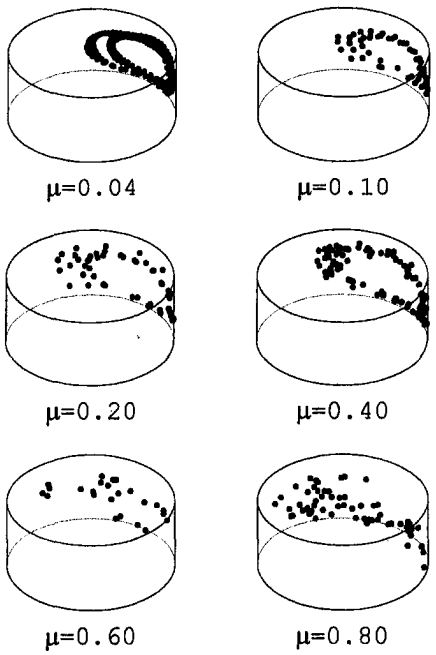

Fig. 5 Experimental return maps indicating a broadening of the chaotic region within the mixing cavity due to increases in the perturbation strength μ with $A = 0.3$, $r_0 = 0.45\ D$, $\theta_0 = \pi/4$, and $z_0 = 0.5\ H$

The situation is shown more clearly in terms of return maps in Fig. 5. These maps give the successive locations of the tracked sphere within the experimental mixing cavity at the completion of each subsequent period. Regular motion is clearly indicated in the return maps when the locations form closed loops or short line segments, depending on the view perspective of the three-dimensional cavity. Only a limited number of locations are shown in Fig. 5 to improve clarity. For $0.04 < \mu < 0.40$, the locus of locations forms loops which suggest regular motion. For $\mu > 0.4$, the locations of the sphere become increasingly uncorrelated, suggesting a broadening region of chaotic motion. Thus, within a region of the mixing cavity containing the point $r_0 = 0.45\ D$, $\theta_0 = \pi/4$, and $z_0 = 0.5\ H$ corresponding to the initial location of the tracked sphere, experimental results indicated that a transition to a markedly broadened chaotic region occurred for $0.4 < \mu < 0.8$. A transition with increasing perturbation strength in this three-dimensional cavity flow is consistent with results reported for chaotic mixing in two-dimensional flows (Aref, 1984; Chien et al., 1986).

In Fig. 6, numerically generated return maps are given for conditions corresponding to those of the experimental results in Fig. 5. Behavior in the vicinity of the hyperbolic flow struc-

tures of Fig. 1 are also shown. Small dots (·) have been used for points initially associated with the elliptic regions and small crosses (+) have be used for points initially associated with the hyperbolic regions. These different symbols can be used to discern the extent of chaotic regions within the cavity. Since the numerical model tracked massless points of zero volume, the locus of elliptic points in Fig. 6 differed somewhat from those measured experimentally with the tracked sphere of finite size. However, it is apparent upon inspection of Figs. 5 and 6 that $\mu \cong 0.6$ when chaotic behavior became evident in both the theoretical calculations and experimental results. The flow structure in the vicinity of the hyperbolic points shown in Fig. 1 is evident in the return maps of Fig. 6 when chaotic behavior is weak. This circulation degenerated at higher perturbation strengths with the degeneration evolving from the vicinity of the hyperbolic point. The closed loop structures in the vicinity of elliptic points in the right portion of the cavity degenerated in response to encroachment by particles from the adjacent chaotic regions. Regions of regular behavior persisted within elliptic regions that were smaller at higher perturbation strengths. A globally chaotic condition occurred at a high perturbation strength for which detectable elliptic regions vanished. This condition is shown in Fig. 6 for $\mu = 0.8$.

Numerical predictions in Fig. 6 show that chaotic motion existed at small perturbation strengths ($0.2 < \mu < 0.4$) near the vicinity of the locus of hyperbolic points in the steady pathlines of Fig. 1. However, the chaotic behavior was confined to small regions and regular motion prevailed throughout the balance of the cavity. The transition in the characteristics of the motion was confirmed by flow visualization with a passive dye injected at $r_0 = 0.45\ D$, $\theta_0 = 1.02\ \pi$, and $z_0 = 0.65\ H$. For $\mu = 0.4$, a dyed minor phase cluster was stretched and folded and ultimately was transformed into a wispy structure of thin filaments. These filaments remained confined within a volume that resembled the hyperbolic structure in the corresponding

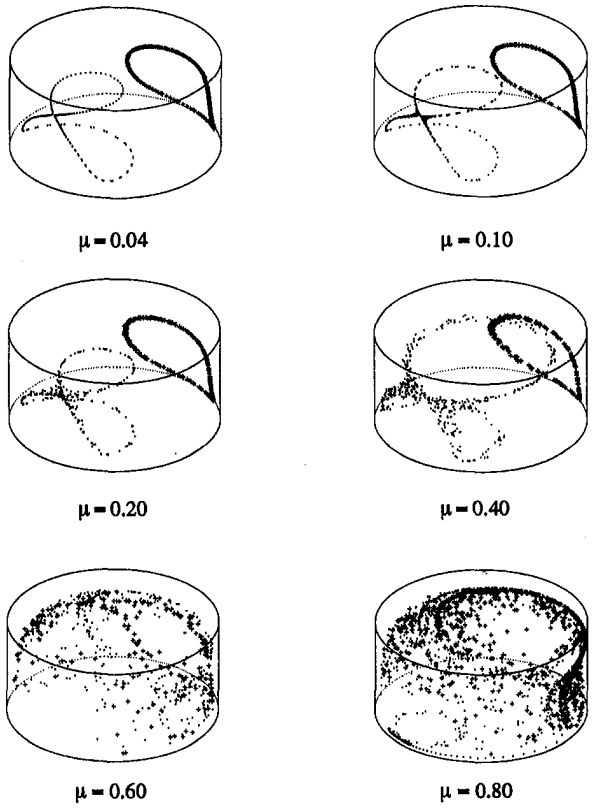

Fig. 6 Numerically generated return maps indicating a transition to chaotic behavior due to increases in the perturbation strength μ with $A = 0.3$

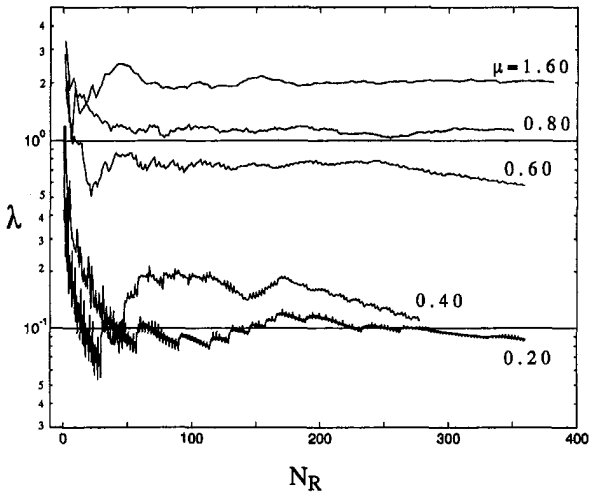

Fig. 7 Calculated Lyapunov exponents from the numerically generated velocity fields with increasing perturbation strength μ for $A = 0.3$, $r_0 = 0.45\ D$, $\theta_0 = \pi/4$, and $z_0 = 0.5\ H$

return map of Fig. 6 for $\mu = 0.4$. Thus, the flow visualization and numerical predictions were consistent. At the location $r_0 = 0.45\ D$, $\theta_0 = \pi/4$, and $z_0 = 0.5\ H$ of Fig. 5, the much simpler loop-like structure was formed with no apparent chaotic behavior. This loop structure was also consistent with the return map of Fig. 6 for $\mu = 0.4$.

The effect of the mixing cavity aspect ratio A was examined over the range $0.3 < A < 0.5$ by repositioning the upper disk in the experimental apparatus (Fig. 2). Increasing the aspect ratio decreased the circulation between the upper and lower surfaces (Fig. 1) in the outer region of the mixing cavity owing to the no-slip condition at the stationary lateral surface. Transition therefore occurred at higher perturbation strengths for larger aspect ratios. In order to determine the onset of chaotic mixing throughout the interior of the cavity for different aspect ratios, return maps of the type shown in Fig. 6 were developed for different perturbation strengths. Chaotic behavior was found to evolve principally from the vicinity of the hyperbolic (x-shaped) structures and encroach upon other portions of the mixing cavity. Regular behavior persisted within elliptical regions that diminished in size with increasing perturbation strength. A transition perturbation strength μ_t was therefore defined to be the perturbation strength at which these elliptic regions vanished. Values of μ_t were 1.25, 1.85, and 2.65 for aspect ratios of 0.3, 0.4, and 0.5, respectively. When plotted, a nearly linear relationship is suggested by these results. Thus, extrapolations to slightly smaller or larger aspect ratios or to aspect ratios within $0.3 < A < 0.5$ seems reasonable in order to ensure effective mixing in similar cylindrical mixing cavities.

The numerical model was used to estimate the Lyapunov exponent λ according to Eq. (4) and thereby confirm the chaotic motion of the fluid particles. In order to reveal conditions for which chaotic mixing can be expected to occur throughout the interior portions of the mixing cavity, the fiduciary and six neighboring particles employed in Eq. (4) were located initially within the more persistent elliptical regions shown in Figs. 5 and 6. Results are given in Fig. 7 for specific perturbation strengths as a function of the total number of rotations N_R of both disks. For $\mu < 0.60$, λ initially decreases and eventually fluctuates about small positive values near zero owing to the sensitivity of the Lyapunov exponent to numerical accuracy. However, for larger perturbation strengths, single positive values for λ are eventually obtained. These positive values are consistent with the onset of a global chaos condition in the return maps of Figs. 5 and 6. Fluctuations in calculated positive Lyapunov exponents pertain to the summation process associ-

ated with the calculation of λ. The positive Lyapunov exponents, dispersed points in the return maps (Figs. 5 and 6), degeneracy in closed pathlines in phase spaces (Fig. 4), and the observed stretching and folding of dyed minor phase clusters at high perturbation strengths are confirmations of chaotic behavior in the mixing cavity.

Conclusions

Three-dimensional chaotic mixing can arise in a cavity formed between a cylindrical surface and upper and lower disks when the disks are rotated periodically. Chaotic motion occurs first near the locations of hyperbolic points associated with the steady flow pathlines for the simultaneous rotations of both disks. A marked broadening of chaotic regions occurs as the angular displacement of the disks increases. The requisite angular displacement for extensive chaotic mixing throughout the cavity is smaller for lower cavity aspect ratios. Specific conditions for chaotic mixing have been disclosed and methodologies are described that are suitable for studies of three-dimensional chaotic mixing in cavity flows.

Acknowledgment

Support for this work was provided by the National Science Foundation of the United States under Grant No. CMS-9253640 and is gratefully acknowledged. The authors also wish to thank Mr. Jonathan Robertson of the South Carolina Governor's School for Science and Mathematics and Mr. Radu Danescu for assisting in the experimental work and calculations.

References

Aref, H., 1984, "Stirring by Chaotic Advection," *Journal of Fluid Mechanics,* Vol. 143, pp. 1–21.

Aref, H., and Balachandar, S., 1986, "Chaotic Advection in a Stokes Flow," *Physics of Fluids,* Vol. 29, pp. 3515–3521.

Chien, W.-L., Rising, H., and Ottino, J. M., 1986, "Laminar Mixing and Chaotic Mixing in Several Cavity Flows," *Journal of Fluid Mechanics,* Vol. 170, pp. 355–377.

Khakhar, D. V., Rising, H., and Ottino, J. M., 1986, "An Analysis of Chaotic Mixing in Two Chaotic Flows," *Journal of Fluid Mechanics,* Vol. 172, pp. 419–451.

Leong, C. W., and Ottino, J. M., 1989, "Experiments on Mixing Due to Chaotic Advection in a Cavity," *Journal of Fluid Mechanics,* Vol. 209, pp. 463–499.

Liu, Y. H., and Zumbrunnen, D. A., 1995, "Emergence of Polymer Composites Due to Chaotic Mixing of Molten Polymers," *Proceedings of the Annual Technical Conference,* Society of Plastics Engineers Vol. II-Materials, pp. 3104–3108; also: *Polymer Composites* (in press).

Moon, F. C., 1992, *Chaotic and Fractal Dynamics,* Wiley, New York, pp. 127–130.

Ottino, J. M., 1989, *The Kinematics of Mixing: Stretching, Chaos, and Transport,* Cambridge University Press, Cambridge, Great Britain.

Pao, H.-P., 1972, "Numerical Solution of the Navier-Stokes Equations for Flows in the Disk-Cylinder System," *The Physics of Fluids,* Vol. 15, No. 1, pp. 4–11.

Patankar, S. V., 1980, *Numerical Heat Transfer and Fluid Flow,* McGraw-Hill, New York.

Zumbrunnen, D. A., Miles, K. C., and Liu, Y. H., 1995, "Auto-Processing of Very Fine-Scale Composite Materials by Chaotic Mixing of Melts," *Composites Manufacturing* (in press).

Prediction of Compressible Flow Pressure Losses in 30–150 Deg Sharp-Cornered Bends

Nia Haidar
Department of Mechanical & Manufacturing Engineering, University of Brighton, Cockcroft Building, Lewes Road, Brighton BN2 4GJ, England

This paper considers the measurement and prediction of the additional total pressure losses of subsonic steady air flow in sharp-cornered bends, similar to those present in the secondary air cooling systems of gas turbine engines. The bends examined ranged between 30 to 150 in 30 deg increments and were circular in cross section. Experimental results covering a wide speed range up to choking are presented for five different bend geometries. An analytical flow model provided results in fairly good agreement with the measurements obtained and equally compared favourably with the experimental findings of other researchers at low Mach numbers. The highest attainable upstream Mach number (M_U) of the average upstream flow was 0.57 for the 30 deg bend. The maximum possible values of M_U represent a limiting condition dictated by downstream choking of the flow. The compressible flow coefficients, caused by the presence of the bends, can be expected to be between 10 to 20 percent higher than those for incompressible flow.

1 Introduction

In the air cooling systems of gas turbine engines, whether for aircraft propulsion or industrial applications, up to 20 percent of the core engine airflow may pass into the air system for various purposes including turbine blade cooling and so some account of the pressure losses is of importance for determining the overall engine efficiency.

This investigation is concerned with the determination of the additional total pressure losses (additional to those arising from wall skin friction losses of a straight duct) occurring in bends, both experimentally and numerically. This paper examines five different sharp-cornered bend geometries ranging between 30 to 150 in 30 deg increments, as shown in Fig. 1. The work involved collaboration with Rolls-Royce Plc. Previous papers by Haidar and Dixon (1988), Haidar and Dixon (1992), and Haidar and Dixon (1994) reported the results of an experimental, theoretical and flow visualization study covering 16 different tee and wye junctions. The available information on the flow and loss characteristics of bend components when the flow is well into the compressible regime is severely limited. Most of the published information for compressible steady air flows have been restricted to right angled pipe bends. Higginbotham et al. (1956), Ward-Smith (1964) and Srivastava (1971) reported experimental results for 90 deg circular pipe bends. However, a considerable amount of data exists for incompressible steady flows. Probably the most comprehensive and recognized data are those of ESDU (1973) and Miller (1978) obtained for bends with circular and rectangular cross-sections. These publications together with Haidar (1994) have established that the additional total pressure loss coefficients are independent of Reynolds number for $Re \geq 10^5$.

A two-dimensional representation of flow in a sharp-cornered bend, shown in Fig. 1, includes hypothetical regions of flow separation which are considered to be the major source of the additional total pressure losses in subsonic flows.

2 Experimental Study

The required test conditions were for steady flows of dry air up to $0.2 \leq M_U \leq 1.0$ and $Re_U \geq 2 \times 10^5$ and based on a duct diameter of 4 cm. The bends examined were all circular in cross section. The angle between the main duct axis and the downstream duct ranged between 30 to 150 deg, in 30 deg increments, as illustrated in Fig. 1. Both ducts were of equal diameter with coplanar axes and sharp intersections. A flow straightener followed by an area reducing section well upstream of the bend ensured that the velocity profile upstream of test section was close to a 7th power-law one. The instrumentation system used comprises of the following: a 48-port scanning valve, a pressure transducer, an analogue to digital converter, a temperature data logger, and a laptop PC. Further details regarding the air supply equipment manufacture, instrumentation, etc., are available in Haidar and Dixon (1994).

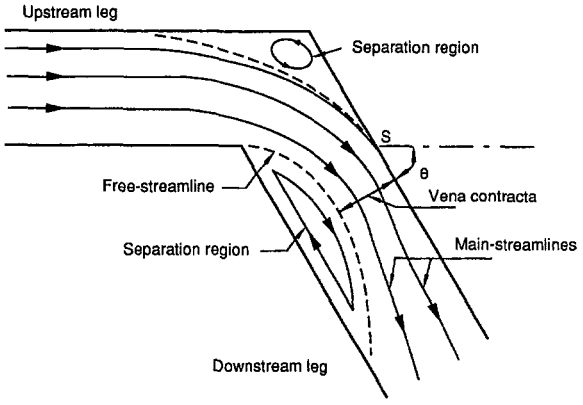

Fig. 1 Flow streamlines in a sharp-cornered bend, θ = 30, 60, 90, 120, and 150 deg

The upstream and downstream stagnation pressures were calculated from the knowledge of the corresponding static pressures and Mach numbers using the compressible isentropic flow pressure equation. The extrapolated pressure loss for one type of flow geometry is sketched in Fig. 2. The additional total pressure loss coefficient, K_{UD}, is defined as:

$$K_{UD} = \frac{P_U - P_D}{P_U - p_U} \quad (1)$$

Contributed by the Fluids Engineering Division for publication in the JOURNAL OF FLUIDS ENGINEERING. Manuscript received by the Fluids Engineering Division May 13, 1994; revised manuscript received February 17, 1995. Associate Technical Editor: Wing-Fai Ng.

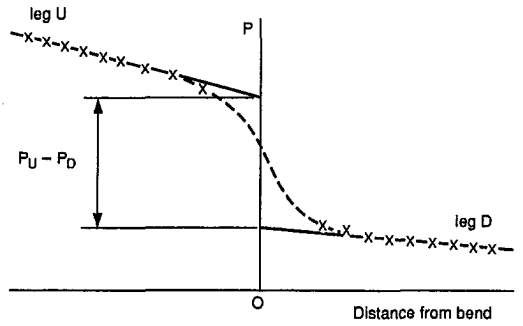

Fig. 2 Extrapolated total pressure loss between legs *U* and *D*

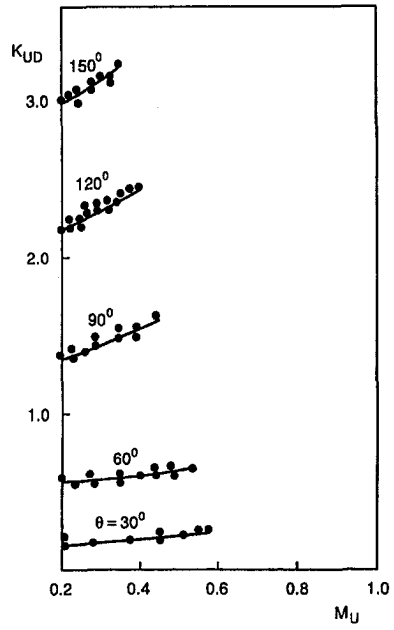

Fig. 3 Compressible flow pressure loss coefficient K_{UD} for θ = 30–150 deg (uncertainty in K_{UD} = ±0.05, in M_U = ±0.012)

The experimental results reported in this paper cover bends with θ = 30, 60, 90, 120, and 150 deg. The loss coefficients, K_{UD}, for the various flow geometries are represented as a function of the upstream Mach number, $M_U \geq 0.2$. The results are presented as a performance chart, as shown in Fig. 3.

3 Loss Coefficient Theory

The analytical model developed here for calculating the total pressure losses is based on the use of the free-streamline potential flow theory, which was first applied to dividing flows in

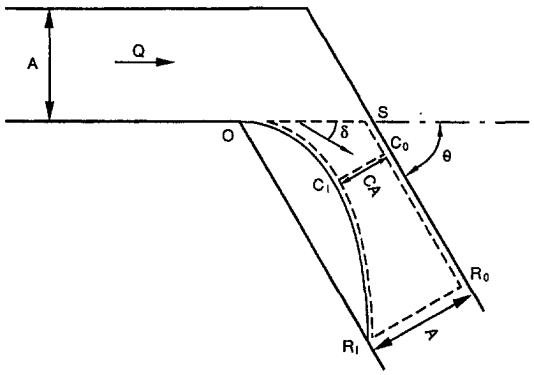

Fig. 4 Control volumes for the downstream duct

tee-junctions, was reported in Haidar and Dixon (1988). From this theory the shape of the downstream duct flow is determined. Control volumes are then selected to divide the flow into regions with either converging or diverging streamlines, a strategy enabling some simplifications to be made. Application of the momentum and energy equations to the contracting control volume yields the contraction coefficient C at the vena contracta, as shown in Fig. 4 for the downstream duct. A further application of the same equations to the diverging control volume is then sufficient to allow the loss coefficient to be determined.

Some important assumptions made are:

(i) The flow is two-dimensional, uniform, steady, irrotational, and incompressible.

(ii) The boundary of the flow separation region is regarded as a streamline

(iii) Average static pressures act along the free-streamline, and duct cross sections.

(iv) The total pressure loss occurring between upstream and downstream duct flows is due to a sudden expansion after the vena contracta.

(v) Point S, in Fig. 4, represents the stagnation point at which the streamline velocity vanishes. Therefore, the static pressure at point S can be assumed as:

$$p_S = p_U + \frac{1}{2}\rho\frac{Q^2}{A^2} \tag{2}$$

A comprehensive computational and flow visualization (Schlieren) investigations have lead to further assumptions:

(i) The velocity of the flow entering the downstream duct can be taken to be equal to the velocity of the flow upstream of the bend.

(ii) The static pressure at point O (p_o) is considered to be equal to p_U.

Nomenclature

A = area of duct
C = contraction coefficient at the vena contracta
K_{UD} = additional total pressure loss coefficient between legs U and D
M = Mach number
P = total pressure
P_D = extrapolated total pressure of leg D
P_U = extrapolated total pressure of leg U
Q = volume flow rate
R = gas constant
Re = Reynolds number
p = static pressure
δ = downstream inlet flow angle with respect to the main duct axis
θ = angle between the main duct axis and the downstream duct
ρ = density of the fluid

Subscripts

C = location where the vena contracta occurs
D = leg carrying the downstream flow
R = location where the free-streamline reattaches to the wall
S = stagnation point at which the main-streamline velocity vanishes
U = leg carrying the upstream flow

(iii) The average inlet flow angle, δ, varies uniformly with the downstream duct angle, θ, such that:

$$\delta = \tfrac{1}{3}\,\theta \tag{3}$$

3.1 Contraction Coefficient. Applying the momentum equation to the control volume *O-S* to C_I-C_O, as shown in Fig. 4, in the downstream duct direction and employing Eqs. (2) and (3):

$$p_U - p_C = \frac{2\rho Q^2}{(1 + C)A^2}\left[\frac{1}{C} - \frac{1}{4} - \cos\frac{2\theta}{3}\right] \tag{4}$$

Applying the energy equation to the above control volume:

$$p_U - p_C = \frac{\rho Q^2}{2A^2}\left[\frac{1}{C^2} - \frac{3}{2}\right] \tag{5}$$

Eliminating $(p_U - p_C)$ from Eqs. (4) and (5) yields a cubic relation for C:

$$C^3 + \frac{2}{3}\left[\frac{1}{2} - 4\cos\frac{2\theta}{3}\right]C^2 + 2C - \frac{2}{3} = 0 \tag{6}$$

For θ = 30, 60, 90, 120, and 150 deg, C is 0.673, 0.470, 0.378, 0.323, and 0.288, respectively.

3.2 Loss Coefficient. Again applying the momentum equation to the control volume $C_I - C_O$ to $R_I - R_O$, as shown in Fig. 4, in the downstream duct direction:

$$p_C - p_R = \frac{2\rho Q^2}{(1 + C)A^2}\left[1 - \frac{1}{C}\right] \tag{7}$$

With energy equation applied to the above control volume:

$$p_C - p_R = \frac{\rho Q^2}{2A^2}\left[1 + K_{UD} - \frac{1}{C^2}\right] \tag{8}$$

Equating Eqs. (7) and (8) the loss coefficient K_{UD} is derived:

$$K_{UD} = \frac{(1 - C)^3}{C^2(1 + C)} \tag{9}$$

Comparisons between the theoretical loss coefficient results, obtained using Eq. (9), and measurements are presented in Fig. 5.

4 Discussion of Results

A comparison between predictions and experimental pressure loss results, obtained for flows in 30–150 deg sharp-cornered bends, is presented in this section.

4.1 Incompressible Flow. Incompressible flow losses which were determined from the knowledge of compressible flow measurements, at M_U = 0.2 and Re = 2×10^5, are compared with the theory presented earlier. Figure 5 compares Eq. (9) with experimental data of loss coefficients, K_{UD}, for 30 deg $\leq \theta \leq$ 150 deg. It can be seen that predictions are generally in good agreement with experiments, especially for 60 deg $\leq \theta \leq$ 120 deg. Additionally, the experimental data of ESDU (1973) and Miller (1978) show good agreement with both predicted and measured results, as shown in Fig. 5. The loss coefficient measured for θ = 150 deg can be about 20 times higher in value than that for θ = 30 deg.

4.2 Compressible Flow. Analysis of the experimental results, shown in Fig. 3, confirms the expected influence of compressibility effects on the magnitudes of the loss coefficients at high values of Mach number for $\theta \geq$ 30 deg. Loss coefficients, K_{UD}, increase with increasing M_U. The highest attainable Mach number is 0.57 for θ = 30°. The relative uncertainty calculations are based on British Standard 1042 (1987). The uncertainties in K_{UD} and M_U are ±0.05 and ±0.012, respectively. For θ = 30 deg, it is evident that subsonic bend loss coefficients for $M_U > 0.57$ could not be obtained despite adequate pressure being available upstream. For $M_U > 0.57$, shock waves became present downstream of the bend and thus escalated the overall bend loss coefficient. The results for K_{UD} were determined over the range $0.2 \leq M_U \leq 0.57$, corresponding to $2 \times 10^5 \leq$ Re $\leq 2 \times 10^6$, for 30 deg $\leq \theta \leq$ 150 deg. At the choking limit, loss coefficients for 30 deg $\leq \theta \leq$ 150 deg are shown in Fig. 5. The loss coefficient measured for θ = 150 deg is about 20 times higher in value than that for θ = 30 deg. It is evident that the results obtained with Eq. (9) compare reasonably well with those obtained at the choking limit, as shown in Fig. 5. The difference between predictions and experimental data is mainly attributed to compressibility effects and secondary flow losses, which are not accounted for in the present two-dimensional theory.

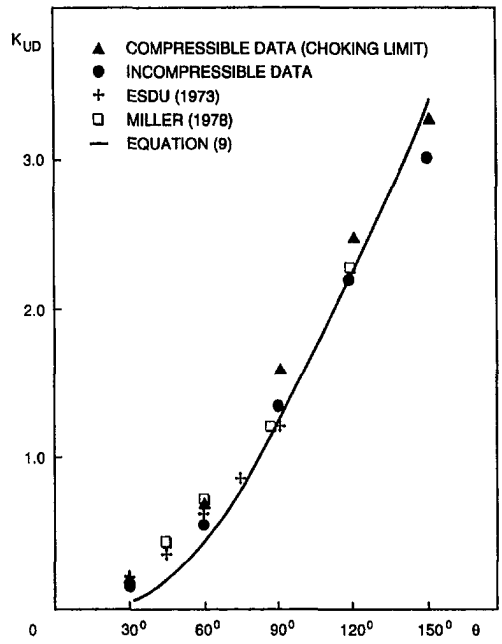

Fig. 5 Comparison between predicted, Eq. (9), and experimental pressure loss coefficient K_{UD} from various sources for θ = 30–150 deg

5 Conclusions

An analytical approach to the problem of predicting the additional total pressure loss coefficients in sharp-cornered 30–150 deg bends has been introduced. The important conclusions reported here are summarized as follows:

1. Comparison between predictions, obtained with Eq. (9), and measurements at low Mach number has in general yielded good agreement with the experimental findings of other researchers, obtained for bends with circular and rectangular cross sections. Moreover, Eq. (9), which is based on a two-dimensional theory, gives an acceptable prediction of the loss coefficients at high values of M_U. The discrepancy between the results is mainly due to compressibility effects and secondary flow losses.
2. The maximum subsonic upstream Mach number, M_U, of the flow is 0.57 for θ = 30 deg, at a limit which is dictated by a combination of choking and flow separation in the downstream duct of the bend. The compressible flow coefficients can be about 10 to 20 percent higher than those for incompressible flow.
3. Loss coefficients K_{UD} increase with increasing angle, θ. For $M_U \geq 0.2$, the loss coefficients for θ = 150 deg can be about 20 times higher in value than those for θ = 30 deg.

References

British Standard 1042, 1987, "Measurement of Fluid Flow in Closed Conduits," BSI.

ESDU, 1973, "Pressure Losses in Three-Leg Pipe Junctions: Dividing Flows and Combining Flows," ESDU, Nos. 73022 and 73023.

Haidar, N. I. A., and Dixon, S. L., 1988, "Compressible Flow Losses in Branched Ducts," *Collected Papers in Heat Transfer,* WAM of ASME, Chicago, IL, HTD-Vol. 104, No. 2, pp. 17–23.

Haidar, N. I. A., and Dixon, S. L., 1992, "Pressure Losses in Combining Subsonic Flows Through Branched Ducts," ASME *Journal of Turbomachinery,* Vol. 114, No. 9, pp. 264–270.

Haidar, N. I. A., and Dixon, S. L., 1994, "Measurement of Compressible Flow Pressure Losses in Wye-Junctions," ASME *Journal of Turbomachinery,* Vol. 116, No. 3, pp. 535–541.

Higginbotham, J. T., Wood, C. C., and Valentine, E. F., 1956, "A Study of High-Speed Performance Characteristics of 90° Bends in Circular Ducts," NACA TN 3696.

Miller, D. S., 1978, "Internal Flow Systems," BHRA.

Srivastava, J. P., 1971, "Steady and Unsteady Compressible Flow in Pipe Bends," *Symposium of Internal Flow,* Salford University, Salford, pp. D29-D40.

Ward-Smith, A. J., 1964, "Subsonic Adiabatic Flow in a Duct of Constant Cross-Sectional Area," *Journal of the Royal Aeronautical Society,* Vol. 68, pp. 117–127.

ERRATA

Journal of Fluids Engineering, September 1995, Vol. 117, pp. 498–504
R. E. A. Arndt, C. R. Ellis, and S. Paul, "Preliminary Investigation of the Use of Air Injection to Mitigate Cavitation Erosion,"
In the above paper, part of the Conclusions section was omitted from the published version. The complete section is printed below.

Conclusions

This study and previous work by others indicate that water tunnel tests are an effective method for isolating the essential flow physics that contribute to cavitation erosion in hydroturbines. The hydrodynamic conditions for the water tunnel tests were carefully chosen "bubble-cloud" cavitation (van der Meulen, 1983).

Although the precise mechanism for cavitation damage is unclear (e.g., van Wijngaarden, 1993), it was determined that the damage initiates in the form of individual pits as observed on the soft aluminum inserts used in this study.

Pitting rate was not directly measured, but three different diagnostic techniques infer that air injection can be very effective in minimizing erosion. Reductions as high as 14 db in the modulation acceleration level were found in these tests.

For the conditions in this study, the modulation analysis technique is the most sensitive to changes in air injection implying a similar sensitivity to erosion rate that needs further verification. A simple analysis indicates that mean square acceleration and mean square pressure are related by the fourth power of pit diameter. If pit diameter scales directly with bubble size, there should be no difference in the velocity scaling for mean square pressure and acceleration. However, there are observed differences in the velocity scaling of the two quantities, implying a velocity scaling for pit diameter which appears to be consistent with previous results.

The piezoelectric film used in these studies shows promise for further research. However, the very short duration of the pressure pulses, much shorter than the Rayleigh bubble collapse time, probably preclude accurate measurement of pulse height spectra. Total impulse can be accurately measured, lending validity to using mean square measurements as a gage of cavitation erosion. Although trends with velocity and σ were noted in the noise signal, the effect of cavitation on the acoustic path makes the monitoring of cavitation noise less effective than the other techniques used.

The results reported herein must be viewed as preliminary until a direct correlation between pitting rate and acoustic emission monitoring is achieved.

Theoretical and Experimental Study of Development of Two-Dimensional Steady and Unsteady Wakes Within Curved Channels

M. T. Schobeiri

K. Pappu

J. John

Turbomachinery Performance Laboratory,
Texas A&M University,
College Station, TX 77843-3123

Development of steady and periodic unsteady wake flows downstream of stationary and rotating cylindrical rods within a curved channel under zero longitudinal pressure gradient is theoretically and experimentally investigated. Wake quantities such as the mean velocity and turbulent fluctuations in longitudinal and lateral directions, as well as the turbulent shear stress, are measured. For the nondimensionalized velocity defect, affine profiles are observed throughout the flow regime. Based on these observations and using the transformed equations of motion and continuity, a theoretical frame work is established that generally describes the two-dimensional curvilinear wake flow. To confirm the theory, development of steady and periodic unsteady wakes in the above curved channel are experimentally investigated. The detailed comparison between the measurement and the theory indicates that the complex steady and unsteady wake flows are very well predicted.

Introduction

The flow through compressor and turbine blade channels of aero- and stationary gas turbine engines is characterized by a periodic unsteady wake flow through the stator and rotor cascades. The wake flow significantly influences the aerodynamic, heat transfer, and the aeroelastic behavior of the subsequent blades. The wake flow itself is strongly affected by the spanwise distributions of blade specific loading, flow coefficient, and degree of reaction as well as the centrifugal and Coriolis forces. In the past, there have been several investigations on compressor and turbine component performance, aerodynamics and heat transfer (see extensive literature review by Schobeiri et al., 1994a). Investigations by Raj and Lakshminarayana (1973) involved studying the effects of unsteady wake and turbulence on the compressor blade performance. In the area of turbine unsteady flow, Hodson and Addison (1989) and Blair et al. (1988) investigated the impact of unsteady flow on turbine aerodynamics and heat transfer. Rotating wake generators have been used to simulate the unsteady flow as reported by Pfeil and Schröder (1981), O'Brien and Capp (1989), and several others (refer to Schobeiri et al., 1994a).

Despite a large number of published reports and papers concerning the effect of unsteady flow and wake on various performance aspects of turbomachines, there has been considerably less information available on the mechanism of the steady and unsteady wake development within turbomachinery blade channels. Accordingly, the first author initiated an unsteady flow research program with the following objectives: (1) to develop a theoretical framework that describes the two-dimensional steady and unsteady wake flows through curved channels; (2) to carry out a systematic experimental investigation with the objective to generate a consistent set of data necessary for further theoretical treatment; and (c) to compare the theory with measurements to quantitatively predict the wake flow behavior within curved channel under steady and periodic unsteady flow conditions.

Contributed by the Fluids Engineering Division for publication in the JOURNAL OF FLUIDS ENGINEERING. Manuscript received by the Fluids Engineering Division April 20, 1995; revised manuscript received May 25, 1995. Associate Technical Editor: Wing-Fai Ng.

Theoretical Framework

For the following theoretical considerations, we assume an incompressible turbulent flow through a two-dimensional curved channel. We further assume that the velocity vector can be decomposed into a time independent mean and a time dependent turbulent fluctuation vector. Based on experimental results by Schobeiri et al. (1994a) and in accordance with the earlier investigation by Pfeil and Eifler (1975) and recently by Nakayama (1987), we further assume that for free turbulent flow, the viscosity effect can practically be neglected. Under these assumptions, the conservation equations of fluid mechanics in a coordinate invariant form are treated by transforming them into an orthogonal curvilinear coordinate system by using tensor analytical tools (for tensor analytical details see Schobeiri, 1990 and Schobeiri et al., 1994a).

Conservation Laws. The continuity equation in time averaged sense can be written as:

$$\bar{U}_{,1} + \left[\left(1 + \frac{\xi_2}{R}\right)\bar{V}\right]_{,2} = 0 \qquad (1)$$

The combination of continuity and momentum equations results in a more appropriate version of momentum equation (for details, see Schobeiri et al., 1994a), which when decomposed into ξ_1, ξ_2 components, leads to:

$$\frac{R}{R+\xi_2}\left(\frac{\bar{p}}{\rho} + \bar{U}^2 + \overline{u^2}\right)_{,1} + (\bar{U}\bar{V} + \overline{uv})_{,2}$$

$$+ \frac{2}{R+\xi_2}(\bar{U}\bar{V} + \overline{uv}) = 0 \qquad (2)$$

$$\frac{R}{R+\xi_2}(\bar{U}\bar{V}+\overline{uv})_{,1}+\left(\frac{\bar{p}}{\rho}+\bar{V}^2+\overline{v}^2\right)_{,2}$$

$$-\frac{1}{R+\xi_2}(\bar{U}^2-\bar{V}^2+\overline{u}^2-\overline{v}^2)=0 \quad (3)$$

Equations (2) and (3) are of practical interest for estimating the order of magnitude of each individual term compared to the others. For the special case of zero longitudinal pressure gradient, presented in this paper, the changes in static pressure in longitudinal direction is set equal to zero. Furthermore, as the experimental results show, the longitudinal fluctuation velocity $|u|$ is considerably smaller than the mean velocity $\bar{U}$. The lateral fluctuation velocity $|v|$, however, has the same order of magnitude as the mean lateral velocity $\bar{V}$, while it is negligible compared to $\bar{U}$. This comparison leads to the conclusion that the contributions of the fluctuation velocity momenta are negligibly small compared to the contribution of the longitudinal mean velocity momentum $\bar{U}^2$.

Nondimensional Parameters. In order to solve Eqs. (1) and (2), we assume that from a definite distance downstream of the wake origin, the velocity as well as the momentum defect profiles are similar. This assumption implies that for arbitrary points located on the wake center with the longitudinal coordinate ξ_1, a corresponding length scale $b = b(\xi_1)$ on the lateral coordinate ξ_2 can be found to define the dimensionless variable:

$$\zeta = \xi_2/b \quad (4)$$

The wake velocity and momentum defects are defined as:

$$\bar{U} = U_p - \bar{U}_1, \quad \bar{U}^2 = U_p^2 - \bar{U}_1^2 \quad (5)$$

In Eq. (5), the time-averaged velocity and momentum defects are represented by $\bar{U}_1$ and $\bar{U}_1^2$. Furthermore, U_p represents the hypothetical velocity distribution which is an extension of the undisturbed wake-external velocity into the wake. In the vicinity of the wake center, it can be approximated as:

$$U_p = U_{p0}\left(1-\frac{\xi_2}{R}\right) \quad (6)$$

with U_{p0} as the hypothetical velocity at the wake center, $\xi_2 = 0$. Thus, for the zero pressure gradient case presented in this paper, U_p is a function of ξ_2 only. The similarity assumption, stated previously, requires the following dimensionless wake velocity defect as well as the momentum defect functions,

$$\varphi_1 = \bar{U}_1/\bar{U}_{1m}, \quad \varphi^2 = \bar{U}_1^2/\bar{U}_{1m}^2 \quad (7)$$

where $\bar{U}_{1m}$, $\bar{U}_{1m}^2$ represent the maximum wake velocity and momentum defects at the wake center.

Expressions for Wake Characteristics. Introducing the wake velocity defect, Eq. (7), in connection with Eq. (5) into continuity equation (Eq. (1)), separating the variables and integrating the resulting equation, after some rearrangement of terms we obtain:

$$\left(1+\frac{\xi_2}{R}\right)\bar{V}=\frac{d(\bar{U}_{1m}b)}{d\xi_1}\int\varphi_1 d\zeta-\frac{db}{d\xi_1}\bar{U}_{1m}\varphi_1\zeta$$

$$-\frac{dU_{p0}}{d\xi_1}b\int\left(1-\frac{\zeta b}{R}\right)d\zeta+c \quad (8)$$

Equation (8) shows that the lateral velocity is determined by the turbulent mixing and the decay process in longitudinal direction characterized by the longitudinal changes of the velocity-width product $\bar{U}_{1m}b$. Experimental investigations from the past (Eifler, 1975; and Pfeil and Eifler, 1975) and our own measurements show that changes of the above product can be set equal to zero if the longitudinal pressure gradient is approximately zero. Also, for the case of zero longitudinal pressure gradient, the variations in U_{p0} with streamwise distance can be neglected. Since the lateral velocity component $\bar{V}$ is zero at the wake center, the integration constant in Eq. (8) must identically vanish. Implementing the above approximations, Eq. (8) simplifies to:

$$\bar{V} = -\frac{R}{R+\xi_2}\frac{db}{d\xi_1}\bar{U}_{1m}\varphi_1\zeta \quad (9)$$

With Eq. (9), the distribution of the lateral velocity component can be found provided the wake velocity defect function φ_1, the distribution of the wake width $b = b(\xi_1)$ as well as the distribution of $\bar{U}_{1m}$ are known. Considering the similarity assumptions stated previously, we choose the maximum wake velocity defect and the wake width as the appropriate velocity and length scales to define a nondimensional relationship for the wake velocity defect, which will be a function of ξ_2/b, i.e., $\varphi_1 = \bar{U}_1/\bar{U}_{1m} = f(\xi_2/b) = f(\zeta)$.

From the experimental investigations by Eifler (1975) and others, it was concluded that the nondimensional wake velocity defect (φ_1) distribution in the case of a straight channel with zero streamwise pressure gradient follows the Gaussian distribution. Investigations by Schobeiri et al. (1994a) also show that similar solution for φ_1 exists for curved channels at zero longitudinal pressure gradient that follows the Gaussian distribution presented below.

$$\varphi_1 = e^{-\zeta^2} \quad (10)$$

Our recent experimental measurements in curved channels at different longitudinal pressure gradients were also found to follow the above distribution as well, proving validity of the similarity assumption in wake velocity defect profiles.

Using the time-averaging procedure, the turbulent shear stress is calculated as the difference of total and partial impulses, i.e., $\overline{uv} = \overline{UV} - \bar{U}\bar{V}$. Since the expressions for the two mean velocity components are known from Eqs. (5) and (9), and with the approximation for U_p from Eq. (6), final expression for the nondimensional partial impulse can be written as:

$$\frac{\bar{U}\bar{V}}{\bar{U}_{1m}^2}=-\frac{R}{R+\xi_2}\frac{db}{d\xi_1}\zeta\varphi_1\left[\frac{U_{p0}}{\bar{U}_{1m}}\left(1-\frac{\zeta b}{R}\right)-\varphi_1\right] \quad (11)$$

To determine the expression for total impulse, a step-by-step derivation procedure (refer to Schobeiri et al., 1994a) is carried out. From that procedure, the final expression for the nondimensional total impulse can be shown to be:

$$\frac{\overline{UV}}{\bar{U}_{1m}^2}=\frac{R}{R+\xi_2}\frac{db}{d\xi_1}$$

$$\times\left[\zeta\varphi_1+\frac{U_{p0}}{\bar{U}_{1m}}\left(-2\zeta\varphi_1+\frac{b\varphi_1}{R}(1+2\zeta^2)\right)\right]+\frac{c}{\bar{U}_{1m}^2} \quad (12)$$

Nomenclature

b = wake width, $b = (1/2\gamma)\int_{-\infty}^{+\infty}(\bar{U}_1/\bar{U}_{1m})d\xi_2$

r = radial position of probe from the center of the convex wall

r_i = radius of convex wall, $r_i = 500$ mm

R = radius of wake centerline

u, v = time dependent fluctuation components in ξ_1, ξ_2 directions

$\bar{U}, \bar{V}$ = mean velocity components in ξ_1, ξ_2 directions

ξ_1, ξ_2 = curvilinear coordinates

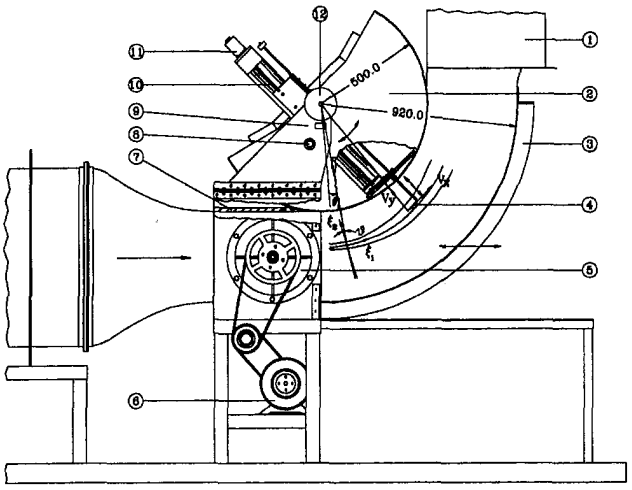

Fig. 1 Test section: 1-exit duct; 2-convex wall; 3-concave wall; 4-probe; 5-wake generator; 6-motor; 7-top wall; 8-safety pin; 9-rotary vernier; 10-traversing system; 11-stepper motor; 12-locking wheel

Now, the expression for Reynolds shear stress is obtained from the difference of total and partial impulses, i.e., Eqs. (12) and (11), as:

$$\frac{\overline{uv}}{\bar{U}_{1m}^2} = \frac{R}{R+\xi_2}\frac{U_{p0}}{\bar{U}_{1m}}\frac{db}{d\xi_1}\left[-\zeta\varphi_1 + \frac{b\varphi_1}{R}(1+\zeta^2)\right] + \frac{R}{R+\xi_2}\frac{db}{d\xi_1}\zeta\varphi_1(1-\varphi_1) + \frac{c}{\bar{U}_{1m}^2} \quad (13)$$

The constant of integration in the above expression is a function of ξ_1 and needs to be evaluated from the experimental results at $\zeta = 0$. For the straight wake case with no streamwise pressure gradient, it is known from experimental results that the shear stress is zero at the wake center with the distribution being symmetric about the wake center. In that case, the constant of integration evaluates to be zero. But for the case of curved channel flow, the shear stress distribution is strongly asymmetric with a non-zero value at the wake center thus reflecting the influence of curvature.

Experimental Research Facility

The layout of the test section is shown in Fig. 1. The inlet of the curved test section has a free-stream turbulence intensity of 1.25 percent. For detailed information about the design description and performance tests, refer to Schobeiri and Pardivala (1992) and Schobeiri et al. (1994a, b).

The wake generator consists of a series of circular rods arranged circumferentially on two parallel rotating disks. A fiber-optic proximity sensor mounted close to the pulley of the wake generator provides a signal for monitoring the rotational speed of the wake generator and for external triggering of the analog to digital (A/D) conversion board needed for phase-averaged measurement.

Instrumentation, Data Acquisition, and Analysis

The test facility was instrumented for fully automated digital data acquisition. The data acquisition system is controlled by a personal computer that incorporates a 12-bit A/D (analog to digital conversion) board. The mean velocity and turbulent stress components are obtained using a three-channel, constant temperature anemometer (TSI, IFA 100) system. The hot-film sensors are calibrated (refer to John and Schobeiri, 1993 for details) frequently in a low turbulence, uniform flow, open jet calibrating facility. The uncertainties of the measurements for the velocity components using the X-probe are estimated to be about 1.2 percent for longitudinal velocity and 3 percent for the lateral velocity components. For details about data reduction and analysis procedures, refer to Schobeiri et al. (1994b).

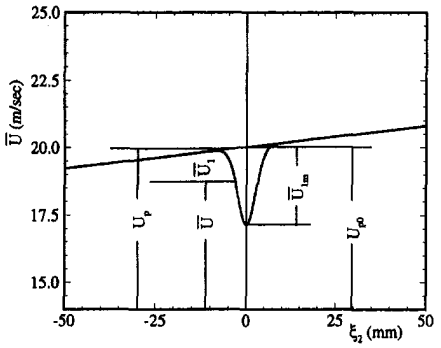

Fig. 2 Schematic velocity distribution, definitions

Results and Discussion

Steady Wake Flow Development. The wake behind a stationary cylinder, with the diameter $d = 2$ mm located at mid height of the wake generating section, was measured using a X-hot-film probe. The wake profiles were obtained at fifteen angular positions (also referred to as longitudinal positions) from $\theta = 0$ to 70 deg in 5 deg intervals. Based on the results of theoretical and experimental investigations of wake flows through straight channels, it was found unnecessary to vary the cylinder diameter as a parameter for the wake flow through curved channels. The wake development in the longitudinal direction depends primarily upon the ratio ξ_1/d (x/d for straight wake) regardless of the separate variation of the parameters involved in this ratio.

The wake center is defined as the location of maximum velocity defect. The path of the wake center represents the direction of the curvilinear coordinate ξ_1 at $\xi_2 = 0$. As the wake convects through the channel, the trajectory of the wake center gradually moves towards the convex wall up to a longitudinal location $\xi_1/d = 240$ ($\theta = 33.66$ deg) and from there onwards it moves away from the convex wall. The maximum velocity defect and the potential velocity are sketched in Fig. 2.

The decay of the maximum velocity defect $\bar{U}_{1m}$ normalized by the potential velocity at the wake center U_{p0} and the wake growth characterized by b/d are shown in Fig. 3. The solid lines represent a power law fit with $\bar{U}_{1m}/U_{p0}$, $b/d \sim (\xi_1/d)^m$. The experimental results suggest that the exponent m is a function of pressure gradient and curvature and may assume different values. In the present study, m can be approximated as being equal to -0.71 for the wake decay, $\bar{U}_{1m}/U_{p0}$, and 0.74 for the

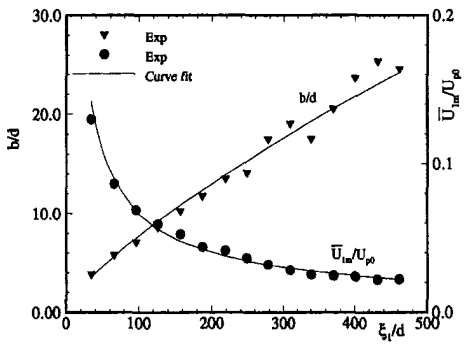

Fig. 3 Nondimensional maximum velocity defect and wake width as a function of ξ_1/d

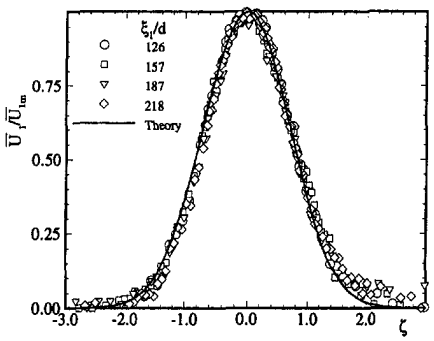

Fig. 4 Nondimensional mean velocity defect distribution with ξ_1/d as parameter

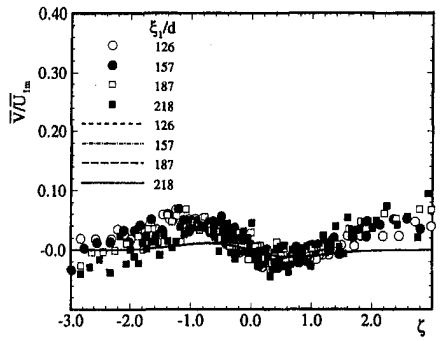

Fig. 6 Mean lateral velocity distribution with ξ_1/d as parameter

wake growth, b/d. Considering the relationships for $\bar{U}_{1m}$ and b/d, the product $\bar{U}_{1m}b$ leads to almost a constant value, which is a characteristic of turbulent wake flow at zero longitudinal pressure gradient.

Mean Velocity Distribution. The distribution of the mean velocity defect function $\varphi_1 = \bar{U}_1/\bar{U}_{1m} = f(\zeta)$ for different longitudinal locations is shown in Fig. 4. The lateral distance ξ_2 is nondimensionalized by the wake width b.

Considering the asymmetric behavior of the velocity distribution, the introduction of the velocity defect has resulted in a fully symmetric defect function. In Fig. 4, the experimental results (symbols) are compared with the developed theory (solid line). The solid lines are based on the velocity defect function, $\varphi_1 = e^{-\zeta^2}$, which is proved to be a general representation of the wake defect for curved and straight wakes. The mean velocity defect profiles are symmetric and almost identical to the straight wake. In general, it may be considered that the effect of curvature on mean velocity defect distribution is small.

The distribution of the experimental and theoretical mean longitudinal velocity components are shown for different longitudinal locations in Fig. 5. As shown, the velocity distribution exhibits a strong asymmetric character with higher velocities at the positive side of ξ_2, corresponding to the locations closer to the convex wall with $\xi_2 = 0$ as the geometric location of the wake center. The wake velocity defect decreases resulting in a continuous increase of the wake width with downstream location. The individual velocity profiles are characterized by a highly dissipative vortical core inside the wake region surrounded by external potential flow region. A comparison with the theory developed shows a detailed prediction of this behavior over the entire velocity range. The agreement between theory and measurements confirms the validity of the assumptions made.

The distribution of the nondimensionalized lateral velocity component $\bar{V}/\bar{U}_{1m}$ for various longitudinal locations is presented in Fig. 6. The experimental results reveal an asymmetric behavior with a minimum at $\zeta > 0$, a maximum at $\zeta < 0$ and zero velocity at the center with non-zero values at the edges. The lines represent the theoretical results for the lateral velocity distribution obtained from the continuity equation. Although the theoretical results exhibit the same tendency, they deviate slightly from the experimental results. The main reason for this deviation is that the lateral velocity component is in general very small compared to the longitudinal velocity component. Considering the transformation of the velocity components from the probe coordinate system into the wake eigen-coordinate system, the deviation is within the accuracy tolerance of the probe associated with inevitable scatter in the measurement. In this connection, it should be noted that many relevant papers on wakes, including the ones dealing with symmetrical wakes, have not reported the lateral velocity distribution probably due to very high scatter in experimental data.

Reynolds Shear Stress. The experimental results (symbols) for Reynolds shear stress distribution at various longitudinal locations are presented in Fig. 7 and are compared with the theory (lines) developed in the previous section. As shown in Fig. 7, unlike the straight channel case, the curved channel shear stress is nonzero at the wake center because of the curvature effect that causes a pressure gradient in lateral direction resulting in a highly asymmetric distribution of shear stress profiles. Raj and Lakshminarayana (1973) also observed nonzero Reynolds shear stress at the wake center.

The Reynolds shear stress in the hypothetical potential flow outside the wake is not exactly equal to zero due to the turbulence existing in that region. Measurements at selected longitudinal locations without the wake showed a lateral gradient of $\overline{uv}$ with a negative value near the concave wall and a positive value near the convex wall. The radial position where $\overline{uv} = 0$ was located between the convex wall and the mean radius of the channel.

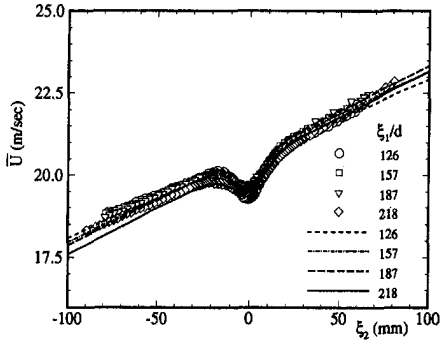

Fig. 5 Mean longitudinal velocity distribution with ξ_1/d as parameter

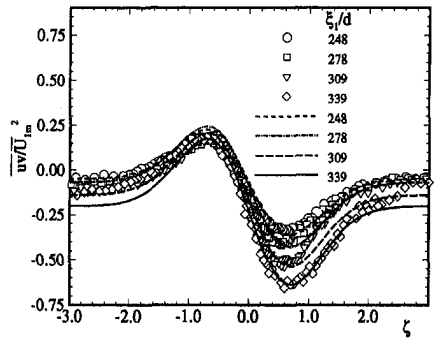

Fig. 7 Nondimensional Reynolds shear stress distribution with ξ_1/d as parameter

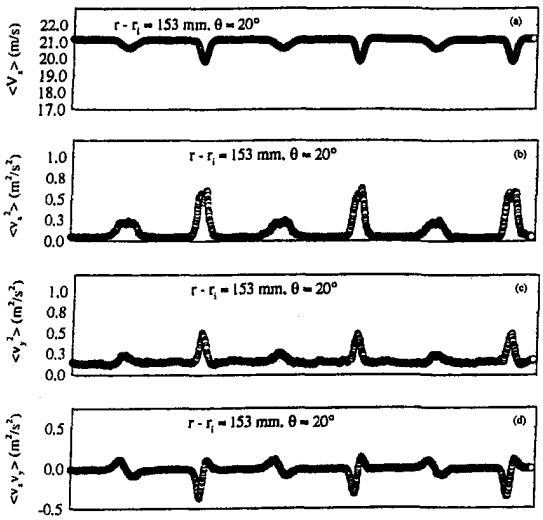

Fig. 8 Phase averaged velocity and Reynolds stresses in stationary frame of reference for the periodic unsteady wake, rpm = 300

The experimentally determined shear stress distributions shown in Fig. 7 are compared with the theory developed in the previous section. As can be seen from Fig. 7, the excellent agreement between the theory and the measurement over the entire range, particularly the precise prediction of the asymmetric pattern proves the validity of the assumptions made in developing the theoretical framework.

Unsteady Wake Flow Development. Measurements were made at five angular positions from $\theta = 0$ to 40 deg in 10 deg intervals. The rotational speed of the wake generator was 300 rpm which corresponds to a Strouhal number of $s = \omega d/V_{in} = 0.031$, a value which is within the range found in turbomachinery. The experimental investigations with Strouhal numbers $s = 0.031$, 0.041, 0.051, 0.062 have shown that the effect of Strouhal number on turbulence characteristics, the profiles of mean velocity defect, normalized Reynolds normal and shear stress distributions is very small.

Temporal Distribution of Velocity and Turbulence Quantities in Probe Coordinates and Stationary Frame of Reference. As a representative example, Fig. 8(a) shows the phase-averaged tangential velocity component $\langle V_x \rangle$ as a function of time at $\theta = 20$ deg and the radial position $r - r_i = 153$ mm. During the rotational motion of the wake generator, each rod produces a primary and a secondary wake that, respectively, are generated during the up- and downward movement of the rods. The radial position $r - r_i$ corresponds to the location where the primary wakes are in the middle of the secondary wakes. These radial locations are selected so that they provide data with minimum interference between primary and secondary wakes.

The phase-averaged distribution of Reynolds normal and shear stresses displayed in Figs. 8(b–d) reveal an asymmetric behavior with respect to the wake center. Measurements at different longitudinal positions have shown that the phase-averaged Reynolds normal stresses outside the wake increase with downstream location. The secondary wake has lower values of Reynolds normal stress by the time it reaches the probe (Figs. 8(b, c). In fact, the magnitude of the radial component of Reynolds normal stress, $\langle v_y^2 \rangle$, of the secondary wake is comparable to the magnitude of radial component of Reynolds normal stress outside the wake. Similar to the wake of stationary cylinder in the curved channel, the Reynolds shear stress distribution, shown in Fig. 8(d), has a pronounced asymmetric character. The Reynolds shear stress for primary and secondary wakes have opposite nature, i.e., the left side of the wake has a negative $\langle v_x v_y \rangle$ for primary wake and positive $\langle v_x v_y \rangle$ for secondary wake.

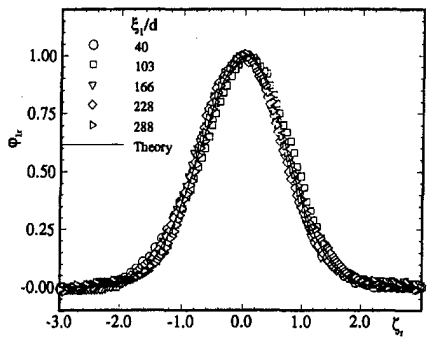

Fig. 9 Lateral distribution of nondimensional velocity defect for the periodic unsteady wake

Conversely, opposite trends are observed for the right side of the wake.

Spatial Distribution of Velocity and Turbulence Quantities in Curvilinear Coordinates and Relative Frame of Reference. The temporal development of the periodic unsteady wake is transformed into a curvilinear spatial coordinate system relative to the moving cylinder (for details, refer to Schobeiri et al., 1994b). The results are shown in Fig. 9 for five downstream locations at a constant rotational speed of 300 rpm, which corresponds to a Strouhal number of $s = 0.031$.

The lateral distributions of mean velocity defect for different longitudinal locations are plotted in Fig. 9. The mean velocity defect is normalized by its maximum value and the lateral distance by the wake width b. The solid line represents the function $\varphi_{1r}, \varphi_{1r} = \bar{U}_{1r}/\bar{U}_{1mr} = e^{-\zeta_r^2}$, where $\zeta_r = \xi_{2r}/b$. The mean velocity defect profiles are symmetric and identical to the steady wake defect profiles. They also follow exactly the same law found for the steady wake which was discussed previously. This observation results in a conclusion that the wake defect is frame indifferent, which can easily be proved mathematically.

The lateral distributions of the experimentally obtained nondimensional Reynolds shear stresses at various longitudinal locations are plotted in Fig. 10. To analytically predict these shear stress distributions, the earlier developed theory is applied to the relative frame of reference and plotted as lines in Fig. 10. A comparison with the experimental results (symbols) shows a detailed prediction of this behavior over the entire velocity range. The Reynolds shear stress distribution shows the strong asymmetry due to the curvature. The value of Reynolds shear stress is higher on the inner half of the wake than on the outer half. The good agreement between theory and measurements confirms the validity of the theory.

Conclusions

The development of steady and periodic unsteady wake flows downstream of a stationary cylinder and the cylinders of a rotat-

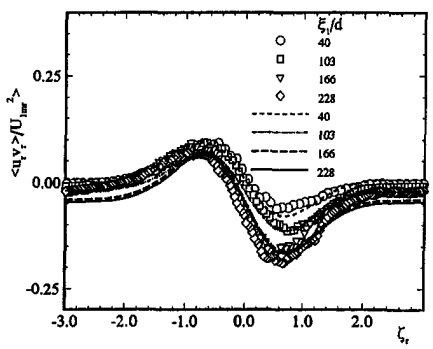

Fig. 10 Lateral distribution of nondimensional Reynolds shear stress for the periodic unsteady wake

ing wake generator in a curved channel at zero longitudinal pressure gradient was theoretically and experimentally investigated. The theoretical framework generally describes the wake flow through two-dimensional curvilinear and straight channels within the absolute as well as relative frame of reference. Detailed experimental results are presented and compared with the developed theory. The introduction of the velocity defect function and the wake width as a single length scale resulted in a fully symmetric distribution of the nondimensionalized velocity defect in absolute and also relative frame of reference. The detailed comparison between measurement and theory showed that the presented theoretical framework is capable of predicting the zero-pressure gradient wake flow in curved channels within absolute and relative frame of reference.

References

Blair, M. F., Dring, R. P., and Joslyn, H. D., 1988, "The Effect of Turbulence and Stator/Rotor Interactions on Turbine Heat Transfer," Part I: ASME-Paper, 88-GT-125, Part II: ASME-Paper, 88-GT-5.

Eifler, J., 1975, "Zur Frage der freien turbulenten Strömungen, insbesondere hinter ruhenden und bewegten Zylindern," Dissertation D-17, Technische Hochschule Darmstadt, Germany.

Hodson, H. P., and Addison, J. S., 1989, "Wake-Boundary layer Interactions in an Axial Flow Turbine Rotor at Off-Design Conditions," ASME *Journal of Turbomachinery,* Vol. 111.

John, J., Schobeiri, T., 1993, "A Simple and Accurate Method of Calibrating X-Probes," ASME JOURNAL OF FLUIDS ENGINEERING, Vol. 115, pp. 148–152.

Nakayama, A., 1987, "Curvature and Pressure-Gradient Effects on a Small-Defect Wake," *Journal of Fluid Mechanics,* Vol. 175, pp. 215–246.

O'Brien, J. E., Capp, S. P., 1989, "Two-Component Phase-Averaged Turbulent Statistics Downstream of a Rotating Spoked-Wheel Wake Generator," ASME *Journal of Turbomachinery,* Vol. 111, No. 4, pp. 475–482.

Pfeil, H., Eifler, J., 1975a, "Zur Frage der Schubspannungsverteilung für die ebenen freien turbulenten Strömungen," *Forschung,* Ing.-Wes. 41, Nr. 4, pp. 105–112.

Pfeil, H., Eifler, J., 1975b, "Messungen im turbulenten Nachlauf des Einzelzylinders," *Forschung,* Ing.-Wes. 41, Nr. 5, pp. 137–145.

Pfeil, H., Schröder, Th., 1981, "Decay of the Wake Behind A Cylinder Crossing Rapidly The Flow," American Institute of Aeronautics and Astronautics, Paper No. AIAA-81-0209.

Raj, R., Lakshminarayana, B., 1973, "Characteristics of the Wake behind a Cascade of Airfoils," *Journal of Fluid Mechanics,* Vol. 81, part 4, pp. 707–730.

Schobeiri, T., 1990, "The Influence of Curvature and Pressure Gradient on the Flow Temperature and Velocity Distribution," *International Journal of Mechanical Sciences,* Vol. 32, pp. 851–861.

Schobeiri, T., and Pardivala, D., 1992, "Development of a Subsonic Flow Research facility for Simulating the Turbomachinery Flow and Investigating its Effects on Boundary layer Transition, wake Development and Heat Transfer," *Fourth International Symposium on Transport Phenomena and Dynamics of Rotating Machinery,* pp. 98–114.

Schobeiri, T., John, J., and Pappu, K., 1994a, "Development of Two-Dimensional Wakes Within Curved Channels, Theoretical Framework and Experimental Investigation," 94-ASME-GT-367, presented at the ASME-IGTI-Conference in Hague.

Schobeiri, T., Pappu, K., and John, J., 1994b, "Theoretical and Experimental Study of Development of Two-Dimensional Steady and Unsteady Wakes Within Curved Channels," AD-Vol. 40, presented at 1994 International Mechanical Engineering Congress and Exposition, Chicago, Illinois.

P. S. Cumber

M. Fairweather

British Gas plc, Research and Technology,
Gas Research Centre,
Loughborough LE11 3QU, England

S. A. E. G. Falle

Department of Applied Mathematics,
The University of Leeds,
Leeds LS2 9JT, England

J. R. Giddings

Mantis Numerics Ltd., 46 The Calls, Leeds
LS2 7EY, England

Predictions of the Structure of Turbulent, Highly Underexpanded Jets

A mathematical model capable of predicting the shock and flow structure of turbulent, underexpanded jets is described. The model is based on solutions of the fluid flow equations obtained using a second-order accurate, finite-volume integration scheme together with an adaptive grid algorithm. Closure of these equations is achieved using a k-ϵ turbulence model coupled to the compressible dissipation rate correction proposed by Sarkar et al. (1991a). Extending earlier work which demonstrated the ability of this model to predict the structure of moderately underexpanded jets, the present paper compares model predictions and experimental data, reported in the literature, on a number of highly underexpanded releases. The results obtained demonstrate that the model yields reliable predictions of shock structure in the near field, inviscid region of such jets, while in the far field results derived using the compressibility corrected turbulence model are adequate for predicting mean flow properties, and are superior to those obtained using a standard k-ϵ approach.

Introduction

Underexpanded, axisymmetric free jets are one of the simplest flows involving both turbulent mixing and compressibility effects. As well as being of interest to fundamental studies of the interaction of turbulence and compressibility, the ability to predict the detailed structure of such flows also has numerous practical applications. Of particular interest in the present work is the use of predictions of such jets in consequence and risk assessments of leaks of high pressure gas arising from both accidental and operational releases.

The flow pattern of a jet issuing from a straight or convergent nozzle depends primarily on the ratio of the pressure at the nozzle exit to the ambient pressure. A number of types of flow are possible depending on this pressure ratio. For the case of air, and neglecting the singular case of an expanded sonic jet at a pressure ratio $P_o/P_a = 1$, subsonic jets exist for pressure ratios less than 1. In the range $P_o/P_a = 1.0$ to 1.1 a weak shock forms in the nozzle, whilst for pressure ratios in the range 1.1 to 2.1 moderately underexpanded jets occur with such jets being characterised by the existence of a system of oblique shocks which form downstream of the nozzle.

Highly underexpanded jets, the subject of the present paper, exist at pressure ratios above 2.1 and are characterised by the existence of one or more shocks that are normal to the direction of flow downstream of the nozzle exit. At pressure ratios $P_o/P_a > 2.1$, therefore, expansion of the jet causes the pressure along its centre-line to become so low relative to the ambient value that recompression can no longer take place through the conical, or intersecting oblique, shocks which characterise moderately underexpanded jets. Instead, the required compression takes place through a characteristic normal shock, or Mach disk. Immediately downstream of this first disk the flow is subsonic, although since supersonic flow persists in the surrounding region a slip line exists at the boundary of these two concentric domains. If the pressure ratio P_o/P_a is sufficiently high ($\simeq 4$), then the subsonic core of the jet is quickly accelerated and becomes supersonic once again so that a second Mach disk forms. In contrast, for very high pressure ratios the first Mach disk grows sufficiently in both strength and diameter to dominate the flow field, thereby preventing the formation of other normal shocks. Downstream of these normal shock structures the flow then decays through a series of oblique shocks, although in practice the latter shocks are often distorted by large scale, low frequency instabilities in the flow. All of these shocks are embedded in a potential core which is surrounded by a mixing region. Radial diffusion in the latter region is however small, with the result that the potential core of highly underexpanded jets is extremely long relative to other free jet flows. Far downstream, these jets decay in the usual subsonic manner.

A number of research groups have formulated mathematical models of underexpanded jets, with the most frequently used approach being to base predictions on a simplified system of parabolized transport equations, derived by neglecting streamwise diffusion. Examples include the models reported by Dash and Wolf (1983) and by Chuech et al. (1989). More recently, Cumber et al. (1994) described a model which derives solutions from elliptic versions of the fluid flow equations using a second-order accurate, finite-volume integration scheme in conjunction with an adaptive grid algorithm. In general, the models referred to above have been shown, through comparison with a range of experimental data, to yield reliable predictions of moderately

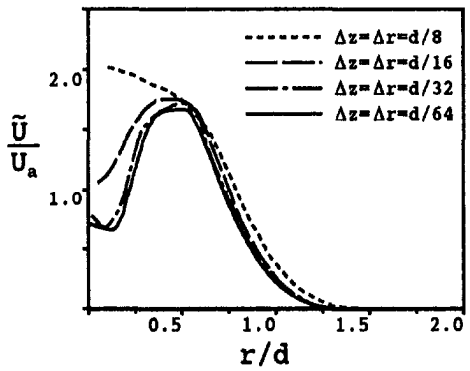

Fig. 1 Effect of grid resolution on radial predictions of mean streamwise velocity at $z/d = 3.92$ for Donaldson and Snedeker's (1971) air jet (d = 13.0 mm, $P_o/P_a = 3.57$, $M = 1$)

Contributed by the Fluids Engineering Division for publication in the JOURNAL OF FLUIDS ENGINEERING. Manuscript received by the Fluids Engineering Division July 11, 1994; revised manuscript received February 17, 1995. Associate Technical Editor: G. Karniadakis.

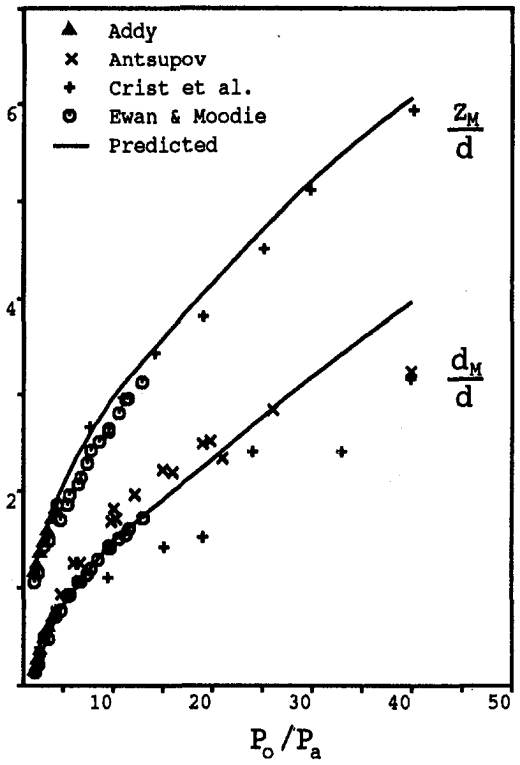

Fig. 2 Variation of dimensionless Mach disk diameter and stand-off distance with pressure ratio

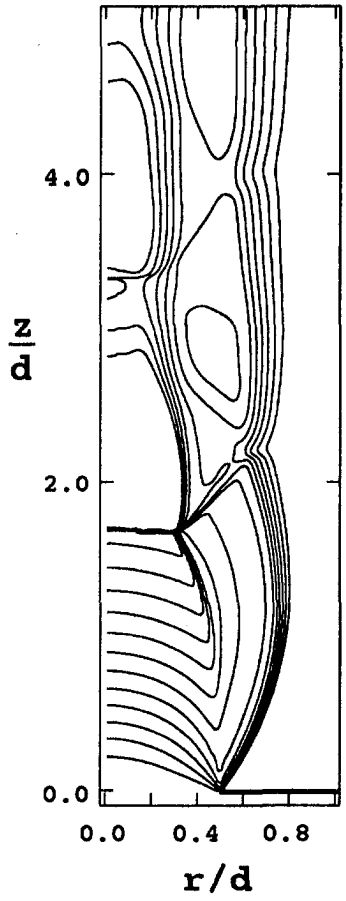

Fig. 3 Predicted Mach number contours within the near field region of Donaldson and Snedeker's (1971) air jet (d = 13.0 mm, P_o/P_a = 3.57, M = 1)

underexpanded jets provided the influence of compressibility effects on turbulence dissipation is modeled.

Some predictions of highly underexpanded jets have also been made. For example, Dash and Wolf (1983) simulated a heated, highly underexpanded jet ($P_o/P_a = 5$), and successfully predicted the existence of a single Mach disk downstream of the nozzle. Palacio et al. (1990) similarly predicted the location of the first and second Mach disks in a jet (P_o/P_a = 3.57) studied experimentally by Donaldson and Snedeker (1971). In general, however, the ability of such models to predict highly underexpanded jets has not been thoroughly assessed through a systematic comparison with available experimental data.

The present paper describes the application of the model outlined by Cumber et al. (1994) to predicting highly underexpanded jets, and validates model predictions against appropriate experimental data on Mach disk diameter and stand-off distance, and on the velocity and concentration fields within such jets.

Mathematical Model

In the interest of brevity, only the essential details of the mathematical model employed in the present work are reproduced below. Full details may be found in Cumber et al. (1994).

Governing Equations. The model was based on solutions of the high Reynolds number versions of the fluid flow equations, expressed in axisymmetric and steady state form (Jones and Whitelaw, 1982). Transport equations for the conservation of mass, momentum, total energy and a strictly conserved scalar variable (mixture fraction) were therefore solved, with density-weighted (Favre) averaging being used as most appropriate for the variable density flows of interest. Closure of this set of equations was achieved through the use of a standard two-equation, k-ϵ turbulence model (Jones and Launder, 1972), with a gradient diffusion model for the turbulent flux of mixture fraction being employed in the conserved scalar equation. Modeling constants employed were standard values found to give acceptable agreement between theoretical predictions and experimental data in a wide range of flows (Jones and Whitelaw, 1982). The system of equations was augmented by the ideal gas law for solution.

Although the standard k-ϵ turbulence model has been used extensively for predicting incompressible flows, in compressible situations it is known to overpredict turbulence levels, and hence mixing rates, because it does not account for the effect of compressibility on turbulence dissipation. Predictions were therefore also derived using a second version of this turbulence model,

Nomenclature

a = local speed of sound
d = nozzle diameter
d_M = Mach disk diameter
f = mixture fraction
k = turbulence kinetic energy
M = Mach number [= U/a]
P = pressure
r = radial coordinate
U = mean velocity
U_a = reference velocity [= $(P_a/\rho_a)^{0.5}$]
z = axial coordinate
z_M = axial distance to Mach disc
Δr = grid spacing in r direction
Δz = grid spacing in z direction
ϵ = dissipation rate of k
ρ = density

Subscripts

a = ambient value
o = nozzle exit condition

Superscript

~ = density-weighted average

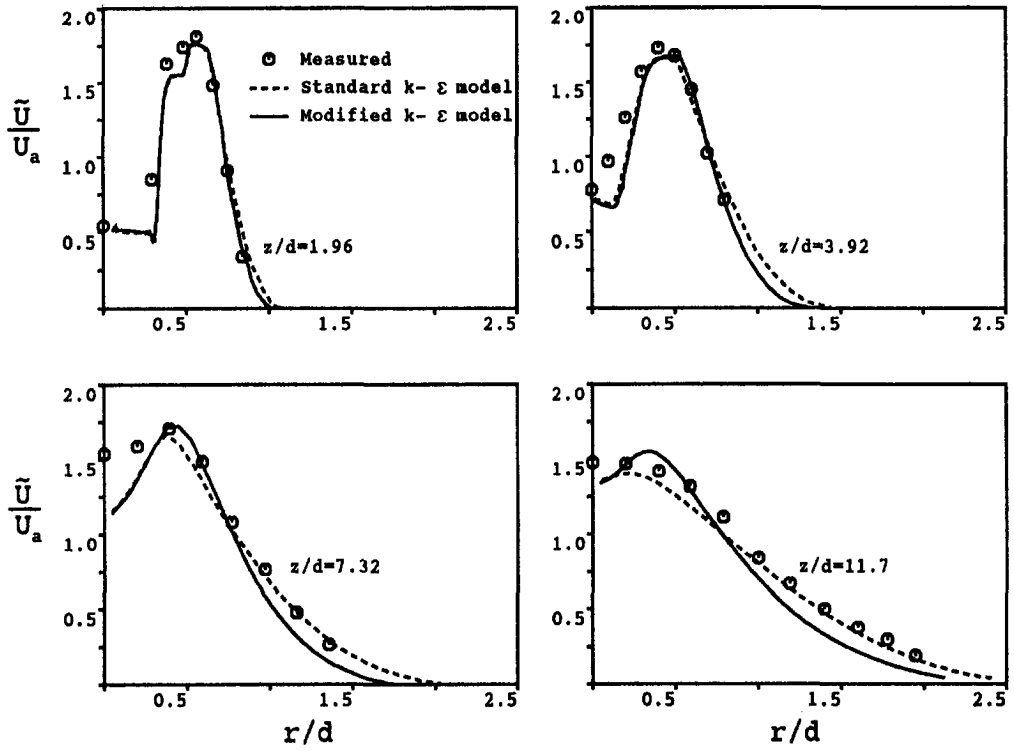

Fig. 4 Radial values of mean streamwise velocity at four downstream stations for Donaldson and Snedeker's (1971) air jet (d = 13.0 mm, P_o/P_a = 3.57, M = 1)

modified in line with the recommendations of Sarkar et al. (1991a). Earlier work by the present authors (Cumber et al., 1994) has demonstrated that results derived using this modification are capable of accurately predicting both mean and fluctuating quantities in moderately underexpanded jets. A fuller description of the compressible turbulence model used may be found in Cumber et al. (1994).

Computational Procedure and Boundary Conditions. To compare predictions of the model with the experimental data considered later, solution of the axisymmetric form of six (for air jets) or seven (for natural gas jets) coupled partial differential equations is required. Solutions were obtained using a general purpose computational fluid dynamics code (see Acknowledgments) in which the equation set was expressed in cylindrical coordinates, with the time-dependent form of these equations being integrated numerically by time-marching to a steady state. Integration was achieved using a second-order accurate, finite-volume scheme, with discretisation of the descriptive equations following a conservative, control volume approach. Diffusion and source terms in the modelled equations were approximated using central differencing, while approximations to the inviscid (advective and pressure) fluxes were derived using a second-order accurate variant of Godunov's method. The rate of convergence was increased using a diagonalised implicit scheme. In order to avoid the normally excessive computational cost involved in capturing shock structures, an adaptive finite-volume grid algorithm was employed. This method used a two-dimensional, rectangular mesh, with local adaption being achieved by overlaying successively refined layers of computational grid. In the results given later, up to five levels of grid were used.

The boundary conditions used in all of the computations were as described previously (Cumber et al., 1994), with the location of the free boundaries having been varied in order to ensure that solutions were insensitive to the boundary conditions imposed on these surfaces. Flat profiles of all dependent variables were prescribed at the nozzle exit for all simulations, and in the absence of appropriate experimental data initial turbulence kinetic energy levels corresponding to 5 percent of the mean velocity were used, with the dissipation rate specified by assuming a turbulence length scale of 0.05 d. The latter values are typical of those found in fully developed turbulent pipe flows. Predictions made for initially plug flows with varying levels of k_o and ϵ_o, both in the present and previous (Cumber et al., 1994) work, did however demonstrate that results were insensitive to the actual nozzle exit values employed.

The fineness of computational grid required to obtain grid independent solutions was examined for each of the jets studied. As an example, simulations of the P_o/P_a = 3.57 air jet studied by Donaldson and Snedeker (1971) required a grid spacing of $\Delta r = \Delta z = \Delta d/64$ for essentially grid independent resolution of the shock structure. Figure 1 shows the sensitivity of predictions of the mean streamwise velocity at one downstream station of this jet to the grid resolution used in the computations. In this figure the predicted peak velocity changes by less than 2 percent when the grid spacing is reduced from $d/32$ to $d/64$,

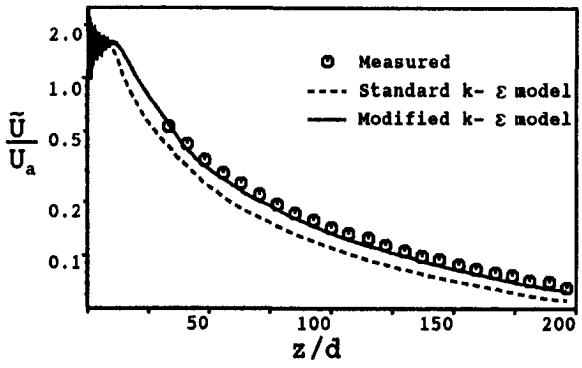

Fig. 5 Centerline values of mean streamwise velocity for Birch et al.'s (1987) P_o/P_a = 3.1 air jet (d = 2.7 mm, M = 1)

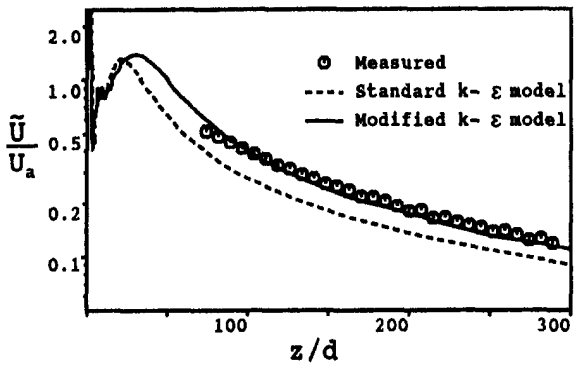

Fig. 6 Centerline values of mean streamwise velocity for Birch et al.'s (1987) P_o/P_a = 16.1 air jet (d = 2.7 mm, M = 1)

equivalent to a numerical error of less than 1 percent in the $d/64$ results when Richardson extrapolation is used to estimate the exact value.

Results and Discussion

Measurements of Mach disk diameter and stand-off distance, or barrel length, in the near field of highly underexpanded air jets have been made by Addy (1981) and Ewan and Moodie (1986). The latter authors used shadowgraphy to determine values of d_M and z_M for the first Mach disk in jets issuing from 12.7 and 25.4 mm diameter contoured nozzles, while Addy (1981) made similar measurements in jets from a 12.7 mm convergent nozzle. Data at higher pressure ratios than those considered by these authors are also available in the literature. Antsupov (1974) used a 14.6 mm diameter convergent nozzle to study Mach disk diameters in air jets with pressure ratios up to 40, whilst Crist et al. (1966) measured both Mach disk location and diameter in nitrogen jets from convergent nozzles with diameters over the range 0.7 to 3.0 mm. Figure 2 compares all these data with predictions of the present model in this mainly inviscid flow region where, as anticipated, identical results were obtained using both the standard and compressibility corrected turbulence models. At low and very high pressure ratios predictions of the model are in good agreement with the data for stand-off distance, although the barrel length does tend to be slightly overpredicted over most of the pressure range shown in this figure with a maximum error of approximately 10 percent. Predictions of Mach disc diameter are in excellent agreement with the data of Addy (1981) and Ewan and Moodie (1986), although at high pressure ratios significant differences in the data make it difficult to assess the model's accuracy. Overall, however, predictions of the model are in reasonable accord with all four data sets noted above.

Donaldson and Snedeker (1971) made measurements of the mean velocity field in an air jet issuing from a 13.0 mm convergent nozzle with a pressure ratio of 3.57. The shock structure within this jet was also examined using continuous light schlieren photography. Figure 3 shows predicted Mach numbers in the near field of this jet, where results are given in terms of contours of constant Mach number which range from 0.8 (at large r/d) to 3.4 (close to the nozzle exit) in increments of 0.2. Similar to experimental observations, the predicted jet has two Mach disks downstream of the nozzle. The characteristic features of a highly underexpanded jet are also evident. The first Mach disk therefore has a well defined triple point (at r/d, z/d = 0.3, 1.7) where the Mach disk, and intercepting and reflected oblique shocks terminate. The slip line downstream of this Mach disk (extending almost vertically upwards from the triple point) which separates the subsonic inner core of the jet from the surrounding supersonic flow is also clearly visible. Good agreement is obtained between measured (from schlieren photographs) and predicted Mach disk locations, with observed centerline distances of z_M/d = 1.58 and 3.36 comparing with predicted values of 1.68 and 3.33. In addition, observed Mach disk diameters of d_M/d = 0.59 and 0.30 compare well with predicted values of 0.62 and 0.32.

Figure 4 compares radial profiles of mean streamwise velocity at four downstream locations within the same jet. Within the shock containing region of the jet, at z/d = 1.96 and 3.92, agreement between model predictions and experimental data is good, although the standard k-ϵ model does tend to overpredict slightly the spreading rate of the jet. Predictions at these two measurement stations faithfully reproduce the existence of subsonic regions in the flow close to the centerline of the jet and just downstream of the first and second Mach disks. At the last two downstream locations however, where the core of the jet is now supersonic, predictions derived using Sarkar et al.'s (1991a) compressibility correction tend to underpredict the spreading rate of the jet, whilst those obtained using a standard k-ϵ approach are in reasonable agreement with observations. This finding is at variance with results for the first two measurement stations within this jet, and also for the moderately underexpanded jets considered by Cumber et al. (1994). Donaldson and Snedeker (1971) do, however, state that their velocity profiles, obtained using Pitot and static pressure probes, were subject to the influence of a flapping instability, i.e., a relatively low frequency lateral oscillation of the entire jet about its mean location. This instability was noted to be most influential downstream of the two Mach disks, and as a consequence mean velocity profiles in this region were judged to be spatially as well as time-averaged; causing measured mean velocity profiles to appear flattened within the core of the jet and spread out at its edges. The effect of this instability on the measurements is therefore consistent with earlier findings regarding the superiority of predictions derived using a compressibility corrected turbulence model, although since the extent of the instability was not quantified it is not possible to simulate numerically its influence on the results presented in Fig. 4.

Thus far the present numerical model has been compared, as far as available data allows, with measurements in, and just downstream of, the shock containing region of a number of highly underexpanded jets. Birch et al. (1984 and 1987) have also obtained far field measurements of mean streamwise velocity and mixture fraction (fuel mass fraction) along the centerline of jets of air and natural gas, making comparison in the totally subsonic regions of such jets possible. Figures 5 to 7 show model predictions and measurements of mean velocity obtained in air jets with pressure ratios of 3.1, 16.1, and 36.9. In all three jets, predictions of the standard k-ϵ model are seen to underestimate mean velocities significantly due to the overprediction of turbulence production dissipating the velocity on the axis. In contrast, incorporation of the compressibility correction

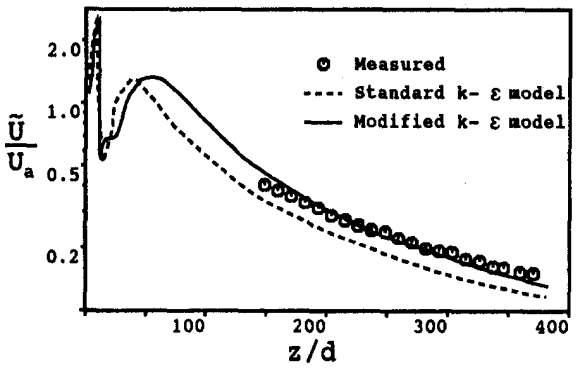

Fig. 7 Centerline values of mean streamwise velocity for Birch et al.'s (1987) P_o/P_a = 36.9 air jet (d = 2.7 mm, M = 1)

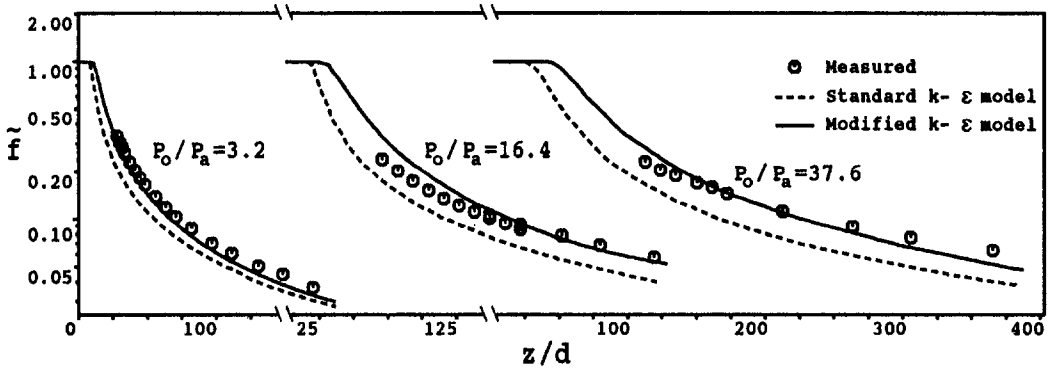

Fig. 8 Centerline values of mean mixture fraction for Birch et al.'s (1984) natural gas jets (d = 2.7 mm, P_o/P_a = 3.2, 16.4 and 37.6, M = 1)

of Sarkar et al. (1991a) leads to an increase in turbulence energy dissipation rates which is sufficiently large to bring predictions in line with experimental data. Results obtained using the latter model do tend to overpredict velocities slightly in the near field of the jets and underpredict those in the far field. A progressive deterioration of the predictions with increasing pressure ratio is also apparent. However, in the near field of these jets the experimental techniques used were susceptible to small errors due to compressibility and sample volume effects (Birch et al., 1984 and 1987), while the logarithmic scale employed as the ordinate of these figures does accentuate differences between theory and experiment. Overall, therefore, reasonable agreement between predictions derived using the modified k-ϵ model and measurements is achieved.

Figure 8 compares measurements and predictions of mean mixture fraction along the centerline of three jets of natural gas with pressure ratios of 3.2, 16.4, and 37.6. Again, results obtained using a standard k-ϵ turbulence model are seen to overpredict mixing rates within the jets, whereas the incorporation of a compressibility correction significantly improves agreement with experimental data. In agreement with findings for mean centerline velocities in this type of jet, predictions of the latter model also tend to overpredict mass fractions slightly in the near field of the higher pressure ratio jets, with an underprediction of far field data being apparent in all three jets. In view of the considerations noted above, however, reasonable agreement is achieved between predictions of the modified k-ϵ model and experimental observations.

Finally, the progressive deterioration of model predictions with increasing pressure ratio noted in Figs. 5 to 8 may be to some extent due to the simplicity of the compressibility correction employed, and the fact that the standard k-ϵ approach is known to overpredict the spreading rate of incompressible round jets. Predictions for the highest pressure ratio jets were therefore also derived using Sarkar et al.'s (1991b) more elaborate compressibility corrections which explicitly allow for both compressible dissipation rate and pressure-dilatation terms as sinks in the turbulence kinetic energy budget of compressible flows. Unfortunately, incorporation of the latter modifications did not improve on the level of agreement obtained between model predictions and experimental data. Likewise, modification of the modelling constants used in the k-ϵ model to account for its overestimation of the spreading rate of axisymmetric jets, using the suggestions of Pope (1978), was found to decrease significantly the level of agreement between theory and experiment noted in Figs. 7 and 8. Further work is required in order to explain these findings and the differences between model predictions and experimental observations in high pressure ratio jets, although more detailed experimental data, particularly in terms of radial profiles of mean and r.m.s. velocities, is needed before such work can proceed.

Conclusions

A mathematical model capable of predicting turbulent, underexpanded jets has been described, and the model's ability to predict the shock and flow structure of highly underexpanded jets has been assessed by comparing predictions with experimental data available in the literature and obtained at pressure ratios characteristic of such flows. In the near field, inviscid region of these jets, model predictions were found to be in close agreement with experimental observations of Mach disk location and diameter. Further downstream, and particularly in the far field subsonic region of such jets where turbulence dominates the flow field, predictions derived using a compressibility corrected (Sarkar et al., 1991a) k-ϵ turbulence model were found to be in reasonable agreement with data on mean velocity and mixture fraction, with results derived using the latter model being, in general, superior to those obtained using a standard k-ϵ approach.

Acknowledgments

The calculations reported in this paper were made using a modified version of the Mantis Numerics Ltd. code, COBRA. This paper is published by permission of British Gas plc.

References

Addy, A. L., 1981, "Effects of Axisymmetric Sonic Nozzle Geometry on Mach Disc Characteristics," *American Institute of Aeronautics and Astronautics Journal,* Vol. 19, pp. 121–122.

Antsupov, A. V., 1974, "Properties of Underexpanded and Overexpanded Supersonic Gas Jets," *Soviet Physics: Technical Physics,* Vol. 19, pp. 234–238.

Birch, A. D., Brown, D. R., Dodson, M. G., and Swaffield, F., 1984, "The Structure and Concentration Decay of High Pressure Jets of Natural Gas," *Combustion Science and Technology,* Vol. 36, pp. 249–261.

Birch, A. D., Hughes, D. J., and Swaffield, F., 1987, "Velocity Decay of High Pressure Jets," *Combustion Science and Technology,* Vol. 52, pp. 161–171.

Chuech, S. G., Lai, M.-C., and Faeth, G. M., 1989, "Structure of Turbulent Sonic Underexpanded Free Jets," *American Institute of Aeronautics and Astronautics Journal,* Vol. 27, pp. 549–559.

Crist, S., Sherman, P. M., and Glass, D. R., 1966, "Study of the Highly Underexpanded Sonic Jet," *American Institute of Aeronautics and Astronautics Journal,* Vol. 4, pp. 68–71.

Cumber, P. S., Fairweather, M., Falle, S. A. E. G., and Giddings, J. R., 1994, "Predictions of the Structure of Turbulent, Moderately Underexpanded Jets," ASME JOURNAL OF FLUIDS ENGINEERING, Vol. 116, 707–713.

Dash, S. M., and Wolf, D. E., 1983, "Shock-Capturing Parabolized Navier Stokes Model (SCIPVIS) for the Analysis of Turbulent Underexpanded Jets," *American Institute of Aeronautics and Astronautics* Paper 83-0704.

Donaldson, C. DuP., and Snedeker, R. S., 1971, "A Study of Free Jet Impingement. Part 1. Mean Properties of Free and Impinging Jets," *Journal of Fluid Mechanics,* Vol. 45, pp. 281–319.

Ewan, B. C. R., and Moodie, K., 1986, "Structure and Velocity Measurements in Underexpanded Jets," *Combustion Science and Technology,* Vol. 45, pp. 275–288.

Jones, W. P., and Launder, B. E., 1972, "The Prediction of Laminarization with a Two-Equation Model of Turbulence," *International Journal of Heat and Mass Transfer,* Vol. 15, pp. 301–314.

Jones, W. P., and Whitelaw, J. H., 1982, "Calculation Methods for Reacting Turbulent Flows: A Review," *Combustion and Flame,* Vol. 48, pp. 1–26.

Palacio, A., Malin, M. R., Proumen, N., and Sanchez, L., 1990, "Numerical Computations of Steady Transonic and Supersonic Flow Fields," *International Journal of Heat and Mass Transfer,* Vol. 33, pp. 1193–1204.

Pope, S. B., 1978, "An Explanation of the Turbulent Round-Jet/Plane-Jet Anomaly," *American Institute of Aeronautics and Astronautics Journal,* Vol. 16, pp. 279–281.

Sarkar, S., Erlebacher, G., Hussaini, M. Y., and Kreiss, H. O., 1991a, "The Analysis and Modelling of Dilatational Terms in Compressible Turbulence," *Journal of Fluid Mechanics,* Vol. 227, pp. 473–493.

Sarkar, S., Erlebacher, G., and Hussaini, M. Y., 1991b, "Compressible Homogeneous Shear: Simulation and Modelling," *Eighth Symposium on Turbulent Shear Flows,* 9th–11th Sept.

Calculation of Laminar Separated Flow in Symmetric Two-Dimensional Diffusers

Yeng-Yung Tsui
Associate Professor.

Chia-Kang Wang
Graduate Student.

Department of Mechanical Engineering,
National Chiao Tung University,
Hsinchu 300, Taiwan

This study is concerned with numerical analysis of laminar separated flow in symmetric, two-dimensional, straight-walled diffusers. With Reynolds numbers Re = 56 and 114 and expansion ratios ER = 3 and 4, totally, there are four cases considered. At the low Reynolds number and the low expansion ratio the flow in the diffuser is nearly symmetric to the center line, irrespective of the diffusion angle. As Reynolds number or expansion ratio increases, a large recirculation region forms at one side wall and a small one at the other side. For the case with Re = 114 and ER = 4 the small recirculating flow disappears at small diffusion angles and a third recirculating flow appear in the same side of the small main recirculation region for large diffusion angles. The pressure recovery reaches its peak value somewhere downstream of the reattachment point of the large recirculating flow. The effectiveness of the diffuser deteriorates as the diffusion angle increases, apart from that at Re = 56 the effectiveness increases from θ = 15 to 30 deg. Symmetric flow solutions can be obtained by incorporating a symmetric relaxation method. The pressure recovery is higher for the symmetric flow than that for the asymmetric flow owing to the weaker recirculating strength in the former.

1 Introduction

In internal flow systems it is often necessary to decelerate the flow to recover static pressure by means of diffuser. The diffuser forms an important component in many flow devices, such as piping systems, wind tunnels and turbomachines. Though the geometry of a diffuser may look simple, the flow in it is complex. The working concept of a diffuser is to gradually enlarge its cross-sectional area such that the flow is decelerated. According to the Bernoulli's principle, the static pressure increases. However, due to the adverse pressure gradient the flow may separate from the side walls. The flow separation causes large pressure losses and deteriorates the function of diffuser.

In the past decades, a lot of efforts have been devoted to the turbulent flow in diffusers (see, e.g., Fox and Kline, 1962, Reneau et al., 1967). As for laminar flow, not much work was done. Most studies were concentrated on single backward-facing steps or double backward-facing steps (i.e., symmetric sudden expansions). Armaly et al. (1983) employed the LDA to measure velocities and reattachment lengths downstream of a single backward-facing step. The Reynolds number was in the range $70 < \mathrm{Re} < 8000$, which covers the laminar, transition and turbulent regimes. Their results showed that the reattachment lengths are characterized by Reynolds number. In addition to the main recirculating flow downstream of the step, there exists a secondary vortex forming on both sides of the channel as the Reynolds number becomes sufficiently large.

Durst and Pereira (1988) calculated impulsively starting backward-facing step flow with the step being mounted in a planar, two-dimensional duct. Results were presented for Reynolds numbers of Re = 10, 368 and 648. For the last two Reynolds numbers comparisons were given between experimental and numerical results obtained for the final steady-state flow conditions. It was important to note that separation regions occur on both walls of the step during the transitional period of the flow development. Some of these regions vanish as time approaches infinity and, hence, the steady-state flow does not reflect the complex flow structure that occurs during the phase of the starting step flow.

Durst et al. (1974) used the LDA to measure velocities in flow over a symmetric sudden expansion. At the low Reynolds number Re = 56 symmetric velocity profiles exist downstream of the expansion. As Reynolds number increases to 114 and 252, the flow becomes asymmetric with separation regions of unequal size on opposite sides of the expansion. A third recirculation region was observed at Re = 252. Flow visualization showed that the flows at high Reynolds numbers are not two-dimensional. Further increasing in Reynolds number leads to larger flow oscillations.

Cherdron et al. (1978) continued the work of Durst et al. (1974) They described detailed velocity characteristics of the asymmetric flow which is formed in the ducts with symmetric sudden expansions. Their results indicated that the cause of asymmetry lies in the disturbances generated at the edges of the expansion and amplified in the shear layers. The spectral distributions of the velocity fluctuations are quantitatively related to the dimensions of the two unequal regions of flow recirculation.

In this study the recirculating flows in symmetrical, two-dimensional, straight-walled diffusers are examined using numerical method. Attention is focused on laminar regime with Reynolds number Re = 56, 114. The expansion ratio of the diffuser is fixed at 3 and 4. The half diffusion angle varies from 15 to 90 deg.

2 Numerical Method

The configuration of a diffuser is shown in Fig. 1. In this figure θ is the half diffusion angle. For $\theta = 90$ deg the diffuser becomes a double-step profile. To cope with the irregular boundaries the governing equations for the steady, two-dimensional, incompressible flow in diffuser are written in curvilinear nonorthogonal coordinates while the Cartesian velocity components are retained (Tsui and Wang, 1994). Discretization of the equations is performed using the control volume technique. In order to alleviate numerical diffusion as encountered by the

Contributed by the Fluids Engineering Division for publication in the Journal of Fluids Engineering. Manuscript received by the Fluids Engineering Division July 27, 1994; revised manuscript received March 1, 1995. Associate Technical Editor: S. P. Vanka.

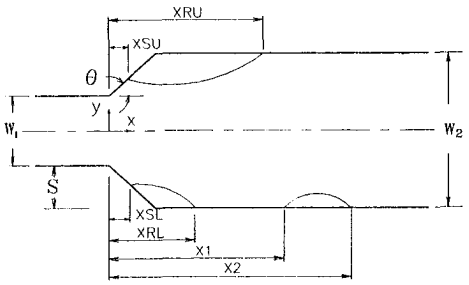

Fig. 1 Configuration of a diffuser and nomenclature

upwind difference the linear upwind difference (Price et al., 1966) is employed for approximation to the convection terms. In this scheme the transported properties at the faces of each control volume are estimated using linear extrapolation from two grid points upstream of the considered face. Just like other high-order schemes, the linear upwind difference may produce unphsical oscillations in solution, i.e., the solution may not be bounded. However, as shown by Tsui (1991), among a number of high-order schemes the linear upwind difference leads to best compromise between the numerical diffusion and the solution unboundness.

The grids used in this study are arranged in the nonstaggered manner, i.e., the velocity components and the pressure are placed at the center of each control volume. It is known that the nonstaggered arrangements may lead to decoupling between velocity and pressure and, thus, produces checkboard oscillations in solution. To avoid this problem the momentum interpolation method of Rhie and Chow (1983) is adopted to calculate the velocities across the faces of control volume. Then the SIMPLE type algorithm is adopted to tackle the coupling between the continuity and momentum equations.

3 Results

Schematic illustration of two different grid arrangements is shown in Fig. 2. In Fig. 2(a) the grid lines in the streamwise direction gradually expand from the center line to match the side walls of the diffuser. It is obvious that with large diffusion angles the skewness of the grids near the diffuser walls become quite large. This might affect the prediction accuracy and the solution stability. Thus, the second type of grid given in Fig. 2(b) is employed for the half diffusion angles greater than 50 deg.

The computational domain extends to 30S downstream of the diffuser entrance, where S denotes the height of diffuser (see Fig. 1). As will be seen below, the reattachment locations of the main recirculating flows will not exceed 10S in all considered cases. Thus, it is expected that the numerical boundary conditions imposed at the outlet will not affect the flow in the region near the diffuser.

In this study two Reynolds numbers, Re = 56 and 114, and two expansion ratios, ER = 3 and 4, are considered. Following Durst et al. (1974), the Reynolds number is defined as Re = U_sW_1/υ, where U_s is the maximum velocity in the channel upstream of the diffuser and W_1 is the height of the upstream channel (see Fig. 1). The expansion ratio is defined as ER = W_2/W_1, where W_2 is the height of the downstream channel (see Fig. 1). The inlet velocity is assumed to be fully developed and, at the outlet, the zero gradient conditions are imposed. The half diffusion angle θ varies in the range $15 \le \theta \le 90$ deg.

The grid refinement tests are undertaken for a flow over a sudden expansion (θ = 90 deg) with Re = 114 and ER = 3. Four kinds of grid have been used to examine the sensitivity of the solution to the grid spacing: 80 × 40, 100 × 60, 130 × 80 and 160 × 100 (Tsui and Wang, 1994). The resulted solutions are in good agreement to each other. Thus, the 100 × 60 grid is adopted in the following calculations for ER = 3. Since the computational dimension in each direction is enlarged by about 30% for cases with expansion ratio ER = 4, the numbers of mesh node are increased to 130 × 80.

To validate the solution method comparison between the predictions with the measurements of Durst et al. (1974) is made. In the experiments of Durst et al. the flow over a sudden expansion with ER = 3 was examined. At Re = 56 the predictions have good agreement with the experimental data (Tsui and Wang, 1994). For Re = 114, it is seen from Fig. 3 that the agreement between the two studies is less satisfactory and the degree of flow asymmetry is less significant in the predictions. It is believed that the cause of discrepancy is mainly due to the three-dimensional flow effects in the regions of recirculation. As shown by Durst et al., the apparent mass flow rate varies along the duct downstream of the expansion until the flow returns to become fully developed. The greatest disagreement, which occurs at X/S = 5.0, could be as high as 20 percent. The end-view photographs taken by them supports this fact that complex three-dimensional flow patterns prevail in the separation regions.

As mentioned above, two Reynolds numbers and two expansion ratios are examined. Totally, there are four cases considered:

Case I Re = 56, ER = 3
Case II Re = 56, ER = 4
Case III Re = 114, ER = 3
Case IV Re = 114, ER = 4

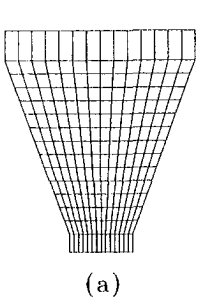

Fig. 2 Schematic illustration of two grid arrangements

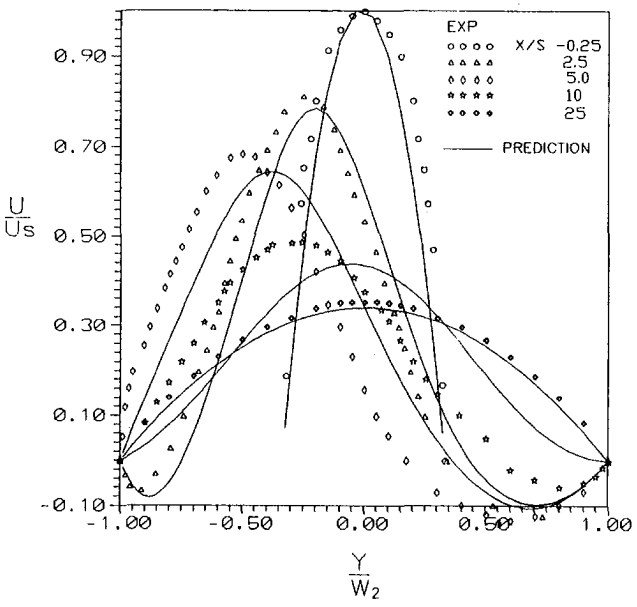

Fig. 3 Comparison between predictions and measurements for Re = 114

Most half diffusion angles are fixed at θ = 15, 22, 30, 45, 60, 75, and 90 deg. The streamlines for θ = 15 and 75 deg are depicted in Fig. 4. At the low Re and the low ER the flow attaches to the side walls and the flow is nearly symmetric to the center line for θ = 15 deg. As ER increases to 4, a small recirculation region near the diffuser exit can be seen. At the high Re large recirculating flows on both sides can easily be identified for ER = 3. As for ER = 4, the high Re flow leads to a very large flow recirculation on one side wall and the flow attaches to the wall on the other side. At the large diffusion angle θ = 75 deg the flow always separates at the diffusion entrance on both walls. At Re = 56 and ER = 3 the sizes of the two recirculation regions are nearly identical and the flow remains nearly symmetric. For the other cases a small recirculation region is formed on one side and a large one is formed on the other side. It is interesting to note that a secondary eddy can be found on the lower wall opposite to the tail of the large eddy on the upper wall in case IV.

The origin of the asymmetry is related to the instability of the shear layers formed by the flow separation. The instability originates from small perturbations embedded in the shear layers, being amplified to form wavy flow pattern and, then, vortex-like structure. Sato (1959) observed that velocity fluctuates in the vicinity of the shear layers near a nozzle exit in two-dimensional jet flow. Photographs of jet emerging from a sharp-edged slit and from an orifice taken by Beavers and Wilson (1970) revealed vortex shedding from the jet exit plane. Other measurements made in the shear layer formed by a laminar boundary layer separating from a single step also showed similar flow oscillation (Sato, 1956, Browand, 1966). The flow characteristics is complicated in the present study because of the confinement of the ducts following the diffusers. Due to the small dimensions of the ducts the two layers adjacent to the two recirculating flows are interdependent. The interaction between the two layers results in alternating shedding of vortices and, thus, flow asymmetry. This phenomenon has been examined in detail by Cherdron et al. (1978) in the flow over a double step.

In numerical calculations there are two sources to generate asymmetric disturbance. One is the rounding error and the other is the relaxation method used during iteration. The TDMA (tri-diagonal matrix algorithm) has been incorporated as basic solver on each vertical grid line and relaxation is conducted to sweep from the inlet plane to the exit plane. This arrangement leads to symmetric flow solution. This result is not unexpected when it is understood that the TDMA is a direct solver on a line and, thus, it is a symmetric solver. The result of symmetric flow implies that the rounding error does not play any role in producing flow asymmetry in this study. The TDMA has been applied

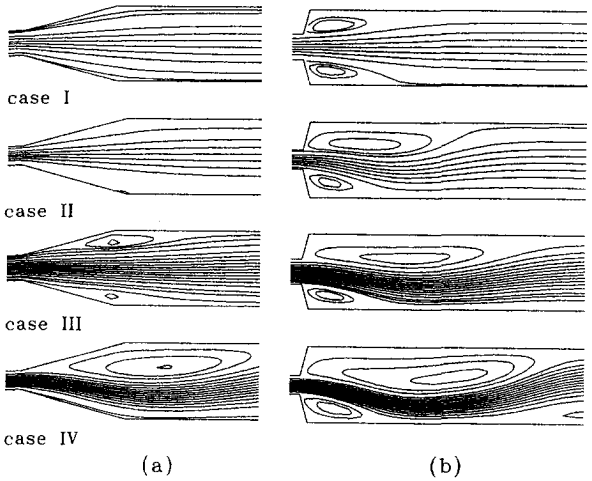

Fig. 4 Flow streamlines for (*a*) θ = 15 deg and (*b*) θ = 75 deg

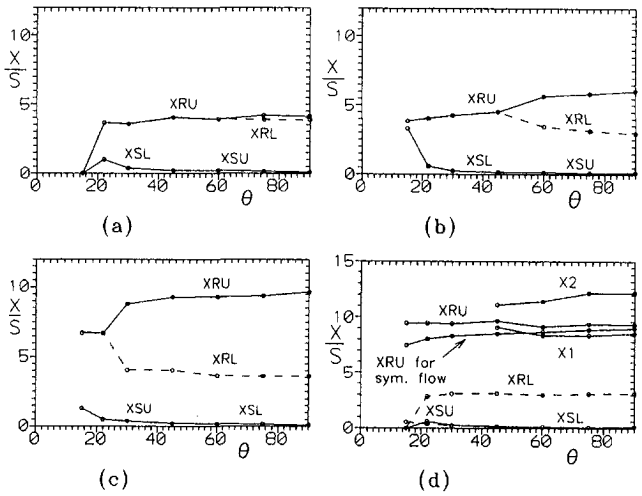

Fig. 5 Separation and reattachment lengths for (*a*) case I, (*b*) case II, (*c*) case III, and (*d*) case IV

to each horizontal line. In this way asymmetric results are obtained. In one case the horizontal line relaxation sweeps from the bottom to the top wall and in another case from the top to the bottom wall. When the sweep direction changes, the flow structure is reversed, i.e. the location of the large recirculating flow changes from one side to the other side. The results shown in Fig. 4 are obtained by using the Stone's SIP (Stone, 1968). The SIP method is an asymmetric solver because two additional points are involved in the computational molecule during the LU decomposition. In the solutions of all cases considered the large eddy is always located at the upper wall side, as plotted in Fig. 4. An only exception is the case with θ = 90 deg of case IV. In this case the location of the large eddy is on the lower wall side.

The flow separation lengths and reattachment lengths for the four cases are exhibited in Figs. 5. The corresponding nomenclature is referred to in Fig. 1. The size of the recirculating eddy is just the difference between the reattachment and the separation lengths. For case I the results just reflect the fact that the flow is nearly symmetric. The flow is unseparated for θ = 15 deg and separated at a certain distance downstream of the diffuser inlet for θ = 22 deg. For $\theta \geq$ 30 deg the flow separation point is close to the diffuser inlet and the eddy size is around 4S. The upper eddy is slightly larger than the lower one as $\theta \geq$ 60 deg. For case II the eddy size increases from 4S at θ = 30 deg to 6S at θ = 90 deg. However, the flow becomes asymmetric for $\theta \geq$ 60 deg and the small eddy size is about 3S. It is interesting to note that the mean size of these two eddies stays in the range of 4 ~ 4.5S. It is noted that the diffuser height S is proportional to the expansion ratio.

Comparing cases III and IV with cases I and II, respectively, indicates that the size of the recirculating flow is greatly enlarged by increasing Reynolds number. For cases III and IV both the upper eddy and the lower eddy remain nearly at constant sizes when the diffuser angle becomes sufficiently large. The upper eddy size is around 9S in both cases whereas the lower eddy size is about 3.5S in case III and 3S in case IV. The size of the secondary eddy downstream of the smaller main eddy in case IV is smaller than 3.5S.

The distributions of pressure coefficient along the x coordinate for cases I and IV are illustrated in Fig. 6. The pressure coefficient C_P is defined as

$$C_P = \frac{\frac{1}{A}\int_A P dA - \frac{1}{A_1}\int_{A_1} P_1 dA_1}{\frac{1}{2}\rho u_1^2}$$

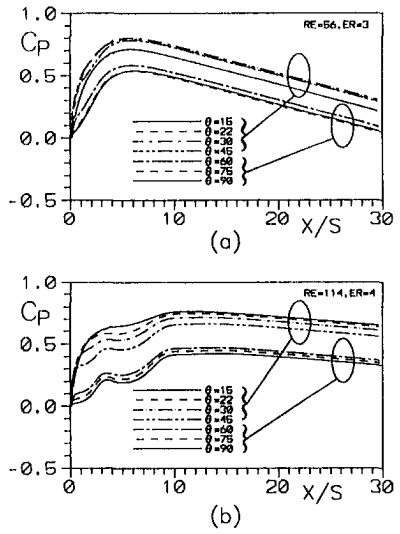

Fig. 6 Variation of C_P against diffusion angle for (*a*) case I and (*b*) case IV

where the subscript 1 denotes the diffuser inlet, A is the cross-sectional area, and u_1 the mean velocity across the inlet. It is seen that the pressure increases quickly in the diffuser and reaches its peak value somewhere downstream of the reattachment point of the large eddy. Afterwards, the pressure gradually decreases and approaches a linear relation with x. This is because of the fact that the flow returns to become fully developed after it recovers from separation. For fully developed flow the pressure drop, caused by frictional effects, is inversely proportional to Reynolds number. Hence, the slope for Re = 114 is lower than that for Re = 56. It can also be observed that the pressure curves exhibit a wavy pattern in the recovery region for case IV. Examination of the reattachment lengths of the smaller eddies reveals that this phenomenon is caused by the appearance of these small eddies.

In view of the C_P distributions it can be seen that the maximum pressure recovery occurs at around x = 6S and 12S for Re = 56 and 114, respectively. The pressure coefficients at these locations are denoted as recovery coefficient C_{PR} and are presented in Fig. 7 for all the cases. At Re = 56 the pressure recovers more effectively for $\theta \leq 45$ deg as the expansion ratio is increased from 3 (case I) to 4 (case II). When the diffusion angle is enlarged, the pressure recovery coefficient of case II becomes lower than that of case I due to appearance of the large recirculating eddy in case II. As for high Re cases the case IV always possesses lower pressure recovery than the case III. An interesting phenomenon noticed is that contrary to the high Reynolds number cases the maximum pressure recovery does not occur at the lowest diffusion angle in cases I and II. The coefficient C_{PR} increases with diffusion angle to a peak value at about θ = 30 deg, and then decreases. This result can be viewed in Fig. 6(a) as well. Similar observations can also be found in turbulent flow (Reneau et al., 1967).

The above results clearly demonstrate that for sufficiently large Reynolds number and expansion ratio the flow is stable only in the form of asymmetry. As described previously, symmetric solution can be obtained by using the vertical line relaxation. Another way to generate symmetric solution is to solve for half of the duct and to impose symmetry boundary conditions at the mid-plane. The reattachment lengths and recovery coefficients C_{PR} for the symmetric flows corresponding to case IV are sketched in Figs. 5(d) and 7, respectively. The eddy lengths of the symmetric flow are slightly smaller than the lengths of the large eddies of the asymmetric flow. Intuition tells that the pressure recovery will become worse because of appearance of two large recirculation regions instead of one large and one small eddy in the asymmetric flows. Actually, the eddy strength of the symmetric flow is much weaker. As an example, consider the case of θ = 75 deg. The height of the symmetric eddy gradually decreases from the diffuser inlet whereas, as seen from the streamlines shown in Fig. 4, the height of the large eddy in the asymmetric flow gradually enlarges till the mid-station of the recirculation region. As a consequence, the flow passage in the symmetric flow is wider than that in the asymmetric flow. Therefore, the pressure recovery is higher in the former, as can be seen in Fig. 7.

4 Conclusions

A numerical method incorporating nonorthogonal, nonstaggered grids has been successfully applied to calculate laminar flow in two-dimensional, symmetric diffusers. Some conclusions can be summarized in the following:

(1) Symmetric and asymmetric solutions are possible, depending on whether the iterative solver is symmetric or not. The flow structure of the asymmetric solution can be reversed by changing the sweep direction of the solver.

(2) Comparison with measurements indicates that good predictions can be obtained for Re = 56. But the agreement deteriorates at Re = 114. The cause of poor predictions at the high Reynolds number lies in that the real flow in the experiments is three-dimensional in the recirculation region.

(3) At low Reynolds number (Re = 56) and low expansion ratio (ER = 3) the flow is almost symmetric to the center line. However, as Re increases to 114 or ER increases to 4, the flow becomes asymmetric when the diffusion angle is large enough, i.e., a large recirculation forms at one side wall and a small one at the other side. For the extreme case (Re = 114, ER = 4) with small diffusion angles the flow attaches to one side wall while the large recirculation at the other side retains its size as in the large angle cases. Another interesting phenomenon observed is that a secondary eddy can be seen in the same side of the small recirculation region and is located near the end of the large recirculation region in case IV.

(4) Roughly, the size of the recirculation region is scaled by the expansion ratio. At sufficiently large diffusion angles the mean eddy size is around 4 ~ 4.5S for the small Reynolds number cases. At high Reynolds number the size of the large eddies is about 9S and that of the small ones is about 3 ~ 3.5S.

(5) The static pressure is recovered in the diffuser. It reaches a peak value somewhere downstream of the reattachment point of the large recirculating flow. Due to appearance of the small recirculating flow the pressure recovery exhibits wavy form.

(6) Generally, the performance of pressure recovery deteriorates as the diffusion angle increases. A particular exception is that at low Reynolds number (Re = 56) the pressure recovery increases from θ = 15 to 30 deg.

(7) The eddy length of the symmetric solution is close to the length of the large recirculation region in the asymmetric solution. The pressure recovery effectiveness is higher in the

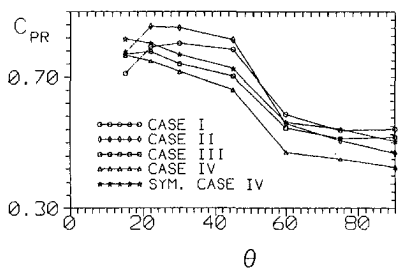

Fig. 7 Variation of C_{PR} against diffusion angle

former due to its much weaker eddy strength than the strength of the large eddy in the latter.

References

Armaly, B. F., Durst, F., Pereira, J. C. F., and Schonung, B., 1983, "Experimental and Theoretical Investigation of Backward-Facing Step Flow," *Journal of Fluid Mechanics,* Vol. 127, pp. 473–496.

Beavers, G. S., and Wilson, T. A., 1970, "Vortex Growth in Jets," *Journal of Fluid Mechanics,* Vol. 44, Part 1, pp. 97–112.

Browand, F. K., 1966, "An Experimental Investigation of the Instability of an Incompressible, Separated Shear Layer," *Journal of Fluid Mechanics,* Vol. 26, Part 2, pp. 281–307.

Cherdron, W., Durst, F., and Whitelaw, J. H., 1978, "Asymmetric Flows and Instabilities in Symmetric Ducts with Sudden Expansions," *Journal of Fluid Mechanics,* Vol. 84, pp. 13–31.

Durst, F., Melling, A., and Whitelaw, J. H., 1974, "Low Reynolds Number Flow Over a Plane Symmetric Sudden Expansion," *Journal of Fluid Mechanics,* Vol. 64, pp. 111–128.

Durst, F., and Pereira, J. C. F., 1988, "Time-Dependent Laminar Backward-Facing Step Flow in a Two-Dimensional Duct," ASME JOURNAL OF FLUIDS ENGINEERING, Vol. 110, pp. 289–296.

Fox, R. W., and Kline, S. J., 1962, "Flow Regimes in Curved Subsonic Diffusers," ASME JOURNAL OF BASIC ENGINEERING, Vol. 84, pp. 303–316.

Price, H. S., Varga, R. S., and Warren, J. E., 1966, "Applications of Oscillation Matrices to Diffusion-Correction Equations," *Journal of Mathematical Physics,* Vol. 45, pp. 301–311.

Reneau, L. R., Johnston, J. P., and Kline, S. J., 1967, "Performance and Design of Straight, Two-Dimensional Diffusers," ASME *Journal of Basic Engineering,* Vol. 89, pp. 141–150.

Rhie, C. M., and Chow, W. L., 1983, "Numerical Study of the Turbulent Flow Past an Airfoil with Trailing Edge Separation," *AIAA Journal,* Vol. 21, No. 11, pp. 1525–1532.

Stone, H. L., 1968, "Iterative Solution of Implicit Approximations of Multi-Dimensional Partial Differential Equations," *SIAM Journal of Numerical Analysis,* Vol. 5, pp. 530–558.

Sato, H., 1956, "Experimental Investigation on the Transition of Laminar Separated Flow," *Journal of the Physical Society of Japan,* Vol. 11, p-702.

Sato, H., 1959, "The Stability and Transition of a Two-Dimensional Jet," *Journal of Fluid Mechanics,* Vol. 7, pp. 53–80.

Tsui, Y.-Y., 1991, "A Study of Upstream-Weighted High-Order Differencing for Approximation to Flow Convection," *International Journal for Numerical Methods in Fluids,* Vol. 13, pp. 167–199.

Tsui, Y.-Y., and Wang, C.-K., 1994, "Laminar Flow Calculation in Planar Diffusers," *Proceedings of the 18th National Conference on Theoretical and Applied Mechanics,* Hsinchu, Taiwan.

Mass Flow and Thrust Performance of Nozzles With Mixed and Unmixed Nonuniform Flow

Reiner Decher
Professor.
Department of Aeronautics & Astronautics,
Box 352400,
University of Washington,
Seattle, WA 98195-2400

The calculated thrust and mass flow rate of a nozzle depend on the uniformity of the entering flow. The one-dimensional flow equations are extended to arrive at analytic expressions for the predicted performance of a nozzle processing two streams whose properties are determined ahead of the throat. The analysis approach forms the basis for the understanding of flows which have more complex distributions of total pressure and temperature. The uncertainty associated with mixing is examined by the consideration of the two limiting cases: compound flow with no mixing and completely mixed flow. Nozzle discharge and velocity coefficients accounting for non-uniformity are derived. The methodology can be extended to experimentally measured variations of flow properties so that proper geometric design variables may be obtained.

Introduction

In many practical applications, the total pressure and temperature of the flow through a nozzle may be such that the assumption of uniform, one-dimensional flow is invalid (Oates and Presz, 1979). This may be encountered in the use of a single nozzle to expand flows from two sources such as the fan and core of a turbofan aircraft propulsion engine, in flows involving non-adiabatic processes (such as chemical reactions, e.g., in an afterburner with zonal burning), or in flows with wakes. Even a so-called uniform flow will necessarily involve boundary layers which are regions of reduced total pressure and perhaps with altered total temperature, depending on any heat transfer involved. Thus a truly one-dimensional nozzle flow is, in fact, difficult to realize in practice. Yet, adiabatic and reversible flow assumptions are readily made to yield simple equations for the mass flow rate and the exit velocity from a nozzle. For accurate performance prediction, these relations must be modified to account for non-uniformities when these are significant. As an example for the motivation of this work, the accurate determination of nozzle thrust in model testing and projection to full scale is critical to thrust/drag accounting and the related problem of performance guarantee specification for aircraft (Gillette et al., 1975; Tegeler et al., 1975; and Kimzey et al., 1985).

The following is an examination of the effect of flow uniformity on the performance of a single throat nozzle as a thrust production and mass flow rate controlling device, by considering the situation where the flow consists of two portions of different total pressures and temperatures. This is the simplest model useful to obtain the results sought since non-uniformity profiles can be infinitely variable. The underlying motivation is an understanding of the inherent accuracy of the performance prediction. The point of departure for this study is the 1-D nozzle flow description developed in standard textbooks. Although one can speak of the flow at the throat as having specific total properties, the usual practical approach is to measure total pressure and temperature ahead of the throat in a flow region where the local Mach number is sufficiently low so that the inherent uncertainty in the measured values is small. The description required for a general non-uniform nozzle flow with reversible and adiabatic flow for each of a number of streamtubes flowing parallel to one another and sharing the local static pressure is given by Bernstein et al. (1967) and developed further by Decher (1978, 1994). A criterion for choking through the "compound flow indicator" is identified in Bernstein et al. The important role of the local static pressure (rather than the Mach number of the uniform flow) is developed as the proper flow description parameter. The complexity of the governing equations is such that it is normally difficult to draw useful conclusions except through their implementation on a computer.

The objective of this work is to develop a sufficiently simple situation to show: First, how does a nonuniform flow differ from a uniform one? What parameters characterize the nonuniformity and what is the coupling between total pressure and temperature nonuniformities as it affects nozzle predicted performance? Second, since the measurements of total pressure and temperature are almost always made ahead of the throat, what is the change in predicted performance associated with mixing that might or might not take place between the measurement location and the throat? To answer these questions, general descriptive relationships of a non-uniform flow are derived. These are linearized for a flow with a small degree of total pressure non-uniformity. Performance increments associated with the non-uniformity as a departure from uniform flow are developed for 1. unmixed flow and 2. fully mixed flow, to illustrate the performance consequences of mixing. Figure 1 shows schematically the results sought: differences of type A between unmixed and uniform flow, type B for mixed and uniform flow, and C to show the difference between mixed and unmixed non-uniform flows.

Generally, the accurate determination of total mass flow rate through the nozzle and its momentum are the performance measures of greatest interest. These quantities are represented nondimensionally by the *discharge* coefficient (C_d = actual divided by ideal mass flow rates) and the *velocity* coefficient (C_v = jet momentum divided by the product of ideal velocity and actual mass flow rate). In addition to the expressions for C_d and C_v, the results of interest include expressions for appropriate averages useful for the 1-D relations and a criterion for choking. The analytic expressions are readily evaluated as corrections to 1-D results, especially if the corrections are small, as they often are. Under these circumstances, linearization of the resulting

Contributed by the Fluids Engineering Division for publication in the Journal of Fluids Engineering. Manuscript received by the Fluids Engineering Division April 11, 1994; revised manuscript received February 23, 1995. Associate Technical Editor: O. Baysal.

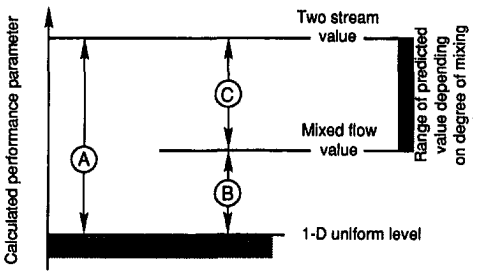

Fig. 1 Predicted performance levels and differences for mixed and unmixed nonuniform flows as these differ from uniform flow

equations is justified and the relationship to uniform flow becomes clear. For this purpose, one of the two flows is used as a reference to measure the departure from uniformity. The deviation between uniform and nonuniform flow results may be viewed as the prediction error made assuming a uniform flow, when in fact, the flow is nonuniform.

The practical situations which might be examined include the following: 1. A fixed geometry nozzle processes a mass flow which is affected by its nonuniformity. For this nozzle and flow one might be interested in determining the C_d associated with the non-uniformity. 2. A known mass flow rate of non-uniform flow is processed and the goal is to find the proper flow area which must be provided. 3. When the proper throat size is used and a known mass flow rate is provided, what is the effect of the non-uniformity on thrust (or equivalently, momentum) performance? This is equivalent to identifying C_v, associated with the non-uniformity. The results are always written so that well understood limiting cases can be easily examined as a check for consistency with known results. The algebraic complexity of the results displayed in this paper may be daunting, but is unfortunately unavoidable. Extension of the approach to a multiplicity of streamtubes and non-uniform properties such as γ and R is not considered here, although inclusion of such effects can be readily incorporated into a machine computation (Decher 1994).

Compound Flow

A flow may be assumed quasi-one-dimensional when it may be said that streamtubes with differing stagnation properties proceed through a duct in such a way as to share a common static pressure (Bernstein et al., 1967). This is the case when the streamtube curvature is small. The static pressure is the link between the two flows which makes it the key parameter in describing the flow. By contrast, the Mach number is commonly used to describe uniform 1-D flows.

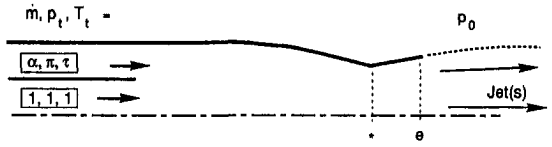

Fig. 2 Schematic of a two stream nozzle. The primary stream serves as a reference.

Consider the flow of two streams with different total temperatures and pressures coming into contact in the low Mach number section of a duct and exiting a common nozzle, Fig. 2. The flow plane where the streams come in contact is the nozzle charging station and * is used for conditions at the throat. The nozzle is assumed properly expanded so that for an unchoked flow, the diverging portion shown in Fig. 2 is absent. Thus the exit static pressure p_e equals the ambient pressure, p_0.

At any station in this nozzle, the two flows are described as a primary flow (1) and a secondary flow (2). For convenience, the stagnation conditions of the primary flow are used as reference. Thus T_{t1}, p_{t1}, and $\dot{m}_1$ are used to form nondimensional parameters which characterize similar quantities in the other flow:

$$T_{t2} = \tau T_{t1}; \quad p_{t2} = \pi p_{t1}; \quad \dot{m}_2 = \alpha \dot{m}_1 \tag{1}$$

Since the static pressure is shared by the two flows, an expression for the total mass flow rate is written in terms of the static pressure as a measure of location along the nozzle. A particularly convenient indicator for this pressure is an entropy-like parameter defined by

$$s \equiv \left(\frac{p}{p_{t1}}\right)^{\gamma-1/\gamma} = \left(1 + \frac{\gamma - 1}{2} \mathrm{M}_1^2\right)^{-1} \tag{2}$$

The use of this quantity minimizes the algebraic complexity of the expressions to be derived. The Mach number M_1 is that in the reference streamtube. The best nondimensional measure of velocity in the streamtube i, =1 or 2, is the ratio of the actual velocity to the value reached by the primary stream upon expansion to zero pressure:

$$V_i = \frac{u_i}{u_{1,\max}} = \frac{u_i}{\sqrt{\dfrac{2\gamma}{\gamma - 1} RT_{t1}}} \tag{3}$$

The energy equations (constant total enthalpy along each streamtube) relate the static temperatures to the velocities as

$$\frac{T_i}{T_{ti}} = 1 - \frac{V_i^2}{\tau_i} = \left(1 + \frac{\gamma - 1}{2} \mathrm{M}_i^2\right)^{-1} \tag{4}$$

Nomenclature

A = flow area
b = collection of stagnation properties, $= \sqrt{2\gamma/(\gamma - 1)}\, p_{t1}/\sqrt{RT_{t1}}$
C_d = discharge coefficient based on primary reference conditions
C_p = specific heat at constant pressure
C_v = velocity coefficient based on primary reference conditions
$\dot{m}$ = mass flow rate
M = Mach number
p, p_t = static and total pressure
R = ideal gas constant
u = flow velocity
V = velocity nondimensionalized by reference enthalpy, $u/\sqrt{(2\gamma/\gamma - 1)RT_{t1}}$
s = static pressure parameter, $(p/p_{t1})^{(\gamma-1)/\gamma}$
T, T_t = static and total temperature
w_R = temperature corrected mass flow fraction of the secondary flow, $\alpha\sqrt{\tau}/(1 + \alpha\sqrt{\tau})$
α = stream mass flow rate ratio, $\dot{m}_2/\dot{m}_1$
Φ = total temperature nonuniformity parameter, $(1 + \alpha\sqrt{\tau})^2/(1 + \alpha)(1 + \alpha\tau)$
γ = specific heat ratio
π = total pressure uniformity parameter, p_{t2}/p_{t1}
Π = Total pressure loss factor in mixed flow
σ = modified total pressure uniformity parameter, $(p_{t2}/p_{t1})^{(\gamma-1)/\gamma}$
τ = total temperature uniformity parameter, T_{t2}/T_{t1}
ψ_i = mass flow function, $1 + 1/\gamma([1/M_{1,i}^2] - 1)$

Subscripts

1 = primary
2 = secondary
e = nozzle exit
i = 1, 2, or m
m = mixed
t = total
u = uniform
* = throat

where $\tau_1 = 1$ and $\tau_2 = \tau$ from the notation definition in Fig. 2. Since the flow in each tube is isentropic, the velocities in the two flows are related to the *pressure* through

$$V_1 = \sqrt{1 - s} \quad \text{and} \quad V_2 = \sqrt{\tau}\sqrt{1 - \frac{s}{\sigma}} \tag{5}$$

Here $\sigma \equiv (p_{t2}/p_{t1})^{(\gamma-1)/\gamma} = (\pi)^{(\gamma-1)/\gamma}$ is defined to characterize the total pressure non-uniformity ($\pi \neq 1$). The static and stagnation states for the two flows are related to the local Mach numbers. Thus with Eq. (4) one can write the Mach numbers at any station where the pressure is given by s as

$$\mathrm{M}_1^2 = \frac{2}{\gamma - 1}\frac{1 - s}{s} \quad \text{and} \quad \mathrm{M}_2^2 = \frac{2}{\gamma - 1}\frac{\sigma - s}{s} \tag{6}$$

Thus when $\sigma < 1$ ($p_{t2} < p_{t1}$), it follows that $\mathrm{M}_2 < \mathrm{M}_1$.

The mass flow rates are given in terms of the local static pressure by the mass conservation relation

$$\dot{m}_i = \frac{p}{p_{t1}}\left[\frac{p_{t1}}{\sqrt{RT_{t1}}}\sqrt{\frac{2\gamma}{\gamma - 1}}\right]\left(\frac{T_{t1}}{T_{ti}}\frac{T_{ti}}{T_i}V_i A_i\right)$$

$$= b\frac{\mathrm{p}}{\mathrm{p}_{t1}}A_i\frac{V_i}{\tau_i - V_i^2} \tag{7}$$

where the constant b is a characteristic ρu for the primary flow defined by the group of variable in the square bracket.

The total mass flow rate for the two flows can be written in terms of s and the velocities as

$$\dot{m} = bs^{\gamma/(\gamma-1)}A\left\{\frac{A_1}{A}\left(\frac{V_1}{1 - V_1^2}\right) + \frac{A_2}{A}\left(\frac{V_2}{\tau - V_2^2}\right)\right\} \equiv \dot{m}_1(1 + \alpha) \tag{8}$$

The mass flow rate ratio, α, is defined here and with Eq. (7), is given by:

$$\alpha \equiv \frac{\dot{m}_2}{\dot{m}_1} = \frac{A_2}{A_1}\left(\frac{V_2}{\tau - V_2^2}\right)\left(\frac{1 - V_1^2}{V_1}\right) \tag{9}$$

since the static pressure is the same for the two streams. This equation can be used to calculate the streamtube area ratio A_2/A_1 implicit in Eq. (9). By eliminating the area ratio, the total mass flow rate can be written in terms of only the *pressure*, s, as

$$\dot{m} = bAs^{1/(\gamma-1)}\sqrt{1 - s}\left\{\frac{1 + \alpha}{1 + \alpha\sqrt{\tau}\left[\frac{1}{\sigma}\sqrt{\frac{1 - s}{1 - s/\sigma}}\right]}\right\} \tag{10}$$

$A = A_1 + A_2$ is the available flow area. This expression is valid for any value of the total temperature uniformity, τ, and total pressure non-uniformity as characterized by σ. All non-uniformity effects are incorporated in the term in brackets. The bracket term reduces to the unity when there is only one flow ($\alpha = 0$) or the flow is uniform, $\pi = \tau = 1$. The quantity in square brackets appears frequently in the work to follow and may be interpreted as a stream velocity ratio.

Choking. A flow is said to be choked when the flow conditions through the nozzle become independent of downstream conditions, i.e., when the mass flow rate is maximized for the given upstream conditions. Equation (10) for a uniform flow, expressed in terms of M, can be differentiated with respect to M and set equal to zero to determine the maximum mass flow rate. Corresponding to the resulting $M = 1$, a uniform flow reaches a static pressure given in terms of s by (see Eq. 2) s^* (uniform) $= 2/(\gamma + 1)$. For nonuniform flow, the more general expression for s^* is found by a null differentiation of Eq. (10) with respect to s. The resulting expression is

$$\frac{\gamma - 1}{2}\frac{s^*}{(1 - s^*)} = \frac{1 + \dfrac{\alpha\sqrt{\tau}}{\sigma\left(\dfrac{1 - s^*/\sigma}{1 - s^*}\right)^{1/2}}}{1 + \dfrac{\alpha\sqrt{\tau}}{\sigma^2\left(\dfrac{1 - s^*/\sigma}{1 - s^*}\right)^{3/2}}} \tag{11}$$

This relation for s^* as a function of α, τ, and π (i.e., σ) is seen to be algebraically implicit and simplifies if the pressure non-uniformity term σ is close to 1.

Nearly Uniform Two Stream Flow. Restriction to this situation allows an overview of a number of instructive results. From the definition of σ (Eq. (5)), it follows that for a small difference in total pressure for the two streams:

$$\sigma \approx 1 + \frac{\gamma - 1}{\gamma}(\pi - 1); \quad |\pi - 1| \ll 1 \tag{12}$$

The stream velocity ratio, when linearized, reads

$$\sigma\sqrt{\frac{1 - s/\sigma}{1 - s}} \approx 1 + \psi(\pi - 1) \tag{13}$$

where ψ is a primary flow Mach number function defined in the Nomenclature section. This function arises in connection with expressions for the mass flow rate and is ≥ 1. Expanding Eq. (11) gives the choked throat static pressure:

$$s^* \approx \frac{2}{\gamma + 1}\left(1 + \frac{\alpha\sqrt{\tau}}{1 + \alpha\sqrt{\tau}}\frac{\gamma - 1}{\gamma}(\pi - 1)\right)$$

$$= \frac{2}{\gamma + 1}\left(1 + w_R\frac{\gamma - 1}{\gamma}(\pi - 1)\right) \tag{14}$$

Here, and in the work ahead, the frequent appearance of the *secondary flow temperature corrected mass fraction*, w_R (see Nomenclature), justifies the short-hand definition.

The Mach numbers *in the choked flow throat* may be determined using Eqs. (6) and (14). The flow with larger total pressure will be supersonic while the other is subsonic:

$$(\mathrm{M}_1^*)^2, (\mathrm{M}_2^*)^2 \approx 1 - w_R\frac{\gamma + 1}{\gamma}(\pi - 1)$$

$$\text{and} \quad 1 + (1 - w_R)\frac{\gamma + 1}{\gamma}(\pi - 1) \tag{15}$$

Note the role of the weighting factor, w_R. For the determination of mass flow rate, one is normally interested in the relation between the upstream conditions and the pressure at the throat. The (linearized, small $(\pi - 1)$, see Eq. (12)) expression for the mass flow rate (Eq. (10)) for the unchoked and choked cases is:

$$\dot{m} \approx bAs^{1/(\gamma-1)}\sqrt{1 - s}\left[\frac{1 + \alpha}{1 + \alpha\sqrt{\tau}}\right]$$

$$\times (1 + \psi_{1^*}w_R(\pi - 1)) \tag{16}$$

Here A is the flow area and ψ_{1^*} is evaluated at M_{1^*}, the Mach number reached by the primary flow on expansion to the throat pressure given by $s^* = (p^*/p_{t1})^{\gamma-1/\gamma}$. When $\mathrm{M}_{1^*} = 1$ (to first order), this flow with a small total pressure variation is choked and the expression yields the expected result for choked flow

with an effective value of the total temperature related to the fraction in square brackets. If the variation in p_t is absent ($\pi = 1$), only the effective total temperature term changes the result from that for a uniform, 1-D flow expression. These results are consistent with the work of Bernstein et al., 1967.

These results may be summarized in non-dimensional form to give the ratio of mass flow rate for a two part non-uniform flow ratioed to the mass flow which would be obtained through *the same flow area* if it were uniform with the properties of the flow portion used as a reference, (1 in this case). This ratio is a discharge coefficient based on the reference (primary) flow conditions, C_d:

$$C_d = \left\{\frac{\dot{m}\ (2\ \text{stream})}{\dot{m}\ (\text{uniform})}\right\}_{\text{Fixed area}} = \frac{1+\alpha}{1+\dfrac{\alpha\sqrt{\tau}}{\sigma}\sqrt{\dfrac{1-s^*}{1-s^*/\sigma}}} \cong \frac{1+\alpha}{1+\alpha\sqrt{\tau}} \times \{1+\psi_{1^*}w_R(\pi-1)\} \tag{17}$$

This value of C_d identifies the change in mass flow rate processing capability relative to a uniform flow as the flow becomes more non-uniform. The choice of the primary flow as a reference allows it to be eliminated when a similar C_d is developed for the nozzle with complete mixing prior to the throat. The last expression in Eq. (17) is the linearized result for a small $\pi - 1$, but arbitrary τ ratio.

Jet Momentum and Thrust. With the mass flow rate known and held constant as flow properties are varied, the thrust may be investigated by calculation of the momentum per unit mass flow rate. For a properly expanded flow, the mass average velocity of the exiting stream is desired. This depends on total quantities and on the local static pressure. The exit pressure ($s_{1,e}$) is such that the primary flow reaches $M_{1,e}$. The velocities V_1 and V_2 are computed from Eq. (5), from which the mass flow weighted velocity is a velocity coefficient *relative to the primary flow conditions,* C_v (2 stream):

$$C_v\ (2\ \text{stream}) \equiv \frac{\overline{V}}{V_1} = \frac{V_1+\alpha V_2}{(1+\alpha)V_1} = \frac{1+\alpha\sqrt{\tau}\sqrt{\dfrac{1-s_{1,e}/\sigma}{1-s_{1,e}}}}{1+\alpha} \cong \frac{1+\alpha\sqrt{\tau}}{1+\alpha} \times \left[1+\frac{w_R(\pi-1)}{\gamma M_{1,e}^2}\right] \tag{18}$$

Thus raising π and τ above unity in the secondary flow increases the jet velocity by the amounts given. Note the temperature affects the pressure term through its presence in the weighting term, w_R defined by Eq. (14). This velocity coefficient is independent of choking.

Ideal Constant Pressure Mixer Flow

As a contrast to the two stream case described above, we consider next the alternate extreme where complete mixing takes place in the region between the station where stagnation measurements are made and the throat. The constant pressure mixer is assumed ideal in that friction losses are neglected, although losses that do occur may be assigned to the entering flow before mixing takes place. The mixer is assumed to fully

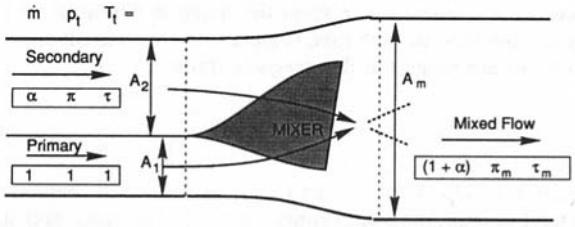

Fig. 3 Schematic of a complete, constant pressure mixer. Values of the variables noted are given for each flow. A_1 and A_2 are the flow areas of the incoming flows while A_m applies to the exit flow.

combine the entering flows to a single exit flow. Figure 3 shows the geometry and identifies the important parameters. The subscript m is used to describe the mixed flow. M_{1m} is directly related to the chosen design value of the pressure in the mixer. In contrast to the flow with coflowing streamtubes, the mixing flow is not reversible.

To determine nozzle performance, the mixture total pressure and total temperature are required. Also of interest is the area ratio across the mixer. The theory for the mixer is an adaptation of that developed by Oates (1984). The conservation of total enthalpy gives the mixed total temperature as

$$\tau_m = \frac{1+\alpha\tau}{1+\alpha} \tag{19}$$

The conservation of momentum gives the mixed flow velocity. For any of the three flow conditions, the energy equation is used to relate the velocity to the static pressure. Thus, one has for the mixed flow at the mixer exit (following Eq. (5)):

$$V_m^2 = \tau_m\left(1-\frac{s_{1,m}}{\sigma_m}\right); \quad \sigma_m \equiv \left(\frac{p_{tm}}{p_{t1}}\right)^{\gamma-1/\gamma} \equiv (\pi_m)^{\gamma-1/\gamma} \tag{20}$$

π_m and σ_m describe the mixed flow stagnation pressure. In the mixer, $s_{1,m}$ is a measure of the local static pressure which can be written in terms of primary flow Mach number there, $M_{1,m}$ using Eq. (2).

From the force-free conservation of momentum statement, the mixed flow velocity, V_m, in terms of the incoming velocities is $V_m = (V_1 + \alpha V_2)/(1+\alpha)$. Eliminating V_m with Eq. (20) gives an expression for the desired total pressure parameter of the mixed flow, σ_m as a function of σ and $s_{1,m}$:

$$\sqrt{\frac{1-\dfrac{s_{1,m}}{\sigma_m}}{1-s_{1,m}}} = \frac{1+\alpha\sqrt{\tau}\sqrt{\dfrac{1-\dfrac{s_{1,m}}{\sigma}}{1-s_{1,m}}}}{\sqrt{(1+\alpha)(1+\alpha\tau)}} \tag{21}$$

Solution for σ_m is straightforward, but the equation is written in this form for symmetry.

Linearized Mixer Analysis. In Eq. (21), the total pressure of the mixed flow (p_{tm} or equivalently σ_m) cannot be stated in terms of (p_{t2}/p_{t1} or $\pi - 1$) without linearization of σ, although a machine computation is direct. The linearization of the square root term gives (for π, σ close to 1):

$$\sqrt{\frac{1-\dfrac{s_{1,m}}{\sigma_i}}{1-s_{1,m}}} \approx 1+\frac{\sigma_i-1}{(\gamma-1)M_{1,m}^2} \approx 1+\frac{\pi_i-1}{\gamma M_{1,m}^2} \tag{22}$$

and the total pressure of the mixer exit flow is

$$\pi_m \approx 1-\gamma M_{1,m}^2(1-\sqrt{\Phi})+w_R(\pi-1)\sqrt{\Phi} \tag{23}$$

The total temperature difference is embodied in the definition of a parameter describing the total temperature nonuniformity:

$$\Phi \equiv \frac{(1 + \alpha\sqrt{\tau})^2}{(1 + \alpha)(1 + \alpha\tau)} \tag{24}$$

Physically, Φ the ratio of the square of the momentum to the energy (per unit mass). The magnitude of Φ is close to unity even for the rather substantial property variations. Note that $\sqrt{\Phi}$ modifies the pressure term, while the mixing term, $1 - \sqrt{\Phi}$, approaches zero as τ approaches 1. From Eq. (23), the following may be concluded:

1. There are two terms which affect the mixed flow total pressure: a decrease due to entropy production associated with heat transfer at finite Mach number and an increase proportional to the weighted contribution of the higher pressure flow ($\pi - 1$). The mixer Mach number term vanishes under either of two conditions: the total temperatures are equal (in which case Φ is unity) or $M_{1,m}$ vanishes.
2. The effect on the mixture total pressure is weighted in proportion to the total temperature corrected mass flow rates.

Mixer Area Ratio. To fix its geometry, the ratio of flow areas across the constant pressure mixer is determined using the mass flow conservation equations for each of the streams, Eq. (7) applied to the entering streams as well as the mixed stream. The resulting area ratio is, for the general and linearized cases:

$$\frac{A_m}{A_1 + A_2} = \frac{1}{\sqrt{\Phi}} \frac{(1 + \alpha\sqrt{\tau})\left(\sigma_m \sqrt{\dfrac{1 - s_{1,m}/\sigma_m}{1 - s_{1,m}}}\right)^{-1}}{1 + \alpha\sqrt{\tau}\left(\sigma \sqrt{\dfrac{1 - s_{1,m}/\sigma}{1 - s_{1,m}}}\right)^{-1}}$$

$$\approx \frac{1}{\sqrt{\Phi}} \{1 - \psi_{1,m}(1 - \sqrt{\Phi})(\Pi - 1)\} \tag{25}$$

A total pressure rise parameter $\Pi - 1$ (incorporating the combined total temperature and total pressure non-uniformity as well as the mixer Mach number) is the grouping:

$$\Pi - 1 \equiv \gamma M_{1,m}^2 + w_R(\pi - 1) \tag{26}$$

Evidently, the primary total temperature influence ($1/\sqrt{\Phi}$) is the most important factor in determining the area ratio of the constant pressure mixer. The total pressure influence is connected not only with the mixer Mach number but also with the T_t influence through its presence in the weighting factor, w_R and the modifier ($1 - \sqrt{\Phi}$). To the extent that the factor Φ is close to unity, a constant pressure mixer is also a constant area mixer.

The term ($\Pi - 1$, related to the type difference C in Fig. 1) also arises from the difference of second order terms in the expressions for mixed flow ($\pi_m - 1$, Eq. 23, type B) and for coflowing streams ($w_R(\pi - 1)$, see for example Eq. (15), type A):

$$(\pi_m - 1) - w_R(\pi - 1) \equiv -(\Pi - 1)(1 - \sqrt{\Phi}) \tag{27}$$

Mixed Flow Nozzle Mass Flow Rate. The mass flow rate of the mixed flow through the nozzle is given by a variation of Eq. (10) where the total pressure and temperature are π_m and τ_m respectively:

$$\dot{m}_{\text{Tot}} = bA_{\text{Tot}}\left(\frac{s}{\sigma_m}\right)^{1/(\gamma-1)} \sqrt{1 - \frac{s}{\sigma_m}} \frac{\pi_m}{\sqrt{\tau_m}}$$

$$= bA_{\text{Tot}} s^{1/(\gamma-1)} \sqrt{1 - \frac{s}{\sigma_m}} \frac{\sigma_m}{\sqrt{\tau_m}} \tag{28}$$

This nozzle is choked when $s/\sigma_m = 2/(\gamma + 1)$.

The mass flow rate through a nozzle of a non-uniform flow relative to a uniform flow for fixed area is obtained from the ratio of Eq. (28) to a similar one with σ, π, and $\tau = 1$. This ratio is (using Eq. (20)):

$$C_d \equiv \left\{\frac{\dot{m}\ (\text{mixed})}{\dot{m}\ (\text{uniform})}\right\}_{\text{Fixed area}} = \sqrt{\frac{1 - s_{1*}/\sigma_m}{1 - s_{1*}}} \frac{\sigma_m}{\sqrt{\tau_m}}$$

$$\approx \sqrt{\frac{1 + \alpha}{1 + \alpha\tau}} [1 + \psi_{1*}(\pi_m - 1)] \tag{30}$$

Here s_{1*} is the pressure at the throat area where the primary Mach number is M_{1*}. The equations for A^* and C_d show that it is the deviation of π_m from unity that controls the departure of the nozzle from the uniform and 1-D performance. For low Mach number (unchoked) flow in the throat, ψ_{1*} can be quite large which amplifies the deviation of C_d from unity.

Mixed Flow Nozzle Thrust. The exit pressure as used in Eq. 18, $s_{1,e}$ is related to $M_{1,e}$ by Eq. (2). The energy equation for the mixed flow (Eq. 20) gives the jet velocity. The ratio of this velocity to that for a uniform flow is C_v (mixed), again referenced to the primary flow conditions:

$$C_v = \frac{V_m}{V_1}$$

$$= \sqrt{\tau_m} \sqrt{\frac{1 - s_{1,e}/\sigma_m}{1 - s_{1,e}}} \cong \sqrt{\frac{1 + \alpha\tau}{1 + \alpha}} \left(1 + \frac{(\pi_m - 1)}{\gamma M_{1,e}^2}\right) \tag{31}$$

Note that expansion to infinite Mach number ($s_{1,e} = 0$) gives a mean velocity corresponding to the mean enthalpy available.

Comparison of Mixed and Two-Stream Flow Performance

The results for two stream and mixed flows are both referenced to a uniform primary flow so that a comparison between them may be readily made for flows through a single, properly expanded nozzle by forming ratios of relevant quantities. The schematic in Fig. 1 gives the relationship between total pressure rise parameters identified for the models discussed here. The design parameter of interest is the choked flow area ratio given by the ratio of the flow areas:

$$\frac{A_m^*}{A^*\ (2\ \text{stream})} \approx \frac{1}{\sqrt{\Phi}} \{1 + (1 - \sqrt{\Phi})[\Pi - 1]\} \tag{32}$$

Evidently the throat areas are identical when the total temperature is uniform, i.e. when τ and therefore Φ are unity. When this is not the case, both the mixer Mach number and the total pressure non-uniformity are important, albeit the dominant effect is due to the first Φ term.

The static pressures at the throat are also important so that the divergent section may be designed for complete expansion. The mixed flow is choked when $s/\sigma_m = 2/(\gamma + 1)$ so that an expression corresponding to Eq. (15) is:

$$s^* = \frac{2}{\gamma + 1}\left[1 + \frac{\gamma - 1}{\gamma}(\pi_m - 1)\right] \quad \text{(mixed flow)} \tag{33}$$

Note here that the choked flow static pressures at the throat are the same for the two cases when the total temperature is uniform (see Eq. (23) with $\Phi = 1$).

The mass flow rate change associated with having mixed rather than coflowing flows through a given area nozzle is given by the ratio of Eqs. (30) and (17). For arbitrary values of σ, σ_m known from a solution of Eq. (21), one has:

$$\left\{\frac{\dot{m}\ (\text{mixed})}{\dot{m}\ (2\ \text{stream})} = \frac{C_{d,m}}{C_{d,2s}}\right\}_{\text{Fixed area}}$$

$$= \frac{\sqrt{\Phi}}{\left(\frac{1}{\sigma_m}\sqrt{\frac{1 - s_{1*}}{1 - s_{1*}/\sigma_m}}\right)} \times \frac{1 + \alpha\sqrt{\tau}\left(\frac{1}{\sigma}\sqrt{\frac{1 - s_{1*}}{1 - s_{1*}/\sigma}}\right)}{1 + \alpha\sqrt{\tau}}$$

$$\approx \sqrt{\Phi}\{1 - \Psi_{1*}(1 - \sqrt{\Phi})(\Pi - 1)\} \quad (34)$$

One may think of this ratio as the change in C_d experienced when the flow is changed from unmixed to mixed. This change is strongly influenced by the total temperature non-uniformity through Φ.

Similarly the velocity (or thrust per unit mass flow) for the mixed flow and coflowing cases may be determined for the general case from a combination of Eqs. (5), (18), and (31):

$$\left\{\frac{V_m}{\bar{V}} = \frac{C_{v,m}}{C_{v,2s}}\right\} = \frac{1}{\sqrt{\Phi}} \frac{(1 + \alpha\sqrt{\tau})\sqrt{\frac{1 - s_{1,e}/\sigma_m}{1 - s_{1,e}}}}{1 + \alpha\sqrt{\tau}\sqrt{\frac{1 - s_{1,e}/\sigma}{1 - s_{1,e}}}}$$

$$\approx \frac{1}{\sqrt{\Phi}}\left[1 - \frac{(1 - \sqrt{\Phi})}{\gamma M_{1,e}^2}(\Pi - 1)\right] \quad (35)$$

The first order impact of nonuniformity on thrust per unit mass flow rate is the energy term embodied in Φ. The coupled effect correction terms is typically quite small.

Large Total Pressure Ratio Results

The results obtained can be extended to situations involving large total pressure ratio across the two streams. A report describing such cases is available from the author.

Summary

This work was carried out to derive the important relationships governing non-uniform nozzle flow performance. Further, this led to identification of the parameters which influence calculated performance of a nozzle whose total properties are measured upstream of a nozzle throat. Thus, bounds in the calculated performance uncertainty associated with subsequent mixing are identified. In general, and in particular within the limit of small total pressure variations which are most often encountered in practice, one may conclude the following for non-uniform nozzle flows:

(i) The difference in predicted nozzle performance (throat area, sonic throat pressure, C_d, and C_v) between coflowing streams and a uniform one is controlled by:

a. the total temperature which influences results through a parameter given by $(1 + \alpha\sqrt{\tau})/(1 + \alpha)$ while
b. the total pressure influence parameter is a combination of total pressure and total temperature non-uniformity, namely $w_R(\pi - 1)$ where the temperature corrected mass fraction $w_R = (\alpha\sqrt{\tau})/(1 + \alpha\sqrt{\tau})$, and
c. solutions for non-uniformities of arbitrary magnitudes requires machine computations.

(ii) A similar mixed flow nozzle analysis gives a different set of parameters:

a. for the total temperature, $\sqrt{(1 + \alpha\tau)/(1 + \alpha)}$, and
b. for the total pressure, $(\pi_m - 1)$ which involves the chosen mixer Mach number, $M_{1,m}$, and a combination of π and τ given by Eq. (27):

$$\pi_m - 1 = -\gamma M_{1,m}^2(1 - \sqrt{\Phi}) + w_R(\pi - 1)\sqrt{\Phi}$$

where the parameter Φ, the non-dimensional ratio of momentum to energy (both per unit mass) is defined in the Nomenclature section or Eq. (24).

(iii) A comparison of the unmixed and mixed flow results involves parameters which are combinations of those identified in (i) and (ii) above, including a pressure/mixer effect non-uniformity parameter given by $\Pi - 1 = \gamma M_{1,m}^2 + w_R(\pi - 1)$. The total temperature non-uniformity effect enters the calculation of the mass flow rate and exhaust velocity through multiplication of $(\Pi - 1)$ by a factor $(1 - \sqrt{\Phi})$. This fact makes the difference between mixed and coflowing performance independent of a modest total pressure non-uniformity if the total temperature is uniform. The difference between mixed and unmixed flow performance provides boundaries for the calculated behavior of a real nozzle.

(iv) A constant pressure mixer is close to constant area device as seen by the proximity of $\sqrt{\Phi}$ to unity.

(v) To the extent that there is an uncertainty as to whether the degree of mixing is complete, there will necessarily be an uncertainty in the calculated values of the mass flow rate and jet velocity.

Acknowledgement

The author acknowledges the support of The Boeing Co., Commercial Airplanes, Propulsion Research Group for this work.

References

Bernstein, A., Heiser, W., and Hevenor, C., 1967, "Compound-Compressible Nozzle Flow," ASME *Journal of Applied Mechanics,* Vol. 34, pp. 548–554.

Decher, R., 1978, "Non-uniform Flow Through Nozzles," *AIAA Journal of Aircraft,* Vol. 15, p. 7.

Decher, R., 1994, *Energy Conversion,* Oxford University Press, New York, pp. 378–435.

Gillette, W. B., Tegeler, D. C., and Decher, R., 1975, "Nacelle-Airframe Integration: Model Testing for Nacelle Simulation and Measurement Accuracy," *Proceedings of the Wind Tunnel Design and Testing Techniques Conference,* Agard CP174, London, UK.

Kimzey, W. F., Wehofer, S., and Covert, E. E., 1985, "Gas Turbine Engine Performance Determination," *Thust and Drag: Its Prediction and Verification,* E. E. Covert, ed., *Progress in Aeronautics and Astronautics Series,* Vol. 98, AIAA, New York, pp. 49–115.

Oates, G. C., and Presz, W., 1979, "Effects of Nonconstant Enthalpy Addition on Fan-Nozzle Combinations," *AIAA Journal of Aircraft,* Vol. 16, No. 12, pp. 891–93.

Oates, G. C., 1984, *Aerothermodynamics of Gas Turbine and Rocket Propulsion,* AIAA, New York.

Tegeler, D. C., and Decher, R., 1975, "High Accuracy Force Accounting Procedures for Turbo-Powered Simulator Testing," AIAA Paper No. 75-1324.

W. L. Chow
Professor. Fellow ASME.

Z. P. Ke
Graduate Assistant.

J. Q. Lu
Graduate Assistant.

Department of Mechanical Engineering,
Florida Atlantic University,
Boca Raton, FL 33431

The Interaction Between a Jet and a Flat Plate—An Inviscid Analysis

The problem of jet-plate interaction has been examined. It is shown that the problem of this type is governed by the mechanisms of inviscid interaction. The method of hodograph transformation has been employed to formulate the problem, and the solution is obtained from numerical computations in the hodograph plane. The flow pattern in the physical plane is produced from additional integrations. Extensions to the compressible flow regime with practical applications have also been mentioned.

I Introduction

When a jet flows toward a flat plate, the interior portion of the jet slows down due to the obstruction of the plate, while the free surfaces gradually turn toward the direction of the plate. A stagnation point appears on the surface of the plate, and the jet is divided into two parts moving parallel along the plate. Eventually, when the effects of streamline-curvature disappear, the original velocity is completely recovered across the jet only when the plate is mathematically infinite in length, and the momentum of the oncoming jet normal to the plate is completely destroyed. This is true whether the jet approaches the flat plate in the normal or oblique direction. The condition of infinite length of the plate is necessary since the mathematical solution of a differential equation must be continuous including its derivatives of higher orders, and the uniform flow condition can only be asymptotically reached at the far upstream or far downstream positions. Nevertheless, the condition of mathematically infinite length of the plate can be practically satisfied by a plate of finite physical length.

A question naturally arises as to the flow condition when the plate is relatively short. Under this situation, it is recognized that the total force acting on the plate is not sufficient to completely annihilate the momentum of the oncoming jet normal to the plate, and the asymptotic direction of the jet flow after leaving the plate will be dependent upon the total force of interaction between the fluid and the plate. The total force of interaction is the integral of the detailed pressure distribution on the plate, which can only be evaluated after the solution of the governing differential equation is established. On the other hand, the solution of the differential equation must be dependent upon the boundary condition provided by the asymptotic flow direction of the downstream jet. Thus the solution and the boundary condition of the differential equation are coupled. Since the viscous effects are indeed very small and are negligible, flow problems of this nature are classified in the category of inviscid interaction, and the Bernoulli's principle is applicable everywhere throughout this region. The free surfaces are the lines of constant velocity of the approaching flow.

Problems governed by mechanisms of inviscid interaction are not new. For example, a jet discharge from a nonsymmetric duct, as shown in Fig. 1, is one typical case of this nature. When the downstream jet flow becomes uniform, its flow direction depends upon the total force acting on the solid wall of the conduit. This problem has been solved by Von Mises (1917) by employing the method of conformal mapping. One may imagine that the method of approach to solve the problem of this type is through iteration. For the present problem, the asymptotic direction of the jet flow after leaving the plate may be assumed, and the solution may be found accordingly. A momentum balance is subsequently applied to check and correct the assumed asymptotic direction. The correct solution is established when this process of iteration is converged. However, it has been found that the method of hodograph transformation is extremely suitable to solve the present problem of jet-plate interaction.

Hodograph transformation (Von Karman, 1941) was originally devised to study the flow problems in the compressible flow regime where the governing differential equation is nonlinear. By taking the speed V and the streamline angle θ of the flow as independent variables while treating all other quantities, including the coordinates x, y, as the dependent variables, the governing differential equation becomes linear. Since this method is not a direct approach to the problem, and its basic difficulty lies in the satisfaction of the boundary condition in the physical plane, it has not been extensively employed to solve the engineering problems. However, with the advent of high speed computation, the difficulty of satisfying the boundary condition in the physical plane can be easily overcome. This method has been applied to solve some problems in open channel flows (Chow and Han, 1979; Han and Chow, 1981), and also the subcritical and supercritical discharge from a valve in the axisymmetric configuration (Chow et al., 1987; Weng et al., 1987). In all these cases, other than the possible numerical errors of computation, the solutions so established are exact. It is the intention here to show that by specifying the important parameters related to the jet-plate interaction, straight forward numerical computations would lead to the geometric pattern of the flow including the length of the plate compatible to the selected parameters.

II Theoretical Considerations

Upon choosing the speed V and the streamline angle θ of the flow as the independent variables, it can be shown (Shapiro, 1953) that the stream function ψ governing the incompressible potential flow satisfies

$$V^2\psi_{VV} + V\psi_V + \psi_{\theta\theta} = 0 \tag{1}$$

where the subscripts indicate differentiations. The corresponding physical coordinates x, y are related to V and θ through

$$dx = -(\psi_\theta \cos\theta/V^2 + \psi_V \sin\theta/V)dV + (\psi_V \cos\theta - \psi_\theta \sin\theta/V)d\theta \tag{2}$$

Contributed by the Fluids Engineering Division for publication in the JOURNAL OF FLUIDS ENGINEERING. Manuscript received by the Fluids Engineering Division June 27, 1994; revised manuscript received September 6, 1994. Associate Technical Editor: D. P. Telionis.

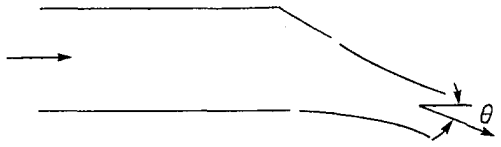

Fig. 1 Jet discharge from a nonsymmetric duct

$$dy = (-\psi_\theta \sin \theta/V^2 + \psi_V \cos \theta/V)dV + (\psi_V \sin \theta + \psi_\theta \cos \theta/V)d\theta \quad (3)$$

Referring to Fig. 2, where a jet of width b and velocity V_∞ approaching a flat plate is depicted, it is convenient to choose V_∞, $b/2$ and α as the reference quantities. Upon defining

$$\psi' = \psi/(V_\infty b/2), \quad V' = V/V_\infty, \quad \beta = \theta/\alpha, \quad \beta_u = \delta_u/\alpha$$

$$\beta_l = -\delta_l/\alpha, \quad x' = x/(b/2), \quad y' = y/(b/2)$$

and after normalization, Eqs. (1) through (3) become

$$V^2\psi_{VV} + V\psi_V + \frac{1}{\alpha^2}\psi_{\beta\beta} = 0 \quad (4)$$

$$dx = -(\psi_\beta \cos \alpha\beta/\alpha V^2 + \psi_V \sin \alpha\beta/V)dV + (\alpha\psi_V \cos \alpha\beta - \psi_\beta \sin \alpha\beta/V)d\beta \quad (5)$$

$$dy = (-\psi_\beta \sin \alpha\beta/\alpha V^2 + \psi_V \cos \alpha\beta/V)dV + (\alpha\psi_V \sin \alpha\beta + \psi_\beta \cos \alpha\beta/V)d\beta \quad (6)$$

where the prime has been intentionally eliminated for simplicity. The upper and lower bounding streamlines of the jet can assume 1 and -1, respectively, as the values of their stream functions. For a given approaching flow angle α, one may select ψ_d ($-1 < \psi_d < 1$) as the value of the stream function of the dividing streamline, and the upper asymptotic streamline angle β_u, which must be positive and less than or equal to unity, i.e., $\delta_u \leq \alpha$. The lower asymptotic streamline angle β_l can be solved from

$$(1 - \psi_d) \cos \alpha(1 - \beta_u) + (1 + \psi_d) \cos \alpha(1 - \beta_l) = 2 \cos \alpha \quad (7)$$

which is the statement of conservation of the momentum tangential to the plate. A typical hodograph for this problem is shown in Fig. 3, whose domain is bounded by constant stream function values of 1, ψ_d, and -1. The stream function within the domain may be established through numerical computations, either through the Gauss-Seidel iteration or the successive-line-over-relaxation (SLOR) scheme. The finite difference form of Eq. (4) may be written symbolically as

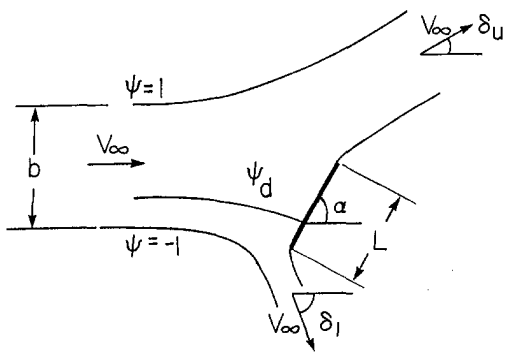

Fig. 2 The schematic of a jet past a flat plate

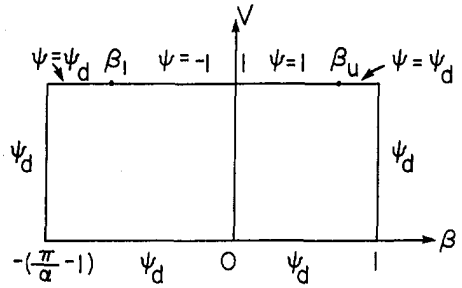

Fig. 3 The hodograph diagram for the jet-flow

$$a_j\psi_{i,j+1} + b_j\psi_{i,j} + c_j\psi_{i,j-1} + d_j(\psi_{i+1,j} + \psi_{i-1,j}) = 0 \quad (8)$$

where i, j are the grid indices. For the Gauss-Seidel scheme, the stream function at each grid point may be updated through

$$\psi_{i,j} = \psi_{i,j} - \mathrm{RF}[a_j\psi_{i,j+1} + b_j\psi_{i,j} + c_j\psi_{i,j-1} + d_j(\psi_{i+1,j} + \psi_{i-1,j})]/b_j \quad (9)$$

where RF is the over relaxation factor. After the successive change of the stream function is less than an arbitrarily small value (e.g., 10^{-5}) for all the grid points in the domain, the solution is established. ψ_V and ψ_β may be subsequently evaluated through differentiations. Numerical integration of Eqs. (5) and (6) would establish the corresponding configuration in the physical plane, including the length of the flat plate required to produce such a flow pattern. The plate length is obtained through integrations along the two vertical boundaries of the hodograph, while the free streamlines are obtained from integrations along the $V = 1$ line. Finally, the path of the dividing streamline may be traced by joining all points of ψ_d in the hodograph through interpolations, and then performing the x–y integration along this curve.

III Results of Numerical Computations

Numerical computations have been carried out for many symmetric or nonsymmetric flow patterns. Second-order finite difference formula was employed for all computations. Results of different flow cases are separately presented below.

1 Figure 4 shows the symmetric flow for $\alpha = 90$ deg, $\psi_d = 0$, $\beta_u = 1$, when the approaching flow is normal to a plate of infinite length. The free streamlines obtained from computations are plotted in the figure. This problem can also be solved by conformal mapping, and the results for the top free surface are given by (Milne-Thomson, 1950) as

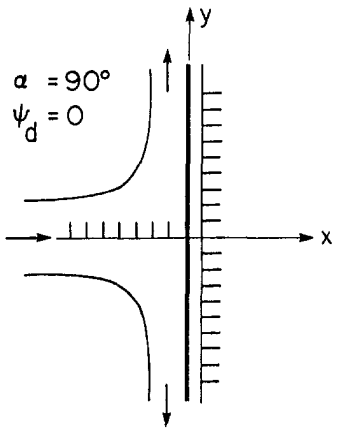

Fig. 4 Results of the free streamlines for the jet flow past a normal infinitely long plate—tick marks are spaced by $b/4$

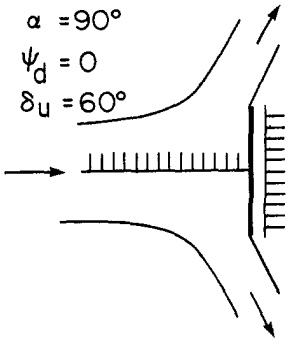

Fig. 5 Results of the free streamlines for the jet flow past a short plate—symmetric flow pattern. Tick marks are spaced by $b/8$.

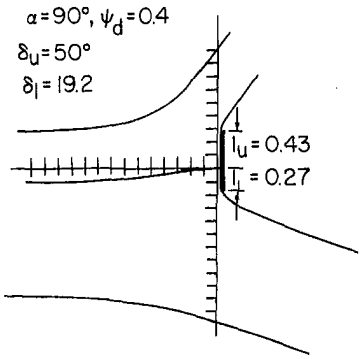

Fig. 7 Results of the free streamlines for the jet flow past a short and misaligned normal plate. Tick marks are spaced by $b/12$.

$$\frac{x}{b/2} = 2/\pi \text{ Ln } (\tan \theta/2) - 1 \qquad (10)$$

$$\frac{y}{b/2} = 2/\pi \text{ Ln } [\tan (\theta/2 + \pi/4)] + 1 \qquad (11)$$

When these results are compared with that in the figure, there is no observable difference between the two. This excellent agreement instills confidence in the numerical computation with the method of hodograph transformation.

2 Figure 5 shows the symmetric flow pattern for $\alpha = 90$ deg, $\psi_d = 0$, and $\delta_u = 60$ deg ($\delta_l = 60$ deg). The plate now has a finite length. When δ_u varies between 0 and 89 deg, the corresponding length of the plate is also obtained. These results are plotted in Fig. 6. It indicates that as the plate length approaches zero, so should the asymptotic jet flow angle after interaction. Furthermore, the asymptotic angle of 90 deg is practically reached when the length of the plate, based on the half width of the approaching jet, is 8. It provides the evidence that the viscous effects of these problems are indeed negligible, and the problem is completely governed by inviscid interaction.

3 Figure 7 shows the results for a normal plate ($\alpha = 90$ deg). However, the plate is short and misaligned with respect to the jet, and a non-symmetric flow pattern is obtained for $\psi_d = 0.4$, and $\delta_u = 50$ deg ($\delta_l = 19.2$ deg). The length of the plate is only 0.7. The dividing streamline has also been traced from the results established in the hodograph. It appears from Fig. 8 that the dividing streamline approaches the plate in the normal direction ($\beta = 0$ deg), which is the trend indicated by all grid points away from the stagnation point. It should be noted that the values of the stream function of all grid points surrounding the stagnation point are different from ψ_d only by a very small margin (on the order of 10^{-3}). Since computation inevitably involves numerical error, a slight error in the proximity of the stagnation point tends to modify the original trend of normal approach (indicated by the two black dots in the Fig. 8). Nevertheless, with these errors included into tracing the dividing streamline, it did not cause much deviation from the normal approach as indicated in Fig. 7.

4 Figure 9 shows the pattern when the plate is not normal to the approaching jet, but has infinite length. The selected parameters are $\alpha = 60$ deg, $\psi_d = -0.5$, $\delta_u = \alpha = 60$ deg, and δ_l was found to be 120 deg from Eq. (7). Since β_u ($\beta_u = 1$) and β_l ($\beta_l = -2$) are located at the two upper corners of the hodograph, only the outside upper and lower free streamlines are traced and shown in the figure. The dividing streamline is also shown in the physical plane. The pressure coefficient C_p ($C_p = p - p_\infty/\rho V_\infty^2/2 = 1 - V^2/V_\infty^2$) is also presented to indicate the velocity variation along the plate.

5 Figure 10 shows the results for a shorter plate but with the same α ($\alpha = 60$ deg) and ψ_d ($\psi_d = -0.5$) as those of the case presented in Fig. 9. δ_u was 40 deg, and δ_l was found to be 85 deg. These values yielded the total plate length of 2.5, based upon the half-width of the jet. The streamline pattern is shown in the Fig. 10. Figure 11 presents the results obtained for the same α and ψ_d, but with different δ_u values. The flow is never symmetric. The location of the stagnation point with respect to the center line of the jet L_0, the upper plate length L_u, the lower plate length L_l, and the total plate length L_p are presented against δ_u in the figure. All these curves (except L_0) should converge toward the origin as δ_u approaches zero. As δ_u becomes less than 31 deg, the plate is so short that the centerline of the jet no longer intersects the plate.

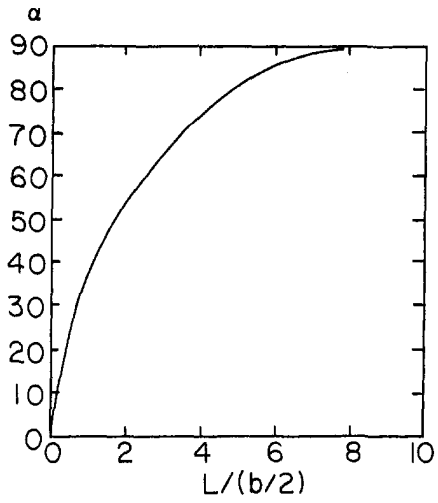

Fig. 6 The deflection angle δ_u versus the length of the plate for symmetric flow

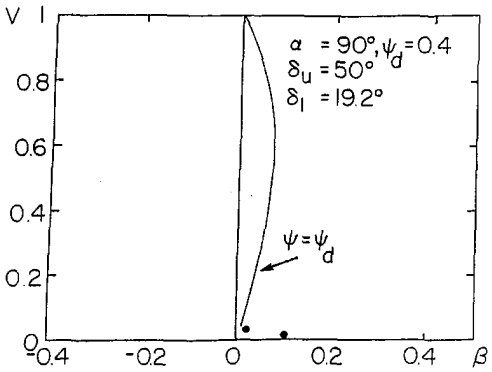

Fig. 8 Tracing of the dividing streamline within the hodograph

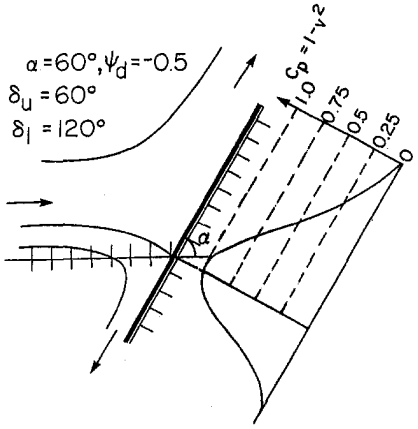

Fig. 9 Results of the free streamlines for the jet flow past an infinitely long and oblique plate. Tick marks are spaced by $b/4$.

IV Discussion and Conclusion

It has been learned from this series of study that the method of hodograph transformation is indeed very efficient and useful for this type of jet-plate interaction. From the present approach, the length of the plate and its location are uniquely related and derived from the results of calculations. It should be noted that satisfaction of the tangential momentum balance in conjunction with the employment of the Bernoulli's principle implies that the momentum relationship normal to the plate is automatically satisfied. This is indeed the case. A post check of all cases presented here indicated that the normal momentum relationship agreed within one percent. For a direct problem, where the orientation, the length of the plate and its location relative to the jet are given, iteration must be relied upon to obtain the corresponding important parameters of the present scheme to match the given condition. Since the present scheme is quite efficient (on the order of seconds needed on a Vax 6320 computing system for each set of computations), this iteration would rapidly converge to the final solution. There should be only one set of the important parameters uniquely related to the given condition in a direct problem.

It is interesting to see that for the whole class of problems of inviscid interaction, solutions of the differential equation must be supplemented with an overall momentum balance in order to single out the physically correct boundary condition for the problem. This fact also implies that the differential equation may yield solutions even with the seemingly reasonable but physically inappropriate boundary conditions. A good practice to establish a physically realistic solution is to verify the conservation of the integral quantities after the solution has been obtained from the differential equation governing the flow.

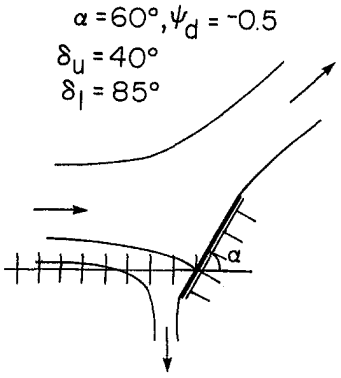

Fig. 10 Results of the free streamline for the jet flow past a short and oblique plate. Tick marks are spaced by $b/4$.

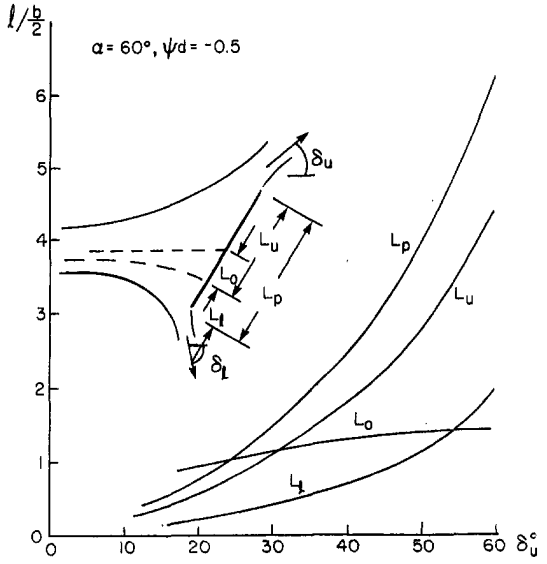

Fig. 11 Plate length and its location relative to the jet versus δ_u for $\alpha = 60$ deg, $\psi_d = -0.5$

The present method of attack can be extended to solve the problems in the axisymmetric geometry, and in the compressible flow regime. A useful and practical extension to the study of thrust reversal device can be anticipated.

References

Chow, W. L., and Han, T., 1979, "Inviscid Solution for the Problem of Free Overfall," ASME *Journal of Applied Mechanics,* Vol. 46, No. 1, Mar. pp. 1–5.

Chow, W. L., Ting, Alice A. L., and Tsai, P. H., 1987, "Discharge from a Vessel Through as Axisymmetric Control Valve," ASME *Journal of Applied Mechanics,* Vol. 54, No. 2, pp. 447–452.

Han, T., and Chow, W. L., 1981, "The Study of Sluice Gate and Sharp Crested Weir Through Hodograph Transformation," ASME *Journal of Applied Mechanics,* Vol. 48, No. 2, pp. 229–238.

Milne-Thomson, L. M., 1950, *Theoretical Hydrodynamics,* Second Edition, The MacMillan Co., New York, pp. 278.

Shapiro, A. H., 1953, *The Dynamics and Thermodynamics of Compressible Fluid Flow,* Chapter 11, Vol. 1, The Ronald Press Co., New York.

Von Karman, Th., 1941, "Compressibility Effects in Aerodynamics," *Journal of Aeronautical Sciences,* Vol. 8, No. 9, p. 337.

Von Mises, R., 1917, "Berechnung von Ausfluss und Veherfallzahlen," *Zeitschrift des Vereines Deutshen Ingenieure,* Vol. 61, No. 22, pp. 469–474.

Weng, Z. M., Ting, Alice A. L., and Chow, W. L., 1987, "Discharge of a Compressible Fluid Through a Control Valve," ASME *Journal of Applied Mechanics,* Vol. 54, No. 4, pp. 955–960.

Addendum

It should now be emphasized that the present analysis is based on the premise that the jet is always surrounded by the constant pressure of the approaching jet flow (the ambient pressure). It would be interesting to see that when the size of the plate normal to the jet is small in comparison with the width of the approaching jet (i.e., $b/L \to \infty$), the effect of viscosity tends to modify the pressure behind the plate into a lower-than-ambient value (the base pressure) and the wake behind the plate is closed, if a steady flow condition is maintained. The actual flow under this situation is unsteady, as a result of periodic vortex shedding. However, the steady flow condition can be maintained if a solid plane wall is inserted along the centerline of the wake to suppress the vortex shedding. This type of steady stste problem was usually classified in the category of viscid-inviscid interaction, where the effects of viscosity must be accounted for before a solution to the problem can be reached. Under such a situation, a jet-mixing (usually turbulent) process between the recirculating wake flow and the external flow occurs along the wake boundary, after the flow leaves from the edge of the plate. Processes of recompression, as a result of

confluence of the upper and lower streams, and redevelopment of the viscous wake flow subsequently follow. Nevertheless, there exists a "corresponding" inviscid flow which is entirely different from the pattern described for the present investigation. It depends upon the level of the base pressure, and the lowest base pressure is usually reached for the turbulent wake flow at high Reynolds numbers. The senior author has some experience in the study of problems of this type (Chow and Spring, 1976; Chow, 1985). The flow situation becomes even more complicated when the plate is not normal to the approaching jet flow.

Although the above discussion applies to the situation when b/L approaches infinity, it is believed that this type of viscid-inviscid interaction flow would also occur at large finite b/L values. Certainly, much more research is needed before the problem of this kind can be completely understood.

Acknowledgment

The authors wish to express their deep appreciation and gratitude toward the Technical Editor of the Journal, Professor D. P. Telionis, for his handling of the review of this paper, for his many valuable suggestions and discussions of the problem, which led to the appearance of this paper in this final form.

Additional References

Chow, W. L., and Spring, D. J., 1976, "The Viscous Interaction of Two-Dimensional Incompressible Separated Flows," *Journal of Applied Mechanics*, Vol. 43, pp. 387–395.

Chow, W. L., 1985, "Base Pressure of a Projectile Within the Transonic Flight Regime," *American Institute of Aeronautics and Astronautics Journal*, Vol. 23, No. 3, pp. 388–395.

Tumbling Flow in Loop-Scavenged Two-Stroke Engines

Yeng-Yung Tsui
Associate Professor.

Hong-Ping Cheng
Graduate Student.

Department of Mechanical Engineering,
National Chiao Tung University,
Hsinchu 300, Taiwan

A multidimensional calculation procedure is used to investigate the flow in loop-scavenged two-stroke engine with curved cylinder heads. Five different cylinder heads are considered. The curvature of cylinder head increases from case I to case IV. In case V the head curvature is further increased, but it is shaped in the radially outer region. Calculations reveal that a tumbling vortex forms after the exhaust port is closed and the vortex constantly dominates the flow structure in the cylinder throughout the compression period. With high head curvatures the vortex is well organized and occupies the entire cylinder volume in the late compression stage. Due to compression of the better organized tumbling vortex by the moving piston more energy cascades from mean flow to turbulence in the high curvature cases III and IV. As for case V, the larger clearance in the bowl center region leads to lower shear stresses and, thus, the turbulence augmentation phenomenon is less prominent than that for cases III and IV.

1 Introduction

The importance of in-cylinder air flow has been recognized a long time ago in the history of engine development. A key factor affecting the burning rate in internal combustion engines is the turbulence generated from the mean gas flow in the cylinder; the higher the turbulence, the faster the flame propagation speed, provided that the flame will not be extinguished due to over stretching and heat loss. Very high levels of turbulence could be produced during the induction period. However, it decays rapidly in the compression period and reaches the level of 0.4 $\sim$ 0.5 times the mean piston speed at TDC (Heywood, 1987). A usual way to sustain the gas flow well into the compression stage is to create a significant vortical motion in the intake process. The swirl, a flow rotating in the direction of the cylinder axis, has been widely adopted in four-stroke engines. Recently, another type of vortical flow, the tumbling flow, which rotates in the direction normal to the cylinder axis, draws much attention. The vertical vortex of the tumbling flow is compressed by the piston motion during compression period. In order to preserve angular momentum the flow tries to spin up and then releases stored energy to turbulence in the late compression period (Gosman et al., 1985). The results of Gosman et al. (1985) showed that, by the end of compression, the mean turbulence intensity in the cylinder could be as high as 0.7 times the mean piston speed. Thus the tumbling motion is a more effective turbulence generator than the swirling flow (Arcoumanis et al., 1990, Haworth et al., 1990). A lot of researches have been devoted to this area since the publication of Gosman et al. (1985). In recent years, four-valve designs with pentroof cylinder head gather popularity. In these engines a pair of directed ports are placed on one side of the pentroof head. Because of this port arrangement a tumbling vortex flow is formed in the cylinder during the induction period. Experiments (Hadded and Denbratt, 1991, Endres et al., 1992) showed that incorporating the tumbling flow in four-valve engines leads to reduction in ignition delay and burning duration, higher EGR (exhaust gas recirculation) tolerance and, thus, lower emissions.

For loop-scavenged two-stroke engines a looped circuit is formed during the scavenging period so that the exhaust gas is scavenged out of the cylinder by the fresh charges. This looped flow is transformed into a vertical vortex after the scavenge and exhaust ports are closed. This process could be identified in the previous studies (Tsui and Cheng, 1994; Tsui et al., 1994; Ahmadi-Befrui et al., 1989). However, the structure of the tumbling vortex in two-stroke engines have never been examined in detail. A computational method employing the EPISO algorithm was developed by the present authors to study the scavenging process in the engine with flat cylinder head (Tsui and Cheng, 1994) and, then, a spray model was added to simulate direct fuel injection into the two-stroke spark-ignition engines (Tsui et al., 1994). In the present study, the method is further extended to allow the cylinder head to be curved. The effects of the cylinder head on the tumbling flow are examined through gradual increase of the curvature. However, before making this examination, a test run has been conducted to validate the solution method.

2 Mathematical Method

The governing equations are written in the density-weighted Favre-averaged form to account for density variations in the cylinder. The k-ϵ model of Launder and Spalding (1974) is adopted to characterize the turbulence. Since the cylinder head is of curved shape, the computational domain is divided into two regions (see Fig. 1): one is the expanding/contracting (E/C) region, and the other is the head region. The volume in the E/C region expands/contracts in accordance with the motion of the piston. Therefore, the grids in the axial direction are allowed to expand and contract with the piston motion. As shown in Fig. 1, there are two lines corresponding to the upper edges of the scavenge and exhaust ports, respectively. The two lines divide the E/C region into three subregions. Whenever the piston moves into one subregion, the grid lines in that region are set in motion with the piston. Governing equations are transformed onto such a moving coordinate system. Detailed information can be found in Tsui and Cheng (1994). The head region is assumed to be a volume of revolution. Hence the axisymmetrically curvilinear-orthogonal coordinate system is employed to fit the curved boundaries. Unlike the E/C region, the grid lines in this region are fixed without motion because the piston does not sweep across this space. Details about the coordinate transformation in this region are refered to Begleris (1987). The ports of the engine are arranged in a symmetric manner. Thus there exists a symmetric plane and only half a cylinder volume is considered in the calculations (see Fig. 1). The specifications of intake and exhaust flows at the openings

Contributed by the Fluids Engineering Division for publication in the JOURNAL OF FLUIDS ENGINEERING. Manuscript received by the Fluids Engineering Division July 8, 1994; revised manuscript received April 12, 1995. Associate Technical Editor: S. P. Vanka.

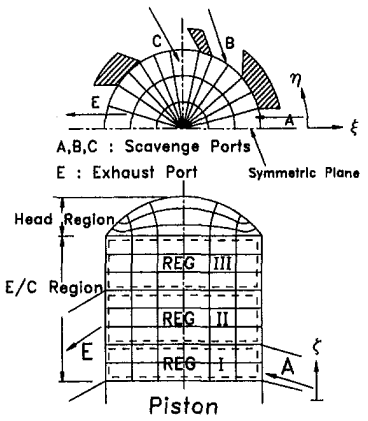

Fig. 1 A typical grid layout

of scavenge and exhaust ports are essential to calculations. The mass flow rates through these ports are modelled by an one-dimensional orifice flow. Given the pressures in the crankcase and outside the exhaust port, the mass fluxes can be determined through overall mass and energy balances in the cylinder (Tsui and Cheng, 1994). The velocity is assumed to be uniformly distributed over the opening area. This plug profile is justified in the experiments of Fansler and French (1992). However, their measurements indicated that the flow entry angle did not follow the port design angle, that is, the entry angle varied with the port opening height. To account for this effect the measurements of Fansler and French (1992) are employed and an interpolation procedure is used to obtain required flow angles.

The discretization is performed using the finite-volume approach. The grid in the head region is generated, following Gosman and Johns (1978), by solving a set of Laplace equations. The system of difference equations are solved by using the EPISO algorithm which has been proved to be an efficient method in calculation of reciprocating engine flows (Tsui and Cheng, 1994, Tsui, 1987). For details about the solution procedure it can be found in the cited references.

3 Validating Tests

Fansler and French (1992) have made a detailed examination of the flow in a loop-scavenged two-stroke engine using the LDV. Amsden et al. (1992) employed the KIVA-3 code to simulate the same engine. In their simulations the flows in cylinder and in all scavenge ports and exhaust port are included in the calculations. The experimentally measured pressures in the crankcase and outside the exhaust port are specified at the open boundaries of scavenge and exhaust ports, respectively. Unlike the study of Amsden et al. (1992), only the flow in cylinder is considered in the present study. Using the measured crankcase and outside the exhaust port pressures the mass fluxes through scavenge ports and exhaust port can be determined via overall mass and energy balances and one-dimensional flow assumptions. With the assumed plug profile along with the measured flow angles, the velocities at cylinder-port interfaces can be determined. However, it should be mentioned here that with this calculation procedure the effects of pressure wave are ignored, i.e., the flow inertia is not accounted for. To avoid the lengthy and costly calculation of the detailed flow in the manifold as done by Amsden et al. (1992) a much easier and convenient way is to incorporate a quasi one-dimensional manifold calculation procedure. This approach will be undertaken in the future study. Figure 2(*a*) presents the variation of cylinder pressure against crank angle obtained from different studies. Generally speaking, the present predictions are quite similar to the measurements of Fansler and French and the calculations of Amsden et al. In Fig. 2(*b*) the variation of cylinder mass is shown. In this figure M_f stands for the mass of fresh air captured in the cylinder, M_r the mass of residual gas left in the cylinder from the previous cycle, and M_t is the sum of the two. It is apparent that during the scavenging period, i.e., the period between the scavenge port opening (SPO) and the scavenge port closing (SPC), there exists strong oscillations for the "new" and "old" masses. This is due to the neglect of the flow inertia. However, the total mass in the cylinder is not much affected. By the end of scavenging period the two predictions are similar. Comparison of trapping ratio and scavenging efficiency is made in Table 1. In this table M_d is the mass of fresh air delivered by the scavenge ports, the trapping ratio is defined as M_f/M_d, and the scavenging efficiency as M_f/M_t. The results indicate that the difference between the two calculations is within about five percent. Both predictions and experimental results indicate that a tumbling vortex dominates the flow in the cylinder after all ports are closed. It is this vortex flow being the main concern of the next section.

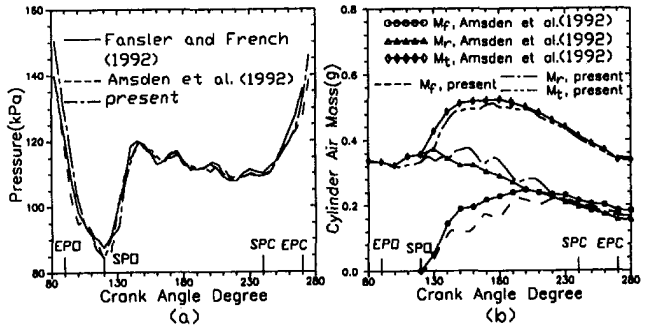

Fig. 2 Comparison of variation of (*a*) cylinder pressure and (*b*) cylinder mass

Table 1 Comparison of trapping ratio (M_f/M_d) and scavenging efficiency (M_f/M_t)

	Amsden et al. (1992)	Present	Relative error (%)
M_t	0.339(g)	0.344(g)	1.5
M_f	0.183(g)	0.176(g)	3.8
M_d	0.306(g)	0.307(g)	0.33
M_f/M_d	0.598	0.573	4.2
M_f/M_t	0.54	0.512	5.2

4 Results

As shown in Fig. 3, five kinds of cylinder head are considered. In case I the cylinder head is flat. The head curvature gradually increases from case I to case IV. In case V the head curvature is further increased, but it is shaped in the outer region such that the compression ratio remains identical to the other cases. The radii of curvature for case II through V are 117, 63, 49 and 32 mm, respectively. The corresponding ratios of head arc length to engine bore are 1.017, 1.069, 1.133 and 1.227.

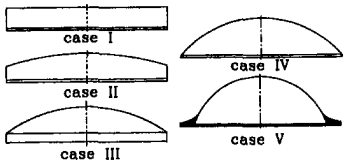

Fig. 3 Illustration of test cases

Table 2 Engine specifications

engine speed	3000 rpm
cylinder bore	74.0 mm
stroke	75.0 mm
clearance (flat cylinder head)	10.2 mm
effective compression ratio	5.8
exhaust port opening	100° ATDC
exhaust port closing	260° ATDC
scavenge port opening	125° ATDC
scavenge port closing	235° ATDC

Specifications of the engine are shown in Table 2. The grid used contains 32 × 45 × 45 (radial × circumferential × axial) nodes in the E/C region and 32 × 45 × 18 nodes in the head region. The grid employed in the E/C region is similar to that used in Tsui and Cheng (1994), which has been shown to be adequate to present the flow characters in the cylinder with a flat cylinder head. This grid is also used in the validating tests shown previously. Calculations commence at EPO (exhaust port opening) and end at TDC.

In order to illustrate the flow fields, velocity vectors and turbulence intensity contours in the symmetric plane at a number of crank angles are presented. To avoid clustering, the velocity vectors are plotted every two nodal points along the grid lines. The turbulence intensity is normalized by the mean piston speed ($\bar{V}_P = 7.5$ m/s). Focus is concentrated on the compression period. The results are shown in Figs. 4 and 5 for cases I and IV, respectively. Obviously, from the vector plots, a tumbling vortex forms after the exhaust port is closed. At CA = 270 deg, the center of the vortex is located near the left head corner. Because of the smoother geometry contour the vortex is better organized in case IV. In the flat head case the vortex center is elongated and is placed closer to the head. As a result, a high shear layer forms in this region. It can be identified from the contour plots that, due to the high shear stresses, very high turbulences are generated around the vortex center in case I, but not in case IV. The maximum turbulence intensity is 1.117 for case I and 0.958 for case IV. At mid-compression (CA = 300 deg), although the flow is compressed in the axial direction by the moving piston, the center region of the vortex expands in the radial direction. Peak values of turbulence are still visible

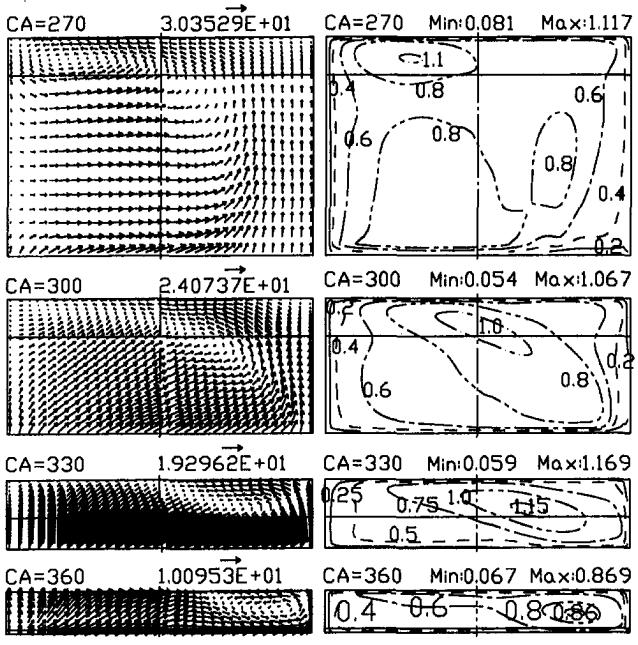

Fig. 4 Mean flow and turbulence intensity fields for case I

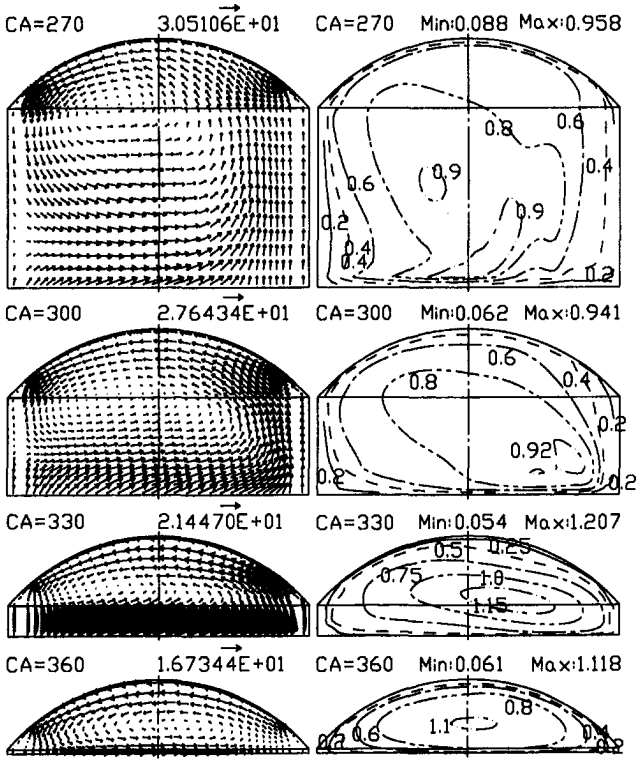

Fig. 5 Mean flow and turbulence intensity fields for case IV

around the vortex center in case I. At 330 deg CA, the vortex flow constantly dominates the flow structure in the cylinder for the high curvature case IV. For the flat head case the vortex has already been twisted and is restricted in the right half cylinder region. The high turbulence zone follows the vortex center, which is true even in the case IV. It should be noticed that, compared with 300 deg CA, the turbulence is enhanced in both cases with the level being higher for case IV than that for case I. The turbulence augmentation phenomenon will be examined in detail later. By the end of compression, the mean flow and turbulence attenuate by a large degree because the piston loses its driving speed. However, the tumbling vortex persists in a good form in case IV. The peak turbulence value at TDC is 1.118 $\bar{V}_P$ for case IV, compared to 0.869 $\bar{V}_P$ for case I.

Although no detailed flow patterns shown here, the flow fields for case II and case III behave similar to case I and case IV, respectively, owing to their geometric similarity. This point can be demonstrated in Figs. 6(a) and 6(b). In Fig. 6(a), the evolution of cylinder-averaged mean kinetic energy during the compression period is shown. Initially, the mean energy is higher and the decay rate is lower for cases III and IV than those for cases I and II. This is attributed to the better organized vortex flow in the former cases, as seen in Fig. 5. However, the decay rate become greater for cases III and IV after mid-compression. This behavior will be clear in the following.

The evolution of cylinder-averaged turbulence intensity normalized by the mean piston speed in the compression stage is illustrated in Fig. 6(b). Up to mid-compression the turbulence remains nearly at a constant level for each case. Higher turbulences are generated in the flatter cases I and II due to the high shear region around the vortex center observed in Fig. 4. In the range around 310 deg < CA < 340 deg, the turbulence is greatly intensified and then decays rapidly. The amplification of turbulence is caused by compression of the tumbling vortex (Gosman et al., 1985). By the end of compression the mean turbulence levels in the cylinder are 0.56 $\bar{V}_P$, 0.60 $\bar{V}_P$, 0.65 $\bar{V}_P$ and 0.68 $\bar{V}_P$ for case I through case IV, respectively. The enhancement in turbulence is more than 20 percent from the

flat head case I to case IV. Looking back to Fig. 6(a), it can be seen that when the turbulence is largely intensified, the mean kinetic energy of the high curvature cases III and IV decays more rapidly. This simply implies that more energy cascades from mean flow to turbulent fluctuations.

To illustrate the turbulence augmentation, the temporal variations of the cylinder integral of the turbulence dissipation and production terms for cases I and IV are respectively exhibited in Figs. 7(a) and 7(b). Also shown in the figures are the separate contributions to turbulence production due to shear stresses, normal stresses and compression. The total generation is sum of these three parts. Comparison between Figs. 6(b) and 7 indicates that the rate of change of turbulence level is roughly proportional to the difference between the total production and dissipation. The normal stresses hardly have any contribution to the turbulence production. The difference in compression production between the two cases is negligible. This is due to that this part of production is directly proportional to the volumetric change rate of the cylinder volume, which is the same for all considered cases because the compression ratio does not change. The maximum dilatation rate occurs at about 330 deg CA, which roughly corresponds to the timing of turbulence production peak in Fig. 7. However, the peak value of turbulence production is much higher and the augmentation period extends closer to the TDC for the high curvature case. This can be ascribed to the well-constructed vortex quickly compressed by the piston during this period in this case.

The cylinder heads of the above four cases can be said to be geometrically "affine", i.e., they have similar shapes but with different rates of curvature. The head shape of case V shown in Fig. 3 is different from the other four cases. Its curvature in the center region is even greater than that of case IV. The mean flow patterns for case V are similar to those for case IV. The temporal variations of mean kinetic energy and turbulence intensity are shown in Figs. 6(a) and 6(b), respectively. Two points can be drawn. The first is that the decay rate of mean energy for this case is much lower than that for the others in the later compression stage. For case V there exists a "squish" region (hatched in Fig. 3) outside the hemispherical bowl. When the piston approaches TDC, air in the squish region is forced to flow into the bowl (Begleris, 1987), resulting in a strong radially inward flow. Since the compression ratio of the present engine is low (5.8) and the squish region is small, the squish effects are not significant. However, it helps to slow down the mean flow decay. By the end of compression the mean energy for case V is two times higher than cases I, II, and III. The second is that the turbulence generation is not so effective. At TDC the turbulence intensity of case V is 0.623 $\bar{V}_P$, which is ranked third in the five cases. The cause of the low turbulence enhancement is mainly attributed to the low shear stresses generated by the tumbling flow in the augmentation period. In view of the geometries of the various cases shown in Fig. 3, the case V has larger clearance in the bowl

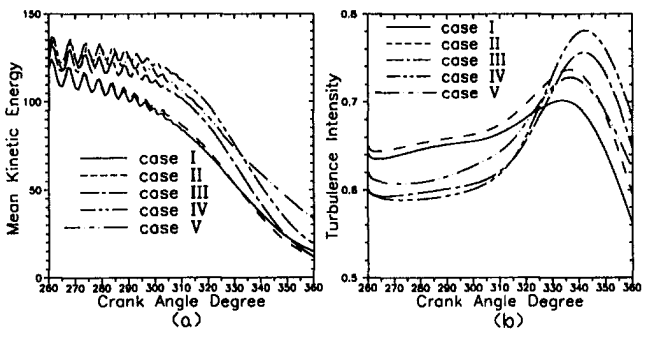

Fig. 6 Temporal variation of (a) mean kinetic energy and (b) turbulence intensity during compression period

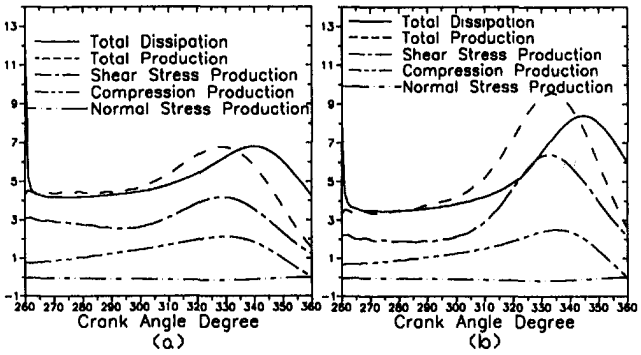

Fig. 7 Temporal variation of turbulence production and dissipation rate during compression period: (a) case I; (b) case IV

center region, when the tumbling vortex dominates the flow in the late compression stage. As a consequence, the shear effects are less prominent.

Finally the scavenging efficiencies obtained from calculations are compared. They are 0.3887, 0.3892, 0.4029, 0.4042, and 0.3925 for cases I through V, respectively. This result reveals that with increasing head curvature the scavenging process is also more effective. It is interesting to notice that in terms of scavenging efficiency the case V also ranks in the middle of the five cases.

5 Conclusions

A model for the flow in a loop-scavenged two-stroke engine has been developed. Results have shown the following main findings.

(1) A tumbling vortex forms after the end of scavenging process. The flow structure is dominated by the vortex flow throughout the compression period.

(2) In the early compression stage, the vortex is located close to the cylinder head and gradually elongated and distorted in the low curvature cases. As a result of the high shear effects around the vortex center region higher turbulence prevails in these cases than in the high curvature cases.

(3) In the later compression stage, the vortex continues to distort in cases I and II and, then, is restricted in part of the cylinder volume whereas the vortex occupies the entire cylinder in the high curvature cases III and IV. Because of the high compression effects turbulence is greatly augmented in the period 310 deg $<$ CA $<$ 340 deg. Compression of the well-organized vortex leads to more energy transfer from mean flow to turbulence in the high curvature cases.

(4) Although the head curvature for case V is the highest among considered cases, its large clearance results in lower shear stresses. Thus, the turbulence augmentation is not so effective.

(5) The cylinder head curvature also affects the scavenging efficiency: the higher the curvature, the higher the scavenging efficiency.

Acknowledgments

This work was supported by the National Science Council under contract numbers NSC 80-0401-E009-18 and NSC 83-0401-E-008.

References

Ahmadi-Befrui, B., Brandstatter, W., and Kratochwill, H., 1989, "Multidimensional Calculation of the Flow Processes in a Loop-Scavenged Two-Stroke Cycle Engine," SAE Paper 890841.

Amsden, A. A., O'Rourke, P. J., Butler, T. D., Meintjes, K., and Fansler, T. D., 1992, "Comparisons of Computed and Measured Three-Dimensional Velocity Fields in a Motored Two-Stroke Engine," SAE Paper 920418.

Arcoumanis, C., Hu, Z., Vafidis, C., and Whitelaw, J. H., 1990, "Tumbling Motion: A Mechanism for Turbulence Enhancement in Spark-Ignition Engines," SAE Paper 900060.

Begleris, P., 1987, "Three-Dimensional Flow Predictions in Motored Diesel Engines," Ph.D. thesis, Imperial College, University of London.

Endres, H., Neußer, H. J., and Wurms, R., 1992, "Influence of Swirl and Tumble on Economy and Emissions of Multi Valve SI Engines," SAE Paper 920516.

Fansler, T. D., and French, D. T., 1992, "The Scavenging Flow Field in a Crankcase-Compression Two-Stroke Engine-A Three-Dimensional Laser-Velocimetry Survey," SAE Paper 920417.

Gosman, A. D., and Johns, R. J. R., 1978, "Development of a Predictive Tool for In-Cylinder Gas Motion in Engines," SAE Paper 780315.

Gosman, A. D., Tsui, Y. Y., and Vafidis, C., 1985, "Flow in a Model Engine with a Shrouded Valve-A Combined Experimental and Computational Study," SAE Paper 850498.

Hadded, O., and Denbratt, I., 1991, "Turbulence Characteristics of Tumbling Air Motion in Four-Valve S. I. Engines and Their Correlation with Combustion Parameters," SAE Paper 910478.

Haworth, D. C., El Tahry, S. H., Huebler, M. S., and Chang, S., 1990, "Multidimensional Port-and-Cylinder Flow Calculations for Two- and Four-Valve-Per-Cylinder Engines: Influence of Intake Configuration on Flow Structure," SAE Paper 900257.

Heywood, J. B., 1987, "Fluid Motion Within the Cylinder of Internal Combustion Engines-The 1986 Freeman Scholar Lecture," ASME JOURNAL OF FLUIDS ENGINEERING, Vol. 109, pp. 3–35.

Launder, B. E., and Spalding, D. B., 1974, "The Numerical Computation of Turbulent Flow," *Computer Methods in Applied Mechanics and Engineering,* Vol. 3, pp. 269–289.

Tsui, Y. Y., 1987, "Calculation of Three-Dimensional Flow in Motored Engines," Ph.D. thesis, Imperial College, University of London.

Tsui, Y. Y., and Cheng, H. P., 1994, "Flow Calculation in a Loop-Scavenged Two-Stroke Motored Engine," *International Journal of Numerical Methods for Heat and Fluid Flow,* Vol. 4, pp. 249–267.

Tsui, Y. Y., Chen, P. J., and Yu, S. J., 1994, "Flow Calculation in a Loop-Scavenged Direct-Injection Two-Stroke Engine," *Journal of the Chinese Society of Mechanical Engineers,* Vol. 15, No. 1, pp. 56–70.

Velocity and Turbulence Characteristics of Isothermal Lobed Mixer Flows

P. Koutmos
Assistant Professor,
Laboratory of Applied Thermodynamics,
Department of Mechanical Engineering,
University of Patras,
Patras, Rio 26110,
Greece

J. J. McGuirk
Professor,
Department of Transport Technology,
Loughborough University of Technology,
Leics LE11 3TU,
United Kingdom

This work describes an experimental and computational study of flows in model multilobed mixers. Laser Velocimetry was used to obtain the velocity and turbulence fields in the downstream mixing duct. Flow development was quantified by examination of the large cross-plane velocities whose direction implied the formation of two streamwise vortices per lobe. A change from coplanar to scarfed geometry increased vortex strength by 25 percent. Vortex cell formation, roll-up and breakdown to fine scale mixing was attained within a distance of 5 lobe heights. The computational investigation of the coplanar configuration adopted a non-aligned mesh to solve the 3-D Reynolds averaged Navier-Stokes equations. The calculations of the lobe and mixing duct flows were coupled to predict the complete mixer. Comparisons between measurements and calculations using a standard k-ϵ model suggested good qualitative agreement with maximum disagreement of about 20 percent in peak radial velocities.

Introduction

Multilobed mixers have become popular as low loss mixing elements in a variety of fluid mechanical applications (Werle et al., 1987; Presz et al., 1988). Such devices are exploited in turbofan engines (Fig. 1) where hot turbine flow is mixed with cooler fan flow prior to exhaust improving performance and reducing noise for many turbofan cycles. Overall gain depends upon the balance between increased mixing and extra pressure losses. Extended nacelle weight and drag must also be offset by performance gains. Advantages of the lobed geometry are that it increases (i) the interfacial mixing area and (ii) the scales across which mixing takes place. Performance is primarily controlled by the strong cross-flows generated by the lobes.

Early investigations (Shumpert, 1980 and Kozlowski and Kraft, 1980) confirmed the increased performance of this mixer through measurements of performance variations associated with changes in lobe geometry. More recently, a comprehensive study of a full scale mixer (Paterson, 1984) detailed the strong secondary flows originating within the lobes and leading to an array of streamwise vortices.

The complicated three-dimensional mixer geometry makes it difficult to choose the best lobe configuration thus initiating the exploitation of CFD methods. Early computations concentrated in the region downstream of the lobe exit (Kreskovsky et al., 1984; Provinelli and Anderson, 1984) and emphasized the importance of accurate knowledge of the 3-D velocity field at lobe exit for use as inlet boundary conditions. More recently, Barber et al. (1986a,b) and Koutmos and McGuirk (1989a) have modeled the lobe flow itself. Koutmos and McGuirk (1989a) computed the complete lobe/nozzle system for a coplanar mixer (lobe exit plane perpendicular to engine axis) using a finite-volume method and the k-ϵ model demonstrating the possibility of predicting the streamwise vorticity generated within the lobes. Although these calculations were promising, confidence in the predictions requires rigorous testing against suitable measurements. The work described here aims at achieving this objective.

In an initial study, Koutmos and McGuirk (1989b) described a controlled validation experiment, but measurements were taken only in a coplanar mixer with a fan-side area ratio (FAR) higher than what is found in applications. This contribution supplements the above work by providing velocity and turbulence information for the mixing region of both a coplanar and a scarfed mixer representative of current practice. In order to facilitate LDV measurements, a water flow was used together with a perspex containing pipe simulating a simple nozzle. This is complementary to concurrent measurements of the flow *within* the lobes where refractive index matching techniques and suitable working liquids are used (tetraline/turpentine, $\rho \approx 1000$ kg/m^3) to investigate the complete system. Although water flow results only cautiously may be extrapolated to practice, restrictions may well be tolerated in a controlled validation experiment. Further, the use of an isothermal experiment to simulate hot/cold stream mixing is strongly supported by the investigations of Paterson (1984) and Greitzer et al. (1985) who suggest that the cold velocity ratio (Fan/Turbine) should be higher than the equivalent hot by a factor $[T_{TUR}/T_{FAN}]^{1/2}$. The present cold flow corresponds to a hot with Fan/Turbine velocity and temperature ratios of 0.74 and 0.67 (values found in practice). Considerable efforts were made to ensure accurate geometry and approach flow alignment so as to restrict attention to a single lobe.

Subsequently, the calculation of the measured flows with the method of Koutmos and McGuirk (1989a) is undertaken for two coplanar configurations with fan-side area ratios of 0.7 and 0.85. Only inlet boundary conditions *upstream* of the lobes are required and were supplied from the measurements. The performance of the method is then assessed by comparing predictions with measurements.

Flow Configuration

The experimental facility has been described in Koutmos and McGuirk (1989b); sketches of this and the model mixer geometries used here are shown in Figs. 2 and 3. The mixers consisted of twelve equispaced lobe peaks projecting into the fan stream and twelve corresponding gulleys. The coplanar lobe height (h) was 17.6 mm and its length (L_M) was 31.3 mm. Scarfing was achieved by truncating or extending the lobe exit planes alternately backwards and forwards (Fig. 3). The central plug started upstream of the lobes and terminated one lobe height downstream of the coplanar exit (mixing plane). The outer perspex tube between lobe inlet and exit could be adjusted to produce a range of fan-side area ratios (FARs of 0.7 and

Contributed by the Fluids Engineering Division for publication in the JOURNAL OF FLUIDS ENGINEERING. Manuscript received by the Fluids Engineering Division January 31, 1994; revised manuscript received May 24, 1995. Associate Technical Editor: W. S. Saric.

0.85 are discussed). The turbine-side area ratio was maintained at 1.15. Downstream of the lobes a mixing region was formed by a constant diameter tube.

Axisymmetric axial velocity profiles with turbulence levels of 3 and 4.5 percent and boundary layer thicknesses of 0.085 h and 0.128 h were measured at GG′ inside the turbine and fan feeds. Corresponding mass flows of 1.87 and 2.32 kg/s were metered by calibrated orifice plates (uncertainty ±3 percent) giving rise to bulk axial velocities at GG′ of 0.8 and 0.72 m/s for the respective sides.

Experimental Method

Measurements of the three mean velocities and turbulence intensities were obtained with a Laser Doppler Velocimeter operating in dual beam forward scatter mode. The optical arrangement is shown in Fig. 2; Table 1 summarizes its principle characteristics. A detailed description of this instrumentation may be found in Koutmos (1985). Measurements were obtained on a lobe peak and a lobe gulley plane. For the scarfed mixer planes through a short and a long gulley were investigated. Measurement locations are depicted in Fig. 3 (and Table 2). Because of periodic repetition of the lobe geometry (every 30 deg for the coplanar and 60 deg for the scarfed) and the absence of swirl in the approach flow, as demonstrated by Koutmos and McGuirk (1989b), the azimuthal planes at peak and gulley (coplanar) and at long and short gulley (scarfed) are symmetry planes and the time-averaged W component is zero there. Nonetheless, measurements of the circumferential normal stress allowed evaluation of the turbulence energy. Intermediate θ planes should however be measured to provide a more detailed description of the secondary velocities.

Uncertainty Estimates

Uncertainties in model/test section dimensions are: pipe radii: ±0.4 mm, lobe height: ±0.3 mm, lobe exit position: ±0.2 mm, plug contour: ±0.1 mm, FAR: ±5 percent. LDV probe position: ±0.5 mm.

The Doppler signals were demodulated by a frequency tracker (Cambridge Consultants CC01). The analogue output was passed to an A/D converter and mean and RMS values were obtained in an Apple microcomputer. Suitable frequency shifts (provided by a rotating grating) helped to obviate tracking range and slew rate restrictions while flow seeding by milk additives minimized signal drop-out (Taylor, 1981).

Nonturbulent broadening (systematic) errors arise from mean velocity gradient across the probe volume, finite transit time, grating jitter and tracker output voltage errors (Koutmos, 1985). Maximum systematic errors in the mean velocity have been estimated: mean velocity gradient (Melling, 1975): $10^{-4}\ U_b$, tracker output error (Taylor, 1981): $4*10^{-2}\ U_b$. In the RMS these have been estimated: transit time broadening (Zang and Wu, 1987): 0.0316 U_b, stability of rotating grating: 0.003 U_b, velocity gradient broadening: 0.012 U_b, tracker output error: 0.015 U_b. The largest statistical (random) errors for the sample collected (5–7000 values), were 1.8 and 2.2 percent for the mean and RMS, for a 95 percent confidence level (Yanta and Smith, 1978). The uncertainty pertaining to data in the Figures is: U, V/U_b: less than ±4.3 percent, RMS: less than ±6.54 percent, $k^{0.5}/U_b$: less than ±9.8 percent, (U_b = 0.57 m/s).

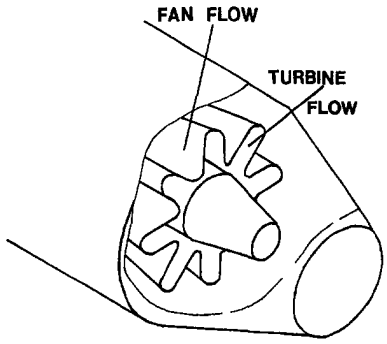

Fig. 1 Typical turbofan lobed mixer

Computational Method

The prediction of the coplanar mixer only was undertaken due to the difficulty in handling the scarfed geometry. Comparisons are performed with the data of Koutmos and McGuirk (1989b) where the fan-side area ratio was 0.7 and with present measurements with a FAR of 0.85. This represents a severe test of the method since the fan flow is subjected to different adverse pressure gradients and the crossflow strength varies in the two cases.

The full 3-D elliptic forms of the equations for conservation of mass and momentum in time-averaged form were solved; using tensor notation these may be written:

$$\frac{\partial}{\partial x_i}(\rho U_i) = 0$$

$$\frac{\partial}{\partial x_j}(\rho U_i U_j) = -\frac{\partial P}{\partial x_i} - \frac{\partial}{\partial x_j}(\rho\overline{u_i u_j})$$

The high-Reynolds number k-ϵ turbulence model was used for closure:

$$-\rho\overline{u_i u_j} = \mu_t\left[\frac{\partial U_i}{\partial x_j} + \frac{\partial U_j}{\partial x_i}\right] - \frac{2}{3}\delta_{ij}\rho k$$

$$\mu_t = C_\mu \rho \frac{k^2}{\epsilon}$$

$$\frac{\partial}{\partial x_j}(\rho U_j k) = \frac{\partial}{\partial x_j}\left(\frac{\mu_t}{\sigma_k}\frac{\partial k}{\partial x_j}\right) - \rho\overline{u_i u_j}\frac{\partial U_i}{\partial x_j} - \rho\epsilon$$

$$\frac{\partial}{\partial x_j}(\rho U_j \epsilon) = \frac{\partial}{\partial x_j}\left(\frac{\mu_t}{\sigma_\epsilon}\frac{\partial \epsilon}{\partial x_j}\right) - C_{\epsilon_1}\frac{\epsilon}{k}\rho\overline{u_i u_j}\frac{\partial U_i}{\partial x_j} - C_{\epsilon_2}\rho\frac{\epsilon^2}{k}$$

Nomenclature

c_μ, $c_{\epsilon 1}$, $c_{\epsilon 2}$ = constants in k-ϵ turbulence model
FAR = fan-side area ratio (A_{in}/A_{out})
h = lobe height
k = turbulence kinetic energy
L_M = mixer length
P = static pressure
R = containing duct radius
U, V, W = mean velocities in x, r, θ system
$\overline{u_i u_j}$ = Reynolds stress tensor
x, r, θ = cylindrical polar coordinates
δ_{ij} = Kronecker delta (=1 for $i = j$; =0 for $i \neq j$)
ϵ = turbulence energy dissipation rate
μ_t = turbulent viscosity
ρ = density
σ_k, σ_ϵ = constants in k-ϵ turbulence model

Superscripts

− = denotes mean value

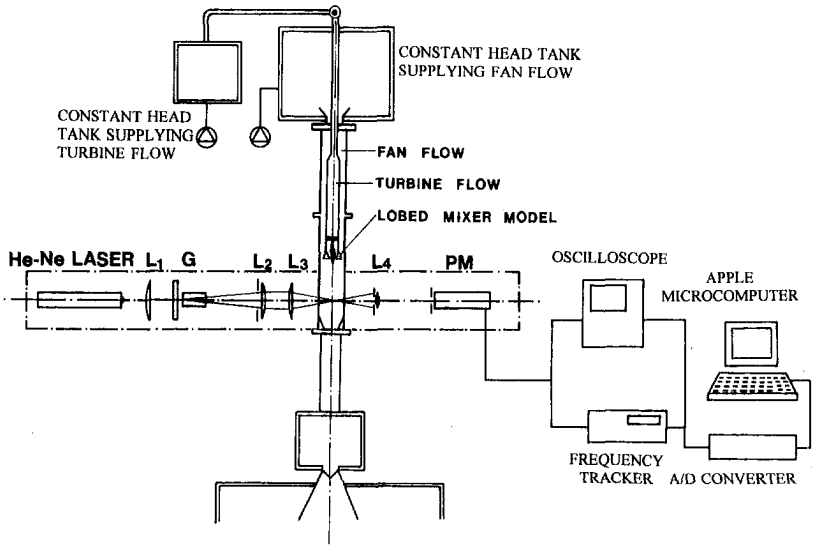

Fig. 2 Experimental arrangement

with the standard set of constants:

$$c_\mu = 0.09,\ c_{\epsilon 1} = 1.44,\ c_{\epsilon 2} = 1.92,\ \sigma_k = 1.0,\ \sigma_\epsilon = 1.3.$$

The solution of the above six equations was obtained using a finite-volume scheme. The basic formulation comprised a staggered mesh, hybrid differencing, a pressure-correction technique and log-law based wall functions (see Koutmos and McGuirk, 1989a and Koutmos, 1985 for details).

The flow within the lobes and mixing duct was predicted with the method of Koutmos and McGuirk (1989a). A nonaligned cylindrical polar grid covers the lobe geometry and its walls are represented in a piecewise planar approximation. The intersection points between the surface and the mesh identify cells which lie inside or outside the flow. For cells intersected by the boundary the finite volume equations are suitably modified. The calculation of the mixer/nozzle system was divided into three stages. The lobe flow prediction (domains A and B, Fig. 3) was obtained first. The predicted fan and turbine exit fields were then used as inlet conditions for the mixing duct (Domain C). The second stage introduces a two-way coupling between domains A, B, and C; the static pressure field at the mixing duct *inlet* obtained previously is now used as *downstream* boundary condition in a re-calculation of the fan and turbine regions. The thus modified lobe exit conditions are used to re-calculate the mixing duct in the second stage. A third pass finally ensures convergence of the iterative coupling procedure.

For the coplanar mixer, flow symmetry and geometric repeatability define a 15 deg solution domain from peak to gulley. A grid of 40*16*25 (r, θ, x) nodes (14,000 points) represented the lobe domain. A separate mesh of 40*16*25 (r, θ, x) nodes was used for the mixing duct. In the r-θ plane lines were spaced every 1 deg while in the mixing duct an axial expansion of 1.085 was maintained; the same r-θ node distribution was used to match the lobe/nozzle regions. In an effort to assess numerical diffusion errors, grid refinement was undertaken and the QUICK differencing scheme (Leonard, 1979) was also used into the basic model. Its implementation into the standard method is described in Barata et al. (1989). For the present boundary wall treatment its application is restricted at cells internal to the flow and located one node away from the boundary node. The performance of the two schemes was evaluated by calculating the results obtained for a FAR of 0.7 both with the mesh described above and with a finer mesh (QUICK only) of 55*25*32 (r, θ, x) (for each region). Figure 4 displays predictions of the axial, radial, velocity, and turbulence energy profiles at stations b, a, and c, respectively. The hybrid scheme

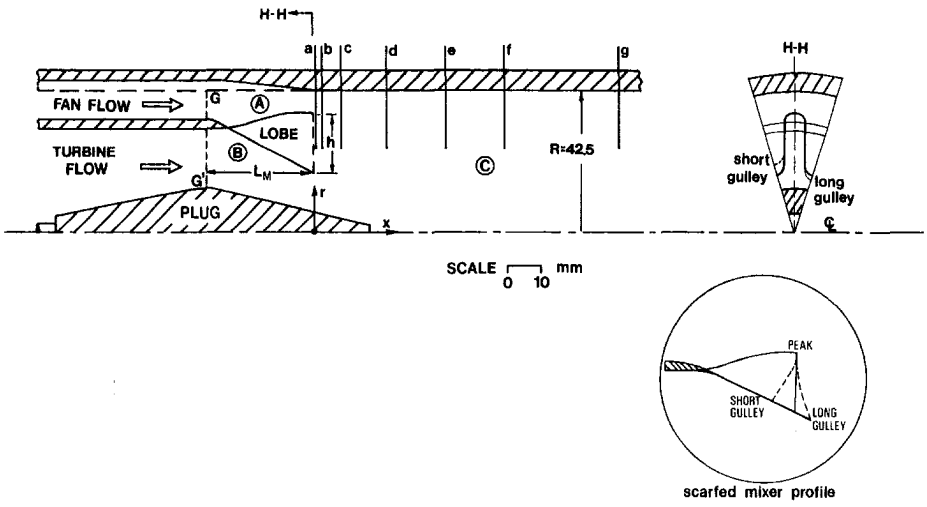

Fig. 3 Model mixer geometries and measurement positions

Table 1 Characteristics of optical setup

5 mW He-Ne laser	λ = 632.8 nm
Fringe separation (μm)	3.037
Intersection volume diameter at $1/e^2$ intensity (mm, in water)	0.101
Intersection volume length at $1/e^2$ intensity (mm, water)	1.287
Calculated number of fringes within $1/e^2$ intensity band with no frequency shift	34

Table 2 Axial measurement positions

	x/R	*x/h*
a	0.016	0.039
b	0.062	0.147
c	0.207	0.494
d	0.523	1.250
e	0.940	2.244
f	1.357	3.238
g	2.190	5.227

underestimates peak values but flow features are not obscured by false diffusion as implied by these comparisons. All significant variations seem adequately resolved by the mesh/scheme combination used to produce the present results. Nonetheless, a refined and/or boundary-fitted mesh may further improve predictions.

Results and Discussion

I Experiments. Figure 5 displays the centerline velocity and turbulence energy for both coplanar and scarfed mixers (FAR = 0.85) starting at the plug end. The velocity profile rises steeply from the plug vicinity reaching a near fully-developed value by station g. In the opposite sense turbulence levels rapidly decay in the first half radius finally reaching lobe inlet levels. The scarfed model produces a quicker velocity development and 25 percent higher turbulence up to x/R = 1.5 giving the first indication of improved mixing.

Profiles of the axial velocity and turbulence intensity are presented for the peak and gulley planes in Figs. 6(*a*, *b*) for the coplanar mixer (FAR = 0.85). Uniform levels are obtained for both turbine stream planes at station b. The fan flow accelerates over the lobe peak causing the local maximum (station b) and decelerates in the expanding trough producing a wake-like distribution. Slow mixing is observed initially with rapid changes appearing only by station d. The velocity deficit previously seen at station c on the *gulley* plane is now identified on the peak plane suggesting circumferential transport and the presence of large scale crossflow. By station f azimuthal variations have smoothed out with only a core of accelerating fluid persisting near the centerline. Uniform axial intensities are found at turbine exit while the local flow deceleration at the fan gulley gives rise to twice as high turbulence levels (station b). The three-dimensionality of the turbulence field is indicated by the different distributions at station c; these high stresses are then circumferentially convected from gulley to peak by stations c and d. The turbulence structure achieves azimuthal uniformity only by station g.

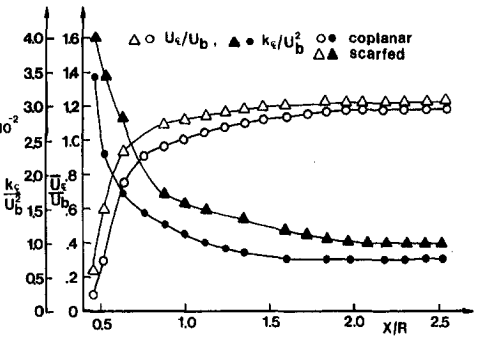

Fig. 5 Centerline development of axial velocity and turbulence energy

Figure 7 compares radial velocity profiles for the coplanar and scarfed mixer (FAR = 0.85). The coplanar mixer produces velocities of order 15 and 25 percent of the lobe inlet velocity at peak and gulley. Similar magnitudes were reported by Paterson (1984) for a full scale mixer. The expanding lobe and contracting plug shapes result in different peak and gulley profiles with the turbine flow being split outwards and inwards. By station g, strong upward and downward radial flows occupy the top 60 percent of the radius on the peak and gulley planes implying a counter-clockwise rotating axial vortex in the left half of the lobe (looking upstream). The comparisons in Fig. 7 suggest that scarfing increases by about 25 percent the secondary flows at the mixer exit and produces vortices of larger size with the steeper gulley penetration producing the stronger crossflow. Alternating deep and shallow gulleys set up radial flows of unequal strength and radial extent injecting vorticity and promoting mixing over a larger area. By station g radial veloci-

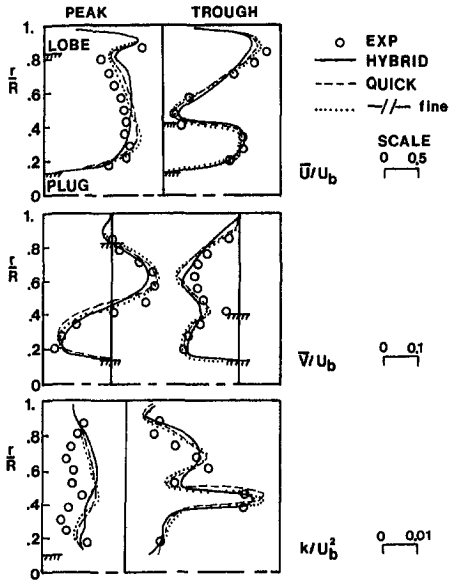

Fig. 4 Comparisons between hybrid and QUICK differencing schemes

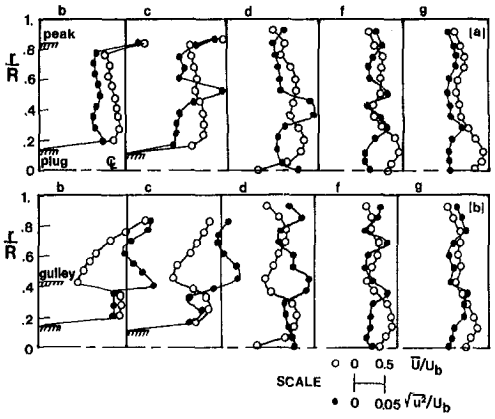

Fig. 6 Velocity and turbulence intensity fields (coplanar model) (*a*) peak and (*b*) gulley

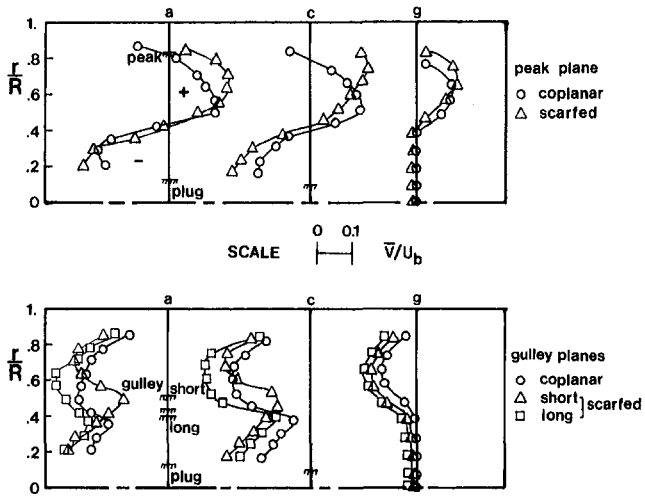

Fig. 7 Radial velocity fields for coplanar and scarfed model

ties are reduced by 40 percent and the vortex extent there is one lobe height signifying the scaling of this circulation.

Turbulence energy profiles are compared for the two mixers in Fig. 8 (due to plug obstruction the W stress was not measured at station c and was assumed equal to V). The highest off-axis k levels, in line with the long gulley trailing edge, are associated with generation in the shear layers formed as the two streams emanate from the lobes. The beneficial effects of scarfing on mixing can again be seen in the higher turbulence energy produced by the scarfed model.

II Computations. Figure 9 displays streakline plots of the predicted cross-flows at mixer exit (Fig. 9(a)) and in the mixing duct (Fig. 9(b)) for a FAR of 0.7. A clockwise rotating vortex (looking *downstream*) occupies the upper half of the sector (enlarged 4 times) with its center close to the lobe interface. 24 vortices are present at the mixer periphery. The vortex size is underestimated by 12 percent.

Calculated and measured radial velocities are compared for the peak and gulley planes and for FARs of 0.7 and 0.85 in Figs. 10(a) and (b). Near the plug the radial flows are well predicted for both planes and FARs. The peak plane upward velocities are underpredicted by about 20 percent while near the gulley trailing edge secondary velocities are overpredicted by about 25 percent. The size of the vortical structure is reproduced better at the initial stages and on the peak plane. At stations f, g its extent is underestimated and its strength is

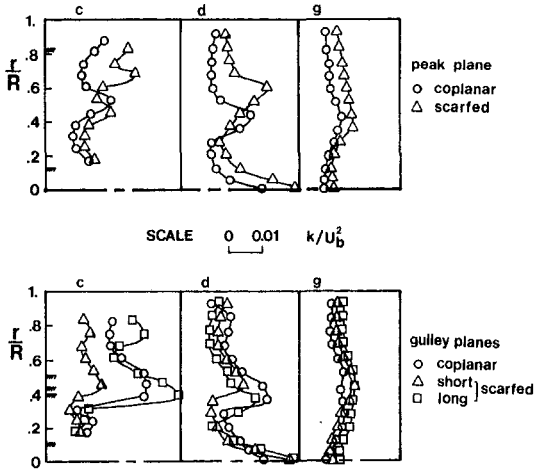

Fig. 8 Turbulence energy fields for coplanar and scarfed model

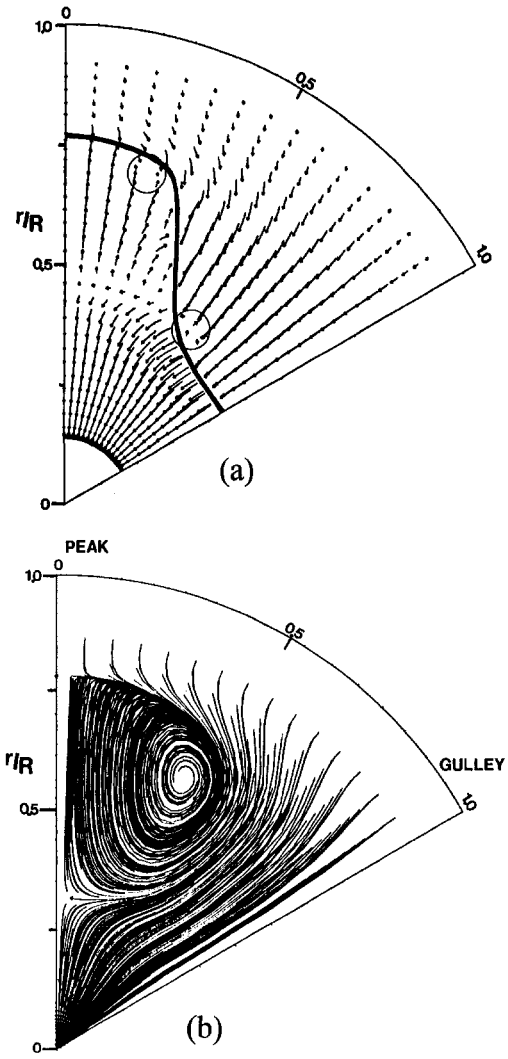

Fig. 9 Predicted flow patterns at (a) lobe exit, (b) mixing duct exit

underpredicted by about 30 percent with discrepancy increasing for the most diffusive FAR (=0.7).

Figure 11(a, b) shows the predicted turbulence energy fields for the two FARs. The energy peak due to the strong shear near the gulley trailing edge (station c) is better resolved for the lower FAR case with the peak plane levels overpredicted by about 40 percent. It is noteworthy that the k-ϵ model has adequately reproduced the azimuthal non-uniformities in the mix-

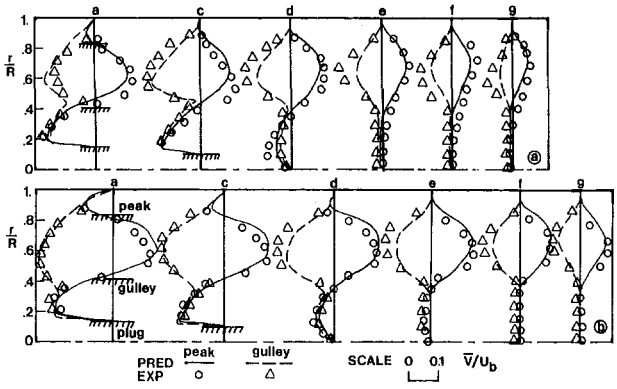

Fig. 10 Comparisons between measured and calculated radial velocities (a) FAR = 0.7, (b) FAR = 0.85

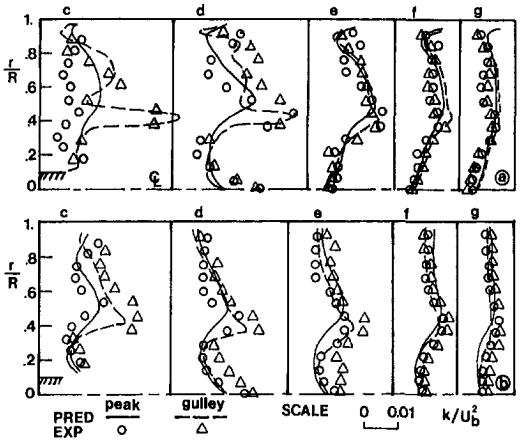

Fig. 11 Comparisons between measured and calculated turbulence energies (*a*) FAR = 0.7, (*b*) FAR = 0.85

ing region despite the significant anisotropies measured near the mixing plane. Rapid circumferential transport from gulley (station c) to peak (station d) is predicted as in the measurements but at a slower rate with agreement improving from station e onwards. The use of a low-Re-number model (within the context of a more refined or surface-fitted mesh) to resolve better the flows developing on the curved lobe surfaces may further improve predictions.

Summary

1. The isothermal three-dimensional velocity and turbulence fields inside the mixing region of two lobed mixers have been presented. The measurements provided information about mixing rates between fan and turbine streams, levels of three-dimensionality in the mixing region and the development of the crossflows that characterize this mixer.

2. Radial velocities of order 25 and 15 percent of the lobe inlet velocity were measured at the fan and turbine exits. These set up a strong axial vortex of the order of the lobe height. Radial velocities were reduced by 40 percent within 5.2 lobe heights downstream of the lobe exit.

3. The introduction of scarfing increased radial velocities by 26–30 percent. Variable penetration gulleys helped to set up two adjacent vortices per lobe with unequal strength, size and radial position. Interaction between these two vortices resulted in a uniform pair within 5.2 lobe heights.

4. Moderate turbulence levels were generated through the mixing region with maximum values of 4 percent of U_b^2 found in the shear layers in line with the long gulley; these decayed to 1 percent of U_b^2 at the duct exit.

5. A finite-volume procedure (Koutmos and McGuirk, 1989a) has been used to compute the coplanar lobe flows. This prediction provided the necessary inlet conditions for the mixing duct calculation. The method adequately reproduced the streamwise vorticity generated on exit from the lobes. Comparisons between measurements and calculations suggested good qualitative agreement with maximum discrepancies of order 20 percent.

Acknowledgments

The authors acknowledge the financial support of the Powerplant Technology section at Rolls-Royce plc.

References

Barata, J. M. M., Durao, D. F. G., and McGuirk, J. J., 1989, "Numerical Study of Single Impinging Jets through a Crossflow," *AIAA Journal of Aircraft,* Vol. 26, No. 11, pp. 1002–1008.

Barber, T. J., Muller, G. L., Ramsey, S. M., and Murman, E. M., 1986a, "Three Dimensional Inviscid Flow in Mixers, Part I: Mixer Analysis Using a Cartesian Grid," *AIAA Journal of Propulsion and Power,* Vol. 2, No. 3, pp. 275–281.

Barber, T. J., Muller, G. L., Ramsey, S. M., and Murman, E. M., 1986b, "Three Dimensional Inviscid Flow in Mixers, Part II: Analysis of Turbofan Forced Mixers," *AIAA Journal of Propulsion and Power,* Vol. 2, No. 4, pp. 339–344.

Greitzer, E., Paterson, R. W., and Tan, S. C., 1985, "An Approximate Substitution Principle for Viscous Heat Conducting Flows," *Proceedings of the Royal Society of London,* Vol. 401, No. 5, pp. 162–192.

Koutmos, P., 1985, "An Isothermal Study of Gas Turbine Combustor Flows," Ph.D. Thesis, University of London.

Koutmos, P., and McGuirk, J. J., 1989a, "Turbofan Forced Mixer/Nozzle Temperature and Flow Field Modelling," *International Journal of Heat and Mass Transfer,* Vol. 32, No. 6, pp. 1141–1152.

Koutmos, P., and McGuirk, J. J., 1989b, "Isothermal Velocity and Turbulence Measurements Downstream of a Model Multilobed Turbofan Mixer," *Experiments in Fluids,* Vol. 8, No. 8, pp. 183–191.

Kozlowski, H., and Kraft, G., 1980, "Experimental Evaluation of Exaust Mixers for an Energy Efficient Engine Propulsion System," AIAA paper 80-1088, AIAA 18th Aerospace Science Meeting, Pasadena, CA.

Kreskovsky, J. P., Briley, W. R., and McDonald, H., 1984, "Investigation of Mixing in a Turbofan Exaust Duct. Part 1: Analysis and Computational Procedure," *AIAA Journal,* Vol. 22, No. 3, pp. 374–389.

Leonard, B. P., 1979, "A Stable and Accurate Convective Modelling Procedure Based on Quadratic Upstream Interpolation," *Computer Methods in Applied Mechanics and Engineering,* Vol. 19, No. 1, pp. 59–98.

Melling, A., 1975, "Investigation of Flow in Non-Circular Ducts and other Configurations," Ph.D. Thesis, University of London.

Paterson, R. W., 1984, "Turbofan Mixer Nozzle Flow Field-A Benchmark Experimental Study," ASME *Journal of Engineering for Gas Turbines and Power,* Vol. 106, pp. 692–698.

Povinelli, L. A., and Anderson, B. H., 1984, "Investigation of Mixing in a Turbofan Exhaust Duct. Part II: Computer Code Application and Verification," *AIAA Journal,* Vol. 22, No. 4, pp. 518–525.

Presz, W. M., Gousy, R., and Monin, B., 1988, "Forced Mixer Lobes in Ejector Designs," *AIAA Journal of Propulsion and Power,* Vol. 4, No. 4, pp. 350–355.

Shumpert, P. K., 1980, "An Experimental Model Investigation of Turbofan Engine Internal Exhaust Gas Mixer Configurations," AIAA paper 80-0228, AIAA 18th Aerospace Sciences Meeting, Pasadena, CA.

Taylor, A. M. K. P., 1981, "Confined Isothermal and Combusting Flows Behind Axisymmetric Baffles," Ph.D. Thesis, University of London.

Werle, M. J., Paterson, R. W., and Presz, W. M., 1987, "Flow Structure in a Periodic Axial Vortex Array," AIAA paper 87-0610, AIAA 25th Aerospace Sciences Meeting, Reno, NV.

Yanta, W. J., and Smith, R. A., 1978, "Measurements of Turbulent Transport Properties with a Laser-Doppler Velocimeter," AIAA paper 73-169, 11th Aerospace Sciences Meeting, Washington.

Zhang, Z., and Wu, J., 1987, "On Principal Noice in Laser-Doppler Velocimeter," *Experiments in Fluids,* Vol. 5, No. 7, pp. 193–196.

Numerical Simulation of the Effects of Rotor-Stator Spacing and Wake/Blade Count Ratio on Turbomachinery Unsteady Flows

W.-S. Yu

B. Lakshminarayana

Center for Gas Turbines and Power,
The Pennsylvania State University,
University Park, PA 16802

A two-dimensional time-accurate Navier-Stokes solver for incompressible flows is used to simulate the effects of the axial spacing between an upstream rotor and a stator, and the wake/blade count ratio on turbomachinery unsteady flows. The code uses a pressure-based method. A low-Reynolds number two-equation turbulence model is incorporated to account for the turbulence effect. By computing cases with different spacing between an upstream rotor wake and a stator, the effect of the spacing is simulated. Wake/blade count ratio effect is simulated by varying the number of rotor wakes in one stator passage at the computational inlet plane. Results on surface pressure, unsteady velocity vectors, blade boundary layer profiles, rotor wake decay and loss coefficient for all the cases are interpreted. It is found that the unsteadiness in the stator blade passage increases with a decrease in the blade row spacing and a decrease in the wake/blade count ratio. The reduced frequency effect is dominant in the wake/blade count ratio simulation. The time averaged loss coefficient increases with a decrease in the axial blade row spacing and an increase in the wake/blade count ratio.

Introduction

Turbomachinery flows are inherently unsteady. Two major sources of unsteadiness are potential interaction of blade rows and wake/blade interaction. Unsteadiness could also arise from the vortex shedding, turbulence fluctuation, tip vortex, and secondary flow.

Recent trends in the design of turbomachinery are toward closer axial spacing of blade rows, increased blade loading, and fewer blade rows. This results in increased unsteadiness and interactions between the rotor and the stator. Understanding the source of these unsteady flows and their dependency on flow and geometrical variables, and their effects on the turbomachinery performance are vital for improving the performance and design that includes these unsteady effects. The unsteady flow effects depend on the upstream wake profile, blade loading, blade row spacing, rotor/stator blade count, blade geometry of the rotor and the stator, Mach number, Reynolds number, freestream turbulence, and the endwall boundary layers. The emphasis hitherto has been to understand the potential effect and viscous interaction effect. With the maturity of computational codes, parametric study can now be carried out with confidence.

In the past decade, there have been many investigations on the computation of unsteady flows in turbomachinery. Based on the fundamental equations used, the investigations fall into three categories: (1) inviscid Euler analysis (e.g., Giles, 1990); (2) coupled inviscid/viscous analysis (e.g., Fan and Lakshminarayana, 1994); (3) full viscous analysis (e.g., Rai, 1987; Ho and Lakshminarayana, 1995). Generally, all three methods can predict the unsteady blade pressure fluctuations reasonably well. The major shortcoming of the first two methods is that neither method allows the physical decay of the upstream wake, both upstream of the leading edge and inside the blade passage. The decay of the upstream wake and its interaction with the viscous flow in the downstream passage necessitates the use of a Navier-Stokes procedure.

One of the major concerns of the designer is the aerodynamic loss and efficiency, due to both the blade boundary layer and the upstream wake. Major objectives of this paper are to investigate the effects of blade row spacing and the rotor/stator blade count on the unsteady pressure, flow field and losses, including accurate prediction of the wake transport and its properties as it progresses from upstream of the blade row to the downstream. The emphasis is not only on the flow physics, but also on the loss generating mechanism. The losses generated upstream of the blade and inside the passage are of interest.

Numerical Approach

Detailed information on the governing equations and the numerical procedures employed in this paper can be found in Basson and Lakshminarayana (1994) and Ho and Lakshminarayana (1995). This unsteady two-dimensional, incompressible Navier-Stokes solver uses the SIMPLE type pressure-based method. Chien's (1982) low-Reynolds-number form of the two-equation model is used to capture the turbulence effects. In order to stabilize the second order central difference scheme used for the momentum equations, the second and fourth order artificial dissipation terms are added.

The numerical scheme is the PISO scheme by Issa (1985) coupled with the *E*-factor scheme by Van Doormaal and Raithby (1984). A control volume approach is used in the discretization procedures for the system of governing equations and the resulting equations are solved by an ADI scheme. Proper choice of optimum grid size and the artificial dissipation coefficients is crucial for accurate prediction of the unsteady flow. The coefficients of the artificial dissipation are limited to minimum values to maintain a stable and convergent solution. Details on the numerical procedure, optimization of grid and selection of artificial dissipation coefficients can be found in Ho and Lakshminarayana (1995).

Contributed by the Fluids Engineering Division for publication in the JOURNAL OF FLUIDS ENGINEERING Manuscript received by the Fluids Engineering Division April 20, 1994; revised manuscript received June 8, 1995. Associate Technical Editor: Wing-Fai Ng.

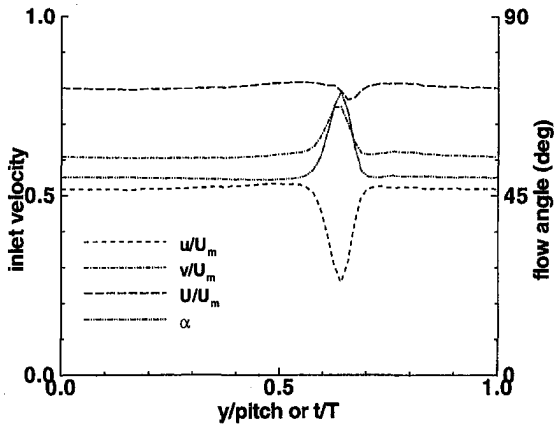

Fig. 1 Inlet velocity profiles for cases 1 to 4 (linear interpolation from data of Stauter et al., 1991 at 36 percent axial chord upstream of the stator)

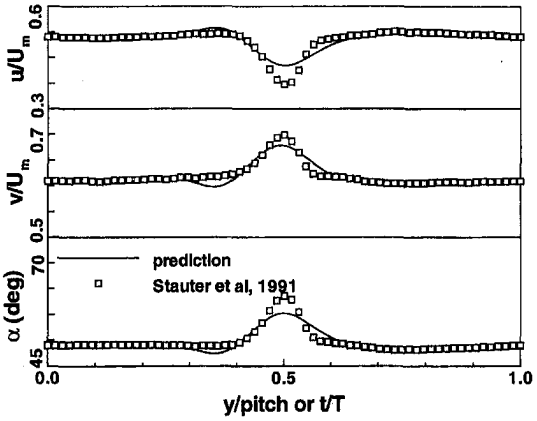

Fig. 2 Rotor wake profile at 13 percent axial chord upstream of the stator

Simulation Test Case

The mid-span section of the second stage stator of a two-stage compressor at the United Technologies Research Center (Stauter et al., 1991) is chosen as the test case for the simulations. The second stage stator and its upstream rotor has 44 blades in each row. The hub/tip ratio is 0.8 with a tip radius of 0.76 m. Rotation speed of the upstream rotor is 650 rpm. The compressor is operated at a flow coefficient of 0.51 and Reynolds number based on the stator blade chord length is 2.5×10^5. The corresponding reduced frequency ω_r is 8.48. Stauter et al. (1991) measured the rotor wake profile at 8 percent axial chord downstream of the rotor trailing edge using a Laser Doppler Velocimeter. Using this profile as the inlet condition, Ho and Lakshminarayana (1995) computed the stator unsteady flow field and validated the code against these data. In this paper, the same geometry is used while certain parameters are varied in order to simulate the effects of axial gap and the wake/blade count ratio. For the sake of brevity, only representative results are shown in this paper. For example, the unsteady pressure are shown on the suction surface only. For complete details, see Yu (1996).

The measured wake profile (Stauter et al., 1991) at 8 percent axial chord downstream of the rotor (36 percent of axial chord upstream of the stator) for a spacing of 0.44 C_x is shown in Fig. 1. At this measuring plane, the maximum angle variation across the rotor wake is 22°. The predicted velocities at 13 percent axial chord upstream of the stator leading edge show considerable decay of the wake, with angle changes of 10° (Fig. 2). The total velocity defect in the wake at both 44 percent of the axial chord and 13 percent of the axial chord upstream is small. The measured and predicted wake profiles are in good agreement. The major effect here is the change in the flow angle due to a "jet" type of profile in the tangential gust and the "wake" type of profile for the axial velocity gust, and the resulting unsteady incidence to the stator.

The simulation includes this case ($s/C_x = 0.44$) as well as $s/C_x = 0.8$ and 0.3. The case with $s/C_x = 0.8$ is simulated by moving the same wake, as in Fig. 1, to 72 percent axial chord upstream. Likewise $s/C_x = 0.3$ is simulated by moving the wake closer to the stator blade at 0.22 C_x. In all cases the wake is located at 0.08 C_x downstream of the rotor.

The characteristics of the wake for various simulation cases are shown in Table 1 for the spacing effect simulation and Table

Nomenclature

C = chord of the stator
C_f = skin friction coefficient = $\tau_w/(0.5\ \rho U_\infty^2)$
C_p = pressure coefficient = $(p - p_{te})/(0.5\ \rho U_\infty^2)$
C_x = axial chord of the stator
F_x, F_y = axial and tangential components of total aerodynamic force on the blade
F_{x1}^+, F_{y1}^+ = = $F_{x1}/F_{x0}, F_{y1}/F_{y0}$
n = coordinate normal to the blade surface
p = static pressure
P_o = total pressure
$P_{o,\text{avg}}$ = passage and mass averaged time mean total pressure
r = rotor wake/stator blade count ratio
s = axial spacing between rotor and stator
t = time
T = upstream rotor wake passing period
u,v = axial and tangential velocity
U = total flow velocity
U_m = blade speed at mid radius
w = relative tangential velocity
x = axial coordinate ($x = 0$ is the stator leading edge)
x_r = distance between stator computational inlet plane and rotor trailing edge
x_{in} = distance between stator computational inlet plane and stator leading edge
y = tangential coordinate/distance normal to the blade
α = absolute flow angle measured from the axial direction
δ = boundary layer thickness
ζ = loss coefficient = $(P_{o,\text{avg},in} - P_{o,\text{avg}})/(0.5\ \rho U_\infty^2)$
θ = momentum thickness, = $\int_0^{n>\delta} (U/U_e)\ (1 - (U/U_e)dn$
ρ = density of fluid
τ_w = wall shear stress
ϕ = phase angle (with reference to inlet wake)
Ω = vorticity normalized by U_∞/C
ω = upstream rotor wake passing frequency
ω_r = reduced frequency = $0.5\ \omega C/U_\infty$

Subscripts

∞ = upstream value
0,1,2 = time mean value, first, and second harmonic
d = maximum defect or variation
exit = stator computational exit plane
e = freestream or edge value
le,te = leading edge, trailing edge
in = inlet of stator computational domain

Table 1 Test cases for blade row spacing effect simulations

Case	x_r/C_x	x_{in}/c_x	s/C_x	u_d/u_e	v_d/v_e	U_d/U_e	$\alpha_d-\alpha_e$	r
1	0.08	0.72	0.80	0.52	0.24	0.06	22°	1
2	0.08	0.36	0.44	0.52	0.24	0.06	22°	1
3	0.08	0.22	0.30	0.52	0.24	0.06	22°	1
4	0.08	0.36	0.44	0.0	0.0	0.0	0°	0

Case 5: Steady-state run for the second stage rotor to predict the decay of wake downstream of the rotor in the absence of the stator.

2 for the wake/blade count simulation. The wake/blade count simulation effect is carried out for the actual geometry measured by Stauter et al. (1991). The configuration, inlet plane and the notations used are shown in Fig. 3.

Effect of Axial Spacing Between Blade Rows

As mentioned earlier, the rotor location is changed to simulate the effects of rotor/stator spacing (Table 1, Fig. 3). The measured wake profile is assumed to be the same as that shown in Fig. 1 for 0.44 C_x spacing. This neglects the effect of the stator pressure field on the rotor viscous flow field. The effects of the stator pressure field on the rotor wake are included from the measurement plane onwards. Thus the unsteadiness caused by the stator on the rotor wake (moving gust) is included.

In the present simulation study, the effect of varying turbulence intensity across the wake is not included. A 9 percent turbulence intensity is used as suggested by Stauter et al. (1991). To capture the wake decay and the unsteady viscous flow through the stator passage accurately, 200 × 96 grid points are used with 61 grids upstream and 72 grids inside the passage; except for case 1 which has a longer inlet, where the corresponding numbers are 81 and 62, respectively.

Unsteady Blade Pressure and Velocity Field. The time-averaged blade pressures are found to be nearly identical to the steady state pressure for all the cases. The unsteady pressures on the blade surface are Fourier decomposed to derive the first and second harmonic components, which are normalized by the tangential gust amplitude v_1,

$$C_{pi} = \frac{p_i}{\rho v_1 U_\infty}, \quad i = 1, 2 \tag{1}$$

The chordwise distribution of the first harmonic of the unsteady pressure on the suction surface is shown in Fig. 4. The value of C_{p1} decreases, as expected, as the spacing is increased. On the pressure surface, the distribution of the first harmonic has the same trend with smaller magnitude. Hence, the pressure fluctuation on the blade, especially in the leading edge region, is higher for smaller blade row spacing. This is supported by the unsteady velocity distribution shown in Fig. 5, which is a snap shot of the unsteady velocity corresponding to the maximum unsteady pressure fluctuations for cases 1 and 3. The vectors shown are the difference between the instantaneous velocity vector and the time-mean velocity vector.

The unsteady velocity vectors for $s/C_x = 0.8$ and 0.3, indicate that the velocity fluctuations are larger for the latter case. As indicated by several earlier investigators, the passage of wake results in two counter rotating vortices on either side, clockwise on the leading edge of the wake and anticlockwise on the trailing side of the wake. Before the wake impinges on the leading

Table 2 Test cases for wake/blade count effect simulations

Case	x_r/C_x	x_{in}/c_x	s/C_x	u_d/u_e	v_d/v_e	U_d/U_e	$\alpha_d-\alpha_e$	r
2	0.08	0.36	0.44	0.52	0.24	0.06	22°	1
6	0.08	0.36	0.44	0.52	0.22	0.08	22°	2
7	0.08	0.36	0.44	0.51	0.22	0.09	22°	3

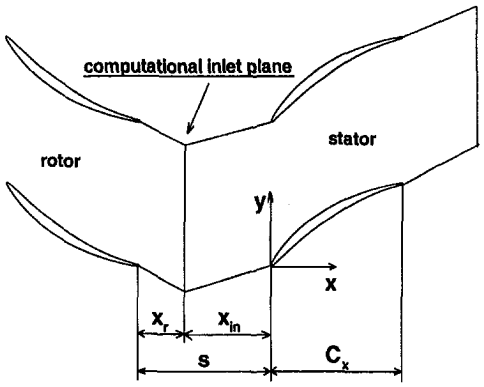

Fig. 3 The second stage rotor and stator blade setting used as the test case

edge the incidence decreases, increases near the impingement location and decreases again after its passage.

The magnitude of the unsteady pressure decreases rapidly (Fig. 4) with distance from the leading edge and this is caused by the guidance of the flow by the blade. A decrease in the streamwise velocity is predicted in the leading edge area on the suction surface with the arrival of the wake, corresponding to an increase in the local incidence and a decrease in the static pressure. Two distinct phenomena are responsible for large unsteady pressure near the leading edge, one of them is the incidence change (Fig. 5), the other is deceleration and acceleration of the flow near the blade surface during the passage of the wake.

The unsteady pressure and flow field downstream of the leading edge is strongly affected by the recirculation or the vortex pattern. This is clear from the unsteady velocity vectors shown in Figs. 5, as well as vorticity ($\Omega = (\partial u/\partial y - \partial v/\partial x)/(U_\infty/C)$, where counter clockwise vorticity is positive) contours shown in Fig. 6. Large positive and negative vorticity is present on either side of the wake centerline and the vorticity associated with the wake decays rapidly downstream. The vorticity and recirculation pattern is the major source of unsteadiness in the pressure downstream of the leading edge. On the suction surface, the clockwise vortex on the leading side of the wake tends to decrease the local instantaneous velocity and increase the static pressure on the suction surface, while the counter-clockwise vortex on the trailing side of the wake tends to increase the local instantaneous velocity and decrease the static pressure. In addition, due to the orientation of the wake with respect to the blade surface, the streamwise component of the unsteady velocity inside the wake is in the opposite direction to the

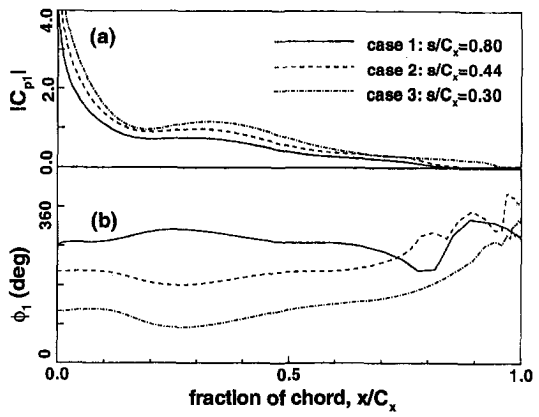

Fig. 4 The first Fourier component of the suction surface unsteady pressure distribution, C_{p1}, (a) magnitude, (b) phase angle

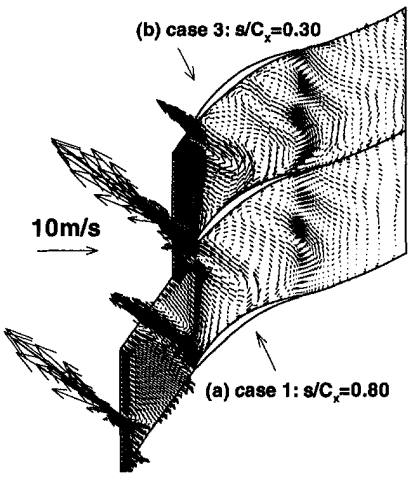

Fig. 5 Unsteady velocity vector $U(t) - U_0$: (*a*) case 1: $s/C_x = 0.80$ at $t/T = 0.80$ (*b*) case 2: $s/C_x = 0.44$ at $t/T = 0.75$

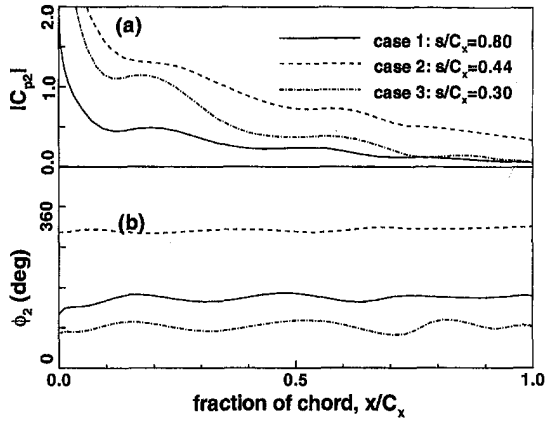

Fig. 7 The second Fourier component of the suction surface unsteady pressure distribution, C_{p2}, (*a*) magnitude, (*b*) phase angle

mainstream. This amplifies the effects of the clockwise vortex. The hump on the suction side (Fig. 4) in the 20–30 percent chordwise location is caused by this effect.

C_{p1} is very small on the suction side very near the trailing edge. This is because of the flow separation. The inception of the separation occurs approximately between 82–90 percent chord, the larger spacing case has a larger flow separation region. This seems to indicate that larger unsteadiness in the flow delays separation. The pressure fluctuations are much smaller in the separated region.

It is clear from unsteady velocity vectors and vortices (Figs. 5 and 6) that the vortices upstream and downstream of the wake centerline are much weaker for the larger spacing. Case 1, with the largest gap, has the smallest hump in C_{p1} near 20–30 percent chord (Fig. 4).

Large variations of the phase angle at and near the leading edge for various blade row spacing (Fig. 4(*b*)) are caused by the differences in the convective time for these cases. Larger rotor/stator spacing requires longer time, hence, larger phase angle difference. The phase angles in regions of very low amplitude fluctuations (e.g., trailing edge regions) are not accurate.

The second harmonic of the pressure fluctuations on the suction surface are plotted in Fig. 7 (see Yu, 1996, for results on the pressure surface). The magnitude of the second harmonic for the larger gap is much smaller. This is consistent with the decay characteristics of the wake, as the first harmonic dominates in the far wake profile. Surprisingly, case 2, with wake farther upstream, has higher magnitudes than case 3 on the suction surface. This may have been caused by the non-linear effects, shift in energy from lower to higher harmonics. The second harmonic of the phase angle differences are similar to those of the first harmonic (Fig. 7(*b*)). Once again, the scatter in the phase angle distribution on the pressure surface is due to low amplitudes of unsteady pressure and the associated inaccuracy.

The axial and tangential components of the total unsteady aerodynamic forces (first harmonic) for various cases investigated are shown and compared with Gallus et al.'s (1982) data in Fig. 8. It should be emphasized here that the blade geometry, configurations used in the test case here are very different from the geometry used by Gallus et al. The comparison is shown mainly to confirm the qualitative trend and not the magnitude. The agreement with the data is reasonably good for the tangential force fluctuations. The trend as well as magnitude are predicted well. The agreement with the axial force fluctuations is not good. The predicted value of F_{x1}^+ is much smaller than the data of Gallus et al.. The measurement indicated that the force fluctuations are large in the region of $s/C_x = 0.05$ to 0.2. This region is dominated by both the potential effect (unsteady pressure interaction) and the viscous wake effect. Resolution of flow in this region has to be carried out with a multistage code, where the rotor and the stator flow is solved simultaneously.

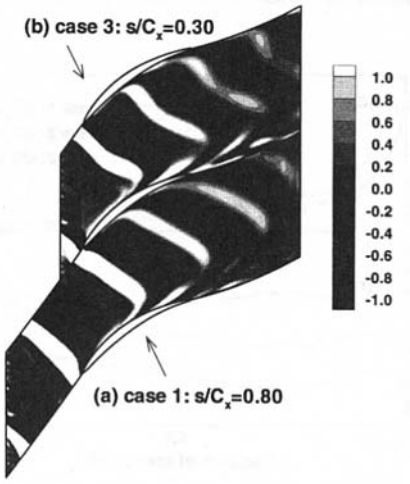

Fig. 6 Unsteady vorticity $\Omega(t) - \Omega_0$ contours: (*a*) case 1: $s/C_x = 0.80$ at $t/T = 0.80$ (*b*) case 2: $s/C_x = 0.44$ at $t/T = 0.75$

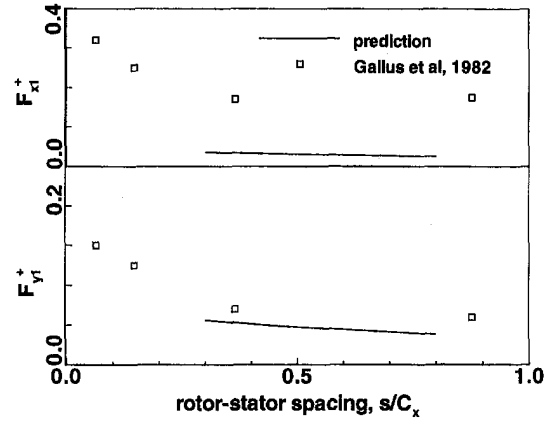

Fig. 8 The first Fourier harmonic of the unsteady total blade force as a function of the spacing, s/C_x. (*a*) axial component, (*b*) tangential component

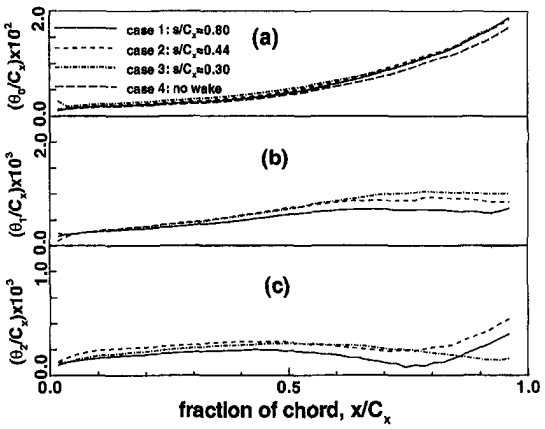

Fig. 9 momentum thickness on the suction surface, θ/C_x (*a*) time mean, (*b*) first harmonic, (*c*) second harmonic

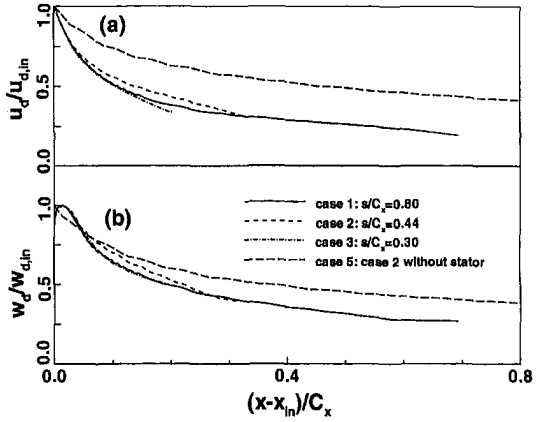

Fig. 11 Decay characteristics of the upstream rotor wake (*a*) axial velocity defect, (*b*) maximum relative tangential velocity variation across the wake

Steady and Unsteady Blade Boundary Layer. The harmonic content of the momentum thickness θ is shown in Fig. 9. The time averaged values are not significantly different. Near the trailing edge, maximum values of θ_0 occur for the closest blade row spacing. This is clear evidence that the profile losses are higher for closer blade spacing. It should be cautioned here that this conclusion is valid when there is no transition.

The first harmonic of the amplitude of the momentum thickness θ_1, shows that the smallest spacing has the maximum amplitude, the amplitude of fluctuations are of the order of 5 percent of the time averaged value near the trailing edge. A similar trend is observed in the second harmonic, with the exception that case 2 (0.44 C_x spacing) has a higher second harmonic component, which is consistent with the predicted second harmonic of unsteady pressure distribution (see Fig. 7). Furthermore, the first and second harmonic of momentum thickness are of the same order of magnitude and as expected, the second harmonic content is more sensitive to the spacing effect. This can be explained on the basis of momentum and energy transport from the first component to the second component as the wakes become more shallow and wider during the transport through the blade row.

The harmonic content of the skin friction coefficient on the suction surface is shown in Fig. 10. The differences in C_{f0} are small, except in the trailing region. Flow separation occurs near the trailing edge for the large blade row spacing and disappears for the smaller spacing. This is consistent with the observations made earlier. The prediction also indicates that this flow is fully turbulent. This is due to high turbulence levels at the inlet (9 percent). The smallest spacing has the maximum effect on the first and the second harmonic of C_f. It should also be observed that both the first and second harmonics are of nearly the same order of magnitude, especially for closer spacing.

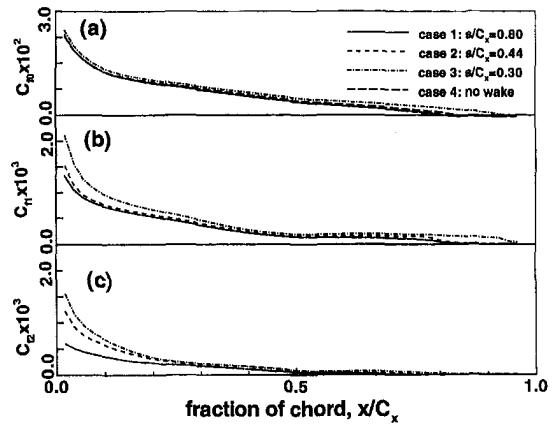

Fig. 10 Skin friction coefficient on the suction surface, C_f (*a*) time mean, (*b*) first harmonic, (*c*) second harmonic

Rotor Wake Decay and Loss Coefficient. The wake decay characteristics are plotted in Fig. 11. The rate of decay of the wake (in the rotor reference frame) is nearly identical for all three cases of the spacing effect simulation. The rotor wake decays faster when there is stator downstream of the rotor and this is caused by the potential interaction. The mechanism responsible for the faster decay of the wake is the unsteadiness in the wake profile introduced by the stator-rotor interaction. This indicates that the unsteady interaction between the rotor and the stator increases the rate of rotor wake decay.

The aerodynamic loss coefficient is evaluated from the equation

$$\zeta = (P_{o,\text{avg},in} - P_{o,\text{avg}})/\tfrac{1}{2}\,\rho U_\infty^2 \tag{2}$$

where $P_{o,\text{avg}}$ is the local passage averaged time mean stagnation pressure and $P_{o,\text{avg},in}$ is $P_{o,\text{avg}}$ at the computational inlet plane. The passage averaged time mean total pressure is defined as:

$$P_{o,\text{avg}} = \int_s^p P_o u_o dy \Big/ \int_s^p u_0 dy \tag{3}$$

where p and s stands for pressure and suction surfaces. The distribution of loss should provide information on the losses due to wake decay upstream, inside the passage and its effect on profile losses on the blade surfaces.

The loss predictions upstream of the stator are shown for five cases in Fig. 12(*a*). The additional cases are stator with uniform flow (case 4), and rotor wake flow without stator (case 5). A comparison of these cases should provide information on additional losses arising from the wake decay and the loss mechanisms upstream and downstream of the stator leading edge. The losses upstream are mainly caused by wake decay. The loss for case 4, is insignificant upstream of the stator, which indicates that the numerical dissipation is very small in these computations. The interesting feature to observe is the effect of the stator on wake losses. The presence of the stator decreases the rotor wake defect. This is clearly evident by comparing case 2 and 5, the latter without a stator. The losses are higher for case 2 as compared with case 5 due to faster decay of the wake and unsteadiness caused by the stator pressure field. The trend in losses observed for cases 1, 2, and 3 are as expected. The losses are highest for case 1, which is located far upstream of the stator, hence, losses due to wake decay are higher. The

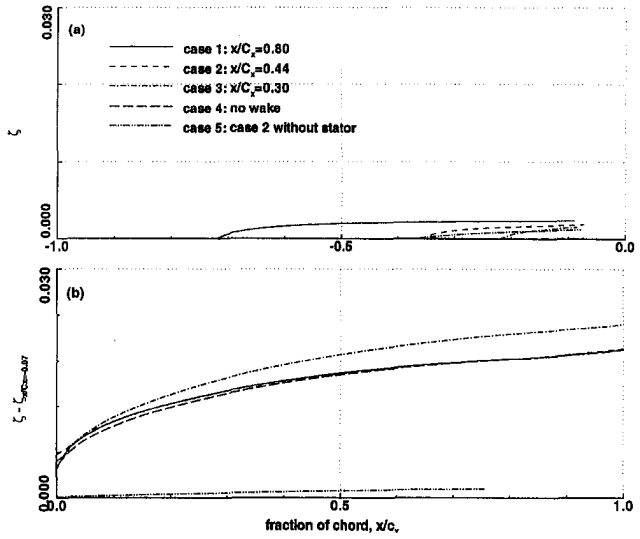

Fig. 12 Distribution of the loss coefficient (*a*) upstream of the stator leading edge (*b*) inside the stator blade passage

losses very near the leading edge are not accurate due to errors in interpolating the results, hence losses are shown only up 7 percent axial chord upstream of the stator.

The losses inside the passage are shown in Fig. 12(*b*). This should provide information on the losses due to the wake decay and change in profile losses due to the passing of the wake inside the passage. This would not include the wake losses upstream of the stator. Case 3, with the closest blade row spacing has the highest losses. The increase in loss is much higher than the losses due to wake decay in the absence of a stator. Thus the non-linear and interaction effects increase losses due to upstream wakes. In addition, the smallest blade row spacing with the largest velocity defect, causes the highest losses due to the presence of strong counter-rotating vortices (Fig. 5(*b*). This is also responsible for additional losses. The total losses due to wake decay alone (case without stator) is lower than the increase in losses (from steady state case) for case 2.

The total loss coefficient at the exit plane of the stator for all the cases is shown in Fig. 13. The total losses include the loss from the computational inlet plane to the exit of the stator, and thus include losses due to the decay of the wake both upstream and inside the passage. The losses upstream of the blade leading

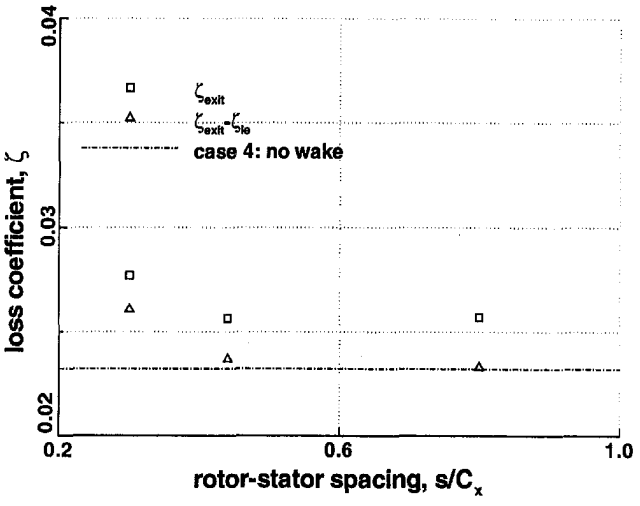

Fig. 13 Loss coefficient at the exit of the stator as a function of spacing, s/C_x

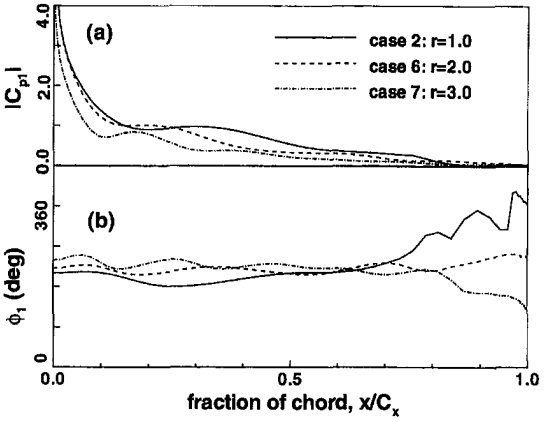

Fig. 14 The first Fourier component of the suction surface unsteady pressure distribution, C_{p1}, (*a*) magnitude, (*b*) phase angle

edge are small compared with the losses inside the blade passage. As indicated earlier, the difference between case 1, 2, 3, and 4 represents additional losses due to wake decay inside the passage and the losses due to the interaction of the wake with the viscous layers inside the stator passage, this being highest for case 3 with the closest spacing. The total losses for cases 1(s/C_x = 0.80) and 2(s/C_x = 0.44) are smaller than the sum of total losses for cases 4 and 5. At these range of spacing between rotor and stator, the unsteadiness of the flow decreases the total loss very slightly. But when the spacing between rotor and stator goes smaller as in case 3, the total losses is found to be larger than the sum of losses for cases 4 and 5.

Effect of Wake/Blade Count Ratio

The ratio of rotor wake/stator blade count (r) is a significant parameter in the evaluation of aeromechanical and aeroacoustic performance of turbomachinery. The effect of r on unsteady performance is evaluated for r = 1,2,3. The wake/blade count ratio (r) is varied by incorporating two and three wakes within one stator passage upstream. The time averaged properties are kept identical for all these cases by increasing the freestream velocities to keep the same mass flow and average flow inlet angles (Table 2). By doing so, the time mean pressure distribution on the stator blade is kept the same.

The effect of the wake/blade count is two-fold. One is the effect of the reduced frequency. It is well known that an increase in the reduced frequency ($\omega_r = 0.5\omega C/U_\infty$) decreases the unsteady pressure. The other effect is mainly caused by viscous and turbulence effects, and disturbance to the flow field caused by larger number of wakes, counter rotating vortices and the associated losses.

The first harmonic content of the unsteady pressure on the suction surface is shown in Fig. 14. It is clear that the unsteady pressure near the leading edge decreases with an increase in the wake/blade count or an increase in the reduced frequency. The unsteady flow vectors for cases 7 and 8, shown in Figs. 15(*a*) and 15(*b*), respectively, clearly reveal the interaction effects inside the passage. The wakes at higher blade count (r) decay more rapidly due to mutual interaction, hence, the lowest blade count should have the largest influence inside the passage away from the leading edge. This is clear from Fig. 14(*a*). The unsteady pressure decreases inside the passage (beyond $0.25C_x$) with an increase in the wake/blade count due to a decreased disturbance caused by the wake. As explained earlier, the interaction vortices located on either side of the wake centerline generate the humps in the unsteady pressure distribution. These effects increase with an increase in r in the region 10–25 percent of chord as revealed in Figs. 14 and 15. This accounts for nearly similar values for C_p at these locations. There are opposing

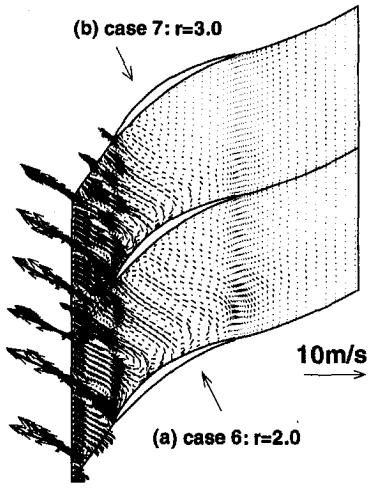

Fig. 15 Unsteady velocity vector $U(t) - U_0$: (*a*) case 6: $r = 2.0$ at $t/T = 0.15$ (*b*) case 7: $r = 3.0$ at $t/T = 0.15$

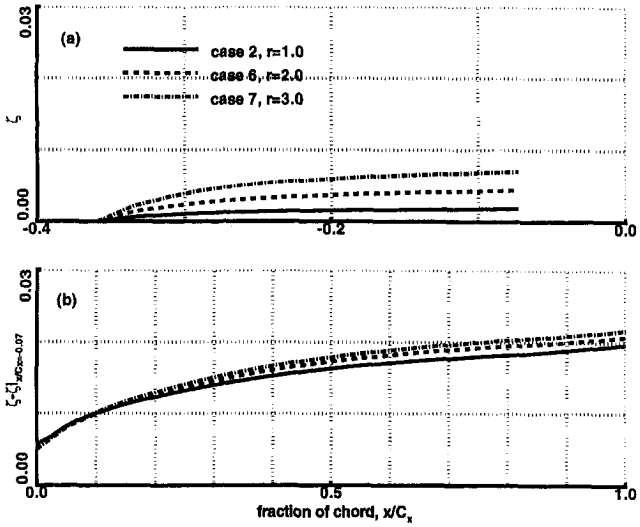

Fig. 17 Distribution of the loss coefficient, (*a*) upstream of the stator leading edge (*b*) inside the stator blade passage

mechanisms here. Higher reduced frequency reduces the unsteady pressure near the leading edge, but generates a larger number of interaction vortices, especially up to about the quarter chord point, thus increasing the unsteady pressure in this region. The appearance of the large number of humps in C_p distribution at higher r is due to the presence of a larger number of wakes. The phase angle distribution is nearly identical for all cases and the prediction beyond $x/C_x = 0.65$ is not accurate due to the low amplitude of fluctuations.

Steady and Unsteady Boundary Layer and Losses. The harmonic content of unsteady momentum thickness θ on the suction surface for various ratios of r, are plotted in Fig. 16. Even though the differences are not significant, the smallest wake/blade count ratio has the highest time-averaged momentum thickness and this is consistent with the highest unsteady pressure and largest flow disturbance caused (especially beyond $x/C_x = 0.25$) at this wake/blade count ratio. This also confirms the earlier conclusion that larger unsteadiness results in higher time-averaged losses. The first harmonic, θ_1, is higher for $r = 1$ beyond $x/C_x = 0.25$, this again is consistent with the distribution of the first harmonic of unsteady pressure shown in Fig. 14(*a*). The second harmonic, θ_2, is the highest for $r = 1$, and this is attributed to the slower decay of the wake inside the passage for this case (compare Figs. 5(*b*) and 15(*b*)).

The chordwise distribution of aerodynamic loss is shown in Fig. 17. The increase in aerodynamic losses with an increase in the ratio r upstream of the leading edge and inside the passage is as expected. From the computational inlet plane to the leading edge, the losses increase almost exactly in proportion to the number of wakes. The losses inside the passage increases with an increase in the wake/blade count ratio. The total losses at the exit plane of the stator increase substantially with an increase in the wake/blade count. This is mainly caused by the losses due to the increased number of rotor wakes inside the stator passage. Furthermore, the losses at all wake/blade count ratios are higher than the steady state value. Hence, the aerodynamic losses increase due to rotor-stator interaction, which strongly depends on the wake/blade count ratio.

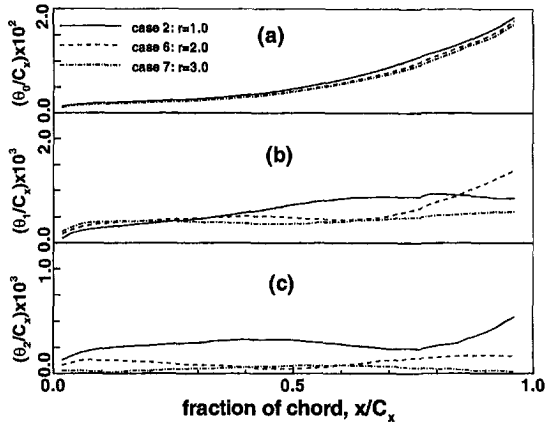

Fig. 16 momentum thickness on the suction surface, θ/C_x (*a*) time mean, (*b*) first harmonic, (*c*) second harmonic

Concluding Remarks

The simulation study carried out in this paper using a Navier-Stokes solver has provided useful information on the effect of rotor-stator blade row spacing and the rotor/stator blade count ratio on the turbomachinery unsteady flows. A decrease in the rotor-stator blade row spacing increases the unsteady pressure on the blade. This is mainly caused by the decay of the wake upstream of the stator. The nonlinear effects and variations in the harmonic content are captured by the Navier-Stokes code. The unsteady flow field data (unsteady velocity and vorticity) indicate that additional mechanisms are responsible for the unsteady pressure and flow field variation inside the passage. The loss mechanisms include: (1) losses due to the decay of the wake upstream of the blade row; (2) losses due to the decay of the wake inside the passage, including modification of the wake profile by the stator pressure field; and (3) the blade profile losses, which are affected by the passage of the wake. The loss budget for various blade row spacings are evaluated. The losses are the highest for the smallest blade row spacing, and they are higher than the steady state case for all the cases investigated.

The wake/blade count ratio effect is dominated by the reduced frequency effect near the leading edge. The wake interaction and vortex formation has a major influence in the 10–25 percent chord region. Beyond this region, the smallest wake/blade count ratio has the most pronounced influence on the unsteady flow and pressure field. The increased interaction effect at higher wake/blade count ratio results in a more rapid decay of the wake, thus reducing the influence of the wake beyond the 25 percent chord location. The losses increase significantly as the wake/blade count is increased. This increase is mainly brought about by the increased number of wakes and

the losses associated with their decay upstream and inside the blade passage.

Acknowledgment

This work is supported by the Office of Naval Research under Contract No. N00014-90-J1182 with J. Fein as the contract monitor. The authors are thankful to Y.-H. Ho for assistance with the code and useful comments. Dr. D. E. Thompson provided valuable suggestions during the course of this work. The authors also would like to acknowledge NASA for providing the supercomputing resources at the NAS Facility at NASA Ames Research Center.

References

Basson, A. H., and Lakshminarayana, B., 1994, "An Artificial Dissipation Formulation for a Semi-Implicit Pressure Based Scheme for Viscous and Inviscid Flows," *International Journal of Computational Fluid Dynamics,* Vol. 2, p. 253.

Chien, K.-Y., 1982, "Prediction of Channel and Boundary-Layer Flows with a Low-Reynolds Number Turbulence Model," *AIAA Journal,* Vol. 20, No. 1, pp. 33–38.

Fan, S., and Lakshminarayana, B., 1994, "Computation and Simulation of Wake-Generated Unsteady Pressure and Boundary Layers in Cascades, Part 1: Description of the Approach and Validation, Part 2: Simulation of Unsteady Boundary Layer Flow Physics," ASME Papers 94-GT-140 and 141.

Gallus, H. E., Grollius, H., and Lambertz, J., 1982, "The Influence of Blade Number Ratio and Blade Row Spacing on Axial-Flow Compressor Stator Blade Dynamic Load and Stage Sound Pressure Level," ASME *Journal of Engineering for Power,* Vol. 104, pp. 633–641.

Giles, M. B., 1990, "Stator-Rotor Interaction in a Transonic Turbine," *Journal of Propulsion and Power,* Vol. 6, pp 621–627.

Ho. Y.-H., and Lakshminarayana, B., 1995, "Computation of Unsteady Viscous Flow Through Turbomachinery Blade Row Due to Upstream Rotor Wakes," ASME *Journal of Turbomachinery,* Vol, 117, Oct.

Issa, R. I., 1985, "Solution of the Implicitly Discretised Fluid Flow Equations by Operator-Splitting," *Journal of Computational Physics,* Vol. 62, pp. 40–65.

Rai, M. M., 1987, "Navier-Stokes Simulations of Rotor-Stator Interaction Using Patched and Overlaid Grids," *Journal of Propulsion and Power,* Vol. 3, pp. 387–396.

Stauter, R. D., Dring, R. P. and Carta, F. O., 1991, "Temporally and Spatially Resolved Flow in a Two-Stage Axial Compressor, Part 1: Experiment," ASME *Journal of Turbomachinery,* Vol. 113, p. 219.

Van Doormaal, J. P., and Raithby, G. D., 1984, "Enhancement of the SIMPLE Method for Predicting Incompressible Fluid Flows," *Numerical Heat Transfer,* Vol. 7, pp. 147–163.

Yu, W.-S., 1996, "Numerical Simulation of 3D Unsteady Turbulent Flows through Turbomachinery including Rotor-Stator Interaction," PhD thesis (in preparation), The Pennsylvania State University.

A. Arnone
Department of Energy Engineering,
University of Florence, Via S. Marta, 3,
50139 Florence, Italy

R. Pacciani
Institute of Energetics,
University of Perugia,
Perugia, Italy

A. Sestini
Department of Energy Engineering,
University of Florence,
Florence, Italy

Multigrid Computations of Unsteady Rotor-Stator Interaction Using the Navier-Stokes Equations

A Navier-Stokes time-accurate solver has been extended to the analysis of unsteady rotor-stator interaction. In the proposed method, a fully-implicit time discretization is used to remove stability limitations. A four-stage Runge-Kutta scheme is used in conjunction with several accelerating techniques typical of steady-state solvers, instead of traditional time-expensive factorizations. Those accelerating strategies include local time stepping, residual smoothing, and multigrid. Direct interpolation of the conservative variables is used to handle the interfaces between blade rows. Two-dimensional viscous calculations of unsteady rotor-stator interaction in a modern gas turbine stage are presented to check for the capability of the procedure.

Introduction

One of the most challenging aspects in turbomachinery design and analysis is the extensive use of Computational Fluid Dynamics (CFD). With the recent evolution of computer performance, scientists are encouraged to look more and more at realistic simulations of the various components. Aspects like heat transfer, secondary flows, leakage flow, and radial mixing can be predicted on the basis of viscous procedures. In the last few years, several schemes have been developed for predicting three-dimensional viscous flows through an isolated blade row (i.e., Subramanian and Bozzola, 1987; Chima and Yokota, 1988; Choi and Knight, 1988; Davis et al., 1988; Hah, 1989; Nakahashi et al., 1989; Weber and Delaney, 1991; Dawes, 1991; Jennions and Turner, 1992; Arnone, 1993). Lately, important steps have also been made in the analysis of a multistage environment (i.e., Ni et al., 1989; Adamczyk et al., 1990; Dawes, 1990), and viscous computations based on the Navier-Stokes equations have become feasible for industrial applications and are routinely used in every-day turbomachinery design.

The real flow inside a turbine or compressor is unsteady and strongly influenced by the interaction of pressure waves, shock waves, and wakes between stators and rotors. Even if important efforts are being made in time-accurate simulations of viscous rotor-stator interaction, this approach is still very expensive when applied in three dimensions, and contributions are needed in this field in order to provide efficient tools for the design of the next generation of turbomachinery.

In this paper, a viscous, time-accurate solver (TRAF, Arnone et al., 1993b) has been extended to the analysis of rotor-stator interaction. The procedure is based on the extension of conventional steady-state acceleration techniques, specifically multigrid and residual smoothing, to unsteady problems. The basic idea is to reformulate the governing equations so that they can be handled by an explicit, accelerated scheme. If the time discretization is made implicit, stability restrictions are removed and accelerating techniques can be used instead of traditional time-expensive factorizations (i.e., ADI, LU).

In viscous flow calculations, the grid is stretched close to the walls and the characteristic time step can vary several orders of magnitude inside the computational domain. The time step required for accuracy is quite often similar to the characteristic time step of the inviscid core, while in the shear layer, the stability restriction of purely explicit schemes is very severe. With the proposed method, depending on the size of the time stepping, residual smoothing and multigrid can be progressively introduced in order to speed up the calculation of the viscous layer.

The procedure is validated by applying it to a typical modern gas turbine first stage. A grid sensitivity analysis is presented along with a study of the influence of the time step size.

With the proposed procedure, an unsteady rotor-stator analysis can be carried out in few hours on a modern workstation.

Governing Equations

Let t, ρ, u, v, p, T, E, and H denote respectively time, density, the absolute velocity components in the x and y Cartesian directions, pressure, temperature, specific total energy, and specific total enthalpy. The two-dimensional, unsteady, Reynolds-averaged Navier-Stokes equations can be written for a moving grid in conservative form in a curvilinear coordinate system ξ, η as,

$$\frac{\partial (J^{-1}Q)}{\partial t} + \frac{\partial F}{\partial \xi} + \frac{\partial G}{\partial \eta} = \frac{\partial F_v}{\partial \xi} + \frac{\partial G_v}{\partial \eta} \tag{1}$$

where,

$$Q = \begin{Bmatrix} \rho \\ \rho u \\ \rho v \\ \rho E \end{Bmatrix}, \quad F = J^{-1} \begin{Bmatrix} \rho U \\ \rho u U + \xi_x p \\ \rho v U + \xi_y p \\ \rho H U - \xi_t p \end{Bmatrix},$$

$$G = J^{-1} \begin{Bmatrix} \rho V \\ \rho u V + \eta_x p \\ \rho v V + \eta_y p \\ \rho H V - \eta_t p \end{Bmatrix} \tag{2}$$

The contravariant velocity components of Eqs. (2) are written as,

$$U = \xi_t + \xi_x u + \xi_y v, \quad V = \eta_t + \eta_x u + \eta_y v \tag{3}$$

and the transformation metrics are defined by,

$$\xi_x = J y_\eta, \quad \xi_y = J x_\eta, \quad \xi_t = -x_t \xi_x - y_t \xi_y$$
$$\eta_x = J y_\xi, \quad \eta_y = J x_\xi, \quad \eta_t = -x_t \eta_x - y_t \eta_y \tag{4}$$

Contributed by the Fluids Engineering Division for publication in the JOURNAL of FLUIDS ENGINEERING. Manuscript received by the Fluids Engineering Division, April 20, 1994; revised manuscript received February 17, 1995. Associate Technical Editor: Wing Fai-Ng.

where the Jacobian of the transformation J is,

$$J^{-1} = x_\xi y_\eta - x_\eta y_\xi \tag{5}$$

The viscous flux terms are assembled in the form,

$$F_v = J^{-1}\begin{Bmatrix} 0 \\ \xi_x\tau_{xx} + \xi_y\tau_{xy} \\ \xi_x\tau_{yx} + \xi_y\tau_{yy} \\ \xi_x\beta_x + \xi_y\beta_y \end{Bmatrix},$$

$$G_v = J^{-1}\begin{Bmatrix} 0 \\ \eta_x\tau_{xx} + \eta_y\tau_{xy} \\ \eta_x\tau_{yx} + \eta_y\tau_{yy} \\ \eta_x\beta_x + \eta_y\beta_y \end{Bmatrix} \tag{6}$$

where,

$$\begin{aligned} \tau_{xx} &= 2\mu u_x + \lambda(u_x + v_y) \\ \tau_{yy} &= 2\mu v_y + \lambda(u_x + v_y) \\ \tau_{xy} &= \tau_{yx} = \mu(u_y + v_x) \\ \beta_x &= u\tau_{xx} + v\tau_{xy} + kT_x \\ \beta_y &= u\tau_{yx} + v\tau_{yy} + kT_y \end{aligned} \tag{7}$$

and the Cartesian derivatives of (7) are expressed in terms of ξ-, and η-derivatives using the chain rule, i.e.,

$$u_x = \xi_x u_\xi + \eta_x u_\eta \tag{8}$$

The pressure is obtained from the equation of state,

$$p = \rho RT \tag{9}$$

According to the Stokes hypothesis, λ is taken to be $-2\mu/3$ and a power law is used to determine the molecular coefficient of viscosity μ as a function of temperature. The eddy-viscosity hypothesis is used to account for the effect of turbulence. The molecular viscosity μ and the molecular thermal conductivity k are replaced with,

$$\mu = \mu_l + \mu_t \tag{10}$$

$$k = c_p\left[\left(\frac{\mu}{\mathrm{Pr}}\right)_l + \left(\frac{\mu}{\mathrm{Pr}}\right)_t\right] \tag{11}$$

where c_p is the specific heat at constant pressure, Pr is the Prandtl number, and the subscripts l and t refer to laminar and turbulent quantities respectively. The turbulent quantities μ_t and Pr_t are computed using the two-layer mixing length model of Baldwin and Lomax (1978).

Spatial Discretization and Artificial Dissipation

The space discretization is based on a cell-centered finite volume scheme. Traditionally, using a finite-volume approach, the space discretization starts from an integral formulation without any intermediate mapping. In the present work, due to the large use of eigenvalues and curvilinear quantities, it was found more convenient to map the Cartesian space (x, y) in a generalized curvilinear one (ξ, η) where the equation of motion (1) can be easily rewritten in integral form by means of Green's theorem. The transformation metrics are evaluated so that the projected areas of the cell faces are given by the ratios of the appropriate metric derivatives to the Jacobian ones i.e., ξ_x/J is the projection onto the x axis of a cell face at a fixed ξ location (i.e., Arnone et al., 1993a, Arnone 1993). On each cell boundary, fluxes are calculated after computing the necessary flow quantities at the side center. Those quantities are obtained by a simple averaging of adjacent cell-center values of the dependent variables.

In viscous calculations, dissipating properties are present due to diffusive terms. Away from the shear layer regions, the physical diffusion is generally not sufficient to prevent the odd-even point decoupling of centered schemes. Thus, to maintain stability and to prevent oscillations near shocks or stagnation points, artificial dissipation terms are also included in the viscous calculations.

The artificial dissipation model used in this paper is basically the one originally introduced by Jameson et al. (1981). In order to minimize the amount of artificial diffusion inside the shear layer, the eigenvalues scaling of Martinelli and Jameson (1988), and Swanson and Turkel (1987) have been used to weight these terms (e.g., Arnone and Swanson, 1993, Radespiel et al., 1990).

The computation of the dissipating terms is carried out in each coordinate direction as the difference between first and third difference operators. Those operators are set to zero on solid walls in order to reduce the global error on the conservation property and to prevent the presence of undamped modes (Pulliam, 1986; Swanson and Turkel, 1987).

Boundary Conditions

In cascade-like configurations there are four different types of boundaries: inlet, outlet, solid wall, and periodicity. In the case of a multistage environment, more than one blade row is taken into consideration, and inlet and outlet refer to the first row inlet and last row exit, and the link between rows must then be provided by means of some technique.

According to the theory of characteristics, the flow angle, total pressure, total temperature, and isentropic relations are used at the subsonic-axial first row inlet, while the outgoing Riemann invariant is taken from the interior. At the subsonic-axial last row outlet, the average value of the static pressure is prescribed and the density and components of velocity are extrapolated.

On the solid walls, the pressure is extrapolated from the interior points, and the no-slip condition and the temperature condition are used to compute density and total energy. For the calculations presented in this paper, all the walls have been assumed to be at a constant temperature equal to a fraction of the total inlet one.

Cell-centered schemes are generally implemented using phantom cells to handle the boundaries. The periodicity is, therefore, easily overimposed by setting periodic phantom cell values. For high turning blade geometries, nonperiodic H- and C-type grids have proven to be effective in order to minimize the mesh skewness (Arnone et al., 1992, Arnone, 1993). On non-periodic H-type grids, the point-to-point mesh correspondence is broken on the periodic boundaries before the leading edge and on the wake. On non-periodic C-type grids, the mesh periodicity is removed only on the wake, while it is retained on the external boundary. On the periodic boundaries where the grids do not match, the phantom cells overlap the real ones. Linear interpolations are then used to compute the value of the dependent variables.

The link between rows is handled by means of interface lines. Stator and rotor grids have a common interface lines and the match is provided through appropriate calculation of phantom cell values. For the blade passage under examination, the phantom cells relative to the interface line lie on the adjacent blade passage, and linear interpolations are used to provide the flow variable values. This approach, similar to the one used on periodic boundaries, where grids do not match, is not strictly conservative. However, a monitoring of the errors in the conservation of mass, momentum, and energy has indicated a very good level of accuracy. For the practical applications considered up to now, relative errors in conservation were always less than 10^{-4}, which was considered accurate enough.

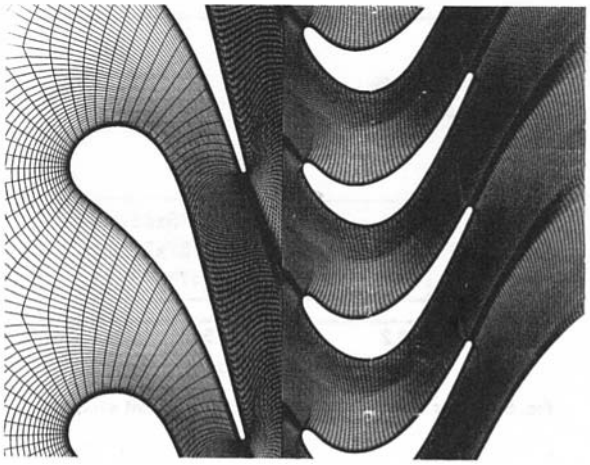

Fig. 1 Mixed C-type and H-type grids for the first stage of the PGT2 heavy duty gas turbine

Basic Time-Stepping Scheme and Acceleration Techniques for the Steady Problem

The system of governing equations is advanced in time using an explicit four-stage Runge-Kutta scheme until the steady-state solution is reached. A hybrid scheme is implemented, where, for economy, the viscous terms are evaluated only at the first stage and then frozen for the remaining stages.

Good, high-frequency damping properties, important for the multigrid process, have been obtained by performing two evaluations of the artificial dissipating terms, at the first and second stages.

In order to reduce the computational cost, three techniques are employed to speed up convergence to the steady state-solution. These techniques: 1) local time-stepping; 2) residual smoothing; 3) multigrid; are briefly described in the following.

Local Time-Stepping. For steady-state calculations, a faster expulsion of disturbances can be achieved by locally using the maximum allowable time step. In the present work, the local time step limit Δt is computed, accounting for both the convective (Δt_c) and diffusive (Δt_d) contributions, as follows,

$$\Delta t = c_0 \left(\frac{\Delta t_c \Delta t_d}{\Delta t_c + \Delta t_d} \right) \tag{12}$$

where c_0 is a constant usually taken to be the Courant-Friedrichs-Lewy (CFL) number. Specifically, for the inviscid and viscous time step we used,

$$\Delta t_c = \frac{1}{\lambda_\xi + \lambda_\eta} \tag{13}$$

$$\Delta t_d = \frac{1}{K_t \dfrac{\gamma \mu}{\rho \mathrm{Pr}} J^2 (S_\xi^2 + S_\eta^2)} \tag{14}$$

where:

$$\lambda_\xi = |U| + a\sqrt{\xi_x^2 + \xi_y^2}, \quad \lambda_\eta = |V| + a\sqrt{\eta_x^2 + \eta_y^2} \tag{15}$$

are the scaled spectral radii of the flux Jacobian matrices for the convective terms, a is the speed of sound, γ is the specific heat ratio, and:

$$S_\xi^2 = x_\xi^2 + y_\xi^2, \quad S_\eta^2 = x_\eta^2 + y_\eta^2 \tag{16}$$

K_t being a constant whose value has been set equal to 2.5 based on numerical experiments.

Residual Smoothing. An implicit smoothing of residuals is used to extend the stability limit and the robustness of the basic scheme. The variable coefficient formulations of Martinelli and Jameson (1988) and Swanson and Turkel (1987) are used to obtain effective viscous calculations on highly stretched meshes. The time step is then computed on the basis of a fixed Courant number, typically 5.0.

Multigrid. In this work, the multigrid technique is based on the Full Approximation Storage (FAS) schemes of Brandt (1979), and Jameson (1983). A V-type cycle with subiterations is used where the process is advanced from the fine grid to the coarser one without any intermediate interpolation, and when the coarser grid is reached, corrections are passed back. One Runge-Kutta step is performed on the fine grid, two on the first coarse grid, and three on all the other coarser grids.

For viscous flows with very low Reynolds numbers or strong separation, it is important to compute the viscous terms on the coarse grids, too. The turbulent viscosity is evaluated only on the finest grid level and then interpolated on the coarse grids.

On each grid, the boundary conditions are treated in the same way and updated at every Runge-Kutta stage.

Reformulation of the Governing Equations

Explicit Runge-Kutta schemes in conjunction with residual smoothing and multigrid have proven to be very efficient for steady problems, however those time-dependent methods are no longer time accurate. As shown by Jameson (1991) for the Euler equations, the system of (1) can be reformulated to be handled by a time-marching steady-state solver. Equations (1) are rewritten in a compact form as,

$$\frac{\partial Q}{\partial t} = -\mathcal{R}(Q) \tag{17}$$

where $\mathcal{R}$ is the residual which includes convective, diffusive, and artificial dissipation fluxes. By the introduction of a fictitious time τ the unsteady governing equations can be reformulated and a new residual $\mathcal{R}^*$ defined as,

$$\frac{\partial Q}{\partial \tau} = \frac{\partial Q}{\partial t} + \mathcal{R}(Q) = \mathcal{R}^*(Q) \tag{18}$$

now τ is a fictitious time and all the accelerating techniques developed in steady-state experiences, can be used to efficiently reduce the new residual $\mathcal{R}^*$, while marching in τ. Following the approach of Jameson (1991), derivatives with respect to the real time t are discretized using a three-point backward formula which results in an implicit scheme which is second-order accurate in time,

$$\frac{\partial Q}{\partial \tau} = \frac{3Q^{n+1} - 4Q^n + Q^{n-1}}{2\Delta t} + \mathcal{R}(Q^{n+1}) = \mathcal{R}^*(Q^{n+1}) \tag{19}$$

where the superscript n is associated with the real time. Between

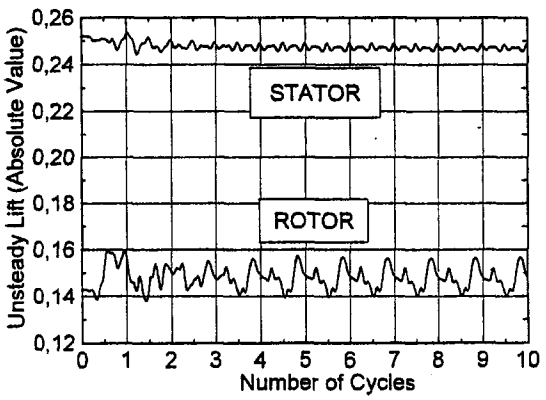

Fig. 2 Unsteady lift evolution

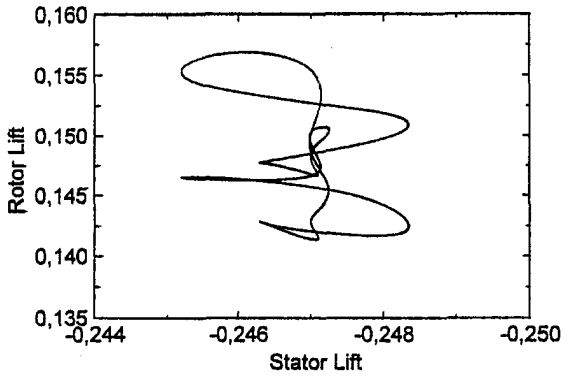

Fig. 3 Phase plot for the stage

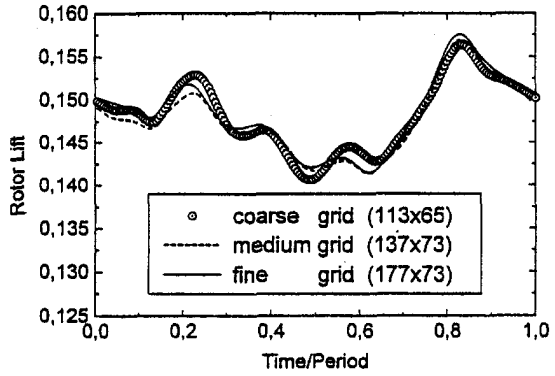

Fig. 5 Effect of the rotor grid density on the lift evolution

each time step the solution is advanced in a non-physical time τ and acceleration strategies like local time stepping, implicit residual smoothing, and multigridding are used to speed up the residual $\mathcal{R}^*$ to zero to satisfy the time-accurate equations.

The time discretization of (19) is fully implicit, however, when solved by marching in τ, stability problems can occur when the stepping in the fictitious time τ exceeds the physical one. This generally occurs in viscous calculations where core-flow cells are much bigger than those close to shear-layer. Based on a linear stability analysis of the four-stage scheme, the stepping in τ must be less than $\frac{2}{3}$ CFL*Δt. The time step $\Delta\tau$ can then be corrected as follows,

$$\Delta\tau = \text{MIN}\left(\Delta\tau, \frac{\Delta t}{2^{m-1}\,\frac{3}{2}\,\frac{\text{CFL}}{\text{CFL}^*}}\right) \tag{20}$$

where the contribution of the multigrid speed-up is included through 2^{m-1}, m being the total number of grids used in the multigrid process. After limiting the time step $\Delta\tau$ with (20) the scheme becomes stable and the physical time step Δt can be chosen safely only on the basis of the accuracy requirement.

At the end of each time step in real time, the time derivative $\partial Q/\partial t$ is updated and a new sequence in the fictitious time τ is started.

To provide a good initialization of the solution at the new time step, a three-point backward formula is used as a predictor,

$$Q^* = Q^n + \frac{3Q^n - 4Q^{n-1} + Q^{n+2}}{2} \tag{21}$$

where Q^* is the predicted value of Q^{n+1}.

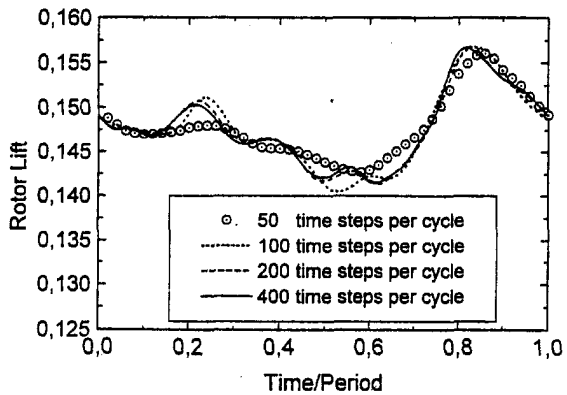

Fig. 4 Effect of the time step size on the rotor lift evolution

Results and Discussions

As a validation of the proposed procedure, the unsteady release of the TRAF code has been used to study the first stage transonic blading of a 2 MW industrial gas turbine produced by Nuovo Pignone (PGT2). This turbine features state-of-the-art design with an inlet temperature of 1370 K and 12.5:1 pressure ratio in two stages. For the analysed configuration of the first stage, the absolute Mach number is slightly above 1 at the stator exit with a Reynolds number of about 1.5 million.

Figure 1 shows an enlargement of the computational grid for a blade-to-blade surface close to midspan. Due to the stator's blunt rounded leading edge, a C-type grid (177 × 33) structure has been selected. On the contrary, it was found convenient to use an H-type structure for the rotor blading. In fact, away from the leading edge, the C-type structure tends to increase the grid size and thus induce a smear of the incoming wakes. With an H-type structure, it is much easier to control the uniformity and density of the grid before the blade passage. Three different grid sizes have been tested for the rotor: coarse 113 × 65, medium 137 × 73, fine 177 × 73. The fine grid has twice as many as points as the coarse one on the blade surface. Figure 1 reports the medium grid which is the one used for most of the calculations presented herein. In order to reduce the grid skewness, both the C-type and H-type grids are of a nonperiodic type (e.g., Arnone et al., 1992, Arnone, 1993).

At the present stage of the research, the fact that stators and rotors generally have different numbers of blades has been addressed by including more blade passages in the calculation. A ratio of one stator blade to two rotor blades was used to approximate the stage configuration. With respect to the machine geometry, the rotor blade distance in the pitchwise direction has been slightly reduced to accommodate the 1:2 stator:rotor configuration.

Figure 2 shows the unsteady lift evolution starting from a steady state solution obtained at a fixed rotor position with respect to the stator. Calculations refer to the previously mentioned medium grid for the rotor and to 200 time steps within a cycle (two rotor blade passings). As experienced by other

Table 1 Performance of the proposed scheme for the investigated case

TIME STEPS PER CYCLE	CFL MINIMUM/ AVERAGED/ MAXIMUM	OPTIMUM NUMBER OF GRIDS	CPU TIME PER CYCLE IBM RISC/6000-320H
50	0.58/3.52/2456	3	4940 s
100	0.29/1.76/1228	2	5560 s
200	0.14/0.88/614	1	7840 s
400	0.072/0.44/307	1	11200 s

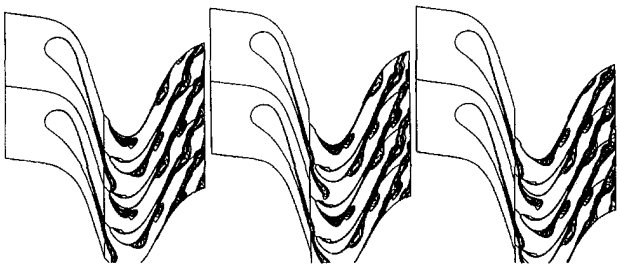

Fig. 6 Instantaneous entropy rise contours for three different rotor positions

researchers (e.g., Rai, 1987; Jorgenson and Chima, 1988; Rao et al., 1992) from five to seven cycles are needed to reach a satisfactory level of periodic behaviour. Figure 3 reports the phase plot relative to the extra five cycles (from cycle 10 to 15). The five curves lie one on top of the other, proving a good level of periodicity in the calculation.

An issue which was believed important is the influence of the time step size and of the number of mesh points on the solution. An analysis of this parameter should provide an indication of the grid size to be used and the number of time steps to be performed per cycle. The effect of the time step size on the rotor lift evolution is reported in Fig. 4. From 50 up to 400 time steps per cycle were tested. Only the solution with 50 divisions within a cycle shows a poor level of accuracy. On the contrary, solutions obtained with 200 and 400 time steps look very similar and indicate a good level of time step independence.

The situation is somehow similar in terms of dependency on the grid density (see Fig. 5). The grid size was chosen on the basis of a previous grid dependency analysis for steady cases (Arnone et al., 1992). Therefore, as most of the unsteady pulsations are expected in the rotor blade passages, only the rotor grid has been changed. Even if the medium and fine grids have very similar lift evolutions, it seems that grid independence has not yet been completely achieved.

Numerical experiments have indicated that the grid density at the rotor exit has some impact on the rotor lift evolution. The vorticity coming from the stator wakes is intercepted by the rotors. The mechanism of this process is quite clear in Fig. 6, where three consecutive stator:rotor relative positions are reported. Contours of entropy rise give a net description of wake evolutions. As there are two rotor blades for each stator, the stator wake is cut twice in a cycle by the rotor's leading edge. Once stator wakes are cut by the rotor's leading edge, an entropy spot is generated and convected downstream in the rotor blade passage. Because of the pitch-wise pressure gradient, these spots move toward the rotor's suction side and eventually interact with the rotor wakes. As a consequence, the rotor wakes become unstable after about half a rotor axial chord. It is suspected that, if the space and time resolutions are made fine enough, the previously described mechanism could induce wake shedding and therefore move the target in the dependency analysis. At the present stage of the research, interest is mostly focused on the validation of the procedure for practical applications, and overall predictions and the level of independence of the calculations from the time stepping and grid density has been considered satisfactory.

Figure 7 shows instantaneous absolute Mach number and static pressure contours for the stage. Both the stator and rotor work in transonic conditions. The stator has a throat shock system and a slightly supersonic exit. On the rotor blades, the trailing edge shock system has a fish-tail structure. Such a system is weakened when the stator wake enters the rotor blade passage.

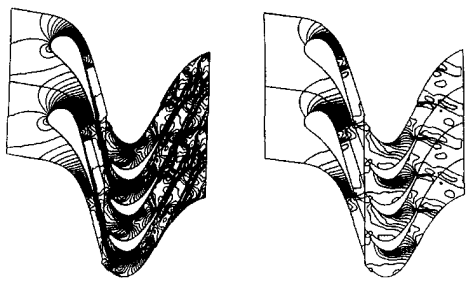

Fig. 7 Instantaneous absolute Mach number and pressure contours

Code Performance

The performance of the proposed method is summarized in Table 1. Calculations refer to the medium grid (137×73) for the rotor blades and correspond to a total of about 26,000 grid points to discretize the stage (one stator and two rotors). In Table 1 the maximum, area averaged, and minimum CFL numbers are reported. Those quantities have been evaluated as the ratios of the physical time step and the characteristic maximum, area averaged, and minimum time step. The local characteristic time step is defined by Eq. (12) with $c_0 = 1$. The code was run at a local CFL number of 5.0 with implicit residual smoothing adjusting the number of grids (used in the multigrid) in order to optimize the CPU time. At each time step subiterations are performed until the averaged root mean square of the residuals is less than 10^{-6}, which generally requires from 2 to 5 multigrid cycles.

As previously pointed out, the averaged CFL is close to the characteristic one. Using 200 time divisions within a cycle, the CFL number is less than one for most of the computational cells. On the other hand, in the boundary layer the CFL increases up to several hundreds. In such a circumstance, the advantage of using multigrid is restricted to the viscous layer and decreases when increasing the time step division per cycle. As can be noticed in Table 1, if using more than 200 time division per cycle, there is no CPU time reduction in running with more than one grid. Although, those considerations are related to the particular application and to the grid density, they are believed to give an idea of effectiveness of the scheme in rotor-stator analysis.

An explicit computation with the four-stage Runge-Kutta scheme has also been carried out. For the sake of accuracy in time, residual smoothing has not been included in the calculation which was performed with a CFL of 2.5. The explicit test has required 50,000 time steps per cycle and about 230,000 s on the IBM RISC/6000 mod. 320 H. With the present method and 200 divisions per cycle the CPU time is $\frac{1}{30}$ of the one of the purely explicit code. The extra memory requirement, due to the implicit time discretization, which requires the storage of the flow variables at three time levels, is limited to about 20 percent.

Concluding Remarks

A viscous time-accurate method has been extended to the analysis of unsteady rotor-stator interaction. Accelerating strategies typical of steady state solvers have been successfully utilized also in the unsteady case. The application to a first stage of a modern gas turbine has indicated up to 97 percent reduction in the computational effort with respect to classical explicit schemes. Those results encourage the extension of the proposed method to three-dimensional calculations.

It is stressed that, as the basic scheme is explicit, the procedure is highly vectorizable.

Acknowledgments

The authors would like to express their gratitude to MURST and to Nuovo Pignone for providing support for this work. Thanks are also due to Prof. Ennio Carnevale and Prof. Francesco Martelli of the University of Florence, for encouraging this work.

References

Adamczyk, J. J., Celestina, M. L., Beach, T. A., and Barnett, M., 1990, "Simulation of Three-Dimensional Viscous Flow Within a Multistage Turbine," ASME *Journal of Turbomachinery,* Vol. 112, July, pp. 370–376.

Arnone, A., Swanson, R. C., 1993, "A Navier-Stokes Solver for Turbomachinery Applications," ASME *Journal of Turbomachinery,* Vol. 115, Apr., pp. 305–313.

Arnone, A., Liou, M.-S., and Povinelli, L. A., 1992, "Navier-Stokes Solution of Transonic Cascade Flow Using Non-Periodic C-Type Grids," *Journal of Propulsion and Power,* Vol. 8, No. 2, Mar.-Apr., pp. 410–417.

Arnone, A., Liou, M.-S., and Povinelli, L. A., 1993, "Multigrid Calculation of Three-Dimensional Viscous Cascade Flows," *Journal of Propulsion and Power,* Vol. 9, No. 4, July-Aug., pp. 605–614.

Arnone, A., 1993, "Viscous Analysis of Three-Dimensional Rotor Flows Using a Multigrid Method," ASME Paper 93-GT-19.

Arnone, A., Liou, M.-S., and Povinelli, L. A., 1993, "Multigrid Time-Accurate Integration of Navier-Stokes Equations," AIAA Paper 93-3361-CP.

Baldwin, B. S., and Lomax, H., 1978, "Thin Layer Approximation and Algebraic Model for Separated Turbulent Flows," AIAA paper 78-257.

Brandt, A., 1979, "Multi-Level Adaptive Computations in Fluid Dynamics," AIAA paper 79-1455.

Chima, R. V., and Yokota, J. W., 1988, "Numerical Analysis of Three-Dimensional Viscous Internal Flows," NASA TM 100878.

Choi, D., and Knight, C. J., 1988, "Computation of Three-Dimensional Viscous Linear Cascade Flows," *AIAA Journal,* Vol. 26, No. 12, Dec., pp. 1477–1482.

Davis, R. L., Hobbs, D. E., and Weingold, H. D., 1988, "Prediction of Compressor Cascade Performance Using a Navier-Stokes Technique," ASME *Journal of Turbomachinery,* Vol. 110, pp. 520–531.

Dawes, N. W., 1990, "Towards Improved Throughflow Capability: The Use of 3D Viscous Flow Solvers in a Multistage Environment," ASME Paper 90-GT-18.

Dawes, N. W., 1991, "The Simulation of Three-Dimensional Viscous Flow in Turbomachinery Geometries Using a Solution-Adaptive Unstructured Mesh Methodology," ASME Paper 91-GT-124.

Hah, C., 1989, "Numerical Study of Three-Dimensional Flow and Heat Transfer Near the Endwall of a Turbine Blade Row," AIAA paper 89-1689.

Jameson, A., 1983, "Transonic Flow Calculations," MAE Report 1651, MAE Department, Princeton University, July 1983.

Jameson, A., 1991, "Time Dependent Calculations Using Multigrid with Applications to Unsteady Flows Past Airfoils and Wings," AIAA Paper 91-1596.

Jameson, A., Schmidt, W., and Turkel, E., 1981, "Numerical Solutions of the Euler Equations by Finite Volume Methods Using Runge-Kutta Time-Stepping Schemes," AIAA paper 81-1259.

Jennions, I. K., and Turner, M. G., 1992, "Three-Dimensional Navier-Stokes Computations of Transonic Fan Flow Using an Explicit Flow Solver and an Implicit k-ϵ Solver," ASME Paper 92-GT-309.

Jorgenson, P. C. E., and Chima, R., 1988, "An Explicit Runge-Kutta Method for Unsteady Rotor/Stator Interaction," AIAA Paper 88-0049.

Martinelli, L., and Jameson, A., 1988, "Validation of a Multigrid Method for the Reynolds Averaged Equations," AIAA paper 88-0414.

Nakahashi, K., Nozaki, O., Kikuchi, K., and Tamura, A., 1989, "Navier-Stokes Computations of Two- and Three-Dimensional Cascade Flowfields," *Journal of Propulsion and Power,* Vol. 5, No. 3, May, pp. 320–326.

Pulliam, T. H., 1986, "Artificial Dissipation Models for the Euler Equations," *AIAA Journal,* Vol. 24, No. 12, Dec., pp. 1931–1940.

Radespiel, R., Rossow, C., and Swanson, R. C., 1990, "Efficient Cell-Vertex Multigrid Scheme for the Three-Dimensional Navier-Stokes Equations," *AIAA Journal,* Vol. 28, No. 8, Aug., pp. 1464–1472.

Rai, M. M., 1987, "Unsteady Three-Dimensional Navier-Stokes Simulations of Turbine Rotor Stator Interactions," AIAA paper 87-2058.

Rao, K. V., and Delaney, R. A., 1992, "Investigation of Unsteady Flow Through a Transonic Turbine Stage, Part I, Analysis," AIAA paper 90-2408.

Subramanian, S. V., and Bozzola, R., 1987, "Numerical Simulation of Three-Dimensional Flow Fields in Turbomachinery Blade Rows Using the Compressible Navier-Stokes Equations," AIAA paper 87-1314.

Swanson, R. C., and Turkel, E., 1987, "Artificial Dissipation and Central Difference Schemes for the Euler and Navier-Stokes Equations," AIAA paper 87-1107.

Weber, K. F., and Delaney, R. A., 1991, "Viscous Analysis of Three-Dimensional Turbomachinery Flows on Body Conforming Grids Using an Implicit Solver," ASME paper 91-GT-205.

M. G. Dunn

C. W. Haldeman, Jr.

Calspan-UB Research Center,
Buffalo, NY 14225

Phase-Resolved Surface Pressure and Heat-Transfer Measurements on the Blade of a Two-Stage Turbine

Phase-resolved surface pressure, and unsteady pressure measurements are reported for the first-stage blade row of the Space Shuttle Main Engine two-stage fuel-side turbine. Measurements were made at 10, 50, and 90 percent span on both the pressure and suction surfaces of the blade. Phase-resolved and unsteady heat-flux measurements are also reported.

Introduction

Phase-resolved measurements obtained for the first blade of the SSME two-stage turbine are presented. Time-averaged results were presented previously by Dunn et al. (1992). The measurements presented here represent a data set that is in addition to the one reported in the earlier publication. These experiments were designed to obtain the unsteady heat-flux loading and to significantly improve the accuracy of the surface-pressure measurements in order to be able to obtain phase-resolved (unsteady) surface-pressure data on the first blade. Because there is a relatively small pressure change across each vane or blade row for this particular turbine, careful calibration of the pressure transducers was an important issue. The transducer calibration accuracy will be demonstrated to be very good.[1]

The shock-tunnel facilities at Calspan have been used for several previous measurement programs to obtain time-resolved heat-flux or surface-pressure data on the blade of a high-pressure turbine at high rotational speed, but for different turbine stages, e.g., Dunn et al. (1986), Dunn, Bennett et al. (1990). This last reference concentrated on time-resolved surface-pressure measurements for the blade of a high-pressure transonic turbine and comparison of the data with prediction. More recently, Rao et al. (1994) reported a further comparison of the time-resolved pressure data and a comparison with the time-resolved heat-flux data.

Description of the Experimental Technique, the Turbine Flow Path and the Instrumentation

The Experimental Technique. The measurements are performed utilizing a shock tunnel to produce the heated and pressurized air that subsequently passes through the turbine. The facility is described in Dunn et al. (1992). The turbine used for these measurements was the full two-stage SSME fuel-side turbopump. The first stage vane has 41 vanes, the first stage rotor has 63 blades, the second stage vane has 39 vanes, and the second stage rotor has 59 blades.[2]

In order to initiate an experiment, the test section is evacuated while the driver tube, the double diaphragm section, and the driven tube are pressurized to predetermined values. The tube pressure values are selected to produce conditions which duplicate the design flow conditions. The flow function ($\dot{m}\sqrt{\theta}/\delta$), wall-to-total temperature ratio (T_w/T_O), stage total-to-total pressure ratio, and corrected speed are all duplicated. With this facility the value of T_O can be set at any desired value in the range of 800°R to 3500°R, and the test gas mixture can be selected to duplicate the desired specific heat ratio. The pressure ratio across the turbine is established by altering the throat area of the flow-control nozzle located downstream of the second rotor. A geometry difference between this set of experiments and the ones previously reported is that the flow-control nozzle for this series of measurements was moved much closer to the turbine exit.

Surface-Pressure Instrumentation. Surface-pressure measurements were obtained using twenty-four dynamic pressure transducers mounted in the blade skin and flush with the contour of the blade. The transducers in use are Kulite Model LQ-062-600A, with an active pressure area of 0.64 mm by 0.64 mm and a frequency response of about 100 kHz in the installed configuration. Only the active chip is installed in the blades, thus there is no cavity or screen over the chip. These chips are installed approximately 2 mm below the blade surface and are covered with a layer of RTV (a silastic material) to make them flush with the surface. This thin layer of RTV acts both as a thermal barrier and as a particle barrier to protect the chip from damage. As demonstrated later by the fast response of the transducer, the dynamic response of the sensor has not been compromised. External temperature compensation was used with these transducers.

The 600 psi transducers would not have been selected if the option of designing the instrumentation for the particular experiment reported had been available. However, these particular transducers were used because the measurement program was designed to be extended to an inlet pressure consistent with the 4,137 kPa (600 psi) value in order to duplicate the full SSME inlet Reynolds number. Transducers were placed at 10, 50, and 90 percent span at the locations given in Dunn et al. (1994) and were distributed over several different blades (at relative positions with respect to a stage index marker as described in the reference just noted) so as to not disturb the integrity of the surface.

Heat-Flux Instrumentation. The heat-flux measurements were performed using thin-film resistance thermometers. These thin-film gauges are described in Dunn et al. (1992). The gauges were calibrated to obtain the temperature coefficient of resistance. The temperature variable thermal properties of the substrate material were available from previous measurements.

[1]A more detailed version of this paper is given in Dunn and Haldeman, 1994.

[2]A complete description of the vanes and blades, including coordinates, is given in Dunn, Kim, and Haldeman, 1994.

Contributed by the Fluids Engineering Division for publication in the JOURNAL OF FLUIDS ENGINEERING. Manuscript received by the Fluids Engineering Division April 20, 1994; revised manuscript received May 31, 1995. Associate Technical Editor: Wing-Fai Ng.

The resistance versus temperature calibration is used to convert the resistance change of the thin film to surface temperature. This calibration is updated every run by recording the resistance of the sensor, and scaling the calibration factor by any increase in resistance. Having previously measured the thermal properties of the substrate as mentioned above, the heat-flux can be determined from the temperature-time trace using a semi-infinite model (Cook-Felderman, 1966). The accuracy of the heat-flux data reported herein is on the order of ±2.5 percent.

Pressure-Transducer Calibration Technique and Results

The blade, flow path, and flow path rake pressure transducers were all absolute semiconductor devices and thus could be calibrated simultaneously through the entire data acquisition system prior to each run. In general, one run was performed each day, and the pre-run calibration served as the post-run calibration for the previous run. The pressure standard used was an Omega transducer which had been calibrated several times over the previous year against a NIST traceable, 1379 kPa MKS Baratron unit. The total variation in the Omega was less than the ±0.7 kPa calibration accuracy over this time period.

Pressure data obtained during the experiments are converted to engineering units using a relative scheme where the only important calibration constant is the scale of the transducer (output in kPa/volt). In this type of system, the base-line at the beginning of a run is averaged to create a set voltage level, and a secondary pressure measurement system (the Omega transducer) provides a pressure measurement in the test section immediately before a run. The voltage readings are converted to pressure by subtracting the base-line voltage from the voltage at any point in time, multiplying this voltage difference by the scale factor, and then adding the measured offset pressure (which is generally quite close to zero).

This system is more impervious to electronic drift, but does require good calibrations over the entire pressure range from vacuum to maximum anticipated pressure and not just over the pressure range expected on the blade surfaces. For these measurements, the pressure fluctuations were expected to vary between 140 and 345 kPa. Because the plan was to extend the measurements to a higher pressure condition, the calibration was done from 0 to 483 kPa. The calibration was performed by pressurizing the test section containing the instrumented turbine, and then opening a small valve and allowing the tank to bleed while sampling the transducers at fixed time intervals (generally 5 seconds, both during pressurizing and venting). Each of these data points is the average of 100 data points sampled at 1 kHz for 0.1 seconds (although these values can be changed by the user). Several different types of calibrations were done to examine the effects of different procedures on the calibration results, several pressurization and depressurization cycles were checked at levels both above and below atmospheric conditions. Some hysteresis was noted in the system, but it was on the order of the calibration accuracy. Generally, several hundred data points were used. Calibration was done by performing a linear least-squares regression on the data and plotting the residuals.

Calibration accuracy can be shown in many forms. This paper examined both the effects of how the generated scale factor changed from calibration to calibration as well as how accurate the individual transducers calibrations were. Four main calibrations were done which examined either 30 or 31 sensors (depending on the run) for a total of 121 sensor calibrations. When examining these data to observe how the scale factors changed from calibration run to calibration run (which was shown as a percent of reading), 78.5 percent (95 measurements) were within ±0.5 percent of reading and 91 percent (110 measurements) were with ±1 percent of reading. The second method calculated the deviation from the measured pressure standard for each transducer during a calibration. For every calibration, the deviations were averaged and a standard deviation (σ) generated. Assuming that the distribution is Gaussian, then 95 percent of the data should exist within $\pm 2\sigma$. Of the 121 measurements made 57 percent were within ±1 kPa, 84 percent within 2 kPa, 92.5 percent within 3 kPa, and 98 percent were within 4 kPa (all of these measurements reflect a 95 percent confidence level).

More detailed comparisons of individual transducers indicated that the calibration deviations are by far the largest contributor to the overall uncertainty of the pressure measurements, and that the variation in the scale factor is largely due to these calibration deviations. It is, however, important to realize that even for the sensors with the largest variations (±4 kPa, none of which were on the blades), the overall accuracy is ±0.1 percent of transducer full-scale, and that the majority of the sensors have a variation of ±1 kPa, which corresponds to an overall accuracy of ±0.02 percent of the transducer full-scale reading.

Table 1 Summary of flow parameters

Run #	$\dot{m}$* (Kg/s)	Full turbine $\frac{P_{T,\text{in}}}{P_{T,\text{out}}}$	Reflected shock pressure (kPa)	Reflected shock temp. (°K)	% Design speed
22	2.34	1.42	6412	507	102
24	2.54	1.46	6855	521	101
26	2.10	1.39	6228	510	102
27	2.26	1.40	6438	514	100
28	2.25	1.38	6289	512	102

* Obtained from vane flow rig data as experimental value of $P_{T,\text{in}}/P_{S,\text{out}}$ t for first vane (see Table 2).

Experimental Conditions

Table 1 provides a summary of the reflected-shock conditions, the full turbine total-to-total pressure ratio, the turbine mass flow, the average speed during the data collection period, and the percent of corrected turbine speed. These experiments were performed at a reflected-shock pressure and temperature of approximately 6.44×10^3 kPa (936 psia) and 513°K (923°R), respectively. This reflected-shock condition results in a first vane inlet Reynolds numbers (based on first vane axial chord) of approximately 1.4×10^5. Measurements were obtained with the turbine speed set at 101 percent ± 1 percent of the design value.

Table 2 presents the inlet total pressure, the first vane total-to-static pressure ratio, the first stage total-to-static pressure ratio, and the overall turbine total-to-total pressure ratio. The average inlet total pressure for the 5 runs was 346 kPa, the average first vane pressure ratio was 1.11, the average first stage

Nomenclature

T_W = wall temperature [K]
T_O = inlet total temperature [K]
$\dot{m}$ = mass flow [Kg/s]
θ = total temperature/reference temperature
δ = total pressure/reference pressure
P_T = total pressure [kPa]
P_S = static pressure [kPa]
N_{phy} = physical speed [rpm]
N_{corr} = corrected speed [rpm] = $N_{\text{phy}}/\sqrt{T_T} = 291.36$

Table 2 Component pressure ratios

Run #	P_T into 1st vane (kPa)	First vane* $\frac{P_{T,\text{in}}}{P_{S,out}}$	First stage $\frac{P_{T,\text{in}}}{P_{S,\text{out}}}$	Full turbine $\frac{P_{T,\text{in}}^{**}}{P_{T,\text{out}}}$
22	345	1.11	1.25	1.42
24	366	1.12	1.27	1.46
26	334	1.10	1.22	1.39
27	348	1.11	1.23	1.40
28	335	1.11	1.22	1.38

* Static pressures were measured at the outer shroud.
** $P_{T,\text{out}}$ is averaged pressure from 7 flow path transducers.

pressure ratio was 1.24, and the average total-to-total pressure ratio was 1.41. The target pressure ratio was 1.45, which could have been achieved by altering the flow-control nozzle throat area. However, for the purposes of this measurement program, it was not necessary to make a throat area change. The first blade tip clearance was 2.14 percent of blade height (0.0187 in.).

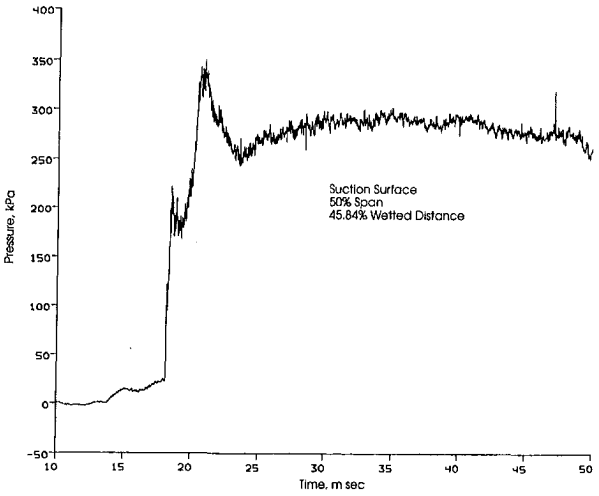

Fig. 2 Pressure history on first blade at 50 percent span

Experimental Results

This paper will concentrate on the following; (a) the ensemble averaged surface pressure on the blade as it passes through a vane exit passage, (b) the unsteady envelope of surface pressure on the blade, (c) the ensemble averaged surface heat flux on the blade as it passes through a vane exit passage, and (d) the unsteady envelope of surface heat flux on the blade.

Reservoir and Flow Path Pressure History. Figures 1(a) and 1(b) are the reflected-shock reservoir and the flow path pressure time history just upstream of the vane entrance that were sampled at a frequency of 100 kHz with an anti-aliasing Bessel filter at 40 kHz. Dunn and Haldeman (1994), present additional time histories for the locations between the first vane and the first blade, between the first blade and the second vane, and downstream of the second blade. The time required to establish local steady flow is noted on Fig. 1(b). During the flow establishment time, the wave system being established between the flow-control nozzle and the inlet (which determines the turbine mass flow and the bypass flow) can be seen in the pressure data. A one-dimensional calculation has been used to demonstrate that the wave system moves through the stage at near the local speed of sound. After flow has been established in the stage, the interstage pressure remains relatively uniform. The occasional spike on the trace is the result of electronic interference which does not affect the result, but could not be eliminated from the electrical circuit without excessive filtering, which was not desirable.

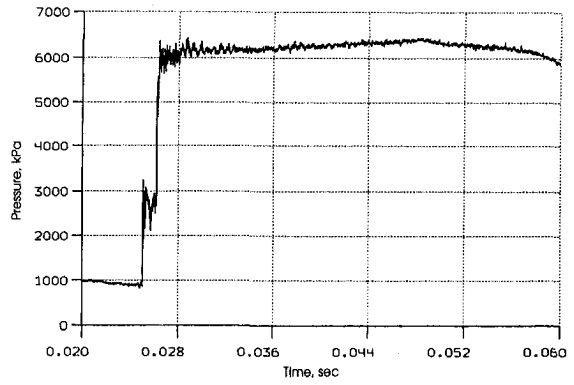

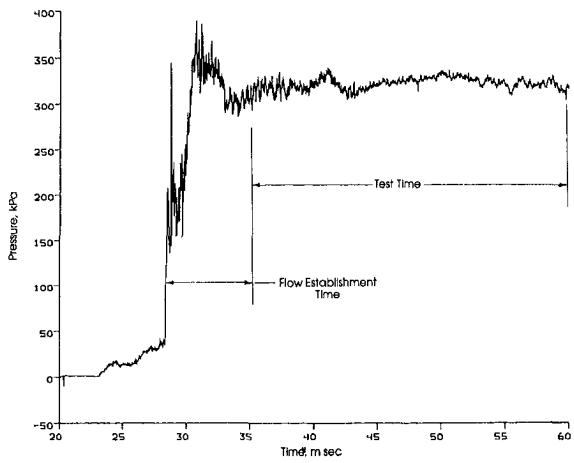

Fig. 1(*a*) Reflected-shock pressure history; Fig. 1(*b*) Static pressure at outer wall just upstream of first vane

Blade Phase-Resolved Surface-Pressure Results. Phase-resolved measurements are taken by describing the circumferential position of the blade leading edge within the vane passage. Phase-averaged results are presented as a percentage of the passage from 0 to 100 percent, where 100 percent corresponds to 8.78 degrees.

Figures 2 and 3 present typical time histories of blade pressure at 50 percent span (45.8 percent wetted distance) and at 90 percent span (16.6 percent wetted distance) from which the

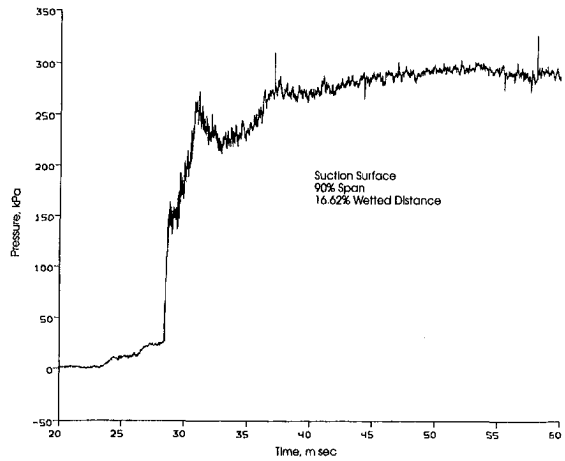

Fig. 3 Pressure history on first blade at 90 percent span

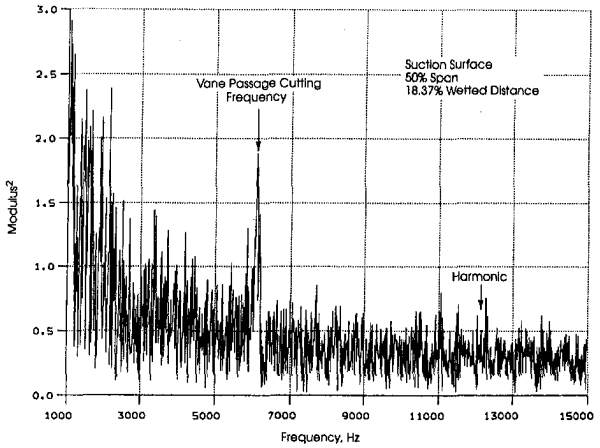

Fig. 4 FFT of blade pressure data

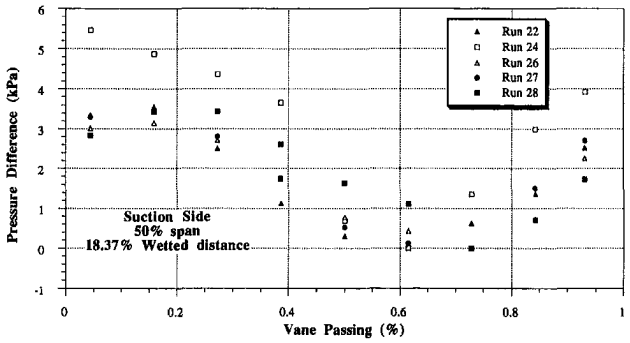

Fig. 6 Ensemble average of pressure at 18.37 percent on suction surface

phase-resolved pressure histories have been derived. Wetted distance is defined as the distance from the geometric stagnation point along the blade surface to the gauge location. These pressure transducers have been sampled at a frequency of 100 kHz with a 40 kHz anti-aliasing Bessel filter and no other filtering has been done.

Figure 4 is an FFT for a blade pressure transducer (run 27) located at mid span on the suction surface at 18.37 percent wetted distance. The rotor speed for this run was 8885 rpm which corresponds to a passage cutting frequency of 6.07 kHz. Figure 4 illustrates the presence of vane passage cutting at this frequency, but the harmonic at 12.14 kHz is buried in the background signal. The signature at 6.07 kHz suggests that the unsteady component of the blade pressure signal is the result of vane exit passage cutting. The flow Mach number at the vane exit is relatively small and no shock waves are present to influence the unsteady pressure signature on the blade. Thus the blade unsteady pressure is dominated by the passage and wake influences. In this regard, it is important to note that the SSME turbopump in-flight configuration was faithfully duplicated for these measurements meaning that there were 13 struts located across the flow path just ahead of the first vane row. Because the unsteady pressure signal for this particular turbine is small, the FFT is not sharp and clean as was shown in Dunn et al. (1990) for which the magnitude of the unsteady pressure signal was more than an order of magnitude greater.

The pressure and heat-flux instrumentation is distributed among several different blades and to compare phase-resolved data from different blades, the relative location of this instrumentation must be indexed to a common reference point in the turbine. Thus, a once per revolution marker is derived from the shaft encoder which, during the experimental set up, is adjusted to correspond to the time at which the blade containing the contoured leading edge heat-flux gauge insert is aligned with the trailing edge of a particular vane. The vane pitch is 8.7805 deg. and the blade pitch is 5.714 degrees. The reader is referred to Dunn and Haldeman (1994) for a detailed map of the blade instrumentation, and for the data necessary to reference all of the phase-resolved pressure and heat-flux data to a particular passage location.

Blade surface-pressure data similar to those presented in Fig. 2 and 3 were used to obtain passage average pressure profiles and the corresponding unsteady pressure envelope. In ensemble averaging the blade data, the blade pressure histories were filtered at 20 kHz (approximately three times the vane passage cutting frequency). For many cases, the surface-pressure data were sufficiently steady to allow the ensemble average to be performed over a time period corresponding to one, two, three, or four revolutions. However, it was found in performing the data analysis that ensemble averaging over one or two revolutions provided essentially the same result as averaging over four revolutions (see Fig. 5 for a position of 90 percent span at 16.6 percent wetted distance). The unsteady pressure variation is plotted as a function of percent of vane passage with 0 and 100 percent corresponding to the vane trailing edge. A revolution of the rotor requires approximately 6.7 milliseconds to complete which corresponds to a vane-passage cutting frequency of about 6.15 kHz. The rotor speed increases by about two per cent over the entire test time. The initial rotor speed is set so that the speed during the test time is the desired speed ± 1 percent which results in a change in the incidence angle. The results presented in Fig. 5 reflect this change in incidence angle.

Figures 6 and 7 are two additional ensemble averaged results for locations at mid span. The data from all five runs have been included on these figures. The ordinate is the difference between the maximum and the minimum pressure at the particular location. Because the individual runs have a slightly different vane inlet total pressure, only the unsteady component of the pressure is presented. For Fig. 6 the run-to-run variation in ensemble averaged pressure is relatively small and the results from indi-

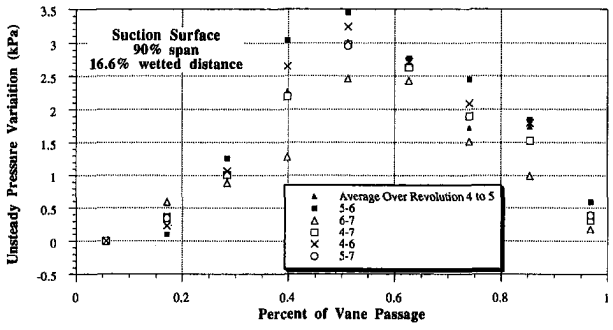

Fig. 5 Ensemble average of pressure over various number of revolutions

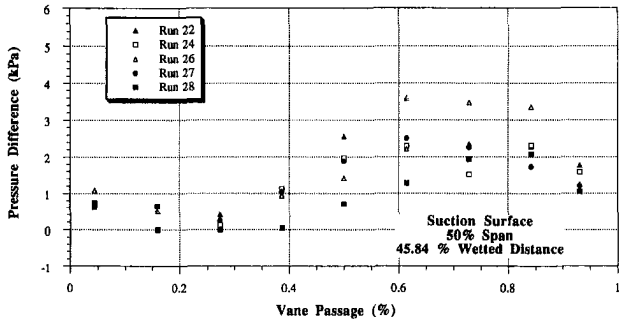

Fig. 7 Ensemble average of pressure at 45.85 percent on suction surface

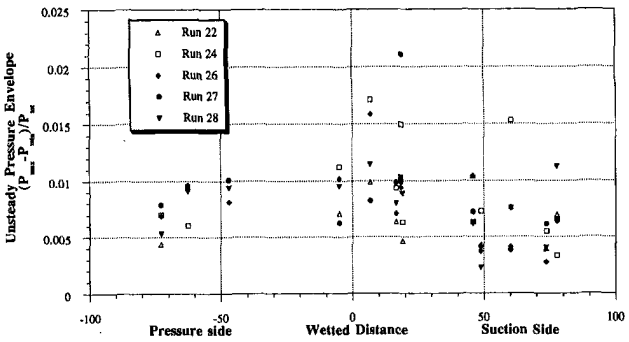

Fig. 8 Measured unsteady pressure envelope for first-stage blade

vidual runs are in good agreement except for the results of run 24. This run was performed for the largest mass flow and the largest pressure ratio and when this is accounted for, the results are consistent. Figure 7 is a corresponding plot for a location further along the suction surface at mid span. In general, the ensemble averaged pressure at this location over the duration of the measurement program are in reasonably good agreement with each other.

Unsteady Pressure Envelope on First Blade. Figure 8 presents the measured unsteady pressure envelope. The ordinate of this plot is the maximum pressure minus the minimum pressure divided by the first vane inlet total pressure and the abscissa is the wetted distance along the blade surface. Experimental data from all span wise locations have been included on Fig. 8.

There is relatively little pressure change across the various components of this turbine which causes the magnitude of the unsteady pressure envelope to be small and difficult to measure. By comparison, the magnitude of the unsteady pressure envelope for the measurements reported in Dunn et al. (1990) (using an Allison turbine with a vane exit Mach number greater than one) was more than fifty times larger.

Blade Time-Resolved Heat-Flux Results. Figure 9 illustrates the surface heat flux (for run 27) on the suction surface of the blade at mid span and 17.71 percent wetted distance for a time period of a little over two revolutions of the rotor. Thin-film gauges were placed at 10, 50, and 90 percent span and in the tip of the blade. The heat-flux history for each gauge was calculated from the temperature-time history of the thin-film gauge (which is derived from the gauge voltage history and the gauge calibration data) using a technique described by Cook and Felderman (1966). The thin-film gauge voltage history was recorded at a sampling frequency of 100 kHz. The resulting temperature history was then filtered at 20 kHz prior to calculating the heat-flux history which was subsequently used to obtain the unsteady heat-flux envelope and the phase-resolved heat-flux profile for selected locations on the blade as a function of position within the passage. The magnitude of the time-averaged heat flux shown in Fig. 9 is consistent with the results of the earlier measurements reported by Dunn et al. (1992). The spikes in the trace seen at approximately 31.5 ms, 33.6 ms, 38.8 ms, and 43.5 ms are electrical interference.

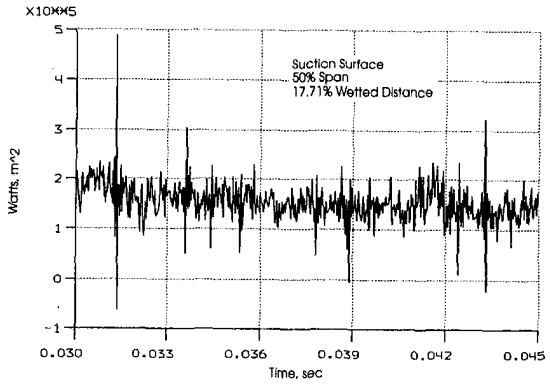

Fig. 9 Heat-flux history during test time

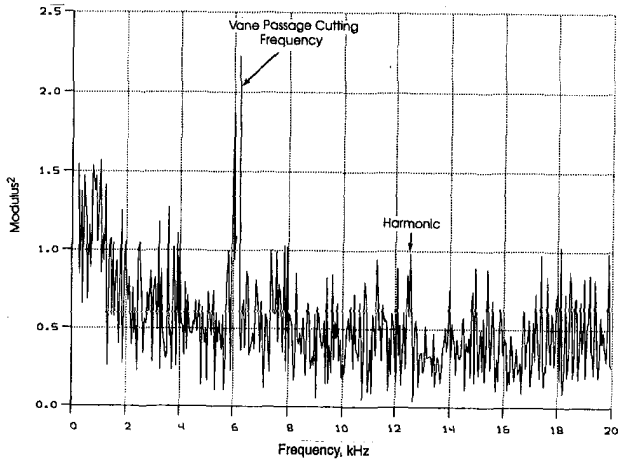

Fig. 10 FFT of blade heat-flux data

Two specific locations were selected at the mid span location on the suction surface of the first-stage blade in order to compare the qualitative behavior of the phase-resolved surface pressure with the surface heat flux; one position in a region of a strongly favorable pressure gradient (approximately 18 percent wetted distance) and a second position in a region of a mildly unfavorable pressure gradient (approximately 47 percent wetted distance). The predicted mid-span pressure distribution is given in Fig. 5 of Dunn et al. (1992) and that figure illustrates that the pressure gradient is mildly favorable over the entire pressure surface, strongly favorable over that portion of the suction surface from 0 to 33 percent wetted distance, and unfavorable from 33 to 100 percent wetted distance on the suction surface. The vane exit Mach number is subsonic (on the order of 0.5 or less). As noted earlier, there are a large number of upstream struts associated with this engine configuration which tend to confuse the issue. However, the FFT of the blade surface-pressure (see Fig. 4) and heat-flux (see Fig. 10) data suggest that the unsteady behavior on the blade for this turbine is dominated by the vane wakes. For these turbine conditions, one would anticipate that the influences of the inviscid flow field would be transmitted through the boundary layer with little or no phase lag and thus one should anticipate the phase-resolved pressure and heat-flux profiles to be qualitatively similar.

Figure 11 is a similar comparison between the phase-resolved heat flux and the phase-resolved surface pressure for a location

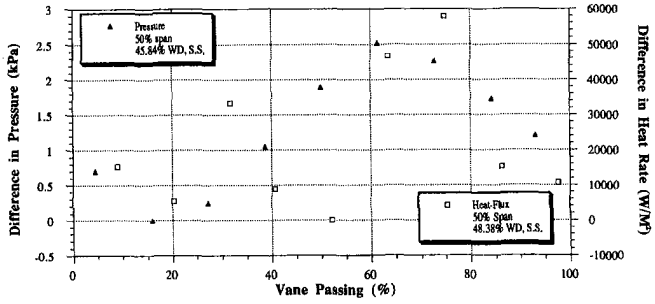

Fig. 11 Comparison of phase-resolved heat flux and surface pressure on the blade at approximately 47 percent wetted distance

a little further along on the blade where the pressure gradient is unfavorable instead of favorable. With the exception of the heat-flux data point at approximately 50 percent of the passage, the two profiles are in qualitative agreement with each other. Comparisons similar to that shown in Fig. 11 were found generally to have a point within the passage that didn't line up to give unequivocal agreement between the two profiles. This is felt to be due to the small reaction of the individual blade rows of the SSME turbine which produces relatively small unsteady effects which, in turn, make resolution of events difficult.

Blade Unsteady Heat-Flux Envelope. Figure 12 presents the unsteady heat-flux envelope for the first blade. This figure presents the maximum minus the minimum heat flux normalized by the stagnation value for the particular run as a function of wetted distance on the blade. Data from all five runs and 10, 50, and 90 percent span are included on this plot. These results were obtained from data like that presented in Fig. 9. The magnitude of the unsteady envelope on the suction surface is relatively independent of location on the blade and reflects the unsteady pressure envelope results presented earlier on Fig. 8. For the pressure surface, the unsteady heat-flux envelope appears to be rather small (by comparison with the suction surface) in the region from 0 to 30 percent wetted distance and then becomes of comparable magnitude from 40 to 70 percent wetted distance. Beyond 70 percent wetted distance on the pressure surface, the magnitude of the unsteady heat-flux envelope is small by comparison to any other location on the blade. Whereas an average value for the unsteady pressure on the suction surface was less than 1 percent, the average of the unsteady heat flux was much larger, being on the order of 10 percent. This result is qualitatively consistent with the results of the measurement program for the Allison turbine that are reported in Rao, et al. (1994).

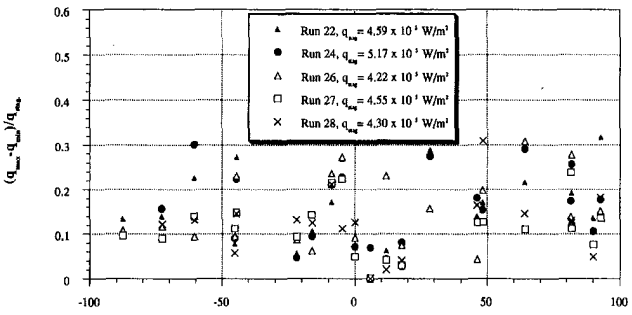

Fig. 12 Unsteady heat-flux envelope on SSME first stage blade

Conclusions

The unsteady envelope of surface pressure and heat flux along with the corresponding phase-resolved (in moving through a vane passage) pressure and heat-flux profiles have been measured for the first blade. The relative magnitude of the heat-flux envelope was found to be significantly larger than the pressure envelope which is consistent with previous measurements.

Measurements obtained at several different blade locations were presented to demonstrate that the ensemble average of the phase-resolved surface pressure data was well defined and the run-to-run variation at a given location on the blade was relatively small.

Representative comparisons between the phase-resolved surface pressure and heat-flux were presented for two locations on the blade suction surface; one in the region of a favorable pressure gradient and the other in a region of an unfavorable pressure gradient. For this subsonic turbine, these two quantities are qualitatively in phase with each other.

Acknowledgments

This research was supported under Grant NAG3-581 and monitored by Dr. Raymond Gaugler and Mr. Kas Civinskas of the NASA Lewis Research Center.

References

Cook, W. J., and Felderman, E. J., 1966, "Reduction of Data From Thin-Film Heat-Flux Gages: A Concise Numerical Technique," *AIAA Journal,* pp. 561–562.

Dunn, M. G., George, W. K., Rae, W. J., Woodward, S. H., Moller, J. C., and Seymour, P. J., 1986, "Heat-Flux Measurements for the Rotor of a Full-Stage Turbine: Part II-Description of Analysis Technique and Typical Time-Resolved Measurements," ASME *Journal of Turbomachinery,* Vol. 108, pp. 98–107. (ASME Paper No. 86-GT-78)

Dunn, M. G., Bennett, W., Delaney, R., and Rao, K., 1992, "Investigation of Unsteady Flow Through a Transonic Turbine Stage: Part II-Data/Prediction Comparison for Time-Averaged and Phase-Resolved Pressure Data," AIAA/SAE/ASME/ASEE 26th Joint Propulsion Conference, Orlando, FL, 1990, AIAA Paper No. 90-2409 ASME *Journal of Turbomachinery,* Vol. 114, pp. 91–99.

Dunn, M. G., Kim, J., Civinskas, K. C., and Boyle, R. J., 1992, "Time-Averaged Heat Transfer and Pressure Measurements and Comparison With Prediction for a Two-Stage Turbine," ASME *Journal of Turbomachinery,* Vol. 116, pp. 14–22, 1994 (ASME Paper No. 92-GT-194).

Dunn, M. G., and Haldeman, C. H., 1994, "Phase-Resolved Surface Pressure and Heat-Transfer Measurements on the Blade of a Two-Stage Turbine," *Unsteady Flows in Aeropropulsion,* ASME AD 40, Ng, W., Fant, D., and Povinelli, L., eds.

Dunn, M. G., Kim, J., and Haldeman, C. H., 1994, "Final Report for NASA Grant NAG3-581-Experimental Measurements and Analytical Analysis Related to Gas Turbine Heat Transfer: Part I: Time-Averaged Heat-Flux and Surface-Pressure Measurements on the Vanes and Blades of the SSME Fuel-Side Turbine and Comparison With Prediction and Part II: Phase-Resolved Surface-Pressure and Heat-Flux Measurements on the First Blade of the SSME Fuel-Side Turbine," CUBRC Final Report No. 640II.

Rao, K. V., Delaney, R. A., and Dunn, M. G., 1994, "Vane-Blade Interaction in a Transonic Turbine, Part I-Aerodynamics and Part II-Heat Transfer," *AIAA Journal of Propulsion and Power,* Vol. 10, No. 3, pp. 305–317.

Vidal, R. J., 1956, "Model Instrumentation Techniques for Heat Transfer and Force Measurements in a Hypersonic Shock Tunnel" Cornell Aeronautical Laboratory Report AD-917-A-1.

High-Frequency Heat Flux Sensor Calibration and Modeling

D. G. Holmberg

T. E. Diller

Mechanical Engineering Department,
Virginia Polytechnic Institute
and State University,
Blacksburg, VA 24061-0238

A new method of in-situ heat flux gage calibration is evaluated for use in convective facilities with high heat transfer and fast time response. A Heat Flux Microsensor (HFM) was used in a shock tunnel to simultaneously measure time-resolved surface heat flux and temperature from two sensors fabricated on the same substrate. A method is demonstrated for estimating gage sensitivity and frequency response from the data generated during normal transient test runs. To verify heat flux sensitivity, shock tunnel data are processed according to a one-dimensional semi-infinite conduction model based on measured thermal properties for the gage substrate. Heat flux signals are converted to temperature, and vice versa. Comparing measured and calculated temperatures allows an independent calibration of sensitivity for each data set. The results match gage calibrations performed in convection at the stagnation point of a free jet and done by the manufacturer using radiation. In addition, a finite-difference model of the transient behavior of the heat flux sensor is presented to demonstrate the first-order response to a step input in heat flux. Results are compared with shock passing data from the shock tunnel. The Heat Flux Microsensor recorded the heat flux response with an estimated time constant of 6 μs, which demonstrates a frequency response covering DC to above 100 kHz.

Introduction

One method of measuring heat flux to or from a surface is to measure the rate of change of temperature of the material. With appropriate transient conduction modeling and material properties, the heat flux that caused the measured temperature history can be determined. The most common method is to assume that the material responds as a one-dimensional, semi-infinite substrate (Scott, 1976; Jones, 1977; Diller, 1993). Because this assumption is only valid for sufficiently short times, its use in short-duration flow facilities is natural. The temperature response is proportional to the inverse of $\sqrt{(k\rho C)}$ of the substrate. The surface temperature measurements are usually made on a low conductivity ceramic substrate to maximize the sensor response for short time measurements. The temperature response on a high conductivity substrate is proportionately smaller.

The use of thin-film resistance gages to measure the required surface temperature history to calculate heat flux is detailed by Schultz and Jones (1973) and has been successfully used for many years. Analog electrical circuits are sometimes used for the conversion of the temperature signal to heat flux, but digital data processing or a combination of the two has also been effectively used (George et al., 1991; Dunn et al., 1986). For use in continuous flow facilities a pre-heated model can be injected into the flow to provide the required transient conditions (O'Brien, 1990). Several groups have used the transient temperature method to measure heat flux in transient flow facilities with applications from gas turbine engines to hypersonic flow (Dunn, 1990; Nicholson et al., 1987; Camci and Arts, 1991; Miller, 1985).

Roberts et al. (1990) used a shock tube to study the transient response of a hot-film sensor mounted in the tunnel wall. The time required for the incident shock to pass over the gage was estimated as 2 μs for the pressure ratios used. Direct measurements of transient heat transfer were made by Hayashi et al. (1989) in a Mach 4 supersonic flow, and by Hager et al. (1993) during the starting transients of a Mach 2.4 flow.

Contributed by the Fluids Engineering Division for publication in the JOURNAL OF FLUIDS ENGINEERING. Manuscript received by the Fluids Engineering Division April 20, 1994; revised manuscript received February 16, 1995. Associate Technical Editor: Wing-Fai Ng.

Baker and Diller (1993) demonstrated a method of calculating surface temperature from time-resolved heat flux measurements. This has the advantage that the effects of electrical noise are diminished because the data processing technique is an integration type process. They used a Heat Flux Microsensor in a low frequency combustion flame to demonstrate the correspondence between the heat flux and temperature signals. The results were within the experimental uncertainties of the sensor calibrations and material property determinations. Holmberg et al. (1994a) demonstrated this method with heat flux and surface temperature measurements for Mach 3 flow in a shock tunnel.

When using heat flux sensors in a high-speed flow, there are two important gage parameters: the gage sensitivity (voltage output/heat flux) and the time response. Neither are easy to measure accurately, particularly in a convective flow environment. A shock tunnel using a supersonic nozzle provides an environment with fast transients, high speed flows, and moderately high heat fluxes. This is ideal for characterizing the transient response of sensors. The present paper documents a method for using shock tunnel data to determine both the heat flux sensitivity and the time response of the Heat Flux Microsensor. The experimental results are compared to a numerical model of the thermal response of the sensor and substrate. The potential for in-situ calibration of heat flux is also examined. Because the individual sensor measurements are not limited by length of time, the sensors once calibrated can be used in any type of flow facility.

Experimental Facilities and Instrumentation

Shock Tunnel Facility. The shock tunnel used for these tests has an 8 ft (2.44 m) driver section and a 20 ft (6.1 m) long driven section; both sections made of 3 in. inside diameter steel pipes. A Mach 3 two-dimensional supersonic nozzle is attached to the end of the driven section to obtain supersonic flow. The driver section of the shock tunnel is filled with compressed gas from a bottle, with the driven section, for the present research, left open to the atmosphere. A mylar diaphragm is sized to break at a specified driver gas pressure, which allows the high pressure gas to expand into the low pressure driven section, producing a traveling shock wave.

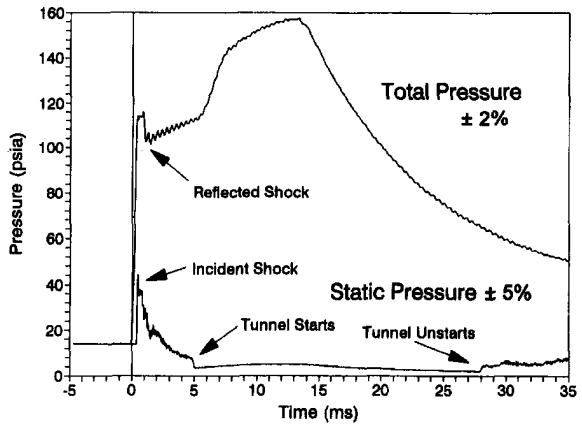

Fig. 1 Total and static pressures for shock tunnel test

Upstream total and exit static pressure measurements for a sample run with an air driver at 210 psig (1.45 MPa) and 300 K are given in Fig. 1. The incident shock wave is the initial spike in the pressure trace at 0 ms. Unsteady wave formation and transmission in the nozzle persist until about 5 ms at which time the nozzle starts. The region of low static pressure in the nozzle defines the time of supersonic flow. The nozzle unstarts at 28 ms and the remaining flow is subsonic. Calculations and measurements of the total temperature in the nozzle indicate an initial total temperature of approximately 600 K.

For the present tests, both air and helium were used as driving gases. For a fixed driver gas to driven gas pressure ratio a lighter driver gas with a larger specific heat yields a faster and stronger incident shock wave. Thus, helium was used both to produce a faster passing shock for time response estimation, as well as a stronger heat flux signal compared to an air driver.

Shock Tunnel Instrumentation and Data Acquisition. The heat transfer measurements were carried out with a Heat Flux Microsensor (HFM-3) manufactured by Vatell Corp. The HFM consists of two separate sensors in close proximity to independently measure the heat flux and surface temperature at one location. The heat flux sensor, as described by Hager et al. (1991), uses a differential thermopile across a thin thermal resistance layer and is made with microfabrication techniques. The sensor outputs a voltage directly proportional to the heat flux. A schematic of the sensor pattern is shown in Fig. 2. The heat flux is measured using the output of 280 copper-nickel thermocouple pairs arranged above and below a 0.8 μm layer of silicon monoxide. The size of the heat flux sensor on the surface is approximately 4 mm by 6 mm.

A radiation calibration was performed by the manufacturer according to the method outlined by Kidd (1992) using a 200 watt tungsten filament lamp with a highly polished ellipsoidal reflector. A circular foil heat flux gage that was calibrated at AEDC by the same method was used as the standard. The sensitivity was reported with an uncertainty of ± 10 percent as

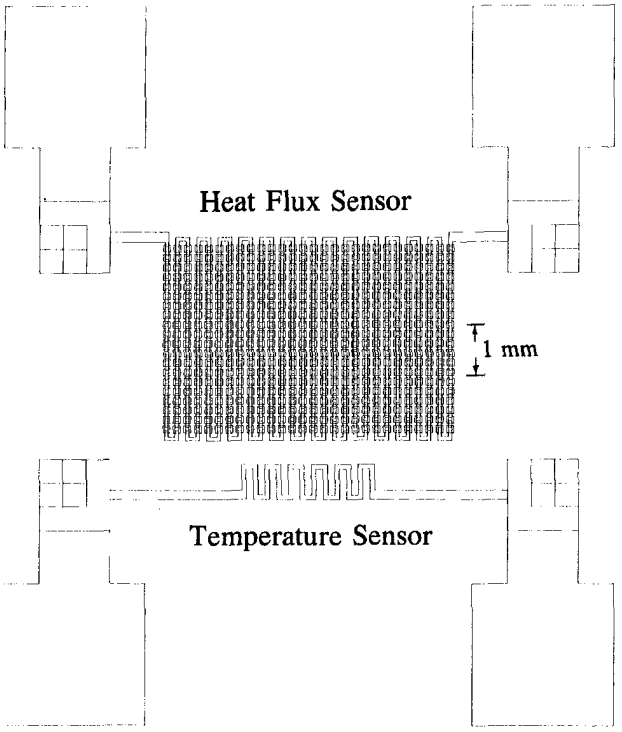

Fig. 2 Detail of HFM pattern

$$S = \frac{E_q}{q} = 50.0\ \mu\text{V}/(\text{W}/\text{cm}^2) \qquad (1)$$

where E_q is the output voltage from the sensor and q is the heat flux. A separate convection calibration was performed using an impinging air jet with the sensor placed at the stagnation point perpendicular to the jet as detailed by Holmberg et al. (1994a). Using a measured heat transfer coefficient for this configuration of 213 W/m^2·K produced a sensitivity of 49.2 μV/(W/cm^2) ± 5 percent.

The second HFM sensor, also shown on Fig. 2, is a platinum resistance element which provides an independent measure of the surface temperature. A 0.1 mA current is supplied to the sensor through an amplifier unit supplied with the sensor to provide the resistance measurement. The manufacturer's calibration to convert the voltage signal to temperature T_s is

$$T_s - T_i = (28.0°\text{C}/\text{mV})E_T \qquad (2)$$

where E_T is the unamplified voltage, and T_i is an initial reference temperature. The estimated uncertainty in the calibration coefficient in Eq. (2) was reported as ± 4.0 percent. The corresponding error in the measurement of the temperature change, $T_s - T_i$, is ± 4.3 percent.

The sensor was fabricated on a 1.0 in. (2.5 cm) diameter, 0.625 cm thick aluminum nitride substrate by a sputtering pro-

Nomenclature

C = specific heat, J/kg·K
E_q = heat flux sensor output, V
E_T = temperature sensor output, V
k = thermal conductivity, W/m·K
n = number of thermocouple pairs in differential thermopile
q = heat flux, W/cm^2
q_{calc} = heat flux calculated from surface temperature, W/cm^2
q_{exp} = measured heat flux, W/cm^2
q_{max} = maximum heat flux, W/cm^2
S = sensitivity of Heat Flux Microsensor, μV/(W/cm^2)
t = time, s
T_i = reference for temperature sensor, °C
T_0 = initial substrate temperature, °C
T_s = surface temperature, °C
T_{calc} = surface temperature calculated from heat flux, °C
T_{exp} = measured surface temperature, °C
T_{num} = surface temperature calculated from numerical model, °C
ρ = substrate density, kg/m^3
σ = thermocouple sensitivity, μV/°C
τ = first-order time constant, μs

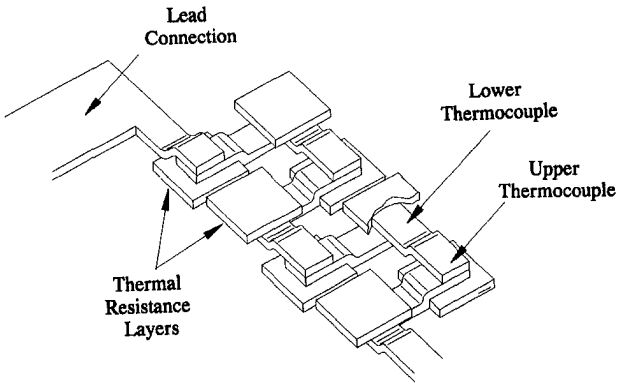

Fig. 3 Heat flux thermopile construction

cess. The thermal properties of the substrate were measured by independent laboratories (Holometrix and Anter Laboratories) as $k = 165$ W/m·K, $C = 713$ J/kg·K, and $\rho = 3290$ kg/m^3. The corresponding value of $\sqrt{(k\rho C)}$ is 19,670 in SI units, with an uncertainty calculated from the reported individual measurements of ± 5 percent. All of these values are close to those of the aluminum nozzle where the gage is mounted. Four pins were countersunk into the substrate to bring the surface temperature and heat flux signals from the surface to the tunnel exterior without disturbing the flow. The HFM was mounted flush with the bottom surface of the shock tunnel, near the exit plane of the nozzle.

For the purpose of gage sensitivity analysis, two channels of data were sampled using an HP 3562A Dynamic Signal Analyzer. Heat flux and temperature signals from the HFM were sampled at different frequencies from 25 kHz for 80 ms up to 250 kHz for 8 ms. Simultaneously, a LeCroy 6810 Waveform Digitizer was used to sample the HFM at a 1 μs interval. The faster sample rate allowed better resolution of the incident shock for time response estimation.

Data Conversion, Digital Data Processing Routine. To convert measured heat flux to the corresponding calculated surface temperature a one-dimensional, semi-infinite model of the heat transfer in the substrate was used. The substrate was assumed to initially be at a uniform temperature, T_0. Baker and Diller (1993) developed a method for calculating time-resolved surface temperature from the measured heat flux signal. Using a Green's function approach, individual heat flux impulse solutions were combined to include a series of heat flux data points.

$$T_s(t_n) - T_0 = \frac{2}{\sqrt{\pi}\sqrt{k\rho C}} \sum_{j=0}^{n-1} q_j \left[\sqrt{t_n - t_j} - \sqrt{t_n - t_{j+1}} \right] \quad (3)$$

A computer code was written making use of this equation to process the E_q signal from the HFM. In addition to converting heat flux, the code calculates a heat flux sensitivity based on each data set by minimizing the sum of the errors between individual time values of the measured surface temperature, T_{exp} and the temperature calculated from the heat flux, T_{calc}. By this method, an independent measure of gage sensitivity can be obtained for each data sample (one test run of the shock tunnel). This is equivalent to obtaining an in-situ calibration of the heat flux sensor while tests are being performed.

Numerical Model of HFM

To provide an analytical basis for the heat flux sensor and substrate thermal response, a numerical model was developed. A close-up of the sputtered gage surface can be seen in Fig. 3. The gage consists of resistance layer (silicon monoxide) square pads interconnected with copper and nickel leads forming thermocouple junctions above and below alternating pads. The numerical model is a one-dimensional implicit finite-difference code which has fifteen nodes across the 1.4 μm of sputtered gage thickness, shown as a cross-section of the pads in Fig. 4. There are ten nodes (not shown) across the 0.8 μm thick resistance layer. Below the gage are 50 nodes with increasing spacing across the quarter inch thick substrate of aluminum nitride. As can be seen in Fig. 4, the sputtering pattern for HFM-3 consists of two separate layering orders. Thermocouple junctions alternate from top to bottom of the resistance layer, rather than being present on the top and bottom of each resistance layer pad as in previous sensors (Hager et al., 1991).

The approximate dimensions (thicknesses of layers based on manufacturer given sputtering rates), are shown in Fig. 4, where the width to thickness ratio of an individual pad is 230 μm/1.4 μm = 164. Consequently, a one-dimensional model was considered justified. Because of the different layering orders for the alternating pads, two separate node networks were set up across the gage itself, but joined at the substrate surface to become one. The model assumed an adiabatic condition on the back surface of the substrate, which is valid for time less than 0.15 seconds for the substrates used (Baker and Diller, 1993).

The material properties used for the aluminum nitride substrate were as given earlier. Properties for all of the sputtered layers (except SiO) were taken as the same as the bulk properties. The model (and gage itself) is most sensitive to the SiO resistance layer properties, which were estimated based on the measured sensor response.

The program solves for the temperature profile across the sensor and through the substrate at each time step. The theoretical voltage output of the sensor can then be calculated from the temperature difference between the thermocouple junctions above and below the thermal resistance layer

$$E_q = n\sigma\Delta T \quad (4)$$

where n is the number of thermocouple pairs (280) and σ is the thermoelectric output, which was taken as 21.5 μV/°C for copper and nickel. This allows comparison of input heat flux to heat flux output from the modeled sensor. In addition, three surface temperature versus time traces can be compared: the experimental temperature, T_{exp}, the temperature from the numerical model, T_{num}, and the temperature from the converted experimental heat flux signal, T_{calc}.

Results

As an example of the conversion method, the heat flux and temperature signals for one of the tests (air driver at a pressure of 1.65 MPa) are presented in Fig. 5 using the manufacturer's calibrations in Eqs. (1) and (2). Notice the initial passing shock and accompanying unsteadiness before the tunnel starts at 5 ms. The tunnel unstarts at 35 ms (refer back to Fig. 1 for pressure traces of a typical run at these conditions). While the heat flux is initially strong, it becomes negative by 40 ms. The corre-

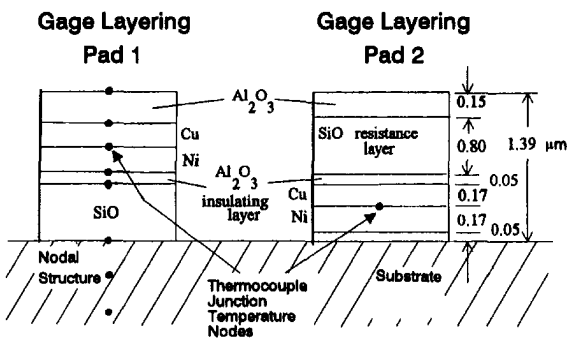

Fig. 4 Numerical model of heat flux sensor

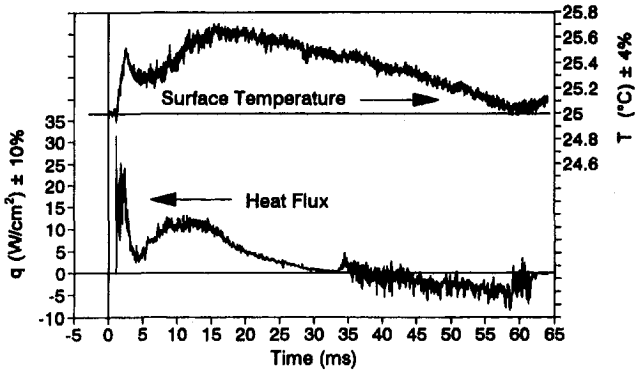

Fig. 5 Heat flux and surface temperature for shock tunnel

sponding temperature change is very small because of the high thermal conductivity of the substrate and the short duration of the flow. Consequently, the effects of electrical noise on the signal are noticeable, and the uncertainty due to it (±0.05°C) is in addition to the 4 percent bias error (from calibration) indicated on the Fig. 5 axis label. The high-frequency fluctuations seen on the heat flux trace are actual flow phenomena, with the signal to noise ratio being much higher than for the temperature signal.

The HFM heat flux signals were converted to the corresponding surface temperature values using equation (3). Comparison of the actual gage surface temperature (T_{exp}) with the calculated gage surface temperature (T_{calc}) is shown in Fig. 6. There is good agreement between T_{exp} and T_{calc}, demonstrating the accuracy of the data processing based on the one-dimensional model. The values of T_{calc} in the 5 to 15 ms range rising slightly above the values of T_{exp} was a common result, although not always present. The values of T_{calc} dropping below T_{exp} past 25 ms was also observed frequently. Although not seen in Fig. 6, longer data sets show that the disagreement between T_{calc} and T_{exp} shown in Fig. 6 does not continue to diverge, but in fact the agreement in the two curves is excellent at longer times. The agreement holds for approximately half a second. A reason for the disagreement at short times (first 50 ms) is possibly related to the radiation from the high temperature flow to the cold (room temperature) sensor. Neither the aluminum-nitride substrate nor the HFM absorb all of the radiation at the surface, which the conversion model assumes.

As evidence of the strength of the conversion methodology of going from heat flux to temperature, note that the temperature curve calculated from the heat flux is much smoother than the measured temperature curve because of the integration process represented by Eq. (3). Comparison of the actual heat flux (q_{act}) with the calculated heat flux (q_{calc}) can also be used to determine S, but q_{calc} is an extremely noise curve. Because heat flux is proportional to the time rate of change of temperature, the effects of electrical noise are increased when converting from temperature to heat flux because the data processing is a differentiation type process (Baker and Diller, 1993).

Heat Flux Sensitivity Calibration. By comparing the temperature and heat flux signals from the Heat Flux Microsensor (HFM) processed according to the digital-data-processing routine presented above, an independent measure of gage sensitivity S, can be found. This measure of S is particularly valuable because it is determined in the actual high speed flow and high temperature environment of the test.

There are several conceptual issues that underlie the calibration method. Instead of relying on a known input heat flux as the standard for comparison, the change in temperature of the surface is used with the substrate properties as the standard. Because the two sensors are located close together physically on the surface, it is assumed that they measure the same thermal phenomena, as demonstrated in Fig. 6. The advantages of this calibration method are that temperature is easier to calibrate than heat flux and calibration of the heat flux sensor can be checked during the start of every experiment. The uncertainty of the method is the combination of the uncertainties of the heat flux and temperature measurements plus the uncertainty of the substrate properties, which in this case is estimated as a total uncertainty in S of ± 8 percent.

Heat flux sensitivities were calculated for 12 separate shock tunnel runs. The driver pressures used were set between 1.21 and 2.07 MPa, using helium or air. Run time lengths varied from 8 to 64 milliseconds. All data sets were 2048 points in length. Raw voltages were input to the conversion program described earlier, and the sensitivity that minimized the error between the resulting T_{exp} and T_{calc} curves (such as shown in Fig. 6) was found for each run. An average value for the 12 runs of S = 49.3 μV/(W/cm^2) was obtained with a 95 percent confidence interval of ± 12 percent. This value is in excellent agreement with the manufacturer supplied radiation calibration of S = 50.0 μV/(W/cm^2) and the value obtained in convection calibration of S = 49.2 (μV/W/cm^2). The confidence interval was higher than the expected uncertainty of the measurements, which was attributed to noise in the temperature signal. To minimize this effect, an average value of many data points prior to tunnel startup was used as the initial T_0 upon which the converted heat flux signal T_{calc} was built. In order to have accurate sensitivities calculated from the data, input signals with high signal to noise ratios (aided by high heat fluxes), and high sampling frequencies (to get more data points) are necessary. As this implies, the shorter shock tunnel data sets (8 ms) had higher uncertainties than the longer ones (64 ms).

It should be noted that the accuracy of the data conversion routine is limited to short run-times due to the semi-infinite conduction assumption. The resulting sensitivity and the individual measurements of temperature and heat flux, however, are valid for any length of time.

Numerical Model. The heat flux sensitivity, S, found from the shock tunnel results was used to calculate the appropriate thermal conductivity of the silicon monoxide layer in the sensor. The value obtained was 0.97 W/m·K, which is lower than the assumed bulk value of 1.38 W/m·K. It is much higher than the value reported by Hager et al. (1991) for sputtered silicon monoxide of 0.1 W/m·K. Properties of sputtered materials are known to be highly dependent on the conditions used during the sputtering process.

Because of the flexibility of the numerical model, a wide range of input signals can be used. One important test is to

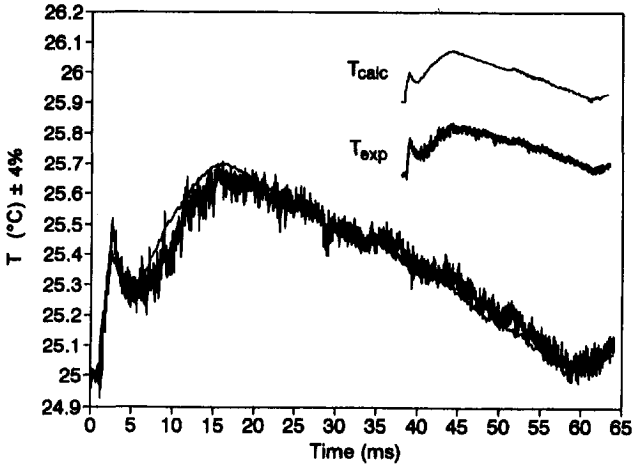

Fig. 6 Calculated and experimental surface temperature

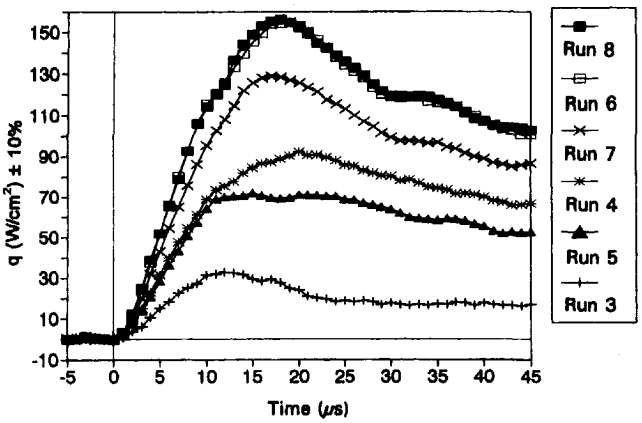

Fig. 7 HFM record of passing shocks in shock tunnel

determine if the sensor alters the measurement of heat flux. To model this situation, measured heat flux data (Fig. 5) were used as input to the numerical model. The heat flux sensor output from the numerical model, q_{num}, differed by less than 1 percent from the input as a result of high-frequency attenuation effects. Therefore, the sensor should not alter the measurement over these time scales. It also demonstrates that the HFM outputs a heat flux signal directly proportional to the actual surface heat flux.

Likewise, the resulting surface temperature, T_{num}, predicted by the model can be compared with the HFM temperature signal, T_{exp} shown in Fig. 5. The temperature at the surface of the substrate below the heat flux gage was found to agree nearly exactly with T_{calc} in Fig. 6 (less than 1 percent difference). This indicates that the one-dimensional numerical model of the substrate matches the analytical representation in Eq. (3) and can be used to convert heat flux to surface temperature.

The temperature at the top surface of the heat flux sensor was also compared with the temperature at the substrate surface. The difference in temperature was found to be a maximum of 0.1°C at the point of maximum heat flux (q = 20 W/cm^2 on Fig. 5). This difference is negligible for most applications, and is a small fraction of a percent of the total temperature difference from the fluid to the surface. This illustrates the extremely small thermal disruption due to the sensor presence.

Frequency Response Estimation. Previously, a Bragg cell and laser were used to create a step change of heat flux for estimating the time response of a thin-film heat flux sensor (Hager et al., 1991). One problem with any radiation measurement, however, is that a coating of high absorptivity is required over the sensor to insure uniform absorption of the heat flux. Unfortunately, because the coating is typically thicker than the sensor itself, the time response is severely altered. One big advantage of the shock tunnel is that an absorption coating is not required because the heat transfer is based on convection. The incident shock provides a sharp change in the thermal and flow properties as the shock passes over the wall position of the gage in about 5 μs.

Figure 7 shows six different passing shock records. These traces are expansions of the incident shock passings of the same data used in sensitivity estimation. The scale has been expanded from milliseconds to microseconds and the individual data points are marked for the 1 MHz sampling rate. Note the magnitude of the heat flux pulses. Also, there is no initial dip in heat flux as observed by Roberts et al. (1990). This is confirmation that the dip was an artifact of using a hot-film sensor driven by an anemometer.

The response of the gage to a step input in heat flux was simulated using the numerical model. Results showed a nearly first-order exponential rise (within 10 percent), with no evidence of overshoot in the gage response. Consequently, a first-order model was used to estimate a time constant for the sensor from the passing shock data.

$$\frac{q}{q_{max}} = 1 - e^{-t/\tau} \tag{5}$$

Results based on Fig. 7 show that the passing shocks ramp up in approximately 5 μs as the shock passes over the physical space of the gage, followed by a segment of roughly constant heat flux. To model the passing shock as a step in heat flux, average heat flux values were estimated for the first 10 μs for different runs. These values were used for q_{max} in Eq. (5) yielding an approximate thermal time constant of τ = 6 μs for the data in Fig. 7.

Based on this result, the values of the parameters in the numerical model were adjusted. Originally, the numerical model used the bulk properties of silicon dioxide because no properties of silicon monoxide were available. This resulted in a calculated time constant of τ = 2 μs. To correspond to the experimentally estimated 6 μs time constant, the product of ρC was increased from 1.16 J/cm^3·K (bulk value) to 18.0 J/cm^3·K. Such large differences between properties of sputtered and bulk materials are common (Goodson et al., 1994). It is important to note that this difference only affects the theoretical response of the sensor to high-frequency input (>100 kHz).

The combined results of the numerical model and passing shock experiments demonstrate the first-order response characteristics of the HFM, as well as a method for estimating frequency response of a heat flux sensor in a convective environment.

Conclusions

A method has been developed for determining heat flux sensitivity for the Heat Flux Microsensor (HFM) from shock tunnel test data. Using a simple data processing code, it was demonstrated how measured heat flux can be converted to surface temperature and compared with the measured temperatures. By minimizing the difference between these two data sets, an independent measure of sensitivity can be determined for each test run. Values from 12 runs were compared with sensitivity calibrations performed by other means. The results were well within the calibration uncertainties.

A numerical model of the heat flux sensor and substrate was used to predict the heat flux response of the sensor to an actual heat flux signal. In addition, the transient surface temperature predicted by the model agrees with the experimental surface temperature. The model also shows first-order characteristics in response to a step input of heat flux. Analysis of heat flux resulting from passage of the incident shock gave an approximate first-order time constant for the heat flux sensor of 6 μs. The data and model, therefore, support a frequency response better than 100 kHz, with a flat response across the entire bandwidth.

Because the high speed and high temperature flow in a shock tunnel is similar to the environment often encountered in heat flux testing, the sensitivities and time response determined in the shock tunnel are particularly appropriate.

Acknowledgments

The authors gratefully acknowledge support for this research from the U. S. Air Force Office of Scientific Research under the supervision of Major Dan Fant, program manager.

References

Baker, K. I., and Diller, T. E., 1993, "Unsteady Surface Heat Flux and Temperature Measurements," ASME Paper No. 93-HT-33.

Camci, C., and Arts, T., 1991, "Effect of Incidence on Wall Heating Rates and Aerodynamics on a Film-Cooled Transonic Turbine Blade," ASME *Journal of Turbomachinery,* Vol. 113, pp. 493–501.

Diller, T. E., 1993, "Advances in Heat Flux Measurements," *Advances in Heat Transfer,* Vol. 23, J. P. Hartnett et al., eds., Academic Press, Cambridge, pp. 279–368.

Dunn, M. G., George, W. K., Rae, W. J., Woodward, S. H., Moller, J. C., and Seymour, P. J., 1986, "Heat-Flux Measurements for a Full-Stage Turbine: Part II-Description of Analysis technique and Typical Time-Resolved Measurements, ASME *Journal of Turbomachinery,* Vol. 108, pp. 98–107.

Dunn, M. G., 1990, "Phase and Time-Resolved Measurements of Unsteady Heat Transfer and Pressure in a Full-Stage Rotating Turbine," ASME *Journal of Turbomachinery,* Vol. 112, pp. 531–538.

George, W. K., Rae, W. J., Seymour, P. J., and Sonnenmeier, J. R., 1991, "An Evaluation of Analog and Numerical Techniques for Unsteady Heat Transfer Measurement with Thin Film Gauges in Transient Facilities," *Experimental Thermal and Fluid Science,* Vol. 4, pp. 333–342.

Goodson, K. E., Flik, M. I., Su, L. T., and Antoniadis, D. A., 1994, "Prediction and Measurement of the Thermal Conductivity of Amorphous Dielectric Layers," ASME *Journal of Heat Transfer,* Vol., 116, pp. 317–324.

Hager, J. M., Simmons, S., Smith, D., Onishi, S., Langley, L. W., and Diller, T. E., 1991, "Experimental Performance of a Heat Flux Microsensor," ASME *Journal of Engineering for Gas Turbines and Power,* Vol. 113, pp. 246–250.

Hager, J. M., Onishi, S., Langley, L. W., and Diller, T. E., 1993, "High Temperature Heat Flux Measurements," *AIAA Journal of Thermophysics,* Vol. 7, pp. 531–534.

Hayashi, H., Aso, S., and Tan, A., 1989, "Fluctuation of Heat Transfer in Shock Wave/Turbulent Boundary-Layer Interaction," *AIAA Journal,* Vol. 27, pp. 399–404.

Holmberg, D. G., Mukkamala, Y. S., and Diller, T. E., 1994a, "Shock Tunnel Evaluation of Heat Flux Sensors," AIAA Paper No. 94-0730.

Holmberg, D., Reid, T., Kiss, T., Moses, H. L., Ng, W. F., and Diller, T. E., 1994b, "Effects of Shock Wave Passage on Heat Transfer in a Transonic Turbine Cascade," ASME Paper No. 94-GT-179.

Jones, T. V., 1977, "Heat Transfer, Skin Friction, Total Temperature, and Concentration Measurements," *Measurements of Unsteady Fluid Dynamic Phenomena,* B. E. Richards, ed., Hemisphere Publishing, Washington DC, pp. 63–102.

Kidd, C. T., 1992, "High Heat Flux Measurements and Experimental Calibrations/Characterizations," NASA CP 3161.

Miller, C. G., 1985, "Refinement of an 'Alternate' Method for Measuring Heating Rates in Hypersonic Wind Tunnels," *AIAA Journal,* Vol. 23, pp. 810–812.

Nicholson, J. H., Forest, A. E., Oldfield, M. L. G., and Schultz, D. L., 1987, "Heat Transfer Optimized Turbine Rotor Blades-An Experimental Study Using Transient Techniques," ASME *Journal of Engineering for Gas Turbines and Power,* Vol. 106, pp. 173–182.

O'Brien, J. E., 1990, "A Technique for Measurement of Instantaneous Heat Transfer in Steady-Flow Ambient-Temperature Facilities," *Experimental Thermal and Fluid Science,* Vol. 3, pp. 416–430.

Roberts, A. S., Jr., Ortgies, K. R., Gartenberg, E., and Caraway, D. L., 1990, "Convective Response of a Wall-Mounted Hot-Film Sensor in a Shock Tube," *International Symposium on Nonsteady Fluid Dynamics,* J. A. Miller and D. P. Telionis, eds., ASME, N.Y., pp. 253–258.

Schultz, D. L., and Jones, T. V., 1973, "Heat Transfer Measurements in Short Duration Hypersonic Facilities," AGARDograph 165.

Scott, C. J., 1976, "Transient Experimental Techniques for Surface Heat Flux Rates," *Measurements in Heat Transfer,* E. R. G. Eckert and R. J. Goldstein, eds., McGraw-Hill, New York, pp. 375–396.

The Ducted Tip—A Hydrofoil Tip Geometry With Superior Cavitation Performance

S. I. Green

S. Z. Duan

Department of Mechanical Engineering,
University of British Columbia,
Vancouver, Canada V6T 1Z4

A novel hydrofoil design, consisting of a small diameter flow-through duct affixed to the tip, has been studied. The tip vortex cavitation inception index, σ_i, of this hydrofoil geometry is about a factor of 2 lower than that of a conventional rounded hydrofoil tip. This inception improvement comes with little associated performance penalty. For angles of attack greater than 8 deg the noncavitating lift-drag ratio is actually superior to that of an unducted hydrofoil of equal span, although with lower wing loadings the hydrofoil performance is diminished by application of the ducted tip. The ducted tip is effective at reducing the tip vortex inception index because, in contrast with the rounded tip, for which vorticity in the Trefftz plane is confined to a line, the ducted tip shed vorticity at the trailing edge is distributed over a line and circle. Distributing the vorticity in this fashion causes the trailing vortex to roll up less tightly, and hence have a higher core pressure and lower σ_i, than a conventional hydrofoil tip. It is also suspected that the interaction at the microscale level between the flow through the duct, and the flow around it, makes the vortex core size larger, and therefore σ_i smaller. The ducted tip design has many potential marine applications, including to ship and submarine propellers, submarine control fins, and ship rudders.

1 Introduction

Wherever a lifting surface terminates in a fluid, a tip vortex is formed. This tip vortex is almost always an important, and often a central, feature of the flowfield.

1.1 Motivation for Tip Vortex Research. Arguably, the four most important flows in which tip vortices play a central role are the following plane interaction problem, helicopter blade-vortex interaction, airplane wing lift/drag inefficiency, and propeller/hydrofoil tip vortex cavitation.

In the following plane problem, the tip vortices generated by one aircraft may be sufficiently strong that a following plane accidentally entering into one of the vortices experiences a loss of control. This accidental interaction is most likely to occur during aerial refueling and over airport runways. Critchley (1991) has documented that serious incidents involving such interactions occur at an average rate of 9 per year at Heathrow airport! The cost of maintaining sufficient plane separation distances on landing to limit the frequency of such hazardous interactions is about $10 million annually for every major airport (Winter, 1991).

Helicopter rotor blades generate strong tip vortices. If the helicopter is hovering, following rotor blades will pass through the tip vortex generated by leading blades. In passing through the tip vortex, the following blade experiences large fluctuating forces (due to the unsteady aerodynamic loading) that can cause premature rotor blade fatigue and excessive blade noise (Poling et al., 1989).

Tip vortices are also significant because they represent substantial lifting inefficiencies. The downwash associated with wing tip vortices causes aerodynamic induced drag. Induced drag on wings is a particularly salient issue. Approximately 35 percent of the drag on a typical aircraft is lift induced drag (Webber and Dansby, 1983). Due to the small aspect ratio of marine propellers, induced drag on propellers is likely to be a greater percentage of the overall drag than in aeronautical applications. The potential savings to be reaped by reducing airplane induced drag, even fractionally, are staggering—roughly $100 million/year worldwide for each 1 percent induced drag reduction.

Finally, and of greatest relevance in terms of this article, is the tendency for tip vortices generated in marine applications to cavitate even at elevated inception indices. The reason for the high values of σ_i may be traced to the fact that the vortical motion is particularly strong (large U_θ/V_∞) in tip vortices. In order to sustain these large tangential velocities (and hence extremely high centripetal accelerations), there exists a large radial pressure gradient from the vortex core to the surrounding fluid. If the freestream pressure is low enough, or the tangential velocity is high, the pressure in the vortex core will locally fall below the water vapour pressure and cavitation may occur.

1.2 Review of Previous Tip Vortex Research. The literature on tip vortices is very large—over 1000 papers have been published in the field (Green, 1994). Only those contributions having a direct bearing on the research described in this paper will be summarized below. We begin with a discussion of single phase flow results.

It has now been well established that trailing vortices generated by wings roll up exceptionally quickly. In general, roll up is complete, i.e., the tangential velocity field is virtually independent of downstream distance, 1–2 chords downstream of the trailing edge of an airfoil (Shekariz et al., 1992, Stinebring et al., 1991, Green and Acosta, 1991). In contrast with the virtual invariance of the tangential velocity distribution in the axial direction, the axial velocity distribution in general falls markedly with downstream distance. For example, Pauchet et al. (1993) have measured a drop in vortex core axial velocity from $2.5V_\infty$ to $1.5V_\infty$ within two chord lengths downstream of a particular hydrofoil. Reynolds number also has a much more profound effect on axial velocity than it does on tangential velocity (Green and Acosta, 1991).

The precise geometry of the wing that generates the tip vortex also has a substantial influence on the single phase flow charac-

Contributed by the Fluids Engineering Division for publication in the JOURNAL OF FLUIDS ENGINEERING. Manuscript received by the Fluids Engineering Division February 8, 1994; revised manuscript received September 28, 1994. Associate Technical Editor: R. Arndt.

teristics. Changing simply the airfoil section shape (e.g., from an NACA 0020 to an NACA 16020), while keeping the wing planform constant, can change dramatically the single phase tip vortex flow (Pauchet et al., 1993). Similarly, changing the wing planform has a marked influence on the tip vortex. For example, elliptic wing planforms tend to behave quite differently from rectangular planforms (e.g., compare Fig. 4 of Arndt et al. (1991) with Fig. 1 of Green and Acosta (1991). Changing the wing tip shape and even roughness (Green et al., 1988, Stinebring et al., 1991) can also dramatically alter the tip vortex.

We now extend the discussion of tip vortices to include cavitation observations. Platzer and Souders (1979) is a good, though now somewhat dated, review of tip vortex cavitation knowledge.

Cavitation inception generally occurs in the region immediately downstream, to as far as two chords downstream, of the generating wing (Arndt et al., 1991, Maines and Arndt, 1993, Stinebring et al., 1991, Green, 1991). Inception is generally highly unsteady, occurring first at one location and subsequently up or downstream from it. Upon further reducing the flow cavitation number below σ_i, a long portion of the tip vortex cavitates. These observations are consistent with the known minimum of vortex core pressure near the hydrofoil trailing edge (owing to rapid rollup), and with the small axial pressure gradient along a tip vortex centerline (resulting from the small variation in U_θ with downstream distance). The magnitude of the inception index in general correlates well with $-\bar{c}_p$ in the vortex core (Fruman et al., 1991), although there is evidence that unsteadiness in the flow may cause σ_i to be raised above $-\bar{c}_p$ (Green, 1991, Arndt and Keller, 1992).

Tip cavitation inception is highly dependent on small details of the flow near the tip. Stinebring et al. (1991) and McCormick (1962) have shown that merely roughening the pressure surface tip region of a hydrofoil substantially reduces σ_i. Drilling small holes in a hydrofoil from the pressure to the suction surfaces at the tip also reduces σ_i (Arakeri et al., 1985, Sharma et al., 1990). Recently, Chahine et al. (1993) have shown that injection of modest amounts of Polyox solution (a viscoelastic polymer) into a propeller tip vortex can, under optimum conditions, reduce the cavitation inception index by up to 35 percent. They attribute this reduction to a significant thickening of the vortex core caused by the viscoelasticity of the solution. The dependence of tip vortex σ_i on small details of the tip flow is congruent with the known sensitivity of the single phase tip flow to the same details.

There has been fairly heated debate about the exact dependence, and reason for the dependence, of σ_i on Reynolds number. In the now classical work in the field, McCormick (1962) found that σ_i varies as $\mathrm{Re}^{0.35}$. He attributed this Reynolds number dependence to the fact that the size of the trailing vortex core, and hence the inception index for given vortex circulation, is related to the wing boundary layer thickness. Stinebring et al. (1989) have corroborated this hypothesis by measuring the trailing vortex core radius at constant lift coefficient. They found the core radius is proportional to $\mathrm{Re}^{0.26}$, which implies a reduction in core pressure with increasing Re. Falcao de Campos et al. (1989) have observed virtually no dependence of σ_i on Re. In contrast, Pauchet et al. (1993) and Maines et al. (1993) have observed the $\mathrm{Re}^{0.35}$ dependence (Maines et al. use the exponent 0.4 on the Reynolds number).

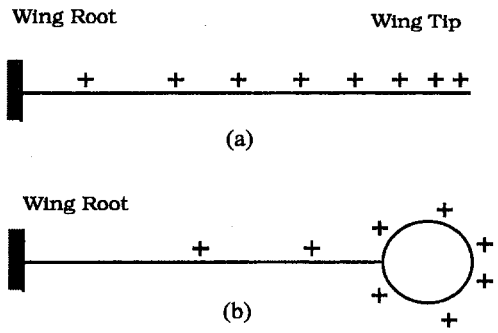

Fig. 1 Shed vorticity in the Trefftz plane from (*a*) conventional and (*b*) ducted tip wings

The size and quality of freestream nuclei also has a substantial impact on σ_i. Arndt and Keller (1992) have measured a doubling of σ_i when the freestream fluid is changed from "strong" water (few and small nuclei) to "weak" water (many, large nuclei).

In summary, the single phase flow in tip vortices is highly complex. The flow, which is highly unsteady, is a function of not merely the wing lift coefficient, but also of the wing planform shape, wing tip shape and roughness, flow Reynolds number (and presumably Mach number too) and wing airfoil section. The cavitating tip vortex flow is much more complex still, depending on all of the above variables and also on the number and size of freestream nuclei.

2 The Ducted Tip Wing Geometry

The tip vortex inception results described in Section 1.2 are both discouraging, in that they reveal our ignorance of tip vortex cavitation, and encouraging, because they imply that we can modify the tip inception index of a wing through simple means.

This paper documents one successful tip cavitation inception delay device—the ducted tip. Before discussing our experimental studies of the ducted tip geometry, we begin with a brief explanation of the rationale for this novel geometry.

As a consequence of Helmholtz vortex laws, the total shed circulation from a wing is essentially established once the wing lift is specified. Therefore, the only way to modify the tip vortex core pressure (and thus σ_i) is to redistribute this shed circulation. In particular, the less concentrated the shed circulation from a wing, the larger the tip vortex core will be, and hence the lower its inception index.

A conventional planar wing sheds (in theory, see e.g. Milne-Thomson (1958)) a line of vorticity in the Trefftz plane (Fig. 1(*a*)). Any wing with an elliptical or near elliptical loading

Nomenclature

c = wing chord [m]
C_D = DRAG FORCE/$0.5\rho V_\infty^2 S$ [1]
C_L = LIFT FORCE/$0.5\rho V_\infty^2 S$ [1]
$\bar{c}_p = \bar{p} - p_\infty/0.5\rho V_\infty^2$ = time mean pressure coefficient [1]
DAC = dissolved air content of water [ppm]
$\bar{p}$ = local time mean pressure [P_a]
p_i = freestream pressure of cavitation inception [P_a]
p_v = vapor pressure of water [P_a]
p_∞ = freestream pressure [P_a]
r = radial distance from vortex centerline [m]
Re = $V_\infty c/\nu$ = Reynolds number [1]
S = planform area of rounded tip wing [m^2]
U_θ = tangential velocity [m/s]
V_∞ = freestream velocity [m/s]
α = geometric angle of attack of airfoil [degrees]
α_o = zero-lift angle of airfoil [degrees]
Θ_p = angle streaklines on airfoil pressure surface make relative to the freestream direction [degrees]
Θ_s = angle streaklines on airfoil suction surface make relative to the freestream direction [degrees]
ν = fluid kinematic viscosity [m^2/s]
ρ = fluid density [kg/m^3]
$\sigma_i = [(p_i - p_v)/0.5\rho V_\infty^2]$ = cavitation inception index [1]

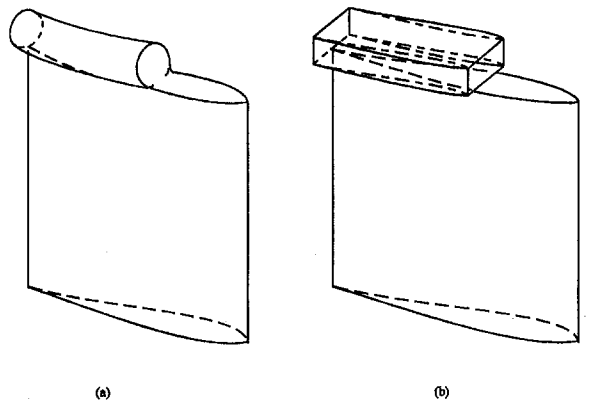

Fig. 2 Schematics of wing tip devices. Flow is right to left. (*a*) Ducted tip. (*b*) Bi-wing tip.

(a desirable characteristic for maximizing L/D) has this shed vorticity concentrated at the wing tips, which accounts in part for the small vortex core radius and hence high σ_i of elliptically loaded wings.[1]

Nonplanar wings (Cone 1963) are not subject to the same near-elliptical loading constraint as conventional wings, and hence do not necessarily shed concentrated vorticity at the wing tip. They therefore potentially have much lower tip vortex cavitation inception indices and, according to Cone, less induced drag, than conventional wings.

The ducted-tip wing is one example of a non-planar wing. It consists of a conventional planar wing to which is mounted a hollow duct, approximately aligned with the wing chord (Fig. 2). Figure 1(*b*) is a Trefftz plane schematic of the configuration. Provided that the flow through the duct has little rotation (a reasonable assumption if the entrance to the duct is near the wing leading edge), and the flow around the exterior of the duct has a significant swirl (again, a reasonable assumption because the large pressure gradient that exists near the wing tip, from the pressure surface to the suction surface, will cause a rapid tangential flow around the tip), there will be significant vorticity shed from the duct, as illustrated in Fig. 1(*b*). Because this shed vorticity is spread over a region of radius comparable to the (large) duct radius, it seems plausible that the resulting tip vortex core radius will also be large. This insight into the distribution of shed vorticity encouraged us to explore experimentally the ducted tip geometry.

3 Experimental Apparatus and Procedures

The line-of-reasoning described in Section 2 leads one to hope that the ducted tip wing geometry has superior tip cavitation characteristics. From a practical standpoint, one is not merely interested in improvements in tip σ_i, one must also know that these improvements are not coincident with a large lift reduction or drag increase. Consequently, the experimental program described here consisted of two discrete parts—measurement of the inception characteristics of a ducted tip wing, and measurement of the lift and drag behavior of such a wing.

The tip vortex inception measurements were carried out in the Low Turbulence Water Tunnel (LTWT) at Caltech. The water tunnel facility has a test section of 30.5 cm × 30.5 cm × 2.5 m long, with a freestream velocity adjustable up to 10 m/s. The freestream pressure, p_∞, can be varied from slightly above atmospheric pressure to 25 kPa by means of a vacuum pump. By using a deaeration system and diatomaceous earth filtration, the freestream nuclei content of the water was controlled. A van Slyke device was used to measure the water's total dissolved air content.

A rectangular planform, untwisted, constant airfoil section (NACA 64-309 modified), hydrofoil was reflection-plane mounted in the LTWT. The chord of this hydrofoil was 15.2 cm, and the semispan was 17.8 cm, resulting in an effective aspect ratio of 2.3. The Reynolds number based on chord length for all the cavitation tests described in this article was in the range $1.1 \times 10^6 < \mathrm{Re} < 1.6 \times 10^6$. This basic wing was fitted with two different tips. The first tip was a duct comprised of a 2.9 cm outside diameter (with a wall thickness of 0.2 cm) cambered brass pipe, 10.2 cm long, attached flush with the hydrofoil trailing edge, with axis aligned with the camberline (Fig. 2(*a*)). The size of the duct selected for these studies is probably not optimum. We designed a duct based on intuition guided by the following considerations: too large a duct will cause excessive parasite drag, while a duct that is too small will have reduced flow through the duct and will cause little change to the shed vorticity distribution. The second tip, which was used for comparison purposes, was a rounded tip geometry with approximately semicircular cross-sections perpendicular to the chordwise direction, fitted onto the end of the basic wing (Fig. 3).

Two different procedures were used to study the flow around these wing tip geometries. Surface flow visualization was accomplished using the paint drop technique (Green et al., 1988). With the hydrofoil out of the water tunnel, drops of oil-based paint were dotted on its surface. The hydrofoil was then returned to the tunnel, and the LTWT was quickly accelerated up to a set velocity, causing the paint drops to be smeared in the direction of the local shearing stress.

The second procedure involved cavitation inception measurement and cavitation photography. The large range of inception numbers encountered precluded us from maintaining a constant Reynolds number for all the tests. Instead, cavitation inception testing consisted of setting the hydrofoil angle of attack and gradually increasing V_∞ and decreasing p_∞ until cavitation inception was observed under stroboscopic illumination. Hydrofoil leading edge inception was defined to occur when cavitation was observed on the foil surface half way between the wing root and tip; trailing vortex inception when at least one cavitation event per second was seen. When the leading edge inception index, $(\sigma_i)_{le}$ was larger than the tip vortex inception index, $(\sigma_i)_{tv}$, it was necessary to achieve $(\sigma_i)_{tv}$ quickly after $(\sigma_i)_{le}$ to avoid erroneous measurements due to the recirculation of cavitation nuclei in the LTWT. Photographs of cavitation were taken by illuminating the hydrofoil and tip vortex in the spanwise direction, and recording on film the light reflected normal to the hydrofoil planform. The cavitation behaviour of the rounded tip was studied first, and several week later, following attempts with different ducted tip geometries, testing of the final ducted tip geometry began.

The aerodynamic performance of the two tip geometries was evaluated in the Low Speed Wind Tunnel (LSWT) at the University of British Columbia. The truncated rectangular cross-section test section of this facility has dimensions 60 cm × 91 cm and is 4 m long. The maximum velocity attainable in the test section is 40 m/s, although the velocity was maintained at 30 m/s for these experiments. A six-axis strain-gauged force balance measures lift and drag forces on models in the test section.

Aerodynamic testing in the LSWT was done on a rectangular planform, untwisted, constant airfoil section (NACA 66-209) basic wing. This acrylic wing is 30.5 cm in chord and 35.6 cm in semi-span, and it is fitted with 92 surface pressure taps. Several different tips were attached to the basic wing, including a series of cambered circular aluminum ducts 3.8 cm in outside diameter (with a wall thickness of 0.2 cm) with lengths ranging from 19.8 cm to 30.5 cm (i.e., 65 percent of wing chord to 100 percent of wing chord). These ducts were aligned with the wing

[1] Real fluid effects that cause the formation of secondary vortices have only a slight impact (addition of a small amount of countersign vorticity near the tips, and smearing of the distribution) on the shed vorticity distribution.

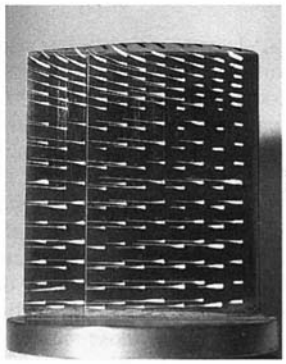

Fig. 3(a)

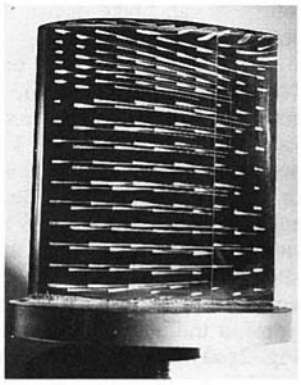

Fig. 3 (b)

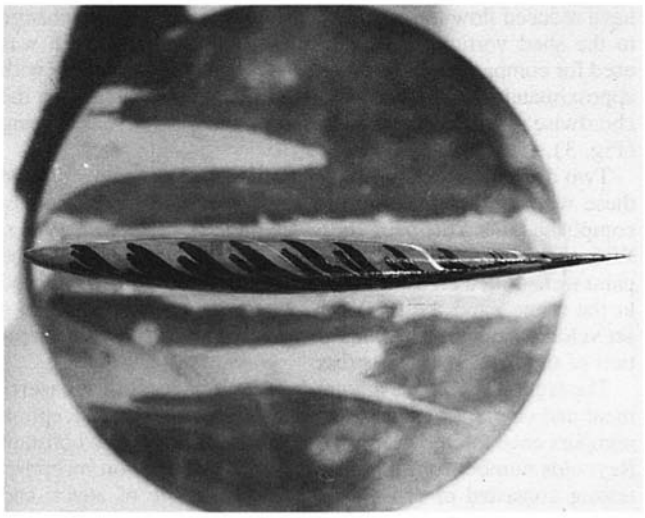

Fig. 3 (c)

Fig. 3 Surface flow visualization on the rounded tip geometry. (*a*) Pressure side. Flow is right to left. (*b*) Suction side. Flow is left to right. (*c*) Inboard view of tip. Flow is left to right. The wing pressure surface is at the top.

trailing edge and were affixed approximately parallel to the wing camberline (Figure 2(*a*)). An elliptical wing tip duct, with major axis 10.5 cm (aligned normal to the wing planform), minor axis 3.9 cm, and length 19.8 cm was also tested. The last type of ducted tip tested was a "bi-wing" configuration.

The "bi-wing" tip (Fig. 2(*b*)) was constructed of two parallel NACA 0006 short airfoils of 15 cm chord and 3.5 cm span joined together at both span ends with thin aluminum plates. The chordline-to-chordline separation of these airfoils was 3.5 cm. This bi-wing tip was attached to the tip of the basic wing with the short airfoils aligned parallel with the basic wing. All plate/wing junctions were then faired with putty before aerodynamic testing.

For comparison purposes, two other tip geometries were also wind tunnel-tested. A semicircular tip constructed of acrylic and body filler 3.8 cm in span was one conventional geometry tested, and a square cut tip (i.e., constant airfoil section to the tip, where the wing chord falls abruptly to zero) 3.8 cm in span was also tested.

In summary, a number of different wing tip geometries were tested in the wind tunnel, all with semi-spans of 39.4 cm, though with aspect ratios varying from 2.58 for the square cut tip, to 2.60 for the rounded tip, to 2.67 for the 65 percent partial chord ducted tip. The aerodynamic test configurations were not geometrically similar with the cavitation test models, but they were nearly so.

Three aerodynamic measurements were made in the LSWT: the lift coefficient, C_L, versus angle of attack α, the drag coefficient, C_D, versus α, and the pressure distribution on both sides of the basic wing.

4 Results and Discussion

4.1 Flow Visualization. Examining the surface flow over an airfoil is perhaps the easiest way to assess qualitatively the

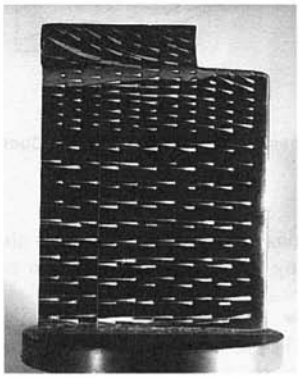

Fig. 4 (a)

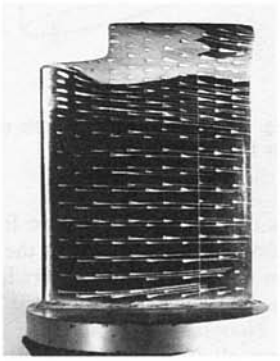

Fig. 4 (b)

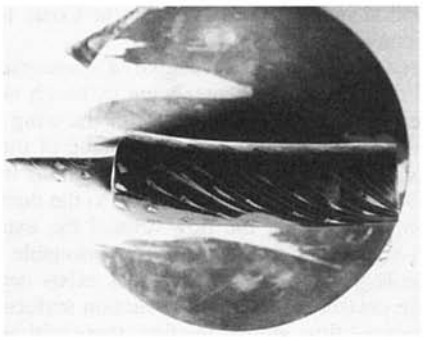

Fig. 4 (c)

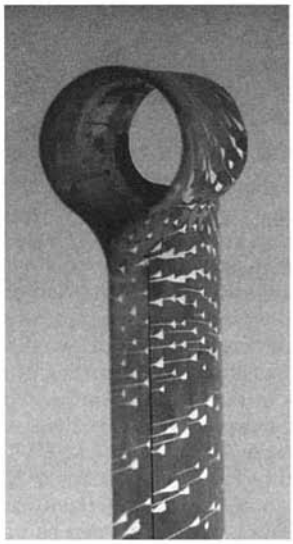

Fig. 4 (d)

Fig. 4 (*a*) Surface flow visualization on the pressure side of the ducted tip wing. The flow is right to left. $\alpha = 7°$, Re $= 1.2 \times 10^6$. (*b*) Suction side view of the wing in Fig. 4(*a*). The flow is left to right. (*c*) Inboard view toward tip of the flow in Fig. 4(*a*). The flow is left to right. The pressure surface is at the top of the photograph. (*d*) Upstream view through the duct of the flow in Fig. 4(*a*). The pressure surface is to the right.

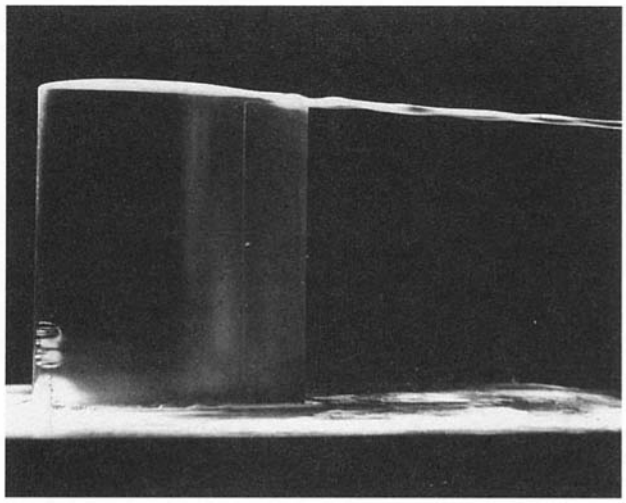

Fig. 5 Developed trailing vortex cavitation behind the rounded tip geometry. α = 7°, Re = 1.3 × 10^6, σ = 1.8, DAC = 5.4 ppm.

performance of different wing tip geometries. Figure 3(a) is a view of the surface flow over the pressure side of the rounded tip geometry. The flow direction is nearly streamwise near the reflection-plane mount (near the bottom of the photograph) and acquires an increasing spanwise component as the tip is approached. Over the majority of the suction side of the wing (Fig. 3(b)) there is also an increasing spanwise velocity component (for this side, directed from the tip to the root) as the tip is approached. Streaklines directed toward the tip on the suction side result from, respectively, the tip vortex rollup in the region near the tip, and an interference vortex near the wing root. The difference between the suction and pressure surface spanwise velocities at each spanwise location is related to the local shed vorticity per unit span length. If the freestream direction component of the velocity (external to the boundary layer) is V_∞, one may show that the shed circulation is approximately $V_\infty(\sin \Theta_p - \sin \Theta_s)$. Θ_p and Θ_s are the angles the streaklines make relative to the freestream at the hydrofoil trailing edge, on, respectively, the pressure and suction surfaces.

Lifting line and lifting surface theory predict that a rectangular planform wing should shed a vortex sheet with vorticity concentrated at the tips—a prediction borne out by Fig. 3.

The surface flow over the ducted tip geometry is quite different from that over the conventional tip geometry. The spanwise velocity component at the trailing edge, on both the suction and pressure surfaces (Fig. 4), is substantially less than that of the rounded tip wing. At one third of the spanwise distance from the reflection plane mount, for example, the angle the rounded tip streaklines make with the freestream direction is about 50 percent greater than the streakline angles of the ducted tip. This difference in spanwise velocity component implies that the ducted tip wing sheds less bound circulation over the majority of the wing span than does the rounded wing tip. Smear lines in the duct (Fig. 4(d)) have little swirl, whereas those on the duct exterior indicate a large tangential velocity. This observation confirms that substantial vorticity is shed from the duct, as indicated in Fig. 1(b).

4.2 Cavitation Characteristics. Figure 5 is a photograph of developed tip vortex cavitation behind the rounded tip geometry. The cavity cross-section is oval immediately downstream of the tip, and becomes nearly circular within one chord of the trailing edge. This shape is consistent with the known transition of the tip vortex velocity field from asymmetric at the hydrofoil trailing edge to nearly axisymmetric a short distance downstream (Fruman et al., 1991, Green and Acosta, 1991). Development of this continuous vapour-filled tip vortex cavity occurs when the cavitation number is decreased by just 10–20 percent below σ_i. The rapidity of the cavitating vortex development implies that the axial pressure gradient along the core of a tip vortex is small, in agreement with recent measurements by Green (1991).

Unlike a developed trailing vortex cavity, which is a steady phenomenon, cavitation inception is highly unsteady. Cavitation inception in the rounded tip vortex is observed 0.3 to 1.5 chords downstream of the hydrofoil trailing edge; the exact location of trailing vortex inception fluctuates in an apparently random manner within this range. It is not known if the fluctuation of the inception location is due to variability in the location at which freestream nuclei are captured by the vortex (Ligneul and Latorre, 1989), or due to the fluctuating pressure field within the tip vortex core (Green, 1991).

Trailing vortex inception occurs for $\sigma_i = 1.8 \pm 0.2$ near the hydrofoil operating angle of attack, α = 7 deg (Fig. 6). As α is varied about the operating angle of attack, the inception index varies much less rapidly than the $(\alpha - \alpha_0)^2$ dependence predicted by a simple Rankine vortex model. Arndt and Keller (1992) have observed the same effect, which they attribute to the significant tension that can be sustained by low-nuclei-content water prior to cavitation inception. Hydrofoil leading edge surface cavitation inception occurs for $\sigma_i = 0.9 \pm 0.1$, substantially lower than the value for tip vortex inception. This observation implies that tip vortex cavitation occurs in many situations for which surface cavitation on the hydrofoil is not present.

The inception indices plotted in Figure 6 were determined in strong (i.e., low nuclei content) water. Water with more freestream nuclei exhibited much higher inception indices (greater by a factor of 2 when the dissolved air content of the water was doubled from 4 to 8 ppm). Arndt and Keller (1992) and Arndt et al. (1991) observed a similarly strong dependence of σ_i on nuclei content.

Cavitation inception from the hydrofoil ducted tip was first observed on the outside edge of the suction surface portion of the duct. This surface cavitation is caused by the separation that occurs as the flow, which has a high tangential velocity around the tip, encounters the duct leading edge. Figure 7 is a photograph of cavitation nuclei generated by the duct surface that have migrated into the ducted tip vortex. Note the diffuse appearance of the vortex.

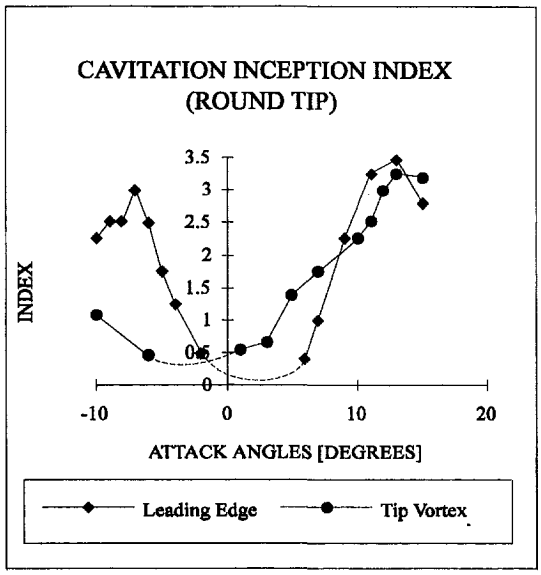

Fig. 6 Cavitation inception index versus angle of attack for the rounded tip geometry. Re = 1.4 × 10^6, DAC = 5.4 ppm (uncertainty in $\alpha = \pm 0.2°$ and in $\sigma_i = \pm 10$ percent at the 95 percent confidence level).

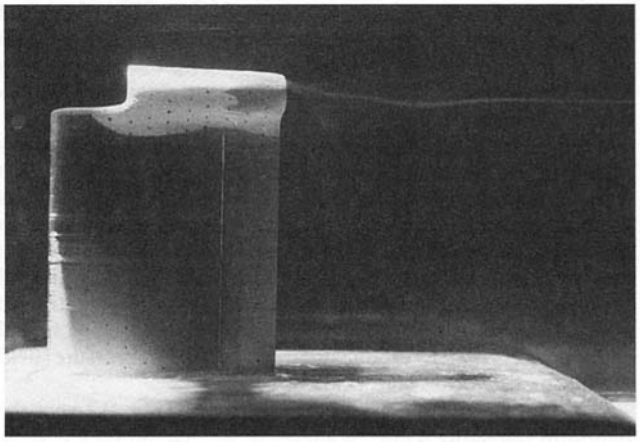

Fig. 7 Ducted tip vortex made visible by migration of cavitation nuclei, generated at the duct leading edge, into the vortex. α = 7°, Re = 1.2 × 10^6, σ = 1.5, DAC = 7.0 ppm.

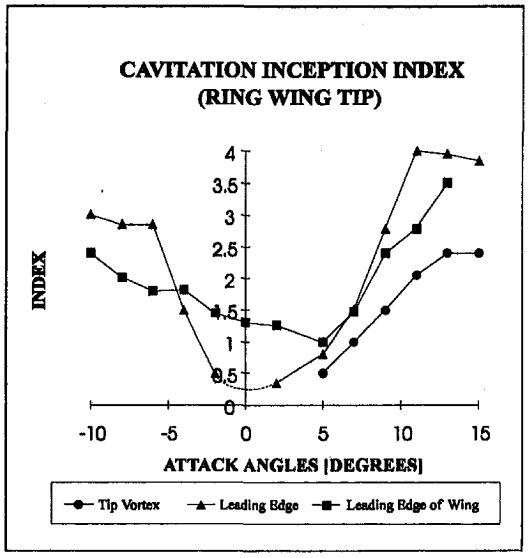

Fig. 8 Cavitation inception index versus angle of attack for the ducted tip geometry. Re = 1.4 × 10^6, DAC = 7.0 ppm. (Uncertainty in α = ±0.2° and in σ_i = ±10 percent at the 95 percent confidence level).

True trailing vortex cavitation occurs only when σ is reduced well below the inception index of both the ducted tip surface cavitation and the hydrofoil leading edge cavitation. As a consequence, cavitation nuclei generated by both the wing leading edge and duct surface cavitation are swept into the tip vortex prior to inception there. Because the tip vortex is exposed to water of much higher nuclei content than the freestream water, the tip vortex will cavitate at relatively higher σ_i. The ducted tip vortex inception measurements are thus biased to high values.

Despite this "unfavorable" bias, the ducted tip vortex data (Fig. 8) show a remarkable decrease in σ_i relative to the rounded tip geometry. For an angle of attack of 7 deg, the inception index of the ducted tip vortex is $\sigma_i = 0.9 \pm 0.1$. In contrast, at the same angle of attack, the rounded tip vortex has $\sigma_i = 1.8 \pm 0.2$ (i.e. σ_i of the ducted tip is 50 percent less). For angles of attack of 5 and 10 deg, the ducted tip vortex σ_i is 0.5 ± 0.05 and 1.8 ± 0.2. These values are respectively 61 and 28 percent less than the rounded tip σ_i values (1.3 ± 0.1 and 2.5 ± 0.1) at the same α.

As explained previously, the inception index of tip vortex cavitation is a strong function of the nuclei content of the water. One might therefore posit that the large reduction of σ_i, when the ducted tip is installed, results from a decrease in the nuclei content of the water between the time of the rounded tip tests and the ducted tip tests. In fact, two observations point to an *increase* in freestream nuclei between the tests. One such observation is the increase in the dissolved air content (from 5 ppm to 7 ppm with an error of ±0.5 ppm) between the rounded and ducted tip tests. The observed increase in hydrofoil leading edge σ_i (from 0.3 to 0.8 at α = 5 deg, from 1.0 to 1.5 at α = 7 deg, and from 3.0 to 3.5 at α = 10 deg) between the rounded and ducted tip tests is another strong indicator of an increase in freestream nuclei concentrations.

In summary, two factors tend to bias the ducted tip σ_i to elevated values—the presence of more naturally-occurring freestream nuclei during testing of that geometry, and the generation of nuclei by cavitation from the hydrofoil leading edge. Despite these two influences, cavitation inception from the ducted tip geometry occurred at much lower inception indices than from the rounded tip geometry.

One may be concerned that the gains in cavitation inception improvement resulting from the ducted tip modification are negated by the increase in other forms of cavitation. For example, one might postulate that the ducted tip geometry would redistribute the hydrofoil loading, causing the wing leading edge σ_i increase referred to above. This is not the case. Except for a small region near the wing tip, the measured pressure distributions on the basic wing were virtually unchanged ($\bar{c}_p$ the same to ±5 percent) with the addition of the ducted tip. The unchanged pressure distribution implies an unchanged wing loading. Therefore, leading edge cavitation is *not* significantly affected by the addition of the ducted tip, whereas tip vortex cavitation is significantly reduced by the ducted tip.

4.3 Aerodynamic Performance. These encouraging inception results prompted a study of the aerodynamic performance of the ducted tip and other tip geometries.

Wind tunnel testing demonstrated that the aerodynamic performance of the square cut and rounded tip wings was identical to within the experimental error (±1 percent drag and ±0.5 percent in lift). The partial chord circular duct tip had the best performance of any of the ducted tip geometries. Consequently, only the partial chord ducted tip and the rounded tip geometries—the same tip geometries whose cavitation behaviour was studied in section 4.2—will be compared here.

For all elevated angles of attack ($\alpha > 7$ deg) the lift coefficient of the ducted tip geometry, when C_L is based on the planform area

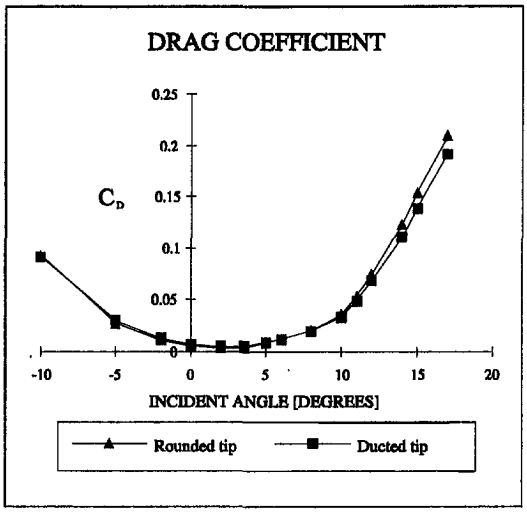

Fig. 9 Drag coefficients of rounded and ducted tip wings. Re = 7.1 × 10^5 (The uncertainty in C_D is ±0.0003 and in α is ±0.1°, both at the 95 percent confidence level).

of the rounded tip, is about 4 percent less than that of the rounded tip. However, the partial chord ducted tip geometry has a 3.4 percent smaller planform area than the rounded tip, and thus the actual lift coefficients for the two geometries are identical to within experimental error. Surface flow visualizations described in Section 4.1 suggest that the ducted tip generates greater lift near the wing root. The implication of the congruity of the two lift coefficients is that the additional lift gained from the root of the ducted tip wing is almost precisely offset by the reduced lift attained in the vicinity of the tip.

Unlike the virtually unchanged wing lift, a significant difference in wing drag is observed when the ducted tip is installed (Fig. 9). For $\alpha < 8$ deg the ducted tip geometry has greater drag than the rounded tip, but for larger α the ducted tip geometry has less drag: 6 percent less at 10 deg, 8 percent less at 12 deg, and fully 10 percent less at 14 deg. Even when allowance is made for the slightly reduced planform area of the ducted tip geometry, there is nonetheless an up to 6 percent drag coefficient benefit arising from the tip modification. This reduction in drag coefficient is somewhat surprising in view of the obviously increased parasite drag of the ducted wing (arising from both its additional wetted area and the likely existence of interference vortices at the duct-wing junction); the only explanation is that the duct attachment to the wing must reduce substantially its induced drag. This conclusion is borne out by the observation that the drag reduction of the ducted tip is most pronounced at elevated angles of attack, for which the induced drag is a larger fraction of the overall drag.

A simple model to explain the reduced induced drag of the ducted tip is shown in Fig. 10. The downwash caused by shed circulation from the duct is less (by the factor cos Θ, where Θ is the angle between a portion of the duct and a portion of the planar wing) than the downwash would be if the same shed circulation were redistributed along the duct diameter, in the spanwise direction. The reduction in downwash causes a consequent reduction in induced drag, as suggested by Cone (1963).

Owing to the large parasite drag of the ducted tip geometry, the lift-drag ratio of this geometry is inferior to the conventional tip geometry at low angles of attack. However, for $\alpha > 8$ deg the aerodynamic performance of the ducted tip is superior. As shown in Fig. 11, the improvement in lift/drag ratio with application of the ducted tip varies from 0 to 6 percent for α between 8 and 17 deg.

5 Conclusions

A novel hydrofoil tip geometry, consisting of a flow-through duct attached to the hydrofoil tip, has been tested for both cavitation inception and lift/drag performance. The principal behind the ducted tip design is to cause the Trefftz-plane shed circulation of the hydrofoil to take the form of a line with an attached circle, rather than the simple line of a conventional hydrofoil.

The tip vortex inception index of the ducted tip geometry is 50 ± 15 percent less than that of a conventional tip at normal operating angles (e.g., $\alpha = 7$ deg), and is at least 30 percent less for all positive angles of attack. Because the ducted tip hydrofoil shed vorticity has been redistributed relative to the baseline hydrofoil, the induced drag on the hydrofoil should also be reduced. Such a reduction in the induced drag has been observed. For $\alpha > 8$ deg the total drag of the ducted tip hydrofoil is less than that of a conventional hydrofoil, despite the fact that the parasite drag of the conventional hydrofoil is less, owing to its much smaller wetted area. The overall lift-drag ratio of the ducted tip hydrofoil, for $\alpha > 8$ deg, is up to 6 ± 1 percent greater than that of a conventional tip. Thus, the much improved cavitation behavior of the ducted tip comes at no cost (for elevated α), and even some benefit, in terms of the hydrodynamic (non-cavitating) performance of the hydrofoil.

The ducted tip geometry is most advantageous when the lifting surface is highly loaded. In practice, propellers on tugs and fishing trawlers are often highly loaded. Studies are presently underway to explore the effectiveness of the ducted tip geometry on such marine propellers.

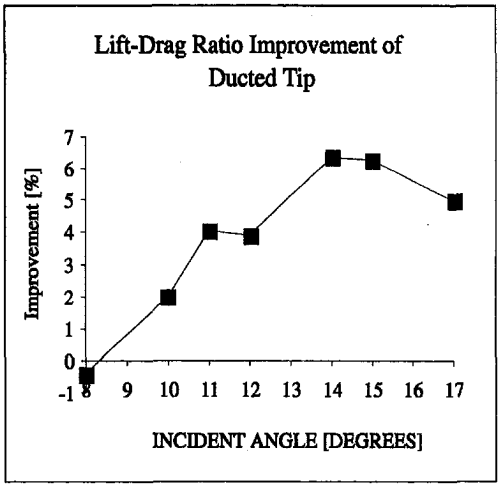

Fig. 11 Lift/Drag ratio improvement of the ducted wing relative to the conventional tip. (The uncertainty in L/D is ±1 percent, and in α is ±0.1° at the 95 percent confidence level).

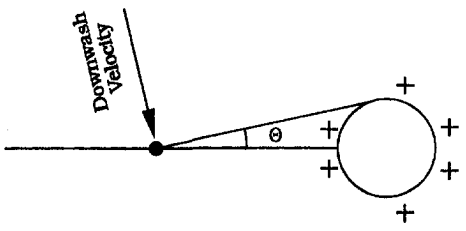

Fig. 10 A simple model for the reduction in induced drag of the ducted tip geometry

Acknowledgments

This research was funded primarily by the Natural Sciences and Engineering Research Council of Canada. The U.S. Office of Naval Research also provided funding. Helpful conversations with Professor Allan Acosta at Caltech are gratefully acknowledged.

References

Arakeri, V. H., Sharma, S. D., and Mani, K., 1985, "A Technique to Delay the Inception of Tip Vortex Cavitation from Marine Propellers," ASME *Cavitation and Multiphase Flow Forum.*

Arndt, R. E. A., Arakeri, V. H., and Higuchi, H., 1991, "Some Observations of Tip Vortex Cavitation," *Journal of Fluid Mechanics,* Vol. 229, pp. 269–289.

Arndt, R. E. A. and Keller, A. P., 1992, "Water Quality Effects on Cavitation Inception in a Trailing Vortex," ASME JOURNAL OF FLUIDS ENGINEERING, Vol. 114, pp. 430–438.

Chahine, G. L., Frederick, G. F., and Bateman, R. D., 1993, "Propeller Tip Vortex Cavitation Suppression Using Selective Polymer Injection," ASME JOURNAL OF FLUIDS ENGINEERING, Vol. 115, No. 3, pp. 497–503.

Cone, C. D., 1963, "The Theory of Induced Lift and Minimum Induced Drag of Non Planar Lifting Systems," *NASA Technical Report* R-139, N63 16288.

Critchley, J. B., 1991, "Wake Vortex—The Program in the United Kingdom," *Proceedings of the FAA Wake Vortices Conference,* Washington, D.C.

Falcao de Campos, J. A. C., George, M. F., and MacKay, M., 1989, "Experimental Investigation of Tip Vortex Cavitation for Elliptical and Rectangular Wings," ASME *Cavitation and Multiphase Flow Forum,* La Jolla, CA.

Fruman, D. H., Dugue, C., and Cerruti, P., 1991, "Tip Vortex Roll-up and Cavitation," ASME *Cavitation and Multiphase Flow Forum,* Portland, OR.

Green, S. I., and Acosta, A. J., 1991, "Unsteady Flow in Trailing Vortices," *Journal of Fluid Mechanics,* Vol. 227, pp. 107–134.

Green, S. I., 1994, "Wing Tip Vortices," to appear in *Fluid Vortices,* S. Green, ed., Kluwer, Dordrecht.

Green, S. I., 1991, "Correlating Single Phase Flow Measurements with Observations of Trailing Vortex Cavitation," ASME JOURNAL OF FLUIDS ENGINEERING, Vol. 113, No. 1, pp. 125–129.

Green, S. I., Acosta, A. J., and Akbar, R., 1988, "The Influence of Tip Geometry on Trailing Vortex Rollup and Cavitation," ASME *Cavitation and Multiphase Flow Forum,* Cincinnati, OH.

Maines, B. H., and Arndt, R. E. A., 1993, "Bubble Dynamics of Cavitation Inception in a Wing Tip Vortex," ASME *Cavitation and Multiphase Flow Forum,* Washington, D.C.

McCormick, B. W., 1962, "On Cavitation Produced by a Vortex Trailing from a Lifting Surface," ASME *Journal of Basic Engineering,* pp. 369–379.

Milne-Thomson, L. M., 1958, *Theoretical Aerodynamics,* Dover, New York.

Pauchet, A., Briancon-Marjollet, L., and Fruman, D. H., 1993, "Recent Results on the Effect of Cross-Section on Hydrofoil Tip Vortex Occurrence at High Reynolds Numbers," ASME *Cavitation and Multiphase Flow Forum,* Washington, D.C.

Platzer, G. P., and Souders, W. G., 1979, "Tip Vortex Cavitation Delay with Application to Marine Lifting Surfaces—A Literature Survey," DTNSRDC Report 79/051.

Poling, D. R., Dadone, L., and Telionis, D. P., 1989, "Blade-Vortex Interaction," *AIAA Journal,* Vol. 27, No. 6, pp. 694–699.

Sharma, S. D., Mani, K., and Arakeri, V. H., 1990, "Cavitation Noise Studies on Marine Propellers," *Journal of Sound and Vibration,* Vol. 138, No. 2, pp. 255–283.

Shekariz, A., Fu, T. C., Katz, J., Liu, H. L., and Huang, T. T., 1992, "Study of Junction and Tip Vortices Using Particle Displacement Velocimetry," *AIAA Journal,* Vol. 30, No. 1, pp. 145–152.

Stinebring, D. R., Farrell, K. J., and Billet, M. L., 1991, "The Structure of a Three-Dimensional Tip Vortex at High Reynolds Number," ASME JOURNAL OF FLUIDS ENGINEERING, Vol. 113, No. 3, pp. 496–503.

Stinebring, D. R., Farrell, K. J., and Billet, M. L., 1989, "The Structure of a Three-Dimensional Tip Vortex at High Reynolds Number," 22nd American Towing Tank Conference, St. John's, Newfoundland.

Webber, G. W., and Dansby, T., 1983, "Wing Tip Devices for Energy Conservation and other Purposes—Experimental and Analytical Work in Progress at the Lockheed-Georgia Company," *Canadian Aeronautics and Space Journal,* Vol. 29, No. 2, pp. 105–120.

Winter, H., 1991, "R and D for a Wake Vortex Warning System in Germany," *Proceedings of the FAA Wake Vortices Conference,* Washington, D.C.

H. Teng
Department of Mechanical Engineering.

C. M. Kinoshita

S. M. Masutani

Hawaii Natural Energy Institute.

University of Hawaii at Manoa,
Honolulu, HI 96822

Capillary Instability of a Liquid Film on a Wire

Capillary instability of a liquid film on a wire in another fluid (gas or liquid) is investigated. The liquid film is found to be unstable whenever the wavelength of the surface disturbance exceeds the circumference of the film surface—this criterion for instability of the liquid film is the same as that established by Rayleigh for a liquid thread. Analysis shows that instability of the liquid film is strongly influenced by film thickness and the properties of the film and the ambient fluid, and that thin, highly viscous liquid films are more stable than thick, low viscosity liquid films.

Introduction

Liquid films on wires are encountered in many phase-contact applications, such as the coating of wires with molten plastics for insulation and of synthetic fibers with water for lubrication. The liquid film on a wire in a fluid different from the film is hydrodynamically unstable due to capillary and/or gravitational forces. Liquid beads or ripples may form on the surface of the liquid film when it is subjected to a surface disturbance.

Boys (1890; 1959) was first to notice hydrodynamic instability of a liquid film on a wire. In comparing the formation of sticky liquid beads on spider webs with the formation of droplets in the breakup of liquid threads, Boys pointed out that a liquid film on a wire is unstable and that the source of the instability is surface tension, the same as for instability of a liquid thread.

Following the approach pursued by Tomotika (1935) in an analysis of linear instability of a liquid thread, Goren (1962) studied a liquid film on a wire in air. Goren reported that for film thicknesses of practical interest, the dimensionless most-unstable wavenumber, η_m, falls in the range $0.60 \lesssim \eta_m \lesssim 0.707$, which brackets the most-unstable wavenumber for an inviscid-liquid thread, $\eta_m = 0.697$ (Rayleigh, 1878). Selected values of the most-unstable wavenumber obtained by Goren are presented in Table 1. In Table 1, $\eta_m = 0$ as $r_0/a \to 0$ (liquid thread) and $\eta_m = 0.707$ as $r_0/a \to 1$ (zero film thickness). These results imply that in the limiting case of zero film thickness, the damping effect of viscosity on instability becomes nil; i.e., the thinner the liquid film, the more unstable the film. This is inconsistent with experimental observation. In the limiting case of a liquid thread, the effect of viscosity is maximum (Weber (1931) showed that $\eta_m = 0$ only when $\mu \to \infty$), which is inconsistent with Weber's classical theory for liquid threads (Weber, 1931). Based on Goren's theory, $0.60 \lesssim \eta_m \lesssim 0.707$ when $r_0/a > 0.25$; however, in Goren's experiments (Goren, 1962), 50 percent of the data fell in the range $0.50 \lesssim \eta_m \lesssim 0.60$ when $0.25 < r_0/a < 0.70$, and no clear relationship for $\eta_m = \eta_m(r_0/a)$ was evident. Therefore, Goren's predictions are suspect.

After Goren, little work on liquid-film instability on a wire was reported. Thus, the phenomenon of liquid-film instability still is not well understood. The objectives of this study are: 1) to investigate capillary instability of a liquid film on a wire in another fluid (gas or liquid); and 2) to determine the effect of film thickness on instability.

Mathematical Formulation

The flow system under consideration is shown in Fig. 1 and consists of an infinitely long, viscous, annular liquid film on a wire of radius r_0 in a stagnant fluid different from the film. Both the film and the ambient fluid are assumed to be Newtonian and incompressible. Heat and mass transfer, and gravitational effects are neglected. It is assumed that any motion in the film is induced by surface disturbance. Instability of the film may be examined via an energy balance on the film (Aris, 1989):

$$\int_V \frac{\partial}{\partial t}\left(\frac{1}{2}\rho u_i^2\right) dV + \int_V \tau_{ij}\epsilon_{ij} dV - \int_S \tau_{ij} u_i n_j dS = 0. \tag{1}$$

The first term in Eq. (1) represents the rate of increase in kinetic energy; the second term, the rate of energy dissipation; and the third term, the rate at which work is performed on the film. The surface integral in Eq. (1) requires that the motion of the ambient fluid and the film/ambient-fluid interfacial conditions be known. The disturbed flows may be modelled as Stokes flows (Tomotika, 1935; Goren, 1962); thus, the motion of the ambient fluid may be described by the momentum and continuity equations:

$$\frac{\partial \hat{\mathbf{u}}}{\partial t} = -\frac{1}{\hat{\rho}}\nabla\hat{p} + \frac{\hat{\mu}}{\hat{\rho}}\nabla^2\hat{\mathbf{u}}, \tag{2}$$

$$\nabla \cdot \hat{\mathbf{u}} = 0; \tag{3}$$

and the film/ambient-fluid interfacial conditions in cylindrical coordinates by (Landau and Lifshitz, 1993):

Kinematic condition

$$u_{rs} = \hat{u}_{rs}, \quad u_{zs} = \hat{u}_{zs}; \tag{4}$$

Dynamic condition

$$\tau_{rrs} = -\hat{p} + 2\hat{\mu}\left(\frac{\partial \hat{u}_r}{\partial r}\right)_s - \sigma\left[\frac{1}{r_s} + \frac{\partial^2 r_s/\partial z^2}{(1 + (\partial r_s/\partial z)^2)^{3/2}} - \frac{1}{a}\right], \tag{5}$$

$$\tau_{rzs} = \hat{\mu}\left(\frac{\partial \hat{u}_z}{\partial r} + \frac{\partial \hat{u}_r}{\partial z}\right)_s, \tag{6}$$

where the caret signifies the properties of the ambient fluid and the subscript s denotes properties at the interface.

Instability Analysis

It is assumed that the film surface is initially perturbed infinitesimally; the radius of the disturbed film surface can be expressed as (Rayleigh, 1878; Weber, 1931)

Contributed by the Fluids Engineering Division for publication in the JOURNAL OF FLUIDS ENGINEERING. Manuscript received by the Fluids Engineering Division May 2, 1994; revised manuscript received December 9, 1994. Associate Technical Editor: Jong H. Kim.

Table 1 $\eta_m = \eta_m(r_0/a)$* **Relationship Obtained by Goren (1962)**

r_0/a	0	10^{-5}	10^{-3}	10^{-1}	0.5	1.0
η_m	0	0.441	0.486	0.586	0.670	0.707

* r_0 and a are the radii of the wire and undisturbed film surface, respectively.

$$r_s = a + \alpha(t)\cos kz, \tag{7}$$

where $\alpha(t)$ is the amplitude of the disturbance, and k is the wavenumber. The film may be modelled as a one-dimensional Cosserat continuum (Bogy, 1978); thus,

$$\frac{\partial A}{\partial t} + \frac{\partial (Au_z)}{\partial z} = 0, \tag{8}$$

where $A = \pi(r_s^2 - r_0^2)$ is the cross-sectional area of the film. Equation (8) and continuity for the film yield

$$u_r = \frac{\dot\alpha \cos kz}{am} r\left(1 - \frac{r_0^2}{r^2}\right), \tag{9}$$

$$u_z = -\frac{2\dot\alpha \sin kz}{kam}, \tag{10}$$

where $\dot\alpha = d\alpha/dt$ and $m \equiv 1 - r_0^2/a^2$ ($m \neq 0$). The above expressions for u_r and u_z can be used to recast the first and second terms in Eq. (1):

$$\int_V \frac{\partial}{\partial t}\left(\frac{1}{2}\rho u_i^2\right) dV = \frac{\pi^2 a^3 \rho}{2\eta^3 m}(8 + n\eta^2)\dot\alpha\ddot\alpha, \tag{11}$$

$$\int_V \tau_{ij}\epsilon_{ij} dV = \frac{\pi^2 a\mu}{2m\eta}\left(24 + 8\frac{r_0^2}{a^2} + n\eta^2\right)\dot\alpha^2, \tag{12}$$

where

$$\ddot\alpha = d^2\alpha/dt^2, \quad \eta \equiv ka, \quad \text{and}$$

$$n \equiv 1 - \left(3 + \frac{4}{m}\frac{r_0^2}{a^2}\ln\frac{r_0}{a}\right)\frac{r_0^2}{a^2}.$$

The integrations are performed over a single wavelength, between $z = 0$ and $\lambda\ (=2\pi/k)$.

Applying the interfacial conditions, the work term in Eq. (1) can be expressed as

$$\int_S \tau_{ij}u_i n_j dS = -\int_S \hat p u_r dS + \int_S 2\hat\mu\left(\frac{\partial \hat u_r}{\partial r}\right)_s u_r dS - \int_S \sigma\left[\frac{1}{r_s} + \frac{\partial^2 r_s/\partial z^2}{(1 + (\partial r_s/\partial z)^2)^{3/2}} - \frac{1}{a}\right]u_r dS + \int_S \hat\mu\left(\frac{\partial \hat u_z}{\partial r} + \frac{\partial \hat u_r}{\partial z}\right)_s u_z dS. \tag{13}$$

The surface integral in Eq. (13) containing the interfacial tension is

$$\int_S \sigma\left[\frac{1}{r_s} + \frac{\partial^2 r_s/\partial z^2}{(1 + (\partial r_s/\partial z)^2)^{3/2}} - \frac{1}{a}\right]u_r dS = -\frac{2\pi^2\sigma}{\eta}(1 - \eta^2)\alpha\dot\alpha. \tag{14}$$

In instability analyses, only unstable disturbance waves are of interest. Equation (14) indicates that the instability of the film is induced by long disturbance waves (Kinoshita et al., 1994); i.e., $\lambda \gg a$. Equations (9), (10), and (4) suggest that $\hat u_{zs} \sim (\lambda/a)\hat u_{rs}$. Thus, $\hat u_z \sim (\lambda/a)\hat u_r$ and $\hat u_z \gg \hat u_r$. Selecting λ and a as characteristic lengths, Eq. (2) can be rewritten in dimensionless scalar form as

$$\frac{\partial \hat u_z^*}{\partial t^*} = -\frac{\partial \hat p^*}{\partial z^*} + \frac{\lambda}{a}\frac{1}{R_e}\left[\frac{1}{r^*}\frac{\partial}{\partial r^*}\left(r^*\frac{\partial \hat u_z^*}{\partial r^*}\right) + \left(\frac{a}{\lambda}\right)^2\frac{\partial^2 \hat u_z^*}{\partial z^{*2}}\right], \tag{15}$$

$$\frac{a}{\lambda}\frac{\partial \hat u_r^*}{\partial t^*} = -\frac{\partial \hat p^*}{\partial r^*} + \frac{1}{R_e}\left[\frac{\partial}{\partial r^*}\left(\frac{1}{r^*}\frac{\partial}{\partial r^*}(r^*\hat u_r^*)\right) + \left(\frac{a}{\lambda}\right)^2\frac{\partial^2 \hat u_r^*}{\partial z^{*2}}\right], \tag{16}$$

where $\hat u_z^* \equiv \hat u_z/U$, $\hat u_r^* \equiv \hat u_r/U$, $t^* \equiv tU/\lambda$, $r^* \equiv r/a$, $z^* \equiv z/\lambda$, and $\hat p^* \equiv \hat p/\hat\rho U^2$ are dimensionless variables. $\mathrm{Re} \equiv Ua\hat\rho/\hat\mu$ is the Reynolds number and U is a characteristic velocity (U is chosen such that $|\hat u_z/U| \leq 1$). Thus, $\lambda/a \gg 1$, $\hat u_z^* \sim 1$, $\hat u_r^* \ll 1$, and $z^* \sim 1$. The order of magnitude of r^* depends on the region of interest; two separate regions are considered (Rayleigh, 1945; Betchev and Criminale, 1967; Kinoshita et al., 1994).

Region 1: $r_s < r < \lambda$. In this region, it is assumed that $r^* \sim 1$. Order-of-magnitude analysis reduces Eqs. (15) and (16) to

$$\frac{\partial \hat u_z^*}{\partial t^*} = -\frac{\partial \hat p^*}{\partial z^*} + \frac{\lambda}{a}\frac{1}{R_e}\frac{1}{r^*}\frac{\partial}{\partial r^*}\left(r^*\frac{\partial \hat u_z^*}{\partial r^*}\right), \tag{17}$$

$$\partial \hat p^*/\partial r^* \to 0. \tag{18}$$

Region 2: $r > \lambda$. In this region, $\lambda/(ar^*) < 1$ and $\partial \hat u_z^*/\partial r^* \ll 1$. The diffusion term in Region 2 is negligible in comparison with the corresponding term in Region 1 (Teng, 1994); thus,

$$\frac{\partial \hat u_z^*}{\partial t^*} = -\frac{\partial \hat p^*}{\partial z^*}, \quad \text{i.e.,} \quad \frac{\partial \hat u_z}{\partial t} = -\frac{1}{\hat\rho}\frac{\partial \hat p}{\partial z}. \tag{19}$$

Modeling the flow in Region 2 as potential flow, $\hat u_z = \partial\varphi/\partial z$. The velocity potential, φ, must satisfy Laplace's equation

$$\frac{\partial^2\varphi}{\partial r^2} + \frac{1}{r}\frac{\partial\varphi}{\partial r} + \frac{\partial^2\varphi}{\partial z^2} = 0. \tag{20}$$

The solutions to Eqs. (17), (19), and (20) are detailed by Teng (1994); only the results are presented here.

$$\hat p = \hat\rho\frac{\ddot\alpha}{k}\cos kz K_0(kr)/K_1(\eta), \tag{21}$$

$$\hat u_z = -\dot\alpha\eta \sin kz[\ln(a/r) + 2/(m\eta^2)] \quad \text{for} \quad r_s \leq r < r + a, \tag{22a}$$

Nomenclature

n_i = projection of unit outward normal
p = pressure
S = area of film surface
t = time
u_i = velocity component in ith direction
V = volume of the film
σ = interfacial tension
ρ = density
μ = viscosity
τ_{ij} = stress tensor
ϵ_{ij} = strain-rate tensor

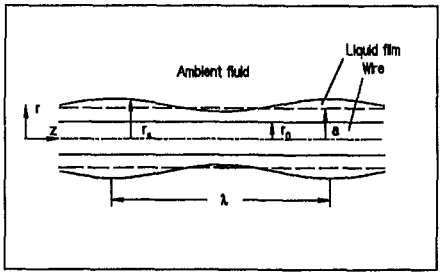

Fig. 1 Flow system configuration. r_0: radius of the wire; a: radius of the undisturbed film surface; r_s: radius of the disturbed film surface; λ: disturbance wavelength.

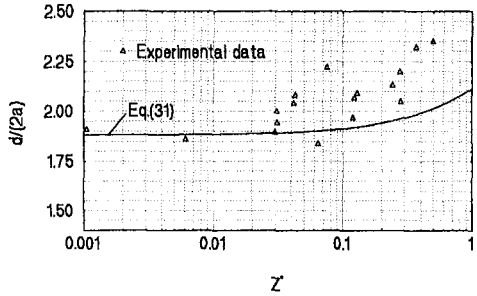

Fig. 3 Comparison of measured and predicted droplet sizes (for limiting case, $m = 1$)

$$\hat{u}_z = \dot{\alpha} \sin kz K_0(kr)/K_1(\eta) \quad \text{for} \quad r > \lambda, \tag{22b}$$

where K_0 and K_1 are the zeroth- and first-order modified Bessel functions of the second kind. Although the velocity in the region $r_s + a < r < \lambda$ is not known, it is not relevant to the solution of those surface integrals in Eq. (13) containing viscosity.

Based on the preceding,

$$\int_S \hat{p} u_r dS = \frac{2\pi^2 \hat{p} a^3}{\eta^2} \frac{K_0(\eta)}{K_1(\eta)} \dot{\alpha}\ddot{\alpha}, \tag{23}$$

$$\int_S \hat{\mu}\left(\frac{\partial \hat{u}_z}{\partial r} + \frac{\partial \hat{u}_r}{\partial z}\right)_s u_z dS + \int_S 2\hat{\mu}\left(\frac{\partial \hat{u}_r}{\partial r}\right)_s u_r dS$$

$$\approx -\frac{4\pi^2 a \hat{\mu} \dot{\alpha}^2}{m\eta}. \tag{24}$$

Substituting Eqs. (14), (23), and (24) into Eq. (13) and combining with Eqs. (11) and (12) in Eq. (1),

$$\left[1 + \frac{\hat{p}}{\rho} \frac{4m\eta}{8 + n\eta^2} \frac{K_0(\eta)}{K_1(\eta)}\right]\ddot{\alpha} + \frac{\mu\eta^2}{\rho a^2(8 + n\eta^2)}$$

$$\times \left(24 + 8\frac{r_0^2}{a^2} + n\eta^2 + 8\frac{\hat{\mu}}{\mu}\right)\dot{\alpha} = \frac{4\sigma m}{\rho a^3} \frac{\eta^2(1 - \eta^2)}{8 + n\eta^2} \alpha. \tag{25}$$

$\alpha = \alpha_0 e^{\omega t}$, where α_0 is the initial disturbance and ω is the growth rate, satisfies Eq. (25). Since $|n| \leq 2$ and $\lambda \gg a$, the term $n\eta^2$ in Eq. (25) can be neglected. Substituting α into Eq. (25) and rearranging yields the following dimensionless characteristic equation

$$\left[1 + \frac{1}{2} m\eta \frac{\hat{p}}{\rho} \frac{K_0(\eta)}{K_1(\eta)}\right]\beta^2 + 2Z\eta^2\beta = m\eta^2(1 - \eta^2), \tag{26}$$

where $\beta \equiv \omega(2\rho a^3/\sigma)^{1/2}$ is the dimensionless growth rate and $Z \equiv [(3 + r_0^2/a^2)\mu + \hat{\mu}]/(2a\rho\sigma)^{1/2}$ is a modified Ohnesorge number. The film is unstable whenever $\beta > 0$ ($\omega > 0$); thus, the criterion for instability is $\eta < 1$, the same as that identified by Rayleigh (1878) for a liquid thread. Equation (26) is valid for either liquid-in-gas or liquid-in-liquid systems provided that the motions of the liquid film and the ambient fluid can be modelled as Stokes flows. If the radius of the wire approaches zero (i.e., $m \to 1$), Eq. (26) reduces to the characteristic equation obtained by Kinoshita et al. (1994) for a liquid thread.

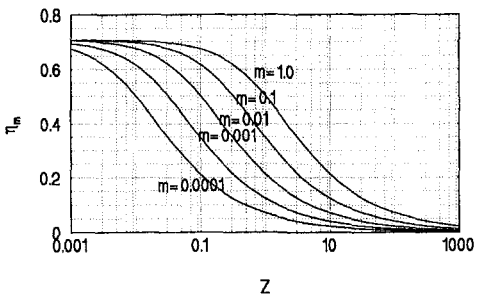

Fig. 2 Dependence of η_m on (Z, m) based on Eq. (28)

Discussion

If $\eta < 1$, then $K_0(\eta)/K_1(\eta) < 1$ and $m\eta K_0(\eta)/K_1(\eta) \ll 1$ ($m < 1$). For $\hat{\rho}/\rho < 2$ (which is generally met in systems of practical interest), Eq. (26) reduces to

$$\beta^2 + 2Z\eta^2\beta = m\eta^2(1 - \eta^2). \tag{27}$$

From an initial disturbance, a number of unstable waves may form on the surface of the film. The wave that controls surface deformation, the "most-unstable wave," is that which has the maximum growth rate in amplitude. The most-unstable wavenumber for the liquid film can be obtained by applying the condition $d\beta/d\eta|_{\eta_m} = 0$ to Eq. (27):

$$\eta_m = \left[\frac{\sqrt{m}}{2(\sqrt{m} + Z)}\right]^{1/2}. \tag{28}$$

Equation (28) is presented graphically in Fig. 2. Figure 2 shows that the instability of the film is strongly influenced by film thickness and the viscosities of the liquid film and the ambient fluid. For a given film thickness, η_m decreases as Z increases; while for fixed Z, η_m decreases as film thickness decreases.

At fixed modified Ohnesorge number, two limiting cases are of particular interest in Fig. 2. One limiting case is $m \to 1$ ($r_0/a \to 0$), wherein the wire becomes nonexistent and the film collapses into a liquid thread. In this limit, Eq. (28) reduces to

$$\eta_m = (2 + 2Z^*)^{-1/2}, \tag{29}$$

where $Z^* = (3\mu + \hat{\mu})/(2a\rho\sigma)^{1/2}$. This result is identical to that obtained by Kinoshita et al. (1994) for a liquid thread. For this limiting case, Teng et al. (1995) derived a relationship between the size of droplets formed from the breakup of a liquid thread and the most-unstable wavenumber:

$$\frac{d}{2a} = \left(\frac{3\pi}{2\eta_m}\right)^{1/3}, \tag{30}$$

where d is droplet diameter. (Note that in this case, a is the undisturbed radius of the liquid thread.) Substituting Eq. (29) into Eq. (30) yields

$$\frac{d}{2a} = \left(\frac{3\pi}{\sqrt{2}}\right)^{1/3}(1 + Z^*)^{1/6}. \tag{31}$$

Figure 3 compares predictions from Eq. (31) with measured droplet sizes for seventeen systems (details are given in Teng et al., 1995) over a wide range of modified Ohnesorge number. Good agreement is observed—the average difference between

predictions and measurements is 8.1 percent and the maximum difference is 25.7 percent.

The other limiting case occurs when $m \to 0 (r_0/a \to 1)$. Here, the film becomes infinitesimally thin relative to the wire and Eq. (28) reduces to $\eta_m = (\sqrt{m}/2Z)^{1/2}$. This implies that the thinner the film, the smaller the most-unstable wavenumber (i.e., the longer the most-unstable wave). In Eq. (27), $\beta \to 0$ as $m \to 0$; thus, the case $m \to 0$ is unconditionally stable. Examination of the two limiting cases shows that the instability of a liquid film behaves consistently with that of a liquid thread at the limit, $m \to 1$; and the thinner the film, the more stable the film.

Figure 2 shows that Eq. (28) has two asymptotic solutions (for $Z \to 0$ and $Z \to \infty$). For inviscid systems (where both the film and the ambient medium are inviscid fluids), $\mu = \hat{\mu} = 0$; thus, $Z = 0$. Equation (28) reduces to $\eta_m = 1/\sqrt{2} = 0.707$; i.e., for inviscid systems, the most-unstable wavenumber is constant, having approximately the same value as an inviscid liquid thread, $\eta_m = 0.697$ (Rayleigh, 1878). Since Z is a damping factor in Eq. (27), and since Z is proportional to the viscosities of the film and the ambient fluid, viscosities have a stabilizing effect ($\eta_m \to 0$ as $Z \to \infty$). Also, Z is proportional to r_0/a; thus, the thinner the liquid film, the greater the damping effect.

For inviscid systems, the present study gives $\eta_m = 0.707$, which lies within the range predicted by Goren (1962), $0.697 \leq \eta_m \leq 0.707$. For viscous systems, Goren (1962) investigated film instability by solving simultaneous equations for the two limiting cases: $\rho \to 0$ and $\mu \to 0$. Since Ohnesorge number is not a free parameter in Goren's approach (Goren, 1962), the present study cannot be compared directly with Goren's analysis. In general, the most-unstable wavenumber is a function of film thickness and Ohnesorge number; therefore, Goren's analysis on viscous systems is incomplete. As shown in Table 1, in Goren's analysis, the effect of viscosity on η_m is overestimated at the limit, $r_0/a \to 0$, and is underestimated at the other limit, $r_0/a \to 1$.

Conclusion

Capillary instability of a liquid film on a wire in another fluid was studied by employing an integro-differential approach. A simple characteristic equation relating the most-unstable wavenumber, η_m, to fluid properties, film thickness, and wire geometry was obtained. By setting the wire radius to zero, the characteristic equation of this study describes the instability of a liquid thread.

The following were found: 1) if $\hat{\rho}/\rho < 2$, the effect of density can be neglected; 2) the damping factor, a modified Ohnesorge number, is proportional to the viscosities of the film and the ambient fluid; thus, viscosities have a stabilizing effect; 3) instability of the liquid film is strongly influenced by film thickness—the thinner the liquid film, the more stable the film; 4) in inviscid systems, η_m is constant, independent of fluid properties and film thickness. The characteristic equation developed in this study has been tested by setting the wire diameter to zero and comparing theoretical predictions for droplet sizes with experimental data taken from the literature. Good agreement was observed over a wide range of modified Ohnesorge number.

Acknowledgment

Partial funding for this study was provided by the Pacific International Center for High Technology Research, Honolulu, Hawaii.

References

Aris, R., 1989, *Vectors, Tensors, and the Basic Equations of Fluid Mechanics,* Dover Publications, Inc.

Betchev, R., and Criminale, W. O., Jr., 1967, *Stability of Parallel Flows,* Academic Press.

Bogy, D. B., 1978, "Use of One-dimensional Cosserat Theory to Study Instability in a Viscous Liquid Jet," *Physics of Fluids,* Vol. 21, pp. 190–197.

Boys, C. V., 1890, "Soap Bubbles and the Forces Which Mould Them," Society for the Promotion of Christian Knowledge, London.

Boys, C. V., 1959, "Soap Bubbles and the Forces Which Mould Them," Enlarged edition, Educational Services, Inc.

Goren, S. L., 1962, "The Instability of an Annular Thread of Fluid," *Journal of Fluid Mechanics,* Vol. 12, pp. 309–319.

Kinoshita, C. M., Teng, H., and Masutani, S. M., 1994, "A Study of the Instability of Liquid Jets and Comparison with Tomotika's Analysis," *International Journal of Multiphase Flow,* Vol. 20, No. 3, pp. 523–533.

Landau, L. D., and Lifshitz, E. M., 1993, *Fluid Mechanics,* 2nd Ed., Pergamon Press.

Rayleigh, Lord, 1878, "On the Instability of Jets," *Proceedings of the London Mathematical Society,* Vol. 10, pp. 4–18.

Rayleigh, Lord, 1945, *Theory of Sound,* Dover Publications, Inc.

Teng, H., 1994, "Laminar Instability of Cylindrical Liquid Jets," Ph.D. thesis, University of Hawaii.

Teng, H., Kinoshita, C. M., and Masutani, S. M., 1995, "Prediction of Droplet Size from the Breakup of Cylindrical Liquid Jets," *International Journal of Multiphase Flow,* Vol. 21, No. 1, pp. 129–136.

Tomotika, S., 1935, "On the Instability of a Cylindrical Thread of a Viscous Liquid Surrounded by Another Viscous Fluid," *Proceedings of Royal Society of London,* Series A, Vol. 150, pp. 322–337.

Weber, C., 1931, "On the Instability of a Liquid Jet," *Zeitschrift fur Angewandte Mathematik und Physik,* Vol. 11, pp. 136–154.

Free Surface Flow Profile and Fluctuations of a Circular Hydraulic Jump Formed by an Impinging Jet

J. W. Stevens
Mechanical Engineering Department,
Mississippi State University,
Mississippi State, MI 39762

A fine wire probe was used to make quantitative measurements of the free surface profile and surface fluctuations around the hydraulic jump formed by a normally impinging free liquid jet. Representative magnitudes of both radial and axial fluctuations were presented for two nozzle sizes and several jet Reynolds numbers and subcritical flow depths. The results were compared to previous measurements of the supercritical flow depth and to theoretical predictions of the circular hydraulic jump size. The agreement appeared reasonable for the supercritical flow depth while the analytical expressions predicted a shorter hydraulic jump than that found by the measurements for the same supercritical flow conditions.

Introduction

Impinging liquid jets are characterized by high transport coefficients in the stagnation region and consequently are used for cooling in a variety of high heat flux applications. In the common configuration of an axisymmetric free liquid jet impinging normally against a plane surface, a hydraulic jump is formed in the jet periphery where the local transport coefficients decrease dramatically. While the fluid mechanics and heat transfer of the stagnation region of impinging jets have been studied extensively, the hydraulic jump region has received comparatively little attention. The flow and transport characteristics of this region are important for cases of cooling with widely spaced, multiple jets, or for cases of a single jet with inadequate or impeded drainage. For many jet configurations of engineering interest, the unsteady fluctuations of the hydraulic jump position make quantitative flow and heat transfer measurements and analysis of this region difficult. As part of a larger study including both flow and heat transfer measurements for the hydraulic jump region, this paper reports measurements of the hydraulic jump surface profile and unsteady fluctuations for two jet diameters and several flow rates and downstream liquid layer depths.

The hydraulic jump occurs when a free surface flow makes a rapid transition from supercritical ($Fr > 1$) to subcritical ($Fr < 1$) flow. Classical hydraulic jumps are formed in smooth, horizontal rectangular channels, and have been widely studied in hydraulic engineering literature (e.g., Rajaratnam, 1967). The jump formed in the radial spread of an impinging jet over a plane surface has been termed a "circular" hydraulic jump. The circular hydraulic jump location for an unsubmerged impinging jet was predicted by Watson (1964), as part of a larger analysis of the laminar and turbulent radial spread of a liquid jet over a flat impingement surface using boundary layer theory. The jump location was determined from mass and momentum balances across the jump using assumed fluid velocity profiles on both sides. Inviscid, laminar, and turbulent cases were considered. The laminar analysis appeared to agree well with experimental measurements. Koloseus and Ahmad (1969) analytically and experimentally compared the circular hydraulic jump with the classical hydraulic jump and found significant differences in the downstream-to-upstream depth and radius ratios for similar upstream Froude numbers. Khalifa and McCorquodale (1979) extended the work of Koloseus and Ahmad (1969) to include the effect of entrained air in the jump. Circular hydraulic jumps were also studied by Craik et al. (1981). Liquid layer depths prior to, and following the jump were measured with an optical technique. Free surface profiles of the jump, and qualitative observations of the jump structure were reported. An eddy which varied in size as the downstream layer depth increased for a fixed flow rate was observed to be an integral part of the jump. Stability of the jump location was considered and related to a critical upstream Reynolds number. Bowles and Smith (1992) performed a theoretical and numerical study of the circular hydraulic jump and found good agreement between their theory and the experimental results of Craik et al. Circular hydraulic jumps were also considered by Lawson and Phillips (1983). The radial flow was formed by the ejection of fluid from between two parallel circular plates, rather than from an impinging jet. A model predicting jump location as a function of flow rate and plate spacing was developed through mass and momentum conservation equations assuming a linear jump profile. Khalifa and McCorquodale (1992) modeled the internal flow of a circular hydraulic jump using an integral method. Experimental treatment of the radial flow on stationary and rotating disks was reported by Thomas et al. (1990). The flow was formed by the radial ejection of the fluid from an axisymmetric orifice. In the experimental portion of the study, fluid layer thicknesses on both sides of the jump were determined with a capacitive probe which measured the air gap between the probe and the liquid free surface. While the probe could not be used on the hydraulic jump itself, measurements were made on the liquid layers on either side. Qualitative descriptions of the jump structure were also reported. A "toroidal roller" was described at the jump which disappeared with increasing flow rates. Numerical predictions for the same case were reported in a companion paper by Rahman et al. (1990a) and similar results shown in Rahman et al. (1990b). The numerical studies also found significant recirculation flows inside and just downstream from the hydraulic jump. Liu and Lienhard (1993) studied the differences between circular hydraulic jumps and those formed by a planar flow. They showed that the two types of jumps exhibit similar features if the planar flow is sufficiently thin. They established the importance of surface tension in determining the shape of the circular hydraulic jump by per-

Contributed by the Fluids Engineering Division for publication in the JOURNAL OF FLUIDS ENGINEERING. Manuscript received by the Fluids Engineering Division July 8, 1994; revised manuscript received December 8, 1994. Associate Technical Editor: J. A. C. Humphrey.

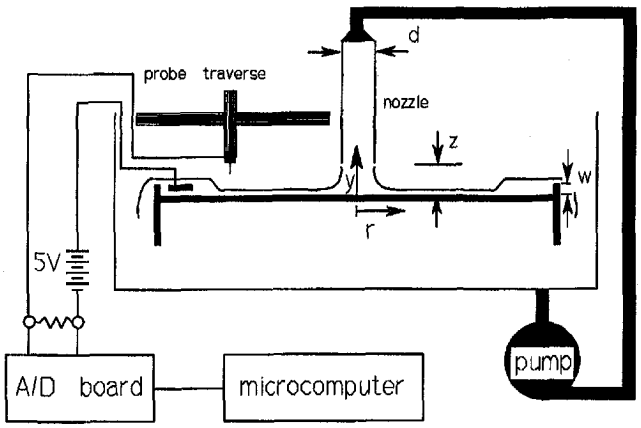

Fig. 1 Schematic diagram of experimental apparatus

forming parametric studies where the liquid surface tension was changed by the addition of a surfactant. A jump Weber number was defined ($We = y_2 \cdot (\rho g/\sigma)^{1/2}$ in the nomenclature of this paper) to represent the balance between hydrostatic forces and surface tension forces. Several circular jump conditions were identified and the evolution, with increasing downstream depth, from a smooth depth increase through single jump and double jump structures to a disordered turbulent jump was described qualitatively.

While the location and internal flow patterns of the circular hydraulic jump have received considerable attention, and the unstable nature of the jump position has been mentioned, previous studies have examined flow rates in the range where unstable fluctuations would be minimized, or have ignored the fluctuations entirely. The objective of this study was to provide quantitative information on the location, shape and unsteady nature of the hydraulic jump formed by an impinging jet. This paper reports the results of measurements of the location of the free surface of the hydraulic jump as a function of nozzle size, jet Reynolds number, and downstream layer depth.

Apparatus and Method

A schematic diagram of the apparatus used for this study is shown in Fig. 1. The jet was formed in a closed loop system with a pump, rotameter-type flowmeter, nozzle, plexiglass impingement plane, and a vessel for collecting the spent water and returning it to the pump. The nozzles were formed with straight pipes of sufficient length to insure fully developed flow at the pipe outlet. The jet Reynolds number range, 20,000 to 50,000, indicated turbulent flow in all cases. Pipes of inside diameter 7.75 mm and 10.16 mm were used to form the jet. The spacing between the nozzle exit and the impingement plane was kept at 1.0 nozzle diameter for all tests. Other studies have shown that the flow field in the impingement region is very insensitive to the nozzle-to-plate spacing for free liquid jets in the ranges of $1 \leq z/d \leq 4$ and $15{,}000 < \mathrm{Re} < 50{,}000$ (Stevens, 1991). It seems reasonable to expect that the flow downstream from the stagnation region would be similarly insensitive. The impingement plane was equipped with a movable weir at the edge of the plane which could be raised or lowered to force the water on the downstream side of the jump to any desired depth. Uncertainty in the jet Reynolds number was less than 9 percent (20:1 odds) in all cases.

The instantaneous position of the free surface was determined by using a fine wire probe (0.25 mm diameter) attached to an A/D board and microcomputer. A small dc voltage was applied to the water, and the voltage probe completed the circuit between the water and the power supply ground. This apparatus returned a non-zero voltage if the tip of the probe was in contact with the water. The probe tip was positioned in the radial and axial dimensions with precision lead screws with 0.132 mm resolution in the radial coordinate and 0.025 mm resolution in the axial coordinate. These resolutions, in combination with bias uncertainty in the zero locations of the coordinates, result in maximum uncertainties of 9 percent (20:1 odds) and 8 percent (20:1 odds) in the absolute radial and axial positions. These uncertainties were calculated for the worst case; in percentage terms the uncertainty was much smaller for nearly all data reported. At each position, a large number of instantaneous measurements were taken, and the percentage of measurements for which the probe tip was in contact with the water was determined. While the data acquisition hardware was capable of sampling rates up to 100,000 samples/s, tests indicated that the hardware and software combined actually produced a maximum sampling rate near 20,000 samples/s. This sampling rate would provide the capability to collect unaliased data up to 10,000 samples/s, which would correspond to fluctuations 0.27 mm in length at the maximum fluid velocity of 2.7 m/s. Most fluid velocities were much slower than 2.7 m/s, and correspondingly smaller features would be detectable. Very small water droplets were formed by splashing of the impinging jet at the higher flow rates. When the probe tip was well clear of the water surface, the splashed droplets would collect and eventually form a water droplet on the probe tip. No such drop was evident when the probe was close to the water surface and it may be assumed that water continued to collect but was rapidly and repeatedly swept away by intermittent contact with the liquid layer. No interference with the measured results was anticipated, however, because the droplet formation time was on the order of seconds, while measurement times were on the order of 10^{-4} seconds. The physically intrusive nature of the probe raised the possibility of two sources of error in the measured results. The tip of the probe could be deflected by the water stream if measurements were made in regions of high velocity flow. For this reason the probe wire was kept short ($\approx$3.0 mm) and regions of high fluid velocity were avoided. The tip of the probe also disrupted the shape of the free surface being measured, particularly as the probe approached 100 percent submersion. The probe and water surface were carefully examined at each data point and no evidence of disruption on the water surface was visible for measurements at less than approximately 80 percent immersion. Nevertheless, some flow disruption had to occur at any time that the probe was in physical contact with the water. This shortcoming limits the applicability of these results to a

Nomenclature

d = nozzle diameter
Fr = Froude number, $V/(gy)^{0.5}$
g = acceleration of gravity
r = radial coordinate
Re = Reynolds number based on jet diameter and mean exit velocity
r_o = radius ratio: r_2/r_1
V = local mean radial fluid velocity
w = height of weir above the impingement plane
y = depth of liquid on the impingement plane
y_o = depth ratio: y_2/y_1
z = distance between the nozzle exit and the impingement plane
ν = fluid kinematic viscosity
σ = fluid surface tension
ρ = fluid density

Subscripts

1 = supercritical region just before the hydraulic jump
2 = subcritical region at the end of the hydraulic jump

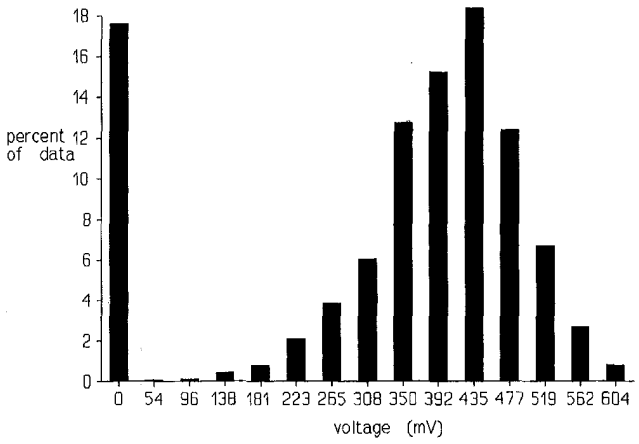

Fig. 2 Histogram of measured voltages at r/d = 14.34, y/d = 0.109, Re = 21,000, w/d = 0.0

general description of free surface profiles, and to an indication of the extent of free surface fluctuations, and precludes their use as exact instantaneous measurements of free surface locations. This physically intrusive experimental method, while suffering from the disadvantages described above, provided fast response, excellent spatial resolution, and the capacity to collect data on both vertical and horizontal fluctuations in the fluid layer near and at the hydraulic jump.

Results

Figure 2 is a histogram showing a typical distribution of measured voltages from the instantaneous measurements used to calculate a single data point. While the magnitude of the measured voltage varied with the position of the probe and flow conditions, the contact/no contact condition was well defined. For each probe position, 2000 individual measurements were taken at temporally uniform spacing. Then, the percentage of time that the probe was in contact with the water was calculated by dividing the number of non-zero voltage measurements by the total number of points.

Figure 3 demonstrates typical data sets for two nozzle sizes, weir settings, and flow rates. The dimensionless distance from the plate is plotted as a function of the percentage of time that the probe was in contact with the water, for various values of the dimensionless radial coordinate. The downward slope of each profile indicates the magnitude of the vertical fluctuations. For example, for the data set r/d = 13.33 in Fig. 3(a), at $y/d \approx 0.3$, the probe was in the water about 5 percent of the time, while at $y/d \approx 0.22$, it was in contact with the water about 95 percent of the time. The deeper downstream depth condition for Fig. 3(b) makes the location of the hydraulic jump slightly more obvious than in Fig. 3(a). The location of the front of the hydraulic jump near $r/d \approx 12.2$ in Fig. 3(b) caused the probe to make contact with the water due to both axial and radial fluctuations in the free surface at that radial location.

In order to generate a more succinct representation of the free surface locations and fluctuations, while providing a consistent treatment to each set of data, a linear regression was performed on each line of data in Fig. 3. While there is no expectation that these curves should be linear, it can be seen from Fig. 3 that the departures from linear behavior are generally small, and the linear regression provides a convenient method of representing each group of data consistently. Samples of the regression lines are shown for $r/d \approx 12.8$ and 13.3 in Fig. 3(a), and for $r/d \approx 12.2$ and 13.1 in Fig. 3(b).

The results from linear regressions for the data of Fig. 3, as well other flow and weir configurations are shown in Figs. 4(a) and 4(b). Figure 4(a) presents data for d = 7.8 mm and Fig. 4(b) contains data for d = 10.2 mm. Each symbol in Fig. 4 represents the y/d location where the probe was in the water 50 percent of the time (based on the linear regression). The vertical error bars on each plotted point represent the 0 and 100 percent intercepts of each regression. Thus, Fig. 4 provides a representation of the approximate mean location of the free surface, along with the approximate vertical extent of the free surface fluctuations. As would be expected, the fluctuations are largest near the front edge of the hydraulic jump, and are greater for higher Re. The progression from a single jump structure to a double jump structure with increasing downstream depth described by Liu and Lienhard (1993) is clearly visible in Fig. 4. Flow visualization by Liu and Lienhard (1993) showed that the double jump was caused by a separated eddy on the wall downstream from a free surface roller. It should be noted that in some cases these profiles do not cover the entire extent of the hydraulic jump, since the depth still appears to be increasing at the downstream end of the data. A comparison of the data sets for a single Reynolds number reveals that the front of the jump gets steeper and the jump gets longer radially with increasing subcritical depth.

The radial fluctuations of the hydraulic jump were measured in a manner analogous to that described above for the vertical fluctuations of the free surface. The probe was positioned at a fixed vertical location slightly above the supercritical flow, then moved radially until it was completely submerged in the subcritical flow. The approximate extent of the radial fluctuations are shown in Fig. 4(a) with horizontal bars. The magnitude of the radial fluctuations increases markedly with increasing downstream flow depth, but the radial fluctuations of the hydraulic jump are still relatively small compared with the total length of the jump. Note that the scales of the abscissa and ordinate

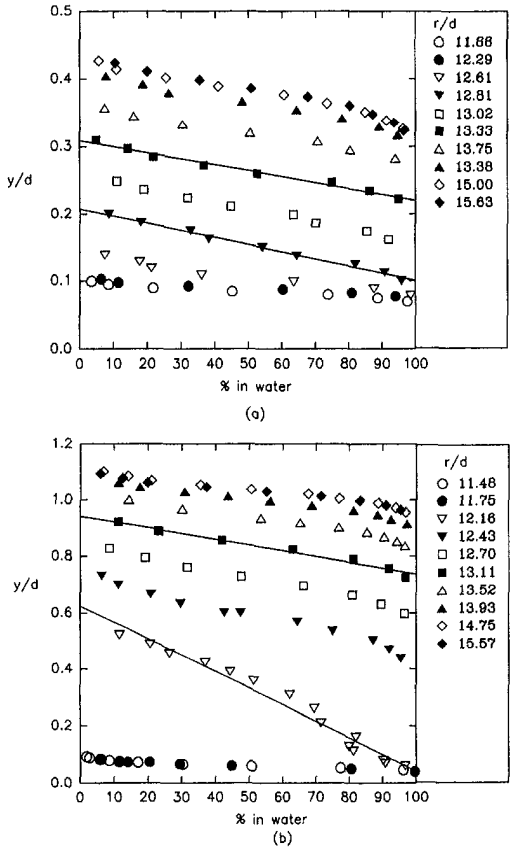

Fig. 3 Liquid layer fluctuations as a function of the radial coordinate: (a) d = 10.16 mm, w/d = 0.0, Re = 19,000; (b) d = 7.75 mm, w/d = 0.5, Re = 31,000

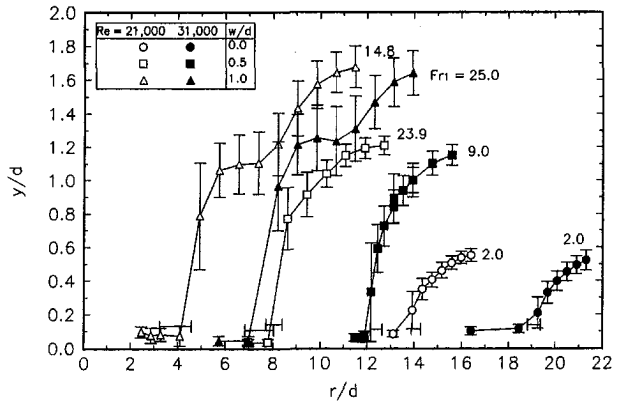

Fig. 4(a)

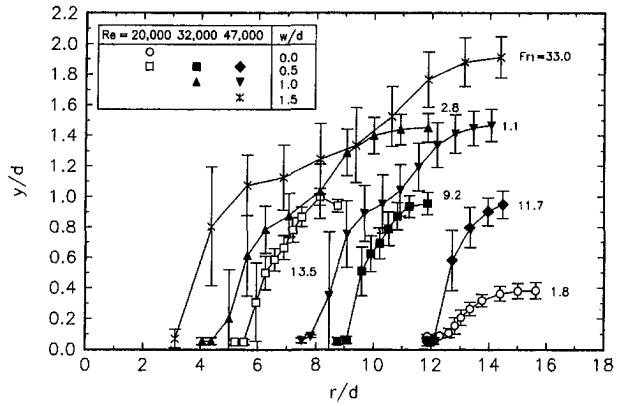

Fig 4(b)

Fig. 4 Hydraulic jump surface profiles and fluctuations: (*a*) *d* = 7.75 mm (*b*) *d* = 10.16 mm

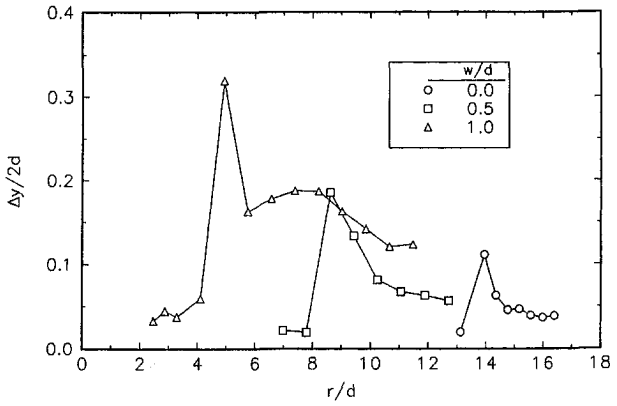

Fig. 6(a)

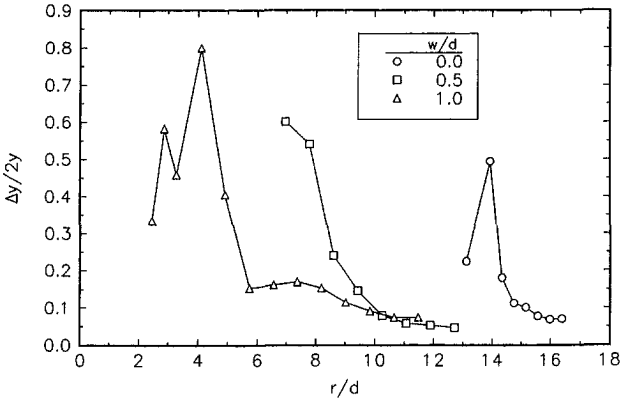

Fig. 6(b)

Fig. 6 Dimensionless free surface fluctuations for *d* = 7.75 mm, Re = 21,000: (*a*) relative to nozzle diameter; (*b*) relative to local layer depth

in Fig. 4(*a*) differ by a factor of approximately seven. Froude numbers calculated at the last supercritical data point in each profile are included in Figs. 4(*a*) and 4(*b*). These numbers may not represent an accurate supercritical Froude number with respect to the jump, since they could only be calculated from the last data point, which was not at the exact foot of the jump in all cases.

The radial fluctuation data in Fig. 4(*a*) is plotted along with additional data in Fig. 5. The mean radial position of the stream face of the jump is shown as a function of Re and *w*/*d*. The 0 and 100 percent immersion intercepts are shown with vertical error bars as in Fig. 4. This figure clearly shows the increase in magnitude of the fluctuations with increasing subcritical depth. In contrast, increasing jet Reynolds number appears to have little effect on the magnitude of the fluctuations, though it does, as expected, change the jump position. The data of Fig. 5 can be correlated reasonably well (±20 percent) for the jump location as a function of Re and *w*/*d*, however, with two independent variables and only 11 data points, such a correlation would not be reliable.

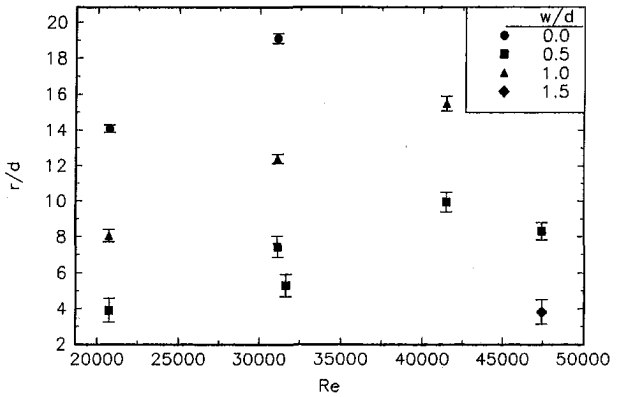

Fig. 5 Radial fluctuations in the front face of the hydraulic jump

Figure 6 demonstrates the extent of the vertical fluctuations of the free surface for several data sets from Fig. 4(*a*). The vertical fluctuations relative to the nozzle diameter are shown in Fig. 6(*a*) and the same fluctuations relative to local layer depth are shown in Fig. 6(*b*). In either view, the fluctuations are very high at the front of the jump, drop off rapidly, then become more uniform toward the back of the jump. These trends were similar for all jet configurations studied.

Relatively few data points were taken in the supercritical region prior to the jump, but these measurements can be compared to a previous empirical correlation for the radial layer depth. Figure 7shows two extremes of the empirical correlation for the layer depth from Stevens and Webb (1992) wherein the average depth was calculated based on LDV measurements of the surface velocity, an assumed velocity profile, and conservation of mass considerations. Also shown in Fig. 7 are data for the time average layer depth measured prior to the hydraulic jump in this study. The agreement is fair, with the data of this study following the same trend but falling mostly to the higher side of the empirical correlation. This would agree with the expected skewing of the average local depth for the intrusive probe of this study. That is, the interference of the probe with the liquid would be expected to cause the apparent liquid layer

depth to be greater than the actual depth. Note that these measurements are in the liquid layer prior to the jump, and that measured average layer depth is less than 1.5 mm. Considering the scatter in the data from which the empirical correlation was derived, the approximations used in that correlation, and the accuracy of the measurement method for this study, the agreement appears reasonable.

The data of this study may also be compared to theoretical predictions of the radial position of the jump. Koloseus and Ahmad (1969) apply conservation of mass and momentum to a circular hydraulic jump to derive an expression relating the downstream-to-upstream depth and radius ratios to the pre-jump Froude number:

$$y_o^3 - \frac{r_o - 1}{2r_o + 1} y_o^2 - \frac{r_o + 6\,\mathrm{Fr}_1^2 + 2}{2r_o + 1} y_o + \frac{6\,\mathrm{Fr}_1^2}{r_o(2r_o + 1)} = 0 \quad (1)$$

Watson (1964) derived an equation for the jump location for turbulent flow of an impinging jet. In the Nomenclature of this paper, this equation can be expressed as:

$$\left(\frac{1}{y_1/d}\right)\left(\frac{1}{y_o}\right)\left(\frac{y_o^3}{2\,\mathrm{Fr}_1^2} + 1\right) = \frac{191.9(r_1/d)}{4.25\left(\frac{(r_1/d)^9}{\mathrm{Re}}\right)^{0.25} + 24.3} \quad (2)$$

Both theoretical expressions involve the depth of the liquid preceding and following the hydraulic jump, and the radius and Froude number of the flow just preceding the jump. In order to compare the measured data with the theoretical expressions, the upstream Froude number, layer depth and radius were taken from the last data point at which the Fr was greater than unity. (The Froude numbers for these points are shown in Fig. 4.) These numbers were then used in the theoretical expressions with successive values of the measured subcritical layer depth until the equation was satisfied. The resulting point should be at (r_2,y_2), that is, the end of the hydraulic jump. Of course, this procedure assumes that the last point for which the Froude number is greater than unity was the beginning of the hydraulic jump, (r_1,y_1), which was not guaranteed. Note that each equation predicts only a single point (r_2,y_2) for each profile, and that the analysis *forces* this point to lie on the curve of measured data. The difference between theory and experiment, then, is composed of the difference between the predicted point (r_2,y_2), and the measured end of the hydraulic jump. The ends for the hydraulic jump predicted by Eqs. (1) and (2) are shown for the data of Fig. 4 in Fig. 8. The theoretical expressions generally indicate jump widths shorter than those determined by the measurements. The difference may be explained by noting that (1) was derived with assumptions of hydrostatic pressure distribution before and after the jump, no air entrained in the jump, and a straight line free surface profile for the jump. The latter two assumptions were violated in the experimental configurations reported here. In addition, Eqs. (1) and (2) are very sensitive to the values used for r_1 and y_1, and, as discussed above, r_1 and y_1 were approximated by using the closest available data point from the experimental data.

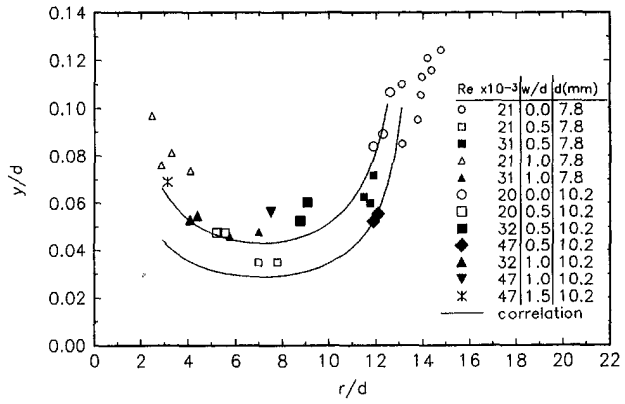

Fig. 7 Comparison of average depth of the supercritical flow layer to the data of Stevens and Webb (1992)

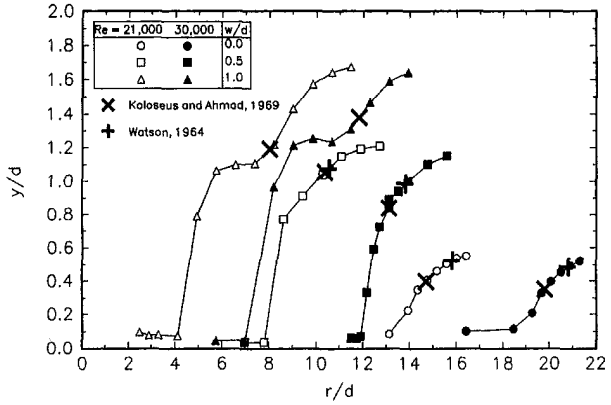

Fig. 8(a)

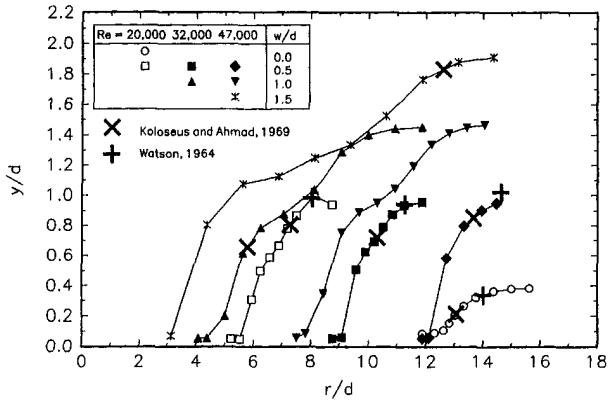

Fig. 8(b)

Fig. 8 Comparison of the data of Fig. 4 with the theoretical expression of Watson (1964), and Koloseus and Ahmad (1969)

Conclusion

Measurements of the profile and unsteady fluctuations of the free surface of the circular hydraulic jump formed by an impinging jet have been presented. The study examined two nozzle sizes, a jet Reynolds number range of 20,000 < Re < 50,000, and a range of downstream weir heights of $0 \le w/d \le 1.5$. The results of measurements of the average liquid layer depth prior to the hydraulic jump agreed reasonably well with previous measurements in this region. A comparison with two theoretical expressions for the size and radial location of the jump found that the measured jump was wider than that predicted by the theories, for given conditions on the beginning of the jump, upstream Froude number, and upstream liquid depth.

References

Bowles, R. I., and Smith, F. T., 1992, "The Standing Hydraulic Jump: Theory, Computations and Comparisons with Experiments," *Journal of Fluid Mechanics*, Vol. 242, pp. 145–168.

Craik, A. D. D., Latham, R. C., Fawkes, M. J., and Gribbon, P. W. F., 1981, "The Circular Hydraulic Jump," *Journal of Fluid Mechanics*, Vol. 112, pp. 347–362.

Khalifa, A. M., and McCorquodale, J. A., 1979, "Radial Hydraulic Jump," *Journal of the Hydraulics Division,* ASCE, Vol. 105, pp. 1065–1078.

Khalifa, A. A. M., and McCorquodale, J. A., 1992, "Simulation of the Radial Hydraulic Jump," *Journal of Hydraulic Research,* Vol. 30, n. 2, pp. 149–163.

Koloseus, H. J., and Ahmad, D., 1969, "Circular Hydraulic Jump," *Journal of the Hydraulics Division,* ASCE, Vol. 95, pp. 409–422.

Lawson, J. D., and Phillips, B. C., 1983, "Circular Hydraulic Jump," *Journal of Hydraulic Engineering,* Vol. 109, pp. 505–518.

Liu, X., and Lienhard, V, J. H., 1993, "The Hydraulic Jump in Circular Jet Impingement and in Other Thin Liquid Films," *Experiments in Fluids,* Vol. 15, pp. 108–116.

Rahman, M. M., Faghri, A., and Hankey, W. L., 1990a, "The Flow of a Thin Liquid Film on a Stationary and Rotating Disk—Part II: Theoretical Prediction," AIAA/ASME Thermophysics and Heat Transfer Conference, *Heat Transfer in Space Systems,* S. H. Chan, E. E. Anderson, R. J. Simoneau, C. K. Chan, D. W. Pepper, B. F. Blackwell, Vol. HTD-Vol. 135, pp. 135–142.

Rahman, M. M., Faghri, A., and Hankey, W. L., 1991, "Computation of Turbulent Flow in a Thin Liquid Layer of Fluid Involving a Hydraulic Jump," ASME JOURNAL OF FLUIDS ENGINEERING, Vol. 113, n. 3, p. 411.

Rajaratnam, N., 1967, "Hydraulic Jumps," *Advances in Hydroscience,* V. T. Chow, ed., Vol. 4, pp. 197–281.

Stevens, J., 1991, "Measurements of Local Fluid Velocities in an Axisymmetric, Free Liquid Jet Impinging on a Flat Plate," Ph.D. thesis, Brigham Young University, Provo, UT, 84602.

Stevens, J., and Webb, B. W., 1992, "Measurements of the Free Surface Flow Structure Under an Impinging Free Liquid Jet," ASME *Journal of Heat Transfer,* Vol. 114, pp. 79–84.

Thomas, S., Faghri, A., and Hankey, W. L., 1990, "The Flow of a Thin Liquid Film on a Stationary and Rotating Disk—Part I: Experimental Analysis and Flow Visualization," AIAA/ASME Thermophysics and Heat Transfer Conference, *Heat Transfer in Space Systems,* S. H. Chan, E. E. Anderson, R. J. Simoneau, C. K. Chan, D. W. Pepper, B. F. Blackwell, eds., HTD-Vol. 135, pp. 125–133.

Watson, E. J., 1964, "The Radial Spread of a Liquid Jet Over a Horizontal Plane," *Journal of Fluid Mechanics,* Vol. 20, part 3, pp. 481–499.

The Introduction of Micro Cells to Treat Pressure in Free Surface Fluid Flow Problems

Peter E. Raad
Associate Professor. Mem. ASME

Shea Chen
Research Associate. Assoc. Mem. ASME

David B. Johnson
Associate Professor. Mem. ASME

Mechanical Engineering Department,
Southern Methodist University,
Dallas, TX 75275-0337

A new method of calculating the pressure field in the simulation of two-dimensional, unsteady, incompressible, free surface fluid flow by use of a marker and cell method is presented. A critical feature of the new method is the introduction of a finer mesh of cells in addition to the regular mesh of finite volume cells. The smaller (micro) cells are used only near the free surface, while the regular (macro) cells are used throughout the computational domain. The movement of the free surface is accomplished by the use of massless surface markers, while the discrete representation of the free surface for the purpose of the application of pressure boundary conditions is accomplished by the use of micro cells. In order to exploit the advantages offered by micro cells, a new general equation governing the pressure field is derived. Micro cells also enable the identification and treatment of multiple points on the free surface in a single surface macro cell as well as of points on the free surface that are located in a macro cell that has no empty neighbors. Both of these situations are likely to occur repeatedly in a free surface fluid flow simulation, but neither situation has been explicitly taken into account in previous marker and cell methods. Numerical simulation results obtained both with and without the use of micro cells are compared with each other and with theoretical solutions to demonstrate the capabilities and validity of the new method.

1 Introduction and Justification

In the numerical simulation of unsteady, incompressible, free surface fluid flow problems, the location of the free boundary is not known a priori. Therefore, in addition to including a method for solving the Navier-Stokes and continuity equations, any solution procedure for free surface fluid flow problems must also include methods for locating and advancing the free surface, as well as for treating the free surface boundary conditions. In fact, the capability of any free surface fluid flow simulation is determined to a very significant extent by the method employed for the numerical treatment of the free surface.

According to Hirt and Nichols (1981), "three types of problems arise in the numerical treatment of free boundaries: (1) their discrete representation, (2) their evolution in time, and (3) the manner in which boundary conditions are imposed on them." In this paper, the discrete representation of the free surface is accomplished by the use of cells that are smaller than the regular cells employed to locate the primary variables. The introduction of micro cells also enables the development of a new approach for the imposition of free surface pressure boundary conditions, which together with the accurate treatment of free surface velocity boundary conditions (Chen et al., 1995) make it possible to use realistic values of the fluid's viscosity and the gravitational constant. Previous marker and cell methods had to use unrealistically high values of viscosity and low values of gravity in order to dampen numerical oscillations due in large part to inaccuracy in the application of free surface boundary conditions.

The height function (Nichols and Hirt, 1976; Bulgarelli et al., 1984; Loh and Rasmussen, 1987; Lardner and Song, 1992), line segment (Chan and Street, 1970; Nichols and Hirt, 1971), marker and cell (Harlow and Welch, 1965; Amsden and Harlow, 1970), volume of fluid (Nichols and Hirt, 1975; Hirt and Nichols, 1981; Torrey et al., 1985; Ashgriz and Poo, 1991), and surface marker (Chen et al., 1991; Johnson et al., 1994; Chen et al., 1995) methods are different solution procedures for free surface fluid flow problems, each employing a different approach for locating and advancing the free surface.

Before proceeding to a description of the new method, an example is presented to emphasize the fact that the inaccurate application of the free surface pressure boundary conditions will lead to an incorrect solution of a free surface fluid flow problem. In this special example, the effects of the inaccurate application of pressure boundary conditions on the shape and position of the free surface are isolated. The system to be considered consists of a stationary container that is partially filled with water initially at rest. Because the fluid is at rest and is undisturbed, neither inertia nor viscous forces should influence the shape or location of the free surface. In the first case, the bottom of the container rests on a horizontal surface, whereas in the second case, depicted in Fig. 1, the container is tilted at 30° to the horizontal. In either case, the free surface should simply remain horizontal if nothing disturbs either the container or the water. For the purpose of simulation, the domain is divided into 20 by 20 cells, with cell dimensions of 0.25 cm by 0.25 cm, the time step is set at $\delta t = 10^{-3}$ s, the gravitational constant is set at $g = 9.8$ m/s^2, and the viscosity is set at $\nu = 1.12 \times 10^{-6}$ m^2/s.

If the horizontal situation is simulated by use of a method in which the free surface pressure boundary conditions are applied at the centers of the surface cells, the free surface remains horizontal, as expected. Even for this situation, however, the value of the hydrostatic pressure will be calculated correctly only if the free surface passes through the centers of the surface cells. Since the pressure boundary conditions are applied at the centers of the surface cells, the calculated pressure field does not depend on the actual location of the free surface within the surface cells. Hence, the calculated pressures can be off by as much as $\pm\rho g \delta y/2$, where ρg is the fluid's specific weight and δy is the cell height.

If, on the other hand, water at rest in the inclined container of Fig. 1(a) is simulated by use of a method in which the free

Contributed by the Fluids Engineering Division for publication in the JOURNAL OF FLUIDS ENGINEERING. Manuscript received by the Fluids Engineering Division August 10, 1994; revised manuscript received April 14, 1995. Associate Technical Editor: O. C. Jones.

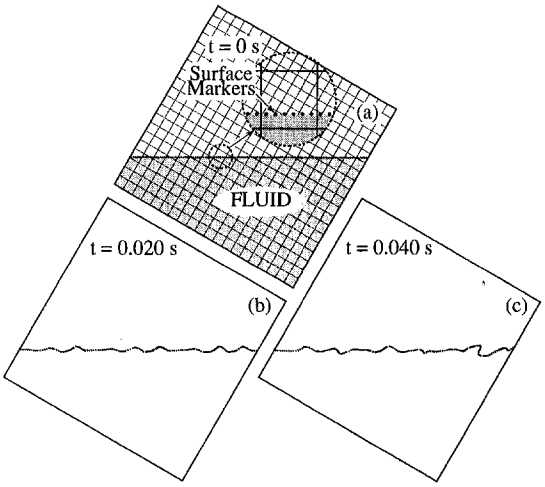

Fig. 1 SM Simulation of stationary water in a container inclined at 30 deg to the horizontal

surface pressure boundary conditions are applied at the centers of the surface cells, unexpected surface oscillations are observable after only 0.02 s as shown in Fig. 1(*b*). These oscillations are due entirely to the fact that the free surface pressure boundary conditions are inaccurately applied, resulting in a stair step representation of the free surface. The oscillations persist, and the description of the free surface worsens with time (Fig. 1(*c*)). It is worth noting that, rather than being unusual, the situation illustrated in Fig. 1(*a*), namely that the free surface is not parallel to the grid lines, is typical.

2 The Micro Cell Method

In all of the finite difference methods mentioned in the preceding section, the same cells are employed to define *both* the locations of the discrete field variables and the location of the free surface. The idea that lead to the development of the micro cell (MIC) method is that it is not necessary that the cells employed to locate the discrete field variables be identical to the cells employed to locate the free surface. In the new method, two types of cells are used. In addition to the standard finite difference/volume cells, hereafter referred to as macro cells, new cells termed micro cells also are introduced. In the MIC method, surface markers are used to advance the free surface; and micro cells, which are smaller than the macro cells, are used to locate the free surface, making it possible to apply the free surface pressure boundary conditions more efficiently and accurately.

2.1 The Computational Cycle. The field variables are advanced from an arbitrary time t_0 to the next time $t_0 + \delta t$ by the following steps.

1. Reflag the micro and macro cells.
2. Assign tentative velocity boundary conditions.
3. Compute a tentative velocity field, $\tilde{u}$ and $\tilde{v}$, at $t_0 + \delta t$ from the velocity field at t_0 by use of

$$\frac{\partial \tilde{u}}{\partial t} = -\frac{\partial u^2}{\partial x} - \frac{\partial uv}{\partial y} + \nu\left(\frac{\partial^2 u}{\partial x^2} + \frac{\partial^2 u}{\partial y^2}\right) + g_x \quad (1)$$

$$\frac{\partial \tilde{v}}{\partial t} = -\frac{\partial v^2}{\partial y} - \frac{\partial uv}{\partial x} + \nu\left(\frac{\partial^2 v}{\partial x^2} + \frac{\partial^2 v}{\partial y^2}\right) + g_y, \quad (2)$$

where (u, v) are the (x, y) velocity components; (g_x, g_y) are the (x, y) gravity components; and ν is the kinematic viscosity of the fluid.

4. Calculate the incompressibility deviation function D defined by

$$D = \partial \tilde{u}/\partial x + \partial \tilde{v}/\partial y. \quad (3)$$

5. Solve for the pressure potential field $\Psi = \delta t\, p/\rho$, where p is pressure and ρ is the fluid density, by use of a new equation developed in Section 2.5.
6. Compute the final velocity components at $t_0 + \delta t$ by use of new equations introduced in Section 2.5.
7. Assign the final velocity boundary conditions.
8. Advect the free surface and manage surface markers.
9. Assign new fluid cell velocities.

The general outline of this computational cycle is similar to those presented in Amsden and Harlow (1970), Chen et al. (1991, 1995), and Johnson et al. (1994). However, Steps 1 and 5–9 are either new or significantly altered.

As far as vorticity is concerned, the tentative velocity field computed by use of Eqs. (1) and (2) is correct. In addition, since vorticity is not a function of pressure, the vorticity associated with the final velocity field at $t_0 + \delta t$ will be the same as the vorticity associated with the tentative velocity field. The tentative velocity field does not, however, necessarily satisfy the continuity equation. A measure of the failure of the tentative velocity field to satisfy the continuity equation is provided by the incompressibility deviation function D defined by Eq. (3). In order to obtain a final velocity field that does satisfy the continuity equation, a pressure potential field, Ψ, must be solved for and used to adjust the tentative velocity field.

2.2 The New Mesh of Macro and Micro Cells. The computational domain is comprised of macro computational and boundary cells. A boundary cell defines the location of a rigid, stationary obstacle, while a computational cell that contains any amount of fluid is called a fluid cell. A fluid cell may be either a surface or full cell. If it contains surface markers and has at least one empty macro cell neighbor, it is flagged as surface, while if it has no empty macro cell neighbors, it is flagged as full. Near the free surface, it is possible for a macro cell that contains surface markers to be flagged as full. Otherwise, full macro cells do not contain markers. The interfaces of the macro cells are called macro grid lines. In general, the fluid free surface passes through the macro surface cells. The staggered grid concept is used to locate the discrete field variables and functions of those variables. The pressure potential $\Psi_{i,j}$ and the incompressibility deviation function $D_{i,j}$ are located at the center of computational macro cell (i, j); the discrete velocities $u_{i,j}$ and $u_{i-1,j}$ are located at the middle points of the right and left faces of the cell, respectively; and the discrete velocities $v_{i,j}$ and $v_{i,j-1}$ are located at the middle points of the top and bottom faces, respectively.

In the new method, the micro cells are created by subdividing each macro cell into N by N micro cells, where N is an odd integer chosen by the analyst. Comparisons between solutions obtained with N = 1 (no micro cells), 3, and 5 are presented in Section 3. The value of N is chosen as an odd integer so that the center of the macro cell, where $\Psi_{i,j}$ and $D_{i,j}$ are defined, coincides with the center of a micro cell. However, at any given time during a simulation, only micro cells near the free surface are involved in the computations. Micro cells, like macro cells, require flags. The definitions of micro boundary, empty, surface, and full cells are similar to those of corresponding macro cells. For example, a micro fluid cell is flagged as surface or full depending on its condition: a surface micro cell is a micro fluid cell that contains surface markers and has at least one empty micro cell neighbor, while a full micro cell is defined as a micro fluid cell that has no empty micro cell neighbors.

As a typical example, nine macro cells near the free surface are shown in Fig. 2, four of which have been subdivided into micro cells. The macro and micro grid lines are represented by

thick and thin lines, respectively. Of the four macro cells that contain micro cells, the one in the center of Fig. 2 is a full macro cell, and the other three are surface macro cells. In these four macro cells, the surface and full micro cells are designated by s and f, respectively, while the empty micro cells are blank. As shown in Fig. 2, one macro cell can contain three different kinds of micro cells at the same instant. It is not necessary, however, for micro cells to be used in each macro cell. For example, no micro cells are used with five of the macro cells shown in Fig. 2. Each of these five macro cells is simply designated with either an E for empty or an F for full. By selectively superimposing micro cells on the macro cells, a better definition of the location of the free surface is possible than can be achieved by the use of macro cells alone.

2.3 The Reflagging Algorithm. Since surface markers are used to track the movement of the free surface, the reflagging algorithm introduced by Chen et al. (1991) is extended to accommodate the reflagging of micro cells. At a given instant, each macro and micro cell possesses *a full, surface,* or *empty* flag. During each computational cycle, the reflagging of micro cells is done prior to the reflagging of macro cells and is similar to it. Before moving the surface markers, all micro cells that contain markers are assigned a temporary *check* flag. After all the markers have been moved and markers have been added as required, the micro cells that now contain markers are flagged as surface. Next, the flag of any remaining check micro cell is changed to empty if the micro cell in question has an empty micro cell neighbor; otherwise, it is changed to full. Finally, the flag of any surface micro cell that now does not have at least one empty micro cell neighbor is changed to full. It must be noted that this micro cell reflagging procedure requires that no marker be allowed to travel in any direction in one time step a distance larger than the dimension of a micro cell in that direction. If nine micro cells per macro cell are used, this consideration imposes no additional restriction on the size of the computational time step, because the use of small time steps is necessary to insure the accuracy of the explicit schemes that are employed to solve the governing fluid flow equations. Hirt and Nichols (1981) state that: "Typically, δt is chosen equal to one-fourth to one-third of the minimum cell transit time." If twenty-five micro cells per macro cell are used, δt must be less than one-fifth of the minimum cell transit time, which is slightly less than the smaller value they suggested.

2.4 Free Surface Pressure Boundary Conditions. Boundary conditions are required for the solution of the pressure potential field, Ψ. Ideally, the boundary conditions along the free surface would be applied at points that are directly on the free surface. In the MIC method, the free surface pressure boundary conditions are applied at the centers of surface micro cells. The result is that the free surface pressure boundary conditions are applied very accurately, with the important added advantage that the locations of the points of application are determined very efficiently. For example, for the situation shown in Fig. 3, with nine micro cells per macro cell, point m is the center of

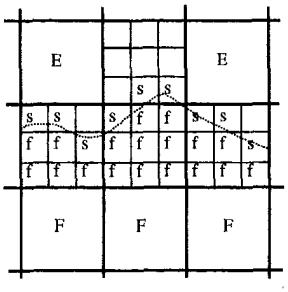

Fig. 2 Macro and micro cells

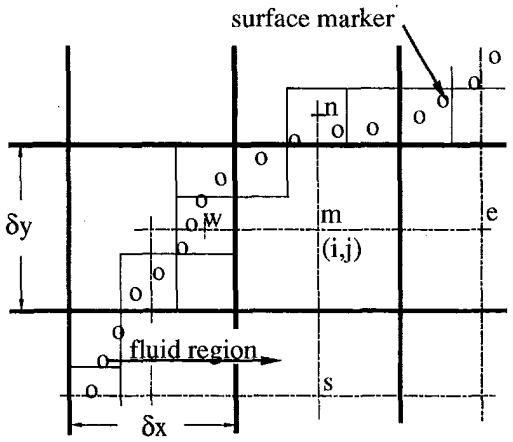

Fig. 3 Points used in pressure potential approximation for cell (i, j)

macro cell (i, j); and points e, n, w, and s are neighboring points to the east, north, west, and south of point m, respectively. The locations of points e, n, w, and s and their respective distances δe, δn, δw, and δs from point m all are required for the computation of the pressure potential at point m. For the example of Fig. 3, points e and s are simply the centers of the full macro cells to the east and south of cell (i, j). Consequently, $\delta e = \delta x$ and $\delta s = \delta y$. On the other hand, points n and w represent points on the free surface and are the centers of the first surface micro cells to the north and west of the center of cell (i, j), respectively. For this particular example, the distances δn and δw are equal to $2\delta y/3$ and $2\delta x/3$, respectively. Points n and w are very near the free surface, and the determination of the lengths δn and δw is simple and efficient. If more than nine micro cells per macro cell were used, the corresponding points of application of the free surface pressure boundary conditions would, in general, be even closer to the free surface, and the determination of the required distances between the free surface and the center of cell (i, j) would still be just as efficient. The determination of "unequal leg lengths" such as δn and δw is required only for some of the macro fluid cells that are near the free surface.

2.5 New Pressure Potential Equation. The MIC method introduces a new equation governing the pressure potential field. Since the objective of the use of the pressure potential field is to provide a final velocity field that satisfies continuity, the new equation is derived by substituting the final velocity equations directly into the continuity equation.

The general expression for the unequal-legs pressure equation used in the MIC method is derived by starting with the usual final velocity equations that make use of the pressure potential field Ψ:

$$u = \tilde{u} - \partial\Psi/\partial x, \tag{4}$$

$$v = \tilde{v} - \partial\Psi/\partial y. \tag{5}$$

Writing Eqs. (4)–(5) in difference form for cell (i, j) yields:

$$u_{i,j} = \tilde{u}_{i,j} - (\Psi_e - \Psi_{i,j})/\delta e_{i,j}, \tag{6}$$

$$v_{i,j} = \tilde{v}_{i,j} - (\Psi_n - \Psi_{i,j})/\delta n_{i,j}, \tag{7}$$

$$u_{i-1,j} = \tilde{u}_{i-1,j} - (\Psi_{i,j} - \Psi_w)/\delta w_{i,j}, \tag{8}$$

and

$$v_{i,j-1} = \tilde{v}_{i,j-1} - (\Psi_{i,j} - \Psi_s)/\delta s_{i,j}, \tag{9}$$

where Ψ_e, Ψ_n, Ψ_w, and Ψ_s represent the pressure potentials at points e, n, w, and s, respectively. Next, these four equations (6)–(9) are substituted into the continuity equation

$$(u_{i,j} - u_{i-1,j})/\delta x + (v_{i,j} - v_{i,j-1})/\delta y = 0 \qquad (10)$$

for the control volume that coincides with cell (i, j). The resulting equation can be written as

$$C\Psi - \frac{\Psi_e}{\delta x \delta e} - \frac{\Psi_n}{\delta y \delta n} - \frac{\Psi_w}{\delta x \delta w} - \frac{\Psi_s}{\delta y \delta s} = -D \qquad (11)$$

where $C = (\delta e^{-1} + \delta w^{-1})/\delta x + (\delta n^{-1} + \delta s^{-1})/\delta y$.

In the MIC method, Eq. (11) is used for cells near the free surface for the determination of the pressure potential field in Step 5 of the computational cycle. It should be noted that Eq. (11) reduces to the standard finite difference form of the pressure potential Poisson equation for a full macro cell that is not near the free surface.

2.6 Calculation of the Pressure Potential Field. Consider the sketch shown in Fig. 4 of fluid sloshing in a container. The computational region consists of twenty five macro cells. The container consists of the square region of nine macro cells in the center of Fig. 4. A single layer of boundary cells completely surrounds the container. The free surface at the instant under consideration is indicated by a dashed line. Micro cells, nine per cell, are shown in five of the macro cells that the free surface passes through.

In general, the pressure potential must be calculated in all full macro cells as well as in any other macro cell whose center micro cell is full. Therefore, in the example of Fig. 4, $\Psi_{i,j}$ must be calculated in all six of the macro cells in the bottom two rows of the cavity. The application of the new pressure potential equation, Eq. (11), requires the determination of leg lengths. A leg length in the direction of a free surface is determined by counting the number of full micro cells between the center of the cell under consideration and the free surface. For the example under consideration, the unequal leg lengths are

$$\delta e_{2,3} = \delta x/3, \quad \delta n_{2,3} = \delta y/3, \quad \delta w_{3,3} = 2\delta x/3,$$

$$\delta n_{3,3} = 2\delta y/3, \quad \delta e_{4,3} = \delta x/3, \quad \delta n_{4,3} = \delta y/3.$$

All other required leg lengths are equal to either δx or δy. Using the preceding leg lengths in Eq. (11) and forcing the gradient of the pressure normal to a solid boundary to vanish leads to the six required pressure potential equations which can be written in matrix form as $\mathbf{M}\ \Psi = \mathbf{R}$. The resulting square matrix $\mathbf{M}$ is positive definite and symmetric. Hence, the PCG method, which is adaptable to parallel and vector processing, can be efficiently applied to obtain an accurate pressure solution. After the pressure potential field has been calculated, the final velocities $u_{i,j}$ and $v_{i,j}$ must be computed. Micro cells also contribute to the implementation of the new set of final velocity equations (Eqs. (6)–(9)).

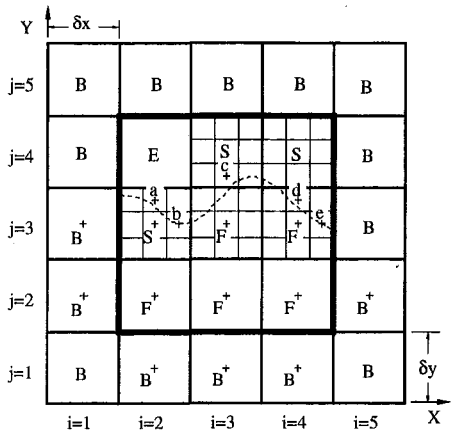

Fig. 4 Micro cells used for calculation of leg lengths in pressure potential equation

2.7 Discussion. The MIC method represents an entirely new approach to the application of free surface pressure boundary conditions. In addition to the other significant differences between the MIC method and the line segment method, the new unequal-legs pressure equation is different than either the "irregular star" approximation that was presented by Chan and Street (1970) or the interpolation/extrapolation technique presented by Nichols and Hirt (1971). Chan and Street used Taylor series expansions to derive their irregular star approximation. Consequently, the continuity equation is not satisfied in full irregular star cells. If the technique of Nichols and Hirt is used, there can be only one free surface location in a surface cell. Consequently, it is not possible to satisfy the free surface pressure boundary conditions at two points in the same surface cell, such as points a and b in cell (2, 3) in Fig. 4. In contrast, the continuity equation will be satisfied in every cell in which the pressure potential is computed in the MIC method, and the free surface pressure boundary conditions can easily be satisfied at points such as a and b in surface cell (2, 3). In addition, in spite of the fact that cell (4, 3) in Fig. 4 has no empty neighbors and, thus, is flagged as a full cell, the new method also allows the imposition of free surface pressure boundary conditions at points d and e, the centers of the two surface micro cells that are found in cell (4, 3). Whereas the irregular star approximation leads to an unsymmetrical system of equations, the new pressure equation leads to a symmetric set of equations. Finally, the use of micro cells allows the efficient determination of the points of application of the pressure boundary conditions and of the associated leg lengths that are required in the new pressure equation.

3 Simulation Results and Validation

In this section, comparisons are made between the simulation results of the surface marker (Chen et al., 1991) and micro cell methods, hereafter referred to as SM and MIC, respectively, in order to demonstrate the significance of the new methods presented in this paper. Additionally, in order to demonstrate its validity, the MIC method is used to simulate problems for which solutions are known.

Simulation results are presented for four different free surface fluid flow examples. Attention is focused on the shape and location of the free surface during each simulation. The size and resolution of the computational grid are specified for each of the problems. In the MIC method, the time step δt is calculated and updated automatically at each time level in order to maintain the accuracy of the solution. For each problem presented here, however, an appropriate fixed time step is chosen for ease of comparison and reporting. A slip flow condition is applied along a solid boundary.

3.1 Still Water Example. At the end of Section 1, a simple problem was considered in order to illustrate the ramifications of the inaccurate application of the free surface boundary conditions. The same problem is revisited here to illustrate the advantages of the use of the MIC method. If the horizontal container problem is simulated by use of the MIC method, the free surface remains horizontal, just as it does when the same problem is simulated by use of the SM method. In addition, however, since each surface cell in the MIC method is subdivided into N by N micro cells, the calculated hydrostatic pressures will be correct if the free surface passes through the centers of any row of surface micro cells. Regardless of the location of the free surface, the maximum discrepancy in the calculated pressure for the MIC method will be no more than $\pm\rho g\delta y/(2N)$, whereas the maximum discrepancy can be as much as $\pm\rho g\delta y/2$ for the SM method. The added accuracy afforded by the use of micro cells is achieved with significantly less

computational expense than would be associated with an N by N fold increase in the number of macro cells which would be required to achieve the same accuracy by the use of macro cells alone.

Next, the inclined container problem in Fig. 1(*a*) is simulated by use of the MIC method. As stated previously, neither inertia nor viscous effects should influence the shape and location of the free surface, and the free surface should remain horizontal. Figures 5(*a*) and 5(*b*) show the solutions for N = 3 at times t = 0.02 s and 0.04 s, respectively. By use of the new method, the surface oscillations clearly visible in Figs. 1(*b*) and 1(*c*) have been significantly reduced and are almost imperceptible. To further improve the accuracy and check the solution's convergence, the number of micro cells subdividing each macro cell can be increased. Figures 5(*c*) and 5(*d*) represent the solutions for N = 5 at times t = 0.02 s and 0.04 *s*, respectively. Some improvement over the results of the N = 3 case is visible, but here again, the surface oscillations are nearly imperceptible, indicating an excellent treatment of the free surface pressure boundary conditions with either N = 3 or 5.

3.2 Small Amplitude Sloshing in a Tank. The next test problem to be considered is that of the sloshing of an inviscid fluid in a tank. The object of this example is to show that the new method can faithfully simulate the small amplitude sloshing of the contained fluid with minimal distortion in either the phase or amplitude of the wave. This problem has been investigated previously by Tadjbakhsh and Keller (1960) and referred to by Torrey et al. (1985). Initially, the quiescent fluid has an average depth of 5 cm, and its surface is defined by one half of a cosine wave with an amplitude of 5 mm. The 10 cm by 6.5 cm computational domain is discretized with 80 cells in the x-direction and 52 cells in the y-direction, resulting in $\delta x = \delta y$ = 1.25 mm. The fluid begins to slosh solely under the influence of a constant gravitational field set at 9.8 m/s^2 in the downward vertical direction. The time step δt is set at 0.25 ms and the viscosity of the fluid is set equal to zero.

In order to demonstrate the significance of the use of micro cells, simulation results at time t = 0.24 s are presented in Fig. 6(*a*) for N = 1 and in Fig. 6(*b*) for N = 3. Superimposed in Fig. 6(*a*) is the shape of the water's free surface at the initial time, t = 0. For N = 1, no micro cells are used, and pronounced oscillations are visible on the free surface in Fig. 6(*a*), representing an irreparable degradation of the anticipated solution. In contrast, the use of micro cells yields the very significantly improved surface representation of Fig. 6(*b*).

Since the exact solution of this transient problem is known, it is possible to quantify the accuracy of the MIC solution

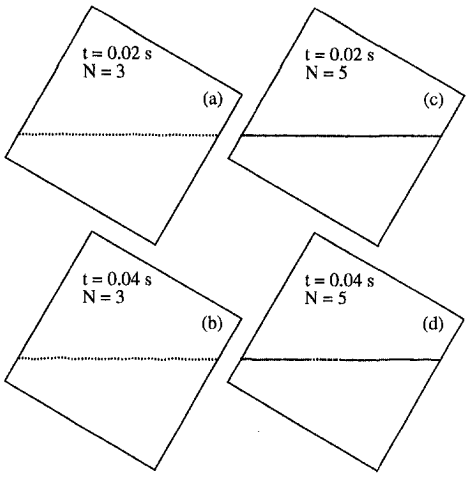

Fig. 5 MIC simulation of water at rest in an inclined container with (*a*)-(*b*) N = 3 and (*c*)-(*d*) N = 5.

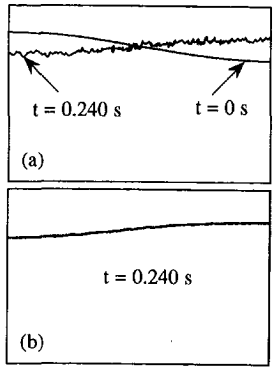

Fig. 6 MIC Simulation of fluid sloshing at t = 0.24 s with (*a*) N = 1 and (*b*) N = 3

by direct comparison of the theoretical and calculated surface distributions at a given instant in the sloshing cycle and of the theoretical and calculated sloshing periods. The theoretical period is given by $P = 2\pi[gk \tanh(kh)]^{-1/2} = 0.3739$ s, where k is the wave number ($= 0.1\pi$ cm^{-1}) and h is the average fluid depth ($= 5$ cm) (Tadjbakhsh and Keller, 1960; Torrey et al., 1985).

Figure 7 shows the surface markers from the MIC simulation with N = 3 at times t = 0.281 s, 0.74475 s, 1.49 s, and 2.23725 s. The results displayed in Fig. 7(*a*) are associated with a time when the free surface is nearly flat, and the velocities of the surface markers essentially have reached their extreme values. The results displayed in Figs. 7(*b*)-(*d*) are associated with times when the free surface has reached an extreme position, and the velocities of all of the surface markers are very close to zero. The period of a sloshing cycle was obtained by monitoring the vertical position of the leftmost marker and capturing the time when it reached its maximum height. The solutions presented in Figs. 7(*b*)-(*d*) correspond to times associated with the completion of the second, fourth, and sixth sloshing cycles, respectively. On the other hand, the time associated with Fig. 7(*a*) was calculated based on the period determined from the simulation results in the manner described above and the knowledge that the free surface should become horizontal at $\frac{3}{4}$ of the period.

3.3 Accuracy and Sensitivity Analysis. In this section, an assessment is made of the temporal and spatial accuracy of the MIC method and its sensitivity to time and space increments by comparing simulation and theoretical results for the problem of small amplitude sloshing in a tank considered in the preceding section.

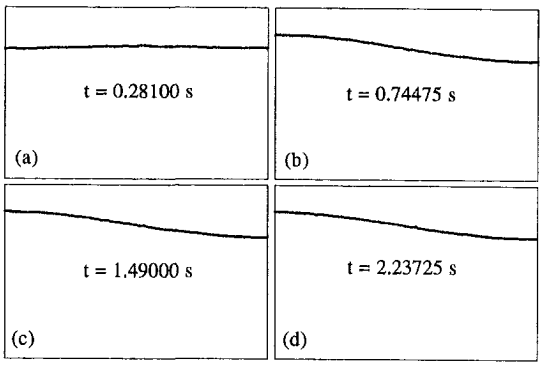

Fig. 7 MIC simulation of fluid sloshing with N = 3 at (*a*) 0.28100 s, (*b*) 0.74475 s, (*c*) 1.49000 s, and (*d*) 2.23725 s

Tables 1, 2, and 3 illustrate the sensitivity to changes in the number of micro cells per macro cell (N × N), the macro space increment ($\delta x = \delta y$), and the time increment (δt), respectively. Two norms, the percent temporal error and the percent spatial error, are used for assessing accuracy. The percent temporal error is defined as

$$100(T_s - T_t)/T_t$$

where T_s and T_t represent the simulation and theoretical times, respectively; and the percent spatial error is defined as

$$\frac{100}{\epsilon M^{1/2}} \left[\sum_{m=1}^{M} (y_s - y_t)^2 \right]^{1/2}$$

where m is the marker counter, M is the total number of surface markers, y_s is the simulation elevation, y_t is the theoretical elevation, and ϵ (= 5 mm) is the initial wave amplitude.

In Table 1, the temporal and spatial errors for N = 3 and N = 5 are shown for the simulation results associated with Figs. 7(*b*)–(*d*). The times obtained by simulation differ from the corresponding theoretical times by 0.44 percent or less for N = 3, indicating a high level of temporal fidelity in the simulation of this problem. When N is increased from 3 to 5, the corresponding differences decrease to 0.06 percent or less, indicating a strong convergence behavior of the new method and further improvement in the accuracy of the placement of the free surface pressure boundary conditions. The spatial accuracy of the MIC simulation of this problem is also quantified in Table 1. For N = 3, the spatial error is 3.5 percent or less. When N is increased from 3 to 5, the spatial errors all decrease. The spatial accuracy of the representation of the free surface is also evident in Fig. 7. The surface markers in the solution shown in Fig. 7(*a*) should theoretically fall on a horizontal straight line located 5 cm from the bottom of the tank, while the solutions in Figs. 7(*b*)–(*d*) should retrace the initial condition of one half of a cosine wave shown in Fig. 6(*a*). In fact, if the original cosine shape were superimposed on Figs. 7(*b*)–(*d*), it would be difficult to distinguish between it and the displayed free surfaces. The same holds true for the straight horizontal line in Fig. 7(*a*).

Table 2 illustrates the sensitivity of the spatial error to the macro cell dimension. When the grid spacing is halved from 2.5 mm to 1.25 mm, the spatial errors decrease by at least 42 percent. When the grid spacing is halved again, there are further decreases in the spatial errors of at least 25 percent. These results indicate a strong spatial convergence behavior.

Table 3 illustrates the sensitivity of the temporal error to the time increment. The results indicate that the temporal error is relatively insensitive to changes in the time increment, provided that an appropriately small time increment is chosen. For a given macro cell dimension, the appropriate time step must be chosen so that no marker moves more than one-fourth to one-third of a cell dimension (Hirt and Nichols, 1981, p. 216). As stated in Section 2.3, the criterion used in the MIC method is that the time step be chosen to prevent a marker from moving more than one micro cell in one time step.

The simulation of relatively small amplitude, spatially sinusoidal and temporally periodic phenomena is especially challenging to methods that use markers and cells since discrete representations of smooth continuous functions require a very large number of cells to minimize the severity of discontinuities inherent in those discrete representations. Yet, the numerical representation of the free surface simulated by the use of the MIC method remains in excellent agreement with the analytical solution even after six sloshing periods, pointing to the advantages of the use of surface markers in tracking the free surface and micro cells in prescribing the pressure boundary conditions as close to the free surface as possible. Micro cells can also be used to advantage in problems which include multi-valued free surfaces as shown in the fountain problem of the next section.

Table 2 Sensitivity of the spatial error to the macro cell dimension with $N = 3$ and $\delta t = 0.125$ ms

Theoretical time	Spatial error (%)		
	δx = 2.5 mm	δx = 1.25 mm	δx = 0.625 mm
2 P	4.2	2.0	1.5
4 P	5.7	3.3	2.0
6 P	9.5	3.6	2.3

3.4 Ideal Flow of a Vertical Jet. In this example, the steady-state solution obtained by simulation of a transient problem is compared with the asymptotic solution for an ideal jet reported by Dias and Christodoulides (1991) (D&C). The problem they considered is the steady irrotational flow of an inviscid incompressible fluid that emerges from a nozzle, rises to a maximum height and falls under the action of gravity. Due to symmetry, only half of the problem is studied, with the vertical midplane assumed to extend to infinity. At the jet's apex, the fluid is assumed to detach from the symmetry plane (or wall) with a zero velocity. The problem is nondimensionalized so that the nozzle velocity (U) and half-width (L) are each equal to 1. For comparison, the case of a Froude number, $\mathrm{Fr} \equiv U(g\,L)^{-1/2}$, equal to 1.04 is chosen. This problem represents a significant test of the MIC method. The flow is inviscid, and the MIC simulation results that are compared with the asymptotic, steady-state solution are obtained after a very large number of time steps (over 2700).

For the MIC simulation of the transient free jet problem, a square, four-unit wide computational region (Fig. 8(*a*)) is discretized with 80 cells in each direction. Initially, a body of fluid with zero viscosity and unit velocity is located between the left solid wall and an internal short obstacle 2 units high. The bottom of the fluid body coincides with the flow inlet which continually supplies fluid with a unit velocity in the upward vertical direction. An outlet boundary condition is specified along the remainder of the lower surface to the right of the vertical obstacle as well as along the right and top sides of the computational domain. Six plots depicting the positions of the markers are shown in Fig. 8 at solution times of 0.03, 1, 2, 3, 5, and 6 nondimensional time units. Figures 8(*b*)–(*f*) illustrate only the square region that is shown in the upper left hand side of Fig. 8(*a*). The round symbols on the plots represent a few of the analytically determined locations of the jet's upper and lower free surfaces as measured from Fig. 3 in D&C. In Fig. 8(*b*) the fluid has risen nearly a full unit and begun to fall to the right and down under the action of gravity. At $t = 2$ (Fig.

Table 1 Temporal and spatial accuracy of MIC simulation with $\delta x = 1.25$ mm and $\delta t = 0.25$ ms

Theoretical time	Temporal error (%)		Spatial error (%)	
	$N = 3$	$N = 5$	$N = 3$	$N = 5$
2 P	−0.44	−0.04	2.0	1.7
4 P	−0.39	−0.06	2.8	2.5
6 P	−0.29	0.001	3.5	3.3

Table 3 Sensitivity of the temporal error to the time increment with $N = 3$ and $\delta x = 1.25$ mm

Theoretical time	Temporal error (%)		
	δt = 0.25 ms	δt = 0.125 ms	δt = 0.0625 ms
2 P	−0.44	−0.38	−0.35
4 P	−0.39	−0.24	−0.37
6 P	−0.29	−0.21	−0.30

8(c)), the fluid column has nearly reached its apex. The representation of the multi-valued free surface by the surface markers is smooth and continuous. At $t = 3$ (Fig. 8(d)), the fluid has overshot moderately the position of the stagnation point on the left wall as both the lower and upper free surfaces are nearing their steady-state profiles. After a time of 5, the flow reaches the steady-state solution and the free surfaces appear stationary thereafter (Figs. 8(e)–(f)). Minor oscillations about the steady-state with no perceptible increase in amplitude continue indefinitely due to numerical truncations.

The temporal accuracy of the MIC method is demonstrated by the close agreement between the shape of the simulated free surfaces and the discrete asymptotic data points of D&C that are shown in Figs. 8(e) and 8(f). In addition, the successful simulation of this problem, in which the viscosity is equal to zero, also demonstrates the robustness of the new method. The agreement in the results is excellent given the fact that the MIC simulation considered only a finite portion of the semi-infinite spatial domain assumed by D&C.

3.5 Uniform Motion of a Circular Body of Fluid. Finally, the uniform motion across the computational domain of a circular body of fluid is simulated by the use of the MIC method. The path of motion is prescribed along a diagonal in order for the markers to traverse the computational cells at a 45 deg angle, thus destroying symmetry about a cell Cartesian system that is parallel to the cell faces. This problem was used by Ashgriz and Poo (1991) to demonstrate, for a problem with a known solution, the improved accuracy of the movement and reconstruction of the free surface that is obtained by use of their FLAIR approach for the advection and reconstruction of the free surface in conjunction with a VOF simulation.

The MIC simulation is performed with a circle of radius equal to 4 cm, $\delta x = \delta y = 1.25$ mm, $\delta t = 3.788$ ms, and $\nu = 10^{-6}$ m^2/s. The fluid moves in a horizontal plane ($g = 0$) with a uniform velocity. Initially, $u_{i,j} = v_{i,j} = 10$ cm/s for all values

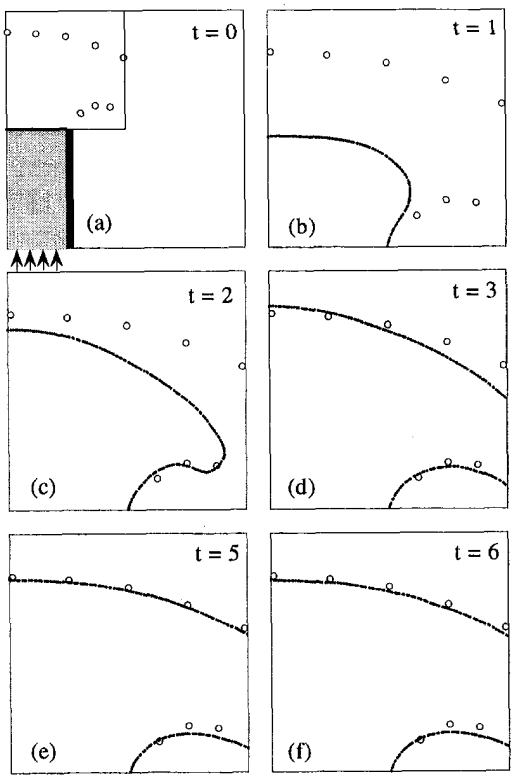

Fig. 8 Comparison of MIC results with asymptotic ideal jet solution of Dias and Christodoulides (1991)

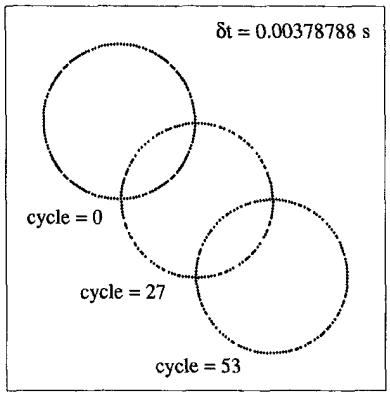

Fig. 9 Uniform motion of a circular body of fluid

of i and j that are associated with cells in the circular fluid region. The progress of the circular body of fluid is shown in Fig. 9. By use of the MIC method, the circular body of fluid proceeds uniformly across the computational domain, as it should. The error in the area of the circle is imperceptible even after 53 calculational cycles.

4 Conclusions

A new method that uses markers and cells is presented. The accuracy and validity of the new method is demonstrated by direct comparisons between simulation results and known solutions of four different example problems. The contributions of the new method can be summarized as follows: (a) The discrete form of the free surface is represented by micro cells which are much smaller than the cells employed to locate the field variables. Therefore, the free surface boundary conditions are located more precisely at micro cell centers rather than at macro cell centers. (b) The advection of the free surface is accomplished with greater precision and computational efficiency by the use of surface markers which are located only along the free surface itself. (c) The introduction of micro cells enables the identification of portions of the free surface that exist in macro cells that have no empty neighbors and, subsequently, the efficient application of free surface pressure boundary conditions in such cells. In addition, the introduction of micro cells enables the application of free surface boundary conditions at multiple points in a single surface cell. Heretofore, such points on the free surface have not been recognized and treated properly. (d) A new unequal leg pressure potential equation is derived for use in the computation of the pressure potential field. The new equation gives rise to a system of algebraic equations whose coefficient matrix is symmetric and positive definite. As a result, the efficient preconditioned conjugate gradient method is used in the new method for the calculation of the pressure field. (e) In order to calculate the final velocity field more accurately, micro cells are also used to improve the computation of pressure potential gradients.

The utilization of surface markers and micro cells in the new method significantly extends the capabilities of the marker and cell approach. The accurate and efficient advection of the free surface, application of free surface pressure boundary conditions, calculation of the pressure field, and computation of final velocities, all of which are made possible by the utilization of surface markers and micro cells, extend the capabilities of free surface fluid flow simulation. These extended capabilities are essential for the successful simulation of free surface fluid flow problems that involve multi-valued free surfaces and breaking fluid fronts.

Acknowledgments

Support for this research has been provided by DARPA as Projects 5-25084 and 5-25085 of Contract MDA093-86-C-

0182, NSF under grant DDM-9114846, Leadwell CNC Machines Manufacturing Corporation, and J. L. Embrey Trustee Professorship in Engineering.

References

Amsden, A. A., and Harlow, F. H., 1970, "A Simplified MAC Technique for Incompressible Fluid Flow Calculations," *Journal of Computational Physics,* Vol. 6, pp. 322–325.

Ashgriz, N., and Poo, J. Y., 1991, "FLAIR: Flux Line-Segment Model for Advection and Interface Reconstruction," *Journal of Computational Physics,* Vol. 93, pp. 449–468.

Bulgarelli, U., Casulli, V., and Greenspan, D., 1984, *Pressure Methods for the Numerical Solution of Free Surface Fluid Flows,* Pineridge Press, Swansea, U. K.

Chan, R. K.-C., and Street, R. L., 1970, "A Computer Study of Finite-Amplitude Water Waves," *Journal of Computational Physics,* Vol. 6, pp. 68–94.

Chen, S., Johnson, D. B., and Raad, P. E., 1991, "The Surface Marker Method," *Computational Modeling of Free and Moving Boundary Problems, Vol. 1, Fluid Flow,* W. de Gruyter, pp. 223–234.

Chen, S., Johnson, D. B., and Raad, P. E., 1995, "Velocity Boundary Conditions for the Simulation of Free Surface Fluid Flow," *Journal Computational Physics,* Vol. 116, pp. 262–276.

Dias, F., and Christodoulides, P., 1991, "Ideal Jets Falling Under Gravity," *Physics of Fluids A,* Vol. 3, pp. 1711–1717.

Harlow, F. H., and Welch, J. E., 1965, "Numerical Calculation of Time-Dependent Viscous Incompressible Flow," *Physics of Fluids,* Vol. 8, pp. 2182–2189.

Hirt, C. W., and Nichols, B. D., 1981, "Volume of Fluid (VOF) Method for the Dynamics of Free Boundaries," *Journal of Computational Physics,* Vol. 39, pp. 201–225.

Johnson, D. B., Raad, P. E., and Chen, S., 1994, "Simulation of Impacts of Fluid Free Surfaces with Solid Boundaries," *International Journal of Numerical Methods in Fluid,* Vol. 19, pp. 153–176.

Lardner, R. W., and Song, Y., 1992, "A Comparison of Spatial Grids for Numerical Modelling of Flows in Near-Coastal Seas," *International Journal for Numerical Methods in Fluids,* Vol. 14, pp. 109–124.

Loh, C. Y., and Rasmussen, H., 1987, "A Numerical Procedure for Viscous Free Surface Flows," *Applied Numerical Mathematics,* Vol. 3, pp. 479–495.

Nichols, B. D., and Hirt, C. W., 1971, "Improved Free Surface Boundary Conditions for Numerical Incompressible-Flow Calculations," *Journal of Computational Physics,* Vol. 8, pp. 434–448.

Nichols, B. D., and Hirt, C. W., 1975, "Methods for Calculating Multi-Dimensional, Transient, Free Surface Flows Past Bodies," *Proceedings of the First International Conference on Numerical Ship Hydrodynamics,* Gaithersburg, MD, pp. 253–277.

Nichols, B. D., and Hirt, C. W., 1976, "Calculating Three-Dimensional Free Surface Flows in the Vicinity of Submerged and Exposed Structures," *Journal of Computational Physics,* Vol. 12, pp. 234–246.

Tadjbakhsh, I., and Keller, J. B., 1960, "Standing Surface Waves of Finite Amplitude," *Journal of Fluid Mechanics,* Vol. 8, pp. 442–451.

Torrey, M. D., Cloutman, L. D., Mjolsness, R. C., and Hirt, C. W., 1985, "NASA-VOF2D: A Computer Program for Incompressible Flows with Free Surfaces," Los Alamos Scientific Laboratory Report LA-10612-MS.

Capsule Transport in Coal Slurry Medium

J. Seaba
Assistant Professor, Department of Mechanical & Aerospace Engineering.

G. Xu
Graduate Student, Department of Mechanical & Aerospace Engineering.

University of Missouri-Columbia, Columbia, MO 65211

The use of coal slurry instead of water in a coal log pipeline (CLP) is investigated for the first time. This investigation reveals significant differences and possible benefits by using coal slurry instead of water in CLPs. The lift-off velocity, and capsule and total pressure gradients are presented for a 51 mm pipeline using two capsule geometries. The fluid velocity was tested from 1 to 3 m/s, which includes the lift-off velocity of the capsule train. The diameter ratio (k) and specific gravity (S) are held constant at 0.75 and 1.3, respectively. Two capsule lengths were studied corresponding to aspect ratios (a) of 2 and 4. Aluminum-Plexiglas capsules are used to simulate the coal logs. The coal slurry significantly lowered the lift-off velocity, and transported more coal per total pressure gradient than coal logs in water. The capsule pressure gradient was nearly constant over the velocity range investigated. This indicates that the optimal operation velocity range may be much larger for coal slurry compared to water. Further tests and abrasion studies are required to fully assess the potential benefits of using coal slurry.

Introduction

The transport of solids through liquid pipelines consist of many different modes such as slurry, capsule, and coal-log pipelines. The coal-log pipeline is an extension of the capsule pipeline, where the coal is made directly into cylindrical capsules for transport through a pipe. CLP is superior to the coal slurry pipeline in that it uses less energy and water to transport coal. The Midwest of the United States uses large quantities of coal transported by trains from Wyoming and other western states approximately 1000 km away. Seventy-five percent of the delivered cost of such coal is due to transportation. Pursuing alternative modes of coal transportation is an important issue with benefits to utilities, coal companies, and society (Liu, 1993; Liu, Richards, and Wu, 1991). The concept of CLP is to transport densely spaced coal logs (capsule trains) over long distances (50 to 1000 km).

The transport of capsules in pipes consist of four regimes (Liu, 1992) is illustrated in Figure 1. Regime I occurs at a low bulk fluid velocity when a capsule is stationary at the pipe bottom. Regime II begins at a slightly higher velocity when the capsule slides on the pipe floor moving slower than the bulk fluid velocity. The initial movement of the capsule along the pipe wall is defined as the incipient velocity (V_i). At higher bulk fluid velocities the capsule moves faster than the bulk fluid velocity (Regime III) and contact friction between capsule and pipe diminishes. The contact friction decreases due to the capsule intermittently lifting off the pipe wall, this is defined as microlift. Regime IV occurs at yet higher velocities when the capsule is well lifted off the pipe floor moving with its leading nose raised, forming an angle of attack. The optimum operational velocity of CLP is between regimes III and IV, or at the lift-off velocity of the capsules. The head loss at lift-off velocity is only slightly (15–30 percent) higher than that of equivalent pipeline flow without capsules at the same bulk velocity (Richards, 1992).

The lift-off velocity (V_L) of capsules in water is given by the following equation (Liu, 1981):

$$V_L = 7.2\sqrt{(S-1)gak(1-k^2)D} \qquad (1)$$

where S is the density ratio between the coal logs and the bulk fluid (ρ_c/ρ_b), ρ_c is the density of the coal logs, ρ_b is the bulk fluid density, g is the acceleration of gravity, a is the aspect ratio (L_c/D_c, refer to Fig. 2), L_c is the length of the coal log, k is the diameter ratio (D_c/D), D_c is the coal log diameter, and D is the pipe diameter. From Eq. (1), the parameters for determining lift-off velocity include capsule geometry (length and diameter), pipe diameter, coal-log density, and fluid density.

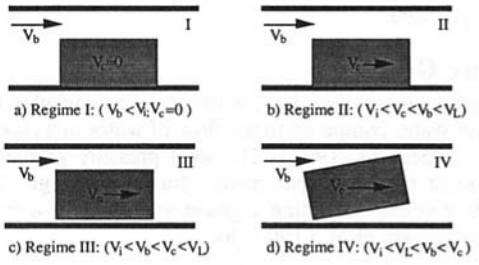

Fig. 1 The four regimes of capsule motion in CLP (after Richards, 1992)

Based on present coal log fabrication research, it is expected that commercial coal logs should have a specific gravity (S) between 1.15 and 1.35 (Gunnink, 1994). Logs with high specific gravity (in excess of 1.25) in large pipes will result in a lift-off velocity greater than 3 m/s. Commercial water pipelines operating at velocities greater than 3 m/s cause significant headloss and should be avoided. The lift-off velocity can be decreased by increasing the density of the bulk fluid by using coal slurry instead of water. Holding g, a, k and D constant in Eq. (1), the ratio of V_L for the water medium versus coal slurry (γ) is:

$$\gamma = \frac{(V_L)_{\text{water}}}{(V_L)_{\text{slurry}}} = \sqrt{\frac{\frac{\rho_c}{\rho_f}-1}{\frac{\rho_c}{\rho_s}-1}} = \sqrt{\frac{S-1}{\beta-1}} \qquad (2)$$

where β is the density ratio of the coal log to coal slurry (ρ_c/ρ_s).

Values of γ are given in Table 1 for coal logs with S between 1.2 and 1.35. From Table 1, the lift-off velocity of the coal log is reduced between 30.7 and 59.4 percent, for S between 1.2 and 1.35. The calculations shown in Table 1 assume that Eq.

Contributed by the Fluids Engineering Division for publication in the JOURNAL OF FLUIDS ENGINEERING. Manuscript received by the Fluids Engineering Division February 7, 1994; revised manuscript received March 29, 1995. Associate Technical Editor: O. C. Jones.

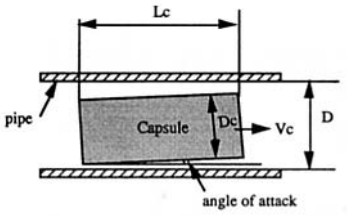

Fig. 2 Capsule at lift-off in pipeline

(1) is valid for coal slurry and the coal slurry behaves as a homogeneous fluid. These calculations are based on a specific gravity of 1.162 for the coal slurry.

Table 1 shows the advantages of using coal slurry as the transporting medium to reduce the lift-off velocity, or operating velocity of CLP. Increasing the density of the fluid medium increases buoyancy of the capsule, thereby decreasing the bulk fluid velocity required for lift-off of the capsule. This study investigates the effects of using coal slurry in a capsule pipeline. The reduction of lift-off velocity using coal slurry would enable coal-logs with specific gravity up to 1.35 to be commercially feasible for pipe diameters up to approximately 50 cm. As a means of providing perspective, a 50 cm diameter coal log pipeline operating at 3 m/s can transport about 20 million tons of coal per year.

Pressure Gradient

A higher pressure gradient is observed as capsules flow in a pipe with water compared to the flow of water in a pipe without capsules (Richards, 1992). The total pressure gradient is one of the most important parameters for CLP design. The total pressure gradient including capsule and fluid in a pipeline is given by Kruyer et al. (1967) as,

$$\left(\frac{dP}{dz}\right)_t = \frac{\Delta P_t - L\left(\frac{dP}{dz}\right)_f}{NL_c} + \left(\frac{dP}{dz}\right)_f \tag{3}$$

where ΔP_t is the total head loss between two pressure taps along the pipeline at a distance L apart; $(dP/dz)_t$ is the total pressure gradient including the presence of both water and capsules; $(dP/dz)_f$ is the pressure gradient of the water; L_c is the length of the capsule; and N is the number of capsules in the train. The first term on the right side of Eq. (3) is the pressure gradient due to the capsule train only. For capsule transport using coal slurry in place of water, Eq. (3) can be rewritten as,

$$\left(\frac{dP}{dz}\right)_t = \frac{\Delta P_t - L\left(\frac{dP}{dz}\right)_s}{NL_c} + \left(\frac{dP}{dz}\right)_s \tag{4}$$

where the subscript s refers to the pressure gradient produced by the coal slurry. Eq. (4) can be expressed in terms of measured quantities, ΔP_c and ΔP_s,

$$\left(\frac{dP}{dz}\right)_t = \frac{\Delta P_c}{NL_c} + \frac{\Delta P_s}{L} \tag{5}$$

where ΔP_c is the measured pressure drop due only to the capsules (Seaba et al., 1993), and ΔP_s is the measured pressure drop produced by the coal slurry. Eq. (5) can also be expressed in terms of the pressure gradients produced by the capsules and slurry flow which sum to the total pressure gradient as follows:

$$\left(\frac{dP}{dz}\right)_t = \left(\frac{dP}{dz}\right)_c + \left(\frac{dP}{dz}\right)_s \tag{6}$$

Table 1 Coal slurry effects on the lift-off velocity

S	β	γ	% Reduction of VL $(1 - 1/\gamma) \times 100$
1.20	1.033	2.462	59.4
1.25	1.076	1.814	44.9
1.30	1.119	1.588	37.0
1.35	1.162	1.443	30.7

Experimental Apparatus and Procedure

The experimental facility consists of a constant-head, open-loop pipeline as shown in Figure 3. The pipeline is made of 51 mm I.D. Excelon-4000 rigid plastic pipe and has a total length of 21.5 meters including the length of three bends with 0.91 meter radii. A 680 liter polyethene tank supplies the coal slurry for the system. The coal slurry is pumped to the head tank which maintains a constant head during the experiment. Overflow from the head tank goes back to the storage tank. The volumetric flow rate through the open loop system is controlled by two valves downstream of the test section, one valve is a gate valve for system shutoff, and the other for throttling.

An ultrasonic flow meter monitors the volumetric flow rate in the test section. The ultrasonic flowmeter was calibrated using a weighing tank (Xu, 1993). The bulk fluid velocity was calculated by dividing the flow rate by the area of the pipe. The uncertainty of the inner pipe dimensions is ±0.03 cm, resulting in an uncertainty of ±2 percent for the flow ranges investigated.

The capsules are loaded at the head tank and released to form a capsule train. The capsules are initially pushed into the open loop using a rod at the head tank to insure the capsules do not separate. The train traverses through the test section where flow rate, pressure, and electromike measurements are recorded. The electromike provides an analog signal corresponding to the distance between the pipe wall mounted sensor and the metal capsule. The measured distance minus the pipe wall thickness defines the gap between the capsule and pipe wall. After passing through the test section, the capsule train is deposited in the

Nomenclature

a = aspect ratio of capsule L_c/D_c
D = pipe diameter
D_c = capsule diameter
g = gravitational constant
He = Hedstrom number, $\tau_y \rho_s D^2/\eta^2$
k = diameter ratio D_c/D
L = distance between pressure taps
L_c = length of capsule
N = number of capsules within distance L in pipeline
ΔP = pressure drop between pressure taps
(dP/dz) = pressure gradient
Re = Reynolds number, $\rho_s D V_L/\eta$
S = specific gravity of coal log (ρ_c/ρ_f)
V = velocity
α = angle of attack of capsule
ρ = density
γ = Lift-off velocity ratio in water and coal slurry
β = density ratio of coal-log to coal slurry
τ = shear stress
η = apparent viscosity

Subscript

b = bulk fluid
c = capsule
f = fluid-water
i = incipient
L = lift-off
s = coal slurry
t = total (capsule and fluid)
trans = transition
y = yield

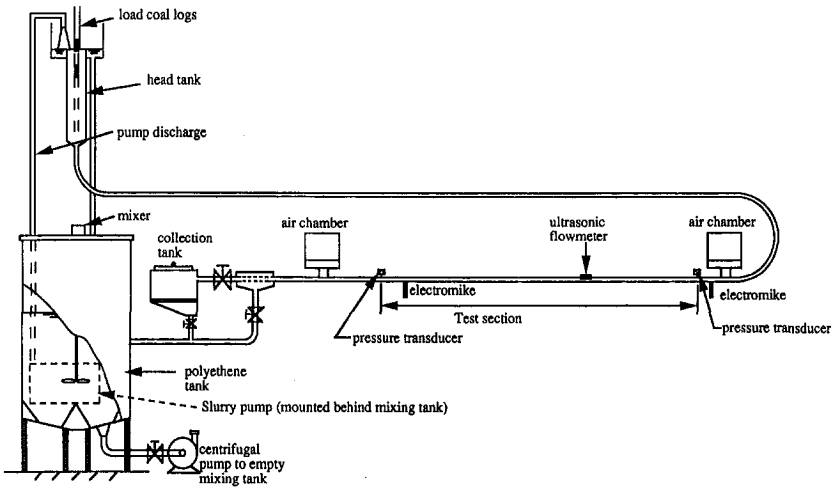

Fig. 3 Experimental apparatus

collection tank. This allows the collection tank to be unloaded without changing the volumetric flow rate of the open-loop system.

Aluminum tubes with Plexiglas ends and a foam center are used as capsules to simulate coal logs. Two different aspect ratios (a) of 2 and 4 are tested. The specific gravity (S) of the capsules is 1.3. The capsule train consists of five capsules, 50 and 100 cm long (NL_c) for aspect ratios 2 and 4, respectively. The distance between pressure taps (L) is 366 cm. This provides a residence time of approximately one second to record the capsule train pressure increase in the lifted regime (maximum velocity). ΔP_c is calculated by averaging several hundred pressure measurements while the train is between the pressure taps. A slight pressure oscillation of ± 0.25 cm of H_2O is observed during this time period (Seaba et al., 1993). ΔP_c and ΔP_b were recorded at flow velocities ranging from 1 to 3 m/s. The test facility cannot operate below 1 m/s due to particle deposition and subsequent blockage in the test loop.

The direct measurement of the capsule train pressure drop $(dP/dz)_c$, is determined by measuring a pressure differential at each tap location. The pressure differential is referenced to the total pressure of the bulk fluid flow without any capsules in the pipe. A valve in parallel with a differential pressure transducer between a pressure tap and piezometer is used to store the steady state pressure at each flow rate. The valve is closed prior to launching the capsule train. The differential pressure transducers determine the pressure difference between the capsule in pipe and pure bulk fluid pressure (previously stored by piezometer). The difference between the two differential pressure transducers is the pressure drop due to the presence of the capsule train (Xu, 1993).

Two air chambers are located before the upstream and after the downstream pressure tap locations. The air chambers are essential to dampen out any pressure fluctuations created in the open-loop system outside of the test section. The same type of electromikes used by Richards (1992) were used to determine the location of the capsules, space between the capsules within the capsule train, capsule orientation, and trigger the data acquisition system. The space between the capsules was less than 2 mm for the test results presented. All instrumentation is connected to a PC based data acquisition system (Xu, 1993).

Characteristics and Rheology of Coal Slurry

Commercial slurry from the Black Mesa Pipeline in Arizona was used in this study. The characteristics of the coal slurry consist of a 48.6% mass coal per mass water mixture corresponding to a specific gravity of 1.162. The maximum coal particle diameter is approximately 1 mm, with a mean particle diameter of 280 μm.

Rheological properties of the coal slurry were analyzed before, during, and after each test condition. The rheological properties were tested using a Brookfield LVRH viscometer. The slurry samples were thoroughly mixed prior to each rheology measurement. The slurry showed no signs of degradation for up to 9 hours of continuous pumping. After 9 hours the viscosity of the coal slurry started to increase, and the slurry was replaced.

A highly concentrated coal slurry can be treated as a Bingham plastic fluid having the following rheological relation (Govier and Aziz, 1972):

$$\tau = \tau_y + \eta\left(\frac{du}{dy}\right) \tag{7}$$

where τ_y is the yield stress of the coal slurry, η is the slurry apparent viscosity (also called "rigidity"), and du/dy (strain

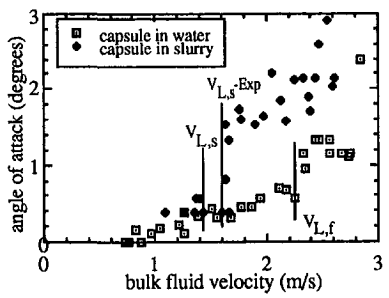

Fig. 4 Angle of attack for capsules with $a = 2$ (uncertainty ± 0.03 degrees, ± 2 percent m/s)

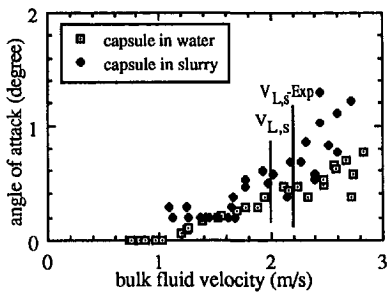

Fig. 5 Angle of attack for capsules with $a = 4$ (uncertainty ± 0.03 degrees, ± 2 percent m/s)

Table 2 Lift-off velocities

a	k	S	β	$V_{L,f}$ (m/s)	$V_{L,s}$ (m/s)	$V_{L,s}$ – Exp (m/s)
4	0.75	1.3	1.119	3.19	2.01	2.2
2	0.75	1.3	1.119	2.26	1.42	1.6

rate) is the velocity gradient normal (radial direction) to the pipe surface. τ_y and η are constants determined from the rheological measurements of the coal slurry. The transition to turbulence (Re_{trans}) in pipe flow involving a non-Newtonian slurry is unlike Newtonian fluids. The Re_{trans} number in Bingham plastic fluids (coal slurry) is a function of the He number. A graphical correlation between Re_{trans} and He is presented by Wasp et al. (1979). The Re number at the lift-off velocity of the capsules in coal slurry is between 9,000 and 13,000. The He number is 7500 which correlates to a transitional Re number of 3,450. Therefore, the coal slurry is in the turbulent regime, and may behave as a pseudo-homogeneous fluid. A pseudo-homogeneous slurry behaves similar to a homogeneous fluid where the larger particles are suspended by turbulent diffusion in the pipe.

Results and Discussion

The lift-off velocity of the capsule is experimentally observed by a change in the angle of attack of the capsule. The angle of the capsules relative to the pipe wall is determined by the electromike signals which are calibrated to represent the distance between the capsule and electromike (or pipe bottom). The first capsule in the train is measured to calculate the angle of attack for both water and coal slurry as shown in Figs. 4 and 5, for aspect ratios of 2 and 4, respectively. Other capsules in the train were also measured, but little difference of the attack angles were observed (Xu, 1993).

The angle of attack increases as the bulk fluid velocity increases for both the short and long capsules. The calculated lift-off velocities in coal slurry using Eq. (1) slightly underestimate the experimental lift-off condition as shown in Figs. 4 and 5. The calculated and experimental lift-off velocities for capsules with S = 1.3 in coal slurry or water is summarized in Table 2. The calculated lift-off velocity ($V_{L,s}$) in coal slurry using Eq. (1) with β replacing S, under predicts the experimental lift-off velocity ($V_{L,s}$-Exp) by approximately 10 percent for both aspect ratios. Further work is required to fully assess the applicability of Eq. (1) for coal slurry.

The angle of attack measurements exhibit scatter at bulk fluid velocities 10 to 20 percent greater than the lift-off velocity. It has been observed in water, that the capsules will start to oscillate up and down under these conditions, which causes scatter in the angle of attack data. Richards (1992) has also shown that coal logs in water show significant degradation at bulk fluid velocities greater than or less than 15 percent of the lift-off velocity.

The uncertainty for the capsule pressure gradients in Figs. 6 and 7 are calculated from the uncertainty of the ΔP measurement divided by the distance between the pressure taps (L). (The pressure is referenced to water at 20°C.) This uncertainty corresponds to ±0.0003 meter of water per meter of pipe. Coal slurry and water are compared for $(dP/dz)_c$ versus the bulk fluid velocity as presented in Figs. 6 and 7 for aspect ratios of 2 and 4, respectively. At low bulk water velocities, $(dP/dz)_c$ increases as the bulk water velocity increases, reaching a maximum of 0.05 meter of water per meter of pipe for $a = 2$ and 0.04 meter of water per meter of pipe for $a = 4$. This corresponds to a bulk water velocity of 1.6 m/s for $a = 2$ and 1.7 m/s for $a = 4$. The maximum $(dP/dz)_c$ represents the transition between regimes 2 and 3 of capsule motion in CLP. In regime 3, $(dP/dz)_c$ decreases as the bulk water velocity increases toward the lift-off velocity.

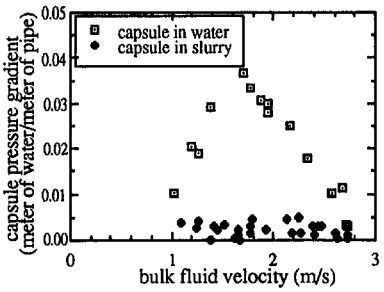

Fig. 7 Capsule pressure gradient for $a = 4$ (uncertainty ±0.0003 m water/m pipe, ±2 percent m/s)

The capsule pressure drop behaves much differently in coal slurry compared to water. $(dP/dz)_c$ is nearly constant (0.005 meter of water per meter of pipe) over the bulk fluid velocity range measured (1.0 to 3.0 m/s). This is an order of magnitude less than the maximum capsule pressure gradient in water. The pressure drop is approximately the same for coal slurry or coal slurry with capsules over the bulk fluid velocity range investigated.

The pressure drop of coal slurry compared to water is shown in Figure 8. The coal slurry has a greater pressure drop compared to water for all bulk fluid velocities from 1 to 3 m/s. The difference between the slurry and water pressure drop is approximately 0.02 meter of water per meter of pipe. The water data follows the Moody diagram for a nondimensional pipe roughness of 0.0002 (Xu, 1993).

The total pressure gradient, $(dP/dz)_t$ increases with increasing bulk fluid velocity for both water and coal slurry capsule flows. $(dP/dz)_c$ shows little difference at 1.7 to 1.8 m/s between the coal slurry and water to transport the capsule as shown in Figs. 9 and 10. This is due to a maximum capsule pressure gradient associated with water and a negligible capsule pressure gradient associated with coal slurry. The added pressure gradient due to the capsule in water is comparable to the pressure gradient associated with coal slurry.

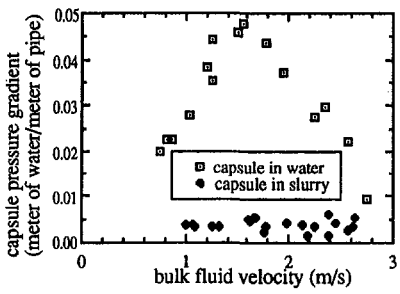

Fig. 6 Capsule pressure gradient for $a = 2$ (uncertainty ±0.0003 m water/m pipe, ±2 percent m/s)

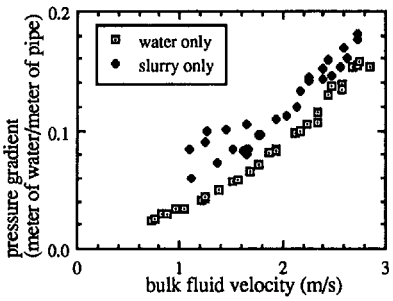

Fig. 8 Water and coal slurry pressure drops in pipe (uncertainty ±0.03 m water/m pipe, ±2 percent m/s)

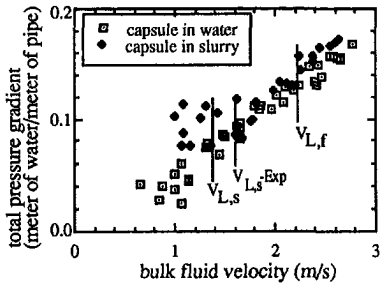

Fig. 9 Total pressure gradient for a = 2 (uncertainty ±0.03 m water/m pipe, ±2 percent m/s)

The total pressure gradient for capsules in water is less than that for capsules in coal slurry for bulk fluid velocities greater than 1.8 m/s. This difference increases with increasing bulk velocity since the capsules in water are approaching the lift-off velocity. The total pressure gradient for capsules in slurry is much greater than capsules in water for bulk velocities less than 1.5 m/s. This is due to large coal particles depositing on the pipe bottom forming a bed flow. Commercial coal slurry pipelines operate at velocities above the bed flow conditions. The uncertainty for the total pressure gradients in Figs. 8, 9 and 10 are calculated from the uncertainty of the ΔP measurement divided by the distance between the pressure taps (L), this is corresponds to ±0.03 meter of water per meter of pipe.

The total pressure gradient of a capsule with aspect ratio 2 at lift-off is approximately 0.08 meter of water per meter of pipe and 0.14 meter of water per meter of pipe, in coal slurry and water, respectively. Assuming a CLP operates at the lift-off velocity, the mass of coal logs transported per unit time in coal slurry decreases by 30 percent, but the total pressure gradient decreases 50 percent. The total pressure gradient is directly related to the power required to operate a CLP. Furthermore, additional coal mass is transported by using coal slurry between the capsule trains which is especially beneficial.

Operational characteristics of CLP also involve the shutdown and restart of the system with the capsules in the pipe. The introduction of coal slurry in place of water would make this a more difficult task. A comparison between a conventional coal slurry pipeline and a coal slurry CLP is discussed. The coal slurry in a coal slurry pipeline at shutdown will deposit on the pipe bottom and slide down to the low point in the pipeline, completely plugging the pipe. In the CLP at shut down, the coal logs quickly deposit on the pipe bottom then the coal particles begin to deposit around them. The coal particles will not slide down to a low point in the pipeline due to the presence of the capsules. Therefore, the area above the capsules will be free from particles providing an area for the water to flow for easier restart of the pipeline. Since the Black Mesa coal slurry pipeline has had little difficulties with shutdown and startup over the last 20 years of operation, the coal slurry CLP should have little additional difficulty with startup after shutdown.

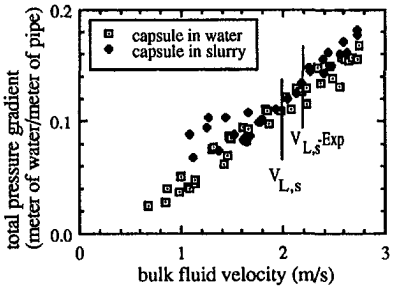

Fig. 10 Total pressure gradient for a = 4 (uncertainty ±0.03 m water/m pipe, ±2 percent m/s)

Conclusion

The coal slurry lowers the lift-off velocity of the capsules which enables one to transport more dense coal logs than the conventional CLP. The lift-off velocity correlation used for capsules in water (Eq. (1)) underestimates the lift-off velocity in coal slurry by approximately 10 percent for the capsules used in this investigation. More data is required to fully evaluate the lift-off equation.

The capsule pressure drop is nearly constant in coal slurry which includes CLP regimes 2, 3, and 4. The added energy loss caused by the capsule train is constant over a large velocity range. Therefore, the operational velocity in coal slurry may have a large velocity range compared to the conventional CLP which must be maintained within ±15 percent of the lift-off velocity. Further work is required to assess the degradation of coal logs in coal slurry for regimes 2, 3 and 4.

The capsules in coal slurry increased the total pressure gradient 3 to 5 percent compared to 15 to 30 percent for capsules in water at lift-off. The coal slurry pressure gradient is greater than the pressure gradient caused by water alone. However, the total pressure gradient is only 5 percent greater for capsules in coal slurry compared to capsules in water. The coal slurry lowers the operational velocity of CLP by 30 percent but decreases the total pressure drop by 50 percent. Therefore, the mass of coal transported per total pressure gradient is greater using coal slurry compared to water.

Acknowledgments

This work has been sponsored by the Capsule Pipeline Research Center and the Department of Mechanical & Aerospace Engineering at the University of Missouri-Columbia. The support of Williams Technologies Inc. is greatly appreciated, in particular Hank Brolick, Joe Anderson, Lowell Hinkins, and Jack Tennant provided the coal slurry and technical insights which proved helpful for this study. Special thanks is extended to Dr. Henry Liu for his guidance and support of this project.

References

Govier, G. W., and Aziz, K., 1972, *The Flow of Complex Mixtures In Pipes,* Van Nostrand Reinhold.

Gunnink, B., 1994, Private communication, Dept. of Civil Engineering, University of Missouri-Columbia.

Kruyer, J., Redberger, P. J., and Ellis, H. S., 1967, "The Pipe Flow of Capsules," *Journal of Fluid Mech.,* Vol. 30, p. 513.

Liu, H., 1981, "Hydraulic Capsule Pipeline," *Journal of Pipelines,* Vol. 1, p. 11.

Liu, H., 1992, "Hydraulic Behaviors of Coal Log Flow in Pipe," *Proceedings of the 7th International Symposium on Freight Pipelines,* Wollongong, Australia, p. 201.

Liu, H., 1993, "Coal Log Pipeline: Economics, Water Use, Right-of Way, and Environmental Impact," *Proceedings of the 10th Annual Pittsburgh Coal Conference,* p. 23.

Liu, H., Zuniga, R., and Richards, J. L., 1993, "Economic Analysis of Coal Log Pipeline Transportation of Coal," CPRC Report No. 93-1, University of Missouri-Columbia, 248 pages.

Rhee, K. H., 1989, "Behavior Of Cylindrical Capsules In Fiber-Water Flow In Pipe," Ph.D thesis, Dept. of Civil Engineering, University of Missouri-Columbia.

Richards, J. L., 1992, "The Behavior Of Coal Log Trains In Hydraulic Transport Through Pipe," M.S. thesis, Dept. of Civil Engineering, University of Missouri-Columbia.

Seaba, J. P., Liu, H., and Xu, G., 1993, "Slurry Suspension of Coal logs—An Exploratory Study," *18th International Technical Conference on Coal Utilization & Fuel Systems,* Clearwater, FL, p. 733.

Wasp, E. J., Kenny, J. P., and Gandhi, R. L., 1979, *Solid-Liquid Flow Slurry Pipeline Transportation,* Gulf Publishing Company.

Xu, G., 1993, "Behavior of Capsules in Slurry Medium in Pipe," M.S. thesis, Dept. of Mechanical & Aerospace Engineering, University of Missouri-Columbia.

Numerical Simulation of Vertical Forced Plume in a Crossflow of Stably Stratified Fluid

Robert R. Hwang
Institute of Physics,
Academia Sinaca,
Taipei

T. P. Chiang
Department of Naval Architecture
and Ocean Engineering,
National Taiwan University, Taipei

In this study, an investigation using a three-dimensional numerical model, which treats conservation of mass, momentum, and salinity simultaneously, was carried out to study the character of a vertical forced plume in a uniform cross-stream of stably linear stratified environment. A k-ϵ turbulence model was used to simulate the turbulent phenomena and close the solving problem. The performance of the three-dimensional model is evaluated by comparison of the numerical results with some available experimental measurements. Results indicate that the numerical computation simulates satisfactorily the plume behavior in a stratified crossflow. The secondary vortex pairs in the cross section induced by the primary one change as the plume flows downstream. This denotes the transformation of entrainment mechanism in stratified crossflow.

1 Introduction

The turbulent mixing of a buoyant jet in a density-stratified crossflow is of significant importance in the application of engineering problems. The plume of smoke from an industrial chimney into the atmosphere is a typical example of the discharge of pollutants as a buoyant jet. The turbulent shear generated by the discharge results in efficient mixing, and this reduces the concentration of pollutants. When compared with a similar flow in unstratified fluid, the major effects of density stratification are to limit the vertical rise of a buoyant jet and to restrict the mixing with the surrounding ambient fluid. Hence, understanding the mixing and dilution processes, and establishing the capability to estimate the rise and width of a buoyant jet in stratified fluid, are necessary for designing and controlling a waste disposal system.

A number of approximate predictive methods for the plume flow in stratified surroundings have been developed in the literature of Abraham (1965), Schwartz and Tulin (1972), Sneck and Brown (1974), Wright (1984), and Hwang and Chiang (1986). All these are basically integral methods based on the simplifying assumptions that the entrainment rate and the similarity profiles for both the velocity and temperature are made. Recently, the differential method was presented, which directly treats the conservations of mass, momentum, and temperature without entrainment and profile assumptions. The differential method employs a turbulence model to predict the turbulent behavior at each point in the buoyant jets. Hence the profiles and entrainment rate are parts of the solution. Studies of Madni and Pletcher (1976) and Mizutori et al. (1990) used a mixing length model to simulate the turbulent diffusion characteristics. Higher order closure models were proposed by Launder and Spalding (1974) and many others. Li and Chen (1985) used the k-ϵ turbulence model to study the behavior of round buoyant jets in quiescent stably linear stratified environments.

Along with recent developments in numerical computations, there has been considerable progress in the construction of turbulence models of wide applicability. It is, therefore, now possible to use an acceptable turbulence model to obtain numerical solutions for jets in a stratified cross flow. The aim of this study is to calculate by a finite-difference method the flow field of a round turbulent buoyant jet issuing vertically into a uniform free stream of density-stratified fluid. In solving the three-dimensional time-averaged governing equations, the two-equation model of standard k-ϵ model is adopted to simulate the turbulent transported quantities.

Contributed by the Fluids Engineering Division for publication in the JOURNAL OF FLUIDS ENGINEERING. Manuscript received by the Fluids Engineering Division April 13, 1994; revised manuscript received May 31, 1995. Associate Technical Editor: G. Karniadakis.

2 Formulation of Flow Problems

2.1 The Governing Equations. We consider the three-dimensional flow field of a round buoyant jet of diameter D_j with constant injection velocity W_j issuing vertically into a uniform velocity cross flow of stably linear stratified fluid. Figure 1 shows the geometry and coordinates of the flow problem. Far upstream, in the frame of reference of the jet exit, the following conditions are assumed to exist:

$$\rho_a = \rho_{ao}(1 - \alpha z)$$

$$U \to U_a$$

$$V, W = 0$$

in which ρ_{ao} is the density of fluid far upstream at the level of the jet exit and

$$\alpha = \lim |d\rho_a/dz|/\rho_{ao}$$

is the stratification parameter, U_a is the velocity of the cross flow. The density of fluid is computed by using Knudsen's formula and the density stratification in the environment is caused only by salinity variation in the fluid.

With the assumptions that α is so small that the Boussinesq approximation is valid and the density variation is accounted for only in the gravitational term, the governing differential equations for the mean velocity, salinity and concentration are: Continuity:

$$\frac{\partial U_i}{\partial x_i} = 0 \tag{1}$$

Momentum:

$$U_j \frac{\partial U_i}{\partial x_j} = -\frac{1}{\rho}\frac{\partial P}{\partial x_i} - \beta g(T - T_a)\delta_{3i} + \frac{\partial}{\partial x_j}(-\overline{u_i u_j}) \tag{2}$$

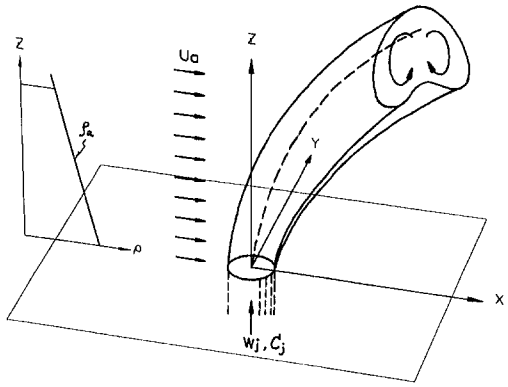

Fig. 1 The considered flow problem

Salinity:

$$U_j \frac{\partial T}{\partial x_j} = \frac{\partial}{\partial x_j}(-\overline{u_j T'}) \tag{3}$$

Concentration:

$$U_j \frac{\partial C}{\partial x_j} = \frac{\partial}{\partial x_j}(-\overline{u_j C'}) \tag{4}$$

where U_i is the time averaged velocity components in the i coordinate direction, ρ is density, P is the mean pressure, T is the salinity, T_a is the local ambient salinity, C is the mean concentration of tracer injecting from the jet, and $-\overline{u_i u_j}$ and $-\overline{u_j T'}$ are the turbulent transport rates of momentum and mass fluxes respectively. Far upstream of the jet exit, the local ambient salinity, or the ambient density, is assumed to be linear in the vertical direction.

2.2 The Turbulence Model. In order to solve Eqs. (1)–(4), a turbulence model for the turbulent stresses and mass flux has to be specified. The model adopted in this study is the standard k-ϵ model in which an isotropic eddy diffusivity is assumed. The eddy diffusivities of salinity and tracer are estimated by using the turbulent Schmidt number σ_t. The local mean state of turbulence can then be characterized by the kinetic energy (k) and dissipation rate (ϵ) of the fluctuating motion. The relationship is

$$-\overline{u_i u_j} = \nu_t\left(\frac{\partial U_i}{\partial x_j} + \frac{\partial U_j}{\partial x_i}\right) - \frac{2}{3}\delta_{ij}k \tag{5}$$

$$-\overline{u_j T'} = \gamma \frac{\partial T}{\partial x_j} \tag{6}$$

$$-\overline{u_j C'} = \gamma \frac{\partial C}{\partial x_j} \tag{7}$$

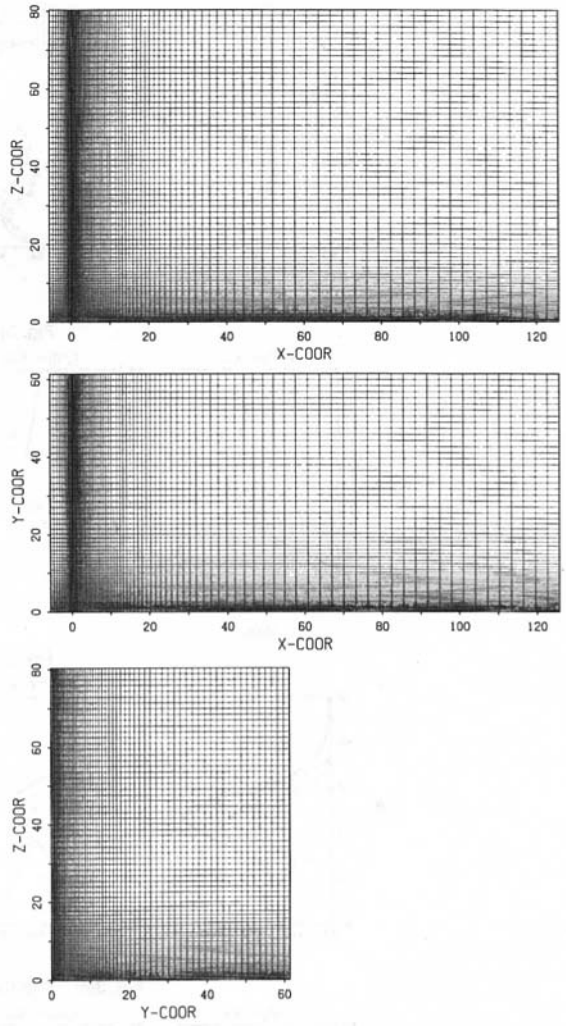

Fig. 2 The arrangement of the computational grid in the computational domain

with

$$\nu_t = C_\mu k^2/\epsilon, \quad \gamma = \nu_t/\sigma_t, \tag{8}$$

where ν_t and γ are the eddy viscosity and diffusivity respectively, and C_μ is a constant.

The equations that govern the distribution of k and ϵ can be found in Rodi (1984) as follows

Nomenclature

C = mean concentration
C_j = injection concentration of the jet
C_1, C_2, C_μ = constants in the turbulence model
D_j = diameter of the jet exit
F = the densimetric Froude number ($=[W_j/(\Delta\rho/\rho_{ao})gD_j]^{1/2}$)
G = the square of Brunt-Vaisala frequency ($=\alpha g$)
g = acceleration of gravity
k = the turbulent kinetic energy ($=\frac{1}{2}(\overline{u^2}+\overline{v^2}+\overline{w^2})$)
P = mean pressure
R = ratio of the jet velocity to the main-stream velocity ($=W_j/U_a$)
R_{ej} = the Reynolds number based on the jet velocity
T = mean salinity
T_a = local ambient salinity
U_a = the crossstream velocity
U, V, W = mean velocity components in the (x, y, z) direction
W_j = injection velocity of the jet
ν_t = eddy viscosity
γ = eddy diffusivity
σ_ϵ, σ_t = constants in the turbulence model
ρ = density
ρ_a = local ambient density
ρ_{ao} = ambient density at the level of jet exit
α = the stratification parameter
ϵ = the dissipation rate of turbulent energy
β = the expansion coefficient of salinity ($=-0.815\times10^{-3}$)

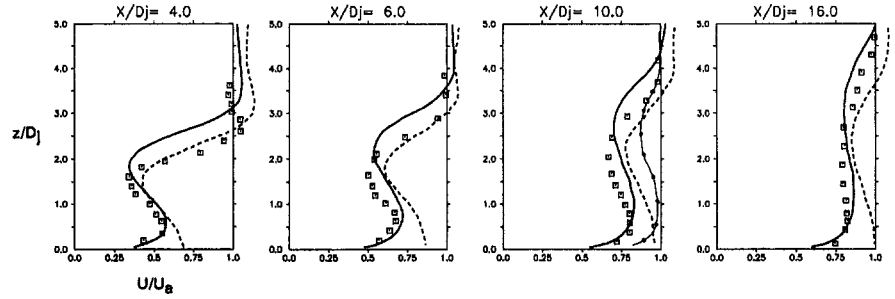

Fig. 3(*a*) Velocity of U

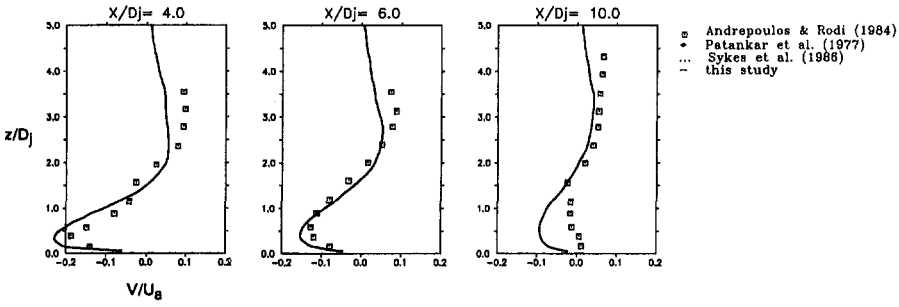

Fig. 3(*b*) Velocity of V

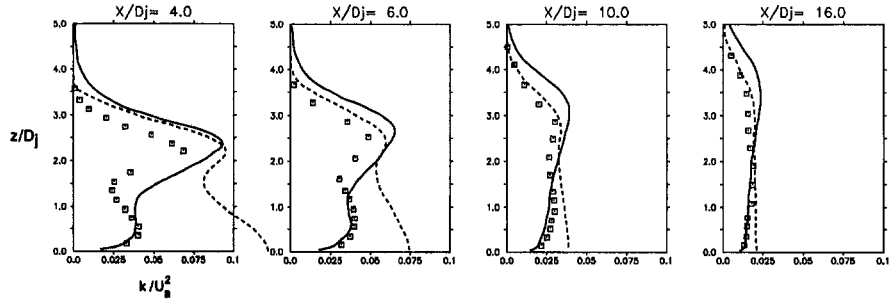

Fig. 3(*c*) The turbulent kinetic energy of k

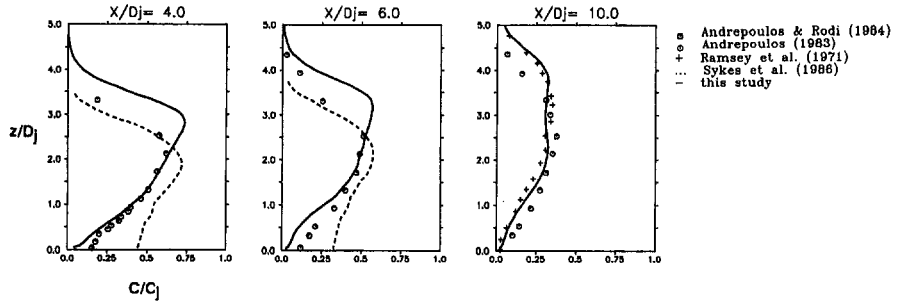

Fig. 3(*d*) The concentration profiles of C

Fig. 3 Comparison of the predicted profiles for $R = 2$ with previous studies

$$U_j \frac{\partial k}{\partial x_j} = \frac{\partial}{\partial x_j}\left(\frac{\nu_t}{\sigma_k}\frac{\partial k}{\partial x_j}\right) + \underbrace{\nu_t\left(\frac{\partial U_i}{\partial x_j} + \frac{\partial U_j}{\partial x_i}\right)\frac{\partial U_i}{\partial x_j}}_{\mathbb{P}} + \underbrace{\beta g_j \frac{\nu_t}{\sigma_k}\frac{\partial T}{\partial x_j}}_{\mathbb{G}} - \epsilon \quad (9)$$

$$U_j \frac{\partial \epsilon}{\partial x_j} = \frac{\partial}{\partial x_j}\left(\frac{\nu_t}{\sigma_\epsilon}\frac{\partial \epsilon}{\partial x_j}\right) + C_1 \frac{\epsilon}{k}(\mathbb{P} + \mathbb{G}) - C_2 \frac{\epsilon^2}{k} \quad (10)$$

where σ_k and σ_ϵ are empirical diffusion constants. Buoyancy effects on the turbulence are accounted for by including the buoyancy terms in the k- and ϵ-equations and leaving the constants uneffected by buoyancy (Rodi 1984). The turbulence model involves six empirical constants. We adopt the same constant values proposed by Rodi (1984) as follows:

$$C_\mu = 0.09, \quad C_1 = 1.44, \quad C_2 = 1.92,$$
$$\sigma_k = 1.0, \quad \sigma_\epsilon = 1.3, \quad \sigma_t = 0.7.$$

As reported in Rodi (1984), these constants have been used for a wide variety of situations to obtain predictions that give satisfactory agreement with experiment.

2.3 Boundary and Exit Conditions. In the flow of a round jet discharged into a stably linear stratified crossflow, it

Table 1 The grid number and resolution conducted for the case of $R = 8$

Run	X_1	X_2	Y_2	Z_2	N_x	N_y	N_z
R8	−6	125	60	80	62	43	56
R8: high resolution	−6	125	60	80	90	64	77

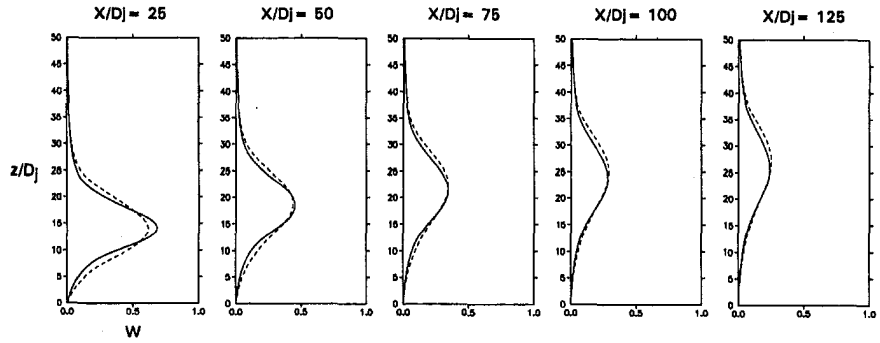

Fig. 4 Comparison of the predicted W profiles at $y = 0$ for $R = 8$ between two grid resolutions. - - - the $62 \times 43 \times 56$ grid size, —— the $90 \times 64 \times 77$ grid size

can be seen from Fig. 1 that the time-averaged flow field is symmetrical about the xz plane passing through the center of the jet. The calculation domain was chosen that, in the y direction, it extended from the symmetry plane to a location where y/D_j is 60. In the z direction, one boundary of the domain considered was the bottom plane, and the other was placed sufficiently far away (say, H) so that uniform crossstream conditions could be approximately assumed there. This location of the outer boundary was found by computational experiments. For a jet-to-crossstream velocity ratio (R) of 8, for example, the outer boundary was located at a z/D_j of 80.

In the x direction, the upstream boundary was placed six jet diameters upstream of the jet and the position of the downstream boundary was located sufficiently far downstream that the flow velocity became almost parallel to the x direction. For example, in the case of the velocity ratio $R = 8$, the downstream boundary was positioned at $x/D_j = 125$.

The boundary conditions for the calculation domain prescribed above were specified as follows:

(1) On the upstream yz plane $x = X_1$, flows were considered to be far away from the jet and the various variables there were treated as

$$U = U_a, \quad V = W = C = 0, \quad T_a = T_{ao} + \frac{dT_a}{dz} z,$$

$$k = 0.04U_a^2, \quad \epsilon = k^{3/2}/(0.06H). \tag{11}$$

(2) At the downstream yz plane $x = X_2$, the normal gradients of the variables were assumed to be zero, i.e., $\partial(V, W, T, k, \epsilon, C)/\partial x = 0$, $U_B^n = U_{B-1}^n$, where n represents the iteration level, and B the boundary point.

(3) On the jet exit, the jet conditions were specified as $W = W_j$, $U = V = 0$, $T = T_j$, $C = C_j$, $k = 0.001W_j^2$, $\epsilon = k^{3/2}/(0.5D_j)$.

(4) The xz plane through the origin ($y = 0$), was treated as a plane of symmetry, i.e.

$$V = 0, \quad \partial(U, W, T, k, \epsilon, C)/\partial y = 0. \tag{12}$$

(5) The other xz plane $y = Y_2$ and the top xy plane $z = Z_2$ were considered to be far from the jet and had the same flow conditions as the upstream yz plane condition of (1).

(6) On the bottom xy plane $z = 0$,

$$W = 0, \quad \partial(U, V, T, k, \epsilon, C)/\partial z = 0. \tag{13}$$

The outflow boundary condition is considered simply to handle the passage of the jet. For the lower boundary, similar to that of Sykes et al. (1986), we use a stress-free wall instead a true wall except for the test case of $R = 2$. This is because the jet flows we considered have relatively large velocity ratios and the flow development will be in jets remote from the wall. The values of the turbulence kinetic energy and dissipation in the main stream and in the jet were as adopted by Demuren (1983) and Li and Chen (1985).

3 Computational Technique

In this study, the numerical computations were performed on a nonuniform and staggered MAC (marker and cell) grid system (Spalding, 1972). In the staggered grid system, the pressure and other dependent scalar variables such as k and ϵ, are calculated at nodal points between those of the velocity to avoid the phenomenon known as the checkboard problem. Figure 2 shows the arrangement of the computational grid in the xz-plane, xy-plan and yz-plane.

To solve the partial differential Eqs. (2), (3), (4), (9), and (10) which are of elliptic type, a computer code based on the power law difference (PLD) method (Patankar, 1972) is constructed for use in the present study. Briefly, in a control volume finite-difference method, the convection together with diffusion terms of transport equation for variable ϕ ($\phi = U, V, k, W, T, C, \epsilon$) of

$$\frac{\partial}{\partial x_j}(\rho U_j \phi) = \frac{\partial}{\partial x_j}\left(\Gamma \frac{\partial \phi}{\partial x_j}\right) + S_\phi \tag{14}$$

is discretized by PLD, source term by second order central difference, and then integrated within a control volume element to obtain an algebraic equation. The pressure field P is solved with SIMPLEC algorithm of Von-Doormaal (1984). The system of linear algebraic equations is solved by the alternating direction line by line iteration method.

To assess the accuracy of the governing equations and the validity of the associated computer program, a case of a turbu-

Table 2 The jet and the ambient flow conditions conducted in this study

	Jet				Ambient flow		Flow parameters		
Case	D_j (cm)	W_j (cm/s)	$\Delta\rho/\rho_{ao} \times 10^{-2}$	R_{ej}	U_a (cm/s)	$\alpha \times 10^{-3}$ (cm^{-1})	R	F	G (s^{-2})
1	0.40	199.7	0.0	8.0×10^3	24.9	0.0	8.0		0.0
2	0.82	82.5	0.76	6.8×10^3	10.3	0.36	8.0	30	0.35
3	0.82	82.5	0.76	6.8×10^3	4.6	0.36	18.0	30	0.35

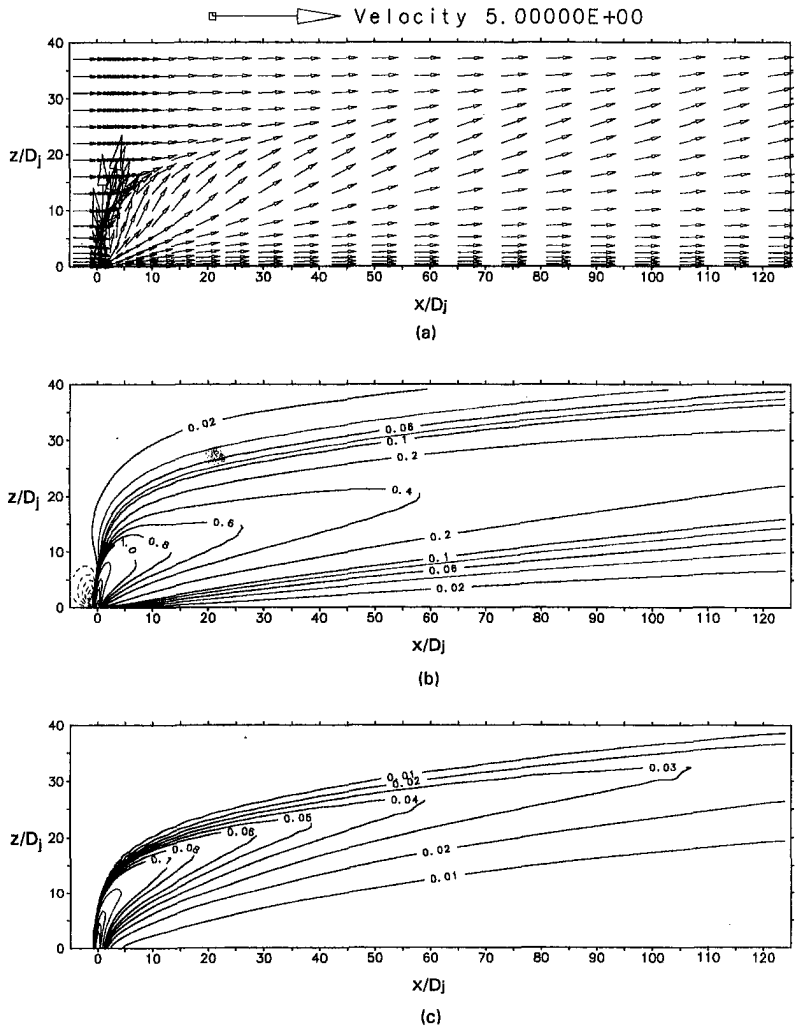

Fig. 5 The computed results on the $y = 0$ plane for $R = 8$, $F = \infty$ and $G = 0$ (unstratified case) (a) The U-W velocity vectors; (b) the W velocity contours; (c) The iso-concentration contours

lent jet emitted normal to a uniform free stream of homogeneous fluid with a jet-to-crossstream velocity ratio $R = 2$ is computed at first, and compared with previous studies of Ramsey and Goldstein (1971), Patankar et al. (1977), Andreopoulos (1983), Andreopoulos and Rodi (1984), and Sykes et al. (1986). In this case, all studies included the bottom xy-plane boundary layer except the study of Sykes et al. (1986). In order to compare with other results, the two-point wall function approach (Chen, 1983) is adopted in this test case to include the bottom xy-plane boundary layer instead of the stress-free boundary condition mentioned previously.

Results are presented for only those quantities which have been reported in the related literature. Profiles of the U, k, and C in the central xz-plane and V at $y/D_j = 0.5$ plane are plotted for several stations downstream from the jet. In Figs. 3(a) and 3(b), we compare the computed velocity of profiles U and V, respectively, with experimental data of Andreopoulos and Rodi (1984) and some predicted results of Patankar et al. (1977) and Sykes et al. (1986). Figures 3(c) and 3(d) show the computed profiles of the turbulent kinetic energy k and concentration C, respectively, compared with the experimental data of Andreopoulos (1983), Andreopoulos and Rodi (1984), and Ramsey and Goldstein (1971) and the predicted results of Sykes et al. (1986). It can be seen that results of different studies do not correlate well among themselves and the computed results of this study seem to fit best with the experimental data. Overall, the agreement with the experimental results is satisfactory.

In the comparison shown in Fig. 3, it is noted that although the study of Sykes et al. treated the lower surface as a stress-free wall instead of a true wall outside the jet-exhaust region, the predicted results of U, k, and C agree quite well with experiment except near the wall. The inclusion of the bottom boundary layer will only have an effect in the region near the wall. This is evidence that the lower boundary does play a role but it is not dominant. If we consider the cases of relatively large jet exit ratios, R, (say $R \geq 8$), the main interest is in the flow remote from the wall, so we have not attempted to model the near-wall region accurately. A free-shear boundary can then be considered instead a true wall for jet flows of relatively large jet exit ratio.

Numerical experiments have also been conducted to determine an adequate grid distribution for the present study. We used two grid distributions to conduct the computations for the case of a turbulent jet injected into a uniform cross stream of homogeneous fluid with $R = 8$. Table 1 indicates the grid number of the two resolutions distributed in the computational domain. Figure 4 shows the comparison of the computed W velocity profiles at the plane of symmetry at several stations along the stream direction from the two grid distributions. Although it indicates a little difference near the exit, the deviation of the

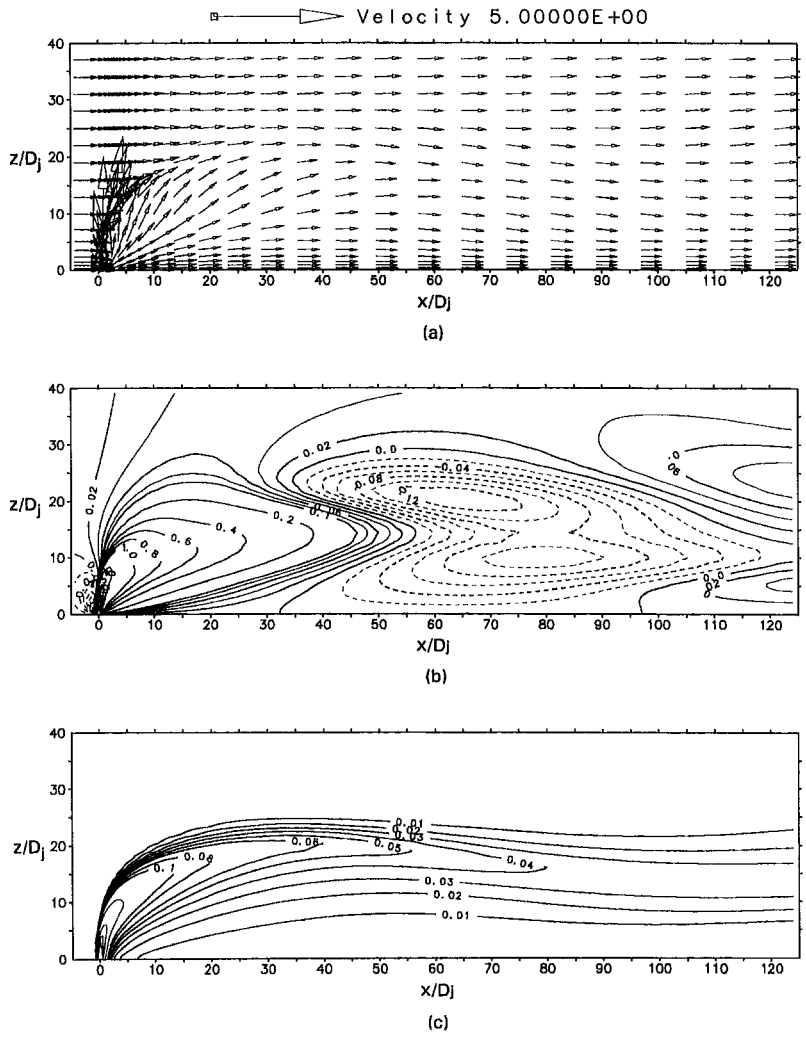

Fig. 6 The computed results on the $y = 0$ plane for $R = 8$, $F = 33.0$ and $G = 0.35\ s^{-2}$, (*a*) The *U-W* velocity vectors; (*b*) The *W* velocity contours; (*c*) The iso-concentration contours

W profiles (especially, the maximum value) of the jet flow between the computed results of the grid size $62 \times 43 \times 56$, and those of the fine grid $90 \times 64 \times 77$ is not significant. Rodi and Srivatsa (1980) also stated that grid refinements in general improve the near-field solution, with without significantly altering the far-field solution. The main interest of this study is in the far-field of the plume behavior in stratified crossflow. Grid refinements then improve a slightly the far-field solution. Therefore, the results that are presented in this study are based on the grid numbers of $(12 + 50) \times 43 \times 56$ distributed nonuniformly in the computational domain $(6.0\ D_j + 125\ D_j) \times 60\ D_j \times 80\ D_j$ in which 12 grids are ahead of the jet (centerline) in the $6.0\ D_j$ length and 50 grids downstream of the jet in the $125\ D_j$ length.

4 Presentation and Discussion of Results

Our objective in the development of this numerical model is to understand flow cases such as the plumes emitted from tall stacks into the atmosphere; hence we only consider relatively large jet exit ratios. Numerical computation of such a three-dimensional jet flow can yield detailed information of flow field. In the present study three flow cases are computed to study the effect of ambient fluid stratification on a jet flow subject to a uniform velocity cross flow. The jet and the ambient flow conditions of these flows are listed in Table 2.

1 The Influences of Ambient Stratifications on the Jet Development. As a turbulent jet issues vertically into a crossflow, the flow field can be described from two views. To the surrounding fluid, the discharged jet behaves similar to an obstacle placed in the flow, where the windward side is the retarding region of high pressure while the lee side is the low-pressure wake region. Secondly, to the jet flow, the horizontal momentum of the crossflow and the shear layer and wake entrainment lead to the deflection of the jet in the cross flow direction and mixing with the surrounding fluid. Since the jet shear layer is permeable and deformable, the surrounding crossflow passes and penetrates through the jet shear layer resulting in the formation of a pair of vortices on the jet cross-section.

Figures 5, 6, and 7 show the U-W velocity vectors, W-velocity contours, and iso-concentration contours of the jet flow interacted with the crossflow for varied jet configurations and ambient stratifications on the plane of symmetry ($y = 0$). Figure 5 shows the computed results for the pure momentum jet in the crossflow of unstratified fluid where $R = 8$, $F = \infty$, and $G = 0$ case. Above the exit the jet, driven by its initial momentum, deflects promptly then continues to move upwards. It can be seen from Fig. 5(b) that the W contours of vertical velocity vary monotonically. The turbulent shear generated by the discharge results in efficient mixing which rapidly reduces tracer concentrations. Figure 5(c) shows the computed concentrations of the

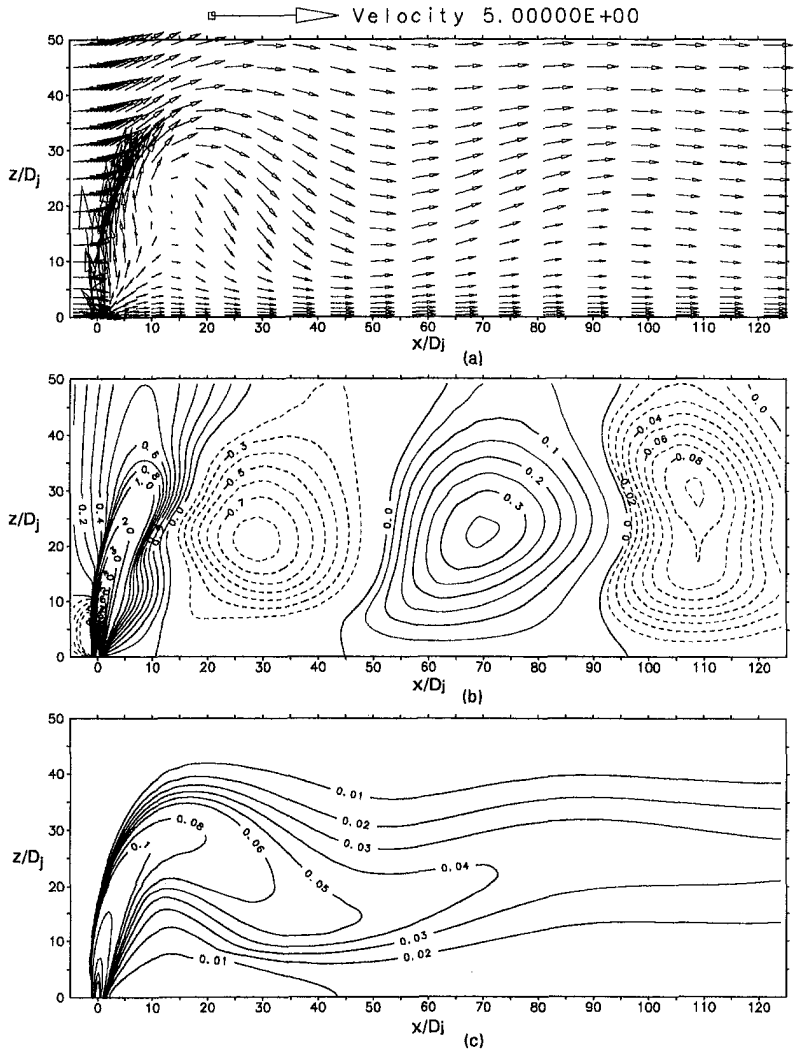

Fig. 7 The computed results on the $y = 0$ plane for $R = 18$, $F = 33.0$ and $G = 0.35\ s^{-2}$, (*a*) The *U-W* velocity vectors; (*b*) The *W* velocity contours; (c) The iso-concentration contours

dyed jet to be reduced down to 10 percent of the undiluted jet concentration in the vicinity of the jet exit.

The other two cases considered show the influences of ambient density stratification on the jet flow development. A major effect of the density stratification is to limit the vertical rise of a buoyant jet and to restrict the dilution compared to a similar flow in an unstratified ambient fluid. Figures $6(a)$ and $6(b)$ show the effects of ambient stratification on the jet development at $y = 0$ plane for flow configuration of $R = 8$, $F = 33.0$, and $G = 0.35\ s^{-2}$. Here $F = W_j/[(\Delta\rho/\rho_{ao})gD_j]^{1/2}$, is the densimetric Froude number, where $\Delta\rho = \rho_{ao} - \rho_j$ is the density difference between the ambient density at the level of jet exit and the jet density, and $G = \alpha g$ is the square of Brunt-Vaisala frequency of the stratified environment. In a stably stratified environment, the plume first behaves like a buoyant jet. The initial momentum and the buoyancy of the plume cause the jet flow to move upward, bend over in the crossstream direction and mix with the heavy bottom fluid. The density deficit of the plume then decreases continuously and becomes zero at a certain level. From here on the buoyancy force is negative and the flow decelerates and turns down after reaching a maximum height. The jet trajectory is illustrated by the iso-concentration contours shown in Fig. $6(c)$.

Increasing the ratio of the jet velocity to the mainstream velocity will increase the initial momentum of jet so that the buoyant jet rises higher and mixes more rapidly with dense bottom fluid. As a result, the density deficit of the plume decreases faster and the jet turns down rapidly. Significant oscillating motion of the jet along the crossflow direction, similar to an internal gravity wave, is then formed. Figure 7 shows the computed results on the $y = 0$ plane for the case of $R = 18$, $F = 33.0$, and $G = 0.35\ s^{-2}$. The upward and downward motion of the jet flow is clearly evident in the W-velocity contours of Fig. $7(b)$. The wavelength of oscillating motion of a buoyant jet in a stratified crossflow from its maximum height-of-rise is inversely proportional to the velocity ratio of R. The larger the jet exit ratio, the smaller the wavelength of the oscillating motion. In the correspondence with the wave-like motion of the jet flow, the jet trajectory also exhibits an oscillating trajectory. This can be seen from the iso-concentration contours shown in Fig. $7(c)$.

2 The Influences of Ambient Stratifications on Vortex Motion on the Jet Cross Section. As described previously, the horizontal momentum of the cross flow causes the jet to be deflected along the flow direction and a pair of vortices to be generated on the jet cross section. As shown in Fig. $8(a)$, the pair of vortices on the cross section is counter clockwise on the left and clockwise on the right. The vortex pair moves upwards and reduces its magnitude of the peak value of the vorticity

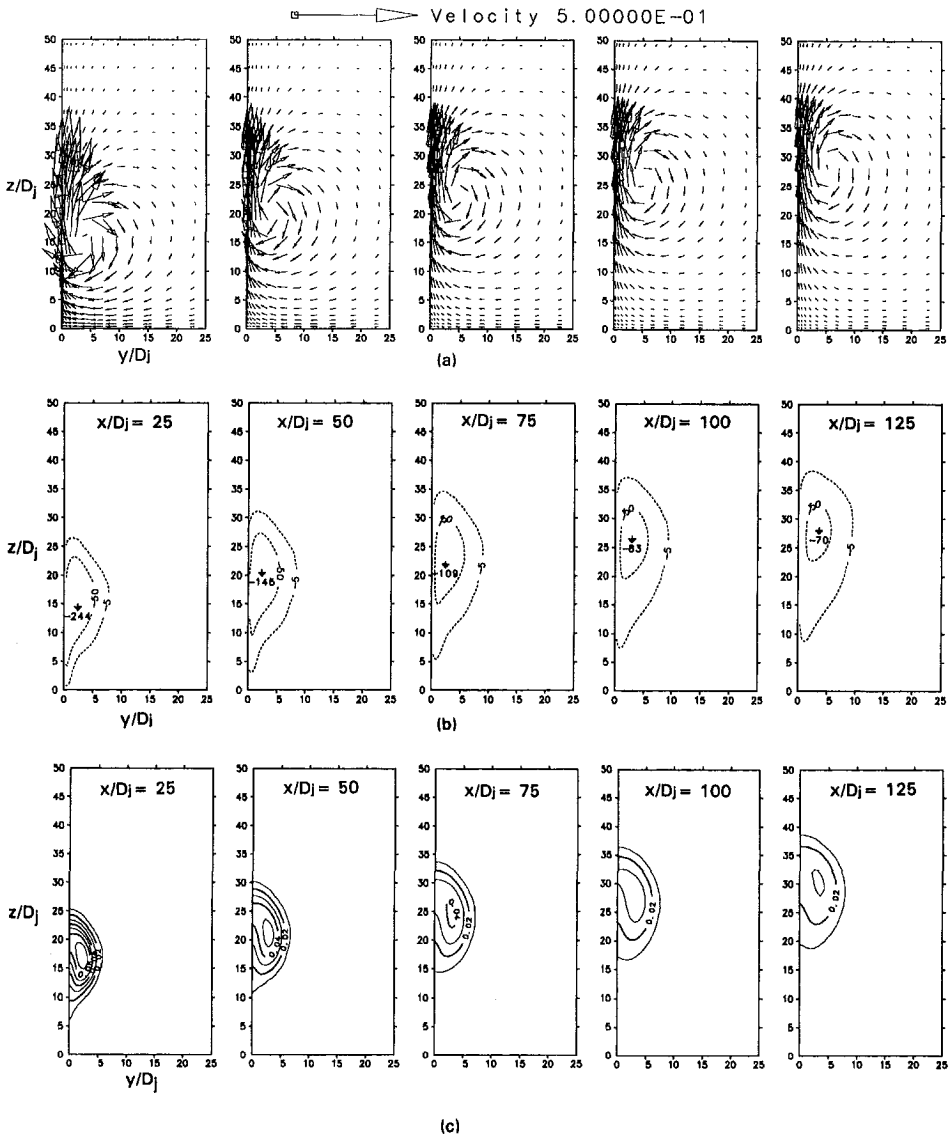

Fig. 8 The evolution of vortex motion on the jet cross section for $R = 8$, $F = \infty$ and $G = 0$ (unstratified case) Fig. 8(*a*) The V-W velocity vectors (*b*) The streamwise-compnent vorticity contours. Contour magnitudes are amplified by 10^3. (c) The iso-concentration contours

along with its diffusion outward. This can be seen more clearly in the various transverse sections of the streamwise vorticity field shown in Fig. $8(b)$. The streamwise-component of vorticity is defined as $\omega_x = (\partial W/\partial y) - (\partial V/\partial z)$. From the vorticity dynamics, it can be noted that the principal feature of the jet flow is a result of injection of vorticity by the jet and subsequent diffusion of that vorticity. The cross-sectional shape of the jet is varied gradually from a circle near the exit to a kidney shape with the indentation on the low-pressure lee side. The deformation of the jet cross-section can also be seen from the iso-concentration contours of Fig. $8(c)$.

In a stably stratified environment, one effect of density stratification is to prevent the vertical rise of the buoyant jet. The retardation of the flow development influenced by the stratified environment then leads to the formation of a secondary pair and a third pair of vortices above and below the primary vortex pair with a reverse direction. It can be noticed at stations of $x/D_j =$ 50 and 75 of Fig. 9 for the case of $R = 8$, $F = 33.0$, and $G = 0.35\ s^{-2}$. The two pairs of vortices in the cross-section grow and suppress the growth of the first one as the plume flows downstream. It then causes the plume to move downward after reaching a maximum height. Figure $9(a)$ shows the evolution of vortex reversion at sections 25 to 125 diameters downstream from the jet exit. As the plume flows further downstream, says at $x/D_j = 100$ and 125, another two pairs of vortices are induced above and below the secondary pair again. These also grow and suppress the growth of the secondly pair simultaneously. The clockwise motion of the two pairs of vortices in Fig. 9 then raises up the plume trajectory again. The various transverse sections of the streamwise-component vorticity field of Fig. $9(b)$ show the evolution process more clearly. The effect of the ambient stratification is to produce the vorticity of opposite sign to the main vorticity. As the stratification of the ambient fluid is increased, the retardation of the jet flow from its source efflux becomes more significant. Influenced by the same mechanism, the development of iso-concentration contours, which have the same shape as the jet cross section, is also altered by the effects of density stratification, as illustrated in Fig. $9(c)$. Both the iso-concentration contours and the shape of jet cross-section have deformed from a symmetric kidney-shape to an oblate ellipse. This can be confirmed by observing the jet trajectory of Figs. 5 and 6 that the jet width (as indicated by the distance between the contours) at far downstream sections is smaller than that of upstream sections. The decaying rate of the tracer concentration

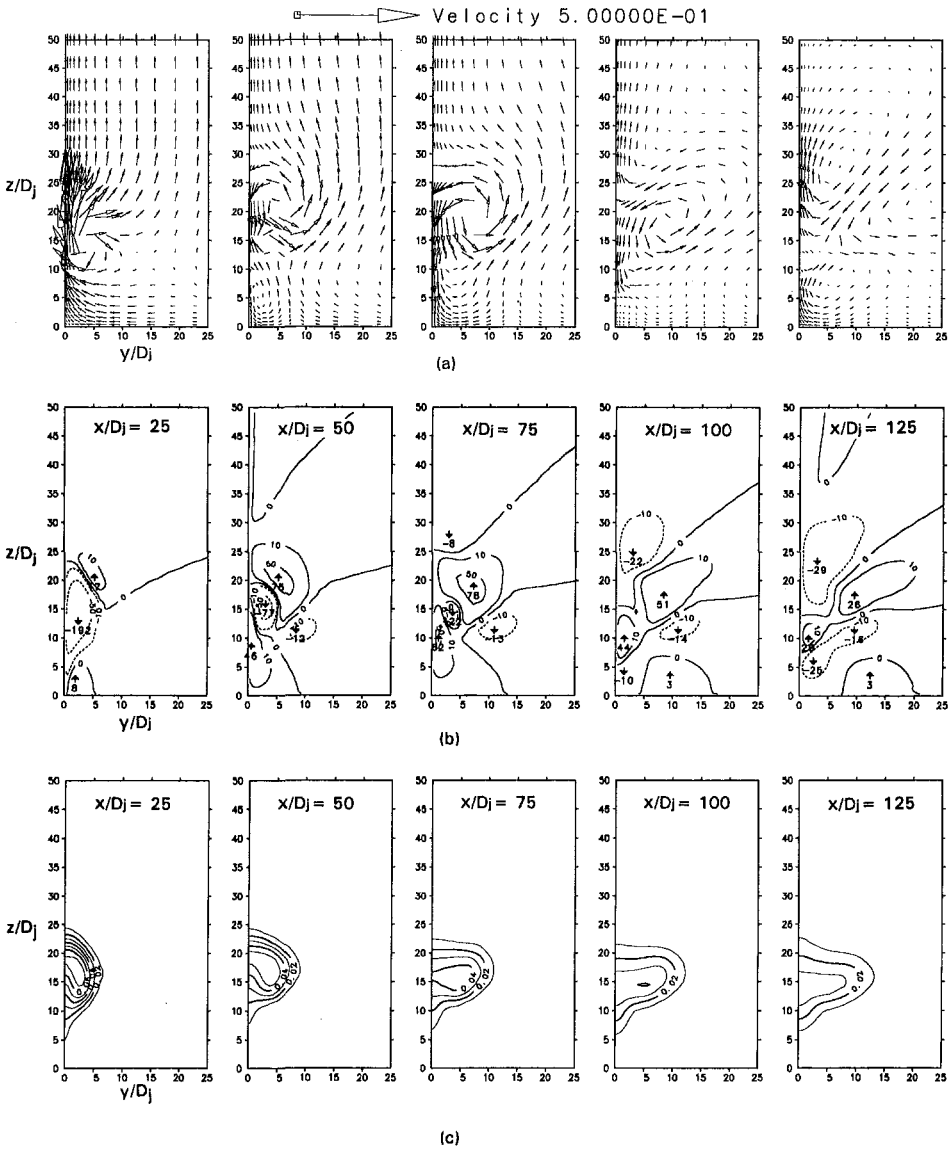

Fig. 9 The evolution of vortex motion on the jet cross-section for $R = 8$, $F = 33.0$ and $G = 0.35\ s^{-2}$ (stratified) (*a*) The *V-W* velocity vectors (*b*) The streamwise-component vorticity contours. Contour magnitudes are amplified by 10^3. (*c*) The iso-concentration contours

is also retarded and decreased due to the effect of ambient stratification, as shown in Figs. 5 and 6.

5 Conclusion

The detailed structure of the flow development for a buoyant jet discharged in a crossflow of stably linear stratified environment is not clear at present. In this study, a three-dimensional numerical model based on a two-equation turbulence model is applied to predict the plume behavior in stratified cross flows. Computations of the model have given results which are, in general, in satisfactory agreement with available experimental data. The formation of the secondary and the third pairs of vortices which are not induced in the unstratified environment causes the jet flow oscillation from its maximum height-of-rise and alteration to the entrainment mechanism in the stratified cross flow. The ambient stratification, prohibits the development of the plume radius and reduces the mixing rate as well as the plume rise and a wave-like trajectory is formed for the case of higher density stratification and higher jet-to-crossstream velocity ratio.

Acknowledgment

This work was supported both by the National Science Council under grant No. NSC82-0209-E001-012 and by the Institute of Physics, Academia Sinica.

References

Abraham, G., 1965, "Entrainment Principle and its Restriction to Solve Jet Problems," *Journal of Hydraulic Research,* Vol. 31, pp. 1–23.

Andreopoulos, J., 1983, "Heat Transfer Measurements in a Heated Jet-Pipe Flow Issuing Into a Cold Cross Stream," *Phys. Fluids,* Vol. 26, pp. 3201–3210.

Andreopoulos, J., and Rodi, W., 1984, "Experimental Investigation of Jets in a Crossflow," *Journal of Fluid Mechanics,* Vol. 138, pp. 93–127.

Chen, C. J., 1983, "Prediction of Turbulent Flows," Central Research Institute of Electric Power Industry Tech. Report 17, Abiko, Japan.

Demuren, A. O., 1983, "Numerical Calculations of Steady Three-Dimensional Turbulent Jets in Crossflow," Computer Methods in Applied Mechanics and Engineering, Vol. 37, pp. 309–328.

Harlow, F. H., and Welch, J. E., 1965, "Numerical Calculation of Time-Dependent Viscous Incompressible Flow of Fluid with Free Surface," *Physical Fluids,* Vol. 8, pp. 2182–2189.

Hwang, R. R., and Chiang, T. P., 1986, "Buoyant Jets in a Crossflow of Stably Stratified Fluid," *Atmospheric Environment,* Vol. 20, pp. 1887–1890.

Launder, B. E., and Spalding, D. B., 1974, "The Numerical Prediction of Turbulent Flows," *Computer Methods in Applied Mechanics and Engineering,* Vol. 3, pp. 269–289.

Li, W., and Chen, C. J., 1985, "On Prediction of Characteristics for Vertical Round Buoyant Jets in Stably Linear Stratified Environment," *Journal of Hydraulic Research,* Vol. 23, pp. 115–129.

Madni, I. K., and Patcher, R. H., 1976, "Prediction of Turbulent Force Plumes Issuing Vertically into Stratified on Uniform Ambients," ASME *Journal of Heat Transfer,* Vol. 99, pp. 99–104.

Mizutori, M., Katano, N., and Nakashiki, N., 1990, "Numerical Simulation of Vertical Forced Plume in Stratified Crossflow," *Proceedings of the 4th International Symposium on Refined Flow Modeling and Turbulence Measurement,* Wu-Han, China, pp. 487–494.

Patankar, S. V., and Spalding, D. B., 1972, "A Calculation Procedure for Heat, Mass, and Momentum Transfer in Three-Dimensional Parabolic Flows," *International Journal of Heat and Mass Transfer,* Vol. 5, pp. 1878–1806.

Patankar, S. V., Basu, D. K., and Alpay, S. A., 1977, "Prediction of the Three-Dimensional Velocity Field of a Deflected Turbulent Jet," ASME JOURNAL OF FLUIDS ENGINEERING, Vol. 99, pp. 758–762.

Patankar, S. V., 1982, "A Calculation Procedure for Two-Dimensional Elliptic Situations," *Numerical Heat Transfer,* Vol. 4, pp. 409–425.

Ramsey, J. W., and Goldstein, R. J., 1971, "Interaction of a Heat Jet with a Deflecting Stream," ASME *Journal of Heat Transfer,* Vol. 93, pp. 365–372.

Rodi, W., and Srivatsa, S. K., 1980, "A Locally Elliptic Calculation Procedure for Three-Dimensional Flows and its Application to a Jet in a Crossflow," *Computer Methods in Applied Mechanics and Engineering,* Vol. 23, pp. 67–83.

Rodi, W., 1984, "Turbulent Models and Their Applications in Hydraulics—A State of the Art Review," *International Association for Hydraulics Research,* Delft.

Schwartz, J., and Tulin, M. P., 1972, "On the Mean Path of Buoyant Bent-Over Chimney Plumes," *Atmospheric Environment,* Vol. 6, pp. 19–36.

Sneck, H. J., and Brown, D. H., 1974, "Plume Rise from Large Thermal Sources Such as Cooling Tower," ASME *Journal of the Heat Transfer,* Vol. 96, pp. 232–238.

Spalding, D. B., 1972, "A Novel Finite Differential Expression Involving Both First and Second Derivatives," *International Journal of Numerical Methods in Engineering,* Vol. 4, pp. 551–559.

Sykes, R. I., Lewellen, W. S., and Parker, S. F., 1986, "On the Vorticity Dynamics of a Turbulent Jet in a Crossflow," *Journal of Fluid Mechanics,* Vol. 168, pp. 393–413.

Van-Doormaal, J. P., and Raithby, G. D., 1984, "Enhancements of the SIMPLE Method for Predicting Incompressible Fluid Flows," *Numerical Heat Transfer,* Vol. 7, pp. 147–163.

Wright, S. J., 1984, "Buoyant Jets in Density-Stratified Crossflow," *Journal of Hydraulic Division,* ASCE, Vol. 110, pp. 643–656.

On the Mechanism of Fluidelastic Instability of a Tube Placed in an Array Subjected to Two-Phase Crossflow*

Y. Joo

V. K. Dhir

Mechanical, Aerospace and Nuclear Engineering Department,
School of Engineering and Applied Science,
University of California, Los Angeles,
Los Angeles, CA 90095

In this work, the fluidelastic instability of a tube placed in an array subjected to two-phase crossflow has been studied. For the determination of fluidelastic instability, acrylic tubes 2.2 cm or 2.37 cm in diameter and 20 cm in length were arranged in a triangular array with pitch to diameter ratio of 1.4 and 1.3. The test tube was flexibly supported with two cantilever beams. By installing cantilever beams horizontally and vertically, drag and lift direction tube vibration were studied. The total damping ratio is found to increase as the liquid gap velocity or void fraction increases. It has been found that the effective spring constant decreases rapidly with increase of liquid gap velocity or void fraction just prior to the onset of instability. For the range of parameters studied in this work, the onset of fluidelastic instability is associated with a rapid decrease of the effective spring constant because for a given applied force the amplitude of the tube vibration is inversely proportional to the spring constant.

1 Introduction

Two-phase crossflow over tubes in many shell-and-tube heat exchangers, steam generators, condensers and other heat exchanger equipment causes flow-induced vibrations. These flow-induced vibrations have been recognized as a major factor in the wear and eventual failure of tubes in heat exchangers. Several mechanisms which induce vibrations have been identified, including turbulence, vortex shedding, and fluidelastic instability. Among these the fluidelastic instability induces the largest amplitude vibrations. When a tube array is subjected to crossflow, the RMS amplitude or the maximum amplitude of the tube vibrations increases slowly with flow velocity, but at a certain flow velocity, it shows a rapid increase. The flow velocity at which a large increase in the amplitude occurs is defined as the critical velocity for the onset of fluidelastic instability.

1.1 Fluidelastic Instability in Two-Phase Crossflow. Connors' (1970) paper is one of the well-documented studies of flow-induced vibrations in single phase crossflows. He developed a stability criterion to predict the onset of instability based on the displacement mechanism (Section 1.2). The critical velocity above which large amplitude vibrations occurred was given by

$$\frac{V_r}{f_n D} = K\left(\frac{2\pi\zeta m}{\rho D^2}\right)^{1/2} \tag{1}$$

where V_r is the critical gap velocity, f_n is the natural frequency of the cylinder, D is the diameter of the cylinder, K is an instability constant, ζ is the cylinder damping ratio in still fluid, ρ is the fluid density, and m is the mass per unit length of the tube, including added mass. The stability criterion was verified with the data from dynamic stability tests on flexibly mounted tubes, and a value of 9.9 for the onset of instability constant was recommended.

Studies of fluidelastic instability of a tube bundle under two-phase crossflow are very limited. Pettigrew et al. (1988a), Remy (1982), and Heilker and Vincent (1981) studied fluidelastic instability and damping of tube bundles in single and air-water two-phase flow. Tube bundles of normal and rotated triangular and square arrays were formed with pitch to diameter ratios varying from 1.32 to 1.47. The flexible tubes were cantilevered. They observed that the excitation in two-phase flow was larger than that in single phase flow, but the onset of instability was less clear in two-phase flow. These studies recommended the values ranging from 4 to 5 for the fluidelastic instability constant in Connors' criterion, but the damping ratios obtained from different flow conditions were applied in implementing the criterion. Pettigrew et al. observed that the critical flow velocity for the all flexible tube bundles was lower than that for a single flexible tube surrounded by rigid tubes in two-phase flow but the critical flow velocities for two cases were almost similar in single phase flow. Axisa et al. (1985) and Gay et al. (1988) measured damping and fluidelastic instability in steam-water and freon-water two-phase flow. They observed that tube behavior at onset of fluidelastic instability was similar to that noted for air-water two-phase flows.

Marn and Catton (1992) numerically studied the fluidelastic instability of a flexible tube in a rigid tube array subjected to single phase flow. From their analysis they identified dynamic instability and divergence. The dynamic instability occurred at a flow velocity smaller than that for divergence. Yetisir and Weaver (1992) have proposed a theoretical model for fluidelastic instability of a single flexible tube in an array of rigid tubes and of an all flexible tube bundle. They showed that for small values of mass-damping parameter, a single tube in an array of rigid tubes is not an unreasonable model. However, for values of mass-damping parameter greater than 200, the interaction between neighboring tubes becomes important and one must use an all flexible tube bundle to model fluidelastic instability.

1.2 Mechanisms of Fluidelastic Instability. Two mechanisms of fluidelastic instability have generally been proposed in the literature: the velocity mechanism and the displacement mechanism. The former assumes that the dominant fluid force is proportional to the velocity of the tubes (fluid-damping force), while the latter assumes that the dominant fluid force

* This work received support from United States Department of Energy under Contract No. DE-FG07-89ER-12902.

Contributed by the Fluids Engineering Division for publication in the JOURNAL OF FLUIDS ENGINEERING. Manuscript received by the Fluids Engineering Division June 7, 1994; revised manuscript received February 10, 1995. Associate Technical Editor: Jong H. Kim.

is proportional to the displacements of the tubes (fluid-stiffness force). In the velocity mechanism, the critical condition for onset of instability is believed to occur when overall damping of the system changes from being positive to negative. In the displacement mechanism, with increase in velocity, the fluid-stiffness force can reduce the modal damping and instability occurs when damping changes from being positive to negative. Depending on the system conditions, either or both of the mechanisms can be present. The velocity mechanism is dominant for the systems with small mass-damping parameter, while the displacement mechanism is dominant for the systems with large mass-damping parameter (Chen, 1987).

Both of these mechanisms assume that the fluidelastic instability occurs when the total damping ratio becomes negative. Only few experimental investigations have documented the decrease of total damping as the flow rate approaches the critical flow rate. The study of Weaver and El-Kashlan (1981) found that total damping approached zero at the onset of instability in single phase flow of air, while other studies (Pettigrew et al., 1988a; Heilker and Vincent, 1981) did not observe such results in their experiments conducted in two-phase flow. None of these studies provide a clear insight regarding the variation of total damping near the onset of instability.

Another commonly accepted explanation of the cause of the fluidelastic instability is that the instability occurs when the energy input by the fluid force exceeds the energy expended in damping. This explanation implies that the total damping ratio does not necessarily have to be negative to cause the instability. As long as the energy input exceeds the energy loss, the instability will occur.

1.3 Damping Ratio. Carlucci and Brown (1983), Pettigrew et al. (1988b), and Hara (1988) measured the damping ratio of a single cylinder or a cylinder in an array in air-water two-phase flow. The flow was either axial flow or crossflow. It was found that the two-phase damping ratio increases with increasing void fraction up to a void fraction of about 0.3, reaches a maximum value at void fractions between 0.3 to 0.6, and decreases as the void fraction increases beyond 0.6.

Blevins (1990) developed a model for the fluid damping ratio of a cylinder in a crossflow. He assumed the tube to vibrate in a harmonic motion. The vibration amplitude was assumed to be small and the tube was assumed to oscillate at its natural frequency. When the structural velocity ($\dot{x}$) was small relative to the mean fluid velocity V, an expression for the fluid damping ratio, ζ_{fluid}, in a cross flow was obtained as

$$\zeta_{\text{fluid}} = \frac{1}{4\pi} \frac{V}{f_n D} \frac{\rho D^2}{m} C_D \qquad (2)$$

where C_D is the drag coefficient for the tube in crossflow.

1.4 Objective of the Present Study. Mass, damping, spring constant, and fluid force are four major components of interest in the study of tube vibrations induced by a fluid flowing across a tube bundle. In order to understand the fluidelastic instability of tubes which are subjected to two-phase crossflow, the investigation and understanding of these four components is necessary. These four components are influenced by several other parameters; such as tube diameter, tube mass, pitch to diameter ratio, natural frequency, flow rate, void fraction, types of tube array, methods in which tubes are supported, and whether the tubes surrounding the test tube are supported rigidly or flexibly, etc. Most of the previous studies concentrated on as to how these parameters affected the critical flow conditions for the onset of fluidelastic instability and on obtaining the instability map. However, the past research did not focus on the manner in which these parameters affected the four components of tube vibrational behavior when fluidelastic instability occurred. As such the mechanism of instability is not clearly explained yet. The objective of the present study is to develop an understanding of the mechanism of fluidelastic instability in tubes subjected to single and two-phase crossflow.

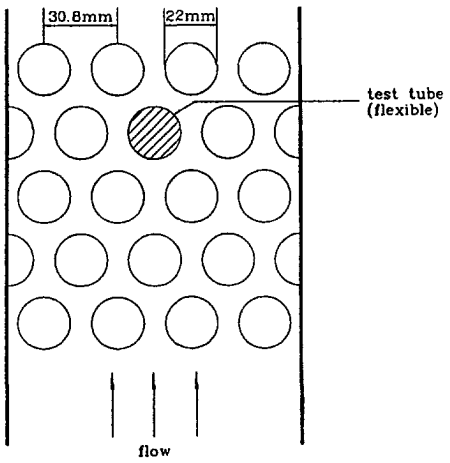

Fig. 1 A normal triangular tube array

2 Experimental Apparatus and Procedure

2.1 The Tube Bundle and Test Tube. The air-water two-phase flow loop which had been used in the study of Joo and Dhir (1994) was used in this study. The flow was bubbly in all cases, and void fractions were nearly uniform across the test section upstream of the tube bundle except for very low liquid flow velocity. In the test section, acrylic tubes are installed horizontally to form a normal triangular array (Fig. 1). The tubes, 2.2 cm in diameter and 20 cm in length, are arranged with pitch to diameter ratio of 1.4. All tubes are rigidly supported at the test section wall except the test tube.

The hollow acrylic test tube, 27 cm in length, is positioned at the center of the fourth row, and extends through holes in the test section wall. The tube is flexibly supported with two cantilever beams which are held outside of the test section wall. The holes in the test section wall are large enough to give the test tube sufficient room to vibrate. Easily removable caps cover the cantilever beams and holes to prevent leaking. The test tube can vibrate in only one direction—normal to the cantilever beams. The cantilever beams are installed horizontally when drag direction vibrations are measured. When lift direction vibrations are measured, the cantilever beams are installed vertically.

The cantilever beams which support the test tube are made from spring steel plates. Spring constants can be varied by using spring steel plates of different thicknesses. The beams are 7 mm in width and 53.5 mm in length. Steel plates of three different thicknesses (t) were used: 0.56 mm, 0.71 mm and 0.89 mm. The natural frequencies in water of these tube-cantilever beam systems are 8.5 Hz, 12.2 Hz, and 17.4 Hz, respectively. In a few experiments, a solid aluminum rod was inserted in the hollow acrylic test tube in order to change the tube mass. The tube mass was changed from 0.062 kg to 0.207 kg. When the aluminum rod inserted tube is supported with 0.71 mm thickness cantilever beams, the natural frequency in water is 10.0 Hz. Uncertainty in the measured frequency is expected to be less than ± 3 percent.

In order to study the effect of pitch to diameter ratio, tubes of 2.37 cm in diameter were used. By arranging the tubes with the same pitch as before (3.08 cm), pitch to diameter ratio of 1.3 was obtained. When the solid acrylic test cylinder, 0.126 kg in mass, is supported with 0.71 mm thickness cantilever beams, the natural frequency in water is 10.0 Hz.

Strain gages were mounted on the top and bottom sides of each cantilever beam. They were installed 6 mm away from the

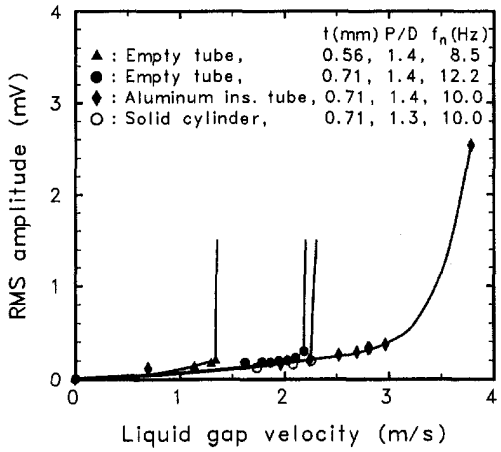

Fig. 2 RMS amplitude change with liquid gap velocity in single phase flow

beam supporting plates. The strain gage out put was read from the strain gage input module of the data acquisition system. Vibration responses were calculated with a personal computer which is connected to the data acquisition system.

2.2 Experimental Procedure. In the two-phase flow experiments, the water flow rate was set constant at some flow rate lower than the single phase instability value, and air flow rate was gradually increased. The vibration response was measured with increasing air flow rate until instability occurred. Time averaged mean value, RMS amplitude and vibration response spectrum were obtained from the strain gage voltage-time data. The strain gages were calibrated before and after measurements for a particular set of tube-cantilever beam system.

Drag coefficients were measured at the normal position of the tube in the array and when the tube was displaced 3 mm and 4 mm from its mean position. Drag coefficients at each position were measured by noting the static pressure distribution at the wall. Details of the procedure are described in the study of Joo and Dhir (1994). In these experiments, the liquid gap Reynolds number was varied from 32,900 to 61,600.

Pressure distributions around the tubes were not measured when the tube was flexibly supported because the displacement of tube in an array was found to affect the measured drag. However, during the experiments for the determination of fluidelastic instability, average drag forces could be obtained from the mean value of strain gage signal.

3 Results

3.1 Single Phase Flow Instability During Tube Vibration in the Drag Direction. The responses of the test tube during tube vibration in the drag direction were measured. Figure 2 shows for single phase flow of water the RMS amplitudes of the empty test tubes supported with 0.56 mm and 0.71 mm thickness cantilever beams and of an aluminum rod inserted test tube installed with 0.71 mm thickness cantilever beams. The tubes were placed in an array of pitch to diameter ratio of 1.4. Figure 2 also shows the RMS amplitude of test tube which was installed with 0.71 mm thickness cantilever beams in an array of pitch to diameter ratio of 1.3. For all of the tubes, the RMS amplitude increases with liquid gap velocity. For the empty tube supported with 0.56 mm thickness cantilever beams in an array of pitch to diameter ratio of 1.4, the RMS amplitude begins to increase rapidly at a liquid gap velocity of 1.3 m/s. This is the onset of instability for single phase flow. A similar behavior at onset of instability was observed for the other cases. For the array with pitch to diameter ratio of 1.4, the critical gap

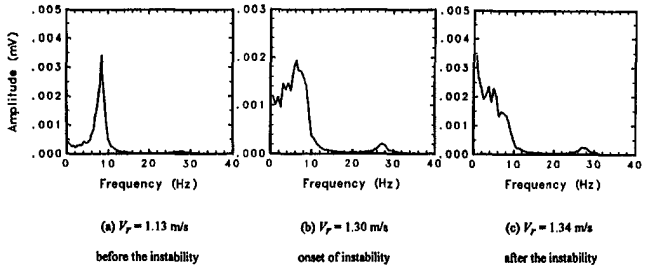

Fig. 3 Vibration response spectrum in single phase flow (empty tube mounted on 0.56 mm thickness cantilever beams)

velocity is seen to increase as the cantilever beam thickness increases and as the tube mass increases. For the same natural frequency of the tube system, the critical gap velocity is seen to increase in Fig. 2 as the pitch to diameter ratio increases. The effect of stiffness of the system, mass, and the pitch to diameter ratio will be discussed further in Section 4.3. The time averaged mean displacements were observed to increase smoothly with liquid gap velocity. However, the slope of the curve through the data for mean displacement was found to increase rapidly just prior to the onset of instability.

The vibration response spectra near the onset of instability are shown in Fig. 3. The spectra are for an empty test tube held with 0.56 mm thickness cantilever beams in an array with pitch to diameter ratio of 1.4. Figure 3(*a*) shows the response spectrum at a liquid gap velocity of 1.13 m/s. This velocity is smaller than the critical gap velocity for the onset of fluidelastic instability. The response spectrum shows a narrow band unique peak at a frequency of 8.1 Hz which is close to the natural frequency of the system. Figure 3(*b*) is a vibration response spectrum at a liquid gap velocity of 1.3 m/s—the critical velocity for the instability. The response spectrum shows a much broad band peak. The first dominant frequency decreases to 6.0 Hz, which is about 75 percent of the natural frequency. The liquid gap velocity corresponding to Fig. 3(*c*) is 3 percent larger than that of Fig. 3(*b*). With this small increase of liquid gap velocity, the response spectrum shows a much different shape than that prior to onset of instability. It has the highest amplitude at a frequency very close to 0 Hz. At this flow velocity the system appeared to degenerate into a static instability mode.

The first dominant frequencies are plotted as a function of liquid gap velocity in Fig. 4. The first dominant frequency decreases slowly with increase of liquid gap velocity. However, just prior to the onset of instability, it shows a rapid decrease with further increase of liquid gap velocity.

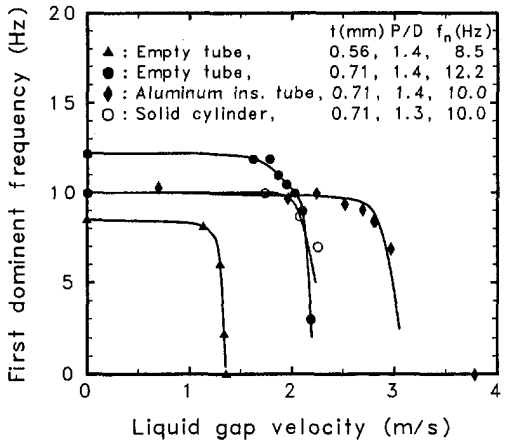

Fig. 4 The first dominant frequency change with liquid gap velocity in single phase flow

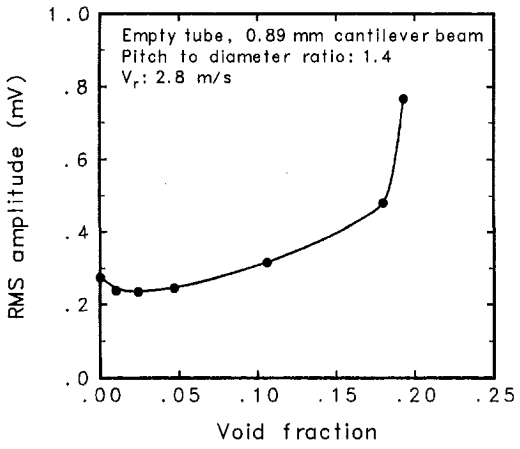

Fig. 5 RMS amplitude change with void fraction in two-phase flow

3.2 Two-Phase Flow Instability During Tube Vibration in the Drag Direction. The vibration response of the test tube in air-water two-phase mixture was measured at superficial liquid gap velocities lower than the critical liquid gap velocity for the instability under single phase flow conditions. Figure 5 is a typical graph of RMS amplitude as a function of the void fraction under two-phase flow conditions. The data plotted in Fig. 5 were obtained when an empty test tube was installed with 0.89 mm thick cantilever beams in an array with pitch to diameter ratio of 1.4. The superficial liquid gap velocity was fixed at 2.8 m/s and tube response was measured as the superficial gas gap velocity or void fraction was increased. The RMS amplitude is seen to increase slowly with the increase of the superficial gas gap velocity or void fraction. However, at a void fraction of 0.18, RMS amplitude increases rapidly with further increase of void fraction. This is the condition for the onset of instability under two-phase flow conditions. In comparison to the single phase case (Fig. 2), the threshold point for the onset of instability is not pronounced in two-phase flow. With decrease in superficial liquid gap velocity, the instability occurred at higher void fractions. However, the threshold point for the onset of instability became even less pronounced for smaller superficial liquid gap velocities. When the liquid gap velocities were smaller than 1.9 m/s, it was hard to determine the threshold point for the onset of instability. A rapid decrease of the first dominant frequency just prior to the onset of instability as observed in single phase flow was also observed in two-phase flow. Onset of instability in two-phase flow is a function of superficial liquid gap velocity and void fraction. As the void fraction increases, instability occurs at lower superficial liquid gap velocities.

The tube responses when cantilever beams were installed vertically to allow the tube to vibrate only in the lift direction were also measured. The sudden increase of RMS amplitude or the sudden decrease of the first dominant frequency as noted in the drag direction was not observed.

3.3 Damping Ratio and Drag Coefficient. For two-phase mixture flow, the damping ratios were obtained from the response spectrum data and from Eq. (2). The drag coefficient in Eq. (2) was calculated from the drag force data which was deduced from the mean value of strain gage signal. The damping ratios obtained in a flowing two-phase mixture were much larger than those obtained in a nearly stagnant two-phase mixture.

The damping ratios for the void fractions close to the critical void fraction for the onset of instability could not be measured because the response spectra were not clear as seen in Fig. 3(b). However, it was observed that the damping ratio at the onset of instability is not zero. It should be stressed that this observation is restricted to the single degree of freedom that was available to the tube in the present experiments. Damping ratio of zero has been used in several previous studies as a criterion for the onset of fluidelastic instability.

An empirical correlation which best fits all of the measured damping ratios in stable flow conditions has been obtained as

$$\zeta_{\text{fluid}} = \zeta_{\text{stillwater}} + \frac{1}{140}\left(\frac{V}{f_n D}\right)\left(\frac{1}{1-\alpha}\right)^3 \quad \text{when} \quad \frac{V}{f_n D} < 13 \quad \text{and} \quad \alpha < 0.3 \quad (3)$$

where $\zeta_{\text{stillwater}}$ are the damping ratios in still water. Ninety percents of measured data were found to be within ± 18 percent of the values calculated from this correlation. The damping ratio predicted from this empirical correlation is similar to that obtained by using Eq. (2).

The pressure distributions around the perimeter of a tube located at the normal position in the array and at positions 3 mm and 4 mm higher than the normal position were measured. The pressure distributions on the upstream portion of the tube were found to be almost the same for all displaced positions. However, pressure on the downstream portion of tubes displaced 3 mm and 4 mm in the vertical direction was smaller than that on tube placed at the normal position. As the test tube moves up, the gap between test tube and upper tubes becomes smaller and flow velocity over the downstream portion of the tube increases. As the velocity increases, the pressure becomes smaller.

The decrease of pressure in the downstream portion manifests in the form of an increase in the drag force on tubes displaced in the vertical or along the flow direction. In Fig. 6, the drag coefficients on a tube in an array are plotted as a function of tube displacement. The drag coefficient increases as the tube displacement increases. Moreover, the rate of increase of drag coefficient with tube displacement ($\Delta C_D/\Delta x$) is seen to increase rapidly when the displacement exceeds 3 mm. This trend is very distinct in single phase flow, but weakens a little as the void fraction increases.

The gradient of drag coefficient with tube displacement (dC_D/dx) is needed for the analysis of the fluidelastic instability mechanism (Section 4.2). In order to obtain dC_D/dx, the drag coefficient was assumed to have the following form,

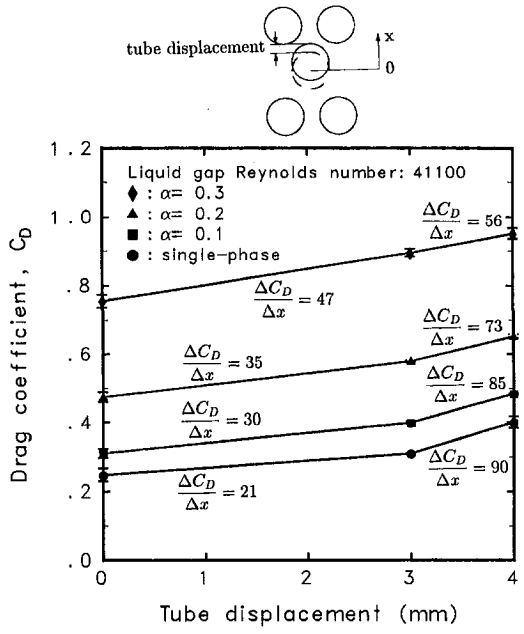

Fig. 6 Change in drag coefficient with tube displacement

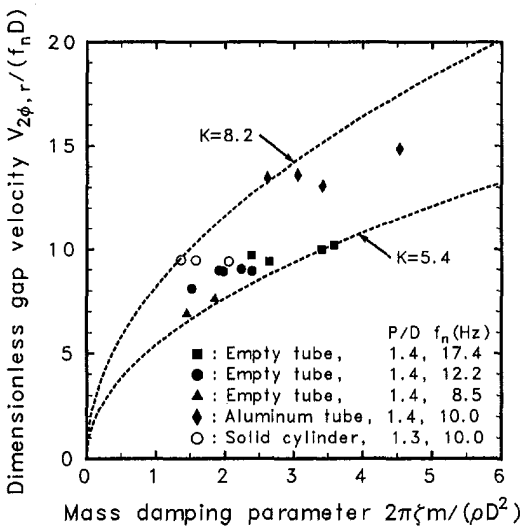

Fig. 7 Onset of instability in two-phase flow

$$C_D(x) = C_D(0mm) + C_1 x^{C_2} \tag{4}$$

where C_1 and C_2 are empirical constants. These constants were determined by substituting the drag coefficients for the tube displaced 3 mm and 4 mm from its normal position. The uncertainty in the drag coefficient itself is calculated to be less than ±10 percent. However, when the gradient of drag coefficient is calculated, the uncertainty is increased. For single phase flow, the uncertainty of the gradient of drag coefficient is calculated to be about ±45 percent.

4 Discussion

4.1 Single and Two-Phase Flow Instability. In the past the flow conditions at onset of instability have been written in terms of two dimensionless groups: $V_r/(f_nD)$ and $2\pi\zeta m/(\rho D^2)$. V_r is the reference gap flow velocity, which is defined as

$$V_r = \frac{P}{P-D} V_l \tag{5}$$

where V_l is a freestream liquid velocity and P is the tube pitch. The mass per unit length, m, includes tube mass and added mass. Added mass was calculated from the correlations suggested by Pettigrew et al. (1988b). Single phase instability data for drag direction vibrations of present study were generally found to lie near the upper band of the data reported in the literature. The possible reason for this will be discussed in Section 4.4.

For correlation of two-phase flow data, the two-phase flow density, $\rho_{2\phi}$, is defined as

$$\rho_{2\phi} = \rho_g \alpha + \rho_l (1-\alpha) \tag{6}$$

where ρ_g and ρ_l are the densities of air and water. For air-water mixture, two-phase mean gap velocity, $V_{2\phi,r}$, is defined as

$$V_{2\phi,r} = \frac{P}{P-D} \times \frac{Q_g + Q_l}{A} \tag{7}$$

where A is the cross-sectional area. In Fig. 7, the flow conditions at onset of instability are plotted for two-phase flow. The plotted data are correlated with Connors' equation when empirical constant K is chosen to have values between 5.4–8.2. This suggests that Connors' criterion combines in an approximate sense all of the parameters that influence the instability.

4.2 Mechanism of Fluidelastic Instability. The tube-cantilever beam system of present study can be simplified as a mass-damper-spring system. The equation of motion can be written as

$$m\ddot{x} + c_s\dot{x} + k_s x = \Sigma F = F_D + F_{\text{turb}} \tag{8}$$

where m is the total mass including added mass, c_s and k_s are the structural damping coefficient and the structural spring constant, x, $\dot{x}$ and $\ddot{x}$ are tube displacement, tube velocity and tube acceleration, respectively. F is the fluid force acting on the tube, which has the component of the drag force (F_D) and the forces caused by turbulence and vortex shedding (F_{turb}). The fluid force caused by vortex shedding is expected to be small in two-phase flow. Drag force can be written as

$$F_D = \tfrac{1}{2}\rho_l V_{\text{rel}}^2 C_D D \tag{9}$$

where V_{rel} is relative flow velocity, and

$$V_{\text{rel}} = V_r - \dot{x} \tag{10}$$

and

$$C_D = C_{D_0} + \frac{dC_D}{dx} x \tag{11}$$

where C_{D_0} is the drag coefficient when the tube is at its normal position in the absence of flow. Since x is measured from zero, dx has been replaced by x in Eq. (11). The term dC_D/dx exists only for a tube in an array and it does not exist for a single tube. Also it should be noted that dC_D/dx represents the total change in C_D and includes the contributions of all the independent parameters. After substituting for C_D and V_{rel}, Eq. (9) becomes

$$F_D = \frac{1}{2}\rho V^2 C_{D_0} D - \rho V C_{D_0} D\dot{x} + \frac{1}{2}\rho C_{D_0} D\dot{x}^2 + \frac{1}{2}\rho V^2 D\frac{dC_D}{dx}x - \rho V D\frac{dC_D}{dx}x\dot{x} + \frac{1}{2}\rho D\frac{dC_D}{dx}x\dot{x}^2 \tag{12}$$

The first term on right-hand side is the static drag force and the second and third terms are damping due to fluid flow. The fourth, the fifth, and the sixth terms are fluid-stiffness force which exists only in a tube array. Among the terms of fluid-stiffness force, the fifth and sixth terms on the right-hand side are negligibly small in comparison to the fourth term and can be deleted. As such, Eq. (8) can be written as

$$m\ddot{x} + \left(c_s + \rho V C_{D_0} D - \frac{1}{2}\rho C_{D_0} D\dot{x}\right)\dot{x} + \left(k_s - \frac{1}{2}\rho V^2 D\frac{dC_D}{dx}\right)x = F_{\text{turb}} + \frac{1}{2}\rho V^2 C_{D_0} D \tag{13}$$

The above equation can be written as

$$m\ddot{x} + c_t\dot{x} + k_e x = \underbrace{F_{\text{turb}}}_{\text{dynamic force}} + \underbrace{\tfrac{1}{2}\rho V^2 C_{D_0} D}_{\text{static force}} \tag{14}$$

In Eq. (14) the total damping coefficient (c_t) is defined as

$$c_t = c_s + \rho V C_{D_0} D - \tfrac{1}{2}\rho C_{D_0} D\dot{x} \tag{15}$$

The structural damping coefficient, c_s, is negligibly small in comparison to the other terms. The second term, $\rho V C_{D_0} D$, is identical with Eq. (2), which showed good agreement with experimental results when the tube vibrated in a stable mode. As the flow rate increases, $\rho V C_{D_0} D$ increases continuously while $\frac{1}{2}\rho C_{D_0} D\dot{x}$ changes in magnitude with change in sign during

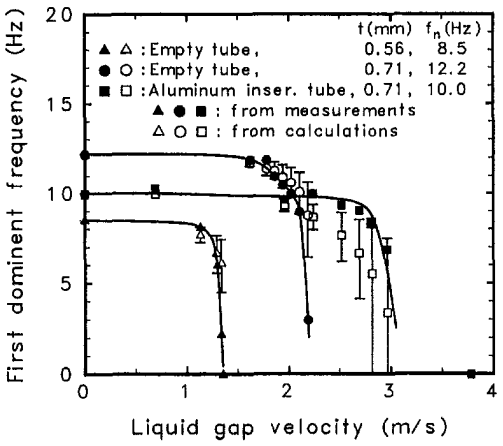

Fig. 8 The first dominant frequencies in single phase flow obtained from the measurements and from the calculations

a cycle. However, the ratio of $\frac{1}{2}\rho C_{D_0} D\dot{x}$ to $\rho V C_{D_0} D$ (i.e., $\dot{x}/2V$) is much less than unity even at the onset of instability. For 2.2 cm diameter empty tube mounted on 0.56 mm thickness cantilever beams subjected to single phase flow, maximum value of $\dot{x}/2V$ is found to be 0.01. Thus in the present experiments the total damping ratio at the onset of instability cannot be zero, which has been used in the past as a criterion for the fluidelastic instability by many investigators.

The effective spring constant (k_e) in Eq. (14) is defined as

$$k_e = k_s - \frac{1}{2}\rho V^2 D \frac{dC_D}{dx} \qquad (16)$$

The fluid-stiffness force ($\frac{1}{2}\rho V^2 D(dC_D/dx)x$) increases as the flow velocity increases. This causes the effective spring constant to decrease. The effective spring constant was calculated by using the data plotted in Fig. 6. In Fig. 8, the first dominant frequencies for single phase flow predicted from the calculated effective spring constant and those obtained from the response of the strain gages are plotted. Closed symbols represent the first dominant frequencies obtained from strain gage signals whereas the open symbols represent the frequencies calculated by using the spring constant given by Eq. (16). For the three cases involving different stiffnesses and masses, the calculated values show a trend very similar to that shown by the data i.e., a rapid decrease of first dominant frequency on approach to onset of fluidelastic instability. The calculated values of the dominant frequency for the tube in which aluminum rod was inserted are found to be somewhat lower than the measured values. However, considering the high uncertainty (±50 percent) in k_e which mainly results from uncertainty in the evaluation of dC_D/dx, the overall agreement is reasonable.

For the two-phase flow case, the effective spring constant predicted from Eq. (16) and deduced from the measured dominant frequency were also found to be in good agreement. The effective spring constant decreased as the void fraction increased. In comparison to the case of single phase flow, the decrease of the effective spring constant prior to the onset of instability was more gradual.

The amplitude of vibrations is inversely proportional to the spring constant. Therefore, rapid decrease in spring constant implies a corresponding rapid increase in the displacement of the tube prior to onset of fluidelastic instability. Increased displacement further reduces the effective spring constant. Thus a feedback exists between displacement and the spring constant.

In several experimental studies reported in the literature, damping was observed to decrease on approach to the instability. With increase in flow velocity, the magnitude of fluid-stiffness force also increases. The instability can occur when, with the increase in flow velocity, either fluid-stiffness increases more rapidly or damping decreases more rapidly. In the present work fluid-stiffness force was found to increase more rapidly.

4.3 Mean Displacement of the Tubes at Onset of Instability. It is noted from Fig. 9 that the mean displacement at onset of instability is generally higher for thicker cantilever beams. The mean displacement is independent of tube mass but is smaller for a tube with reduced pitch to diameter ratio. These observations can be explained with the displacement mechanism described earlier. The spring constant of a thick cantilever beam is larger than that of a thin cantilever beam. In order to decrease the effective spring constant to a given value, a larger flow rate (V) and a larger dC_D/dx are needed for a thicker cantilever beam. A larger dC_D/dx is obtained when the displacement of the tube from its mean position is large.

For the aluminum rod inserted tube (tube with larger mass), the center of the tube mass in still water is lower than that of the empty tube. In order to displace this tube the same distance as an empty tube, a large drag force is needed. Therefore, as seen in Fig. 2, the critical gap velocity for the aluminum inserted tube is larger than that for the empty tube when both tubes are supported with cantilever beams of the same thickness. However, at the onset of instability the displacement of the heavier tube from the normal position (of an empty tube) in the array will be the same as that of the empty tube. This is confirmed by the fact that in Fig. 9 the observed displacement of the heavier tube at the onset of instability is about the same as that of the empty tube. Since pitch to diameter ratio of an array determines the gap between two neighboring tubes, the onset of instability can be identified to occur when the gap between neighboring tubes reaches a critical value. Larger the pitch to diameter ratio of an array, larger will be the required displacement to attain a critical value for the gap. This in turn will mean that fluidelastic instability will occur at higher flow velocities or void fractions. On the other hand, for instability to occur in a closely packed array, smaller displacement or lower velocities will be required. This is what is seen in Fig. 9.

In two-phase flow the critical superficial liquid velocity in the gap is smaller than that for single phase flow. The key reason for this is that drag coefficient generally increases with void fraction. Is should also be noted that for displacement of 3 to 4 mm from the mean position, dC_D/dx for two-phase flow is smaller than that for single phase flow. In order to decrease the effective spring constant the same amount as with single phase flow, a larger dC_D/dx is needed in two-phase flow. As noted earlier dC_D/dx increases with displacement of the tube

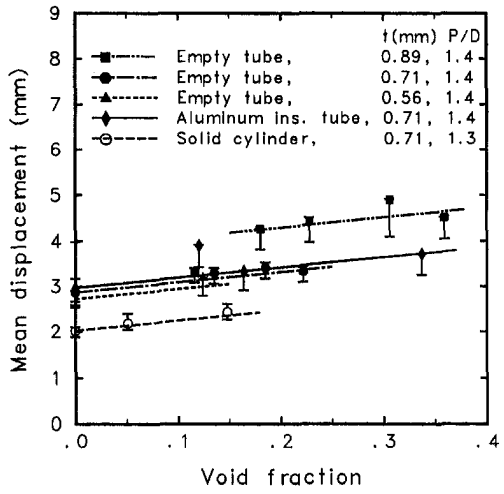

Fig. 9 Mean displacements at onset of instability for different tube-cantilever beam systems

from mean position. Also, under two-phase flow conditions dC_D/dx increases slowly in comparison to single phase flow. As a result the threshold point for instability in two-phase flow is less pronounced than that in single phase flow.

No fluidelastic instability was observed when the tube was allowed to vibrate in the lift direction. When the tube vibrates in the lift direction, the mean displacement is always zero. The amplitude of vibrations in the lift direction was found to be much smaller than that observed in the drag direction. It should be noted that the observations made in this work are specific to the experimental configuration used in the study and for the range of parameters that were investigated.

4.4 Fluidelastic Instability of a Tube With Movement in Two Directions and of an All Flexible Tube Bundle. It was seen in Section 4.1 that the critical flow velocities measured in the present study were generally higher than those obtained in the studies in which tubes were allowed to vibrate in both the lift and drag directions. When the test tube can move in two directions the fluidelastic instability occurs at a lower flow rate than when the tube is allowed to vibrate in one direction. For a triangular array this can be explained by noting that for a given flow rate the resultant displacement when the tube vibrates in both directions is higher than that when the tube is free to vibrate only in one direction. Thus to attain a critical gap thickness between tubes in the adjacent rows, a smaller flow velocity is needed when the tube can vibrate in both the lift and drag directions.

In a heat exchanger, all tubes are flexible and free to vibrate in two directions. When a flexible tube bundle is subjected to crossflow, the vibration center of each tube (the mean displacement of a tube in the present study) will move the same amount in the downstream direction. As the flow rate increases, the vibration centers will move further, but the distance between the vibration centers of each tube will be the same. It has been reported that the tubes generally vibrate in oval orbits somewhat synchronized with neighboring tubes (Blevins, 1990). As the flow rate increases, the amplitude (or the diameter of an oval) will increase, and the minimum distance between two neighboring tubes in one cycle will become smaller. When the two neighboring tubes approach closer than the critical gap for the fluidelastic instability, the tubes will become unstable.

5 Conclusions

From the experiments conducted in this work with a single flexible tube placed in an array of rigid tubes, the following conclusions have been arrived at:

1. The drag coefficient on a tube in an array increases as the tube is displaced in the direction of flow. The drag coefficient increases rapidly when the tube is displaced more than a certain distance (about 3 mm in the present study). This trend is very distinct in single phase flow, but the effect weakens a little as the void fraction increases.
2. The total damping ratio increases with the increase of liquid gap velocity in single phase flow and with the increase of void fraction in two-phase flow. However, the effective spring constant decreases rapidly with the increase of liquid gap velocity or void fraction just prior to the onset of instability. It is mainly due to the rapid increase of drag force in the displaced position prior to the onset of instability.
3. The fluidelastic instability occurs when the mean displacement of a tube exceeds a certain value and the gap between tubes reaches a critical value. The mean displacements at the onset of instability coincide with the distance beyond which the rapid increase of drag coefficient occurs.
4. The fluidelastic instability is caused by rapid decrease of the effective spring constant because the amplitude of tube vibration is inversely proportional to the effective spring constant.

References

Axisa, F., Villard, B., Gibert, R. J., and Boheas, M. A., 1985, "Vibration of Tube Bundles Subjected to Steam-Water Cross Flow: A Comparative Study of Square and Triangular Pitch Arrays," 8th International Conference on Structural Mechanics in Reactor Technology, Paper B1/2, pp. 7–12, Aug., Brussels, Belgium.

Blevins, R. D., 1990, *Flow-Induced Vibration,* 2nd ed. Van Nostrand Reinhold, New York.

Carlucci, L. N., and Brown, J. D., 1983, "Experimental Studies of Damping and Hydrodynamic Mass of a Cylinder in Confined Two-Phase Flow," ASME *Journal of Vibration, Acoustics, Stress, and Reliability in Design,* Vol. 105, pp. 83–89.

Chen, S. S., 1987, *Flow-Induced Vibration of Circular Cylindrical Structures,* Hemisphere Publishing Corporation, Washington.

Connors, H. J., 1970, "Fluidelastic Vibration of Tube Arrays Excited by Cross Flow," *Symposium on Flow Induced Vibration in Heat Exchangers,* ASME Winter Annual Meeting, D. D. Reiff, ed., Dec., New York, NY, pp. 42–56.

Gay, N., Decembre, P., and Launay, J., 1988, "Comparison of Air-Water to Water-Freon Two Phase Cross Flow Effects on the Vibratory Behaviour of a Tube Bundle," *International Symposium on Flow-Induced Vibration and Noise,* ASME Winter Annual Meeting, Vol. 3, M. P. Paidoussis, S. S. Chen, and M. D. Bernstein, eds., Nov., Chicago, IL, pp. 139–158.

Hara, F., 1988, "Two-Phase Fluid Damping in a Vibrating Circular Structure," PVP-Vol. 133, *Damping-1988,* ASME Pressure Vessel and Piping Conference, H. Hara, P. Y. Chen, S. S. Chen, and A. G. Ware, eds., June, Pittsburgh, PA, pp. 1–8.

Heilker, W. J., and Vincent, R. Q., 1981, "Vibration in Nuclear Heat Exchangers Due to Liquid and Two-Phase Flow," ASME *Journal of Engineering for Power,* Vol. 103, pp. 358–366.

Joo, Y., and Dhir, V. K., 1994, "An Experimental Study of Drag on a Single Tube and on a Tube in an Array Under Two-Phase Cross Flow," *International Journal of Multiphase Flow,* Vol. 20, pp. 1009–1019.

Marn, J., and Catton, I., 1992, "On Stability Analysis of a Flexible Cylinder in an Array of Rigid Cylinders," ASME JOURNAL OF FLUIDS ENGINEERING, Vol. 114, pp. 12–19.

Pettigrew, M. J., Tromp, J. H., Taylor, C. E., and Kim, B. S., 1988a, "Vibration of Tube Bundles in Two-Phase Cross-Flow: Part 2-Fluidelastic Instability," *International Symposium on Flow-Induced Vibration and Noise,* ASME Winter Annual Meeting, Vol. 3, M. P. Paidoussis, S. S. Chen, and M. D. Bernstein, eds., Nov., Chicago, IL, pp. 159–179.

Pettigrew, M. J., Taylor, C. E., and Kim, B. S., 1988b, "Vibration of Tube Bundles in Two-Phase Cross-Flow: Part 1-Hydrodynamic Mass and Damping," *International Symposium on Flow-Induced Vibration and Noise,* ASME Winter Annual Meeting, Vol. 2, M. P. Paidoussis, D. A. Steininger, and M. W. Wambsganss, eds., Nov., Chicago, IL, pp. 79–103.

Remy, F. N., 1982, "Flow Induced Vibration of Tube Bundles in Two-Phase Cross Flow," Paper 1.9, 3rd International Conference on Vibration in Nuclear Plants, Vol. 1, Paper 1.9, May, Keswick, U.K., pp. 135–160.

Weaver, D. S., and El-Kashlan, M., 1981, "The Effect of Damping and Mass Ratio on the Stability of Tube Bank," *Journal of Sound and Vibration,* Vol. 76, pp. 283–294.

Yetisir, M., and Weaver, D. S., 1992, "A Theoretical Study of Fluidelastic Instability in a Flexible Array of Tubes," PVP-Vol. 242, *International Symposium on Flow-Induced Vibration and Noise,* ASME Winter Annual Meeting, Vol. 2, M. P. Paidoussis, S. S. Chen, and D. A. Steininger, eds., Nov., Anaheim, CA, pp. 69–87.

P. G. Hicks[1]
Thermal Sciences and Propulsion Center,
School of Mechanical Engineering,
Purdue University,
West Lafayette, IN 47907-1003

D. W. Senser
Coatings Application Laboratory,
Department of Mechanical Engineering,
University of Wyoming,
Laramie, WY
(deceased)

Simulation of Paint Transfer in an Air Spray Process

A methodology for simulating drop transport and deposition in air-spray, paint-application processes is presented. Simulation of the complex physical phenomena involved is made possible through a number of key assumptions based on measurements of typical air paint sprays. The significant advance is the inclusion of the direct effects of turbulent air velocity fluctuations on the trajectories of paint drops via a stochastic separated flow approach. The model accurately predicts the mean air velocity field, paint transfer efficiency, and drop transfer efficiency. Owing to increased inertia, the mechanisms controlling drop transport shift with increasing drop size.

Introduction

The desires to minimize hydrocarbon solvent emissions, improve appearance, and reduce coating costs are stimulating considerable interest in understanding and improving air spray painting. While significant advances in paint formulation, such as high solids and water borne systems (Bentley, 1987), and applicator technologies, such as high volume low pressure (Bunnell, 1988) and super-critical carbon dioxide (Schrantz, 1989), have been made, it is becoming increasingly clear that significant advances will require a better understanding of the basic components of spray coating. These include atomization of the bulk liquid into drops, transport of these drops from the applicator to the workpiece (or inadvertently to the surroundings), film build on the workpiece surface, and curing/drying of the paint film. These components and their interactions are complex. In most cases, even a qualitative understanding of how changes in paint formulation, applicator type, operating conditions, or workpiece geometry will affect performance is beyond the current state-of-the art. There is clearly a need for verified models that encompass the physical processes governing spray painting. Recent advances in particle diagnostics (Lefebvre, 1989) and computational methods for dilute two-phase flows (Faeth, 1987) are particularly relevant to paint sprays and can provide significant insight into the painting process (Snyder et al., 1989; Kwok, 1991; Corbeels et al., 1992).

This article presents a methodology for simulating drop transport and deposition within air spray painting processes. The approach is quite general and applicable to other conventional paint spray systems, including airless and rotary, and can be extended to electrostatic systems (McCarthy, 1995). The flow features of conventional air paint sprays are first described. This is followed by descriptions of the simulation methodology and of the statistical quantities used to describe paint transfer. Simulation results are then compared to the measurements of Kwok (1991) in order to verify the methodology and are examined in order to obtain greater insights into the mechanisms that control paint transport.

Flow Features of Air Paint Sprays

Air paint sprayers have been used for many years since they are fast, simple to operate, and capable of providing a fine finish. The structure of an air paint spray near the nozzle is determined by the liquid flow rate, air flow rates, and nozzle geometry. An example of a spray nozzle is illustrated in Fig. 1. The primary features are the central liquid orifice, the annular atomizing air orifice, the secondary atomizing air orifices, the cleaning air orifices, and the opposing shaping air orifices. Paint, emanating from the center orifice at low velocity (approximately 5 m/s), is atomized by the annular flow of high velocity atomizing air. Consistent with the general behavior of all twin-fluid atomizers, drop size decreases with increasing atomizing air flow (Lefebvre, 1989). Depending on the air supply pressure (which can vary from less than 20 kPa [3 psid] to greater than 345 kPa [50 psid]), the atomizing air flow may be either subsonic or transonic.

A number of small air orifices surround the atomizing air port, as illustrated in Fig. 1. The air jets emanating from these cleaning orifices reduce recirculation near the nozzle face and prevent paint buildup on the nozzle.

Shaping air flowing from the opposing orifices in the horns of the air cap dramatically affects the structure of the spray (Hicks, 1995) and is also thought to affect paint atomization. The shaping air jets impinge upon the central flow of paint and atomizing air at a short distance from the nozzle face. The visible effect of a typical flow rate of shaping air is to pinch the spray in one direction (the minor axis) and to spread it out in the other direction (the major axis), creating an oval cross section that expands downstream, see Fig. 2. Oval cross section aspect ratios are generally large, in excess of four. As well as changing the shape of the spray, the addition of typical shaping air flow rates decreases the transverse gradients in drop size and decreases the axial velocity of both the air and paint phases (Goris, 1990; Chan, 1991; Colwell et al., 1993). The impinging jets of shaping air contribute little axial momentum; yet one would expect the high shear rates at impingement to dramatically increase turbulent transport. Turbulent transport is thought to 1) reduce transverse gradients in drop size by increasing turbulent dispersion of the drops and 2) decrease axial air velocities by increasing entrainment of low-velocity ambient air into the spray (Colwell et al., 1993). As the drop-laden air flow approaches the workpiece, it turns and flows around the workpiece. A shear layer develops above the workpiece producing the velocity profile illustrated in Fig. 2. Drops either penetrate this shear layer or are swept along the workpiece and considered overspray.

In order to provide insight into the spray flow structure and to simplify the modeling effort, the flow between the air spray gun and the workpiece is divided into two regions: the near nozzle and flow development region and the workpiece-interaction region, see Fig. 2.

The Near Nozzle and Flow Development Region. The extent of the near nozzle and flow development region (NNFD) region is determined by the nozzle geometry and spray gun

[1] Currently at Fuel Systems Textron, 700 N. Centenial St., Zeeland, MI 49464.

Contributed by the Fluids Engineering Division for publication in the JOURNAL OF FLUIDS ENGINEERING. Manuscript received by the Fluids Engineering Division February 22, 1994; revised manuscript received April 17, 1995. Associate Technical Editor: O. C. Jones.

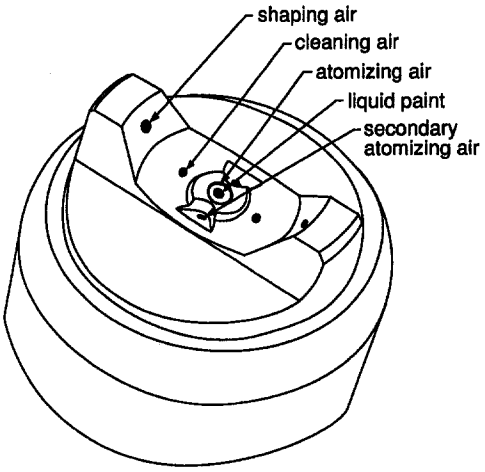

Fig. 1 Schematic of air-spray nozzle

operating conditions. Within this region, the bulk flow of paint is atomized into an ensemble of spherical drops that is described by the atomized drop-size distribution. In addition, the impinging jets of paint, atomizing air, and shaping air form a dense flow. This high-speed dense flow then entrains air from the ambient producing a dilute two-phase flow before passing into the workpiece interaction region.

The Workpiece Interaction Region. Within the workpiece interaction (WI) region, the presence of the workpiece begins to affect the dilute flow of paint drops in air and an ensemble of drops deposit on the workpiece. The size distribution of these drops is termed the deposited drop-size distribution. In addition to the nozzle geometry and spray gun operating conditions that determine the extent of the near nozzle and flow development (NNFD) region, the WI region is influenced by the shape and position of the workpiece. The approaching air flow from the NNFD region, both inside and outside the boundaries of the spray, turns and flows along the workpiece. As discussed later, most of the big drops are able to penetrate the air flow along the workpiece and deposit due to their high axial momentum that is acquired in the NNFD region. In contrast, most of the small drops are unable to penetrate the air flow due to their low axial momentum. The few small drops that deposit, as discussed later, do so as a result of turbulent transport.

The flow in the WI region is considered dilute: the drop density is so small, and the mean free path between drop collisions so large, that the rate of drop collisions is too small to significantly affect the drop-size distribution. In addition, the momentum coupling between the air and paint phases is one way. With one-way momentum coupling, the velocities of individual drops are significantly affected by their aerodynamic drag, yet the cumulative effect of their drag on the air flow is negligible.

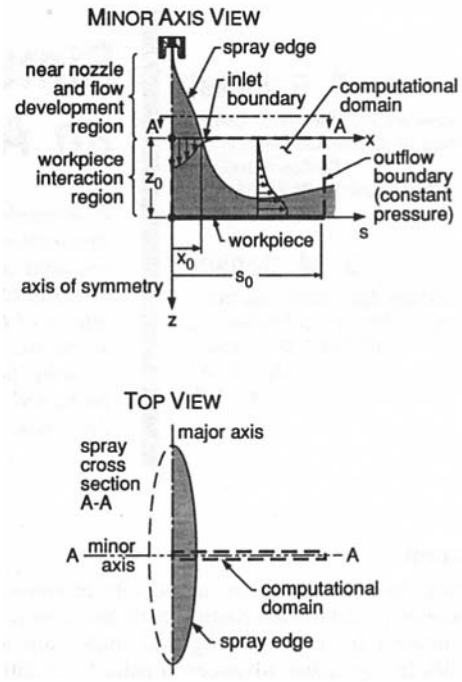

Fig. 2 Key features of the impinging paint spray and corresponding computational domain

Phase Doppler particle analyzer measurements in typical air paint sprays have revealed paint volume concentrations (volume of paint drops per volume of space) of less than 10^{-4} at distances greater than 10 cm downstream of the nozzle (Colwell et al., 1993). These small values indicate that the flow is dilute. In addition, it has been observed that the presence of the workpiece at a typical painting distance of 25 cm begins to influence the air flow at approximately 6 cm above the workpiece. These data suggest that the boundary between the NNFD and WI region for a typical air spray lies between approximately 10 and 20 cm downstream of the spray gun for a painting distance of 25 cm.

Nomenclature

D = drop diameter, μm
D_{min} = minimum drop diameter, μm
D_{max} = maximum drop diameter, μm
k = turbulent kinetic energy, m^2/s^2
$n_{x,D}$ = specific drop flux, a function of inlet position x and drop diameter D, drops/cm-s
$\tilde{n}_{x,D}$ = joint specific drop flux probability density function, a function of inlet position x and drop diameter D, cm^{-1} μm^{-1}
$\tilde{n}_D$ = specific drop flux probability density function of diameter, a function of drop diameter D, μm^{-1}
$\tilde{n}_x$ = specific drop flux probability density function of inlet position, a function of inlet position x, cm^{-1}
$P_{x,D}$ = drop transfer probability—probability that a drop of diameter D that crosses the inlet boundary at position x will deposit on the workpiece, a function of inlet position x and drop diameter D
P_s = scaled spatial transfer probability density function of deposition position s, a function of distance across the workpiece (s) cm^{-1}
q_D = drop volume probability density function of diameter D, a function of diameter D, μm^{-1}
s = position along the workpiece measured from centerline of the spray, cm
s_o = width of the workpiece, cm
T_D = drop transfer efficiency—efficiency at which drops of diameter D that cross the inlet boundary deposit, a function of drop diameter D
TE = transfer efficiency
u = transverse velocity, m/s
w = axial velocity, m/s
x = position along the inlet boundary measured from centerline of the spray, cm
x_o = width of spray at the inlet boundary, cm
z = distance downstream of the applicator, cm
z_o = vertical size of the domain, cm
ϵ = turbulent dissipation rate, m^2/s^3

Simulation Description

The present drop transport simulation considers the individual trajectories of a large number of paint drops through the workpiece interaction (WI) region where the aerodynamic interaction with the workpiece is significant. Owing to the dilute nature of the drop flow in the WI region, the air flow is assumed steady and determined from solution of the continuity, time-averaged Navier Stokes, kinetic energy, and dissipation rate conservation equations. An ensemble of individual drop trajectories is then determined from repeated solution of Newton's second law, considering only the inertia and aerodynamic drag terms to be significant. The gravitational force is neglected because of its small contribution, approximately 0.8% of the aerodynamic drag force. The estimate of the drag force is based on a 30 μm diameter drop traveling at relative speed of 5 m/s. The computations are achieved using KIVA-II (Amsden et al., 1989) a computer code originally developed at Los Alamos National Laboratories for the simulation of an internal combustion engine. The code has been modified to allow for spatially variable inlet boundary conditions.

A stochastic separated flow (Shuen et al., 1984) approach which accounts for direct interaction between the paint drops and the turbulent air flow is incorporated into KIVA-II. At any instance, each drop is assumed to interact with a constant-velocity eddy. The paint drop/eddy interaction continues for either the lifetime of the eddy or the transit time of the drop through the eddy, which ever is shorter. The instantaneous air velocity is determined by randomly selecting a fluctuating eddy velocity from a Gaussian distribution that depends on k and adding it to the local average air velocity. The eddy size and lifetime are determined from relations that depend on both k and ϵ. Owing to the random selection of eddy velocities, each drop exhibits a unique trajectory and a statistical description of the spray is required. Greater detail is given in Amsden et al. (1989). Recently, some questions have arisen concerning the application of the stochastic separated flow model to small drops (MacInnes and Bracco, 1992). However, it was determined in a personal communication (MacInnes, 1992) that the model is applicable to the two-phase flow typical of paint sprays.

Application of the model requires specification of the computational domain and appropriate boundary conditions. Of critical importance are the conditions at the inlet boundary which separates the near nozzle and flow development (NNFD) region from the WI region. These inlet boundary conditions describe the flows of air and paint drops entering the domain and implicitly account for the atomization and flow phenomena that occur in the NNFD region. Consequently, the inlet boundary conditions will vary with gun operating conditions (flow rates and fluid properties) and nozzle geometry.

The two phase flow along the minor axis of the spray is modeled in two dimensions because the minor axis is an axis of symmetry. Results of the drop transport simulation along the minor axis are assumed to be representative of all planes parallel to the minor axis across the spray. Recent results (Hicks, 1995) have indicated this is reasonable and the validity of this assumption is a result of the high aspect ratio of the spray cross sections in the WI region (approximately four).

The simulation is applied to the air spray experiments of Kwok (1991) in which a conventional air spray gun was operated at 25.4 cm above a 30 cm by 61 cm flat workpiece, see Fig. 2. A differential air pressure of 263 kPa (38 psid) and a paint flow rate of 5.57 g/s were used. The corresponding computational domain is also shown in Fig. 2. The domain extends from 14 cm downstream of the applicator to the workpiece surface located at a painting distance of 25.4 cm. The domain extends 15.2 cm along the minor axis of the spray to the edge of the workpiece. Placement of the inlet boundary at 14.0 cm corresponds to an axial station for which measured boundary conditions are available and is consistent with the previous discussion that indicates the boundary between the NNFD and WI regions should be between 10 and 20 cm from the nozzle.

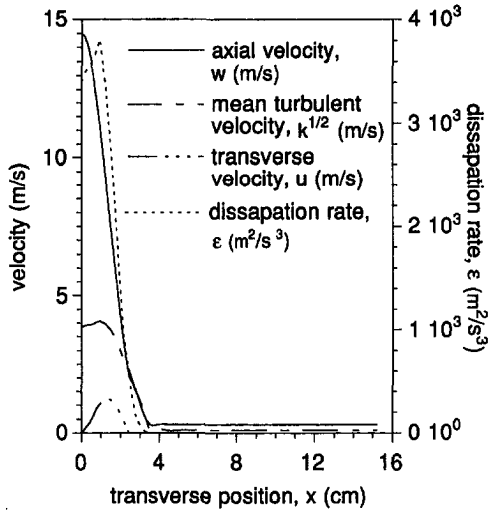

Fig. 3 Inlet air flow boundary conditions

The two-phase flow is solved by dividing the computational domain to 1485 nonuniformly spaced cells, 33 in the axial direction and 45 in the transverse direction. Cells are concentrated in regions of high velocity gradients. Quadrupling the number of cells results in an insignificant change in the velocity flow field of less than 1 percent. The allowed relative error in the implicit mass, momentum and turbulence model equations is set at 10^{-2}. The allowed relative error in the implicit pressure iteration is chosen as 10^{-3}. Decreasing these criterion causes less than a 1 percent change in the gas phase flow solution.

The steady flow solution is obtained by solving the unsteady flow until little change is observed in the gas phase solution. The time step used to perform these calculations is 3×10^{-5} s; i.e., a maximum Courant number of 0.2 (based on the largest velocity and the smallest cell size). This time step is also used to solve for the liquid phase flow and corresponds to 14 response times of the 10 μm diameter drops. Smaller time steps increase computational time significantly and provide an inconsequential change (<0.1 percent) in predicted transfer efficiency.

Air Flow Boundary Conditions. The inlet boundary conditions describing the air flow from the near nozzle and flow development to workpiece interaction (WI) region are summarized in Fig. 3. These are based on the axial and transverse mean velocity measurements reported by Kwok (1991) which were made without paint flow using hot wire and Pitot tube methods. The air flow in the WI region without paint drops is assumed to be a good approximation to the air flow with paint flow since the WI region flow is generally dilute for air sprays (Goris, 1990; Chan, 1991; Colwell et al., 1993).

Unfortunately, measurements of the turbulence model variables, kinetic energy (k) and dissipation rate (ϵ), were not reported. Owing to the similarity of the air flow in the WI region to that of a plane jet, these variables along the inlet boundary are estimated by analogy to plane jet flow. The similarity between the air spray and plane jet flows is illustrated in Fig. 4. As shown, the axial velocity profiles of the air spray at five distances downstream of the nozzle, z (3.2, 7.5, 10.2, 14.0, and 17.2 cm), are in good agreement to plane jet measurements (Bradbury, 1965). The axial velocities have been normalized by the centerline values and the transverse position by the half width, the position at which the axial velocity is equal to half of the centerline value. The k profile is obtained from plane jet measurements (Bradbury, 1965) as recommended by Rodi

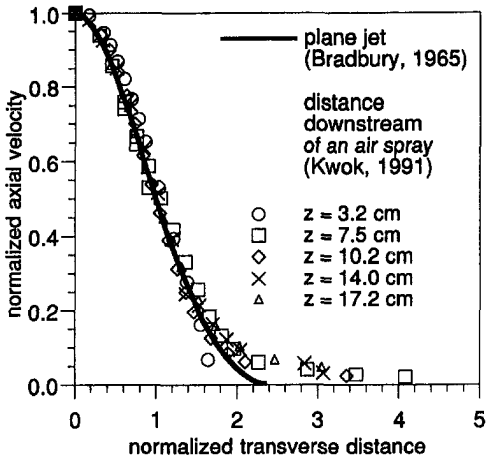

Fig. 4 Similarity of plane jet and air spray transverse profiles of axial velocity at five distances (3.2, 7.5, 10.2, 14.0, and 17.2 cm) downstream of the nozzle

(1975) using the half width of the measured transverse axial velocity profile as the appropriate length scale. Using the same half width, the ϵ profile is obtained from plane jet computations (Rodi and Spalding, 1970).

The remaining air flow boundary conditions are much simpler. Symmetry is applied along the left boundary, outflow (constant pressure, Amsden et al., 1989) along the right boundary and a law-of-the-wall along the workpiece.

Paint Flow Boundary Conditions. The paint flow conditions along the boundary between the near nozzle and flow development region and workpiece interaction (WI) region serve as initial conditions for the drop trajectory calculations. Direct measurements of the paint flow boundary conditions were unavailable; consequently, they were estimated from the measured size distribution of paint drops produced by the gun and a number of simplifying assumptions which are discussed below.

The drop-size distribution of the spray crossing the inlet boundary is assumed to be equal to the overall distribution measured by Kwok (1991). The size distribution measured by Kwok, expressed as a probability density function of diameter on a volume basis, q_D, is shown in Fig. 5. Descriptions of the experimental procedures used to make these measurements are given by Kwok (1991) and Hicks et al. (1993). As shown, the spray spans nearly two orders of magnitude in drop diameter

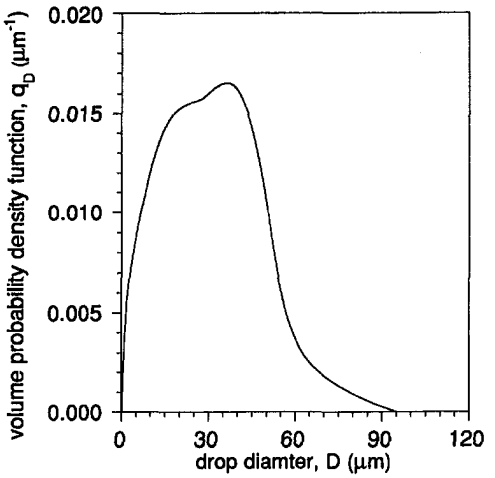

Fig. 5 Measured air spray drop-size distribution

Table 1 Paint flow inlet boundary conditions

Inlet location (cm)	Axial drop velocity (m/s)	Transverse drop velocity (m/s)
0.17	14.2	0.17
0.96	10.4	0.72
1.46	7.25	0.76
2.00	4.73	0.66
2.55	2.84	0.52
Drop diameter (μm)		Number of drops
2, 10		6.5×10^5
20, 30, 40, 50, 60, 70, 90, 120		10^5

from less than 2 μm to approximately 100 μm with a volume median diameter of 38 μm. The drop-size distribution is assumed to be independent of position along the inlet of the domain, based on recent measurements in comparable air sprays (Colwell et al., 1993). They report little variation in drop-size distribution across cross sections of air sprays and attribute this spatial uniformity in air paint sprays to high levels of turbulent mixing.

The number flux profile, or liquid volume flux profile since drop-size distribution is considered independent of position, is assumed proportional to the mean axial air velocity. This assumption is consistent with recent observations (Hicks, 1995). Consequently, the probability density function of position for drops crossing the inlet boundary, $\tilde{n}_x$, is proportional to the axial velocity profile. This results in a paint flux profile that is qualitatively consistent with general observations; the paint flux peaks at the centerline and tapers off rapidly along the minor axis. Consistent with these assumptions, drops are assigned an initial axial velocity that is equal to the mean axial air velocity. This implies no size-velocity correlation. In order to maintain the proper spray angle, drop transverse velocity is chosen as follows: drops at the center are injected with no transverse velocity and drops at the outside of the spray are injected with a transverse velocity such that their trajectory matches the spray angle. Transverse velocities for drops injected between these two extremes are interpolated linearly.

Simulation of paint transport within the WI region is achieved using five discrete positions that span the spray along the inlet boundary and ten discrete drop diameters that span the measured drop size. These are given in Table 1 along with the initial axial and transverse drop velocities for each inlet position. Note that the initial transverse drop velocities are not equal to the transverse air velocities.

At each inlet position, a large number of individual trajectories for each drop diameter are used to resolve the effects of the turbulent air flow on drop transport. These are also reported in Table 1. In order to resolve the stochastic nature of the drop trajectories (for a given drop size and inlet location) the number of drops entering the domain was increased until convergence in the fraction of drops that deposit is achieved. Convergence is achieved when additional drops produce less than a 1 percent change in the fraction of trajectories that intersect the workpiece. Since an inordinate number of stochastic trajectories are required to resolve the motion of the smaller drops, the convergence criterion used for the 2 μm in diameter drops is 5 percent. Relaxing the convergence criterion of the small drops (because of their small contribution to the volume of the spray) has little effect on the predicted transfer efficiency.

The remaining paint flow boundary conditions are as follows. A drop leaving the inlet or right (outflow) boundaries is assumed to never re-enter. While they may re-enter, the likelihood of such a drop depositing on the workpiece surface is small. Drops that impact the surface are assumed to stick and their deposition locations recorded. Paints are viscous fluids and designed to allow limited flow in order to prevent sagging. This

restricts bounce back and splashing. In addition, McCarthy (1991) observed that the rebounding liquid volume flux of even a low viscosity fluid such as water is less than 1 percent at 500 μm above the surface, provided sufficient shaping air is used to obtain a realistic pattern. This suggests that drop bounce or splash is negligible or that it occurs in very small volumes near the surface. In either case, the point of initial impact should be a good estimate of deposition location to a resolution that is small compared to the width of the workpiece.

Statistical Description of Drop Deposition

Calculation of meaningful measures of the painting process, such as transfer efficiency, require the profile of specific paint drop flux along the inlet boundary, $n_{x,D}$, and the scaled spatial transfer probability density function, P_s. The former is a boundary condition that must be specified while the latter results from the drop trajectory simulations.

The specific paint drop flux is the rate per unit length that paint drops of diameter D cross the inlet boundary at position x. This flux profile along the inlet boundary accounts for the effects of the near nozzle and flow development (NNFD) region on the paint flow crossing this boundary. Normalizing the specific paint drop flux results in the joint probability density function of inlet position x and drop diameter D,

$$\tilde{n}_{x,D} = \frac{n_{x,D}}{\int_{D_{\min}}^{D_{\max}} \int_0^{x_o} n_{x,D} dx dD}. \quad (1)$$

Integration of this joint probability density function over finite intervals in drop diameter and inlet position yields the probability that a drop which crosses the inlet boundary will be within the interval in drop diameter and pass through the interval in inlet position.

Consistent with the observation of nearly spatially invariant mean drop size within axial cross sections of the spray (independence of x and D), the joint probability density function reduces to

$$\tilde{n}_{x,D} = \tilde{n}_D \tilde{n}_x, \quad (2)$$

where $\tilde{n}_D$ is the probability density function of diameter for drops crossing the inlet boundary, i.e. the measured size distribution on a number basis, and $\tilde{n}_x$ is the probability density function of position for drops crossing the boundary, i.e. the normalized number flux profile. As noted earlier, $\tilde{n}_x$ is assumed to be proportional to the axial gas phase velocity.

The scaled spatial transfer probability density function, P_s, relates the probability of a drop depositing at a specific location on the workpiece, s, to the drop diameter and position at which the drop crossed the inlet boundary. This function is scaled such that integration over the workpiece yields the probability that a drop of diameter D which enters at position x will deposit on the workpiece, the drop transfer probability ($P_{x,D}$). The function P_s is evaluated from the results of a large number of individual drop trajectory simulations. The individual trajectories must not only resolve the x, D, and s coordinates, but more significantly, they must resolve the stochastic manner in which the drops interact with the turbulent air flow.

The deposition locations for drops of ten discrete diameters and five discrete inlet locations, see Table 1, were determined from the trajectory simulations. These locations were then resolved into 150 equally spaced intervals of s from which values of P_s were estimated. Discrete values of $P_{x,D}$ at the five inlet locations are determined from numerical integration of P_s across the workpiece surface. The continuous function $P_{x,D}$ is evaluated from polynomial interpolation between the discrete values.

The transfer efficiency, TE, defined as the fraction of sprayed paint that deposits on the workpiece, is commonly used to assess spray painting performance and for regulatory purposes. This

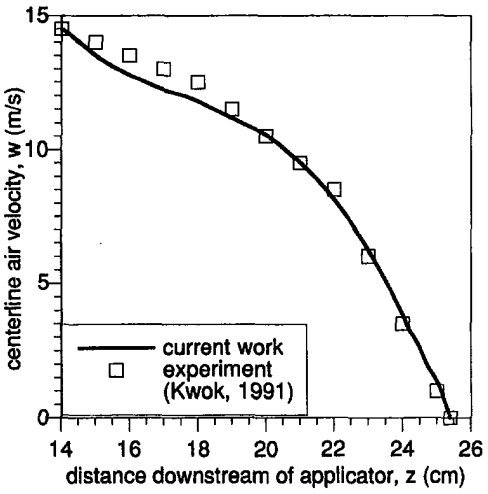

Fig. 6 A comparison of measured and predicted axial air velocity along the centerline of the spray within the computational domain

ensemble average, in terms of the discrete simulation results, is given by

$$TE = \frac{\int_{D_{\min}}^{D_{\max}} \int_0^{x_0} q_D \tilde{n}_x P_{x,D} dx dD}{\int_{D_{\min}}^{D_{\max}} \int_0^{x_0} q_D \tilde{n}_x dx dD} \quad (3)$$

where $\tilde{n}_D D^3$ has been replaced by the volume probability density function of diameter, q_D. The actual integration was performed numerically using the measured size distribution, see Fig. 5, and interpolating between the values of $P_{x,D}$ for the ten discrete diameters and five discrete inlet locations, see Table 1.

It is insightful to examine how the TE depends upon drop diameter. Essentially, this is given by the drop transfer efficiency, T_D,

$$T_D = \int_0^{x_0} \tilde{n}_x P_{x,D} dx. \quad (4)$$

This ensemble average characterizes the size dependence of the transport process to the workpiece. A more detailed discussion of drop transfer efficiency is given by Hicks et al. (1993). This diameter function is analogous to the drop-size distribution function which characterizes the size dependence of the atomization process; however, T_D is not a probability density function that describes the probability of the next depositing drop on the workpiece being of diameter D. Rather, it describes the efficiency at which an air spray process facilitates deposition for drops of diameter D. The actual integration of Eq. (4) was performed numerically in a manner similar to that for Eq. (3).

Results and Discussion

Gas Phase. The gas phase simulation accuracy is established by comparing computed air velocities with corresponding measured air velocities (Kwok, 1991). Once the accuracy of the gas phase flow computations is established, the liquid (paint) phase computations are performed.

The gas phase computations adequately predict the flow field, as illustrated in Fig. 6. Figure 6 illustrates the agreement between predicted and measured axial centerline air velocities within the computational domain. Although the model slightly under predicts the flow near the inlet to the domain, it predicts the flow near the workpiece well. This is significant because the region near the workpiece has the most influence on the deposition of drops. The underprediction of the centerline veloc-

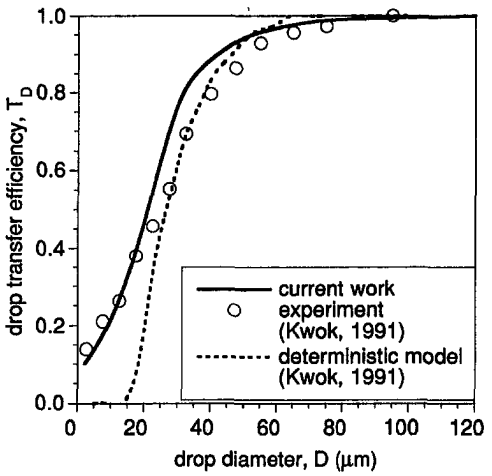

Fig. 7 Comparison of measured and computed drop transfer efficiency functions using the current stochastic simulation and a deterministic simulation

ity near the inlet is most likely to be a result of the selection of k-ϵ model parameters.

Liquid Phase. The liquid phase (paint) simulation accuracy is established by comparing the computed *TE* and size dependence of the drop transfer efficiency, T_D, to the measurements of Kwok (1991). Once verified, greater insights into the physical mechanisms that control air spray painting are developed by examining the relationships between 1) a drop's diameter, 2) the position at which it crossed the inlet boundary, and 3) the probability of it depositing on the workpiece.

The present stochastic simulation that includes the effects of fluctuating air velocities on drop drag yields a paint *TE* of 72 percent which is in good agreement with the measured value of 68 percent. In addition, the stochastic *TE* is more accurate than the 62 percent *TE* computed from a deterministic drop trajectory method that neglects the effects of fluctuating air velocities on drop trajectories (Kwok, 1991).

While the improvement in *TE* accuracy with the stochastic method is relatively small, the improvement in the dependency of *TE* on drop diameter, T_D, and consequently the size distribution of depositing drops, is significant. A comparison between measured and simulated results using both deterministic and stochastic methods is presented in Fig. 7. Experimentally, the drop transfer efficiency is observed to increase rapidly with increasing drop size from approximately 0.1 for the 2 μm drops to 1.0 for the 120 μm drops. Most of the large drops deposit on the surface while most of the small drops flow around the workpiece, forming overspray. The present stochastic model captures this basic behavior and, consequently, it provides an accurate deposited size distribution. There is some overprediction of drop transfer efficiency in the range from 30 μm to 60 μm, and this explains the small overprediction of *TE* with the stochastic model. In sharp contrast to the stochastic simulation, the deterministic simulation seriously under predicts the deposition of smaller drops, below 25 μm in diameter, and fails to account for any deposition of drops that are less than 15 μm in diameter. This explains the under prediction of *TE* with the deterministic model and will result in a skewing of the simulated deposited size distribution to larger drop diameters.

The significant differences between the stochastic and deterministic results indicates that the smaller diameter drops, less than 15 μm, deposit solely due to turbulent velocity fluctuations. This is not surprising since the smallest drops in the spray have turbulent Stokes numbers, based on the ratio of the response time of the drop to the eddy lifetime, of approximately one throughout much of the spray.

The drop transfer probability results from the stochastic simulation are shown in Fig. 8 and provide further insight into air spray deposition. The results show a strong correlation between where drops cross the inlet boundary and whether they deposit for all but the smallest and largest drop diameters. Nearly all of the largest drops (120 μm in diameter) deposit independent of where they cross the inlet boundary. While only a small fraction, approximately 10 percent, of the smallest drops (2 μm in diameter) deposit, their drop transfer probability is also nearly independent of entry location. Between these limiting behaviors, the drop transfer probability exhibits a smooth transition: generally decreasing with increasing distance from the centerline and with decreasing drop diameter. This indicates a gradual shift in mechanisms from one dominated by initial momentum for the high inertia—large Stokes number—big drops to one dominated by aerodynamic drag in the flow field for the low inertia—small Stokes number—little drops. The larger drops are generally able to penetrate the air flow moving along the workpiece surface and deposit due to their greater momentum. In contrast, many of the smaller drops which are unable to penetrate this air flow are swept around the workpiece. A fraction of these smaller drops penetrate the air flow along the workpiece via the fluctuating normal components of air velocity. Without these normal fluctuations (the deterministic model), deposition of the smaller drops is precluded.

The decrease in drop transfer probability with increasing entry location for all but the smallest diameter drops is attributed to the momentum and position at which these drops cross the inlet. The axial momentum of drops crossing the inlet boundary not only decreases with drop diameter, but also with distance from the spray centerline. As shown in Table 1, the average axial drop momentum (velocity) decreases with distance from the centerline in a manner that is consistent with the air flow crossing the inlet boundary. Possessing less initial axial momentum, these drops are less likely to deposit. In addition, drops that cross the inlet boundary at a greater distance from the spray centerline are allowed less transverse displacement before moving beyond the edge of the workpiece.

Summary and Conclusions

A methodology for simulating paint drop transport in air sprays has been developed. Simulation of this complex process is made possible through a number of key assumptions based on experimental measurements of typical air paint sprays. These assumptions include (1) neglecting drop interaction and the momentum source term in the air flow calculations since the flow is dilute in the workpiece interaction (WI) region, (2)

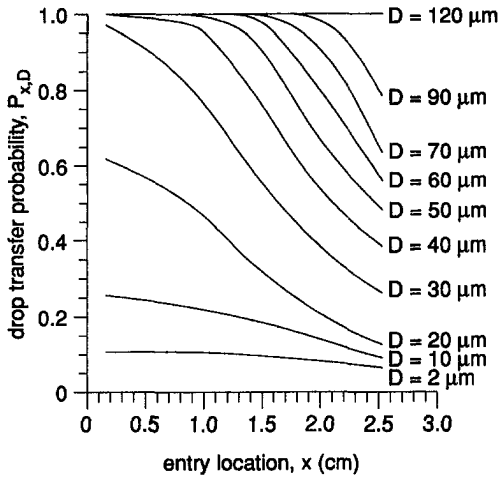

Fig. 8 The influence of entry location and drop diameter on drop transfer efficiency

expressing the specific drop flux crossing the inlet boundary as the product of the atomized drop-size distribution and the local drop flux due to the spatial uniformity of the drop-size distribution crossing the boundary between the near nozzle and flow development (NNFD) and WI regions, and (3) considering the local drop flux crossing the boundary between the NNFD and WI regions to be proportional to the air flux (velocity).

Meaningful measures of paint application performance, such as transfer efficiency (TE) and drop transfer efficiency (T_D) can be determined from key ensemble averages of the simulation results. These results are based on a large number of individual drop trajectory calculations that resolve the relevant coordinates (D, x, s) as well as the stochastic nature of the drop trajectories.

Accurate simulations of paint and drop transfer efficiencies over the range of drop diameters produced by the atomizer are obtained when the direct effects of air turbulence are accounted for with a stochastic separated flow formulation. Deposition of the larger drops is efficient and controlled by their initial momentum when crossing the inlet boundary. As a result the drop transfer efficiency of the 120 μm diameter drops is 1.0 due to their large inertia. In contrast, deposition of the smaller drops is much less efficient, 10 percent for the 2 μm diameter drops, and is controlled by the nature of the turbulent air flow field. Without air turbulence, the smaller drops are unable to deposit.

Acknowledgments

This work was supported by the National Science Foundation under Grant CDR8803017 to the Engineering Research Center for Intelligent Manufacturing Systems.

The efforts of Mr. R. Mongia in reducing the data are greatly appreciated.

References

Amsden, A. A., O'Rourke, P. J., and Butler, T. D., 1989, "*KIVA-II: A Computer Program for Chemically Reactive Flows with Sprays,*" Los Alamos Scientific Laboratory report LA-11560-MS.

Bentley, J., 1987, "Organic Film Formers," *Paint and Surface Coatings,* R. Lambourne, ed., Ellis Horwood Ltd., New York.

Bradbury, L. J. S., 1965, "The Structure of a Self-Preserving Turbulent Plane Jet," *Journal of Fluid Mechanics,* Vol. 23, Part 1, pp. 31–64.

Bunnell, M. H., 1988, "Painting with a Gentle Touch," *Industrial Finishing,* Vol. 64, No. 5, p. 28.

Colwell, J. D., Smith, R. M., and Senser, D. W., 1993, "A Comparison of Supercritical Fluid and Air Paint Sprays," to be submitted to *Atomization and Sprays.*

Corbeels, R. W., Senser, D. W., and Lefebvre, A. H., 1992, "Atomization Characteristics of a High-Speed Rotary-Bell Paint Applicator," *Atomization and Sprays,* Vol. 2, No. 2, pp. 87–99.

Chan, B. M., 1991, "Investigation of the Spray Structure of A High Volume Low Pressure Air-Assist Atomizer," M.S.M.E. thesis, Purdue University.

Faeth, G. M., 1987, "Mixing and Combustion in Sprays," *Progress in Energy Combustion Science,* Vol. 13, pp. 293–345.

Goris, N. H., 1990, "Operational Characteristics and Energy Considerations of Pneumatic Atomizers," M.S.M.E. thesis, Purdue University.

Hicks, P. G., 1995, "Drop Transport in Air Paint Sprays," Ph.D. thesis, Purdue University.

Hicks, P. G., Senser, D. W., Kwok, K. C., and Liu, B. Y. H., 1993, "Drop Transfer Efficiency in Air Paint Sprays," Presented at the Engineering Society of Detroit Advanced Coatings Technology Conference, November 9–11, Dearborn, MI.

Kwok, K. C., 1991, "A Fundamental Study of Air Spray Painting," Ph.D. thesis, University of Minnesota.

Lefebvre, A. H., 1989, *Atomization and Sprays,* Hemisphere Pub., New York.

MacInnes, J. M., 1992, Personal Communication, Sept. 11, 1992.

MacInnes, J. M., and Bracco, F. V., 1992, "A Stochastic Model of Turbulent Drop Dispersion in Dilute Sprays," Presented at the ILASS-Europe Conference, Sept., 1992, Amsterdam, Netherlands.

McCarthy, Jr., J. E., 1991, "Basic Studies on Spray Coating: Drop Rebound From a Small Workpiece with a Conventional Air Applicator," M.S.M.E. thesis, Purdue University.

McCarthy, J. E. Jr., 1995, "Drop Transport in Electrostatic Air Paint Sprays," Ph.D. thesis, Purdue University.

Rodi, W., and Spalding, D. B., 1970, "A Two-Parameter Model of Turbulence, and its Application to Free Jets," *Wärme- und Stoffübertragung,* Bd. 3, pp. 85–95.

Rodi, W., 1975, "A Review of Experimental Data of Uniform Density Free Turbulent Boundary Layers," *Studies in Convection,* Vol. 1, pp. 78–165.

Schrantz, J., 1989, "New CO_2 Spray Finishing Technology!," *Industrial Finishing,* Vol. 65, No. 9, pp. 26–31.

Shuen, J. S., Solomon, A. S. P., Zhang, Q-F., and Faeth, G. M., 1984, "Structure of Particle-Laden Jets: Measurements and Predictions," AIAA Paper 84-0038.

Snyder, H. S., Senser, D. W., and Lefebvre, A. H., 1989, "Drop Size Measurements in Electrostatic Paint Sprays," *IEEE Transactions: Industrial Applications,* Vol. 25, No. 4, pp. 720–727.

Flow Patterns and Pressure Drop in Air/Water Two-Phase Flow in Horizontal Helicoidal Pipes

A. Awwad

R. C. Xin

Z. F. Dong

M. A. Ebadian[1]
Fellow ASME

Department of Mechanical Engineering,
Florida International University,
Miami, FL 33199

H. M. Soliman
Department of Mechanical Engineering,
University of Manitoba,
Winnipeg, Manitoba, Canada

An experimental investigation is conducted for air/water two-phase flow in horizontal helicoidal pipes. The helicoidal pipes are constructed of 25.4 mm I.D. Tygon tubing wrapped around cylindrical concrete forms with outside diameters of 62 cm and 124 cm. The helix angles of the helicoidal pipes vary from 1 to 20 deg. The experiments are performed for superficial water velocity in a range of $U_L = 0.008 \sim 2.2$ m/s and for superficial air velocity in a range of $U_G = 0.2 \sim 50$ m/s. The flow patterns are discerned and recorded photographically. The pressure drop of the air/water two-phase flow in the coils is measured and the Lockhart-Martinelli approach is used to analyze the data. The results are presented in the form of frictional pressure drop multipliers versus the Lockhart-Martinelli parameter. It was found that the flow patterns differ greatly from those of the straight pipe, and that the frictional pressure drop multipliers depend on both the Lockhart-Martinelli parameter and the flow rates. The correlation of the frictional pressure drop has been provided based on the current data. Furthermore, it was also found that the helix angle of the helicoidal pipe had almost no effect on the air/water two-phase flow pressure drop in the present experimental ranges.

Introduction

Helicoidal pipes have been used extensively in steam generators, chemical plants, and nuclear reactors. Depending on their specific application, the coil axis of the helicoidal pipe may be oriented horizontally or vertically, and correspondingly, the pipe is designated as either a horizontal helicoidal pipe or a vertical helicoidal pipe. A few papers have dealt with the hydrodynamic characteristics of two-phase flow in helicoidal pipes, and among them, the investigators were mainly concerned with overall parameters such as pressure drop, void fraction, and flow patterns in the vertical helicoidal pipe. The centrifugal force acting on the fluids causes flow in a helicoidal pipe to be much more complicated than the flow in a straight pipe, and in general, two-phase flow in the horizontal helicoidal pipe differs greatly from that in the vertical helicoidal pipe because of the influence of gravity. Although different flow characteristics exist between two-phase flow in the straight pipe and the helicoidal pipe, the method for analyzing the pressure drop data for the straight pipe is still used or modified to describe two-phase flow in helicoidal pipes. Boyce et al. (1969) indicated that the pressure drop data were adequately correlated by the Lockhart-Martinelli relationships and were in agreement with the findings of Rippel et al. (1966) and Banerjee et al. (1969). The Lockhart-Martinelli method was also used to correlate the pressure drop data of convection boiling (Owhadi et al., 1968) and downward two-phase flow (Rippel et al., 1966) in vertical helicoidal pipes. Some other methods and correlations were proposed to correlate the pressure drop data (Chen and Zhou, 1981; Saxena et al., 1990; and Akagawa et al., 1971). The flow patterns observed for two-phase flow in vertical helical coils were similar to those seen in the two-phase flow in horizontal straight pipe. Banerjee et al. (1969) found that flow patterns could be adequately predicted for all regimes by a Baker's plot. Chen and Zhang (1984) investigated systematically the air/water two-phase flow patterns and their transitions in helical coils in which the effects of the coil diameter and the helix angle on the flow pattern transition were included. Three criteria for predicting the transitions were proposed by the authors. Besides the flow region transition, Kaji et al. (1984) measured the liquid film thickness around the tube periphery for annular flow in air/water flow in a helicoidal pipe. The striking phenomenon in two-phase flow in a helicoidal pipe is film inversion, which was experimentally explored by Banerjee et al. (1967). This phenomenon was further studied by Whally (1980) and Hewitt and Jayanti (1992).

All of the above-mentioned investigations were conducted for two-phase flow in vertical helicoidal pipes. None was related to the air/water two-phase flow in horizontal helicoidal pipes. Therefore, experiments on air/water two-phase flow in horizontal helicoidal pipes have been conducted in the present study and more attention is focused on the flow patterns and frictional pressure drop.

The Experimental Facility and Procedures

The experimental system consists of an air/water flow loop, test section, and associated instrumentation. A schematic representation of the experimental system is shown in Fig. 1. After the flow rates are measured, air and water flow into the mixer. The mixer is designed like a tee-section. The air is discharged into the water flow through a small tube with a closed end and uniformly distributed through small holes around it. The small tube is inserted into the center of the water pipe. The homogenous mixture of air and water then flows into a visual section after a developing section with a length of 60 times the diameter of the tube. This visual section is made of cast acrylic, where the flow patterns located upstream of the test section can be observed. The test section is located beyond the visual section at a distance of about 60 times the tube diameter. After passing the test section, the air/water mixture flows into a separator

[1] Corresponding author.

Contributed by the Fluids Engineering Division for publication in the JOURNAL OF FLUIDS ENGINEERING. Manuscript received by the Fluids Engineering Division March 29, 1994; revised manuscript received March 29, 1995. Associated Technical Editor: Jong H. Kim.

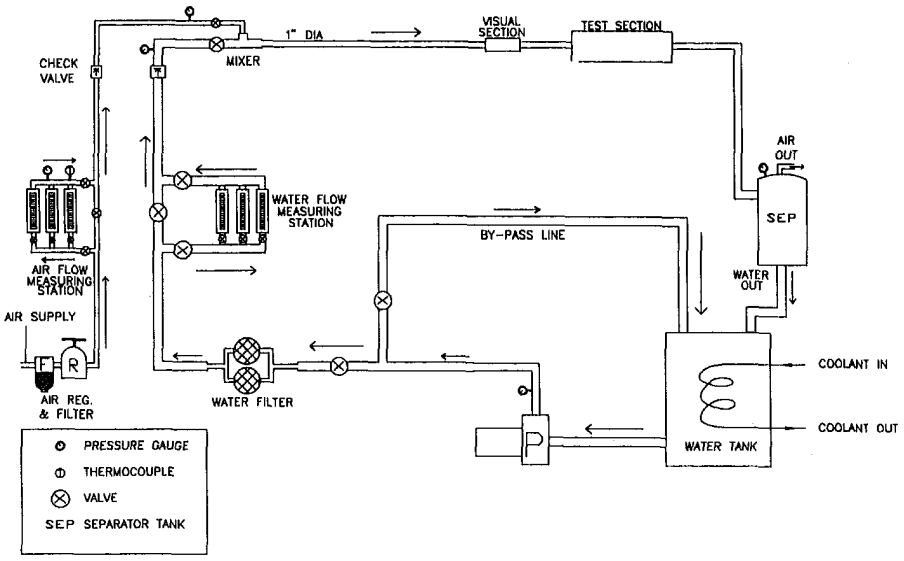

Fig. 1 Schematic representation of the experimental system

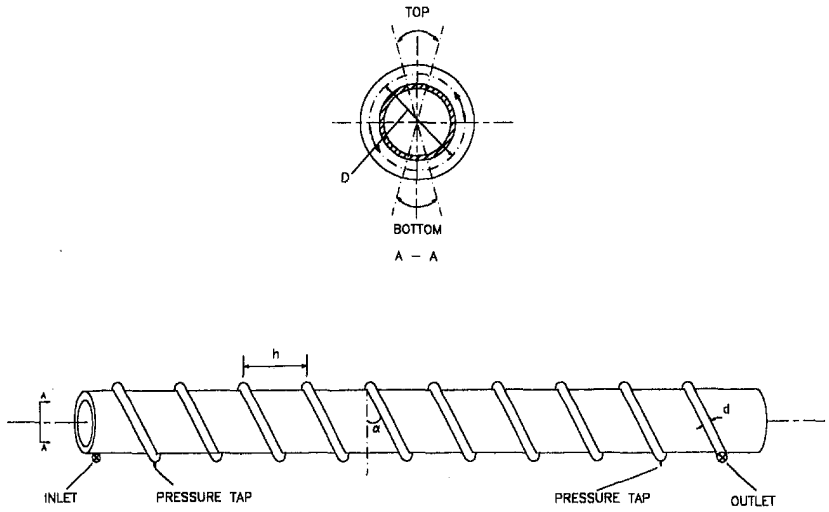

Fig. 2 Configuration of the horizontal helicoidal pipe

from which the air escapes to the ambient, while the water drops and returns to the water tank. In addition, the air-flow rate and water flow rate are monitored by valves and a by-pass mounted in the flow loop. After build-up, both the air line and the water line are carefully checked and adjusted to avoid any leakage.

The test section is shown in Fig. 2. A 6 mm thick-walled transparent Tygon tube with a 25.4 mm inner diameter was wrapped around a cylindrical concrete form. The helicoidal pipe was then fixed and tightened carefully by clamps to avoid large deformations. The whole test section was mounted on a UNI-STRUT frame to avoid vibration.

The pressure taps are located at the bottom of the horizontal helicoidal pipe, as shown in Fig. 2. The pressure difference was measured by a differential pressure transducer (wet/wet). The air/water flow was recorded by a video camera using a shutter

Nomenclature

D = coil diameter, m
De = Dean number
d = tube diameter, m
dp/dz = pressure gradient, Pa/m
$F_d = F_r(d/D)^{0.1}$
Fr = Froude number
f = friction factor
g = gravitational acceleration, m/s^2
h = pitch, m
n = coil turns
Re = Reynolds number
t = turbulent flow
U = superficial velocity, m/s
V = volumetric flow rate
v = laminar flow
X = Lockhart-Martinelli parameter, Eq. (2)
α = helix angle
ΔP = pressure difference
μ = viscosity
ρ = density [kg m^{-3}]
ϕ = pressure drop multiplier, Eq. (1)

Subscripts

G = gas
L = liquid
S = single phase
TP = two-phase

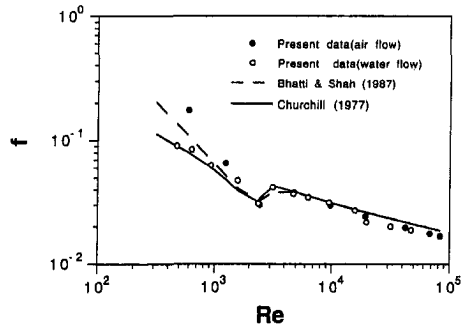

(a) Straight pipe

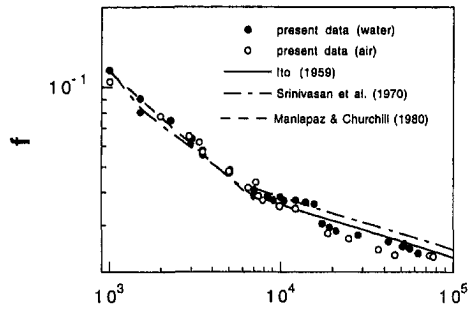

(b) Helicoidal pipe

Fig. 3 Comparison of the friction factor for single-phase flow: (*a*) straight pipe; and (*b*) helicoidal pipe

speed of 4000 frames/sec, which could be replayed at a slow speed in the video cassette recorder (VCR).

The experiments were conducted on the air/water two-phase flow in the 25.4 mm I.D. horizontal helicoidal pipes. The diameters of the coils were 660 mm and 350 mm. The helix angles of the helicoidal pipes were 1 (or 2), 5, 10, and 20 deg. Correspondingly, the numbers of turns of the helicoidal pipes were 10, 10, 6, and 3. Furthermore, the superficial velocities of air and water ranged from 0.2 ~ 50 m/s and 0.008 ~ 2.2 m/s, respectively. Before conducting the two-phase flow experiments, the experimental system was calibrated for single-phase flow in a straight pipe and a helicoidal pipe with a helix angle of 5 deg. The friction factor data are depicted in Figs. 3(*a*) and 3(*b*), and are compared with several empirical formulas from the literature. It was found that excellent agreement was reached for both the laminar flow and the turbulent flow with a maximum deviation of 7 percent. The two-phase flow test of the air/water mixture in a straight pipe was then conducted. Figure 4

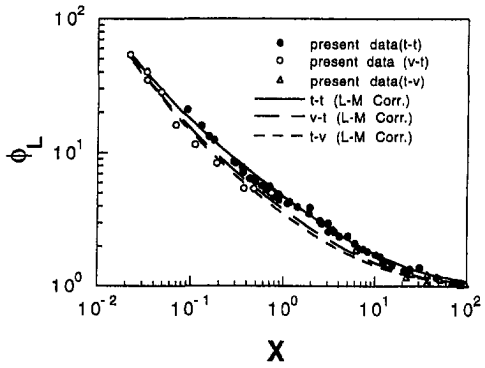

Fig. 4 Comparison of the pressure drop multiplier for two-phase flow in a straight pipe

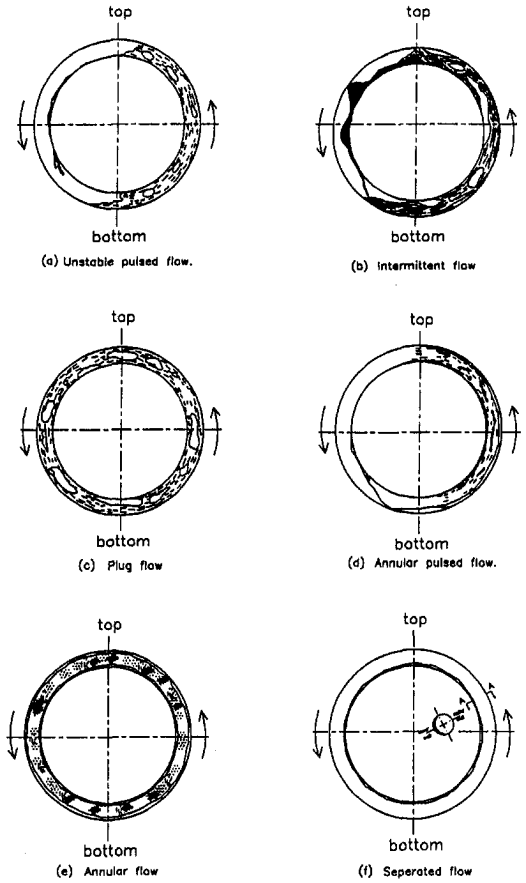

Fig. 5 Flow patterns

shows that the frictional pressure drop multiplier data for two-phase flow in the horizontal straight pipe adhere to the prediction by the Lockhart-Martinelli equation. The two-phase flow test in the helicoidal pipes was then conducted for a variety of air and water flow rates.

Results and Discussion

The Flow Patterns. The flow patterns were discerned based on visual observation of a video tape replay and photographs taken by a high-speed camera with ISO 1600 film. Six typical flow patterns were identified and named as unstable pulsed flow, intermittent flow, plug flow, annular pulsed flow, annular flow, and separated flow (Fig. 5). These flow patterns can be classified into three flow regimes: Unsteady flow (Figs. 5(*a*) and 5(*b*), transitional flow (Figs. 5(*c*) and 5(*d*)) and steady flow (Figs. 5(*e*) and 5(*f*)). In unsteady flow, both the air phase and the water phase flow as a bullet or slug. Neither flow as a continuous phase. However, for the steady flow, both the air phase and water phase flow steadily and continuously in the helicoidal pipe. For the cases shown in Figs. 5(*e*) and 5(*f*), the flow was more like the annular flow and stratified flow in a straight pipe. A film of water formed on the wall of the pipe, and the air phase with dispersed water flowed in the center of the pipe. The flows between the unsteady and steady flows are illustrated in Figs. 5(*c*) and 5(*d*) as transitional flow from unsteady to steady flow in which the plug breaks up, and the air and water mix in certain amounts. Except for the steady flow pattern, different flow patterns were observed in different sections of the horizontal helicoidal pipes. All of the above-mentioned flow phenomena were attributed to the results of the interaction of all the forces, which are gravity force, centrifugal force, and torsion force, in the air/water two-phase flow. The

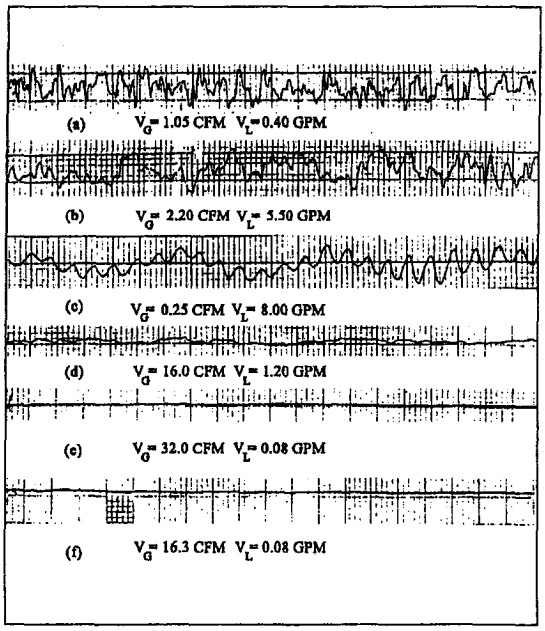

Fig. 6 Pressure fluctuation in two-phase flow

directions and the values of those forces change with the location and the flow rates of the water and the air.

In Fig. 6, the pressure fluctuation is correspondingly displayed for the flow patterns shown in Fig. 5. The pressure fluctuation is recorded for one minute in each case. It is obvious that the pressure fluctuation diminishes as the flow patterns change from unsteady flow to steady flow. In the actual pressure drop measurement, the average reading of the pressure was taken in one minute. It can be seen from Fig. 6 that the time period for the pressure averaged value in one minute was suitable and could be used for the entire pressure drop measurements.

The Pressure Drop. The general method for correlating the two-phase flow frictional pressure drop given by Lockhart-Martinelli is applied in the analysis of the pressure drop data. In the case of air/water two-phase flow in the horizontal helicoidal pipes, the pressure gradients induced by the phase change and gravitation can be ignored. Therefore, it follows that the frictional pressure gradient in two-phase flow, $(dp/dz)_{TPf}$, is related to that for the gas or liquid phase flowing alone in the helicoidal pipes. The results are presented in terms of pressure drop multipliers, ϕ_G and ϕ_L, versus the Lockhart-Martinelli parameter. The ϕ_G and ϕ_L are defined as:

$$\phi_G^2 = \frac{(dp/dz)_{TPf}}{(dp/dz)_G}, \quad \phi_L^2 = \frac{(dp/dz)_{TPf}}{(dp/dz)_L}, \tag{1}$$

and the Lockhart-Martinelli parameter is expressed as:

$$X^2 = \frac{(dp/dz)_L}{(dp/dz)_G}. \tag{2}$$

The single-phase pressure drop used in Eqs. (1) and (2) can be calculated from the standard equations:

$$\left(\frac{dp}{dz}\right)_G = 2f_G\rho_G U_G^2/d, \quad \left(\frac{dp}{dz}\right)_L = 2f_L\rho_L U_L^2/d. \tag{3}$$

The pressure gradient of two-phase flow is determined from the measured pressure drop (ΔP):

$$\left(\frac{dp}{dz}\right)_{TPf} = \frac{\Delta P}{\pi Dn/\cos\alpha}. \tag{4}$$

The friction factors, f_G and f_L, are calculated from the equation by Manlapaz and Churchill (1980) for laminar flow, and from equation by Ito (1959) for the turbulent flow of single-phase flow in a helicoidal pipe. They are cited here, respectively.

$$\frac{f}{f_s} = \left[\left(1.0 - \frac{0.18}{[1 + (35/\mathrm{De})^2]^{0.5}}\right)^m + \left(1.0 + \frac{d/D}{3}\right)^2\left(\frac{\mathrm{De}}{88.33}\right)\right]^{2.5}, \tag{5}$$

where $m = 2$ for $\mathrm{De} < 20$, $m = 1$ for $20 < \mathrm{De} < 40$, and $m = 0$ for $\mathrm{De} > 40$, and $f_s = 16/\mathrm{Re}$, and

$$f\left(\frac{D}{d}\right)^{0.5} = 0.00725 + 0.076\left[\mathrm{Re}\left(\frac{D}{d}\right)^{-2}\right]^{-0.25} \quad \text{for} \quad 0.034 < \mathrm{Re}\left(\frac{D}{d}\right)^{-2} < 300. \tag{6}$$

The Reynolds number and the Dean number in Eqs. (5) and (6) are defined as:

$$\mathrm{Re} = \frac{\rho U d}{\mu} \quad \text{and} \quad \mathrm{De} = \mathrm{Re}\left(\frac{d}{D}\right)^{1/2}. \tag{7}$$

In the following sections, the frictional pressure drop data are presented in terms of the variation of the frictional pressure drop multipliers, ϕ_L or ϕ_G, with the Lockhart-Martinelli parameter, X. Figures 7 and 8 show the variations of ϕ_L and ϕ_G with X for the helicoidal pipes with the large diameter coil, and Figs. 9 and 10 for the helicoidal pipes with the small diameter coil. There are three graphs in each figure for the different helix angles of the helicoidal pipes. All the symbols are data from the present experiment, and the solid line is the prediction of the frictional pressure drop multiplier, ϕ_L or ϕ_G, for two-phase flow in a straight pipe by the Lockhart-Martinelli correlation. It is clearly seen that unlike two-phase flow in a straight pipe, both the frictional pressure drop multipliers, ϕ_L and ϕ_G, depend

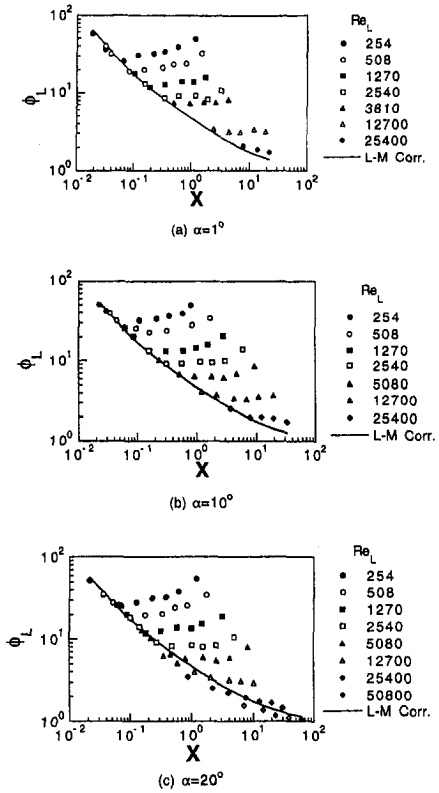

Fig. 7 Variation of ϕ_L versus X for large coils with different helix angles

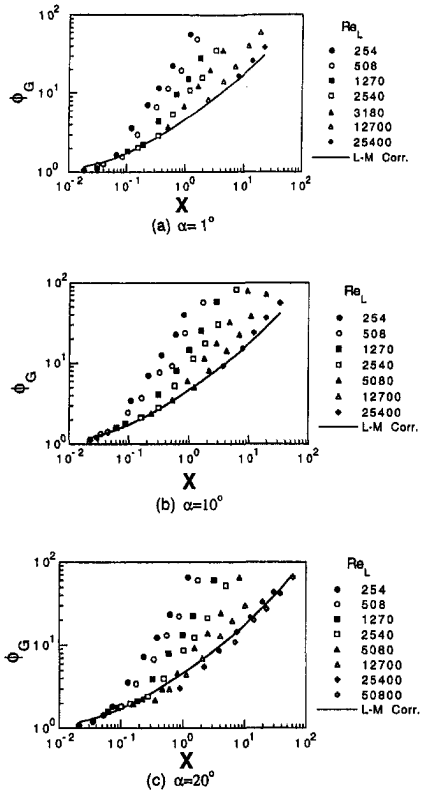

Fig. 8 Variation of ϕ_G versus X for large coils with different helix angles

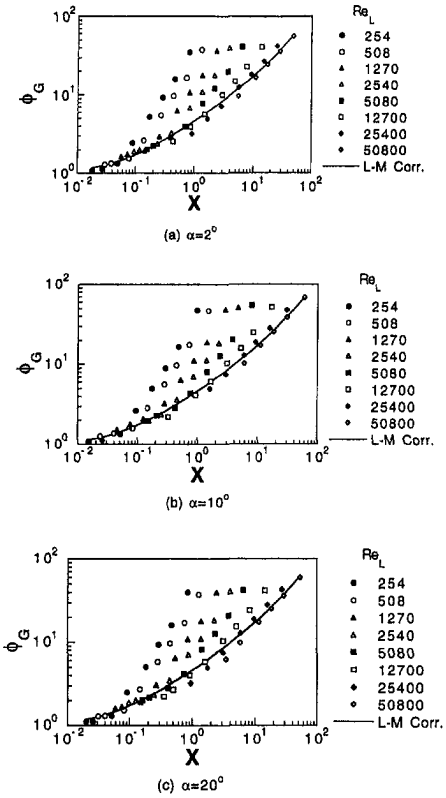

Fig. 10 Variation of ϕ_G versus X for small coils with different helix angles

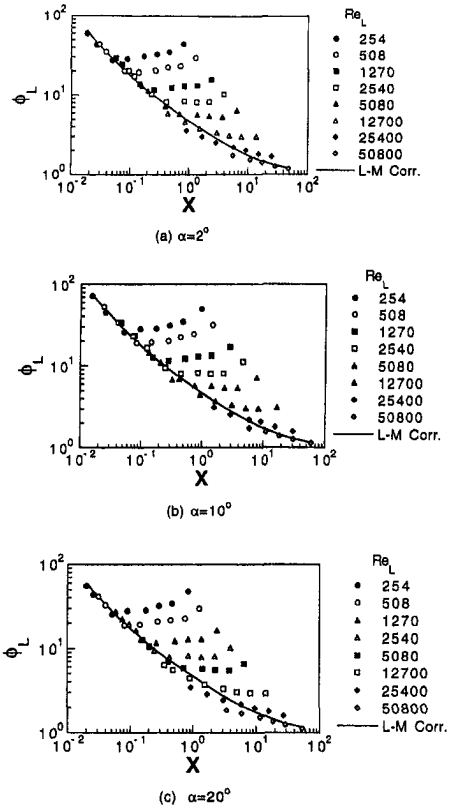

Fig. 9 Variation of ϕ_L versus X for small coils with different helix angles

on the superficial velocity of air or water. Therefore, the third parameter, Re_L, the superficial Reynolds number of water flow, is applied in presenting the experimental results. When Re_L is larger, the experimental data adhere to the solid line by the Lockhart-Martinelli correlation; otherwise, they diverge. An explanation for this follows. In unsteady and transitional flows, the upward side of the helicoidal pipe is full of residual water, which is always present. It is this residual water that blocks the air flow and increases the pressure drop. As the air flow rate increases, the air flow has more kinetic energy to overcome the resistance due to the residual water so that less water remains there. This leads to a decrease in the pressure drop, as shown in Figs. 7 and 9 in the lower flow rate. When the flow rates are higher, there is no residual water in the case of steady flow in

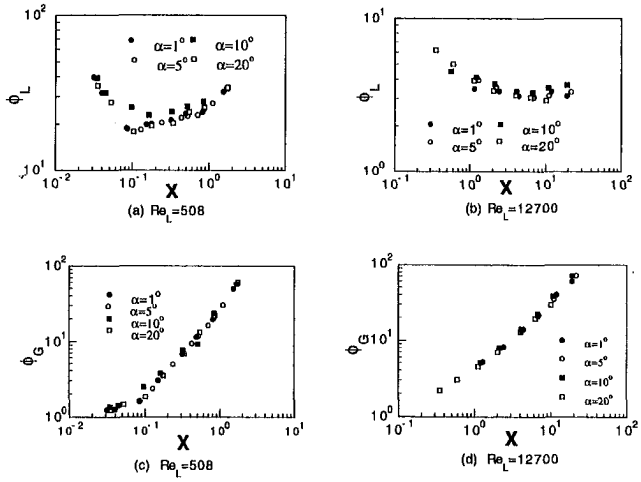

Fig. 11 Effect of the helix angle on the frictional pressure drop multipliers, ϕ_L and ϕ_G, for large coils

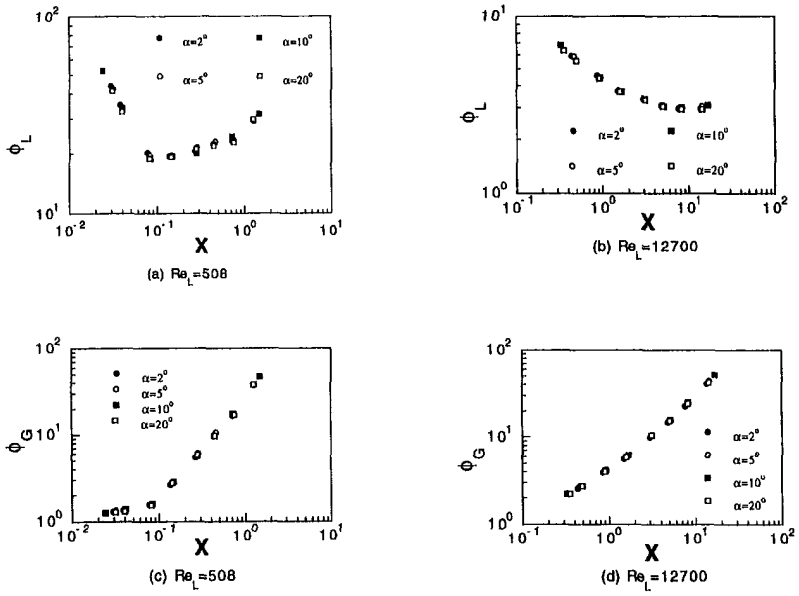

Fig. 12 Effect of the helix angle on the frictional pressure drop multipliers, ϕ_L and ϕ_G, for small coils

the helicoidal pipe, and air and water flow concurrently in both the upward and downward sides of the helicoidal pipe, and the pressure drop increases as the flow rate increases. This phenomenon was observed in both the helicoidal pipes with a large coil diameter and a small coil diameter.

The effect of the helix angle on the frictional pressure drop multipliers, ϕ_L and ϕ_G, in the large coil is shown in Fig. 11 for different flow rates (represented by the superficial Reynolds number of water, Re_L). It is observed from these graphs in Fig. 11 that the helix angle has almost no effect on ϕ_L or ϕ_G. All the data for different helix angles, 1, 5, 10, and 20 deg, are close in value to each other. This is attributed to turbulence in the two-phase flow. The frictional pressure drop will be increased by the turbulence, as well as the torsional force due to the finite pitch (helix angle) of the helicoidal pipe. The intensity of the turbulence in the helicoidal pipe depends on the flow rate ratio of air to water instead of the helix angle. Therefore, there is almost no effect of the helix angle on the frictional pressure drop multipliers, ϕ_L and ϕ_G. This conclusion can also be confirmed by Fig. 12, which shows the effect of the helix angle on ϕ_L and ϕ_G in the helicoidal pipe with a small coil.

The effect of the coil diameter on the pressure drop multiplier, ϕ_L, is displayed in Fig. 13, where the superficial Reynolds number of water is used as a parameter. It was found that only in the cases of lower flow rates does a difference exist between the pressure drop data of the large coils and the small coils. In the case of a high flow rate, the pressure drop data for both coils agree with each other. This can be explained by the fact that in the low flow rate, more water resides in the upward side of the helicoidal pipe because of the large coil diameter, and thus, the pressure drops for large helicoidal pipes are greater than for small helicoidal pipes for the same superficial water velocity.

It has been seen that the Lockhart-Martinelli correlation for the straight pipe is not suitable for calculating the frictional pressure drop in two-phase flow in helicoidal pipes. Based on the present experimental data and by incorporating the Froude number, Fr, a new correlation has been worked out. The basic idea for creating this new correlation is to add one factor to the Lockhart-Martinelli equation to account for the effect of the velocity of the liquid. It is expressed as:

$$\phi_L = \left(\frac{X}{9.63F_d^{0.61}}\right)\left(1 + \frac{12}{X} + \frac{1}{X^2}\right)^{1/2}, \qquad (8)$$

where F_d is defined as $F_d = \mathrm{Fr}\,(d/D)^{0.1} = U_L^2/gd(d/D)^{0.1}$. The

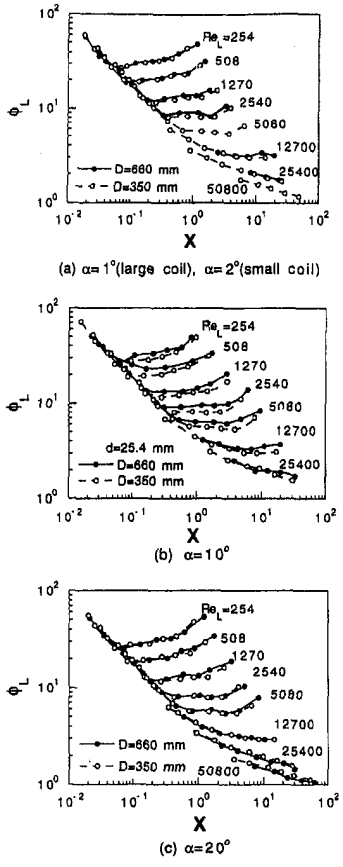

Fig. 13 Effect of the coil diameter on the frictional pressure drop multiplier, ϕ_L, with different helix angles

deviation between the prediction by Eq. (8) and the experimental data is less than 30 percent in the present experimental range.

Experimental Uncertainty. Two quantities of the direct measurements were the flow rate and the pressure drop. Both the air and water flow rates were measured by three Fisher and Porter rotameter-type flow meters with an accuracy of 2 percent. The pressure drop was measured by two Rosemount pressure transducers with an accuracy of 2 percent. The accuracies of other quantities, such as length and properties, were estimated as 1 and 0.25 percent, respectively. It was estimated that the uncertainties of ϕ_L or ϕ_G were 5.14 percent and the uncertainty of X was 9.2 percent.

Conclusion

Air/water two-phase flow in horizontal helicoidal pipes with a 25.4 mm inner diameter has been experimentally investigated. The flow patterns in the coils were discerned and the frictional pressure drop data were analyzed by the Lockhart-Martinelli approach. The experiments were conducted in ranges for superficial air velocity, $U_G = 0.2 \sim 50$ m/s, and superficial water velocity, $U_L = 0.008 \sim 2.2$ m/s. Two coil diameters of 350 mm and 660 mm were used in the experiments. The helix angles of the coils varied from $1 \sim 20$ deg. Six basic flow patterns were identified, which have been classified into three flow regimes: Unsteady flow, transitional flow, and steady flow. In the steady flow regime, both the air phase and the water phase flow in a continuum, but the unsteady flow pattern behaves intermittently, as air and water slug or plug flow. There is a transitional flow between the steady flow and the unsteady flow. On the other hand, it was found that the frictional pressure drop data were strongly related to the flow rates in addition to the Lockhart-Martinelli parameter. A new correlation has been provided based on the present measurement, and it is recommended for use in the present experimental range. In addition, it seems that the helix angle of the helicoidal pipes had almost no effect on the frictional pressure drop, although the coil diameter had some small effect on the pressure drop in certain cases.

References

Akagawa, K., Sakaguchi, T., and Ueda, M., 1971, "Study on a Gas-Liquid Two-Phase Flow in Helically Coiled Tubes," *Bulletin of the Japanese Society of Mechanical Engineering,* Vol. 14, pp. 564–571.

Banerjee, S., Rhodes, E., and Scott, D. S., 1969, "Studies on Concurrent Gas-Liquid Flow in Helically Coiled Tubes, I-Flow Patterns, Pressure Drop and Holdup," *Canadian Journal of Chemical Engineering,* Vol. 47, pp. 445–453.

Banerjee, S., Rhodes, E., and Scott, D. S., 1967, "Film Inversion of Concurrent Two-Phase Flow in Helical Coils," *American Institute of Chemical Engineering,* Vol. 13, No. 1, pp. 189–191.

Bhatti, M. S. and Shah, R. K., 1987, "Turbulent and Transition Flow Convective Heat Transfer in Ducts," *Handbook of Single Phase Convective Heat Transfer,* S. Kakac, R. K. Shah, and W. Aung, Wiley, Chapter 4.

Boyce, B. E., Collier, J. G., and Levy, J., 1969, "Hold-Up and Pressure Drop Measurement in the Two-Phase Flow of Air-Water Mixing Tubes in Helical Coils," *Proceedings of International Symposium on Research in Concurrent Gas and Liquid Flow,* E. Rhodes and D. S. Scott, eds. Plenum Press, New York, pp. 203–231.

Chen, X. J. and Zhang, M. Y., 1984, "An Investigation on Flow Pattern Transition for Gas-Liquid Two-Phase Flow in Helical Coils," *Multi-Phase Flow and Heat Transfer III, Part A: Fundamentals,* T. N. Veziroglu and A. E. Berglers, eds., pp. 185–200.

Chen, X. J., and Zhou, F. D., 1981, "An Investigation of Flow Pattern and Frictional Pressure Drop Characteristics of Air Water Two Phase Flow in Helical Coils," *Proceedings of 4th Miami International Conference on Alternate Energy Sources,* pp. 120–129.

Churchill, S. W., 1977, "Comprehensive Correlation Equations for Heat, Mass and Momentum Transfer in Fully Developed Flow in Smooth Tubes," *Industrial Engineering Chemistry Fundamentals,* Vol. 16, pp. 109–116.

Hewitt, G. F., and Jayanti, S., 1992, "Prediction of Film Inversion in Two-Phase Flow in Coiled Tubes," *Journal of Fluid Mechanics,* Vol. 236, pp. 497–511.

Ito, H., 1959, "Friction Factors for Turbulent Flow in Curved Pipes," ASME *Journal of Basic Engineering,* Vol. 81, pp. 123–134.

Kaji, M., Mori, K., Nakanishi, S., and Ishigai, S., 1984, "Flow Regime Transitions for Air-Water Flow in Helically Coiled Tubes," *Multi-Phase Flow and Heat Transfer III, Part A: Fundamentals,* T. N. Veziroglu, ed., Elsevier, Amsterdam, pp. 201–214.

Manlapaz, R. L., and Churchill, S. W., 1980, "Fully Developed Laminar Flow in a Helicoidal Coiled Tube of Finite Pitch," *Chemical Engineering Communications,* Vol. 7, pp. 57–78.

Owhadi, A., Bell, K. J., and Crain, B., 1968, "Forced Convection Boiling Inside Helically-Coiled Tubes," *International Journal of Heat and Mass Transfer,* Vol. 11, pp. 1779–1793.

Ripple, G. R., Eidt, C. M., Jornan, H. B., 1966, "Two-Phase Flow in a Coiled Tube," *Industrial and Engineering Chemistry,* Vol. 5, pp. 32–39.

Saxena, A. K., Schumpe, A., and Nigam, K. D. P., 1990, "Flow Regimes, Holdup and Pressure Drop for Two-Phase Flow in Helical Coils," *Canadian Journal of Chemical Engineering,* Vol. 68, pp. 553–559.

Srinivasan, P. S., Nandapurkar, S. S., and Holland, F. A., 1970, "Friction Factors for Coils," *Transactions of Institute of Chemical Engineering,* Vol. 48, pp. T156–T161.

Whally, P. B., 1980, "Air-Water Two-Phase Flow in a Helically Coiled Tube," *International Journal of Multi-Phase Flow,* Vol. 6, pp. 345–356.

Journal of Fluids Engineering

Technical Briefs

On the Roughness Reynolds Number Transition Criterion

J. A. Masad[1]

The theoretically validated Fage's transition criterion for predicting transition in flow over a single roughness element is used to show that in the widely used roughness Reynolds number (Re_k) transition criterion, the critical value of Re_k depends strongly on the length of the roughness element. At roughness length where the criterion is valid, the variation of the roughness height with free-stream Reynolds number is quantified.

Introduction

In boundary-layer flow over a roughness element it is known that increasing the roughness element's height moves the transition location upstream. As the roughness element's height exceeds a certain value which is larger than the value that causes separation, transition occurs at the roughness element itself (Schlichting, 1979; Masad and Iyer, 1994) and a further increase in the roughness element's height beyond that value has virtually no influence on the movement of transition location. A widely used empirical criterion which relates the roughness and flow parameters at which transition occurs at the roughness element itself is the Re_k criterion (see Morkovin, 1993). In this criterion Re_k is defined as

$$\mathrm{Re}_k = \frac{k^* U_k^*}{\nu_k^*} \tag{1}$$

where k^* is the dimensional height of the roughness element, U_k^* is the dimensional streamwise velocity of the flow at height k^* in absence of the roughness element, and ν_k^* is the dimensional kinematic viscosity of the fluid at height k^* in absence of the roughness element. In aircraft icing studies, the flow is considered transitional at the roughness (due to ice accretion) itself when (Hansman, 1993) Re_k exceeds a value of 600. Fage and Preston (1941) indicated that the value is above 400 for the case of flow over a circular wire mounted on a body of revolution. The Re_k criterion accounts for the height of the roughness explicitly through k^* in Eq. (1). The free-stream unit Reynolds number is also accounted for almost explicitly through the factor U_k^*/ν_k^* in Eq. (1). The effect of the location of the roughness element is accounted for implicitly because at the same roughness height and at the same free-stream unit Reynolds number U_k^* increases as the roughness is located further downstream of the leading edge due to the growth of the boundary layer. It is clear from Eq. (1) that Re_k increases as k^* increases which is expected. Increasing the flow unit Reynolds number increases U_k^* in Eq. (1) which increases Re_k. Moving the roughness element upstream decreases U_k^* which also decreases Re_k. Increasing the free-stream Mach number thickens the boundary layer and, therefore, reduces U_k^* which results in a reduced Re_k.

It is clear from Eq. (1) and the above discussion that the Re_k criterion does not account for the effect of the length of the roughness element because it is not represented in any of the quantities in Eq. (1). This aspect was pointed out by Masad and Malik (1994). The effect of the length of the roughness element on transition location was found by Masad and Iyer (1994) to be significant. In this work we use the transition prediction formula of Fage (1943) which is based on experimental data to show the dependence of the value of Re_k at which transition occurs at the roughness elements itself on the length of the roughness element. Furthermore, at roughness lengths where the Re_k transition criterion is valid, computations and results for the dependence of Re_k on roughness height and location and flow free-stream unit Reynolds numbers are presented.

Formulation and Results

We consider incompressible flow over a flat plate with a roughness element. We denote the dimensional length of the roughness element by λ^* and we introduce U_∞^* and L^* as the free-stream streamwise dimensional velocity and the dimensional distance from the leading edge of the flat plate to the center of the roughness element. If we use L^* to make distances nondimensional, then we have

$$k = \frac{k^*}{L^*} \tag{2a}$$

$$\lambda = \frac{\lambda^*}{L^*} \tag{2b}$$

and we define

$$\mathrm{Re} = \frac{U_\infty^* L^*}{\nu^*} \tag{2c}$$

where Re is the free-stream Reynolds number based on L^*.

Fage (1943) used his own experimental data on the effects of surface roughness on transition, as well as the experimental data of Walker and Greening, Walker and Cox, and Hislop (as reported in Fage, 1943), to correlate the transition location with the height and length of the roughness element and the Reynolds number at the edge of the boundary layer. If we replace the nondimensional velocity at the edge of the boundary layer with

[1] High Technology Corp., 28 Research Drive, Hampton, VA 23666.

Contributed by the Fluids Engineering Division of THE AMERICAN SOCIETY OF MECHANICAL ENGINEERS. Manuscript received by the Fluids Engineering Division June 1, 1994; revised manuscript received June 8, 1995. Associate Technical Editor: R. W. Metcalfe.

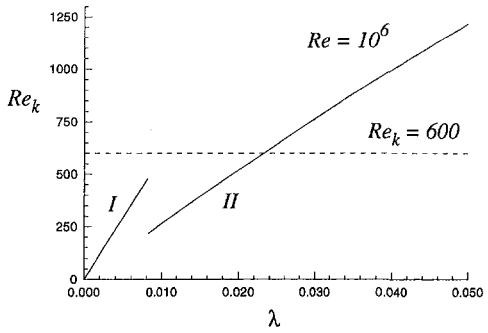

Fig. 1 Variation of Re_k with the nondimensional length of the roughness element

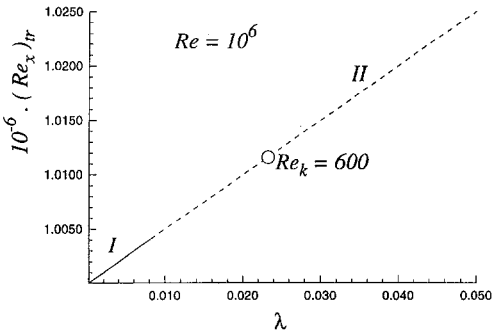

Fig. 3 Variation of transition Reynolds number with the nondimensional length of the roughness corresponding to Figs. 1 and 2

unity and solve for the height k as a function of λ and Re, then Fage's criterion can be written as

$$k = \frac{9 \times 10^6}{(1 + 0.5\lambda)} \sqrt{\frac{\lambda}{\mathrm{Re}^3}} \quad \text{when} \quad \frac{k\,\mathrm{Re}^{1.5}}{9 \times 10^6} > 0.09 \qquad (3a)$$

and

$$k = \frac{13.5 \times 10^6 \sqrt{\lambda}}{(1 + 0.5\lambda)^{1.5}\,\mathrm{Re}^{1.5}} \quad \text{when} \quad \frac{\lambda^{1/6}\,\mathrm{Re}\,k^{2/3}}{(13.5)^{2/3} \times 10^4} < 0.09 \qquad (3b)$$

we define $(\mathrm{Re}_x)_{tr}$ as the value of $\mathrm{Re}_x = U_\infty^* x^*/\nu_\infty^*$ at the transition location. The dimensional distance from the leading edge of the surface is x^*. The nondimensional distance is $x = x^*/L^*$ and it can be shown that

$$\mathrm{Re}_x = x\,\mathrm{Re} \qquad (4)$$

Fage's criterion is valid in a range of $(\mathrm{Re}_x)_{tr}$ that extends from 1 million to 3.5 million. The free-stream Reynolds number Re varied in the experimental data (the basis for Fage's criterion) from 0.5 million to 1 million. The results of the e^N method for transition prediction were found (Masad and Iyer, 1994) to agree well with the results of the experimental correlation of Fage. In the e^N method, transition is assumed to occur when the integrated instability growth rate calculated from linear stability theory reaches a certain value. In the work of Masad and Iyer (1994), various combinations of roughness height k, roughness length λ, and freestream Reynolds number Re were considered. Then the mean flow was computed using interacting boundary layers and the transition location was predicted by performing linear stability calculations for the generated velocity profiles and using the e^N method with $N = 9$.

In the above notation, the roughness element is centered at $x = 1$ and it extends between $x = 1 - \lambda/2$ and $x = 1 + \lambda/2$.

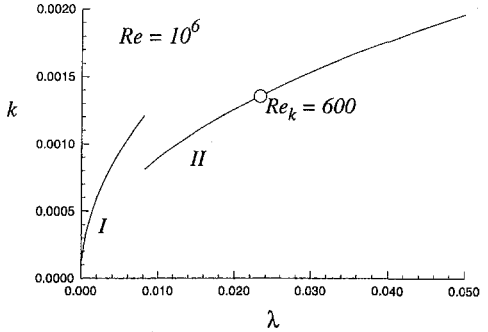

Fig. 2 Variation of the nondimensional roughness height with the nondimensional length of the roughness corresponding to Fig. 1

Therefore, transition first occurs at the roughness element itself when

$$(\mathrm{Re}_x)_{tr} = \mathrm{Re}\left(1 + \frac{\lambda}{2}\right) \qquad (5)$$

where Eq. (4) has been used. Equation (5) has been used to reach Eqs. (3).

We now consider incompressible flow over a flat plate (Blasius flow) which is governed by

$$\frac{d^2U}{d\eta^2} + g\frac{dU}{d\eta} = 0 \qquad (6a)$$

$$U = 0 \quad \text{and} \quad g = 0 \quad \text{at} \quad \eta = 0 \qquad (6b)$$

$$U \to 1 \quad \text{as} \quad \eta \to \infty \qquad (6c)$$

where

$$\eta = y\sqrt{\frac{\mathrm{Re}}{x}}, \quad g = \frac{1}{2}\int_0^\eta U d\eta \qquad (7)$$

and y is made nondimensional using L^*. Therefore,

$$U = 2\frac{dg}{d\eta} = \frac{U^*}{U_\infty^*} \qquad (8)$$

at some height k^* we have

$$y = \frac{k^*}{L^*} = k$$

and at the center of the roughness

$$x = 1$$

therefore

$$\eta_k = k\sqrt{\mathrm{Re}} \qquad (9)$$

It follows from Eqs. (1) and (2) that

$$\mathrm{Re}_k = kU_k\,\mathrm{Re}$$

but at k^*, $\eta = \eta_k^*$, then

$$\mathrm{Re}_k = kU_{\eta_k}\,\mathrm{Re} \qquad (10)$$

Using the above relations it is possible to select λ and Re, calculate k from relations (4), calculate η_k from relation (9), pick the U_{η_k} corresponding to η_k from the computed Blasius profile, and then calculate Re_k from Eq. (10).

The above procedure of calculations was performed. However, the parameters were restricted to those where Fage's correlation is valid, which are

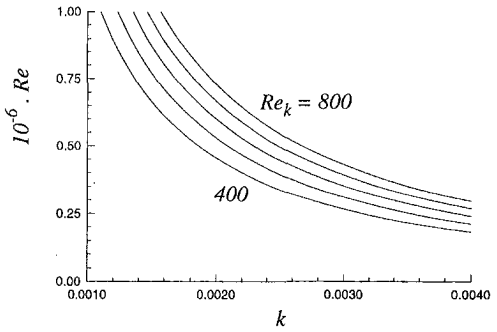

Fig. 4 Variation of the free-stream Reynolds number with the nondimensional height of the roughness element. The values of Re_k proceeding downwards are: 800, 700, 600, 500, and 400.

$$0.5 \times 10^6 \leq \mathrm{Re} \leq 1.0 \times 10^6$$

and

$$1 \times 10^6 \leq (\mathrm{Re}_x)_{tr} \leq 3.5 \times 10^6$$

The considered values of λ extend from 0 to 0.05. In this range and with the above constraints, solutions were found only in the neighborhood of $\mathrm{Re} = 1 \times 10^6$. The results of the variation of Re_k with λ for $\mathrm{Re} = 10^6$ are shown in Fig. 1 and the corresponding variations of k and $(\mathrm{Re}_x)_{tr}$ with λ are shown in Figs. 2 and 3, respectively. Regions I and II in Fig. 3 correspond to relations (3*b*) and (3*a*), respectively. The results of the two relations do not match in the $\mathrm{Re}_k - \lambda$ domain (Fig. 1), or in the $k - \lambda$ domain (Fig. 2), but they match in the $(\mathrm{Re}_x)_{tr} - \lambda$ domain (Fig. 3). The mismatches in Figs. 1 and 2 and the match in Fig. 3 are due to the fact that the curve fit of Fage was performed to fit $(\mathrm{Re}_x)_{tr}$ as a function of k, λ, and Re rather than k as a function of λ, Re, and $(\mathrm{Re}_x)_{tr}$ (Eq. 3) or Re as a function of k, λ, and $(\mathrm{Re}_x)_{tr}$. The large dependence of Re_k on λ is clear from Fig. 1. At $\mathrm{Re} = 10^6$, the $\mathrm{Re}_k = 600$ corresponds to $\lambda \approx 0.0232$ and $k \approx 0.00136$ and at these parameters $(\mathrm{Re}_x)_{tr} = 1.0116 \times 10^6$. The vast variation of Re_k with λ is at $\mathrm{Re} = 10^6$, other values of Re might result in even further variation.

At the roughness length where the Re_k transition criterion is valid, one can quantify its dependence on the roughness height and the flow free-stream Reynolds number based on the location of the roughness element. In that case, one can select a value of Re and assume a value of k, calculate η_k from relation (9), pick U_{η_k} corresponding to η_k from the computed Blasius profile, and then calculate Re_k from Eq. (10). Newton-Raphson iteration can be performed to compute k which drives Re_k to a specific value. The procedure of calculations was performed and the variation of Re with k for various values of Re_k is shown in Fig. 4.

In summary, the theoretically-validated and experimentally-based transition criterion of Fage for predicting transition in flow over a roughness element in certain parameter space is used to show that in the widely used Re_k transition criterion, the critical value of Re_k depends strongly on the length of the roughness element.

References

Fage, A., 1943, "The Smallest Size of Spanwise Surface Corrugation Which Affect Boundary Layer Transition on an Airfoil," British Aeronautical Research Council, Report and Memoranda No. 2120.

Fage, A., and Preston, J. H., 1941, "On Transition from Laminar to Turbulent Flow in the Boundary Layer," *Proceedings of the Royal Society of London,* Vol. 178, pp. 201–227.

Hansman, R. J., 1993, "Microphysical Factors Which Influence Ice Accretion," *Proceedings of the First Bombardier International Workshop on Aircraft Icing and Boundary-Layer Stability and Transition,* I. Paraschivoiu, ed., ISBN 2-553-00422-2, pp. 86–103.

Masad, J. A., and Iyer, V., 1994, "Transition Prediction and Control in Subsonic Flow Over a Hump," *Phys. Fluids,* Vol. 6, No. 1, pp. 313–327. Also NASA CR-4543, Sept. 1993.

Masad, J. A., and Malik, M. R., 1994, "On the Link Between Flow Separation and Transition Onset," AIAA Paper No. 94-2370.

Morkovin, M. V., 1993, "Bypass-Transition Research: Issues and Philosophy," *Instabilities and Turbulence in Engineering Flows,* Ashpis, Gatski and Hirsh, eds., Kluwer Academic Publishers, pp. 3–30.

Schlichting, H., 1979, *Boundary-Layer Theory,* 7th ed., McGraw Hill, New York, pp. 536–537.

Freon Bubble Rise Measurements in a Vertical Rectangular Duct

P. F. Vassallo,[1] P. D. Symolon,[1] W. E. Moore,[1] and T. A. Trabold[1]

Nomenclature

- Ta = Tadaki number
- Re_b = bubble Reynolds number
- Mo = Morton number
- We = Weber number
- ρ_l = liquid density
- ρ_g = gas density
- μ_l = liquid dynamic viscosity
- σ = surface tension
- E = bubble aspect ratio
- h = bubble height
- b = bubble width
- V_r = relative velocity between bubble and liquid
- $V_{r\infty}$ = terminal bubble rise velocity
- K_b = coefficient in Fan-Tsuchiya formulation for viscous bubble regime
- c = coefficient in Fan-Tsuchiya formulation for distorted bubble regime
- η = parameter in Fan-Tsuchiya formulation reflecting system purity
- g = gravitational constant
- d_e = equivalent bubble diameter

1 Introduction

Isolated bubble rise experiments provide data on bubble drag as a function of size and fluid properties. This data is useful in obtaining drag models for higher void fraction bubbly flows. Previous experiments (Haberman and Morton, 1953) have shown that the purity of the fluid affects the bubble rise velocity, and therefore the drag coefficient. For contaminated systems, impurities collecting at the liquid-vapor interface increase the effective viscous drag and decrease the rise velocity.

In the current experimental work, Freon-114 is used to simulate high temperature environments. Freon is chosen as the modelling fluid because it boils at a lower temperature, and may be scaled appropriately. However, if the purity of the Freon test liquid is unknown, using it to model high temperature environ-

[1] Knolls Atomic Power Laboratory, Lockheed Martin Corporation, Schenectady, NY 12301-1072.

Contributed by the Fluids Engineering Division of THE AMERICAN SOCIETY OF MECHANICAL ENGINEERS. Manuscript received by the Fluids Engineering Division August 23, 1994; revised manuscript received April 12, 1995. Associate Technical Editor: O. C. Jones.

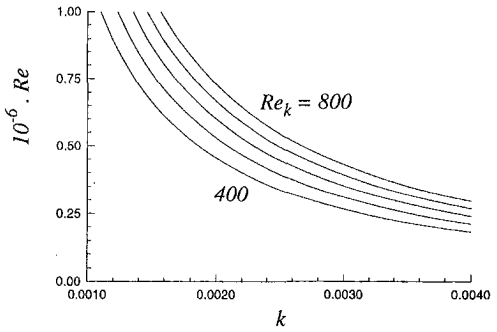

Fig. 4 Variation of the free-stream Reynolds number with the nondimensional height of the roughness element. The values of Re_k proceeding downwards are: 800, 700, 600, 500, and 400.

$$0.5 \times 10^6 \leq \mathrm{Re} \leq 1.0 \times 10^6$$

and

$$1 \times 10^6 \leq (\mathrm{Re}_x)_{tr} \leq 3.5 \times 10^6$$

The considered values of λ extend from 0 to 0.05. In this range and with the above constraints, solutions were found only in the neighborhood of $\mathrm{Re} = 1 \times 10^6$. The results of the variation of Re_k with λ for $\mathrm{Re} = 10^6$ are shown in Fig. 1 and the corresponding variations of k and $(\mathrm{Re}_x)_{tr}$ with λ are shown in Figs. 2 and 3, respectively. Regions I and II in Fig. 3 correspond to relations (3*b*) and (3*a*), respectively. The results of the two relations do not match in the $\mathrm{Re}_k - \lambda$ domain (Fig. 1), or in the $k - \lambda$ domain (Fig. 2), but they match in the $(\mathrm{Re}_x)_{tr} - \lambda$ domain (Fig. 3). The mismatches in Figs. 1 and 2 and the match in Fig. 3 are due to the fact that the curve fit of Fage was performed to fit $(\mathrm{Re}_x)_{tr}$ as a function of k, λ, and Re rather than k as a function of λ, Re, and $(\mathrm{Re}_x)_{tr}$ (Eq. 3) or Re as a function of k, λ, and $(\mathrm{Re}_x)_{tr}$. The large dependence of Re_k on λ is clear from Fig. 1. At $\mathrm{Re} = 10^6$, the $\mathrm{Re}_k = 600$ corresponds to $\lambda \approx 0.0232$ and $k \approx 0.00136$ and at these parameters $(\mathrm{Re}_x)_{tr} = 1.0116 \times 10^6$. The vast variation of Re_k with λ is at $\mathrm{Re} = 10^6$, other values of Re might result in even further variation.

At the roughness length where the Re_k transition criterion is valid, one can quantify its dependence on the roughness height and the flow free-stream Reynolds number based on the location of the roughness element. In that case, one can select a value of Re and assume a value of k, calculate η_k from relation (9), pick U_{η_k} corresponding to η_k from the computed Blasius profile, and then calculate Re_k from Eq. (10). Newton-Raphson iteration can be performed to compute k which drives Re_k to a specific value. The procedure of calculations was performed and the variation of Re with k for various values of Re_k is shown in Fig. 4.

In summary, the theoretically-validated and experimentally-based transition criterion of Fage for predicting transition in flow over a roughness element in certain parameter space is used to show that in the widely used Re_k transition criterion, the critical value of Re_k depends strongly on the length of the roughness element.

References

Fage, A., 1943, "The Smallest Size of Spanwise Surface Corrugation Which Affect Boundary Layer Transition on an Airfoil," British Aeronautical Research Council, Report and Memoranda No. 2120.

Fage, A., and Preston, J. H., 1941, "On Transition from Laminar to Turbulent Flow in the Boundary Layer," *Proceedings of the Royal Society of London,* Vol. 178, pp. 201–227.

Hansman, R. J., 1993, "Microphysical Factors Which Influence Ice Accretion," *Proceedings of the First Bombardier International Workshop on Aircraft Icing and Boundary-Layer Stability and Transition,* I. Paraschivoiu, ed., ISBN 2-553-00422-2, pp. 86–103.

Masad, J. A., and Iyer, V., 1994, "Transition Prediction and Control in Subsonic Flow Over a Hump," *Phys. Fluids,* Vol. 6, No. 1, pp. 313–327. Also NASA CR-4543, Sept. 1993.

Masad, J. A., and Malik, M. R., 1994, "On the Link Between Flow Separation and Transition Onset," AIAA Paper No. 94-2370.

Morkovin, M. V., 1993, "Bypass-Transition Research: Issues and Philosophy," *Instabilities and Turbulence in Engineering Flows,* Ashpis, Gatski and Hirsh, eds., Kluwer Academic Publishers, pp. 3–30.

Schlichting, H., 1979, *Boundary-Layer Theory,* 7th ed., McGraw Hill, New York, pp. 536–537.

Freon Bubble Rise Measurements in a Vertical Rectangular Duct

P. F. Vassallo,[1] P. D. Symolon,[1] W. E. Moore,[1] and T. A. Trabold[1]

Nomenclature

- Ta = Tadaki number
- Re_b = bubble Reynolds number
- Mo = Morton number
- We = Weber number
- ρ_l = liquid density
- ρ_g = gas density
- μ_l = liquid dynamic viscosity
- σ = surface tension
- E = bubble aspect ratio
- h = bubble height
- b = bubble width
- V_r = relative velocity between bubble and liquid
- $V_{r\infty}$ = terminal bubble rise velocity
- K_b = coefficient in Fan-Tsuchiya formulation for viscous bubble regime
- c = coefficient in Fan-Tsuchiya formulation for distorted bubble regime
- η = parameter in Fan-Tsuchiya formulation reflecting system purity
- g = gravitational constant
- d_e = equivalent bubble diameter

1 Introduction

Isolated bubble rise experiments provide data on bubble drag as a function of size and fluid properties. This data is useful in obtaining drag models for higher void fraction bubbly flows. Previous experiments (Haberman and Morton, 1953) have shown that the purity of the fluid affects the bubble rise velocity, and therefore the drag coefficient. For contaminated systems, impurities collecting at the liquid-vapor interface increase the effective viscous drag and decrease the rise velocity.

In the current experimental work, Freon-114 is used to simulate high temperature environments. Freon is chosen as the modelling fluid because it boils at a lower temperature, and may be scaled appropriately. However, if the purity of the Freon test liquid is unknown, using it to model high temperature environ-

[1] Knolls Atomic Power Laboratory, Lockheed Martin Corporation, Schenectady, NY 12301-1072.

Contributed by the Fluids Engineering Division of THE AMERICAN SOCIETY OF MECHANICAL ENGINEERS. Manuscript received by the Fluids Engineering Division August 23, 1994; revised manuscript received April 12, 1995. Associate Technical Editor: O. C. Jones.

ments may lead to inaccurate results. The purpose of the bubble rise experiment is then (1) to identify the purity of the Freon test liquid, and (2) understand the bubble drag mechanism for single bubbles as a building block for multiple bubble drag models.

2 Test Description

In this study, the bubbles were generated in a rectangular Freon test section 3.3 cm thick, 15.2 cm wide, and 55.9 cm long. The bubbles were generated in zero liquid flow using two different methods. The first method used a pitot tube to channel Freon vapor from an externally heated Freon tank directly into the test section. A valve was placed in the line between the tank and the pitot tube to regulate the Freon vapor; first the valve was opened to produce a stream of bubbles, then it was closed to gradually lessen the bubbles until a few remained. Just before the bubbles completely ceased, a few good single bubbles were formed, and the pictures were quickly taken to capture them. The second method utilized a hot wire anemometry probe within the test section to boil Freon bubbles off the surface of the wire. The wire was heated for a very short duration (achieved by quickly turning the power supply on and off) to form individual bubbles.

The photographs of the single bubbles were taken with a Mamiya M645 120 mm camera. The camera was equipped with a combination macro lens and macro spacer to obtain life-size reproduction, and was mounted on a millimeter slide to allow good focusing control. Two fused Silica windows in the test section provided optical access. The camera faced the test section at an approximate angle of 90 degrees (defined as the angle between the camera axis and the plane of the test section window). Directly in line with the camera, on the opposite side of the test section, a 200 W strobe lamp illuminated the bubbles.

The shooting and analysis of the bubble rise photographs were performed as follows. First, a picture of the pitot tube was taken for size calibration. Next, without a change in the camera settings, the bubble rise photos were taken using an appropriate shutter speed to obtain 4 bubble images at the 200 Hz strobe rate. The position of the camera was set well upstream of the bubble generator to ensure that the terminal rise condition had been reached. After the prints were developed (with a known magnification between 8–12) Vernier calipers were used to measure the bubble size and the distance travelled between each image on the photograph. An estimated error of ±10 percent is ascribed to these measurements, due to the uncertainty in positioning the calipers. Since the larger bubbles are deformed, the distance between the centers of the first and fourth bubble image were used to calculate the bubble velocity.

A summary of all the bubble rise data is provided in Table 1. The Freon-114 properties used in the analysis were calculated at an average temperature and pressure of 24.4 degrees C and 209.3 KPa. The drag coefficient was calculated using an expression derived from a force balance on a single rising bubble:

$$C_D = \frac{4g\Delta\rho d_e}{3\rho_l V_r^2}$$

3 Results and Discussion

In this section, the bubble shape and velocity data are compared to available correlations. Particular attention is given to correlations which relate to pure and impure systems.

3.1 Bubble Shape. The shape of a rising bubble is primarily a function of its Reynolds number. At low Reynolds number, when the bubble size is small, surface tension forces predominate, and the bubble shape is approximately spherical. As the bubble size increases, the dynamic pressure acting on the front of the bubble also increases. This produces an inward push against the bubble top surface. At the sides, the liquid must accelerate to maintain the flow and, by Bernoulli's principle, the pressure must decrease. Since the pressure inside the bubble is uniform (due to negligible gas density and viscosity), the local curvature at the sides of the bubble must decrease until the pressure force is balanced by the surface tension force. The extent of the pressure difference increases as the relative velocity between the bubble and the surrounding liquid or the bubble Reynolds number increases. This pressure force explains why the bubble flattens in the direction of its motion as its size increases (Fan and Tsuchiya, 1990).

A general correlation to predict bubble shape in pure and impure systems, as well as in two dimensional or three-dimensional systems, has been provided by Vakhrushev and Efremov (1970). For impure three-dimensional systems, the correlation is:

$$\frac{h}{b} = \begin{cases} 1 & \text{Ta} < 1.0 \\ A & 1.0 \le \text{Ta} < 40 \\ 0.24 & 40 \le \text{Ta} \end{cases} \qquad (1a)$$

$$A = \{0.81 + 0.2 \tanh [2.0(0.80 - \log_{10} \text{Ta})]\}^m$$

And for pure three-dimensional systems, the correlation is:

$$\frac{h}{b} = \begin{cases} 1 & \text{Ta} < 0.3 \\ B & 0.3 \le \text{Ta} < 20 \\ 0.24 & 20 \le \text{Ta} \end{cases} \qquad (1b)$$

$$B = A\{0.81 + 0.2 \tanh [1.8(0.40 - \log_{10} \text{Ta})]\}^m$$

where

$$\text{Ta} = \text{ReMo}^{0.23} = \text{Re}\left(\frac{g\mu_l^4(\rho_l - \rho_g)}{\rho_l^2\sigma^3}\right)^{0.23}$$

In Fig. 1, the Freon bubble shape data is compared with the Vakhrushev-Efremov correlations. Only the pure correlation accurately predicts the Freon data. The impure correlation does not adequately model the distortion of Freon bubbles at equivalent diameters between 0.4 and 2.0 mm. The distortion of Freon bubbles at these diameters is a result of the lack of surface-active impurities in the liquid. In general, conditions at the gas-liquid interface strongly affect the bubble shape. If no impurities exist at the interface, the effective viscous drag is decreased, and the bubble experiences more inertial force. This means for a fixed bubble size, the bubble shape is more flattened in pure liquids than in contaminated liquids.

3.2 Bubble Rise Velocity. A bubble moving freely in a liquid under the influence of gravity will rise at a constant rate after the terminal condition is reached. For bubbles of intermediate to large size, the correlation of Mendelson (1967) has proven to yield the best predictions of bubble rise velocity in purified liquids. He related the rise velocity of bubbles to the hydrodynamic theory of waves. In his model the terminal rise velocity is given by:

$$V_{r\infty} = \sqrt{\frac{2\sigma}{d_e\rho} + \frac{gd_e}{2}} \qquad (2)$$

Fan and Tsuchiya (1990) developed a general model for the terminal velocity of bubbles which is applicable to both pure and contaminated systems and provides a continuous correlation for the viscous and distorted regime. Their expression for terminal speed in the viscous regime is:

$$V_{r\infty}^{vis} = \frac{\rho_l g d_e^2}{K_b \mu_l}$$

K_b was found to vary from one liquid to another:

Table 1 Bubble rise data for single bubbles in stagnant liquid Freon-119

Major axis (mm)	Minor axis (mm)	Aspect ratio	Diameter (mm)	Velocity (cm/s)	Drag coefficient	Reynolds number
0.18	0.18	1.0	0.18	6.85	0.50	52.3
0.20	0.20	1.0	0.20	8.30	0.38	70.4
0.21	0.21	1.0	0.21	9.80	0.28	87.2
0.22	0.22	1.0	0.22	9.67	0.30	90.2
0.23	0.23	1.0	0.23	9.78	0.31	95.3
0.24	0.24	1.0	0.24	9.78	0.32	99.5
0.25	0.25	1.0	0.25	10.50	0.29	111.2
0.25	0.25	1.0	0.25	10.88	0.27	115.3
0.30	0.26	0.87	0.29	11.70	0.27	141.8
0.30	0.28	0.93	0.29	11.55	0.28	143.5
0.29	0.28	0.96	0.29	13.14	0.21	159.2
0.30	0.28	0.93	0.29	12.90	0.23	159.9
0.32	0.28	0.86	0.30	13.86	0.20	178.7
0.46	0.34	0.74	0.41	18.54	0.16	325.7
0.48	0.36	0.75	0.44	17.89	0.18	333.1
0.44	0.30	0.68	0.39	20.74	0.12	342.5
0.51	0.35	0.69	0.45	19.34	0.16	368.1
0.50	0.35	0.71	0.44	19.75	0.15	369.9
0.53	0.35	0.66	0.46	18.94	0.17	370.5
0.48	0.31	0.64	0.42	21.36	0.12	377.2
0.58	0.36	0.62	0.49	18.67	0.18	388.3
0.54	0.36	0.67	0.48	19.34	0.16	389.7
0.60	0.36	0.60	0.51	19.34	0.18	417.9
0.61	0.36	0.59	0.51	19.34	0.18	420.7
0.61	0.36	0.60	0.51	19.71	0.17	428.6
0.62	0.36	0.59	0.52	19.75	0.17	432.8
0.62	0.38	0.61	0.52	19.91	0.17	441.0
0.71	0.36	0.51	0.57	19.83	0.19	478.5
0.73	0.37	0.52	0.58	20.15	0.19	497.1
0.78	0.42	0.54	0.64	18.54	0.24	499.9
0.99	0.46	0.46	0.77	18.14	0.30	589.6
1.21	0.55	0.45	0.93	16.93	0.42	667.7
2.18	0.85	0.39	1.59	14.50	0.98	978.9
2.06	0.75	0.36	1.47	15.72	0.78	980.3
2.66	0.91	0.34	1.86	13.70	1.28	1080.5
2.58	1.24	0.48	2.02	13.00	1.55	1113.6
2.67	1.02	0.38	1.94	14.40	1.21	1182.6
2.84	1.33	0.47	2.20	13.00	1.69	1215.3
2.96	1.02	0.34	2.08	14.81	1.22	1302.9

$$K_b = \max \text{ of } \begin{cases} 12 \\ K_{bo} Mo^{-0.038} \end{cases}$$

where $K_{bo} = 14.7$ for water, and $K_{bo} = 10.2$ for organic solvents and mixtures. In the distorted/capped bubble regime:

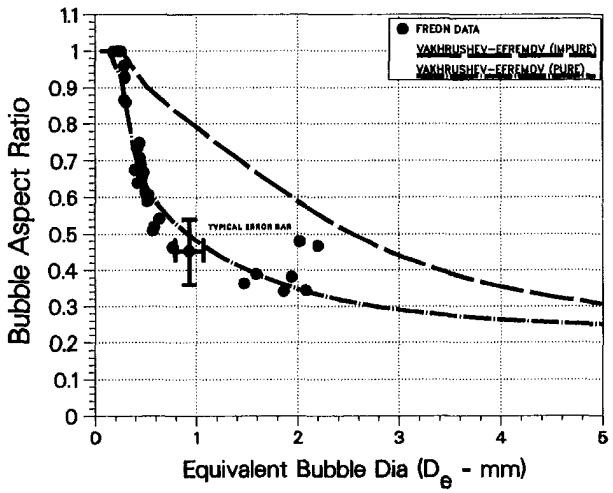

Fig. 1 Bubble aspect ratio compared to several models

$$V_{r\infty}^{\text{dis}} = \sqrt{\frac{2c\sigma}{\rho_l d_e} + \frac{g d_e}{2}}$$

If the coefficient c is 1.0, $V_{r\infty}^{\text{dis}}$ reduces to the Mendelson model. To satisfy the condition that $V_{r\infty}^{\text{vis}}$ dominates when d_e is small, and $V_{r\infty}^{\text{dis}}$ dominates when d_e is large, Fan and Tsuchiya proposed the following function:

$$V_{r\infty} = [(V_{r\infty}^{\text{vis}})^{-\eta} + (V_{r\infty}^{\text{dis}})^{-\eta}]^{-1/\eta} \quad (3)$$

where η is an empirical parameter introduced to accommodate both purified and contaminated systems. Values of c in the range of 1.2 to 1.4 predict the available data. The parameter η usually ranges between 0.6 and 1.6, with the lower values indicating impure substances.

Figure 2 shows a comparison of the Fan-Tsuchiya correlation to the Freon bubble rise data, with $K_{bo} = 10.2$ and $c = 1.4$ for three values of η: $\eta = 0.6$ (contaminated system) $\eta = 1.6$ (purified system) and $\eta = 2.6$ (best fit to Freon data). It is noted that the increase in terminal speed characteristic of a purified system is enhanced in the Freon system, where a peak velocity of 21 cm/s is observed at equivalent bubble diameters near 0.42 mm. The data in the vicinity of this diameter correspond well with the Mendelson prediction for pure systems. However, as the bubble diameter decreases, the Mendelson model becomes inaccurate, and the Fan-Tsuchiya correlation (for pure substances) is required to predict the Freon data. For bubbles greater than about 1.5 mm, the purity of the system becomes less important and the data falls in the rough vicinity of all the correlations.

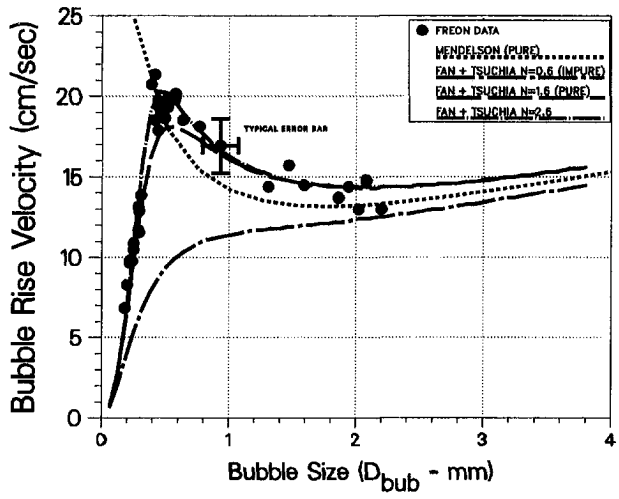

Fig. 2 Predicted bubble rise velocity from several models versus freon data

4 Summary and Conclusions

A photographic technique was used to obtain the terminal velocity and shape of isolated Freon-114 bubbles in a 3.3 × 15.24 cm rectangular test section. A 120 mm still camera equipped with a high magnification lens faced the test section, while a 200 W strobe lamp flashing at 200 Hz illuminated the bubbles from the opposite side. This technique allowed the bubble diameter and velocity to be obtained from a single photograph.

The bubble rise data were taken over a bubble Reynolds number range of 52-1300 for zero liquid flow. At Reynolds numbers less than 118, the bubble shape was spherical. As the Reynolds number increased, the pressure difference between the front and side surfaces of the bubble increased. This caused the aspect ratio (defined as the ratio of bubble height to width) to drop until a relatively constant value of 0.35 was obtained.

The drag coefficient was calculated from the measured values of bubble size and velocity using an expression derived from a force balance on a single rising bubble. This analysis indicates that the drag coefficient varies between 0.12 and 1.69 for the given Reynolds numbers range. Comparisons of bubble velocity and shape data to available correlations show that Freon bubbles behave similarly to bubbles rising in pure liquid. The rise velocity data exhibits a peak of 21.4 cm/s for bubble diameters near 0.42 mm; this peaking is a general characteristic of pure substances.

Acknowledgment

This work was prepared for the United States Department of Energy by Knolls Atomic Power Laboratory, Contract No. DE-AC12-76SN00052.

References

Fan, L. S., and K. Tsuchiya, 1990, *Bubble Wake Dynamics in Liquids and Liquid-Solid Suspensions,* Butterworth-Heinemann, Stoneham, MA.

Haberman, W. L., and R. K. Morton, 1953, "An Experimental Investigation of the Drag and Shape of Air Bubbles Rising in Various Liquids," David W. Taylor Model Basin Report 802, Navy Dept., Washington, DC.

Mendelson, H. D., 1967, "The Prediction of Bubble Terminal Velocities from Wave Theory," *American Institute of Chemical Engineering Journal,* Vol. 13, No. 12, p. 2150.

Vakhrshev, I. A. and G. I. Efremov, 1970, *Chemical Technology of Fuels and Oils (USSR),* Vol. 5/6, pp. 376–379.